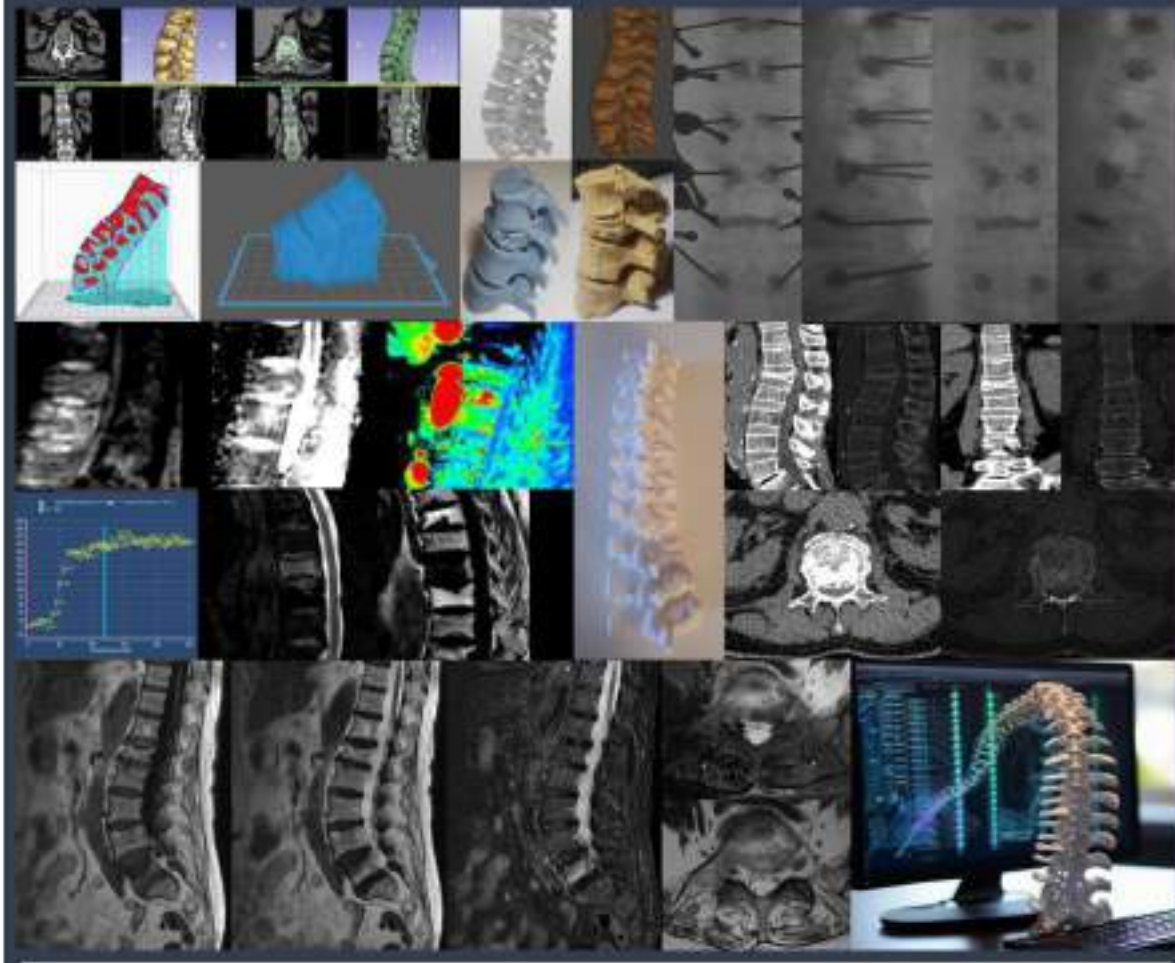

DIAGNÓSTICO Y TRATAMIENTO DE LAS FRACTURAS VERTEBRALES OSTEOPORÓTICAS: APORTACIONES DESDE LA RADIOLOGÍA

ANTONIO JESÚS LÁINEZ RAMOS-BOSSINI

DIRECCIÓN: FERNANDO RUIZ SANTIAGO

UNIVERSIDAD DE GRANADA

TESIS DOCTORAL

PROGRAMA DE DOCTORADO EN MEDICINA CLÍNICA Y SALUD PÚBLICA

UNIVERSIDAD DE GRANADA

DIAGNÓSTICO Y TRATAMIENTO DE LAS FRACTURAS VERTEBRALES OSTEOPORÓTICAS: APORTACIONES DESDE LA RADIOLOGÍA

UNIVERSIDAD DE GRANADA

Programa de Doctorado en Medicina Clínica y Salud Pública

Facultad de Medicina

Departamento de Radiología y Medicina Física

Tesis Doctoral

Antonio Jesús Láinez Ramos-Bossini

Granada, 2023

Editor: Universidad de Granada. Tesis Doctorales
Autor: Antonio Jesús Laínez ramos
ISBN: 978-84-1195-072-5
URI: https://hdl.handle.net/10481/85098

Memoria presentada por Antonio Jesús Láinez Ramos-Bossini para aspirar al grado de DOCTOR por la Universidad de Granada

Dirigida por:

Dr. FERNANDO RUIZ SANTIAGO

Profesor Titular de Universidad

Departamento de Radiología y Medicina Física

Facultad de Medicina

Universidad de Granada

Granada, 2023

Trabajos realizados durante la tesis doctoral:

1. Ruiz-Santiago F, **Láinez Ramos-Bossini AJ**, Wang YXJ, López-Zúñiga D. The role of radiography in the study of spinal disorders. Quant Imaging Med Surg. 2020;10(12):2322-2355. doi: 10.21037/qims-20-1014. FI: 3,837. Q2 (T1).
2. Ruiz Santiago F, **Láinez Ramos-Bossini AJ**, Wáng YXJ, Martínez Barbero JP, García Espinosa J, Martínez Martínez A. The value of magnetic resonance imaging and computed tomography in the study of spinal disorders. Quant Imaging Med Surg. 2022;12(7):3947-3986. doi: 10.21037/qims-2022-04. PMID: 35782254. FI: 2,8. Q2 (T2).
3. López Zúñiga D, **Láinez-Ramos-Bossini AJ**, Ruiz Santiago F. Radiographic diagnosis of osteoporotic vertebral fractures. An updated review. Med Clin (Barc). 2022;158(3):125-132. doi:10.1016/j.medcli.2021.06.019. FI: 3,9. Q2 (T2).
4. **Láinez Ramos-Bossini AJ**, Ruiz Santiago F, Moraleda Cabrera B, López Zúñiga D, Ariza Sánchez A. Imaging of low-energy vertebral fractures. Radiologia (Engl Ed). 2023;65(3):239-250. doi: 10.1016/j.rxeng.2023.01.006. Epub 2023 May 11. PMID: 37268366. FI: 1,3 (cuartil no asignado, primer año con FI).
5. **Láinez Ramos-Bossini AJ**, Gálvez López R, Pastor Rull J. Vertebral artery dissection secondary to hangman's fracture. Med Clin (Barc). 2020;154(5):195-196. English, Spanish. doi: 10.1016/j.medcli.2019.02.008. Epub 2019 Apr 4. PMID: 30954291. FI: 1,725. Q3 (T2).
6. Ruiz Santiago F, **Láinez Ramos-Bossini AJ**, Moraleda-Cabrera B. Factors influencing vertebral collapse in osteoporotic vertebral fractures. Trabajo no publicado en el momento de la lectura de la Tesis Doctoral.
7. **Láinez Ramos-Bossini AJ**, López Zúñiga D, Ruiz Santiago F. Percutaneous vertebroplasty versus conservative treatment and placebo in osteoporotic vertebral fractures: meta-analysis and critical review of the literature. Eur Radiol. 2021;31(11):8542-8553. doi:10.1007/s00330-021-08018-1. FI: 7,034. Q1 (T1).

El doctorando y el director de esta Tesis desean agradecer el apoyo y facilidades proporcinadas por los miembros del Servicio de Radiodiagnóstico del Hospital Universitario Virgen de las Nieves para la realización de la presente Tesis Doctoral, donde se ha realizado gran parte de la investigación presentada, así como a los miembros de 3D Translation S.L., que ha proporcionado material e infraestructura para el desarrollo de varios de los trabajos publicados. Asimismo deseamos mostrar nuestro profundo agradecimiento al profesorado del Máster en Avances en Radiología Diagnóstica y Terapéutica y Medicina Física de la Universidad de Granada por la formación recibida en metodología de la investigación y en la actualización sobre el conocimiento de las técnicas radiológicas aplicadas al ámbito de investigación de la Tesis.

...et tenebrae erant super faciem abyssi… Dixitque Deus: 'Fiat lux'. Et facta est lux."

Genesis 1:3

AGRADECIMIENTOS

En primer lugar, quiero dar gracias a Dios, el motor y centro de mi vida. El esfuerzo y resultados de este trabajo son fruto de su amor, inmenso y paciente. Como decía el poeta Ángel González: “Creo en ti, existes, eres. Me basta”.

En el plano terrenal, sois demasiadas las personas que habéis hecho posible esta tesis doctoral. Afortunadamente, sabéis de sobra que no es necesario que deje por escrito cuánto os agradezco vuestro cariño y apoyo, y no creo necesario extenderme aquí con nombres e historias compartidas porque soy de los que opinan que los actos valen más que en las palabras. Con todo, sí quiero hacer hincapié en mi profundo agradecimiento a quienes habéis sido, sois y seréis pilares fundamentales de mi vida:

A mi prometida Paula María, mi mayor regalo, la luz de mi vida; y a su encantadora familia (¡con mi amigo Pablo en ella, qué curiosa es la vida…!), especialmente a sus padres.

A mis mejores amigos, Mario, Juan Luis y David, cuya amistad incondicional y apoyo constante han sido fundamentales en mi vida. Gracias por quererme tal como soy y por el privilegio de compartir vuestra amistad en una dimensión más profunda de la que quizás merezco.

A mi abuelo Paco, mi modelo a seguir, y a mi abuela Angustias; a mi madre y a mi padre, a Ana y a mis dos soles, Anita y Babi. También a mis queridos amigos y padrinos, Maribel y Paco. Gracias por cuidarme y quererme a pesar del tiempo, la distancia y mis entretenimientos varios.

Aunque sea una sucinta enumeración, no puedo obviar el más que merecido agradecimiento al resto de mi familia paterna y materna (especialmente a Alejandro, Susana, Cari, Fede, Bea, Susi y Ale), a la familia Rivera, a los amigos en la distancia (Juanca, Manu), y a todos aquellos que, a lo largo de mi vida, habéis compartido conmigo. Gracias.

Finalmente, quiero dar las gracias a quienes habéis intervenido de forma más próxima al desarrollo de esta tesis dentro del ámbito laboral y académico:

A mi director de tesis, Fernando Ruiz Santiago, por su inspiración desde que era estudiante para elegir esta maravillosa especialidad médica y perseguir una constante motivación investigadora y docente.

A todos mis demás *profesores* de las distintas secciones del servicio de Radiodiagnóstico, en particular a Ángela Salmerón, Antonio Medina, José Pablo Martínez y María Isabel Romero. Vuestro compromiso con la excelencia han sido y seguirán siendo una inspiración continua para mí, y a muchos os debo en lo personal más que en lo profesional. Este logro no habría sido posible sin vuestra guía.

Finalmente, a los residentes y alumnos con los que he tenido el placer de compartir experiencias asistenciales, investigadoras y académicas, y han compartido conmigo la pasión de aprender y de querer ir más allá. Sois el presente y el futuro; estoy convencido de que esta tesis es apenas un botón de muestra para lo que se viene con vosotros.

Este viaje ha sido un desafío, pero también una bendición. A todos vosotros, ¡gracias de corazón por ser parte de él!

ÍNDICE

RESUMEN

La presente tesis doctoral está dedicada al estudio de las fracturas vertebrales osteoporóticas (FVO) desde el punto de vista radiológico, y más concretamente en sus aportaciones diagnósticas y terapéuticas. Las FVO constituyen un problema de salud global de primer nivel por su alta prevalencia y morbimortalidad asociada. El diagnóstico por imagen de estas fracturas puede realizarse mediante diferentes pruebas radiológicas como la radiografía convencional (RC), la tomografía computarizada (TC) o la resonancia magnética (RM) y existen diversos abordajes terapéuticos, entre los cuales cabe destacar las técnicas de cementación vertebral como la vertebroplastia percutánea (VP) y su variantes posteriores (cifoplastia, vesselplastia, etc.). A pesar de las mejoras en el diagnóstico radiológico de las FVO, se han descrito limitaciones y controversias en la literatura sobre los criterios diagnósticos por imagen y los sistemas de clasificación más útiles. Además, existe un gran interés por determinar los factores pronósticos que permitan seleccionar a los pacientes con mayor riesgo de colapso vertebral con tratamiento conservador, con el fin de tomar decisiones que redunden en un mayor beneficio clínico para el paciente. Por otra parte, la eficacia de la VP se ha puesto en tela de juicio en la última década, a raíz de la publicación de algunos ensayos clínicos y meta-análisis que no mostraron beneficios clínicos en comparación con placebo o tratamiento conservador, pero los resultados en la literatura son inconsistentes. Finalmente, el desarrollo de nuevas tecnologías como la inteligencia artificial (IA) y la impresión 3D basada en imagen médica está abriendo nuevas posibilidades en radiología y su aplicación a las diferentes patologías de la columna vertebral, particularmente a las FVO, aún está por definirse.

Con estos antecedentes, hemos llevado a cabo diversos trabajos con el objetivo general de revisar y profundizar en los avances radiológicos relativos al diagnóstico y tratamiento las FVO, y, de manera más concreta, con los objetivos específicos de: a) revisar los hallazgos de imagen en RC, TC y RM de las principales patologías de la columna vertebral, especialmente las que se incluyen en el diagnóstico diferencial de las FVO, y conocer el *statu quo* de la impresión 3D e IA en este ámbito; b) analizar qué alteraciones radiológicas tienen influencia en la evolución clínica y radiológica de las FVO; y c) determinar si la vertebroplastia percutánea en las FVO es superior al placebo y al

tratamiento conservador, y las potenciales causas de las controversias sobre su eficacia existentes en la literatura científica.

De los resultados obtenidos se concluyen los siguientes puntos. Primero: el conocimiento de los hallazgos radiológicos de la columna vertebral normal y patológica en RC, TC y RM resulta fundamental para realizar un correcto diagnóstico de las FVO. Deben considerarse las indicaciones, ventajas y limitaciones de estas pruebas de imagen en función de la patología que se sospeche (traumática, degenerativa, inflamatoria, infecciosa o tumoral). Segundo: es preciso conocer los diferentes sistemas de clasificación utilizados en el diagnóstico de las FVO, sus ventajas e inconvenientes, y su utilidad en la práctica clínica. La distinción entre sistemas de clasificación cualitativos, cuantitativos y semicuantitativos es útil para este propósito. Tercero: las tecnologías de impresión 3D y los sistemas basados en IA representan áreas emergentes con aplicaciones útiles en el diagnóstico y tratamiento de las FVO. Su implementación clínica se está instaurando progresivamente en los últimos años, por lo que el radiólogo debe familiarizarse con ellas y conocer sus ventajas y limitaciones. Cuarto: una diferencia significativa en la pérdida de altura vertebral posterior entre la RC en bipedestación y la TC en supino, un cociente elevado entre la densidad radiológica del cuerpo vertebral fracturado y el no fracturado, y una edad avanzada, se asocian con un mayor riesgo de colapso vertebral en las FVO, lo que permite orientar hacia la elección de un tratamiento alternativo al conservador. Es necesario validar estos hallazgos mediante series más amplias, idealmente prospectivas y multicéntricas. Quinto: La VP ofrece ventajas significativas en el alivio del dolor, mejora en la funcionalidad y calidad de vida en comparación con el placebo y con el tratamiento conservador. La adecuada selección de pacientes candidatos a este tratamiento es fundamental para obtener resultados óptimos.

El conocimiento derivado de esta tesis doctoral permite profundizar en el estado actual del diagnóstico y tratamiento de las FVO desde la radiología, aporta recursos útiles para la práctica de radiólogos y otros especialistas, y sirve de punto de partida para nuevas investigaciones que redunden en beneficios clínicos significativos para los pacientes con este tipo de fracturas.

INTRODUCCIÓN

I. INTRODUCCIÓN

1. Marco conceptual y cuestiones generales

Esta tesis doctoral aborda los avances diagnósticos y terapéuticos relativos a las fracturas vertebrales osteoporóticas (FVO) desde el punto de vista radiológico, así como a los potenciales factores de riesgo y pronósticos sobre los que desarrollar estrategias de prevención específicas. Convergen en este contexto diversas disciplinas como la anatomía humana, la endocrinología o la medicina preventiva y salud pública. Resulta por ello ineludible situar contextualmente el marco en el que se ha llevado a cabo la investigación, destacando diversos aspectos generales de la anatomía de la columna vertebral y de las modalidades, fundamentos y características esenciales de las técnicas de imagen empleadas en radiología para su estudio. Posteriormente trataremos otras cuestiones de interés sobre la osteoporosis y su relación con las FVO, así como otros conceptos afines que servirán de marco referencial para comprender las hipótesis y objetivos de nuestra investigación, y de la metodología empleada para alcanzar estos últimos.

1.1.La columna vertebral: el eje del cuerpo humano.

La columna vertebral, también conocida como raquis o espina dorsal, es una estructura anatómica esencial en el sistema musculoesquelético humano (Standring, 2016). Está conformada por un conjunto de elementos óseos denominados vértebras, articulados entre sí a lo largo del eje longitudinal de la región posterior del cuerpo. En su extremo cefálico se articula con la base del cráneo y en su extremo caudal con el hueso sacro. Proporciona soporte, estabilidad y protección al organismo y a estructuras vitales como la médula espinal, y puede considerarse el pilar central del cuerpo, ya que conecta sus principales regiones anatómicas y permite la movilidad y la transmisión de fuerzas entre ellas, ejerciendo así una función biomecánica esencial (D'Août, 2016).

Anatómicamente, la columna vertebral se divide clásicamente en cinco regiones o segmentos principales: cervical, torácica, lumbar, sacra y coccígea. Cada uno de estos segmentos presenta un número relativamente constante de vértebras y exhibe características estructurales distintivas adaptadas a funciones específicas. Así, la columna

cervical consta de siete vértebras (C1 a C7) y permite una amplia gama de movimientos del cuello y la cabeza. La columna torácica está compuesta por doce vértebras (D1 a D12) que se articulan con las costillas, brindando soporte y protección a los órganos internos de la cavidad torácica y del hemiabdomen superior. La columna lumbar está conformada por cinco vértebras (L1 a L5) y es la región que soporta una mayor carga; protege las estructuras del abdomen y proporciona estabilidad durante las actividades de carga y movimientos de flexión y extensión. Finalmente, el segmento sacrococcígeo está formado por vértebras fusionadas (S1 a S5 y un número variable de vértebras coccígeas, usualmente de 3 a 5), brindando soporte y estabilidad a la pelvis y a sus órganos internos. Además, los diferentes segmentos actúan como punto de inserción para numerosos músculos y ligamentos (cervicocefálicos, torácicos, de la región lumbosacra y del anillo pélvico) (Láinez Ramos-Bossini et al., 2023).

La estructura de la columna vertebral es compleja y altamente especializada. Cada vértebra está compuesta por una serie de elementos estructurales que son prácticamente comunes en todos los segmentos, a saber, cuerpo, arco posterior, apófisis espinosas y transversas, y carillas articulares (Mahadevan, 2018). No obstante, como se ha mencionado, la configuración de las vértebras presenta algunas variaciones en función del segmento anatómico en el que se localizan, siendo especialmente destacable el caso de las dos primeras vértebras cervicales el atlas (C1) y el axis (C2). El cuerpo vertebral forma la parte anterior de la vértebra y constituye el principal soporte para la carga axial. El arco posterior o neural está constituido por los pedículos y las láminas, que conforman el canal o foramen vertebral, por donde discurre la médula espinal, una prolongación del sistema nervioso central que se extiende desde C1 hasta L1 y se continúa caudalmente por el filum terminale y las raíces de la cola de caballo (Izzo et al., 2013). Las apófisis espinosas, trasversas y otros procesos óseos, proporcionan puntos de inserción para los músculos y ligamentos paravertebrales, lo que contribuye a la estabilidad y movilidad de la columna vertebral (Moore et al., 2013).

La columna vertebral exhibe unas curvaturas características en su eje sagital que ayudan a mantener el equilibrio y a distribuir las fuerzas durante la locomoción y las actividades diarias. Estas curvaturas se denominan lordosis cervical y lumbar, y cifosis torácica, y se desarrollan fisiológicamente a lo largo de la infancia y la adolescencia. El mantenimiento de estas curvaturas dentro de rangos de normalidad resulta esencial para preservar las

propiedades biomecánicas adaptativas propias de la vida diaria y mantener el balance sagital normal del cuerpo (Le Huec et al., 2019).

Como se verá más adelante, la pérdida de la morfología normal de las vértebras, y particularmente la pérdida de altura del cuerpo vertebral, condicionará un grado variable de alteración de las funciones estructurales, biomecánicas y de protección propias de la columna vertebral. Esto es precisamente lo que ocurre en la mayoría de fracturas vertebrales y de aquí deriva la importancia primordial de conocer la anatomía y fisiología de la columna normal como punto de partida para el correcto diagnóstico y, en su caso, tratamiento, de las FVO.

1.2. Principales técnicas radiológicas empleadas en el estudio de la columna vertebral

Las técnicas de imagen más empleadas en el diagnóstico de las FVO en radiología son la radiografía simple o convencional (RC), la tomografía computarizada (TC) y la resonancia magnética (RM). Cada una de ellas permite obtener imágenes del cuerpo humano mediante fuentes de distinta naturaleza. Aunque la explicación de los fundamentos físicos que subyacen a estas pruebas de imagen desborda los objetivos de la presente tesis doctoral, resulta pertinente introducir algunos aspectos generales de interés como paso previo a explorar sus aplicaciones en el diagnóstico de las FVO. En este apartado se llevara a cabo una revisión concisa de los fundamentos físicos, las aplicaciones, ventajas y las limitaciones de la RC, TC y RM.

La RC puede considerarse como la prueba de imagen fundacional de la radiología. Desde el descubrimiento de los rayos X por Wilhelm Conrad Roentgen en 1895 (Premio Nobel de Medicina en 1901), esta técnica ha desempeñado un papel crucial en la medicina, proporcionando información relevante del interior del cuerpo humano. La RC se basa en el uso de rayos X, un tipo de radiación electromagnética de alta energía capaz de desplazar electrones de los átomos, creando iones (radiación ionizante). Mediante un sistema esencialmente basado en una fuente de rayos X y un colimador, los equipos de RC generan un haz de rayos X que atraviesa el cuerpo del paciente, absorbiéndose de forma diferencial por los tejidos del cuerpo en función de su densidad y composición (Mahesh, 2013). Tras atravesar al paciente, los rayos X inciden sobre un chasis donde se ubica el panel digital que transforma los impactos fotónicos en una imagen radiológica, asignando a cada pixel de la imagen un tono en la escala de grises que correlaciona con la energía

incidente en la placa. La imagen resultante corresponde a una proyección bidimensional del objeto (o cuerpo humano) atravesado por el haz de radiación. En la **Figura 1** se muestra un esquema del proceso.

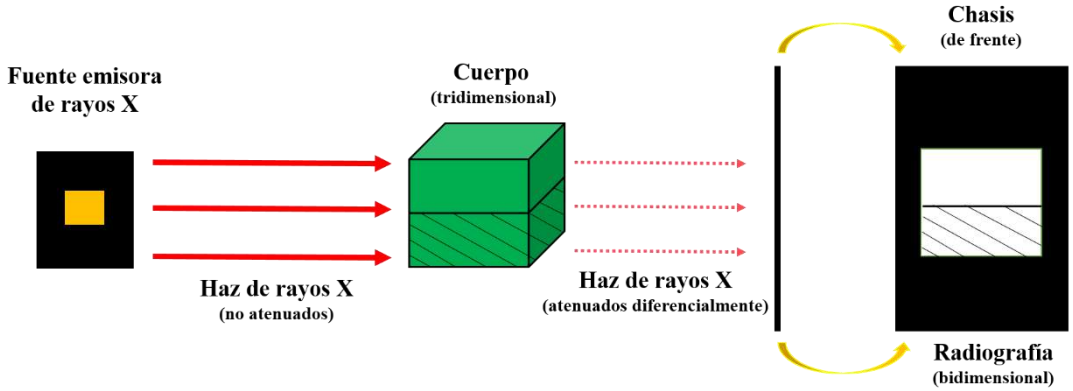

Figura 1. Esquema básico de la obtención de imágenes mediante radiografía simple. El haz de rayos X es emitido desde la fuente (tubo de rayos X) y atenuado de manera diferencial tras atravesar el objeto o cuerpo. A partir de la información de los rayos X que llegan al chasis (placa digital en los equipos actuales) se genera la proyección bidimensional radiológica del objeto, que corresponde a la imagen de una radiografía simple. *Fuente: Elaboración propia.*

A día de hoy, la RC sigue siendo una herramienta diagnóstica ampliamente utilizada en la práctica clínica, resultando especialmente útil en la evaluación de las estructuras óseas del sistemas musculoesquelético (Gyebnar et al., 2018). Las principales ventajas de la RC pueden resumirse en su accesibilidad y eficacia, pues se encuentra presente de forma prácticamente universal en cualquier entorno hospitalario, lo que la convierte en una opción diagnóstica asequible para el abordaje inicial de una amplia variedad de patologías (Gallet and Titus, 2005). A pesar de sus ventajas, no está exenta de limitaciones, entre las que destacan sus efectos biológicos (potencial carcinogénico derivado del uso de radiación ionizante), su bajo contraste o rango dinámico, que ocasiona dificultades para diferenciar entre tejidos de densidad similar, y la superposición de estructuras al no ser una técnica tomográfica, lo que puede limitar la capacidad para detectar o evaluar ciertas patologías (Murphey, 1997).

En la RC se pueden distinguir cuatro densidades radiológicas básicas: hueso, agua, grasa y aire. Además, existe una densidad “metal” que no está presente de forma fisiológica en el cuerpo humano, pero que se encuentra con frecuencia en la práctica clínica, ya que es propia de dispositivos médicos como grapas o implantes, o de los contrastes radioopacos. Esta densidad metálica se muestra en la imagen como un área muy blanca o brillante

(radiopaca) debido a la alta capacidad de los materiales que la producen para atenuar el haz de rayos X. Las estructuras óseas (densidad hueso) muestran una menor densidad que el metal, pero significativamente mayor que los demás tejidos del cuerpo humano, lo que permite su diferenciación clara en la RC. La densidad "agua", propia de este elemento y de las partes blandas (p.ej., músculos y órganos internos), se visualiza en tonos grises, con diferentes grados de opacidad dependiendo de la atenuación diferencial específica de cada tejido. La grasa, debido a su menor densidad, exhibe tonos de gris más oscuro que la densidad agua. Por último, el aire es la densidad radiológica más baja y aparece como áreas completamente negras o radiolúcidas.

El conocimiento de las densidades radiológicas básicas resulta esencial para la correcta interpretación y diagnóstico preciso en RC. Conviene mencionar en este punto el signo radiológico más clásico, de suma importancia en la semiología de la RC, denominado "signo de la silueta", que puede enunciarse de la siguiente manera: los contornos de dos estructuras con la misma densidad que se encuentran en contacto físico directo son indistinguibles entre sí (Broder, 2011). Por último, merece la pena reseñar que las RC actuales, en formato digital, permiten una modificación del contraste y del brillo de la imagen, lo que posibilita visualizar mejor las estructuras de interés.

La TC constituye una técnica más avanzada de imagen médica que actualmente permite generar imágenes multiplanares de muy alta resolución. Esta técnica fue concebida en 1973 por el ingeniero británico Godfrey Hounsfield, cuya contribución pionera fue reconocida con el Premio Nobel de Fisiología y Medicina en 1979, que compartió con Allan M. Cormack. La TC emplea una fuente de radiación ionizante similar a la utilizada en la RC. Sin embargo, en lugar de generar imágenes en un solo plano del espacio, el tubo de rayos X de la TC gira alrededor del cuerpo del paciente, obteniendo imágenes desde múltiples ángulos. Posteriormente, estas imágenes son procesadas mediante algoritmos específicos para obtener representaciones bidimensionales o tridimensionales del organismo. Este proceso de reconstrucción proporciona una imagen detallada que facilita la diferenciación efectiva entre diversas estructuras y tejidos, permitiendo obtener imágenes de alta resolución espacial y generar reconstrucciones multiplanares y tridimensionales del cuerpo (Vosper, 2016).

Además, es posible cuantificar la densidad radiológica de los tejidos, medidas en Unidades Hounsfield (UH), que son unidades de valor relativas respecto al agua (por

convenio, 0 UH); el aire tiene una densidad de aproximadamente -1000 UH y el hueso cortical de >1000 UH. Conviene mencionar en este punto el concepto de "modificación de ventana" (en inglés, "windowing") o mapeo de escalas de grises, que alude al proceso por el cual rango de grises de visualización de la imagen se manipula en función de las UH (**Figura 2**).

La terminología utilizada en la descripción de las imágenes de TC es similar a la que se emplea en RC. Así, las estructuras óseas se visualizan en tonos blancos y se describen como de alta densidad, hiperdensas o, menos frecuentemente, radiopacas. Por otro lado, el gas y la grasa aparecen en tonalidades más oscuras y se describen como de baja densidad, siendo considerados hipodensos o radiolúcidos. Sin embargo, debe tenerse en cuenta que la tonalidad se modificará sustancialmente en función de la ventana empleada; una misma estructura puede verse hipodensa o hiperdensa atendiendo a los parámetros de nivel y anchura seleccionados. De ahí que sea frecuente describir estructuras o áreas en relación a otras regiones de referencia, o medir las UH de las zonas de interés.

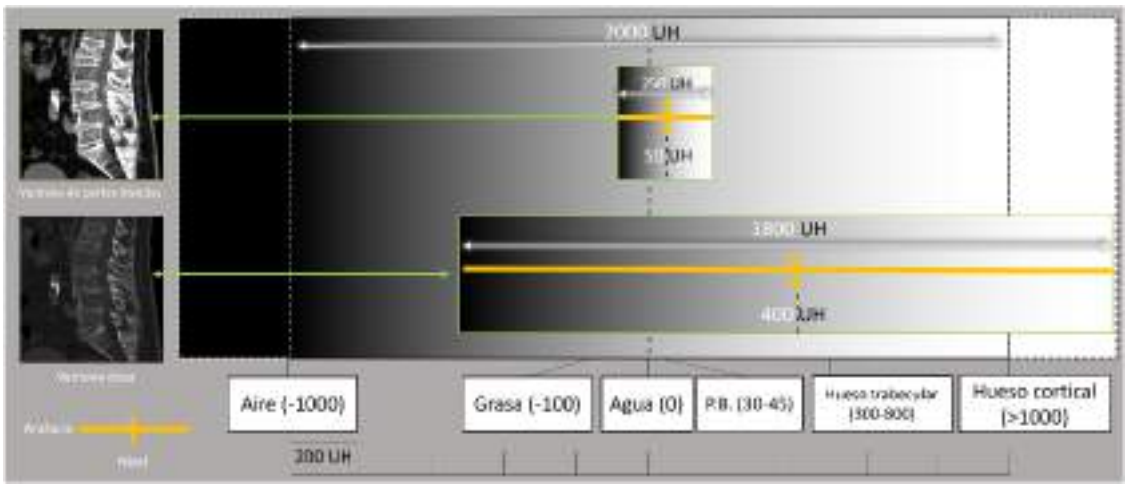

Figura 2. Ventana en tomografía computarizada (TC). Al ajustar los parámetros de la ventana (nivel y anchura), el rango de grises se restringe a los valores incluidos en el intervalo de la anchura. Las estructuras con unidades Hounsfield (UH) por encima o por debajo del límite superior e inferior de la ventana se visualizarán en blanco y negro, respectivamente, y no se distinguirán entre sí. Por el contrario, dos estructuras de densidad similar podrán diferenciarse entre sí si se ajusta adecuadamente la ventana. Existen ventanas con niveles predefinidos de anchura y nivel (ventana de pulmón, mediastino, hueso, cerebro…), como se muestra a la izquierda de la figura. P.B.: partes blandas. *Fuente: elaboración propia.*

A pesar de sus indudables ventajas (rapidez, alta resolución espacial), la TC presenta limitaciones que deben ser tenidas en cuenta, especialmente la exposición del paciente a radiación ionizante, que es significativamente superior a la de una RC. Aunque el riesgo

asociado a una exploración de TC es bajo, la exposición acumulada incrementa la probabilidad de carcinogénesis. Además, su coste es superior al de la RC y su accesibilidad puede ser limitada en entornos extrahospitalarios (Kalra et al., 2015).

La RM es la tercera modalidad de imagen radiológica empleada en el estudio de la columna vertebral. A diferencia de la RC y de la TC, no se basa en el uso de radiación ionizante, lo que constituye una de sus principales ventajas y la convierte en una técnica segura para estudios longitudinales y en poblaciones vulnerables, como los niños y las mujeres embarazadas. En su lugar, la RM emplea campos magnéticos y ondas de radiofrecuencia. El principio físico elemental que subyace a la obtención de imágenes por RM se sustenta en la propiedad de la resonancia magnética nuclear, por cuyo descubrimiento Felix Bloch y Edward Mills Purcell fueron galardonados con el Premio Nobel en 1952. La obtención de imágenes mediante esta técnica es muy compleja y su explicación detallada desborda sobremanera los objetivos de esta introducción. De manera extraordinariamente simplificada, tras aplicar un campo magnético externo de alta intensidad, los núcleos de hidrógeno en los tejidos del cuerpo humano se alinean con el mismo. A continuación, se emiten ondas de radiofrecuencia con unas características específicas (i.e., frecuencia de Larmor) que interrumpen este equilibrio. En este momento, los núcleos de hidrógeno regresan a su estado original de alineación (relajación), emitiendo señales de radiofrecuencia que son captadas por las antenas de la RM y posteriormente procesadas para generar imágenes detalladas y tridimensionales de los tejidos del cuerpo (Bydder, 1991).

En función de diferentes parámetros ajustables (tiempo de eco, tiempo de repetición, etc.), se obtienen "secuencias" específicas. Las más utilizadas en el estudio de la columna son las potenciadas en T1, T2 y STIR, aunque existen otras que también mencionaremos, como las secuencias con supresión o saturación de grasa que, como su nombre indica, permiten eliminar la señal de la grasa, que se visualizará de color negro en la imagen, T1 en fase y fase opuesta (permiten detectar grasa intracitoplasmática) o las secuencias ponderadas en difusión y su correspondiente mapa de coeficientes de difusión aparente (ADC), mediante las cuales es posible analizar fenómenos funcionales relacionados con el movimiento browniano de las moléculas en un tejido. En la descripción de las imágenes de RM, se hará referencia a las estructuras y áreas como de "(intensidad de) señal alta o baja" seguido de la secuencia analizada. Por ejemplo, las estructuras quísticas se visualizarán como áreas de baja intensidad de señal (hipointensas) en T1 y de alta señal

(hiperintensas) en T2. El líquido cefalorraquídeo dentro del canal espinal puede ayudar a distinguir entre secuencias de imágenes si no están etiquetadas. El comportamiento en T1, T2 y STIR permite filiar con bastante fiabilidad la naturaleza de diversos tejidos, incluyendo la grasa, el líquido y el calcio, lo que permite ayudar a diagnosticar lesiones y cambios en la médula ósea.

La RM ofrece la ventaja de producir imágenes con un alto contraste tisular en cualquier plano del espacio. Sin embargo, también tiene limitaciones. En primer lugar, el tiempo de adquisición de la imagen es notablemente más largo en comparación con otras modalidades de imagen, lo que puede resultar incómodo para el paciente y limita su uso en situaciones urgentes. En segundo lugar, es una técnica significativamente más cara, tanto en términos de inversión inicial en el equipo como de mantenimiento, lo que restringe su disponibilidad (Caverly, 2015). Finalmente, la presencia de ciertos tipos de implantes metálicos o dispositivos médicos, como los marcapasos, puede contraindicar su uso debido a los riesgos asociados a la presencia de un campo magnético de alta intensidad (Yang et al., 2022).

1.3.Anatomía radiológica de la columna vertebral

La comprensión de la anatomía radiológica de la columna vertebral normal es fundamental para el diagnóstico y la evaluación de las patologías que pueden alterar su estructura, como es el caso de las FVO. Tanto la RC como la TC y la RM permiten la visualización de los elementos principales de la columna y la identificación de la mayor parte de estructuras anatómicas, con un grado variable de resolución espacial y tisular en función de la técnica de imagen empleada (Valladares-Otero et al., 2014).

La RC permite visualizar los principales elementos vertebrales y la alineación sagital y coronal de la columna, con la especial ventaja de poder realizarse con el paciente de pie, de manera estática o con maniobras dinámicas, principalmente de flexión y extensión (Butt, 1989). Como se ha mencionado previamente, la limitación principal de la RC deriva de su naturaleza bidimensional, lo que se traduce en una superposición de estructuras anatómicas y en la frecuente necesidad de obtener, al menos, dos proyecciones, habitualmente anteroposterior y lateral (Harvey y Blomley, 2003). Por su parte, la TC proporciona imágenes más detalladas de la columna vertebral gracias a su capacidad para obtener imágenes multiplanares y reconstrucciones volumétricas con alta resolución espacial (hasta 0,625 mm de espesor de corte en los equipos actuales) y a la

posibilidad de emplear algoritmos de reconstrucción ósea y de tejidos blandos. Por lo tanto, resulta de gran utilidad en la evaluación de las estructuras óseas y, por consiguiente, en el diagnóstico de las FVO (Sanal and Akay, 2015). Finalmente, la RM permite generar imágenes con elevada resolución tisular, siendo especialmente útil en comparación con las técnicas anteriores en la valoración de la médula espinal, los discos intervertebrales, los ligamentos y los músculos. Además, permite evaluar alteraciones en la médula ósea como la presencia de edema. Como se verá más adelante, conlleva significativas ventajas en el contexto de las FVO, pues permite guiar la toma de decisiones clínicas y monitorizar la evolución de las fracturas, entre otros aspectos (Freund et al., 2019).

Es importante destacar que la interpretación precisa de las imágenes radiológicas de la columna vertebral requiere un conocimiento profundo de la anatomía normal y de las variantes más comunes (Shepard et al., 2020). El radiólogo debe tener en cuenta las características específicas de cada paciente y correlacionar los hallazgos radiológicos con los síntomas clínicos para realizar un diagnóstico preciso. Así pues, la correcta evaluación de las patologías de la columna y, particularmente, de las FVO, debe sustentarse en un conocimiento exhaustivo de la anatomía radiológica normal. Por ello, se describirán las principales características radiológicas de la columna vertebral normal mediante las tres técnicas de imagen revisadas en este apartado, prestando especial atención a la RC, cuya semiología es quizás menos intuitiva debido al solapamiento de estructuras anatómicas. Debe tenerse en cuenta que se repasarán conceptos básicos fundamentales y se mencionarán algunos ejemplos sencillos de alteraciones que permitan comprender la importancia de detectar las desviaciones del patrón radiológico normal. Sin embargo, las diferentes patologías e la columna serán revisadas en el cuerpo de la tesis de forma mucho más minuciosa. Además, puede consultarse una descripción más pormenorizada de los hallazgos radiológicos por TC y RM de la columna vertebral (y del resto de la anatomía) en el **Apéndice 1**.

1.3.1. Anatomía radiológica de la columna vertebral en radiografía simple

En la semiología radiológica de la columna vertebral en RC es posible visualizar las estructuras anatómicas principales que componen cada vértebra: el cuerpo, el arco posterior, las apófisis espinosas y transversas, así como las articulaciones principales (cigapofisarias, unciformes, costovertebrales). Como hemos mencionado previamente, para una correcta evaluación de la columna deben realizarse dos proyecciones

radiológicas: anteroposterior y lateral. No obstante, existen otras proyecciones específicas para evaluar determinadas regiones o patologías específicas que pueden ser útiles en determinados contextos, como la proyección transoral o atlanto-occipital, en flexión-extensión, oblicua, etc. (Smith and Abel, 1975; Waldt et al., 2014). Habitualmente, la región de interés se centra en un único segmento de la columna, atendiendo a la sospecha clínica.

En general, los cuerpos vertebrales muestran una morfología rectangular y deben presentar una densidad uniforme y contornos nítidos (Kricun, 2002). Entre dos cuerpos vertebrales contiguos se define el espacio intervertebral, que corresponde al espacio ocupado por los discos intervertebrales, debiendo preservar una altura similar en los diferentes niveles. La disminución de estos espacios sugiere patología discal, frecuentemente degenerativa. Las estructuras del arco posterior deben mostrar una continuidad clara sin interrupciones o desalineaciones. Las apófisis espinosas y transversas que emergen de las porciones posterior y laterales de dicho arco, respectivamente, deben tener un aspecto simétrico y correctamente alineado en condiciones normales, tanto en la proyección posteroanterior como lateral. Las alteraciones de la forma, posición o densidad de estas estructuras pueden traducir la presencia de lesiones traumáticas, infecciones o procesos neoplásicos. Las articulaciones cigapofisarias o facetarias se evalúan en términos de su alineación y diámetro del espacio articular. El estrechamiento de este espacio, la esclerosis subcondral o los osteofitos son hallazgos que pueden sugerir artrosis facetaria (Waxenbaum et al., 2023).

En la proyección posteroanterior, cada segmento vertebral presenta características anatómicas y semiológicas distintivas. Así, en el segmento cervical, se pueden visualizar las siete vértebras cervicales excepto C1 y C2, debido a la superposición de la mandíbula, y sus respectivas apófisis espinosas, que deben aparecer alineadas en un eje vertical. Cualquier desviación de esta alineación puede indicar fracturas o luxaciones (Kafiabadi and Rangi, 2017). En esta proyección, los forámenes transversos, por donde pasan las arterias vertebrales, no son visibles, pero se pueden apreciar las articulaciones uncovertebrales, cuya alteración puede indicar artrosis. Los cuerpos vertebrales deben presentar contornos claros y definidos y una densidad uniforme. En el segmento dorsal o torácico, se visualizan los cuerpos vertebrales y los arcos posteriores de las costillas, que se articulan con los primeros a través de los procesos costovertebrales (Ombregt, 2013). Es importante evaluar la alineación de las articulaciones costo-vertebrales y se debe

prestar atención a la densidad y morfología de las apófisis espinosas que, al igual que en el segmento cervical, deben disponerse en línea recta. Por último, el segmento lumbar presenta las vértebras de mayor tamaño de la columna vertebral, con forma cuadrangular, y también es posible evaluar la alineación y densidad de las apófisis espinosas. En todas las regiones debe evaluarse el espacio discal, cuyo estrechamiento puede ser indicativo de patología degenerativa; incluso se ha encontrado una asociación entre la disminución de dicho espacio y el riesgo de desarrollar osteoporosis (Sornay-Rendu et al., 2004). Además, la proyección anteroposterior permite evaluar las curvaturas coronales patológicas propias de la escoliosis, permitiendo la medición de ángulos y relaciones que orienten la toma de decisiones clínicas (Ng and Bettany-Saltikov, 2018).

La proyección lateral proporciona una perspectiva complementaria a la anteroposterior, permitiendo evaluar características anatómicas y patológicas específicas de cada región vertebral (Jebri et al., 2015). En el segmento cervical, esta proyección permite una visualización clara de la morfología rectangular de los cuerpos vertebrales y de la altura de los discos intervertebrales, así como de la alineación normal de las apófisis espinosas. En el segmento dorsal se puede observar la morfología de los cuerpos vertebrales y las articulaciones costovertebrales y, al igual que en el segmento cervical, el análisis del espacio discal es fundamental para detectar signos de degeneración. En cuanto al segmento lumbar, se debe visualizar la forma cuadrangular y de mayor tamaño propia de los cuerpos vertebrales. Asimismo deben visualizarse los elementos posteriores, particularmente las articulaciones facetarias, que pueden estar alteradas en el contexto de patologías como la artrosis o espondilólisis (Kwee and Kwee, 2021). Respecto a esta última patología, el famoso signo del "perrito de Lachapelle" suele servir como referencia para la localización de los elementos posteriores en la proyección oblicua, tal y como se revisará más adelante. Para finalizar, cabe recordar que la proyección lateral permite evaluar las curvaturas fisiológicas sagitales (lordosis cervical y lumbar, y cifosis torácica), cuya alteración puede estar asociada a patologías como la enfermedad de Scheuermann, espondilolistesis o enfermedades degenerativas (Furlanetto et al., 2018). Además, puede evaluarse la integridad del canal vertebral y la alineación global de la columna, factores fundamentales en el diagnóstico de enfermedades como la estenosis de canal (Ruiz Santiago et al., 2010).

1.3.2. Anatomía radiológica de la columna vertebral en tomografía computarizada

En la TC de columna vertebral se pueden identificar con mayor claridad las características anatómicas de las vértebras y las estructuras adyacentes, brindando información adicional a la obtenida mediante CR. Resulta especialmente útil en casos de traumatismo, sobre todo en casos de traumatismo de alta energía, donde es la prueba de primera elección dada su mayor sensibilidad y especificidad para la detección de fracturas y otras complicaciones en comparación con la RC (Dreizin et al., 2014). Además, posibilita una valoración parcial de las hernias de disco y la detección de otras patologías no traumáticas, particularmente tumorales. En la evaluación semiológica por TC se utilizan convencionalmente las ventanas ósea (anchura: 1800 UH, nivel: 400) y de partes blandas (anchura: 250; nivel: 50), evaluadas en los tres planos ortogonales del espacio (Quiroga et al., 1982). En ocasiones puede requerirse el uso de contraste intravenoso, sobre todo en pacientes posquirúrgicos. En cuanto al protocolo de adquisición, se deberán ajustar los parámetros de voltaje, corriente, campo de visión, grosor e intervalo de corte, reconstrucciones multiplanares, etc., e incluir algoritmos de reconstrucción óseo y de partes blandas (Tins, 2010). A modo de ejemplo, se describe el protocolo y parámetros de adquisición de la TC de columna lumbar en la **Tabla 1**.

Parámetros técnicos	Descripción
Posición del paciente	Decúbito supino, ambos brazos elevados
Voltaje del tubo	120 (140) kVp
Corriente del tubo	Ajustada automáticamente según el modo de ajuste automático de corriente
Exploración Scout	Desde el diafragma hasta la cadera
Extensión de la exploración	Puede variar según la pregunta clínica, debe incluir T12 y S1
Dirección de exploración	Craneocaudal
Geometría de exploración	Campo de visión (FOV): 120-200 mm (ajustado para aumentar la resolución en el plano de interés)
Grosor de corte	≤0.625 mm
Intervalo	≤0.5 mm
Algoritmo de reconstrucción	Hueso, tejido blando
Administración de contraste	Por lo general, sin contraste, opcionalmente con contraste
Volumen de contraste	70-100 mL (0.1 mL/kg) a una velocidad de 2-3 mL/s
Retraso de la exploración	65-80 segundos
Reconstrucciones/reformateos multiplanares	• Imágenes sagitales: alineadas sagitalmente a través del centro de los cuerpos vertebrales y los procesos espinales • Imágenes coronales: alineadas a los procesos transversos • Imágenes axiales: perpendiculares a la columna lumbar con una reconstrucción en bloques separados
Grosor de corte	Hueso ≤ 2 mm, tejido blando ≤ 3 mm, superposición del 50%

Tabla 1. Protocolo de adquisición de imagen en TC de columna lumbar. Aspectos técnicos principales.

La alta resolución espacial de la TC permite evaluar con gran precisión la forma, tamaño y alineación de los cuerpos vertebrales, los arcos vertebrales, las apófisis espinosas y transversas, unciformes y facetarias, hiperdensas en comparación con las partes blandas adyacentes. Esta técnica también proporciona información detallada sobre la densidad ósea de las corticales y del hueso trabecular, posibilitando su análisis en una, dos o tres dimensiones, lo que permite la identificación de patologías como osteopenia, osteoporosis o enfermedades infiltrativas óseas (Celenk and Celenk, 2012). Otro aspecto a reseñar es la posibilidad de generar mediciones cuantitativas secundarias y ratios con fines

diagnósticos y pronósticos, como se verá posteriormente en nuestra investigación. Además de las estructuras óseas, la TC ayuda a visualizar otros elementos importantes de la columna vertebral como los discos vertebrales, el saco tecal, la grasa epidural y la musculatura paravertebral, aunque su sensibilidad para la detección de alteraciones es, en general, menor que la RM.

1.3.3. Anatomía radiológica de la columna vertebral en resonancia magnética

Actualmente la RM desempeña un papel fundamental en el diagnóstico y manejo de diversas patologías de la columna vertebral, brindando información anatómica y funcional de indudable valor que posibilita una evaluación integral de estructuras óseas y partes blandas (Pressney et al., 2014), y siendo especialmente útil en comparación con la RC y TC en la valoración de los discos vertebrales, ligamentos y estructuras intratecales. Aunque pueden emplearse muchas secuencias para el estudio de la columna, como se ha mencionado previamente las más utilizadas son las ponderadas en T1, T2 y STIR (*short-tau inversion recovery*) y/o T2 con saturación grasa, usualmente en los planos sagital y axial (Neeson and Roberts, 2021). Otras secuencias que pueden resultar de utilidad en determinadas situaciones que veremos más adelante incluyen las potenciadas en difusión (DWI/ADC), T1 o T2 en fase (*in-phase*) y en fase opuesta (*opposed-phase*), además de las secuencias T1 tras la administración de contraste paramagnético (gadolinio) intravenoso. En ocasiones se utilizan también los planos coronales u oblicuos, atendiendo a la patología que se sospeche. A modo de ejemplo, en la **Tabla 2** se detalla el protocolo habitual de RM de columna lumbar.

Parámetros técnicos	**Valores**
Bobina	Bobina posterior, Bobina anterior
Geometría de escaneo	Resolución espacial en el plano: ≤0,7 x 0,7 mm
	Campo de visión (FOV): 300-380 (sagital/coronal), 150-250 (axial)
	Grosor del corte: (≤4 mm) – mejor ≤3mm
Planificación	
Imágenes sagitales	Angulación: paralela al eje espinal lumbar y procesos espinosos
	Volumen: incluye los cuerpos vertebrales completos y las articulaciones facetarias
	Grosor del corte: ≤3 mm
Imágenes coronales	Angulación: paralela al eje espinal lumbar y procesos transversos
	Volumen: incluye el canal espinal del cuerpo vertebral completo y las láminas posteriores
	Grosor del corte: ≤3 mm
Imágenes axiales	Angulación: perpendicular a la columna lumbar
	Volumen: variable, depende de la pregunta clínica y/o patología visible
	Grosor del corte: ≤3 mm
Secuencias	**Planos**
T1 *fast spin echo*	Sagital, axial* (opcional)
T2 Dixon / T2 *fast spin echo*	Coronal, sagital, axial
T2 Dixon / STIR / T2 FS *fast spin echo*	Coronal o sagital, axial

Tabla 2. Protocolo de adquisición de imagen en RM lumbar. Aspectos técnicos principales. STIR: *Short-tau Inversion Recovery*. FS: *fat saturated*.

La RM permite evaluar la morfología vertebral y la intensidad de señal de la médula ósea, que en condiciones normales suele ser hiperintensa en secuencias T1 y T2 e hipointensa STIR por la presencia de médula grasa, aunque esto es variable en función de la edad del paciente. El edema se visualiza como un área de alta intensidad de señal en secuencias sensibles al líquido (STIR, T2 con saturación grasa), y su detección resultará de gran importancia para el diagnóstico y seguimiento de las FVO. La RM también posibilita la evaluación de la integridad de los discos intervertebrales y el diagnóstico de patologías

discales (deshidratación, fisuras, abombamientos, hernias, etc.), siendo esta una de las indicaciones más frecuentes por las que se solicita esta prueba en la práctica (Urban and Winlove, 2007). Por último, resulta especialmente útil para evaluar otros tejidos blandos de la columna, como los ligamentos, que pueden verse afectados en el contexto de una fractura vertebral, la musculatura, las raíces nerviosas y la médula espinal, esta última de gran importancia en el contexto de fracturas con sospecha de mielopatía compresiva secundaria.

En la **Tabla 3** se comparan las ventajas y limitaciones de la RC, la TC y la RM en la evaluación de la columna vertebral.

Criterios	**RC**	**Tomografía computarizada**	**Resonancia magnética**
Radiación	Baja radiación	Mayor exposición a la radiación	No emplea radiación ionizante
Disponibilidad	Ampliamente disponible	Disponible, pero en menor medida que la RC	Disponible en centros especializados
Rapidez	Rápida y de fácil realización	Más tiempo requerido para la adquisición de imágenes que la RC	Requiere un tiempo de adquisición más prolongado
Coste	Coste relativamente bajo	Mayor coste en comparación con la RC	Mayor coste en comparación con la RC
Valoración ósea	Proporciona información sobre la estructura ósea, alineación y fracturas	Ofrece una visualización detallada de las estructuras óseas, incluyendo fracturas y densidad ósea	Permite una evaluación detallada de las estructuras óseas, incluyendo fracturas y cambios degenerativos
Valoración de partes blandas	Limitada visualización de tejidos blandos	Proporciona información limitada sobre los tejidos blandos	Permite una evaluación detallada de los tejidos blandos, como discos intervertebrales, ligamentos y médula espinal
Resolución espacial	Baja resolución espacial	Mayor resolución espacial que la RC	Mayor resolución espacial que la RC
Resolución tisular	Baja resolución tisular	Proporciona una buena resolución tisular para tejidos blandos y órganos	Excelente resolución tisular para tejidos blandos y órganos

Tabla 3. Ventajas y limitaciones de la RC, la tomografía computarizada (TC) y la resonancia magnética (RM) en la evaluación de la columna vertebral.

1.3.4. Impresión 3D basada en imagen médica en la valoración de la columna vertebral

La impresión 3D basada en imagen médica es una tecnología emergente en radiología (Láinez Ramos-Bossini et al., 2022) que permite la creación de modelos físicos tridimensionales a partir de datos de imagen obtenidos mediante técnicas como la TC o la RM (Marro et al., 2016). La impresión 3D ha demostrado ser una herramienta de gran utilidad para el estudio de la anatomía de la columna vertebral normal y patológica (Láinez Ramos et al., 2021) (**Figura 3**), y actualmente debe ser considerada como una tecnología más dentro del arsenal diagnóstico-terapéutico de un servicio de radiología moderno (Wake, 2021). Mediante la conversión de los datos de imagen en un modelo físico, es posible tener una representación tangible y precisa de las estructuras anatómicas de la columna vertebral, proporcionando una mejor comprensión de la relación espacial entre las diferentes vértebras, discos intervertebrales, articulaciones y tejidos blandos (Cai et al., 2018).

Además, existen diversos trabajos en los que se ha demostrado la utilidad de la impresión 3D en la planificación quirúrgica y en la práctica clínica, posibilitando a los cirujanos la simulación de procedimientos complejos con mayor precisión y seguridad, especialmente la evaluación de las relaciones anatómicas y en el ensayo de técnicas quirúrgicas e intervencionistas (Pugliese et al., 2018). Además, facilita el diseño y la fabricación de prótesis y otros dispositivos médicos personalizados para el tratamiento de patologías de la columna vertebral, facilitando su adaptación de forma precisa en función de las características anatómicas específicas de cada paciente, lo que mejora la eficacia y la seguridad de los tratamientos (Provaggi et al., 2016).

Por otra parte, los modelos impresos en 3D permiten una exploración táctil y visual de la estructura anatómica, lo que facilita el aprendizaje y la enseñanza en medicina y cirugía (Láinez Ramos-Bossini et al., 2021; Zheng et al., 2019). Aunque no es el objeto principal de esta tesis doctoral, en el **Apéndice 2** puede consultarse uno de nuestros trabajos sobre la utilidad de estas tecnologías en la enseñanza de la anatomía de la columna. Además, estos modelos pueden utilizarse como herramientas educativas para pacientes y sus familiares, lo que les ayuda a comprender mejor su condición y los posibles procedimientos quirúrgicos (van de Belt et al., 2018).

Figura 3. Ejemplo de modelos impresos en 3D de la columna vertebral utilizados como paradigma de aprendizaje para la enseñanza de la anatomía de la columna vertebral. Los modelos se imprimieron con la impresora 3D Bibo 2 Dual Extrusion. *Fuente: Láinez Ramos-Bossini et al., 2021 (**Apéndice 2**).*

A pesar de todas estas ventajas, la impresión 3D basada en imagen médica también tiene limitaciones. La calidad de los modelos impresos es variable y depende de diversos aspectos, como las imágenes fuente, el proceso de segmentación, la calidad de los materiales o la impresora utilizada. Por otra parte, la necesidad de personal cualificado, el coste y la disponibilidad de los equipos pueden ser limitantes en ciertos entornos clínicos y educativos (Bastawrous et al., 2018). Sin embargo, el rápido avance de estas tecnologías y el abaratamiento de sus costes está permitiendo una implantación cada vez más generalizada en los servicios de radiología.

1.3.5. Inteligencia artificial en el diagnóstico radiológico de la columna vertebral

La inteligencia artificial (IA) es un área de la informática que se ocupa de diseñar sistemas que resuelven problemas complejos para cuya resolución el ser humano debe aplicar inteligencia (Zhang et al., 2021). Es un área surgida en los años 60 del siglo pasado que ha ido evolucionando con la tecnología que le da soporte (ordenadores y *hardware* relacionado). Las técnicas de IA se han venido aplicando a diversos problemas en múltiples áreas de la actividad y conocimiento humanos, y en concreto en medicina (Glissen Brown and Berzin, 2021). En los años 80 hubo una gran expansión de esta área con el desarrollo de los denominados «sistemas expertos» y los progresos en estos últimos

40 años han llevado a crear sistemas inteligentes con rendimientos espectaculares en análisis de datos, modelado y reconocimiento de patrones.

Una de las principales áreas en las que se han realizado grandes avances en este ámbito es la del aprendizaje automático (*machine learning*), que reúne diferentes conjuntos de métodos automatizados para conseguir realizar tareas concretas sin una programación explícita para ello (Singh, 2019). La última generación de estas técnicas recibe el nombre colectivo de aprendizaje profundo (*deep learning*) y se basa en el empleo de modelos mucho más complejos estructuralmente, con parámetros libres cuyo número supera fácilmente los centenares de miles, frecuentemente millones (Fan et al., 2021). A su vez, dentro del aprendizaje profundo, se encuentran las redes neuronales artificiales, modelos inspirados en el funcionamiento biológico del sistema nervioso que han supuesto una revolución metodológica en múltiples campos relacionados con la imagen gracias a sus resultados, similares o incluso superiores al del ser humano (Torres-Velazquez et al., 2021). Debido a la falta de familiaridad de la mayoría de médicos sobre esta disciplina, existen frecuentes confusiones respecto a las relaciones entre IA, aprendizaje automático, aprendizaje profundo y redes neuronales (**Figura 4**).

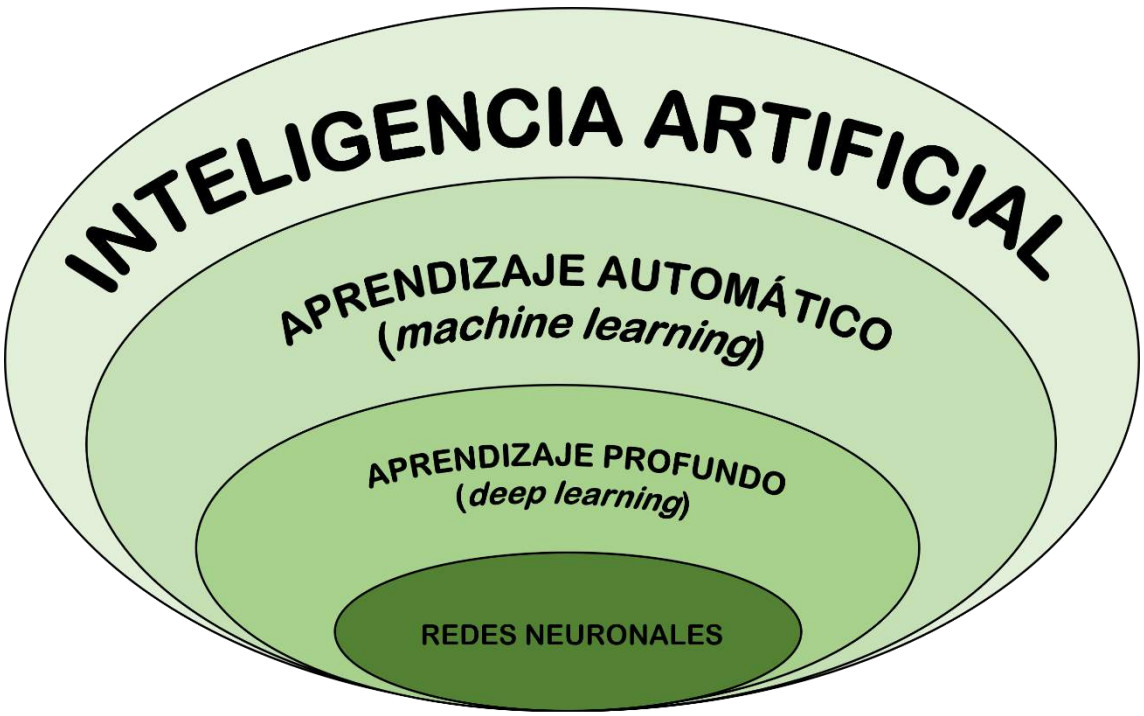

Figura 4. Relaciones entre la inteligencia artificial, aprendizaje automático, aprendizaje profundo y redes neuronales. *Fuente: Elaboración propia.*

En la última década, las nuevas técnicas desarrolladas en IA han tenido una expansión sin precedentes en el ámbito de la medicina, especialmente en el campo de la radiología e imagen médica (Lee et al., 2019). El reconocimiento o detección de patrones en imágenes ha tenido un desarrollo espectacular en estos años y la capacidad de adaptación (aprendizaje) de los nuevos modelos ha permitido la construcción de sistemas de diagnóstico muy eficaces en distintos problemas reales. El diagnóstico de diferentes patologías en pruebas radiológicas es uno de los problemas a los que se pueden aplicar. En efecto, recientemente se han desarrollado algoritmos altamente resolutivos capaces de detectar precozmente patologías de alto impacto en salud como el ictus (Duong et al., 2020), y en la reciente pandemia por COVID-19 se han desarrollado numerosos algoritmos y aplicaciones basadas en IA para el cribado, diagnóstico y pronóstico de estos pacientes, como se puede consultar en trabajos de nuestro grupo (Lastra Leidinger et al., 2022; Redruello-Guerrero et al., 2022).

La columna vertebral fue una de las primeras regiones anatómicas en las que se aplicaron algoritmos de IA en el campo de la imagen médica y actualmente existen herramientas para segmentación y etiquetado vertebral en RC, TC y RM, cambios degenerativos vertebrales, evaluación del riesgo de osteoporosis y detección de metástasis, enfermedades infiltrativas óseas (Martín-Noguerol et al., 2023). En cuanto a las fracturas vertebrales, también existen algoritmos que han demostrado resultados prometedores con una alta precisión diagnóstica, principalmente en RC y TC, y están preparados para su implementación en la práctica radiológica (Zhang et al., 2020). Sin embargo, aún es necesario validar mediante ensayos prospectivos multicéntricos el rendimiento diagnóstico de muchas de estas aplicaciones.

Una de las principales dificultades existentes en este campo es la necesidad de grandes conjuntos de datos etiquetados que no suelen estar fácilmente disponibles. No obstante, se han desarrollado algunas estrategias para paliar este déficit de datos. Por ejemplo, en el contexto del aprendizaje automático han surgido distintos paradigmas y técnicas como los métodos basados en *transfer-learning*, *semi-supervised learning* y *data augmentation* que ayudan a extraer la máxima información posible a partir de problemas diagnósticos similares para los que ya existen modelos entrenados, aprovechar datos no etiquetados, o ampliar el conjunto de datos para facilitar la calidad del sistema final (Cholaquidis et al., 2018; Weiss et al., 2016).

2. Osteoporosis y fracturas vertebrales osteoporóticas

2.1. Osteoporosis: un problema de salud global. Prevalencia e impacto socioeconómico

La osteoporosis es una enfermedad metabólica caracterizada por la reducción de la densidad y microarquitectura del hueso. Desde un punto de vista epidemiológico, representa la enfermedad metabólica ósea más frecuente en el mundo y constituye un problema de salud de primer orden, afectando a más de 200 millones de personas en el mundo, con una prevalencia estimada de 27,6 millones de personas en la Unión Europea (Cosman et al., 2014; Williams et al., 2009). En España, 3,5 millones de personas están afectadas por esta enfermedad y se espera que la cifra ascienda a 4,5 millones en el año 2025 (Hernlund et al., 2013). En concreto, un tercio de las mujeres mayores de 50 años y más de la mitad de las mujeres mayores de 70 años presenta osteoporosis (Naves et al., 2005). Además, el proceso de envejecimiento poblacional generalizado y el estilo de vida propio de los países de nuestro entorno indican que la prevalencia de esta enfermedad aumentará significativamente en los próximos años (Blanch et al., 2017), por lo que se considera un problema de salud pública relevante y un reto para el futuro. La principal consecuencia clínica de la osteoporosis es el desarrollo de fracturas óseas, lo que justifica la necesidad de prevenir y tratar este problema de salud, pese a que las políticas implantadas hasta la fecha han resultado ineficaces (Del Pino Montes, 2010). La detección de los principales factores de riesgo asociados a estas fracturas podría ayudar al desarrollo de estrategias preventivas efectivas.

El impacto económico de la osteoporosis y fracturas derivadas en los sistemas de salud es muy elevado (Nogués Solán et al., 2010). A nivel mundial, el 40% de las mismas ocurren durante la edad laboral; en Europa, la discapacidad secundaria a la osteoporosis es mayor que la causada por la mayoría de los cánceres (Johnell and Kanis, 2006) y, en las mujeres mayores de 45 años, las fracturas osteoporóticas generan un mayor número de días de hospitalización que la diabetes, el infarto de miocardio y el cáncer de mama (Kanis et al., 1997). El coste anual del tratamiento de las fracturas osteoporóticas en trabajadores asciende a 48.000 millones de dólares solo en Canadá, Europa y Estados Unidos, sin tener en cuenta los costes indirectos derivados de la discapacidad y pérdida de productividad (International Osteoporosis Foundation, 2016). En España, la incidencia estimada de fracturas osteoporóticas es de 25.000 casos anuales, lo que conlleva unos

costes directos estimado de 126 millones de euros, que ascienden a 420 millones si se consideran los costes indirectos (Del Pino Montes, 2010). En la **Tabla 4** se recogen los datos más relevantes sobre la epidemiología de la osteoporosis y los costes económicos asociados.

	Osteoporosis	**FCO**	**FVO**	**Todas las FO**
Prevalencia				
Mundial	≈200.000.000 mujeres	1.364.717	≈1.417.000	8.900.000
Unión Europea	27.600.000	≈620.000	≈490.000	≈3.000.000
España	3.528.264 mujeres >50 años y 2.675.627 >70 años^	40.473 >50 años ≈7.2/1000	29.689 (>50 años)	250.000
Coste económico (€/año)				
Mundial	No disponible	No disponible	No disponible	No disponible
Unión Europea	No disponible	19.219.000	1.745.000.000	37.000.000.000
España		No disponible	41.746.930	2.842.000.000

Tabla 4. Datos epidemiológicos y económicos relativos a las fracturas osteoporóticas. FCO: Fractura de cadera osteoporótica. FVO: fractura vertebral osteoporótica. FO: fractura osteoporótica. Entre paréntesis se indica la referencia bibliográfica de la que se han obtenido los datos. ^Cifras extraídas a partir de Naves et al. (2005), actualizado con la prevalencia demográfica en 2019 según datos del Instituto Nacional de Estadística. Fuentes: Blanch et al., 2017; Bouza et al., 2007; Hernlund et al., 2013; Herrera et al., 2006; Johnell and Kanis, 2006; Naves et al., 2005; Odén et al., 2013; The Global Burden of Osteoporosis: a Factsheet, 2019; INE. Instituto Nacional de Estadística, 2019.

2.2. La fractura vertebral osteoporótica (FVO): importancia del diagnóstico precoz

La localización más frecuente de fractura osteoporótica es la vértebra y su presencia incrementa el riesgo de sufrir nuevas fracturas en el futuro hasta 10 veces (Kaptoge et al., 2004), conllevando una morbimortalidad similar a la de la fractura osteoporótica de cadera (Hernlund et al., 2013; Kanis et al., 2004; Lentle et al., 2016; Ross, 1997; Wáng

et al., 2017). Las FVO pueden tener consecuencias muy negativas en la calidad de vida de los pacientes, dando lugar a dolor crónico, deformidad vertebral, discapacidad y al ya citado aumento del riesgo de fracturas diferidas (Yoon et al., 2014). Para evitar estas complicaciones, es necesario realizar un diagnóstico preciso de las FVO lo más precozmente posible e iniciar el tratamiento apropiado para la osteoporosis (Li et al., 2018). En este sentido, mientras que el diagnóstico de la mayoría de fracturas óseas (p.ej. la fractura de cadera) no suele resultar difícil por varios factores (antecedente de traumatismo, sintomatología florida y diagnóstico por imagen usualmente diáfano), en el caso de la FVO la realidad suele ser muy distinta, pues normalmente son asintomáticas o paucisintomáticas y con frecuencia no van precedidas de traumatismos significativos o estos son de muy baja energía. Especial atención merece, como se verá más adelante, la dificultad que entraña en ocasiones la interpretación de la RC para el diagnóstico de algunas FVO, siendo esta la prueba más utilizada para el diagnóstico de FVO dada su amplia disponibilidad en cualquier servicio de Urgencias y en muchos centros de Atención Primaria. Aunque la TC y la RM son mucho más sensibles y específicas que la RC, son menos accesibles y tienen otros problemas añadidos que ya se han mencionado previamente, y a los que cabría añadir la necesidad de médicos especialistas cualificados para su correcta interpretación (radiólogos).

Dada la amplia disponibilidad de la RC, esta técnica de imagen debería servir de herramienta de detección precoz de las FVO. Sin embargo, el diagnóstico mediante radiología simple resulta difícil por varias razones que se detallarán en el siguiente apartado, como la falta de consenso en los criterios diagnósticos, la coexistencia de fenómenos destructivos y reparativos, o la escasa sintomatología asociada en muchos casos (Li et al., 2018). Por todo lo anterior, existe un elevado número de FVO que no son diagnosticadas. Las estimaciones publicadas cifran estos casos perdidos en torno al 30% de las FVO (Williams et al., 2009), lo que se traduce en aproximadamente unos 13.000 casos anuales en nuestro país, considerando la prevalencia de este tipo de fracturas.

Por otra parte, el tratamiento precoz de las FVO es fundamental para minimizar el impacto negativo en la calidad de vida de los pacientes. La identificación temprana y el manejo adecuado de estas fracturas pueden prevenir complicaciones a largo plazo y mejorar los resultados clínicos. El retraso en el tratamiento puede llevar a un mayor dolor, deformidad vertebral progresiva y discapacidad funcional.

2.3. Diagnóstico y tratamiento de la fractura vertebral osteoporótica

La detección y el diagnóstico de las FVO son esenciales debido a sus implicaciones terapéuticas y pronósticas. Así, aunque la prueba de referencia para el diagnóstico de osteoporosis es la absorciometría dual de rayos X (*T score* <2,5 desviaciones estándar en la columna lumbar, cadera o cuello femoral; Riancho et al., 2022), frecuentemente este diagnóstico se realiza en el escenario clínico de una FVO diagnosticada tras un traumatismo mediante pruebas radiológicas (CR, TC y/o RM). A pesar del uso extendido de la RC de columna vertebral y de RC de tórax en la práctica clínica diaria, existe un infradiagnóstico generalizado de las FVO, que puede atribuirse, entre otros factores, a la falta de consenso en los criterios diagnósticos y a la falta de conciencia generalizada por parte de los médicos acerca de su importancia diagnóstica, incluso en casos incidentales. Por lo tanto, es fundamental tener un conocimiento actualizado de los enfoques más relevantes para el diagnóstico de las FVO (Ferrar et al., 2005).

Actualmente, tanto la absorciometría de rayos X de doble energía como la RC, la TC y la RM se utilizan para evaluar las FVO, y la RM puede determinar su evolución temporal (Grados et al., 2009). A pesar de que la RC sigue considerándose la prueba de referencia para la evaluación inicial de las FVO en la región toracolumbar, varios estudios han demostrado la superioridad de la RM en el diagnóstico de las FVO (Rihn et al., 2009). Sin embargo, actualmente no se ha establecido un consenso claro sobre la superioridad de una modalidad de imagen sobre otra para el diagnóstico de las FVO, por lo que son necesarios más estudios para determinar las indicaciones clínicas más apropiadas, teniendo en cuenta diversos factores relativos a la técnica como su disponibilidad, coste y precisión, además de las preferencias del paciente, y la experiencia y habilidades de los médicos implicados en el proceso asistencial, especialmente los expertos en imagen médica (Lentle et al., 2019).

2.3.1. Importancia de la anatomía radiológica del raquis en el diagnóstico de las fracturas vertebrales osteoporóticas

El primer aspecto que debe tenerse en cuenta a la hora de abordar el diagnóstico de las FVO por imagen es la necesidad de un conocimiento exhaustivo de la anatomía radiológica de la columna vertebral normal, de sus variantes anatómicas, y de la columna vertebral patológica (Kim et al., 2015). En este sentido, la máxima de que "solo se diagnostica lo que se sabe", cobra su máxima plenitud, no solo por la compleja anatomía

de la columna sino por la elevada prevalencia de variantes anatómicas (anomalías de transición, particularmente lumbosacras, o variantes que remedan fracturas como la vértebra en limbo), u otras patologías coexistentes que frecuentemente se prestan a diagnóstico diferencial, y por la importancia de diagnosticar complicaciones de las FVO, como afectación compresiva medular o de elementos vasculares (p.ej., arterias vertebrales o aorta). En la práctica los radiólogos frecuentemente tenemos que atender interconsultas de RC por este tipo de hallazgos que plantean dudas diagnósticas para los médicos no especialistas en imagen.

Por otra parte, no solo es importante conocer la anatomía radiológica de cara al diagnóstico preciso (en este caso, diferencial) de las FVO. También debe tenerse en cuenta la elevada frecuencia de hallazgos concomitantes a una FVO que pueden justificar dolor, y que deberán incluirse en el informe radiológico (Link et al., 2005). En muchos de estos casos resultará fundamental prestar atención a los hallazgos de imagen que puedan resultar de ayuda al clínico para realizar un correcto diagnóstico etiológico de la clínica del paciente. Por ejemplo, la existencia de hallazgos sugerentes de cronicidad del foco de fractura en una FVO y de una radiculopatía compresiva herniaria simultánea exigirá una minuciosa correlación con la clínica referida por el paciente, además de priorizar el tratamiento más necesario o accesible.

En tercer lugar, deben considerarse algunas razones pedagógicas para insistir en el conocimiento radiológico de la anatomía radiológica de la columna vertebral. Como en todo proceso de aprendizaje de un campo complejo, lo ideal es abordar los diferentes objetos de conocimiento de forma ordenada. En este sentido, los radiólogos debemos considerar en primera instancia los grupos de patologías más relevantes en los que clasificar los posibles hallazgos de imagen. Este conocimiento previo resulta de gran ayuda inicial, puesto que se parte de unas nociones fisiopatológicas básicas que permiten homogeneizar las patologías y ordenarlas (p.ej., en función de si son de etiología traumática, inflamatoria, infecciosa, tumoral, variantes anatómicas).

Como es esperable y, en efecto, ocurre, los hallazgos por imagen tienen una asociación relativamente alta con los tipos de patologías. Por ejemplo, las fracturas se caracterizan en general por discontinuidades en la cortical ósea y alteraciones morfológicas del hueso normal, las alteraciones degenerativas darán lugar a cambios como la aparición de osteofitos en el hueso, engrosamientos ligamentarios o fenómenos de deshidratación del

fibrocartílago, la patología inflamatoria tenderá a manifestarse con fenómenos edematosos y reactivos locales, la patología infecciosa incluirá estos fenómenos inflamatorios a los que se podrán sobreañadir colecciones purulentas (formación de abscesos), y la patología tumoral a la formación de masas sólidas. Sin embargo, esta simplificación de la realidad resulta sumamente reduccionista cuando se avanza en el conocimiento de las entidades clínicorradiológicas debido, por un lado, a la complejidad de fenómenos simultáneos que subyacen a las diferentes patologías desde un punto de vista fisiopatológico (piénsese en la coexistencia de fenómenos inflamatorios en las enfermedades infecciosas, traumáticas y tumorales), por otro lado, a la frecuente coexistencia de diferentes patologías en una misma localización anatómica, cosa especialmente común en las FVO (fenómenos traumáticos, inflamatorios y degenerativos), y, por último, a las limitaciones intrínsecas de las pruebas de imagen, que permiten observar un número limitado de alteraciones en función de su naturaleza.

Por último, merece la pena reseñar que no solo es fundamental este conocimiento general de la radiología de la columna; en el caso particular de las FVO se hace necesario ahondar en aspectos más circunscritos del grupo de patologías traumáticas, pues en muchos casos la información clínica es limitada y el informe radiológico aportará orientaciones de gran ayuda en la toma de decisiones (Heller and Fink, 2000). Esto resultará especialmente importante en el diagnóstico de fracturas de etiología no osteoporótica, en fracturas localizadas en segmentos donde las FVO son infrecuentes como la columna cervical, o en casos de FVO mínimas. Siguiendo la línea derivada de la necesidad de profundizar en el conocimiento particular de las fracturas vertebrales, debe hacerse hincapié en la importancia de saber diagnosticar aquellos hallazgos que condicionarán el tratamiento del paciente; en este sentido, existen numerosas clasificaciones en la literatura científica sustentadas en hallazgos que han demostrado tener un valor pronóstico en la evolución clínica de los pacientes con fractura vertebral (compresión medular, pérdida de altura significativa, morfología vertebral, edema óseo, afectación de los diferentes elementos vertebrales), y siguen publicándose estudios con la finalidad de descubrir nuevos factores que condicionen el tratamiento, pronóstico y la monitorización del tratamiento (Curfs et al., 2020). A su vez, esto tendrá repercusiones significativas para los clínicos y cirujanos, y para los propios radiólogos intervencionistas que vayan a tratar mediante cementación percutánea u otras técnicas radioguiadas las FVO. Por todos los aspectos previamente

mencionados, es imprescindible partir de una revisión exhaustiva de los hallazgos de imagen típicos de las diferentes patologías de la columna vertebral.

2.3.2. Diagnóstico por imagen de las fracturas vertebrales osteoporóticas. Aspectos básicos.

La RC juega un papel fundamental en el diagnóstico de las FVO y sigue siendo la prueba inicial recomendada en la mayoría de los casos de sospecha de FVO. Proporciona una visión general de la columna vertebral, permitiendo la identificación de deformidades vertebrales y cambios en la alineación que pueden ser indicativos de una FVO. Además, representan una herramienta de diagnóstico accesible y de bajo costo, lo que las hace particularmente útiles en entornos donde la TC y la RM pueden no estar disponibles o ser económicamente inviables. Sin embargo, es importante recordar que la RC puede infradiagnosticar las FVO, especialmente las que son muy pequeñas o están en una etapa temprana. Por lo tanto, si se sospecha una FVO a pesar de una RC normal, se deben considerar técnicas de imagen más sensibles como la TC o la RM. En la **Figura 5** se muestra un ejemplo de fractura vertebral osteoporótica en RC.

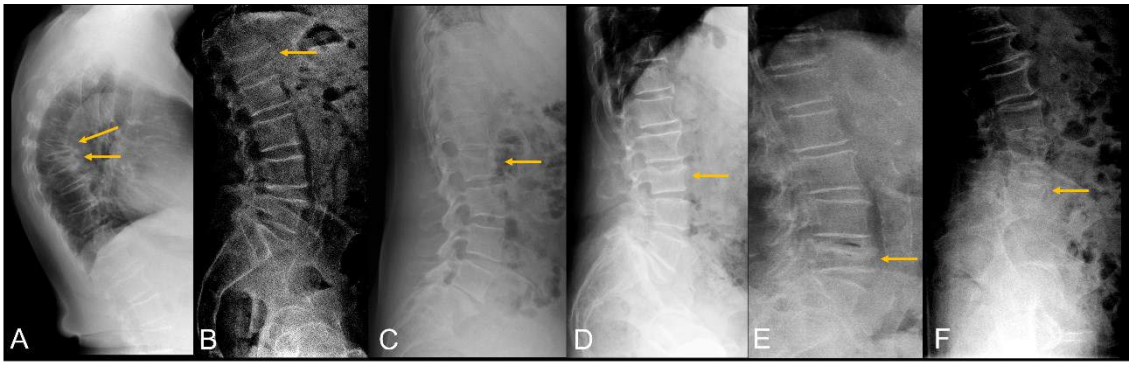

Figura 5. Ejemplos de fracturas vertebrales en proyecciones laterales de radiografía simple (flechas). A. Fracturas vertebrales de D6 y D7 con marcado acuñamiento anterior. B. Fractura de L1. C. Fractura de L2. D. Fractura de L3. E. Fractura de L4. F. Fractura de L5.

En el contexto de pacientes atendidos en el servicio de Urgencias, la prueba empleada cuando existen dudas sobre la presencia de fractura o sus posibles complicaciones es la TC, debido a su mayor disponibilidad y alta resolución. La sensibilidad y la especificidad de esta técnica son significativamente superiores, especialmente si la evaluación de la RC ha sido realizada por observadores inexpertos, algo relativamente habitual en la práctica clínica. Los hallazgos por imagen que deben sugerir una FVO en TC incluyen las discontinuidades focales del córtex en cualquiera de las paredes y el hundimiento de las

plataformas, además de otros signos asociados como la presencia de gas intrasomático o discal, compactación trabecular o quistes o hendiduras subcondrales. Además, permite evaluar de manera precisa las características de la fractura desde el punto de vista morfológico, de densidad y angulación, posibilitando asimismo la obtención de reconstrucciones volumétricas 3D, que pueden exportarse como archivos STL para su posterior impresión 3D (Láinez Ramos-Bossini et al., 2021). En la **Figura 6** se muestra un ejemplo de fractura vertebral osteoporótica en TC.

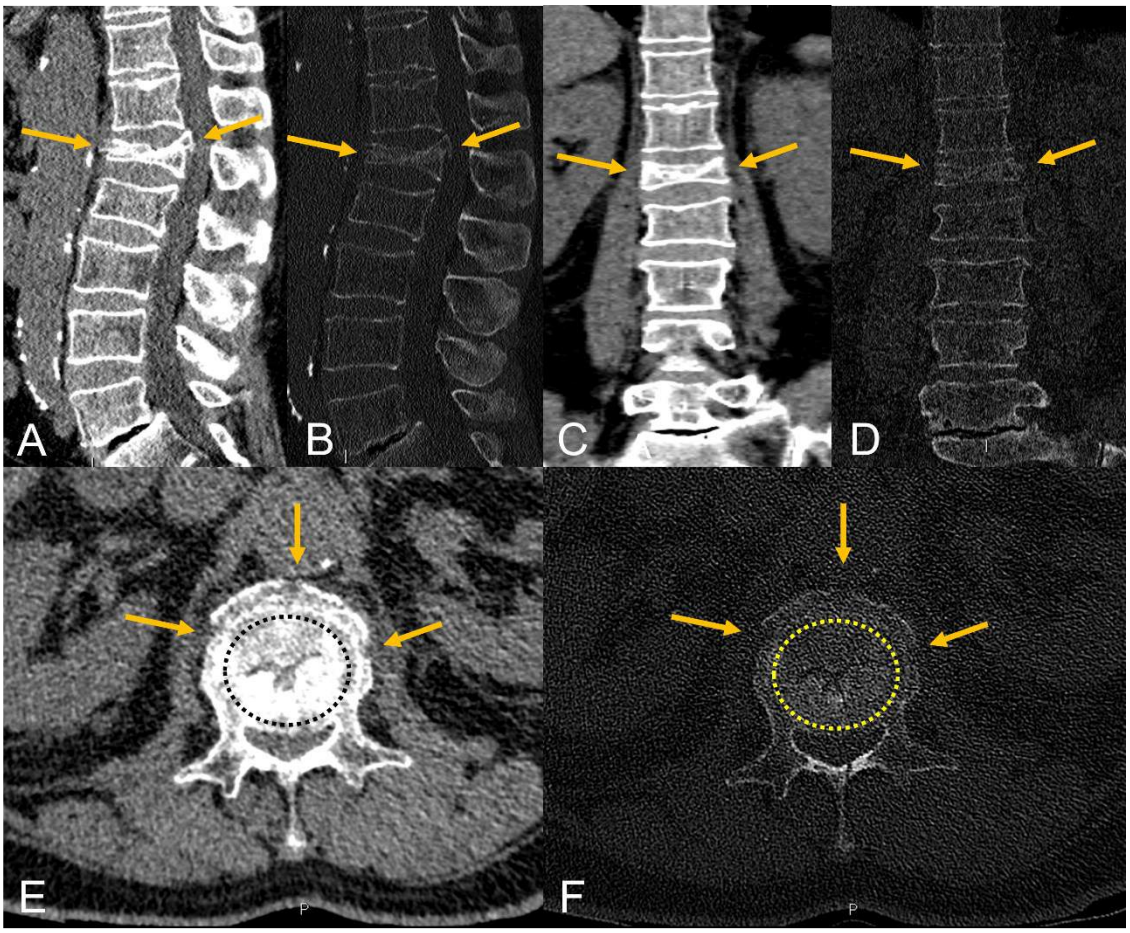

Figura 6. Ejemplo de fractura vertebral de L1 en tomografía computarizada. Imágenes sagitales (A, B), coronales (C, D) y axiales (E, F). En cada pareja de imágenes se muestra el algoritmo de reconstrucción y ventana de partes blandas a la izquierda y el algoritmo de reconstrucción y ventana ósea a la derecha. Se observa una marcada pérdida de altura de la plataforma superior del cuerpo de L1, que adopta una morfología "en cuña" y muestra retropulsión del muro posterior, compatible con fractura (flechas). En las imágenes axiales se señala el foco de fractura intrasomático como un trazo lineal irregular (círculos) y discontinuidades corticales en las paredes anterior y laterales (flechas).

Finalmente, la RM es la técnica más sensible y específica para la detección de FVO, ya que permite la identificación de edema óseo en fracturas sin deformidad asociada. Esto también posibilita monitorizar su evolución y determinar la cronicidad de la fractura, pues

en fracturas crónicas se encontrarán alteraciones del cuerpo vertebral sin edema óseo, o deformidades vertebrales con edema de causa mecánica. Además permite evaluar la relación de la fractura con las estructuras del saco tecal (médula espinal, raíces de la cauda equina), la afectación de otras estructuras como los discos intervertervales y los ligamentos paraespinales, aspectos de gran importancia a la hora de tomar decisiones clínicas, existen secuencias específicas de gran utilidad en la distinción de FVO y fracturas malignas: las potenciadas en difusión (DWI/ADC), T1 o T2 en fase (*in-phase*) y en fase opuesta (*opposed-phase*), además de las secuencias T1 tras la administración de contraste paramagnético (gadolinio) intravenoso. Sin embargo, la resolución espacial es menor en comparación con la TC, y presenta limitaciones para evaluar las corticales en las secuencias habitualmente empleadas en la práctica clínica. En la **Figura 7** se muestra un ejemplo de fractura vertebral osteoporótica en TC.

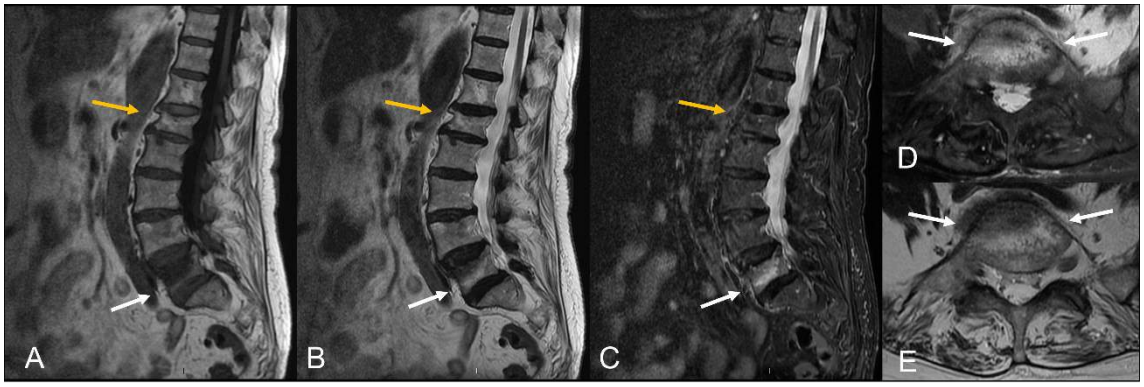

Figura 7. Ejemplos de fractura vertebral en resonancia magnética. Imágenes sagitales de columna lumbar potenciadas en T1 turbo spin-echo (TSE) (A), T2 TSE (B) y *short-tau inversión recovery* (STIR) (C). Imágenes axiales potenciadas en T2 TSE (D) y T2 fat sat (E) a nivel de L5. Fractura crónica de L1 sin edema óseo significativo asociado (flechas amarillas). Fractura aguda/subaguda de L5 con edema óseo significativo en el foco de fractura (flechas blancas).

2.3.3. Abordaje terapéutico de las fracturas vertebrales osteoporóticas

Actualmente existen diversas opciones terapéuticas para el tratamiento de las FVO, que incluyen el tratamiento conservador, farmacológico, técnicas percutáneas y cirugía (Prost et al., 2021). El abordaje conservador se basa en medidas no invasivas que incluyen reposo, analgésicos, fisioterapia y el uso de dispositivos ortopédicos como corsés o fajas. Estas intervenciones suelen ser efectivas en casos de fracturas estables y dolor moderado pero no abordan la causa subyacente de la fractura ni previene futuras fracturas (Ameis et al., 2018). La terapia farmacológica se basa en suplementos de calcio y vitamina D y medicamentos como los bifosfonatos (p.ej., el alendronato y el ácido zoledrónico),

ampliamente utilizados. También se pueden emplear otros fármacos, como los moduladores selectivos de los receptores de estrógeno (p.ej., raloxifeno) en mujeres postmenopáusicas, análogos de la hormona paratiroidea (p.ej., teriparatida) y anticuerpos monoclonales (p.ej., denosumab o romosozumab). Estos medicamentos inhiben los procesos biológicos relacionados con la pérdida de masa y mineralización ósea y disminuyen el riesgo de fracturas (Iolascon et al., 2020).

Por otra parte, los tratamientos percutáneos mediante inyección de cemento biológico, también denominada cementoplastia (vertebroplastia, cifoplastia, vesselplastia), representan abordajes mínimamente invasivos en los cuales se inyecta una sustancia (cemento) biológicamente inerte en la vértebra fracturada, con el objetivo de estabilizar la vértebra y aliviar el dolor (Spivak and Johnson, 2005). La vertebroplastia percutánea (VP) es la modalidad de cementoplastia más antigua y ha demostrado ser eficaz para el manejo del dolor agudo y la mejoría funcional en pacientes con FVO, aunque existen algunas controversias sobre la eficacia de algunas de estas técnicas que serán objeto pormenorizado de análisis en esta tesis.

En cuanto al procedimiento, el paciente se coloca decúbito prono o lateral y se administra anestesia local o sedación general para garantizar su comodidad. Mediante monitorización fluoroscópica, se guía la colocación de las agujas hasta el sitio de la fractura vertebral mediante abordajes trans -, extra- o infrapediculares de forma uni- o bilateral (Ringer and Bhamidipaty, 2013). Una vez que las agujas alcanzan el foco de fractura, se inyecta un cemento acrílico o biológico, generalmente una mezcla de polimetilmetacrilato, que solidifica rápidamente y crea una especie de andamiaje interno que da soporte a la vértebra fracturada, estabilizándola. A medida que se inyecta el cemento, se monitoriza continuamente su distribución para garantizar que se llene adecuadamente el espacio fracturado y que no haya fugas hacia estructuras adyacentes. Después del procedimiento, el paciente se mantiene bajo observación por un corto período de tiempo antes de ser dado de alta. En la **Figura 8** se muestra un ejemplo de VP. La cifoplastia y la vesselplastia son variantes de esta técnica que emplean balones para crear una cavidad en el interior del cuerpo vertebral fracturado antes de la inyección de cemento óseo.

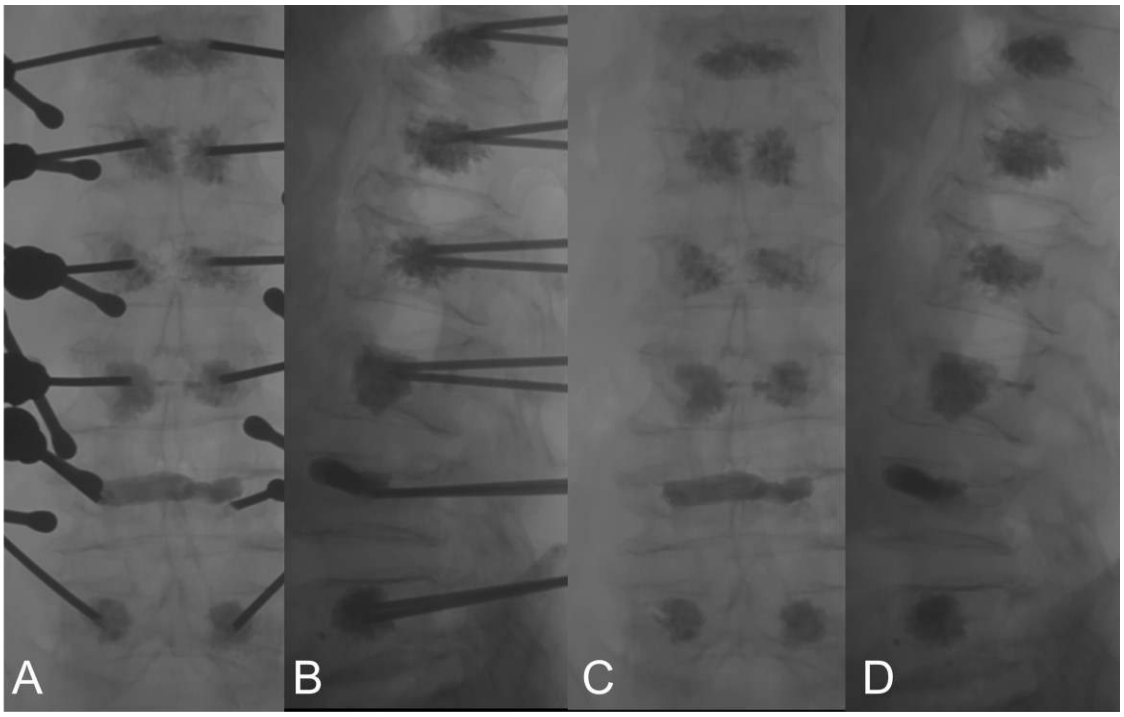

Figura 8. Vertebroplastia percutánea. Inyección de cemento en los cuerpos vertebrales tras posicionamiento de las agujas mediante abordaje transpedicular bilateral (A, proyección posteroanterior; B, proyección lateral). Resultado final tras retirada de las agujas, sin signos de fuga (C, proyección posteroanterior; D, proyección lateral).

Finalmente, en casos graves o cuando las modalidades de tratamiento previas no han sido efectivas, se puede considerar la cirugía. Las opciones quirúrgicas principales incluyen la fusión vertebral, la reparación de fracturas con implantes y la colocación de dispositivos de artrodesis para corregir deformidades y estabilizar el segmento afectado (Takenaka et al., 2014). Estos procedimientos quirúrgicos tienen como objetivo restaurar la estabilidad de la columna vertebral y mejorar la calidad de vida del paciente.

JUSTIFICACIÓN

II. JUSTIFICACIÓN

Los elementos que justifican la línea de investigación sobre los avances en el diagnóstico y tratamiento de las FVO seguida en esta tesis doctoral se pueden resumir en los siguientes puntos:

1. **Evolución del problema de salud**: La elevada prevalencia e incidencia de FVO, que a todas luces ascenderá en los próximos años como consecuencia del envejecimiento de la población, así como la insuficiencia de los tratamientos médicos actuales para la osteoporosis en un número significativo de pacientes, justifican la necesidad de realizar diagnósticos precoces y precisos de este tipo de fracturas. Para ello resulta esencial conocer la anatomía normal y alterada de la columna vertebral en las diferentes técnicas de imagen. Asimismo, es necesario correlacionar los hallazgos radiológicos relativos a los distintos tipos y localizaciones de FVO con variables asociadas a la morbimortalidad de la osteoporosis.

2. **Escasez de revisiones comprehensivas y actualizadas sobre el diagnóstico radiológico de la patología de la columna vertebral y, específicamente, sobre las FVO**: a pesar de que existen diversas revisiones narrativas y pictóricas sobre las patologías de la columna vertebral, son necesarios trabajos que incorporen actualizaciones y sirvan de utilidad para la práctica radiológica habitual. En este sentido, se echan en falta revisiones estructuradas por grupos de patologías que ofrezcan contenido visual claro, con ejemplos reales que frecuentemente ofrecen dudas diagnósticas. Asimismo, en el caso de las fracturas vertebrales y, particularmente, de las osteoporóticas, se hace necesaria la inclusión de sistemas de clasificación útiles para la práctica y destacar las ventajas y limitaciones que ofrecen para el radiólogo.

3. **Necesidad de encontrar factores predictivos de la evolución de las FVO en las pruebas de imagen**: aunque se han publicado varios estudios con el propósito de identificar marcadores de imagen que permitan predecir la evolución de las FVO, su validez en la práctica clínica es escasa. Considerando la capacidad cada vez mayor de diagnóstico precoz de las FVO mediante las pruebas de imagen, el

creciente interés por el desarrollo de clasificaciones útiles para la toma de decisiones y la eficacia diferencial de los tratamientos disponibles en función del perfil de paciente y del tipo de fractura, se hace necesario determinar factores predictivos que permitan una selección óptima de los pacientes, tanto para determinar el tipo de tratamiento (conservador, intervencionista, quirúrgico) como para la monitorización de la evolución de la fractura, especialmente en los casos de tratamiento conservador.

4. **Controversias sobre la eficacia de los tratamientos percutáneos en las FVO**: A pesar de que las técnicas de cementoplastia se utilizan en la práctica clínica desde la década de 1980, se han publicado ensayos clínicos aleatorizados, revisiones sistemáticas y meta-análisis que ponen en tela de juicio su eficacia. Esto es especialmente significativo en el caso de la vertebroplastia percutánea, la técnica más antigua dentro de este grupo de abordajes mínimamente invasivos, donde la revisión sistemática y meta-análisis más reciente publicado en la Cochrane concluye que no existen pruebas de calidad suficientes sobre sus ventajas frente al placebo en términos de alivio del dolor, mejora en la funcionalidad ni en la calidad de vida. Sin embargo, muchos de los estudios en los que se sustentan estas síntesis de la evidencia científica adolecen de limitaciones metodológicas importantes. Se hace, por lo tanto, necesario, profundizar en la evidencia científica disponible y en los posibles motivos que limiten la validez de los resultados encontrados en los ensayos clínicos sobre la eficacia de la vertebroplastia.

HIPÓTESIS

III. HIPÓTESIS

Las principales hipótesis de trabajo que justifican este estudio son las siguientes:

1. El diagnóstico radiológico de las FVO ha experimentado cambios significativos en los últimos años y no existe consenso sobre los sistemas de clasificación más útiles desde el punto de vista clínico y radiológico.

2. La mejor comprensión de la fisiopatología de las FVO permite establecer criterios diagnósticos cualitativos, cuantitativos y semicuantitativos.

3. Es posible determinar factores de riesgo en la evolución de las FVO a partir de hallazgos de imagen en las pruebas radiológicas empleadas de forma rutinaria en la práctica clínica.

4. El tratamiento intervencionista precoz de las FVO en pacientes seleccionados ofrece resultados superiores al tratamiento conservador

OBJETIVOS

IV. OBJETIVOS

El objetivo general de la presente tesis doctoral es revisar y profundizar en los avances radiológicos relativos al diagnóstico y tratamiento las fracturas vertebrales de naturaleza osteoporótica. Como objetivos específicos, se definen los siguientes:

1. Revisar los hallazgos de imagen en RC, TC y RM de las principales patologías de la columna vertebral, y particularmente aquellas que pueden incluirse en el diagnóstico diferencial de las FVO.

2. Determinar qué factores tienen influencia en la evolución clínica y radiológica de las FVO, destacando el tipo de fractura según los diferentes sistemas de clasificación, los parámetros cuantitativos y cualitativos identificables en las pruebas de imagen, y la anatomía de la fractura.

3. Determinar si la vertebroplastia percutánea en las FVO es superior al placebo y al tratamiento conservador, y las potenciales causas de las controversias sobre su eficacia existentes en la literatura científica.

MÉTODOS

V. MÉTODOS

En esta sección se describirá la metodología general utilizada para esta tesis doctoral y los
trabajos que de ella se desprenden, a saber:

- Trabajo 1: The role of radiography in the study of spinal disorders. Se trata de una revisión bibliográfica y pictórica que cubre los objetivos 1 y 2.
- Trabajo 2: The value of magnetic resonance imaging and computed tomography in the study of spinal disorders. Se trata de una revisión bibliográfica y pictórica que cubre los objetivos 1 y 2.
- Trabajo 3: Radiographic diagnosis of osteoporotic vertebral fractures. An updated review. Se trata de una revisión bibliográfica y pictórica que cubre los objetivos 1 y 2.
- Trabajo 4: Diagnóstico por imagen de las fracturas vertebrales de baja energía. Se trata de una revisión pictórica que cubre el objetivo 2 y la parte correspondiente a la RC del objetivo 1.
- Trabajo 5: Vertebral artery dissection secondary to hangman's fracture. Carta al editor sobre los hallazgos de imagen en un caso de complicación tras fractura vertebral de C2 tras traumatismo de baja energía. Cubre parte del objetivo 1.
- Trabajo 6: Factors influencing vertebral collapse in osteoporotic vertebral fractures. Se trata de un estudio de investigación original retrospectivo que cubre el objetivo 2.
- Trabajo 7: Percutaneous vertebroplasty versus conservative treatment and placebo in osteoporotic vertebral fractures: meta-analysis and critical review of the literature. Se trata de una revisión sistemática y meta-análisis que cubre el objetivo 3.

La metodología descrita en esta sección tratará de responder a los objetivos general y específicos planteados y serán detallados en los respectivos artículos (sección Resultados). Los métodos utilizados se pueden agrupar en tres grandes categorías: revisión de la literatura, meta-análisis y estudio de investigación original. Los análisis estadísticos han sido realizados con los programas Review Manager® versión 5.3 y SPSS® versión 23 para Windows.

1. Revisión de la literatura

1.1. Revisión narrativa

Una revisión narrativa es una forma de revisión de la literatura científica que proporciona un análisis exhaustivo, crítico y objetivo del conocimiento actual sobre un tema específico. Esta metodología permite identificar patrones, tendencias y lagunas en la literatura existente, generando un marco teórico para la investigación. La revisión narrativa es una herramienta esencial en el proceso de investigación y puede ayudar a establecer un enfoque o contexto apropiado para el mismo (Ferrari, 2015). Su objetivo principal es proporcionar una comprensión clara del estado actual del conocimiento sobre el tema de investigación y destacar las áreas que requieren más investigación.

El procedimiento recomendado en este tipo de revisiones consiste en recopilar y analizar datos de diversas fuentes, incluyendo estudios de investigación y opiniones de expertos. El objetivo es proporcionar una visión detallada y completa del estado actual del conocimiento sobre el tema de investigación. A través de este proceso, la revisión narrativa puede ayudar a identificar áreas de investigación insuficientemente exploradas y a guiar futuros trabajos de investigación (Rumrill and Fitzgerald, 2001).

Las revisiones narrativas ofrecen varias ventajas. Permiten una visión amplia y completa de un campo de investigación y son flexibles en términos de los tipos de estudios que pueden incluir. Además, las revisiones narrativas pueden ser útiles para generar nuevas hipótesis y teorías (Machi and McEvoy, 2016). Sin embargo, también existen limitaciones. Las revisiones narrativas pueden estar sujetas a sesgos del revisor, ya que la selección y la interpretación de los estudios pueden ser influenciadas por las creencias y expectativas personales del revisor. Además, la falta de un enfoque metodológico estándar puede llevar a variabilidad en la calidad de las revisiones narrativas y a limitar su reproducibilidad. Por último, es posible que las revisiones narrativas no identifiquen todos los estudios relevantes, especialmente si se circunscriben a ciertas bases de datos o términos de búsqueda (Kuhberger et al., 2016), limitación compartida, en mayor o menor grado, con cualquier otro tipo de revisión de la literatura científica.

El proceso de la revisión narrativa comienza con la definición clara del tema de investigación. A continuación, se realiza una búsqueda de la literatura relevante utilizando bases de datos académicas y científicas mediante una o varias combinaciones de palabras clave y términos de búsqueda relevantes para el tema de investigación. En el

caso de los trabajos 1 a 4 se llevó a cabo este proceso en las bases de datos PubMed (Medline), Scopus, EMBASE y Scielo, utilizando las palabras clave “fracture”, “diagnosis”, “imaging”, “spine” y “osteoporosis”. Los estudios identificados se evalúan en función de su relevancia para el tema de investigación, en este caso el diagnóstico por imagen de las patologías de columna vertebral y, particularmente, las FVO. Los criterios de inclusión y exclusión suelen definirse de manera laxa en comparación con otras revisiones; en el caso de los trabajos realizados, dado el amplio espectro de patologías cubiertas, el criterio principal de inclusión consistió en la presencia de descripciones por imagen de las patologías de columna vertebral. Finalmente, la información relevante de los estudios seleccionados se sintetiza para identificar patrones, tendencias y lagunas en la literatura existente, y se presentan de una manera coherente y lógica. En los trabajos 1 a 4 debemos destacar que la revisión narrativa se acompañó de una revisión pictórica profusa, particularmente en los trabajos 1, 2 y 3, cuya metodología se describe en el siguiente apartado.

1.2. Revisión pictórica

Una revisión pictórica es una modalidad de revisión que se caracteriza por ser altamente visual, centrada en imágenes para proporcionar una visión clara y comprensible de un tema determinado (Alesandrini and Rigney, 1981). Este tipo de revisión es particularmente útil en campos donde la interpretación visual es crucial, como ocurre en radiología, por lo que ha servido como sustrato metodológico para los trabajos 1 a 4.

La metodología empleada para realizar una revisión pictórica es similar a la de una revisión narrativa, con la adición de pasos concretos para la selección y presentación de imágenes relevantes. Por lo tanto, la revisión pictórica comienza con la identificación de un tema a abordar, en este caso el diagnóstico por imagen de las patologías de columna vertebral y de las FVO. A continuación, se lleva a cabo una búsqueda exhaustiva de la literatura relevante utilizando bases de datos académicas y otros recursos similares. En los trabajos realizados, esta labor fue realizada por Fernando Ruiz Santiago y Antonio Jesús Láinez Ramos-Bossini en los trabajos 1, 2 y 4, y también por Daniel López Zúñiga en el trabajo 3. Los estudios seleccionados se revisan y se extrae la información relevante, que posteriormente se estructura en apartados pertinentes atendiendo al objetivo general del trabajo. Por último, se seleccionan cuidadosamente las imágenes más representativas o instructivas del tema en cuestión para su inclusión en la revisión (Wcg et al., 2010). En

el caso de los trabajos presentados, todas las imágenes radiológicas incluidas se recuperaron del sistema de información radiológica del Hospital Universitario Virgen de las Nieves, utilizando el visor Carestream Vue® (Phillips), y la imagen de impresión 3D del trabajo 4 se obtuvo con material fotográfico personal. Los elementos visuales añadidos a las imágenes para clarificar y facilitar los elementos de interés se incorporaron con las herramientas de *Impress* (LibreOffice®, https://es.libreoffice.org/descubre/impress/).

Al igual que con las revisiones narrativas, las ventajas de las revisiones pictóricas incluyen la posibilidad de proporcionar una visión general amplia de un tema y la capacidad para identificar tendencias, patrones y brechas en la literatura existente (Alesandrini and Rigney, 1981). Son especialmente útiles para sintetizar y presentar información visual de una manera que puede ser más accesible y atractiva para los lectores. No obstante, las revisiones pictóricas también tienen sus limitaciones; pueden estar sujetas a sesgos de selección y son menos rigurosas que las revisiones sistemáticas en términos de protocolos de búsqueda y evaluación de la calidad del estudio. Además, la presentación de las imágenes es dependiente de la subjetividad del autor. En los trabajos presentados, la revisión conjunta de las figuras por parte de todos los autores resultó de gran utilidad para minimizar este tipo de sesgos subjetivos.

1.3. Revisión sistemática

1.3.1. Metodología general

La revisión sistemática del trabajo 7 se realizó de conformidad con las recomendaciones de las guías *Preferred Reporting Items for Systematic Reviews and Meta-Analyses* (PRISMA) (Page et al., 2021) y se detalla en el cuerpo y material suplementario de dicho trabajo. De manera resumida, tras definir los criterios de inclusión y exclusión de los artículos de interés, se realizó una búsqueda en las principales bases de datos biomédicas (Medline, EMBASE y Cochrane Central Register of Controlled Trials) mediante ecuaciones de búsqueda dirigidas con términos clave, incluidos o no en el MeSH. No se establecieron restricciones en cuanto al lenguaje ni fecha, incluyéndose por lo tanto todos los estudios publicados hasta el momento de realización de la búsqueda (31 de julio de 2020). En el **Apéndice 4** pueden consultarse las estrategias de búsqueda empleadas en cada base de datos. A continuación, se excluyeron los documentos duplicados y dos investigadores (Antonio Jesús Láinez Ramos-Bossini y Daniel López Zúñiga) realizaron

de manera independiente la revisión de los títulos y resúmenes de los artículos obtenidos en la búsqueda, seleccionando aquellos de potencial interés. Finalmente, se procedió a una lectura completa de los artículos para comprobar si se cumplían todos los criterios de inclusión y no se cumplía ningún criterio de exclusión. En caso de discrepancia en la selección de los artículos, un investigador senior (Fernando Ruiz Santiago) resolvió las inconsistencias.

Una vez realizada la selección de artículos, se procedió a la recolección de los datos de interés, que fueron los siguientes: autor, año, publicación, tipo de tratamiento en el grupo de intervención y control, edad y sexo de los pacientes en cada grupo, tiempo de evolución de la FVO y duración del seguimiento. Para la evaluación del objetivo principal del trabajo, se recogieron las puntuaciones de las escalas de interés relativas al dolor (EVA o NRS), discapacidad funcional (RMDQ, ODI) y calidad de vida (QUALEFFO, EuroQoL-5). Además, se recogió información de interés relativa al procedimiento seguido en el grupo de control para realizar análisis de subgrupos. Para la recopilación de datos incluidos en forma de gráficas, se utilizó la versión gratuita de la herramienta *Plot Digitizer*® (http://plotdigitizer.sourceforge.net/).

Las variables fueron agrupadas en función del tiempo en el que fueron medidas como sigue: corto plazo (<3 meses), medio plazo (3-12 meses), largo plazo (>12 meses). Si en algún estudio se midieron las variables de interés en varios momentos dentro de uno de los intervalos definidos en este estudio, se seleccionaron los datos de la última medición realizada en dicho intervalo.

1.3.2. Evaluación del riesgo de sesgos

La herramienta *Cochrane Risk of Bias Tool*® v. 2 fue usada para analizar sistemáticamente la existencia de potenciales sesgos en los estudios incluidos, centrados en diferentes aspectos relativos al diseño, realización y presentación de los resultados de los ensayos. Para cada ensayo clínico se clasificaron los riesgos de sesgos como bajo, intermedio o alto. El sesgo de publicación fue analizado mediante gráficos en embudo (*funnel plots*) para las variables principales de cada estudio. La presencia de un gráfico en embudo truncado se consideró como indicativo de un potencial efecto de estudios pequeños (véase apartado 3.3).

2. Descripción de caso clínico

El trabajo 5 es una carta al editor en la que se comenta el caso clínico de una complicación de fractura vertebral tras traumatismo de baja energía (disección de la arteria vertebral izquierda) en el que se revisan los hallazgos por RM sin contraste intravenoso que permiten detectar dicha complicación. El informe de caso (*case report*) es una forma de publicación científica que tiene como objetivo presentar la descripción de un caso clínico particularmente interesante o poco común. Este tipo de informe se caracteriza por su enfoque descriptivo y detallado, centrándose en la presentación y análisis minucioso de los datos del caso. Por lo general, un reporte de caso incluye información sobre la historia clínica del paciente, los hallazgos físicos, los resultados de las pruebas diagnósticas, el tratamiento y el seguimiento realizado. Además, suele presentar una discusión que analiza el caso en el contexto de la literatura existente, resaltando las características relevantes y las implicaciones clínicas (Târcoveanu et al., 2011).

Los informes de caso son útiles para aumentar el conocimiento científico sobre un tema y puede presentarse de forma más o menos extensa en función de la tipología de artículos que admitan o recomienden las revistas científicas (en este caso, como carta al editor). En primer lugar, brindan la oportunidad de compartir información valiosa sobre situaciones clínicas poco comunes o con características singulares, que pueden ayudar a ampliar el conocimiento médico o científico en general. Además, en muchas ocasiones permiten generar hipótesis o sugerir nuevas áreas de investigación, estimulando el desarrollo de investigaciones posteriores. Asimismo, los reportes de caso permiten a los profesionales de la salud y a los investigadores aprender de experiencias clínicas específicas, lo que puede contribuir a mejorar la práctica clínica y la toma de decisiones (Khan and Arif, 2017).

Sin embargo, los informes de caso también presentan algunas limitaciones. Debido a su naturaleza descriptiva y no experimental, no ofrecen un nivel de evidencia científica tan robusto como los ensayos clínicos o los estudios observacionales. Además, al basarse en casos individuales, existe el riesgo de sesgos y generalizaciones inapropiadas. Por otro lado, la publicación de informes de caso puede estar sujeta a sesgos de publicación, ya que se tiende a reportar más frecuentemente los casos excepcionales o con resultados positivos, dejando de lado aquellos con resultados negativos o menos impactantes (Nissen and Wynn, 2014). A pesar de estas limitaciones, los informes de caso siguen siendo una

valiosa herramienta en la investigación científica, complementando otros tipos de estudios y enriqueciendo la comprensión de la medicina y las ciencias de la salud.

La metodología seguida para la publicación de este caso se sustentó en primer lugar en la detección del interés del clínico y radiológico, que resumidamente consiste en dos aspectos principales: la dificultad de diagnosticas una disección de arteria vertebral sin contraste intravenoso y el consecuente infradiagnóstico de esta complicación, y en la falta de consenso sobre el tratamiento más apropiado en estos casos. A continuación se solicitó consentimiento por escrito al paciente para publicar las imágenes, aspecto fundamental de conformidad con las guías de ética de la publicación científica (Barbour et al., 2016). El siguiente paso consistió en realizar una revisión en la literatura sobre las características principales de la disección de la arteria vertebral (prevalencia, etiología, diagnóstico con particular énfasis en los hallazgos de imagen, tratamiento y pronóstico). Después se estructuró de forma ordenada el contenido del artículo, incluyendo referencias bibliográficas relevantes y apartados pertinentes relativos a los antecedentes que justifican el interés del caso, la presentación del mismo, la discusión derivada de las peculiaridades del caso desde el punto de vista médico, y unas conclusiones apropiadas. Finalmente, se sintetizaron los aspectos fundamentales que revisten interés clínico y radiológico de conformidad con las normas de la revista para el tipo de publicación, en este caso una carta al editor.

3. Meta-análisis

El metaanálisis es una técnica estadística para combinar información de diferentes estudios (Glass, MacGaw y Smith, 1984), proporcionar una estimación global del tamaño del efecto poblacional y analizar las diferencias entre los estudios.

3.1. Obtención de estimadores resumen

Para obtener estimadores resumen, y tras considerar los estudios que presentaron una misma exposición y un mismo desenlace, se procedió a realizar un metanálisis bajo un modelo de efectos aleatorios. Se asumió que los estudios incluidos en el metanálisis no comprenden la totalidad de la evidencia existente, lo que además ayuda a considerar la heterogeneidad entre los estudios seleccionados (Riley et al., 2011). En resumen, dicho modelo asume que el efecto de la exposición varía entre estudios, y estima el promedio de la distribución de dichos efectos. Como consecuencia, los intervalos de confianza

obtenidos como resultado del metanálisis serán más amplios que en el modelo de efectos fijos, el cual asume la homogeneidad entre estudios.

El meta-análisis se realizó utilizando datos secundarios, ya que los datos crudos no estaban disponibles en ninguno de los artículos seleccionados. Las variables recogidas fueron las medias y desviaciones típicas en los grupos de intervención y control para cada variable de interés. Para las variables medidas en distintas escalas, se calculó la diferencia de medias estandarizada con el intervalo de confianza al 95% ($IC_{95\%}$). En el caso de escalas diferentes pero con el mismo rango para la evaluación del dolor, se aplicó el análisis de diferencia de medias, siguiendo el ejemplo del meta-análisis de Shih et al. (2020). Cuando las desviaciones estándar (DE) no estaban disponibles para una variable dada, fueron calculadas mediante el error estándar (EE) usando la fórmula DE= EE· √N; a partir de intervalos de confianza al 95% usando la fórmula $SD = \sqrt{N} \cdot \frac{(L_S - L_I)}{3.92}$ (para muestras mayores a 70 pacientes) o $SD = \sqrt{N} \cdot \frac{(L_S - L_I)}{4.13}$ (siendo L_S y L_I los límites superior e inferior, respectivamente), según las recomendaciones de Cochrane(Higgins JPT, Li T, 2022); o para el rango de valores usando la fórmula DE=f· rango, donde f es un factor de conversión de un tamaño de muestra dado, como se describe en Walter y Yao (2007). Si las DE o los $IC_{95\%}$ no estaban disponibles, los valores de las DE fueron imputados basados en la mediana de las DE de todos los estudios del mismo grupo (Ebrahim et al., 2014).

Una vez obtenidas las medias y desviaciones estándar, se construyeron los diagramas de bosque para cada variable de interés en función de los intervalos temporales preestablecidos correspondientes al corto, medio y largo plazo. Para facilitar la interpretación visual de los resultados, la escala de medida se adaptó a los puntos 2, 5, 10, 20 y 40, atendiendo a los valores de las escalas empleadas en la evaluación de cada variable.

3.2. Análisis de heterogeneidad

Se aplicó el método de la varianza inversa ponderada, usando el estadístico I^2 para analizar la heterogeneidad entre los estudios (no relevante, moderada o considerable, con valores de corte establecidos como $I^2<40\%$, $40\%<I^2<75\%$, e $I^2>75\%$, respectivamente) (Deeks JJ, Higgins JPT, 2022). En caso de duda, se consideró el valor estadístico Q de Cochran (heterogeneidad si valor

p<0,1). Se llevaron a cabo análisis de sensibilidad en los casos de heterogeneidad moderada o considerable (I^2>40%) mediante la eliminación consecutiva de cada estudio para estimar su contribución al conjunto de estudios. Se ejecutaron pruebas a dos colas con el nivel de significación p<0,05.

3.3. Evaluación del sesgo de publicación

Para evaluar el sesgo de publicación se utilizó un enfoque gráfico para analizar el efecto de los estudios pequeños mediante la representación de diagramas de embudo. Según este método, se busca una forma de embudo en el gráfico para garantizar la ausencia de sesgo de publicación. Esto implica que la parte inferior del gráfico debe tener un mayor número de estudios, homogéneamente repartidos a ambos lados del estimador global que marca la línea vertical, y a medida que nos desplazamos hacia arriba, el número de estudios debe ser menor y encontrarse más cerca de la línea vertical. El eje horizontal del gráfico representa la magnitud del efecto medido (el estimador puntual de cada estudio aparece como un punto dentro de la gráfica); la línea vertical divisoria representa el global del meta-análisis y, en el eje vertical, se representa el tamaño de muestra de cada estudio, medido como el inverso del error estándar del estimador (medida de precisión que trata de mostrar indirectamente la calidad de cada estudio). Como resultado, los estudios con mayor tamaño muestral se ubican en la parte superior del gráfico y los estudios más pequeños en la parte inferior. El diagrama en embudo permite analizar de forma visual la existencia de potenciales sesgos de publicación, siendo habitual el sesgo de publicación positiva, donde se observa una asimetría causada por un bajo número de estudios en la parte inferior y derecha de la gráfica debida a la ausencia de estudios publicados con bajo tamaño muestral que resultan favorables al grupo control. Sin embargo, debe tenerse en cuenta que no toda asimetría en el diagrama de embudo es consecuencia de un sesgo de publicación, ya que existen otros factores implicados como la heterogeneidad, el sesgo de información o el azar (Sterne et al., 2011).

4. Estudio de investigación original

4.1. Diseño del estudio

En esta sección, se presentará una descripción detallada del diseño observacional empleado en la investigación original (trabajo 6). Asimismo, se discutirán los principales procedimientos de muestreo utilizados, incluyendo el muestreo consecutivo y por

conveniencia. Por último, se explicará la ausencia de un cálculo del tamaño muestral a priori debido a las restricciones en el reclutamiento de pacientes.

El diseño observacional constituye una aproximación valiosa para la investigación científica en diversas disciplinas, permitiendo la observación y análisis de fenómenos en su contexto natural. En el presente estudio, se utilizó el diseño de series consecutivas de casos con mediciones longitudinales. Este enfoque consiste en la recopilación sistemática y exhaustiva de datos de una serie de casos individuales, permitiendo el seguimiento de variables específicas a lo largo del tiempo.

La elección de este diseño se fundamentó en su idoneidad para explorar la evolución y cambios en las mediciones de interés en el contexto de la población objetivo, así como la factibilidad de emplear este diseño en un contexto clínico. Al emplear mediciones longitudinales, se obtiene información valiosa sobre las trayectorias individuales y las variaciones interindividuales. Esto posibilita el análisis de tendencias, la identificación de patrones y la detección de posibles relaciones causales, aunque este diseño no permite la verificación de hipótesis causales.

En cuanto al procedimiento de muestreo utilizado en este estudio, se empleó un muestreo consecutivo y por conveniencia. El muestreo consecutivo implica la inclusión secuencial de los casos que cumplen con los criterios de selección establecidos, a medida que se van presentando. Esta estrategia se basa en la disponibilidad de los casos en el momento del reclutamiento y ofrece la ventaja de una inclusión continua y constante, evitando sesgos relacionados con la selección arbitraria de los participantes o por motivos determinados. Sin embargo, la ausencia de aleatorización de la muestra supone un posible sesgo de selección, que asumimos por no tener acceso al total de la población de casos que permita realizar esta estrategia. Además, este enfoque permite obtener una muestra razonablemente representativa de la población objetivo en un período de tiempo determinado. Por otro lado, el muestreo por conveniencia se utiliza en situaciones en las que la disponibilidad y accesibilidad de los casos es limitada o restringida. En este caso, los participantes se seleccionan debido a su conveniencia y disponibilidad, lo que puede generar ciertos sesgos y limitaciones en la representatividad de la muestra. Sin embargo, en algunas circunstancias particulares, como en el caso de patologías urgentes o los estudios realizados sin financiación ni recursos, el muestreo por conveniencia puede ser la única opción viable para la investigación.

Es importante destacar que en este estudio no se realizó un cálculo del tamaño muestral a priori. Esta decisión se basó en las limitaciones existentes para el reclutamiento de pacientes. Debido a la naturaleza específica de la población objetivo y las restricciones logísticas, se consideró inviable establecer un tamaño muestral fijo y predeterminado. A pesar de la falta de un cálculo del tamaño muestral a priori, se implementaron medidas para maximizar la validez interna y la representatividad de la muestra dentro de las limitaciones existentes, adoptando criterios de inclusión y exclusión claros y documentando detalladamente las características de los participantes reclutados.

4.2. Extracción de datos y variables de interés

En el caso del trabajo 6 se siguieron las guías *Strengthening the Reporting of Observational Studies in Epidemiology* (STROBE) (von Elm et al., 2014) para la realización de un estudio retrospectivo de casos y controles unicéntrico que incluyó una serie consecutiva de pacientes con FVO aguda de la columna toracolumbar a los que se realizó RC y TC desde enero a septiembre de 2019. Tras aplicar los criterios de inclusión y exclusión descritos en la metodología de dicho trabajo (ver apartado 6.6.), se recogieron diversas variables independientes cualitativas relacionadas con el tipo de fractura en el momento del diagnóstico inicial y al final del seguimiento, incluyendo las clasificaciones morfológica (en cuña, bicóncava, aplastamiento), semicuantitativa de Genant (grado 0, 1, 2, 3), Sociedad Alemana de Ortopedia y Traumatología (OF1, OF2, OF3, OF4, OF5), AOSpine (A1 a A4) y Sugita (hinchado-frontal, en forma de arco, saliente, cóncavo, abollado); y las variables independientes cuantitativas siguientes: edad del paciente, cifosis local, porcentaje de pérdida de área vertebral y de altura anterior, media y posterior, densidad en Unidades Hounsfield de la vértebra fracturada, y ratios derivadas a partir de dichas variables que pueden consultarse en el correspondiente trabajo. La variable dependiente fue el desarrollo o no de colapso vertebral, definido como la pérdida de área o altura mayor del 50% en el control final de la fractura.

Los datos fueron recogidos a partir de los informes radiológicos correspondientes a través de la aplicación informática GSIR de forma retrospectiva, aplicando como criterios de filtro el tipo de estudio (tomografía computarizada de columna dorsal o lumbar), realización en la sala de urgencias e intervalos temporales (enero a septiembre de 2019) y que contuvieran el término clave “fractura” en el cuerpo del informe o en la justificación clínica de la petición electrónica. Para cada informe, se comprobó que correspondía a un

estudio adecuado aplicando los criterios de inclusión y exclusión definidos a priori para el estudio, descartando, en su caso, los que no cumplieran todos los criterios de inclusión y no cumplieran ningún criterio de exclusión. Todas las variables radiológicas fueron medidas por el mismo investigador (Antonio Jesús Láinez Ramos-Bossini), utilizando el visor Carestream Vue® (Phillips). Posteriormente, los datos fueron almacenados en un fichero de datos anonimizado para su tratamiento estadístico.

4.3. Análisis estadístico

Las variables cualitativas categóricas se expresaron como frecuencias absolutas (n) y relativas (%) respecto al total de la muestra y las variables continuas se expresaron como medias y desviaciones estándar. A continuación, se aplicó la prueba de Shapiro-Wilk, un test de bondad de ajuste que permite determinar si una variable cuantitativa sigue una distribución normal mediante la comparación de los valores observados y los esperados bajo la suposición de normalidad. Si el valor p resultante de esta prueba es mayor que un nivel de significación predeterminado (0,05), se considera que los datos siguen una distribución normal (Shapiro y Wilk, 1965). Posteriormente, se realizaron análisis bivariantes, empleando la prueba t de Student para variables independientes en el caso de las variables continuas y la prueba chi-cuadrado de Pearson para las variables cualitativas. La primera es una prueba paramétrica que se basa en la comparación de las medias y la variabilidad de las variables continuas entre los grupos, proporcionando una medida de la significancia estadística de la diferencia entre las medias y se utiliza para determinar si las diferencias observadas son estadísticamente significativas (Student, 1908). La segunda permite determinar si existe una relación significativa entre dos variables categóricas y se fundamenta en la comparación de las frecuencias observadas y esperadas en una tabla de contingencia y genera un valor de chi-cuadrado. Si el valor p asociado a esta prueba es menor que el nivel de significación establecido, se concluye que existe una asociación significativa entre las variables (Pearson, 1900). En este último caso se verificaron las condiciones de aplicación de la prueba antes de realizarla.

Por último, se realizó un análisis multivariante basado en un modelo de regresión logística binaria. El análisis de regresión logística permite evaluar el efecto conjunto de varias variables predictoras sobre la variable de resultado, y proporciona estimaciones de la probabilidad de ocurrencia del evento de interés. La bondad de ajuste del modelo se evaluó utilizando la prueba de Hosmer-Lemeshow, que determina cómo se ajusta el

modelo a los datos observados (Hosmer and Lemeshow, 2005). Para el análisis discriminante se utilizaron curvas ROC (Receiver Operating Characteristic), herramientas gráficas utilizadas para evaluar la capacidad de un modelo de clasificación para distinguir entre dos clases o estados. Representan la relación entre la tasa de verdaderos positivos (sensibilidad) y la tasa de falsos positivos (1-especificidad) con diferentes puntos de corte. La curva ROC proporciona información sobre la precisión y el rendimiento general del modelo (Swets, 1988). En todos los casos se consideró un valor de significación $p<0,05$.

RESULTADOS

VI. RESULTADOS

La presentación de los Resultados se divide en función de los 7 estudios que se han desarrollado durante la presente Tesis Doctoral. Cada estudio ha sido diseñado independientemente de los demás. En aras de la claridad mostraremos en esta sección los estudios completos con sus propias secciones de introducción métodos, resultados, discusión y referencias. El estudio 6 ha sido enviado para publicación y actualmente se encuentra en proceso de revisión, por lo que se presenta el manuscrito enviado a revista.

TRABAJO 1: THE ROLE OF RADIOGRAPHY IN THE STUDY OF SPINAL DISORDERS.

Ruiz-Santiago F, **Láinez Ramos-Bossini AJ**, Wang YXJ, López-Zúñiga D. The role of radiography in the study of spinal disorders. Quant Imaging Med Surg. 2020;10(12):2322-2355. doi: 10.21037/qims-20-1014. FI: 3,837. Q2 (T1).

Se trata de una revisión bibliográfica y pictórica que cubre los objetivos 1 y 2.

Review Article

The role of radiography in the study of spinal disorders

Fernando Ruiz Santiago[1], Antonio Jesús Láinez Ramos-Bossini[1], Yì Xiáng J. Wáng[2], Daniel López Zúñiga[1]

[1]Department of Radiology, Neuro-traumatology Hospital, Hospital Virgen de las Nieves, University of Granada, Granada, Spain; [2]Department of Imaging and Interventional Radiology, the Chinese University of Hong Kong, Prince of Wales Hospital, Shatin, New Territories, Hong Kong, China

Correspondence to: Fernando Ruiz Santiago. Department of Radiology, Neuro-traumatology Hospital, Hospital Virgen de las Nieves, University of Granada, C-Julio Verne 8, 7 B, 18003 Granada, Spain. Email: ferusan12@gmail.com.

Abstract: Despite the growing use of computed tomography (CT) and magnetic resonance imaging (MRI) in the study of spinal disorders, radiography still plays an important role in many conditions affecting the spine. However, the study and interpretation of spine radiograph is receiving less attention and radiologists are increasingly unfamiliar with the typical findings in normal and pathologic conditions of the spine. The aim of this article is to review the radiologic indications of radiograph in different pathologic conditions that affect the spine, including congenital, traumatic, degenerative, inflammatory, infectious and tumour disorders, as well as their main radiographic manifestations.

Keywords: Spine; radiography; back pain; spinal disorder; spinal curvature; osteoporotic fracture

Submitted May 05, 2020. Accepted for publication Aug 31, 2020.
doi: 10.21037/qims-20-1014
View this article at: http://dx.doi.org/10.21037/qims-20-1014

Introduction

The simplest and most accessible technique in the department of radiology is conventional radiography. Paradoxically, clinicians and radiologists are losing their interest in interpreting radiographs, relying more in the source of information provided by tomographic techniques, such as computed tomography (CT) and magnetic resonance imaging (MRI). Although radiography in the digital format remains as one of the most frequently employed techniques in the study of spinal pain, both its role and importance have greatly changed with the widespread use of CT and MRI.

Because CT and MRI have displaced radiography in the study of many spinal conditions, radiographic signs of spinal conditions have become increasingly less studied and thus less known among clinicians and radiologists. The aim of this narrative review is to review the diagnostic findings that radiography may provide in the study of spinal disorders and their role in patient management.

General indications for spine radiographs

Leaving aside extraspinal causes, the most frequent origin of spinal pain is classified as "non-specific" (70%) because the specific nociceptive source cannot be identified, although it is supposedly related to sprain and/or strain of the soft tissues (1). In this setting, no imaging studies are recommended (2). Mechanical back pain is considered the second most prevalent cause (27%) and includes degenerative disorders of the spine, alignment abnormalities and vertebral fractures. In this case, radiographs are recommended as the initial imaging study in patients with history of low-energy trauma and in patients with suspicion of vertebral compression fracture, such as osteoporotic patients or those receiving steroids. Flexion and extension radiographs may also be useful in assessing spinal stability. Finally, back pain may be secondary to specific causes, such as infection, inflammatory or tumor conditions; in this group, radiographs are still recommended to evaluate young patients for ankylosing spondylitis (3).

In children with back pain, algorithms have been developed to avoid unnecessary radiation exposure (4,5). As with adults, non-specific pain is the most common cause of back pain. Therefore, in pain of short duration and no red flags, no imaging is indicated (5). When persistent pain or red flags are present (e.g., fever, trauma, history of malignancy), radiography is still considered the first imaging modality. In some reported studies, radiograph demonstrated abnormalities in approximately 8–13% of paediatric patients with back pain (5-7). However, in patients with an underlying pathology confirmed by other imaging methods, radiographs showed abnormalities in 26–76% of cases, helping therapy guidance or directing further imaging studies (6-8). The most common diagnoses are spondylolysis, spondylolisthesis, Scheuermann's kyphosis, indirect signs of disc pathology, infectious and neoplastic conditions (5,7). Anterior-posterior and lateral radiographs showed a sensitivity of 77.6% for the detection of spondylolysis (9). Radiographs also play a key role in the diagnosis and management of abnormal spine curvature, including scoliosis and kyphosis. Regarding disc pathology, radiography is not sensitive to early changes or disc displacement. Studies using MRI reported a greater frequency of disc pathology undetected by radiography in children (5). Finally, when specific causes of back pain (e.g., tumour or infection) are suspected, radiographs have low sensitivity and can often miss subtle findings (6). If the clinical history, physical examination, and radiographs do not lead to any specific diagnosis, MRI is advocated as the next diagnostic exam because of its high sensitivity to depict the spinal and paraspinal soft tissues, disc and vertebral abnormalities associated to back pain (5).

Congenital pathology

Congenital alterations of the spine can be simple, when there is no associated spinal deformity or have little or no clinical consequence, or complex, when associated with serious deformities such as kyphosis, lordosis or scoliosis, or have neurologic implications (10). Congenital vertebral anomalies can be secondary to defects involving vertebral formation, vertebral segmentation or both (11). In the first case, all or part of the vertebra is not well formed/developed, leading to deformities such as agenesis, hemivertebrae, wedged or butterfly vertebrae (*Figure 1*). In the second case, the embryonic vertebrae are not separated resulting in congenital vertebral block formation. Typical signs that allow differentiation of congenital from acquired vertebral block are the preservation of normal vertebral height of the affected vertebral bodies and the narrow waist of the union between both vertebrae, due to the lack of formation or development of the epiphysial rings at the level of the absent disc. This is known as the wasp-waist sign (12). Combined cases include complex congenital syndromes such as Klippel-Feil, Jarcho-Levin, or Goldenhar, etc. (13,14) (*Figure 1*).

Among patients with congenital spine deformities, 80% had a scoliosis, 14% had a kyphoscoliosis, and 6% had a pure kyphosis. Hemivertebra is the most common cause of a congenital scoliosis followed by unilateral unsegmented bar. An anterior failure of vertebral body formation is the most common cause of congenital kyphosis or kyphoscoliosis (11). It has been classified into posterolateral quadrant vertebra (35%), posterior hemivertebra (7%), butterfly vertebra (13%) and anterior wedged vertebrae (5%) (15).

Radiography is usually the first imaging method to study congenital vertebral abnormalities and related deformities, allowing their classification, evaluation of severity and assessment of risk of progression (16). As the number of bony malformations increases, there is a higher incidence of cord anomalies ranging from 20% to 58% (16-18) and being greater in the presence of combined failures of segmentation and formation (18). MRI is the appropriate technique for complete evaluation of intraspinal abnormalities. CT may also be useful in defining the anatomy of vertebral deformities in pre-surgical planning (19).

Among the simple congenital abnormalities, transitional vertebra is considered a developmental variance that is present in <25% of the population (20-22) (*Figure 2*). The most frequent presentation (around 17% of the cases) is sacralisation of L5 which is fused to the sacrum, followed by lumbarisation (around 2% of the cases), in which S1 is detached from the sacrum. Radiographs of the entire spine, if available, allow the radiologist not only to count vertebral bodies from C2 down, but also to differentiate hypoplastic ribs from lumbar transverse processes (21). In our clinical practice in Granada, Spain, we frequently use both, the AP radiograph of the chest and the radiograph of the lumbar spine, to achieve the same purpose. Identification of the correct vertebral level is essential when spinal surgery is planned (22). The association between transitional vertebra and lumbar pain, i.e., Bertolotti syndrome, is controversial, but there is more consensus on the higher prevalence of degenerative changes of the disc and facet joints at the superior level of the transitional vertebra, as a consequence of the increased stress at the closest mobile segment to the

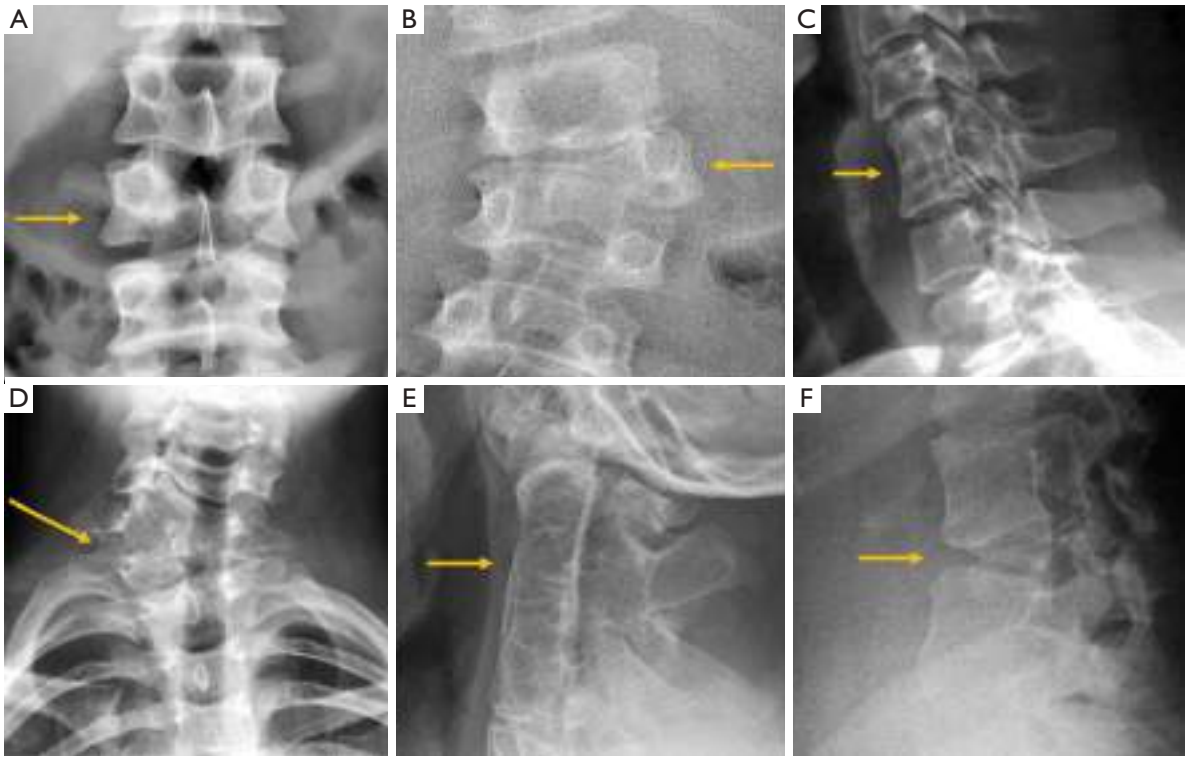

Figure 1 Congenital abnormalities in different patients. (A) Butterfly vertebra; (B) hemivertebra; (C) vertebral block. Complex abnormalities in Klippel Feil (D) and Jarcho-Levin (E) syndromes. (F) Kyphotic deformity secondary to anterior failure of vertebral body formation. Arrows point the main abnormality in each case.

fused transitional vertebral (22).

Transitional anomalies can also affect the cervicothoracic junction. Cervical ribs are the most frequent transitional abnormality and have been described associated with lumbar sacralization. Another less well-known transitional anomaly is the elongation of the anterior tubercle of the cervical transverse process, which may lead to fusion between two vertebrae, typically between C5 and C6 (23) (*Figure 2*).

Traumatic pathology

Radiographs have largely been superseded by CT for the assessment of traumatic cervical spine injury (24). The sensitivity of radiographs compared with CT ranges from 36% to 65% (25,26). Therefore, most guidelines recommend CT as the initial radiological examination when traumatic injury to the cervical spine is suspected, preserving MRI for selected cases with neurological compromise or ligament injury (6,27,28).

Imaging of the cervical spine is indicated if the patient meets at least one of the 5 criteria of the National Emergency X-Radiography Utilization Study (NEXUS), developed with data from 21 centres across the United States (29). The more complex Canadian C-Spine Rule (CCR) clinical criteria can also be used to determine the need for imaging in cervical spine trauma (30).

Despite the many advantages of CT, in hemodynamically stable patients, radiographs may be appropriate in some clinical scenarios and in low risk patients (6,31) to guide in pre-operative planning or follow-up control after medical or surgical treatment. Therefore, interpreting radiographs in the context of traumatic cervical spine is still important for radiologists. The lateral radiograph is the most important view in this context, and interpreting it correctly helps to elucidate bone anatomy and alignment (*Figure 3*). When examining a lateral radiograph of the cervical spine, there are 5 lines that should be observed to rule out spinal fracture or dislocation. From front to back, these correspond to the

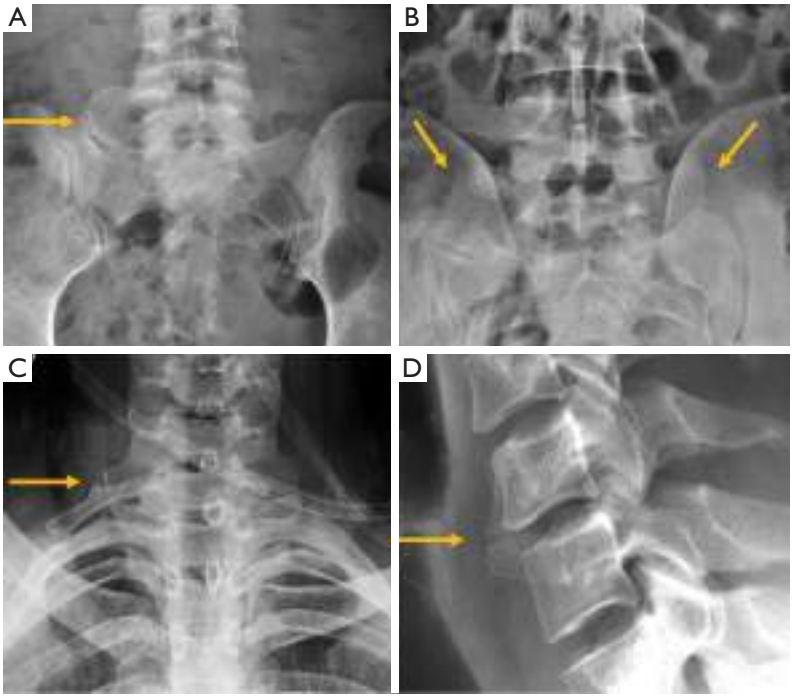

Figure 2 Transitional abnormalities in different patients. (A) Sacralisation; (B) lumbarisation; (C) cervical rib; (D) elongation of the anterior tubercle of the cervical vertebral transverse process. Arrows point the main abnormality in each case.

prevertebral soft tissues, the anterior vertebral, the posterior vertebral, the spinolaminar and the supraspinous lines. Notably, disruption of the posterior vertebral line has the greatest clinical implications due to its proximity to the spinal cord (*Figure 3*). Also, on a well-positioned lateral radiograph, the anterior arch of the normal atlas shows a crescent shape. Finally, the utility of flexion and extension films to evaluate ligamentous injury is debatable but is still employed in a significant number of trauma centres to diagnose posttraumatic instability (31). Nevertheless, the routine and selective use of functional radiographs is questionable as pathological findings are rare (32).

In traumatic thoracolumbar fractures, the reported sensitivity of radiographs ranges from 49% to 62% at the thoracic level and from 67% to 82% at the lumbar level (33-35). In addition, the severity of vertebral fractures may be underrated in radiographs, with up to 25% of burst fractures misdiagnosed as wedge compression fractures (36). Therefore, CT must be performed even after detection of a vertebral fracture in radiographs for proper grading. Nevertheless, it is important to be aware of the radiological signs that allow the diagnosis and grading of severity of traumatic fractures, mainly because there is no current universal availability of CT or MRI and thus radiologists may have to deal with radiographs of trauma patients in an emergency setting. A vertebral fracture is considered as a burst fracture when the posterior vertebral wall is affected. Signs associated with severity and instability of burst fractures include widening of the interpedicular distance, widening of the interspinous distance (manifested in AP radiographs as the "empty vertebra" sign) and the presence of horizontal fracture in the pedicles (*Figure 4*).

Osteoporotic vertebral fracture (OVF)

Osteoporosis is a systemic skeletal disease characterised by a reduction in bone mass and qualitative skeletal changes (macro- and microarchitecture, material properties, geometry, and micro-damage) leading to increased bone fragility and fracture risk. There are two forms of the disease: (I) primary osteoporosis, which includes juvenile, postmenopausal, and male and senile osteoporosis; and (II) secondary osteoporosis, which is caused by a large number of diseases and medications. Fragility fractures may occur in

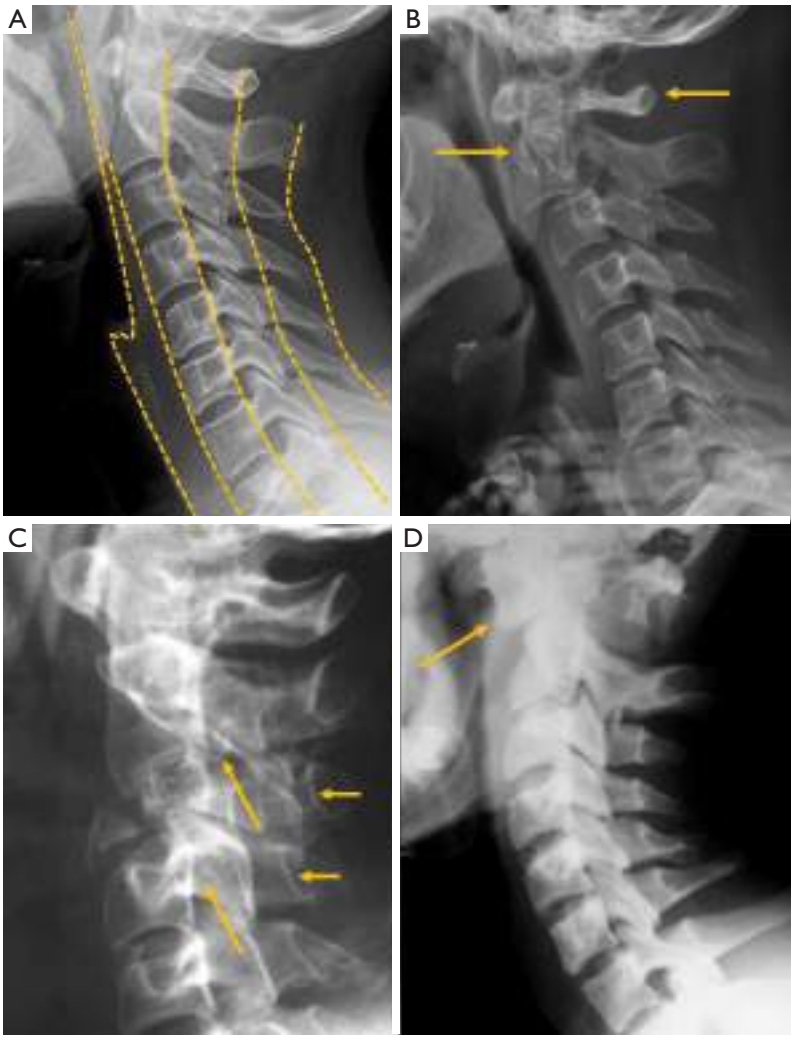

Figure 3 Traumatic pathology of the cervical spine. (A) The 5 normal lines to check in lateral radiographs of the cervical spine; (B) the same patient of A after a car crash suffered a fracture of the C2 pedicles (hangman's fracture) and radiography shows the anterior displacement of the C2 vertebral body and atlas (arrows); (C) C3 burst fracture with disruption of the posterior vertebral and spinolaminar lines (arrows); (D) lateral radiographs showing loss of the normal crescent shape of the anterior arc of the atlas in a patient with rotatory subluxation of the atlas (arrow).

almost all skeletal segments, but the preferential locations are the vertebral column, the proximal ends of the femur and humerus, and the distal end of the radius (Colles fracture). Trauma due to a fall is by far the most frequent cause of fractures affecting long bones (femur, humerus, and radius), while it is more difficult to determine the cause and the exact time of fragility fractures of the vertebral body, which often go undiagnosed. OVF has high prevalence in the elderly population. It affects at least one-fourth of all postmenopausal women, and is commonly seen among women approximately one decade after menopause (37). It is estimated that the prevalence of OVF in elderly men is approximately half of that in age matched women (38). A vertebral fracture, after minor trauma, is a hallmark of osteoporosis.

The detection of OVF in women suggests that the patient's bone strength is compromised, and the risk of future fracture is substantially increased, both for further OVFs and non-vertebral fragility fractures including the hip (39-43).

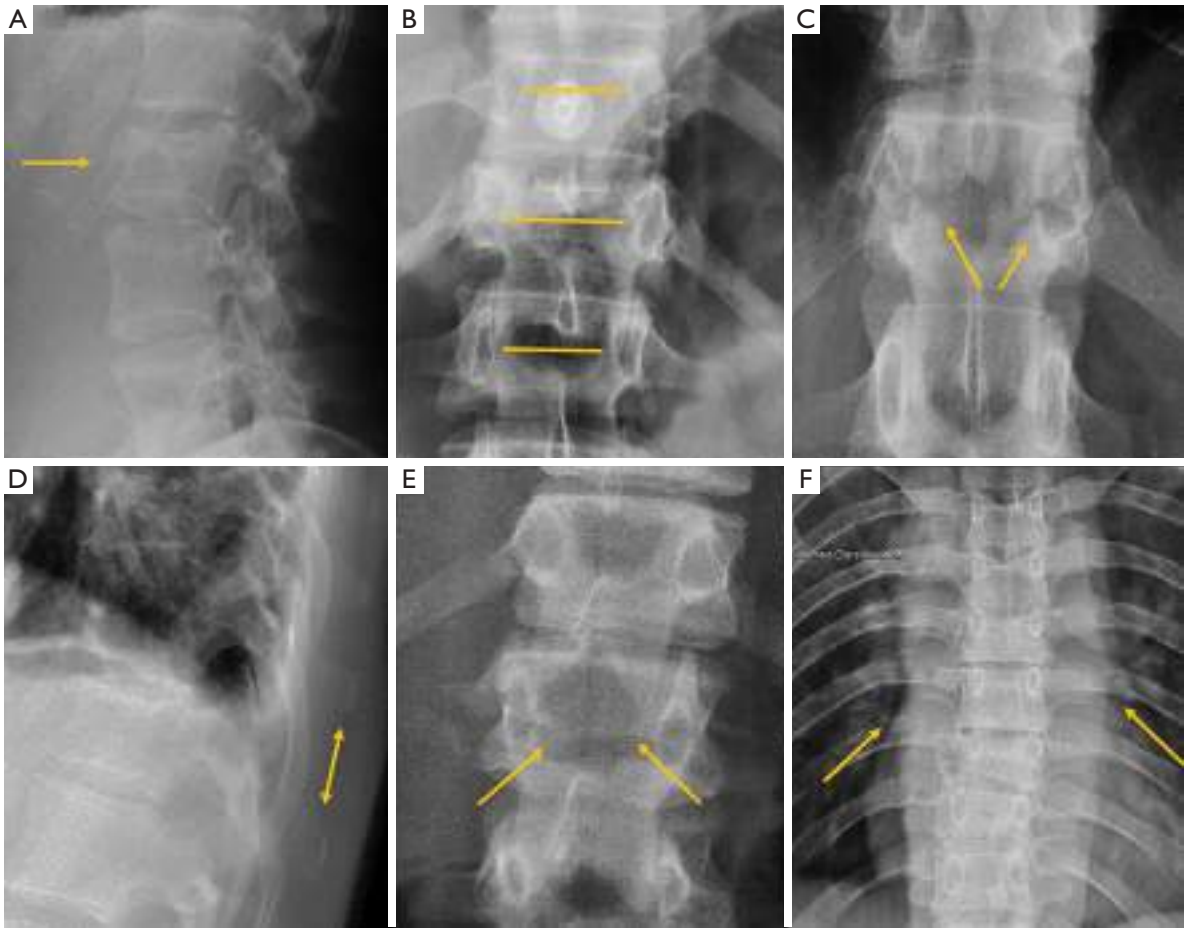

Figure 4 Traumatic pathology of the thoracolumbar spine. (A) Post-traumatic wedge compression fracture; (B) increased interpedicular distance in burst fracture; (C) horizontal fracture through the pedicles; (D) increased interspinous distance; (E) empty vertebra sign; (F) paravertebral haematoma. Arrows point the main abnormality in each case.

OVFs can be associated with decreased trunk extension torque, spinal motion, functional reach, mobility skills and walking distance, and may also influence mortality because of their association with chronic back pain, immobility and postural change (38,41,43). Multiple and more severe grades of OVFs are associated with an even greater fracture risk (41-43). Hip fractures have highly detrimental and very costly individual and social repercussions, and in women over 55 years and older, they are responsible for more hospitalisations than heart attacks, strokes, and breast cancer combined (44). Advances in understanding the biology of osteoporosis have resulted in several medications that have been demonstrated to reduce fracture risk (45,46). Nonpharmacologic approaches to manage osteoporosis, including adequate calcium and vitamin D intake and physical activity, can positively affect bone mass. Coupled with preventing falls and limiting modifiable risk factors, such as smoking and alcohol use, these measures can help reduce the risk for osteoporotic fractures (41,43).

OVF may often be relatively asymptomatic. In the MrOS (USA) follow-up study, Ensrud *et al.* (47) reported that 13.5% of incident radiographic OVFs in elderly men were also clinically diagnosed as incident fractures. In postmenopausal women included in the Fracture Intervention Trial Research study, Fink *et al.* (48) reported that about 25% of incident radiographic OVFs were also diagnosed as clinical VF in women. Patients presenting with back pain typically report sudden or acute onset of pain in

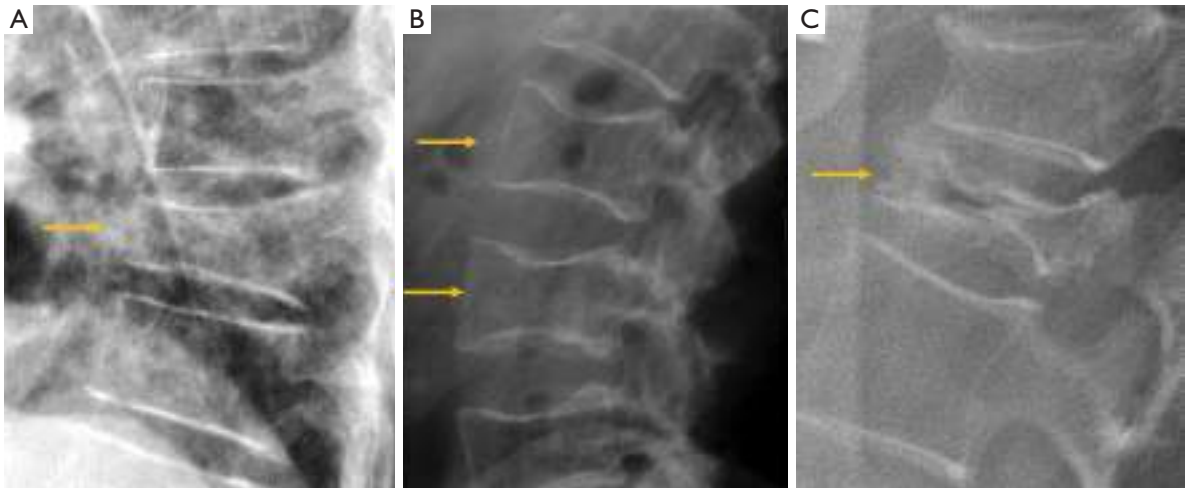

Figure 5 Types of osteoporotic vertebral fractures according to Genant's classification. (A) Wedge; (B) biconcave (with endplates depression); (C) burst fracture. Note the intravertebral vacuum phenomenon in (C). Arrows point the main abnormality in each case.

temporal relationship with relatively atraumatic activities such as bending forward, standing from a seated position, or even with vigorous coughing or sneezing (49). In the absence of localising symptoms, spinal fracture status is usually determined by obtaining lateral radiographs of the spine (50). Low-energy fractures of the spine due to osteoporosis can be detected in radiographs based on their morphologic changes. An alternative method called vertebral fracture assessment (VFA) by DXA (dual-energy X-ray absorptiometry) devices is also available (51). The VFA quality imaging is lower, and the interpretation may be challenging. It is important to identify and report OVF, so that appropriate investigation and treatment can be instigated.

The most frequent site of OVF involvement is the thoracolumbar junction, with the second most frequent region being the midthoracic spine. Vertebral fracture can occur among osteoporotic patients in three possible scenarios: (I) minimal energy trauma which is not noted by patients, (II) low-energy trauma which is defined as forces equivalent to a fall from a standing height or less, and also (III) high-energy trauma. In high-energy trauma the vertebra will fracture even in the absence of osteoporosis, but because the vertebra is osteoporotic, the trauma-induced deformity (i.e., the extent of damage to the vertebra) will be more extensive. Most typical OVFs in epidemiological studies appear as concave deformity, with vertebral middle height loss greater than vertebral anterior height (52-54), which are more associated with minimal traumas unnoticed by the patients. However, in clinical practice OVFs can have various appearances (*Figure 5*), and at least a portion of OVFs may be like traumatic VFs when a low-energy trauma event is involved. Wang *et al.* discussed the endplate fracture differences between OVF and traumatic VF. They noted that traumatic VFs rarely have lower endplate fracture without simultaneously having upper endplate fracture (55). Vertebral fractures due to lower energy trauma or high-energy trauma are likely to be seen in their acute or sub-acute phase in the orthopaedic department or back pain clinics, while OVFs due to minimal energy trauma are more likely to be detected incidentally when undergoing other imaging examinations, or the patients are referred for routine OVF assessment.

Multiple classification systems for OVF have been proposed without general acceptance of a single system to date. The Sugita's classification which considers both deformity and cortex fractures, includes 5 types: swelled-front, bow-shaped, projecting, concave and dented (56) (*Figures 6*,*7*). The author observed that the first three types had a poor prognosis, with a higher incidence of late collapse, frequently showing an intravertebral cleft that can be detected in radiographs as an intravertebral vacuum phenomenon. This observation has been supported by the work of Ha *et al.* (57), who noted that a mid-portion type fracture is a relative risk factor for progressive collapse following the acute fracture event. Sugita *et al.* suggested that mid-portion type fractures lead to vascular injury as

Quantitative Imaging in Medicine and Surgery, Vol 10, No 12 December 2020

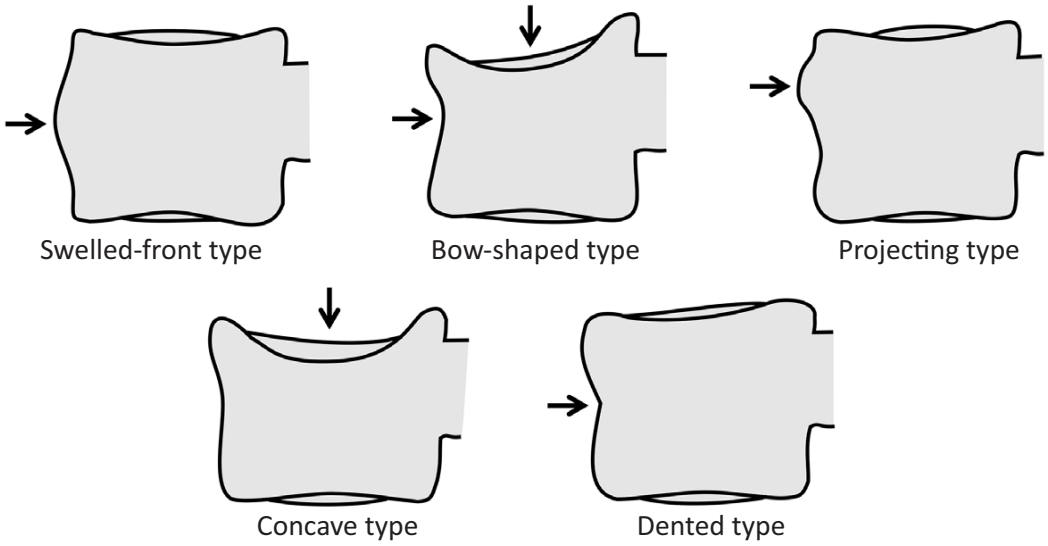

Figure 6 Classification of acute vertebral compression fractures in the elderly according to Sugita *et al.* Modified from (56).

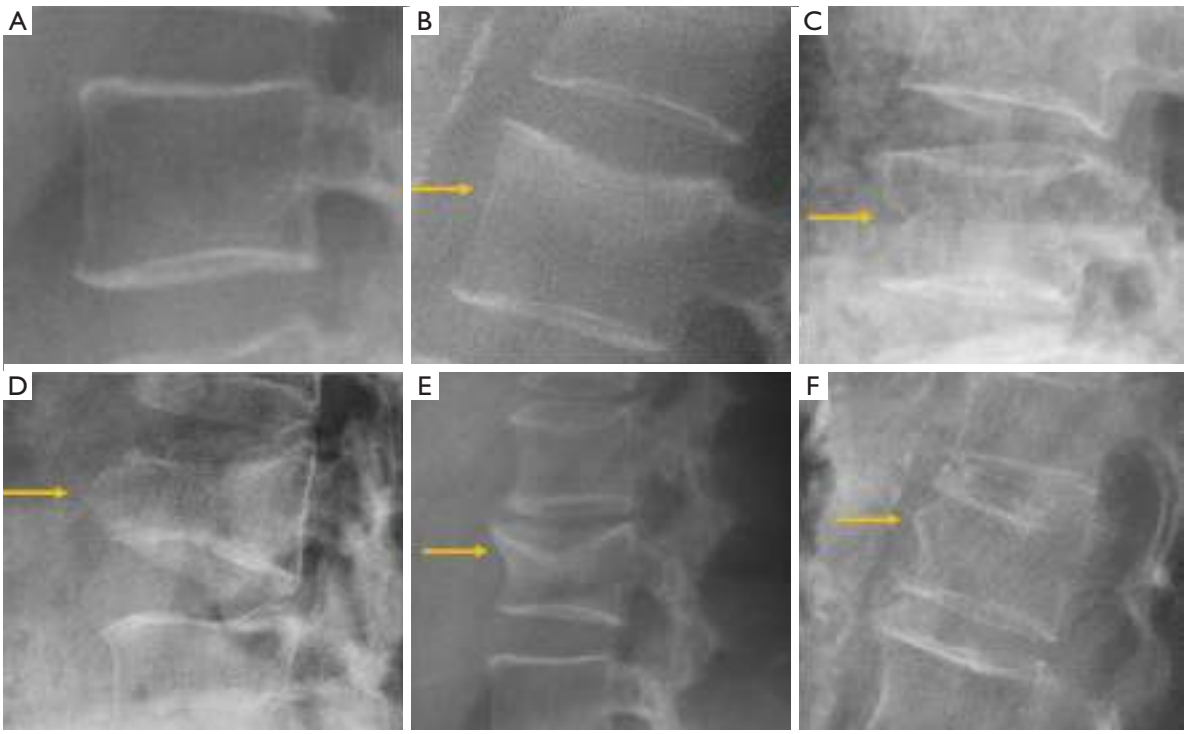

Figure 7 Types of osteoporotic vertebral fractures according to Sugita's classification. (A) Normal; (B) concave; (C) dented; (D) swelled-front; (E) bow-shaped; (F) projecting. Arrows point the main abnormality in each case.

 Quant Imaging Med Surg 2020;10(12):2322-2355 | http://dx.doi.org/10.21037/qims-20-1014

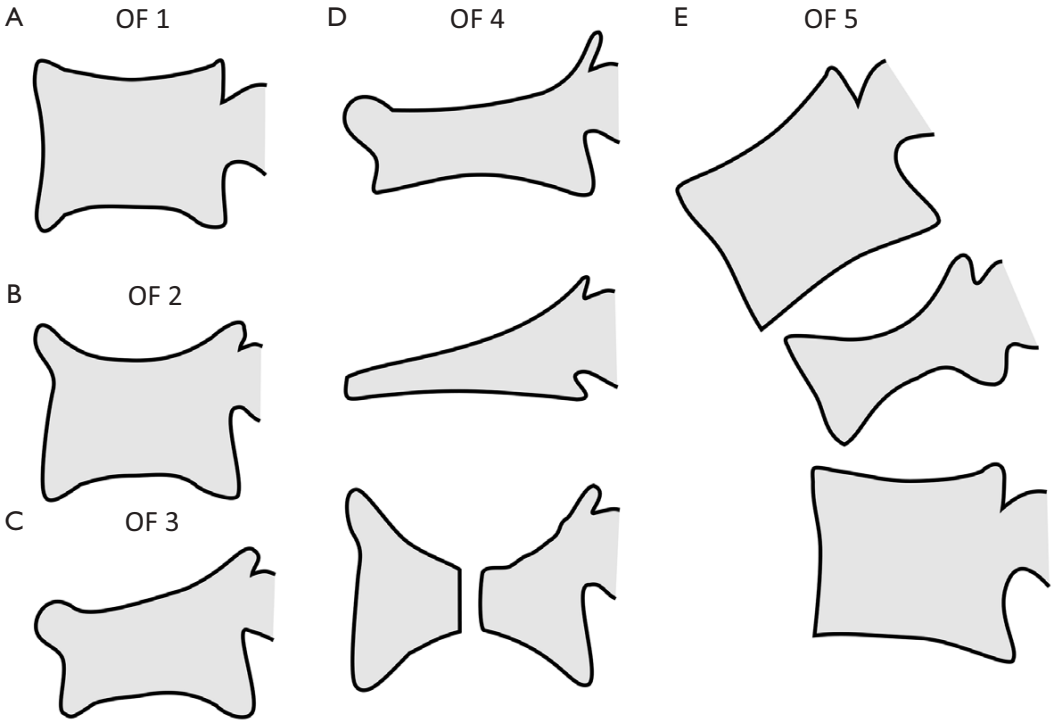

Figure 8 The German Society for Orthopaedics and Trauma (DGOU) Classification of Osteoporotic Thoracolumbar Spine Fractures: (A) Type 1 (OF 1) non deformity; (B) Type 2 (OF 2) deformation with minor involvement of the posterior wall; (C) Type 3 (OF 3) deformation with distinct involvement of the posterior wall; (D) 3 examples of Type 4 (OF 4) loss of integrity of vertebral frame architecture or pincer-type fracture; (E) Type 5 (OF 5) injuries with distraction or rotation. Modified from (59).

opposed to endplate type fractures (56). These works can be summarised by the rule that acute OVFs with anterior cortex fracture seen in the orthopaedic department are more likely to develop further collapse. In their series, Sugita *et al.* found that OVFs of swelled-front-type (13.1%), bow-shaped-type (28.6%), and projecting-type fractures (16.7%), all of which were of mid-portion type, counted for 58.3% of the total VFs, while the concave type counted for 32.1%. They also noted that concave-type fractures mostly occurred without specific trauma, whereas swelled-front-type fractures resulted from apparent accidents. Ha *et al.* reported that 11 of their 75 VFs were mid-portion type fractures (14.7%). On the other hand, Lentle *et al.* (58) reported that only 5% of their epidemiological study participants had 'anterior cortex buckling'. Recently, the German Society for Orthopaedics and Trauma proposed a classification system for Osteoporotic Vertebral Body Fractures (59) (*Figures 8,9*). It offers a comprehensive score of the type of fracture and clinical factors to decide between medical or surgical treatment. A score of more than 6 points may result in surgical management (60). This classification includes five types of vertebral fractures. OF (osteoporotic fractures) 1: No vertebral deformation (vertebral body oedema on MR fat-suppressed image only). The stable injury is clearly visible on fat-suppressed image only. X-rays and CT scan do not show vertebral deformation. OF 2: deformation with no or only minor involvement of the posterior wall (<1/5). This type of fracture affects one endplate only (impression fracture). The posterior wall can be involved, but only slightly. OF 2 are stable injuries. OF 3: deformation with distinct involvement of the posterior wall (>1/5). This type of fracture affects one endplate only, but shows distinct involvement of the anterior and posterior wall (incomplete burst fracture). The fracture can be unstable and may collapse further over time. OF 4: loss of integrity of the vertebral frame structure, or vertebral body collapse, or pincer-type fracture. This subgroup consists of 3 fracture types. In case of loss of integrity of the vertebral

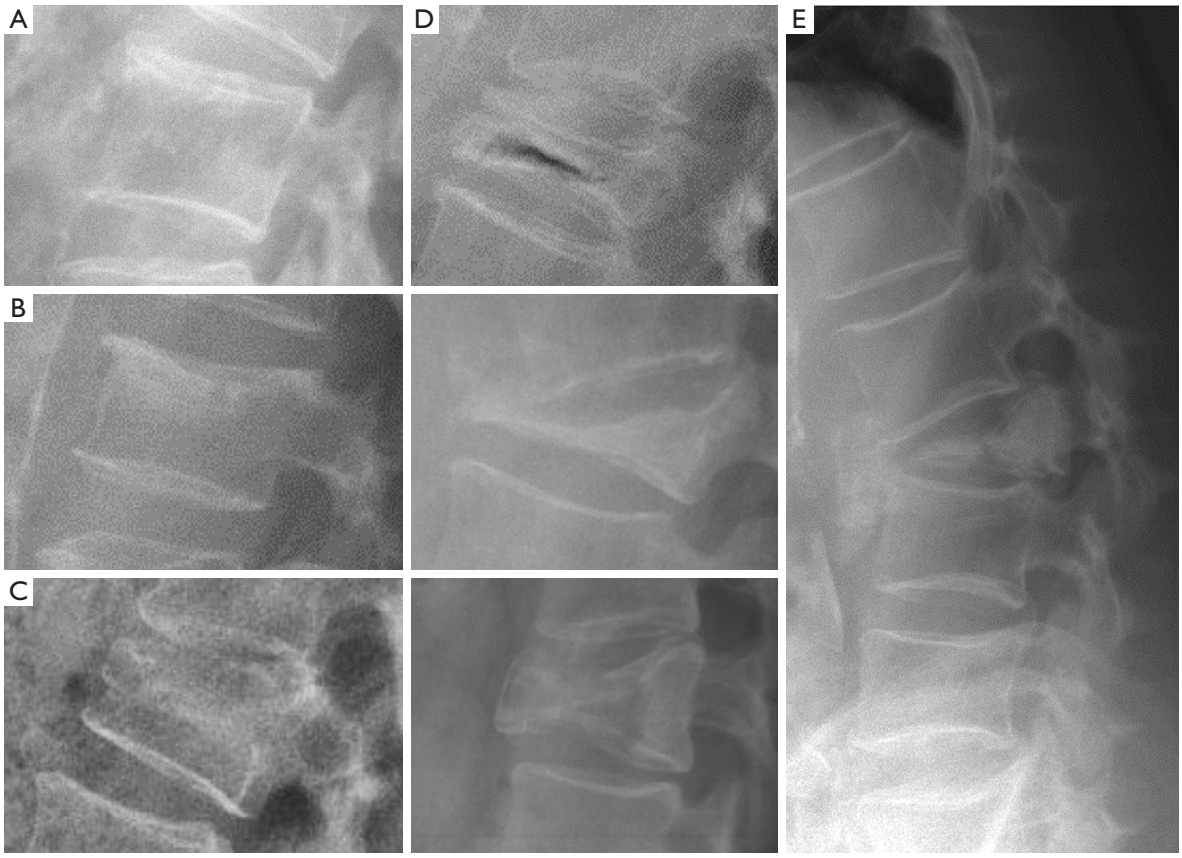

Figure 9 Examples of osteoporotic vertebral fractures according to the German Society for Orthopaedics and Trauma (DGOU) Classification. (A) Type 1—non deformity; (B) Type 2—deformation with minor involvement of the posterior wall; (C) Type 3—deformation with distinct involvement of the posterior wall; (D) 3 examples of Type 4—loss of integrity of vertebral frame architecture or pincer-type fracture; (E) Type 5—injuries with distraction or rotation.

frame structure both endplates and the posterior wall are involved (complete burst fracture). Vertebral body collapse is typically seen as a final consequence of failed conservative treatment and can impose as a plain vertebral body. Pincer-type fractures involve both endplates and may lead to severe deformity of the vertebral body. OF 4 injuries are unstable fractures and intravertebral vacuum clefts are often visible. OF 5: injuries with distraction or rotation. This group is rare but shows substantial instability. The injury includes not only the anterior column but also the posterior bony and ligamentous complex. OF 5 injuries can be caused either by a direct trauma or by ongoing sintering and collapsing of an OF 4.

The semi-quantitative (SQ) criteria proposed by Genant's *et al.* have been commonly used to date for epidemiological studies, with OVFs being classified into three types: wedge, biconcave and crushed fractures (61,62) (*Figure 5*). Semiquantitative grading of vertebral collapse is based on the percentage of vertebral height loss or vertebral area decrease. According to Genant *et al.*, a vertebral body (VB) is graded on visual inspection of the anterior, middle, or posterior heights as normal (Grade-0), mildly deformed (Grade-1, a 20–25% reduction in one of the three heights and a reduction in area of 10–20%), moderately deformed (Grade-2, a 25–40% reduction in any height and a reduction in area of 20–40%) and severely deformed (Grade-3, a 40% or more reduction in height and area). This classification, mainly used in epidemiological studies, has not gained importance in the orthopaedic field. For research purposes, Wáng *et al.* emphasises the importance of measurement-

Figure 10 Digital chest radiograph of an 86 years old female. Compressive vertebral deformity of T12 and L1 is noted (arrows).

Figure 11 Digital abdominal radiograph of a 71 years old female. Compressive vertebral deformity of T10 is noted (arrow). A left urinary tract drainage catheter can be seen.

based grading, rather than visual estimation (63), to improve the comparability of studies by different authors. Recent reports consider that fractures of the vertebral endplate and/or vertebral wall cortex fracture (ECF) have more prognostic implications than isolated vertebral deformities (58,64). Wáng *et al.* (65) proposed that a VF without ECF should be term "osteoporotic vertebral deformity" (OVD), while those VFs with ECF should be called OVF. According to Lentle *et al.*, OVD is an OVF only when diagnosed based on evidence or findings of endplate, cortical, or trabecular damage (66). To facilitate visual grading of OVD/OVF in women, Wáng *et al.* proposed to simplify the Genant's SQ classification into three categories: <1/5 height loss, 1/5–1/3 height loss, and >1/3 height loss. OVD of >1/3 height loss is always associated with ECF (65,67), and OVF of >1/3 height loss in elderly women is associated with increased back pain prevalence (Wang YX *et al.*'s unpublished data).

Despite its importance, many patients with OVF and at high risk for further fracture remain undetected and untreated (68). Particularly, OVFs are often unrecognised on chest radiographs when the radiographs are ordered for non-skeletal conditions (69,70). OVFs are also missed on spine radiograph when not read carefully (71). Based on analysis of digital spine radiograph, Wáng *et al.* (72) reported that moderate to severe VDs (i.e., with >25% vertebral height loss) at middle/lower thoracic and lumbar spine are mostly identifiable on the frontal view, with a small proportion of ambiguous cases that can be clarified by additional lateral view imaging. In clinical practice, frontal chest frontal radiograph is often taken for patients suspected of respiratory diseases, pleural diseases, as well as to assess the heart and large vessels. Abdominal frontal radiograph is taken in patients with abdominal pain, for assessing urinary stone, gastrointestinal gas, etc. It can be envisaged that, depending on the technical condition of the radiograph, a substantial portion of moderate to severe grades of VDs in the mid/lower thoracic spine and lumbar spine are identifiable on a frontal view digital radiograph of the abdomen and chest (*Figures 10,11*). Thus, opportunity exists for detecting OVFs on digital chest/abdominal frontal radiograph for high-risk osteoporotic patients (such as elderly females >65 years) when they are X-rayed for other indications. Radiologists should pay attention to the potential existence of an OVF while reading chest and

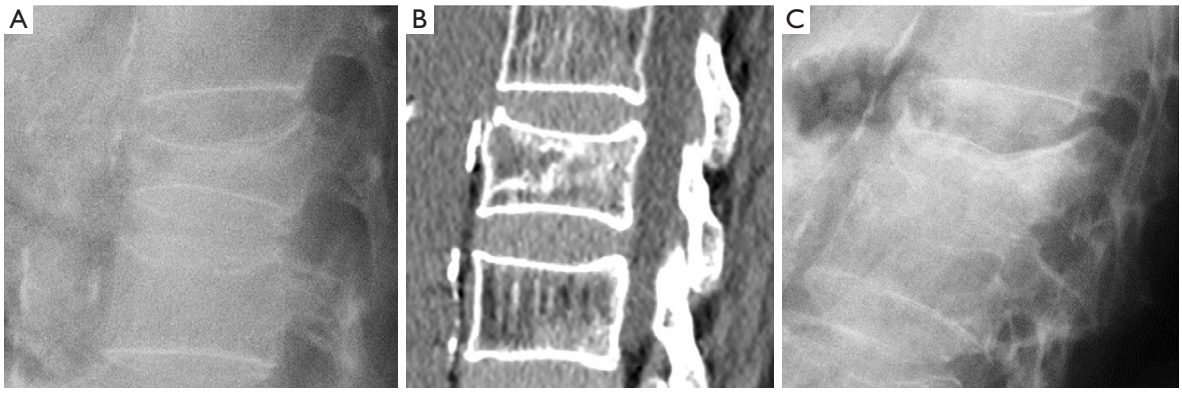

Figure 12 Intravertebral fracture instability. (A) Standing radiograph with marked local kyphosis that is reverted in supine CT (B). (C) Follow-up radiograph showing severe collapse of the vertebral body.

abdominal radiographs of elderly subjects.

Vertebral cleft has been reported in approximately 7–13% of OVF patients seen in orthopaedic clinics and has been associated with osteonecrosis (Kummel disease), non-union fracture and intravertebral instability (73,74). The presence of intravertebral cleft implies intravertebral instability. Accordingly, several methods have been reported in the literature to assess this instability. It can be quantified as the difference in local kyphosis between flexion and extension radiographs, in standing or prone radiographs (75-77), or comparing the difference in local kyphosis in standing or sitting radiographs with local kyphosis on supine CT (78) (*Figure 12*).

Of note, most of the studies on OVF epidemiology are based on female patients. The importance of OVF in males remains less certain (38). Wáng *et al.* reported that for elderly Chinese males (mean age 71.7 years, range 65–91 years), existing OVFs were only very weakly associated with higher risk of further development of OVFs during a 4-year follow-up (54).

Finally, it should be noted that the age group with high prevalence of OVF is also the age group with high prevalence of spine metastatic tumours. Differentiating between OVD and metastatic deformity can be sometimes difficult by sole radiograph. MRI is the preferred imaging technique for the differential diagnosis (79).

Degenerative pathology

Degenerative pathology of the lumbar spine can affect several anatomical locations, including:

(I) Synovial joints: atlantoaxial, facets, costovertebral and sacroiliac.

Facet joints constitute the outer wall of the vertebral foramen. Since they are synovial joints, degenerative signs of osteoarthritis include joint space narrowing, subchondral cysts and/or sclerosis, vacuum phenomenon and osteophyte formation. Due to their posterior location, different projections may be necessary to clearly identify these signs. In lumbar spine, oblique views are more useful with a reported sensitivity of 55% and specificity of 69% (80) (*Figure 13*).

(II) The intervertebral disc, resulting in intervertebral osteochondrosis or scarred disc, and spondylosis deformans or ageing disc.

According to Resnick, osteochondrosis is a process that affects the annulus fibrosus and the nucleus pulposus. It is characterised by narrowing of the intervertebral disc space, central vacuum phenomenon, sclerosis of the vertebral endplates and subchondral bone, and asymmetric osteophytes in any direction (81). From a pathophysiological perspective, osteochondrosis results from radial tears that lead to degeneration of the nucleus pulposus and it is considered a pathologic process associated with vertebral symptoms. Nevertheless, these findings have been described in 19% of asymptomatic subjects (82) (*Figure 13*).

Spondylosis deformans predominantly affects the annulus fibrosus. Radiologic signs include symmetrical anterolateral osteophytes, preservation or mild reduction of disc height, peripheral vacuum phenomenon, sclerosis, and/ or amputation of the

 Quant Imaging Med Surg 2020;10(12):2322-2355 | http://dx.doi.org/10.21037/qims-20-1014

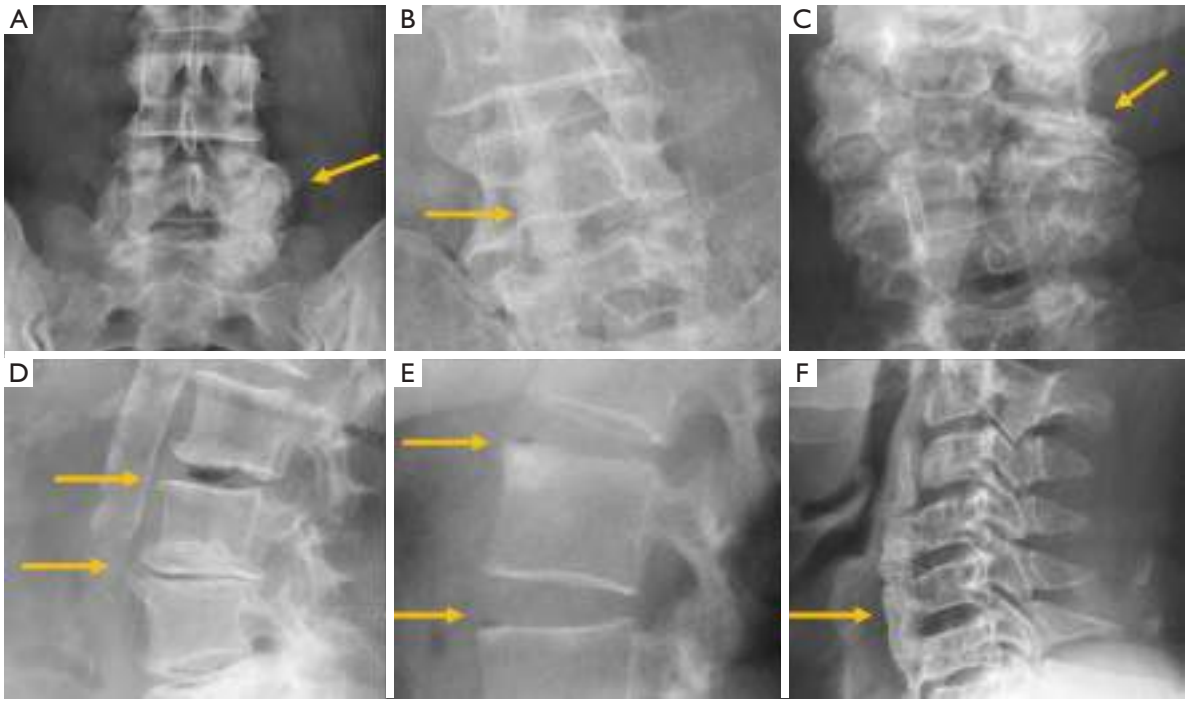

Figure 13 Facet osteoarthritis. AP (A) and oblique (B) lumbar radiographs. (C) Facets osteoarthritis at the cervical spine; (D) vertebral osteochondrosis with marginal osteophytes and central vacuum phenomenon; (E) spondylosis deformans with marginal sclerosis and peripheral vacuum phenomenon; (F) diffuse idiopathic skeletal hyperostosis. Arrows point the main abnormality in each case.

epiphyseal ring. Rim or concentric tears at the annulus fibrosus promote increased instability, while at the insertion of Sharpey fibres, they stimulate osteogenesis, leading to sclerosis and osteophyte formation (83) (*Figure 13*).

(III) Ligaments and their insertions at the bone, resulting in diffuse idiopathic skeletal hyperostosis (DISH).

DISH is a systemic condition, with an estimated prevalence of approximately 10% in people >50 years of age. The radiographic criterion proposed by Resnik for its diagnosis is the presence of large bridging osteophytes in at least four adjacent thoracic vertebrae. Patients with DISH may be largely asymptomatic. The spinal stiffness in the final stages of the disease implies increased spinal vulnerability to low-energy trauma (84) (*Figure 13*). On the other hand, the diagnostic criteria proposed by Utsinger greatly reduced the number of spinal bridges required, but involvement of peripheral entheses was included in order to achieve an early diagnosis (85).

(IV) Degenerative changes of the cervical spine typically involve the uncovertebral processes with formation of posterior osteophytes. Associated abnormalities are decreased disc height and disc bulging or protrusion. Plain films are useful for the evaluation of cervical uncovertebral osteoarthritis. In AP radiograph, the uncinate process becomes blunted and sclerotic, while in lateral radiographs the Mach effect may lead to the false impression of a fracture. The Mach effect is an optical illusion at the margin between areas of different density. In this case presenting as a dark outline of the sclerotic uncinate process (86). The examination should be completed with oblique projections because osteophytes often determine stenosis of the neural foramina and could be missed otherwise (87) (*Figure 14*).

Degenerative disorders may lead to spinal stenosis, although it may be favoured by the coexistence of developmental spinal stenosis. Radiographs show the

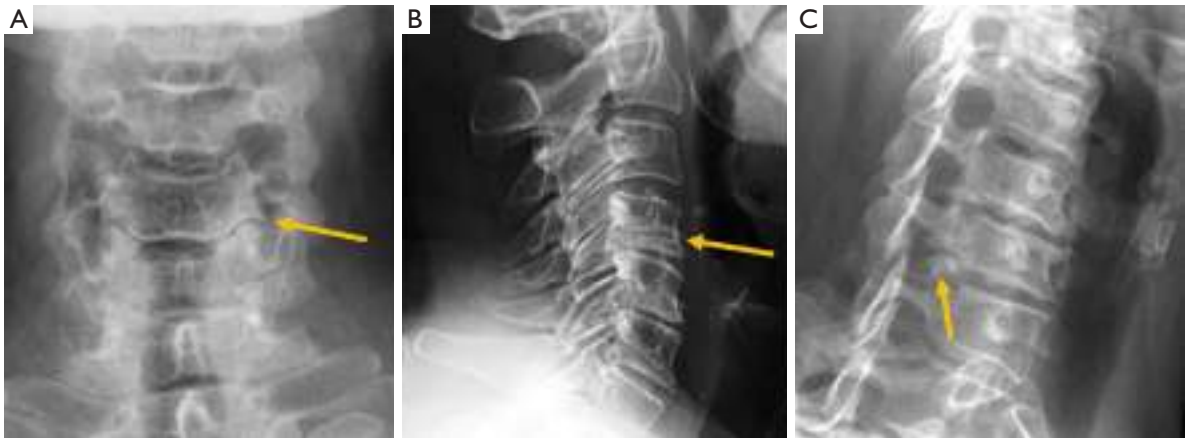

Figure 14 Uncarthrosis. (A) AP radiograph; (B) in the lateral a dark line projected over the vertebral body may simulate a vertebral fracture line; (C) oblique radiograph with osteophytes impinging the vertebral foramen. Arrows point the main abnormality in each case.

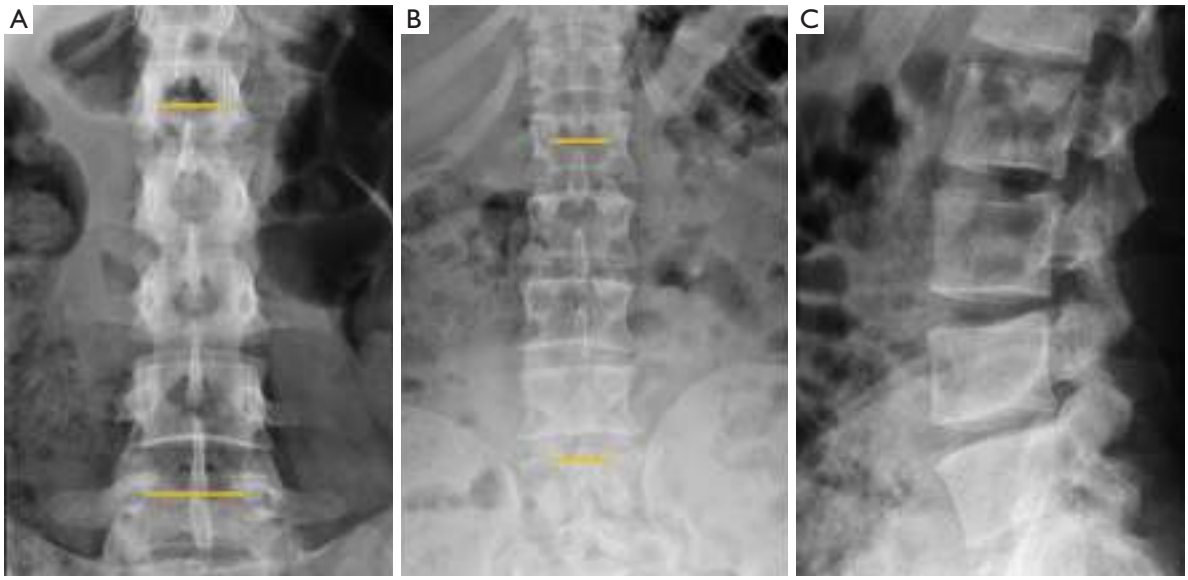

Figure 15 Lumbar spinal canal measurement. (A) Normal AP radiograph showing progressive widening of the interpedicular distance. In congenital stenotic canal; (B) this widening is not present; (C) lateral radiograph of congenital stenotic canal.

bone-related causes of canal stenosis. Congenital stenosis is more frequent in the lumbar tract. It can be part of a skeletal syndrome (e.g., Morquio's disease, achondroplasia, Down syndrome) or be idiopathic. In normal subjects, the interpedicular distance at the lumbar level increases progressively from L1 (range, 17–19 mm) to L5 (20–23 mm). This increase is lower or absent in congenital spinal stenosis (87) (*Figure 15*).

Several indices and measurements have been described in radiographs as diagnostic criteria for developmental stenosis. At the cervical level, a sagittal canal diameter <14 mm between C4 and C7 or a ratio between the sagittal diameter of the canal and that of the vertebral body <0.8 mm are considered signs of central canal stenosis. In the lumbar spine, moderate stenosis is established if the sagittal diameter is between 10 and 14 mm and severe stenosis if the

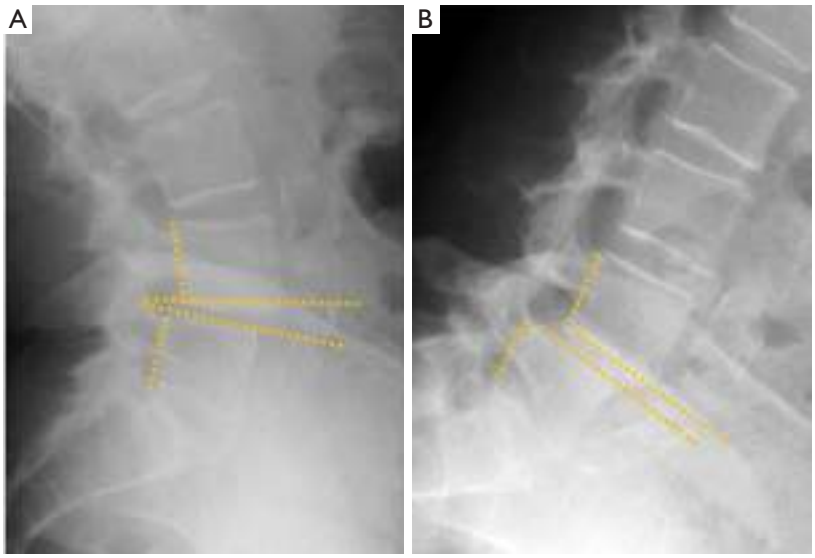

Figure 16 L4–L5 instability. Extension (A) and flexion (B) radiographs demonstrating 5 mm L4 forward displacement, with subsequent change of the L4–L5 disc angle approximately 20 degrees.

diameter is <10 mm (87).

Alignment abnormalities

Radiographs provide direct information of bone structures. Functional information about misalignment and vertebral stability can be obtained by upright dynamic films in flexion-extension. For the lumbar spine, values of 10° for sagittal rotation, measured as the shift of the angle between the vertebral endplates of the unstable disc, and more than 3 mm of sagittal translation are the cut-off conventionally used to diagnose instability (88) (*Figure 16*). Nevertheless, criteria for the diagnosis of cervical spine instability lack universal agreement, ranging from 1 to 3.5 mm based on the literature (89), although a 3-mm slippage appears to be a reliable cut-off point (*Figure 17*). Regarding the atlantoaxial joint, the accepted criteria for instability based on flexion-extension radiographs include an interval greater than 3 mm between the anterior margin of the odontoid process and the posterior cortex of the anterior arch of the atlas (90) (*Figure 17*).

Six types of spondylolistheses have been described: congenital or dysplastic, isthmic, traumatic, pathologic, iatrogenic, and degenerative (pseudospondylolysis) (87).

According to the classic work of Meyerding (91), vertebral displacement in spondylolisthesis is classified into five grades based on the position of the posterior margin of the upper vertebra over the upper end-plate of the inferior vertebra, which is divided into four equal parts from posterior to anterior. Displacements in each of these quarters of vertebral endplate correspond to grades I to IV, while in grade V or spondyloptosis, L5 slippage overpasses the anterior margin of S1. Most of the cases seen in a clinical setting are secondary to degenerative or isthmic spondylolisthesis and correspond to grades I and II, whereas grades III and IV are extremely rare (92). Grade V is also rare, and usually secondary to a dysplastic posterior arch, and less frequently to trauma. On AP radiographs, the frontal orientation of the brim of the upper endplate and the transverse processes of L5 can project an image called "the inverted Napoleon hat" sign (*Figure 18*).

Isthmic spondylolisthesis is the most frequent type of spondylolisthesis in young people and is generally secondary to a stress fracture in a previously normal bone. Spot lateral radiographs allow detecting the bone defect in the pars interarticularis in up to 84% of the cases (93). However, the 45º oblique view provides better definition of the isthmic defect, deploying the whole length of the pars interarticularis as the "neck" of a silhouette resembling a "dog" known as the "Scotty dog" in the English literature and as "le petit chien de Lachapelle" in the French literature. Demonstration of spondylolysis in the oblique

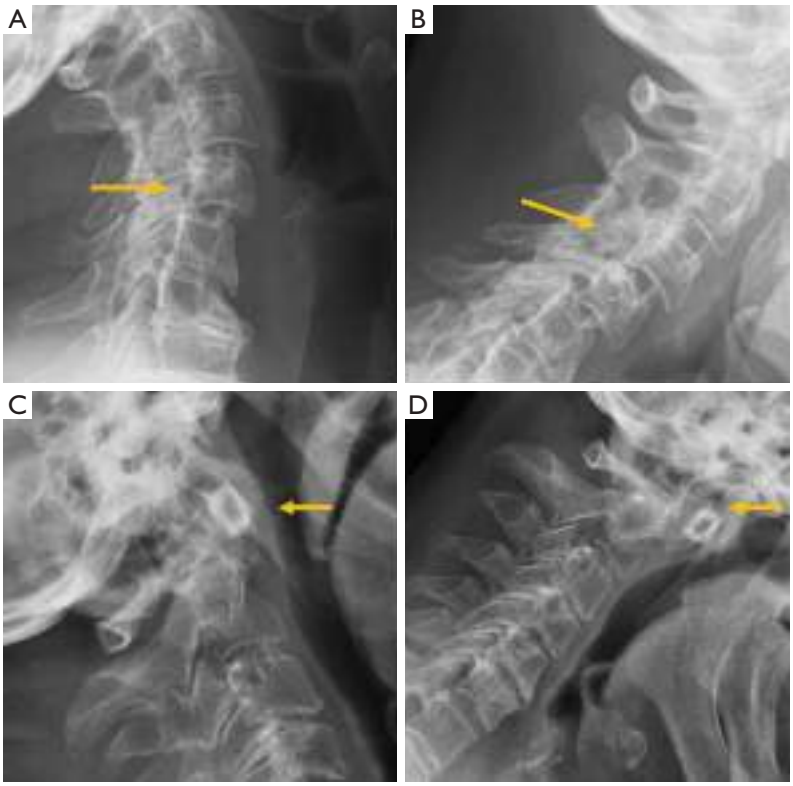

Figure 17 Subaxial cervical instability. Extension (A) and flexion (B) radiographs showing 4 mm forward displacement of C4. Atlantoaxial joint instability. Extension (C) and flexion (D) radiographs showing 4 mm forward displacement of the anterior arch of the atlas. Arrows point the main abnormality in each case.

view is depicted as "the collar or broken neck of the Scotty dog" sign. Other authors found that approximately 20% of defects in the pars interarticularis seen on plain radiographs can only be identified in oblique views (94). Nevertheless, there are secondary signs that help diagnose isthmic spondylolisthesis even if spondylolysis per se is not seen. The spinous process does not shift with the displaced vertebral body and the central canal widens while the foramina are usually stenosed (*Figure 18*).

The second most common site of neural arch injury following pars interarticularis is the vertebral pedicle. It may be associated with unilateral spondylolysis but has been also described without associated spondylolysis in some young athletes or even in osteoporotic patients (95).

Degenerative spondylolisthesis is secondary to facet and disc degeneration while the neural arch remains intact. For this reason, the spinous process is anteriorly displaced with the vertebral body, and the central canal is usually stenosed (*Figure 17*). It is the most frequent cause of spondylolisthesis in elderly subjects (96). It should also be noted that degenerative and isthmic spondylolistheses are not usually clinically relevant, the former being seen in 20% of the elderly population (97). The prevalence of degenerative spondylolisthesis increases with age, being more common in elderly women than in elderly men, being more common in Caucasian compared to East Asian subjects (98).

Traumatic spondylolisthesis is a rare injury, defined as any acute fracture or dislocation of the posterior elements associated with vertebral spondylolisthesis. When located at C2, it is called the "Hangman fracture", with radiological signs analogous to isthmic spondylolisthesis (*Figure 3*).

Retrolisthesis is a manifestation of spondylolisthesis that consist in posterior shifting of a cephalad vertebra over caudal vertebra. It is generally secondary to loss of disc material caused by intervertebral osteochondrosis or acute herniation of the nucleus pulposus (87) (*Figure 19*).

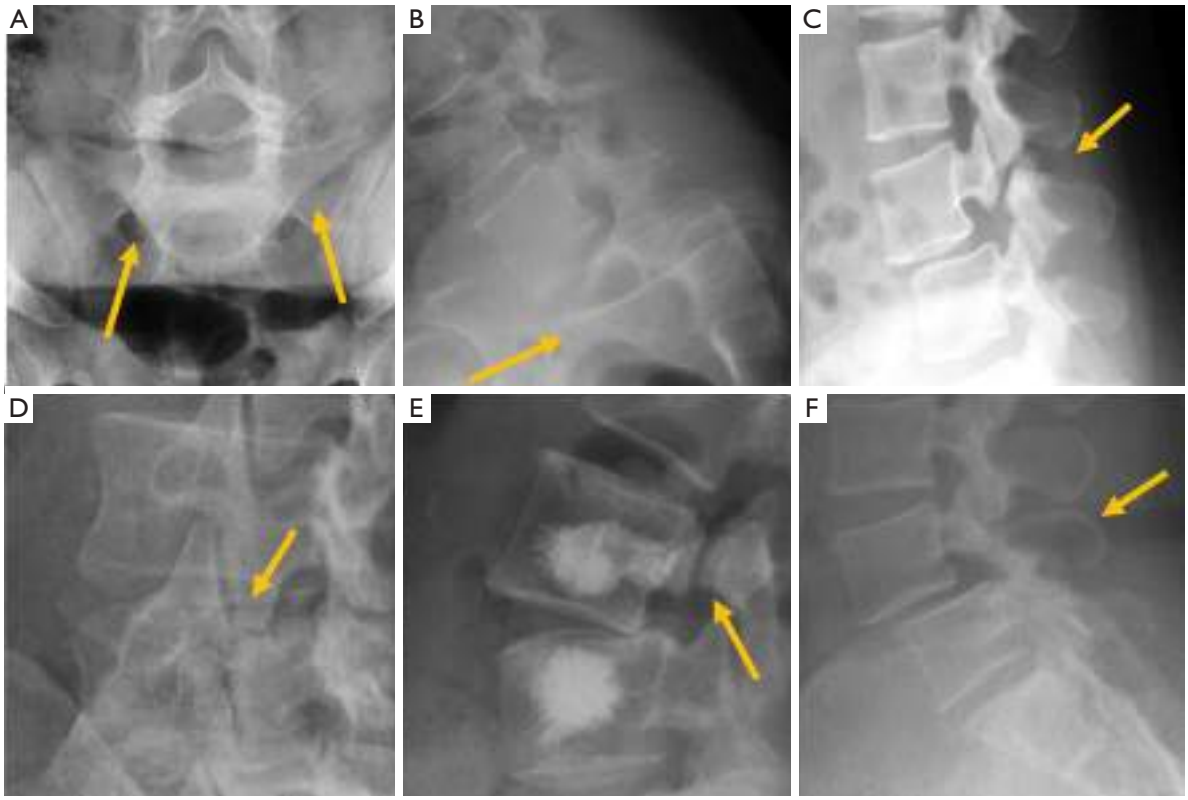

Figure 18 Vertebral spondylolisthesis. (A) Inverted Napoleon hat sign in spondyloptosis (arrows); (B) lateral radiograph in spondyloptosis (arrow points to L5 in front of the sacrum); (C) spondylolysis with spondylolisthesis. The spinous process does not move with the vertebral body; (D) oblique view showing the "broken neck of the Scotty dog" in spondylolysis (arrow); (E) pedicle stress fracture in osteoporotic fracture with previous vertebroplasty; (F) degenerative spondylolisthesis with the spinous process displaced forward (arrow).

Alterations in the spinal curvature

Vertebral alignment and spinal curvatures can be readily assessed and measured using radiographs that provide a global analysis of the spine.

In the sagittal plane, thoracic kyphosis varies with both age and gender, increasing with age more in women than in men. Reported average normal values in adults range from 20º to 42.1º (99-101), with values <30º in people in their 20s, and over 50º in subjects older than 60 years (102). Therefore, there is no uniformly accepted threshold for defining hyperkyphosis or "normal" kyphosis without considering age, sex, and clinical setting (103). The angle is measured between a line parallel to the upper end-plate of the most superior vertebra involved in the kyphotic curve (commonly T4) and another line parallel to the lower end-plate of the transitional vertebra between the thoracic and lumbar curves (commonly T12) (101) (*Figure 20*). Intra- and inter-rater reproducibility of thoracic kyphosis measurement has been demonstrated to be superior for T4–T12 than for T1–T12 or T2–T12 (104), with good agreement (104,105).

During adolescence, juvenile kyphosis—also known as Scheuermann's disease—and idiopathic kyphosis are the two more frequent forms of pathological kyphosis, which is defined by a thoracic kyphotic angle greater than 45°. In Scheuermann's disease, irregular endplates, Schmorl nodes and narrowing of the intervertebral disc can all be found. Vertebral wedging (local kyphosis >5º) must be present in at least one vertebral body, according to Sachs and Bradford's criteria (106), or in three adjacent vertebral bodies, according to Sorensen's criteria (107). When no vertebral abnormalities are present and only anterior wedging of the intervertebral disc exists, the case is classified as idiopathic kyphosis (108) (*Figure 21*). In physiologic vertebral wedging,

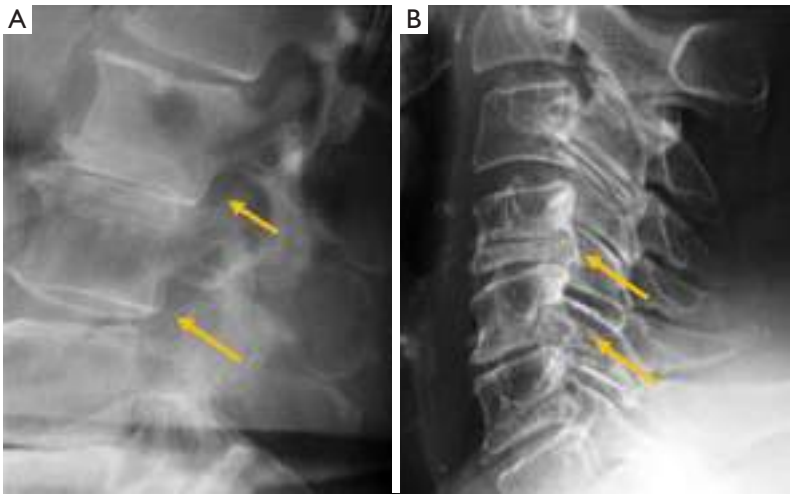

Figure 19 Retrolisthesis (arrow) at lumbar (A) and cervical spine (B).

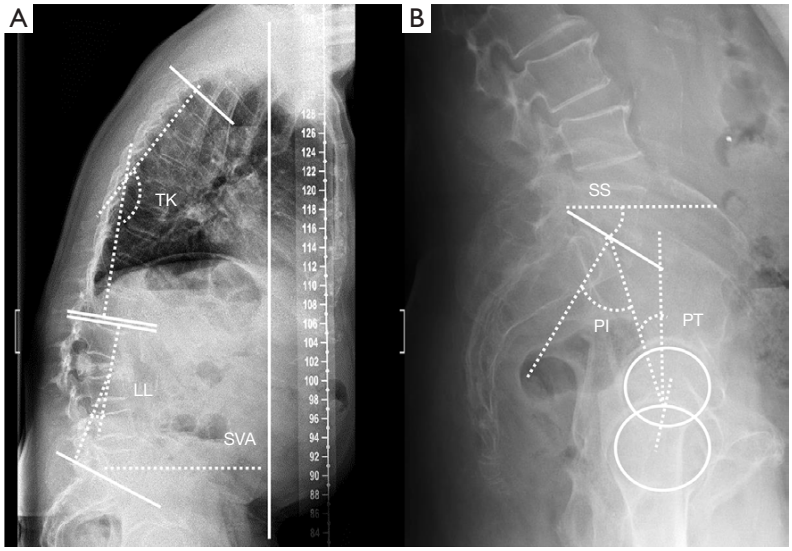

Figure 20 Sagittal alignment of the spine. (A) Measurement of the thoracic kyphosis (TK), lumbar lordosis (LL) and sagittal vertical axis (SVA) showing a positive sagittal balance in a patient with L2 burst fracture; (B) measurement of pelvic incidence (PI), sacral slope (SS), and pelvic tilt (PT).

thoracic kyphosis values are within the normal range and Schmorl's nodes are absent (109,110).

Lumbar lordosis (LL) is measured from the upper endplate of L1 to the upper endplate of S1. Because the normal range of lordosis is very wide (30º–80º using the Cobb method), it is difficult to determine the normal/optimal lordosis angle for an individual (111). Mean values reported in the literature range from 44º–60º in normal individuals (112,113).

In lateral full-length standing radiographs, sagittal balance is determined by a vertical line (sagittal vertical axis) drawn from the centre of the C7 vertebral body that should pass over the posterior-superior corner of S1. If the line lies anterior to the posterior-superior corner of S1, the patient

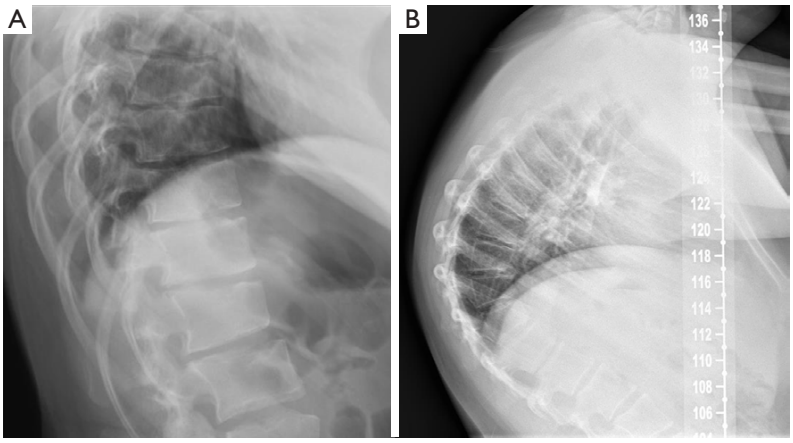

Figure 21 Causes of pathological kyphosis. (A) Typical end-plate changes in Scheuermann's disease; (B) idiopathic juvenile kyphosis.

is said to have a positive sagittal balance (negative sagittal balance in the opposite case). The most common deformity secondary to vertebral fracture is local kyphosis, which may lead to a positive sagittal balance when compensatory mechanisms fail. Physiological spinal ageing or pathologic degenerative loss of disc height may lead to loss of LL and hyperkyphosis, which also disrupts the sagittal balance (114) (*Figure 20*).

The pelvis is the cornerstone of spinal sagittal alignment. Several measurements have been developed to relate the morphology and position of the pelvis to sagittal spinal alignment. Of these, pelvic incidence (PI) is constant, while sacral slope and pelvic tilt are positional. Therefore, PI is the most suitable parameter for surgical planning, being unique for each patient and showing a strong positive correlation with LL (114,115). A parameter, PI minus (–) LL, quantifies the mismatch between the morphology of the pelvis and the lumbar curve. Values <10º are considered the goal of spinopelvic sagittal alignment (116). Nevertheless, compensatory mechanisms must be considered. The decrease in LL is compensated by increased pelvic retroversion and pelvic tilt (117). Ideally, a sagittal vertical axis (SVA)-posterosuperior S1 distance <40 mm, a PI-LL mismatch within 10º and a PT <20º have been considered the goals for appropriate sagittal alignment (114,115).

In the coronal plane, scoliosis is defined as a lateral curvature of the spine greater than 10° when measured on a standing radiograph according to the Cobb method (118). This Cobb angle can be measured manually or digitally (119,120). Idiopathic scoliosis is the most frequent type, although there are rarer cases secondary to congenital vertebral deformities or neuromuscular disorders. In adolescent scoliosis, radiographic findings are used to monitor for curve progression and usually guide the therapeutic options. The AP view should include the iliac crests, which serve to assess skeletal maturation based on the degree of calcification of the iliac crest (Risser method). Lateral bending views are performed to differentiate rigid from flexible curves (*Figure 22*). In the coronal plane, non-flexibility on side bending ≥25° defines a structural curve (121). In adults, degenerative changes and OVFs lead to deformities that may contribute to scoliosis.

Coronal alignment can also be assessed in AP radiographs, with a vertical line drawn from the middle of the C7 vertebral body that should pass over the centre of the sacrum (122). Coronal imbalance has been defined by some authors when this line deviates ≥3 cm from the centre of the sacrum (123). Based on this line, Qiu categorised degenerative lumbar scoliosis into three types according to the value of global coronal malalignment (GCM): Type A = GCM <3 cm; Type B = GCM >3 cm toward the concave side of the main curve; and Type C = GCM >3 cm toward its convex side (124) (*Figure 23*). According to some reports, this classification has an influence in postoperative coronal imbalance (124) and functional outcome (125).

Inflammatory pathology

Despite the improved utility of CT and MRI in spinal inflammatory arthritis, radiography is still recommended

Figure 22 Structural thoracolumbar curve. No significant correction is achieved with bending manoeuvres. (A) Right bending radiograph; (B) AP radiograph; (C) left bending radiograph.

as initial examination to rule out structural damage of the spine (126). According to the modified New York Criteria (NYC), the diagnosis of definite axial spondyloarthropathy (AS) requires the presence of manifest sacroiliitis by radiography (bilateral grade ≥2 or unilateral grade 3–4 sacroiliitis), in addition to clinical criteria (127) (*Figure 24*). Nevertheless, these criteria do not allow detection of individuals with early disease, in which no structural damage in the sacroiliac joints is seen on radiographs. Currently, the ASAS (Assessment in Spondyloarthritis International Society) classification criteria for AS are the most widely used. Sacroiliitis on imaging is one of these criteria in the imaging arm and includes either the diagnosis of definite radiographic sacroiliitis according to the modified NYC, or active sacroiliitis on MRI (127,128). Some authors differentiate between early non-radiographic AS, when no imaging abnormalities are seen on radiographs with or without inflammatory changes on MRI, and late radiographic AS, when signs of sacroiliitis are present on radiographs according to the NYC (129,130). This is because radiographic changes manifest in the chronic phase, between 3 and 7 years from the onset of the disease (131). Compared to MRI, radiographs show a modest sensitivity (79.8–84.3%) and specificity (70.6%/74.7%) for sacroiliitis and considerable intra-observer variability (132).

Seronegative AS pertain to a group of multisystem inflammatory diseases that includes diagnoses such as ankylosing spondylitis, and lumbar and sacroiliac involvement secondary to inflammatory bowel disease, psoriatic arthritis, and reactive arthritis. Classically, it has been said that ankylosing spondylitis and inflammatory bowel disease tend to show symmetric bilateral involvement, psoriatic and reactive spondyloarthropathy tend to be coarser and more asymmetrical (131-133). However, it has been seen that ankylosing spondylitis

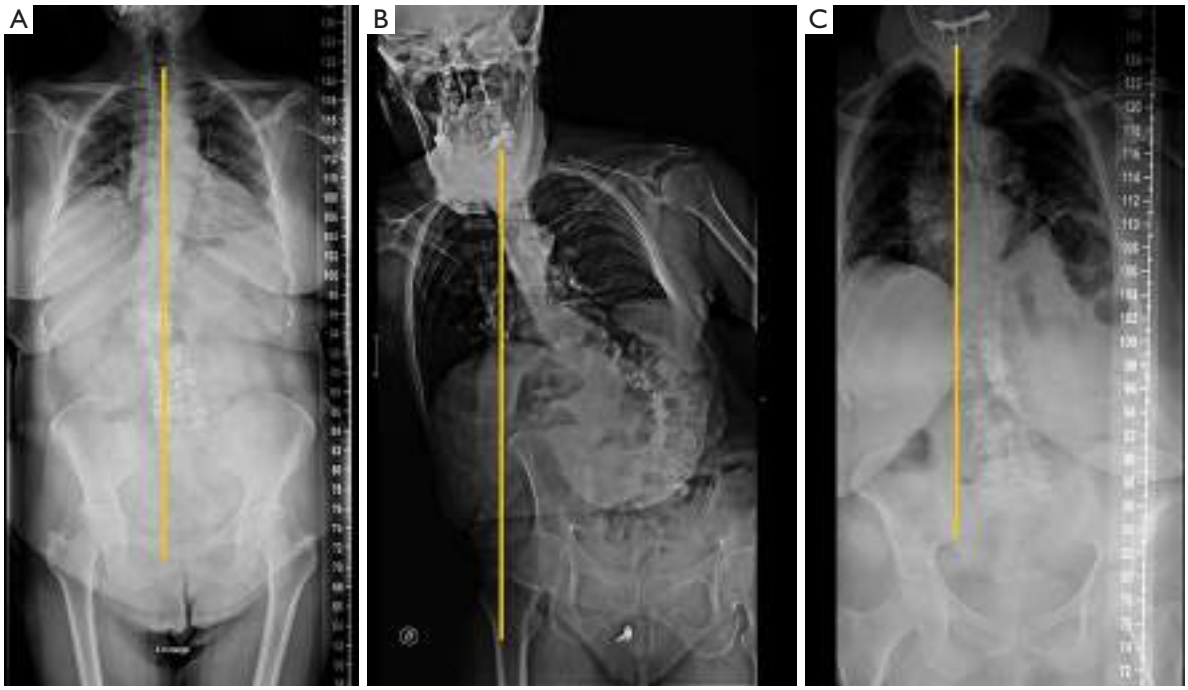

Figure 23 The three types of scoliosis (A,B,C) according to Qiu's classification of global coronal alignment.

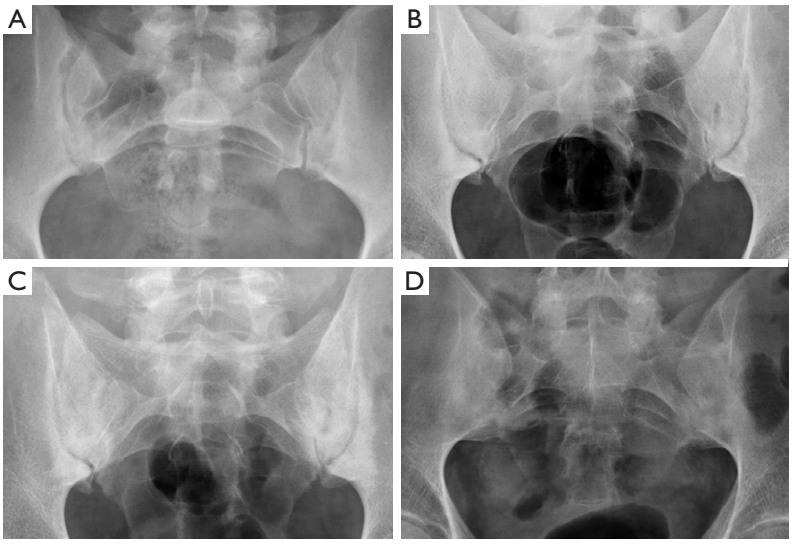

Figure 24 New York sacroiliitis grading. Grade 0 is normal. (A) Grade 1—suspicious changes; (B) Grade 2—minimum abnormality (small localized areas with erosion or sclerosis, without alteration in the joint width); (C) Grade 3—unequivocal abnormality (moderate or advanced sacroiliitis with erosions, evidence of sclerosis, widening, narrowing, or partial ankyloses); (D) Grade 4—severe abnormality (total ankyloses).

 Quant Imaging Med Surg 2020;10(12):2322-2355 | http://dx.doi.org/10.21037/qims-20-1014

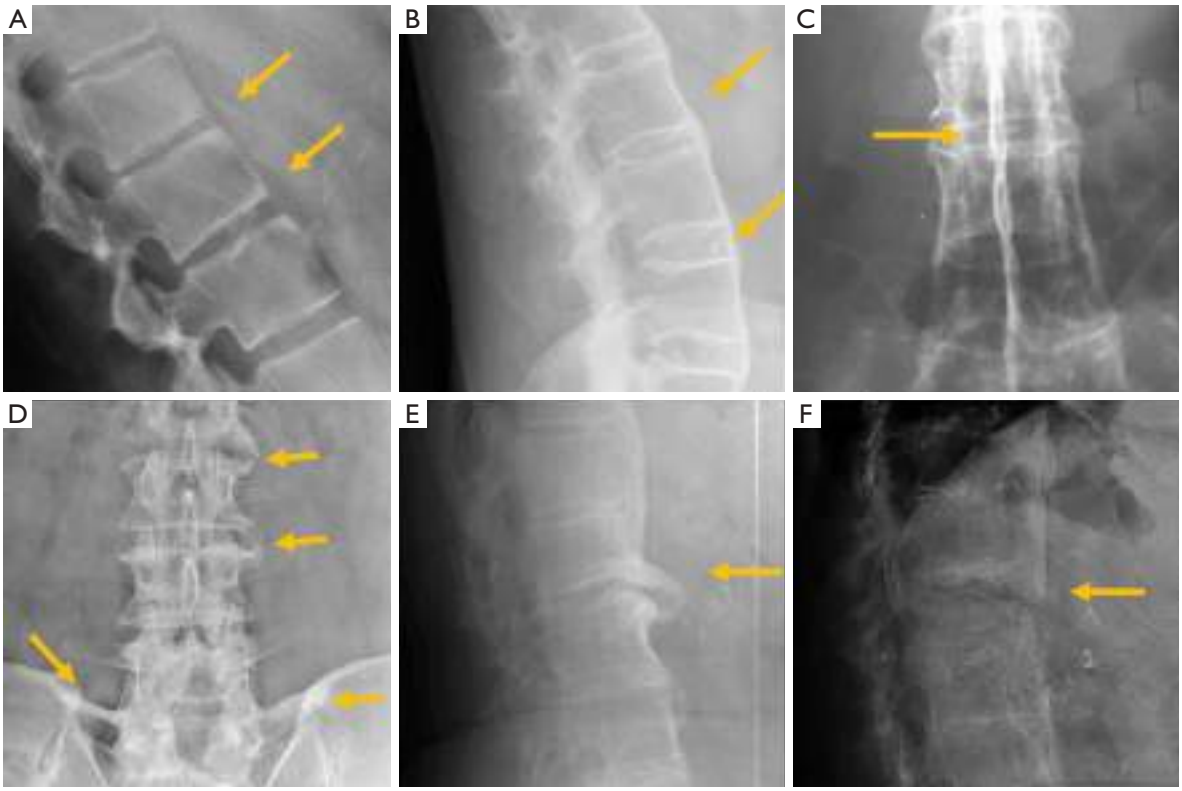

Figure 25 Seronegative spondyloarthropathies. (A) Squaring and shiny corner sign in ankylosing spondylitis; (B) bamboo spine; (C) the dagger sign in ankylosing spondylitis; (D) coarse bone bridges in psoriatic spondyloarthropathy. There is also ossification of the iliolumbar ligaments (lower arrows); (E) bone bridges in psoriatic arthritis before (E) and after bone fractures (F). Arrows point the main abnormality in each case.

can be asymmetrical in the early stages and become symmetrical along the course of the disease (133,134). Changes in psoriatic arthritis can be either symmetrical or asymmetrical, while in reactive arthritis they are symmetrical in about 50% of the cases (135).

Ankylosing spondylitis is the most frequent form of spondyloarthropathy and shows relatively typical radiographic features at the spine. Characteristic early radiographic changes consist of vertebral squaring and sclerosis of vertebral corners (shiny corners or Romanus lesion). Erosive changes within intervertebral spaces (Andersson lesions) have been detected by radiography in approximately 5% of patients with this condition (136). If the disease progresses, slim ossifications between vertebral bodies (syndesmophytes) bridge the vertebral bodies, fusing the discs and the facet joints. Associated arthritis/ankylosis due to ligamentous ossification also contributes to spinal stiffness leading to a complete spinal fusion called “bamboo spine”. A hyperdense line along the central spine secondary to ossification of interspinous and supraspinous ligaments on frontal radiographs is known as the “dagger sign” (126) (*Figure 25*). Fractures of the vertebrae at the ligamentous bridges have been reported to occur in up to 6% of patients with ankylosing spondylitis, especially in patients with long disease duration (137). Psoriatic patients also have an increased risk of vertebral fractures (138). Radiologic findings of spondyloarthropathy secondary to inflammatory bowel disease can be indistinguishable from those of ankylosing spondylitis. Nevertheless, in psoriatic and reactive spondyloarthropathy, bone bridges tend to be coarser and more prominent (126).

In rheumatoid arthritis the focus is the cervical spine, where the atlantoaxial joint may be affected by the inflammatory pannus, leading to structural changes and alignment abnormalities with displacement of the atlas in

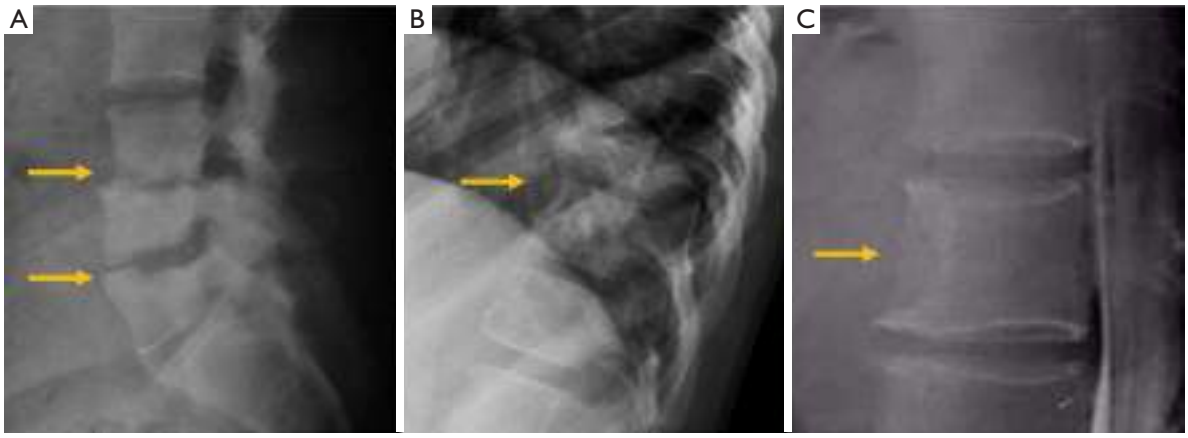

Figure 26 Infectious pathology of the spine. (A) Pyogenic spondylodiscitis in L4–L5 and L5–S1; (B,C) subligamentous spread of the infection in two cases of tuberculous spondylodiscitis. Arrows point the main abnormality in each case.

anterior, posterior, lateral or vertical direction (*Figure 17*). Younes *et al.* recommend cervical spine radiography in all patients with RA lasting >2 years because cervical involvement occurs in over 70% of these patients and up to 17% are asymptomatic (139).

Infectious pathology

For suspected spinal infection, MRI is the preferred imaging technique due to its high sensitivity and specificity. Nevertheless, radiographs may be appropriate in some scenarios, depicting structural changes, such as bone destruction and secondary alignment abnormalities (3).

Spondylodiscitis accounts for 2–4% of all osteomyelitis. Radiographic findings include destruction of two adjacent vertebral endplates with narrowing or disappearance of the disc space which, in turn, can cause an acquired vertebral block (140). In pyogenic spondylodiscitis, the first signs on radiographs may take 2–8 weeks to develop (141).

The evolution of pyogenic infections is much faster compared with tuberculosis due to the release of proteolytic enzymes in the former group. Tuberculosis usually exhibits a more chronic pattern, and radiographic changes take longer to become apparent, between 8–12 weeks (142). Subligamentous spread of tuberculosis can occur before spreading to the intervertebral space. In this case, erosion or scalloping of the anterior vertebral wall can be detected on radiographs (143) (*Figure 26*).

Tumour pathology

Tumour of the spine may be metastatic, primary benign or primary malignant. Because of overlapping of osseous structures of the spine, conventional radiography is often insufficient and further characterisation with CT or MRI is needed (144).

Metastatic lesions can manifest on radiographs with an osteolytic, osteoblastic, or mixed pattern. Plain-film radiography is somewhat insensitive regarding the visualisation of bone destruction or marrow replacement. Based on the size of the lesion, between 30–50% of bone destruction is needed before the lesions become visible on radiographs (145,146).

Destruction of the pedicle typically indicates that the lesion is advanced since it rarely occurs in a primary or isolated form (147). Unilateral destruction of the pedicle is usually responsible for the "winking owl" or "one-eyed vertebra" sign. Occasionally, destruction of both pedicles may lead to the "blind vertebra sign" in which there is no rounded shape of any of the pedicles in the AP view (148). Lung, thyroid and kidney metastases are fundamentally osteolytic lesions (*Figure 27*). Other osteolytic metastases can be secondary to bladder, nasopharyngeal carcinoma, and colon and, in childhood, to neuroblastoma (*Figure 27*) (144,149,150).

The detection of osteoblastic lesions may also be delayed with conventional radiographs. One study reported that in

Figure 27 Osteolytic metastases. (A) "One-eyed vertebra" sign in metastasis of bladder carcinoma; (B) thyroid metastasis in C4; (C) sacral osteolysis in metastasis of kidney tumour; (D) osteolytic metastasis in lung cancer. Arrows point the main abnormality in each case.

the case of breast cancer, radiography detection of these lesions may be delayed up to 3–6 months (151). Most commonly, metastases from breast and prostate cancer present with a sclerotic pattern (*Figure 28*). In adults, other sources of osteoblastic metastases are lymphoma, carcinoid tumours, mucinous adenocarcinoma of the gastrointestinal tract, pancreatic adenocarcinoma, bladder carcinoma or nasopharyngeal carcinoma; in childhood, neuroblastoma and medulloblastoma are the main primary source (144,149,150) (*Figure 28*).

Primary benign tumours may also show osteolytic, osteoblastic or mixed patterns. Osteolytic benign tumours or pseudo tumours include osteoid osteoma, osteoblastoma, haemangioma, giant cell tumour, aneurismal bone cysts or eosinophilic granuloma. Haemangiomas are one of the most frequent benign tumour lesions seen in the spine. On radiographs, they can be observed when enough destruction of the spongy bone marrow occurs. The remaining trabeculae thicken, revealing a classic "corduroy cloth" pattern within the osteolytic area (152). Extreme collapse of the vertebral body, vertebra plana or coin-on-edge vertebra is a typical feature of eosinophilic granuloma, a benign tumour-like disorder characterised by clonal proliferation of Langerhans cells (*Figure 29*).

Benign sclerotic tumours or pseudotumours include bone island (enostosis), sclerosis secondary to osteoid osteoma, or healed benign lesions such as cysts or fibromas. Bone island, or enostoma, is often considered a variant of normality. It appears when compact bone develops within the bone marrow. Sometimes, it may be difficult to differentiate enostomas from malignant osteoblastic lesions (144,152) (*Figure 30*).

Osteochondroma is a benign developmental exophytic lesion rather than an actual tumour. Spinal osteochondromas account for 1–4% and 9% of all solitary and multiple osteochondromas, respectively. Radiographically, osteochondroma is a bone exostosis protruding from the bone and showing varying degrees of chondroid calcification of the cartilaginous cap (153) (*Figure 30*).

Regarding primary malignant tumours, chordoma, plasmacytoma, osteosarcoma and primary lymphoma of the bone are rare, while myeloma is the most common. Chordomas usually present with an osteolytic pattern and soft tissue mass. They usually appear in the sacrococcygeal region (50% of cases), followed by the spheno-occipital region (35%) and the vertebral bodies (15%). Osteosarcoma often presents with osteoid calcification of

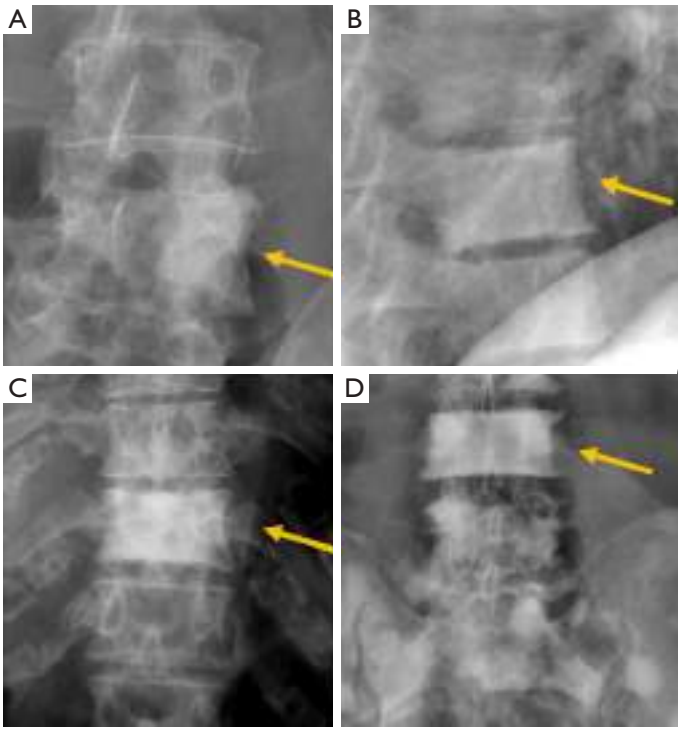

Figure 28 Sclerotic metastases in urothelial tumour (A), nasopharyngeal carcinoma (B), breast cancer (C), and prostate carcinoma (D). Arrows point the main abnormality in each case.

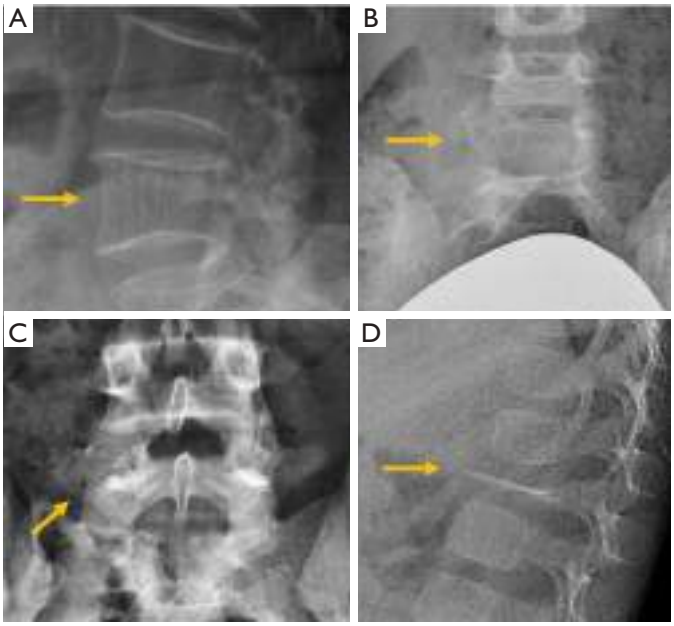

Figure 29 Benign osteolytic tumours and pseudotumours of the spine. (A) "Corduroy cloth" pattern in vertebral haemangioma. (B) "One-eyed vertebra" sign in aneurysmal bone cyst (B) and in osteoblastoma (C). (D) Vertebra plana in eosinophilic granuloma. Arrows point the main abnormality in each case.

 Quant Imaging Med Surg 2020;10(12):2322-2355 | http://dx.doi.org/10.21037/qims-20-1014

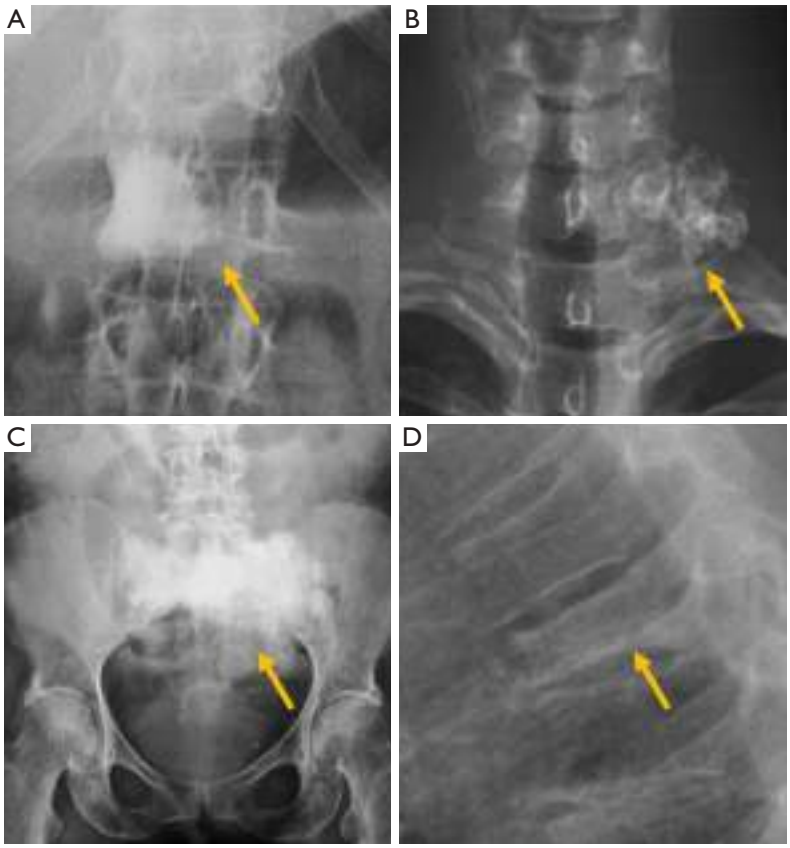

Figure 30 Primary sclerotic tumours and pseudotumours of the spine. (A) Bone island; (B) osteochondroma; (C) sacral osteosarcoma; (D) sclerotic fracture in lymphoma. Arrows point the main abnormality in each case.

the tumour matrix, with marked mineralisation originating in the vertebral body that may manifest as an "ivory vertebra" (144). This sclerotic vertebra can also be seen in bone lymphoma (*Figure 30*).

Solitary plasmacytoma is an uncommon tumour that occurs in 3–7% of patients with plasma cell neoplasms. It is considered to represent the early stages of multiple myeloma (MM) and shows a predominantly lytic pattern (153). Bone disease in multiple myeloma patients is characterised by lytic bone lesions that can result in pathologic fractures and severe pain (154,155). Between 10% and 20% of patients with MM appear normal on radiography (156,157). Osteopenia and osteolytic lesions may present separately or in association. Vertebral fractures have been reported in 50–70% of patients with MM (158,159). It is noteworthy to know that the radiographic appearance of MM may resemble that of OVFs, and the topographic distribution of the fractures is similar in both cases (158) (*Figure 31*).

Conclusions

Radiographs are still useful in assessing the anatomy and pathology of the spine in many clinical settings. The take-home messages are the following: (I) panoramic view of the whole spine is essential in assessing coronal alignment and sagittal balance after fracture, in congenital or developmental abnormalities with associated deformity (scoliosis and kyphosis), or in deformity secondary to degenerative disorders; (II) comparison of standing radiographs with supine radiographs or CT are useful in assessing unstable OVFs; (III) degenerative, inflammatory and tumour pathology can be characterised on radiographs with different degrees of sensitivity.

 Quant Imaging Med Surg 2020;10(12):2322-2355 | http://dx.doi.org/10.21037/qims-20-1014

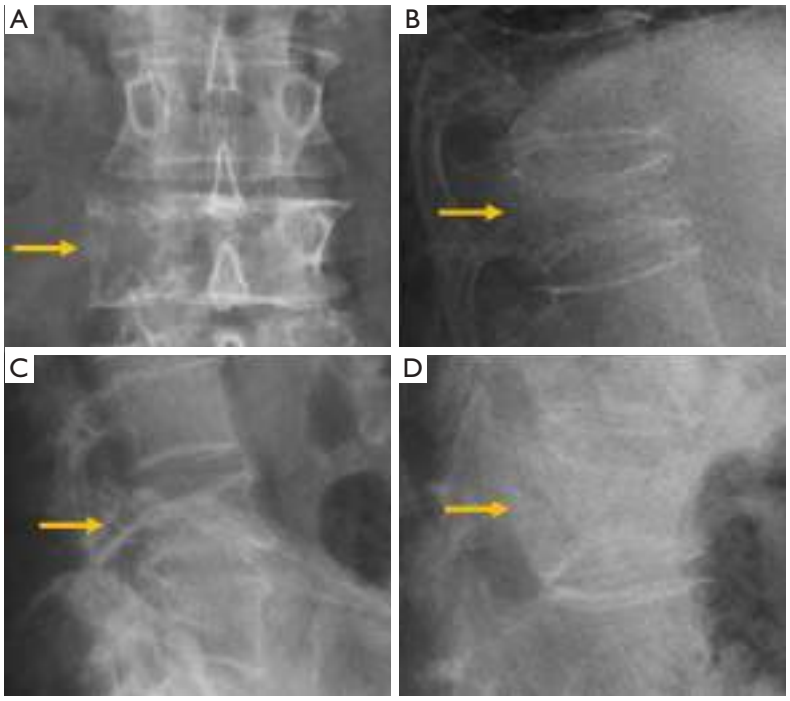

Figure 31 Vertebral involvement of myeloma in different patients. (A) "One-eyed vertebra" sign in myeloma. Burst (B), biconcave (C) and wedge fractures (D) in multiple myeloma. Arrows point the main abnormality in each case.

Acknowledgments

Funding: None.

Footnote

Conflicts of Interest: All authors have completed the ICMJE uniform disclosure form (available at http://dx.doi.org/10.21037/qims-20-1014). YXJW serves as unpaid Editor-In-Chief of *Quantitative Imaging in Medicine and Surgery*. The other authors have no conflicts of interest to declare.

References

1. Deyo RA, Weinstein JN. Low back pain. N Engl J Med 2001;344:363-70.
2. Wáng YXJ, Wu AM, Ruiz Santiago F, Nogueira-Barbosa MH. Informed appropriate imaging for low back pain management: A narrative review. J Orthop Translat 2018;15:21-34.
3. Patel ND, Broderick DF, Burns J, Deshmukh TK, Fries IB, Harvey HB, Holly L, Hunt CH, Jagadeesan BD, Kennedy TA, O'Toole JE, Perlmutter JS, Policeni B, Rosenow JM, Schroeder JW, Whitehead MT, Cornelius RS, Corey AS. ACR Appropriateness Criteria Low Back Pain. J Am Coll Radiol 2016;13:1069-78.
4. Schlemmer E, Mitchiner JC, Brown M, Wasilevich E. Imaging during low back pain ED visits: a claims-based descriptive analysis. Am J Emerg Med 2015;33:414-8.
5. Ramirez N, Flynn JM, Hill BW, Serrano JA, Calvo CE, Bredy R, Macchiavelli RE. Evaluation of a systematic approach to pediatric back pain: the utility of magnetic resonance imaging. J Pediatr Orthop 2015;35:28-32.
6. Expert Panel on Pediatric Imaging:, Booth TN, Iyer

RS, Falcone RA Jr, Hayes LL, Jones JY, Kadom N, Kulkarni AV, Myseros JS, Partap S, Reitman C, Robertson RL, Ryan ME, Saigal G, Soares BP, Tekes-Brady A, Trout AT, Zumberge NA, Coley BD, Palasis S. ACR Appropriateness Criteria® Back Pain-Child. J Am Coll Radiol 2017;14:S13-S24.
7. Bhatia NN, Chow G, Timon SJ, Watts HG. Diagnostic modalities for the evaluation of pediatric back pain: a prospective study. J Pediatr Orthop 2008;28:230-3.
8. Feldman DS, Straight JJ, Badra MI, Mohaideen A, Madan SS. Evaluation of an algorithmic approach to pediatric back pain. J Pediatr Orthop 2006;26:353-7.
9. Miller R, Beck NA, Sampson NR, Zhu X, Flynn JM, Drummond D. Imaging modalities for low back pain in children: a review of spondyloysis and undiagnosed mechanical back pain. J Pediatr Orthop 2013;33:282-8.
10. Chaturvedi A, Klionsky NB, Nadarajah U, Chaturvedi A, Meyers SP. Malformed vertebrae: a clinical and imaging review. Insights Imaging 2018;9:343-55.
11. McMaster MJ. Spinal growth and congenital deformity of the spine. Spine (Phila Pa 1976) 2006;31:2284-7.
12. Nguyen VD, Tyrrel R. Klippel-Feil syndrome: patterns of bony fusion and wasp-waist sign. Skeletal Radiol 1993;22:519-23.
13. Vázquez-López ME, López-Conde MI, Somoza-Rubio C, Pérez-Pacín R, Morales-Redondo R, González-Gay MA. Anomalies of vertebrae and ribs: Jarcho Levin syndrome. Description of a case and literature review. Joint Bone Spine 2005;72:275-7.
14. Zhou PL, Poorman GW, Wang C, Pierce KE, Bortz CA, Alas H, Brown AE, Tishelman JC, Janjua MB, Vasquez-Montes D, Moon J, Horn SR, Segreto F, Ihejirika YU, Diebo BG, Passias PG. Klippel-Feil: A constellation of diagnoses, a contemporary presentation, and recent national trends. J Craniovertebr Junction Spine 2019;10:133-8.
15. McMaster MJ, Singh H. Natural history of congenital kyphosis and kyphoscoliosis. A study of one hundred and twelve patients. J Bone Joint Surg Am 1999;81:1367-83.
16. Expert Panel on Pediatric Imaging:, Jones JY, Saigal G, Palasis S, Booth TN, Hayes LL, Iyer RS, Kadom N, Kulkarni AV, Milla SS, Myseros JS, Reitman C, Robertson RL, Ryan ME, Schulz J, Soares BP, Tekes A, Trout AT, Karmazyn B. ACR Appropriateness Criteria® Scoliosis-Child. J Am Coll Radiol 2019;16:S244-S251.
17. Belmont PJ Jr, Kuklo TR, Taylor KF, Freedman BA, Prahinski JR, Kruse RW. Intraspinal anomalies associated with isolated congenital hemivertebra: the role of routine magnetic resonance imaging. J Bone Joint Surg Am 2004;86:1704-10.
18. Trenga AP, Singla A, Feger MA, Abel MF. Patterns of congenital bony spinal deformity and associated neural anomalies on X-ray and magnetic resonance imaging. J Child Orthop 2016;10:343-52.
19. Wu ZX, Huang LY, Sang HX, Ma ZS, Wan SY, Cui G, Lei W. Accuracy and safety assessment of pedicle screw placement using the rapid prototyping technique in severe congenital scoliosis. J Spinal Disord Tech 2011;24:444-50.
20. Ruiz Santiago F, Guzmán Alvarez L, Tello Moreno M, Navarrete González PJ. Plain-film radiography in the study of spinal pain. Radiologia 2010;52:126-37.
21. Uçar D, Uçar BY, Coşar Y, Emrem K, Gümüşsuyu G, Mutlu S, Mutlu B, Caçan MA, Mertsoy Y, Gümüş H. Retrospective cohort study of the prevalence of lumbosacral transitional vertebra in a wide and well-represented population. Arthritis 2013;2013:461425.
22. Konin GP, Walz DM. Lumbosacral transitional vertebrae: classification, imaging findings, and clinical relevance. AJNR Am J Neuroradiol 2010;31:1778-86.
23. Ortega Herrera R, Ruiz Santiago F, Cañadillas Barea L, Galera L. Elongation of the anterior tubercle of the cervical vertebral transverse process. Radiología 1999;41:531-3.
24. Expert Panel on Neurological Imaging and Musculoskeletal Imaging:, Beckmann NM, West OC, Nunez D Jr, Kirsch CFE, Aulino JM, Broder JS, Cassidy RC, Czuczman GJ, Demertzis JL, Johnson MM, Motamedi K, Reitman C, Shah LM, Than K, Ying-Kou Yung E, Beaman FD, Kransdorf MJ, Bykowski J. ACR Appropriateness Criteria® Suspected Spine Trauma. J Am Coll Radiol 2019;16:S264-S285.
25. Bailitz J, Starr F, Beecroft M, Bankoff J, Roberts R, Bokhari F, Joseph K, Wiley D, Dennis A, Gilkey S, Erickson P, Raksin P, Nagy K. CT should replace three-view radiographs as the initial screening test in patients at high, moderate, and low risk for blunt cervical spine injury: a prospective comparison. J Trauma 2009;66:1605-9.
26. Griffen MM, Frykberg ER, Kerwin AJ, Schinco MA, Tepas JJ, Rowe K, Abboud J. Radiographic clearance of blunt cervical spine injury: plain radiograph or computed tomography scan? J Trauma 2003;55:222-6; discussion 226-7.
27. Veiga JRS, Mitchell K. Cervical spine clearance in the adult obtunded blunt trauma patient: A systematic review. Intensive Crit Care Nurs 2019;51:57-63.
28. Duane TM, Young AJ, Vanguri P, Wolfe LG, Katzen J, Han J, Mayglothling J, Whelan JF, Aboutanos MB,

Ivatury RR, Malhotra AK. Defining the cervical spine clearance algorithm: A single-institution prospective study of more than 9,000 patients. J Trauma Acute Care Surg 2016;81:541-7.
29. Hoffman JR, Mower WR, Wolfson AB, Todd KH, Zucker MI. Validity of a set of clinical criteria to rule out injury to the cervical spine in patients with blunt trauma. National Emergency X-Radiography Utilization Study Group. N Engl J Med 2000;343:94-9.
30. Stiell IG, Wells GA, Vandemheen KL, Clement CM, Lesiuk H, De Maio VJ, Laupacis A, Schull M, McKnight RD, Verbeek R, Brison R, Cass D, Dreyer J, Eisenhauer MA, Greenberg GH, MacPhail I, Morrison L, Reardon M, Worthington J. The Canadian C-spine rule for radiography in alert and stable trauma patients. JAMA 2001;286:1841-8.
31. Peetz AB, Salim A. Clearance of the Spine. Curr Trauma Rep 2015;1:160-8.
32. Sliker CW, Mirvis SE, Shanmuganathan K. Assessing cervical spine stability in obtunded blunt trauma patients: review of medical literature. Radiology 2005;234:733-9.
33. Karul M, Bannas P, Schoennagel BP, Hoffmann A, Wedegaertner U, Adam G, Yamamura J. Fractures of the thoracic spine in patients with minor trauma: comparison of diagnostic accuracy and dose of biplane radiography and MDCT. Eur J Radiol 2013;82:1273-7.
34. Rhea JT, Sheridan RL, Mullins ME, Novelline RA. Can chest and abdominal trauma CT eliminate the need for plain films of the spine? – Experience with 329 multiple trauma patients. Emergency Radiology 2001;8:99-104.
35. Sheridan R, Peralta R, Rhea J, Ptak T, Novelline R. Reformatted visceral protocol helical computed tomographic scanning allows conventional radiographs of the thoracic and lumbar spine to be eliminated in the evaluation of blunt trauma patients. J Trauma 2003;55:665-9.
36. Ballock RT, Mackersie R, Abitbol JJ, Cervilla V, Resnick D, Garfin SR. Can burst fractures be predicted from plain radiographs? J Bone Joint Surg Br 1992;74:147-50.
37. Melton LJ 3rd. Epidemiology of spinal osteoporosis. Spine (Phila Pa 1976) 1997;22:2S-11S.
38. Wáng YX, Lentle BC. Radiographic osteoporotic vertebral fractures in elderly men: a brief review focusing on differences between the sexes. Quant Imaging Med Surg 2020;10:1863-76.
39. Weaver J, Sajjan S, Lewiecki EM, Harris ST, Marvos P. Prevalence and Cost of Subsequent Fractures Among U.S. Patients with an Incident Fracture. J Manag Care Spec Pharm 2017;23:461-71.
40. Delmas PD, Genant HK, Crans GG, Stock JL, Wong M, Siris E, Adachi JD. Severity of prevalent vertebral fractures and the risk of subsequent vertebral and nonvertebral fractures: results from the MORE trial. Bone 2003;33:522-32.
41. Sanchez-Rodriguez D, Bergmann P, Body JJ, Cavalier E, Gielen E, Goemaere S, Lapauw B, Laurent MR, Rozenberg S, Honvo G, Beaudart C, Bruyère O. The Belgian Bone Club 2020 guidelines for the management of osteoporosis in postmenopausal women. Maturitas 2020;139:69-89.
42. Danila MI, Saag KG. Imminent Fracture Risk: A Call to Action for Rheumatologists. Arthritis Care Res (Hoboken) 2020;72:741-3.
43. Nuti R, Brandi ML, Checchia G, Di Munno O, Dominguez L, Falaschi P, Fiore CE, Iolascon G, Maggi S, Michieli R, Migliaccio S, Minisola S, Rossini M, Sessa G, Tarantino U, Toselli A, Isaia GC. Guidelines for the management of osteoporosis and fragility fractures. Intern Emerg Med 2019;14:85-102.
44. Singer A, Exuzides A, Spangler L, O'Malley C, Colby C, Johnston K, Agodoa I, Baker J, Kagan R. Burden of illness for osteoporotic fractures compared with other serious diseases among postmenopausal women in the United States. Mayo Clin Proc 2015;90:53-62.
45. Crandall CJ, Newberry SJ, Diamant A, Lim YW, Gellad WF, Booth MJ, Motala A, Shekelle PG. Comparative effectiveness of pharmacologic treatments to prevent fractures: an updated systematic review. Ann Intern Med 2014;161:711-23.
46. Viswanathan M, Reddy S, Berkman N, Cullen K, Middleton JC, Nicholson WK, Kahwati LC. Screening to prevent osteoporotic fractures: updated evidence report and systematic review for the US preventive services task force. JAMA 2018;319:2532-51.
47. Ensrud KE, Blackwell TL, Fink HA, Zhang J, Cauley JA, Cawthon PM, Black DM, Bauer DC, Curtis JR, Orwoll ES, Barrett-Connor E, Kado DM, Marshall LM, Shikany JM, Schousboe JT; Osteoporotic Fractures in Men (MrOS) Research Group. What Proportion of Incident Radiographic Vertebral Fractures in Older Men Is Clinically Diagnosed and Vice Versa: A Prospective Study. J Bone Miner Res 2016;31:1500-3.
48. Fink HA, Milavetz DL, Palermo L, Nevitt MC, Cauley JA, Genant HK, Black DM, Ensrud KE; Fracture Intervention Trial Research Group. What proportion of incident radiographic vertebral deformities is clinically diagnosed

and vice versa? J Bone Miner Res 2005;20:1216-22.
49. Kim DH, Vaccaro AR. Osteoporotic compression fractures of the spine; current options and considerations for treatment. Spine J 2006;6:479-87.
50. Messina C, Maffi G, Vitale JA, Ulivieri FM, Guglielmi G, Sconfienza LM. Diagnostic imaging of osteoporosis and sarcopenia: a narrative review. Quant Imaging Med Surg 2018;8:86-99.
51. Rosen HN, Vokes TJ, Malabanan AO, Deal CL, Alele JD, Olenginski TP, Schousboe JT. The Official Positions of the International Society for Clinical Densitometry: vertebral fracture assessment. J Clin Densitom 2013;16:482-8.
52. Jiang G, Eastell R, Barrington NA, Ferrar L. Comparison of methods for the visual identification of prevalent vertebral fracture in osteoporosis. Osteoporos Int 2004;15:887-96.
53. Lunt M, Felsenberg D, Reeve J, Benevolenskaya L, Cannata J, Dequeker J, Dodenhof C, Falch JA, Masaryk P, Pols HA, Poor G, Reid DM, Scheidt-Nave C, Weber K, Varlow J, Kanis JA, O'Neill TW, Silman AJ. Bone density variation and its effects on risk of vertebral deformity in men and women studied in thirteen European centers: the EVOS Study. J Bone Miner Res 1997;12:1883-94.
54. Wáng YXJ, Che-Nordin N, Leung JCS, Kwok TCY. Existing severe osteoporotic vertebral fractures in elderly Chinese males were only weakly associated with higher further vertebral fracture risk at year-4 follow-up. Osteoporos Int 2020;31:1593-4.
55. Wang XR, Xu FR, Huang QL, Wáng YXJ. Radiological features of traumatic vertebral endplate fracture: an analysis of 194 cases with 263 vertebral fractures. Chin Med J (Engl) 2020. [Epub ahead of print]. doi: 10.1097/CM9.0000000000000919.
56. Sugita M, Watanabe N, Mikami Y, Hase H, Kubo T. Classification of vertebral compression fractures in the osteoporotic spine. J Spinal Disord Tech 2005;18:376-81.
57. Ha KY, Kim YH. Risk factors affecting progressive collapse of acute osteoporotic spinal fractures. Osteoporos Int 2013;24:1207-13.
58. Lentle BC, Berger C, Probyn L, Brown JP, Langsetmo L, Fine B, Lian K, Shergill AK, Trollip J, Jackson S, Leslie WD, Prior JC, Kaiser SM, Hanley DA, Adachi JD, Towheed T, Davison KS, Cheung AM, Goltzman D; CaMos Research Group. Comparative Analysis of the Radiology of Osteoporotic Vertebral Fractures in Women and Men: Cross-Sectional and Longitudinal Observations from the Canadian Multicentre Osteoporosis Study (CaMos). J Bone Miner Res 2018;33:569-79.
59. Schnake KJ, Blattert TR, Hahn P, Franck A, Hartmann F, Ullrich B, Verheyden A, Mörk S, Zimmermann V, Gonschorek O, Müller M, Katscher S, Saman AE, Pajenda G, Morrison R, Schinkel C, Piltz S, Partenheimer A, Müller CW, Gercek E, Scherer M, Bouzraki N, Kandziora F; Spine Section of the German Society for Orthopaedics and Trauma. Classification of Osteoporotic Thoracolumbar Spine Fractures: Recommendations of the Spine Section of the German Society for Orthopaedics and Trauma (DGOU). Global Spine J 2018;8:46S-49S.
60. Blattert TR, Schnake KJ, Gonschorek O, Gercek E, Hartmann F, Katscher S, Mörk S, Morrison R, Müller M, Partenheimer A, Piltz S, Scherer MA, Ullrich BW, Verheyden A, Zimmermann V; Spine Section of the German Society for Orthopaedics and Trauma. Nonsurgical and Surgical Management of Osteoporotic Vertebral Body Fractures: Recommendations of the Spine Section of the German Society for Orthopaedics and Trauma (DGOU). Global Spine J 2018;8:50S-55S.
61. Genant HK, Wu CY, van Kuijk C, Nevitt MC. Vertebral fracture assessment using a semiquantitative technique. J Bone Miner Res 1993;8:1137-48.
62. Wáng YXJ, Che-Nordin N. Informed communication with study subjects of radiographically detected osteoporotic vertebral deformity. Quant Imaging Med Surg 2018;8:876-80.
63. Wáng YXJ, Diacinti D, Yu W, Cheng XG, Nogueira-Barbosa MH, Che-Nordin N, Guglielmi G, Ruiz Santiago F. Semi-quantitative grading and extended semi-quantitative grading for osteoporotic vertebral deformity: a radiographic image database for education and calibration. Ann Transl Med 2020;8:398.
64. Wáng YXJ, Che-Nordin N, Deng M, Leung JCS, Kwok AWL, He LC, Griffith JF, Kwok TCY, Leung PC. Osteoporotic vertebral deformity with endplate/cortex fracture is associated with higher further vertebral fracture risk: the Ms. OS (Hong Kong) study results. Osteoporos Int 2019;30:897-905.
65. Wáng YXJ. A modified semi-quantitative (mSQ) grading scheme for osteoporotic vertebral fracture in elderly women. Quant Imaging Med Surg 2019;9:146-50.
66. Lentle B, Trollip J, Lian K. The Radiology of Osteoporotic Vertebral Fractures Redux. J Clin Densitom 2016;19:40-7.
67. Deng M, Kwok TCY, Leung JCS, Leung PC, Wáng YXJ. All osteoporotically deformed vertebrae with >34% height loss have radiographically identifiable endplate/cortex fracture. J Orthop Translat 2018;14:63-6.
68. Guggina P, Flahive J, Hooven FH, Watts NB, Siris ES,

Silverman S, Roux C, Pfeilschifter J, Greenspan SL, Díez-Pérez A, Cooper C, Compston JE, Chapurlat R, Boonen S, Adachi JD, Anderson FA Jr, Gehlbach S; GLOW Investigators. Characteristics associated with anti-osteoporosis medication use: data from the Global Longitudinal Study of Osteoporosis in Women (GLOW) USA cohort. Bone 2012;51:975-80.
69. Delmas PD, van de Langerijt L, Watts NB, Eastell R, Genant H, Grauer A, Cahall DL; IMPACT Study Group. Underdiagnosis of vertebral fractures is a worldwide problem: the IMPACT study. J Bone Miner Res 2005;20:557-63.
70. Bartalena T, Rinaldi MF, Modolon C, Braccaioli L, Sverzellati N, Rossi G, Rimondi E, Busacca M, Albisinni U, Resnick D. Incidental vertebral compression fractures in imaging studies: Lessons not learned by radiologists. World J Radiol 2010;2:399-404.
71. Wáng YXJ, Che-Nordin N. Some radiographically 'occult' osteoporotic vertebral fractures can be evidential if we look carefully. Quant Imaging Med Surg 2019;9:1992-5.
72. Wáng YXJ, Du MM, Che-Nordin N, Ye PP, Qiu SW, Griffith JF, Yan ZH. Recognizing osteoporotic vertebral deformity on frontal view radiograph: a cohort analysis and a pictorial review. Arch Osteoporos 2020;15:41.
73. Matzaroglou C, Georgiou CS, Panagopoulos A, Assimakopoulos K, Wilke HJ, Habermann B, Panos G, Kafchitsas K. Kümmell's Disease: Clarifying the Mechanisms and Patients' Inclusion Criteria Open. Orthop J 2014;8:288-97.
74. Venmans A, Klazen CA, Lohle PN, Mali WP, van Rooij WJ. Natural history of pain in patients with conservatively treated osteoporotic vertebral compression fractures: results from VERTOS II. AJNR Am J Neuroradiol 2012;33:519-21.
75. Cho JH, Shin SI, Lee JH, Yeom JS, Chang BS, Lee CK. Usefulness of prone cross-table lateral radiographs in vertebral compression fractures. Clin Orthop Surg 2013;5:195-201.
76. McKiernan F, Jensen R, Faciszewski T. The dynamic mobility of vertebral compression fractures. J Bone Miner Res 2003;18:24-9.
77. Lim J, Choi SW, Youm JY, Kwon HJ, Kim SH, Koh HS. Posttraumatic Delayed Vertebral Collapse : Kummell's Disease. J Korean Neurosurg Soc 2018;61:1-9.
78. Nakamae T, Fujimoto Y, Yamada K, Hashimoto T, Olmarker K. Efficacy of Percutaneous Vertebroplasty in the Treatment of Osteoporotic Vertebral Compression Fractures with Intravertebral Cleft. Open Orthop J 2015;9:107-13.
79. Wáng YXJ, Santiago FR, Deng M, Nogueira-Barbosa MH. Identifying osteoporotic vertebral endplate and cortex fractures. Quant Imaging Med Surg 2017;7:555-91.
80. Pathria M, Sartoris DJ, Resnick D. Osteoarthritis of the facet joints: accuracy of oblique radiographic assessment. Radiology 1987;164:227-30.
81. Resnick D. Degenerative disease of the vertebral column. Radiology 1985;156:3-14.
82. Jensen MC, Brant-Zawadzki MN, Obuchowski N, Modic MT, Malkasian D, Ross JS. Magnetic resonance imaging of the lumbar spine in people without back pain. N Engl J Med 1994;331:69-73.
83. Milette PC. The proper terminology for reporting lumbar intervertebral disk disorders. AJNR Am J Neuroradiol 1997;18:1859-66.
84. Mader R, Verlaan JJ, Eshed I, Bruges-Armas J, Puttini PS, Atzeni F, Buskila D, Reinshtein E, Novofastovski I, Fawaz A, Kurt V, Baraliakos X. Diffuse idiopathic skeletal hyperostosis (DISH): where we are now and where to go next. RMD Open 2017;3:e000472.
85. Utsinger PD. Diffuse idiopathic skeletal hyperostosis. Clin Rheum Dis 1985;11:325-51.
86. Buckle CE, Udawatta V, Straus CM. Now You See It, Now You Don't: Visual Illusions in Radiology. RadioGraphics 2013; 33:2087-102.
87. Gallucci M, Limbucci N, Paonessa A, Splendiani A. Degenerative disease of the spine. Neuroimaging Clin N Am 2007;17:87-103.
88. Leone A, Guglielmi G, Cassar-Pullicino VN, Bonomo L. Lumbar intervertebral instability: a review. Radiology 2007;245:62-77.
89. Jiang SD, Jiang LS, Dai LY. Degenerative cervical spondylolisthesis: a systematic review. Int Orthop 2011;35:869-75.
90. Fielding JW, Cochran Gv, Lawsing JF 3rd, Hohl M. Tears of the transverse ligament of the atlas. A clinical and biomechanical study. J Bone Joint Surg Am 1974;56:1683-91.
91. Meyerding HW. Spondylolisthesis. Surgical, Gynecology, & Obstetrics 1932;54:371-7.
92. Wáng YX, Deng M, Griffith JF, Kwok AW, Leung JC, Ahuja AT, Kwok T, Leung PC. Lumbar Spondylolisthesis Progression and De Novo Spondylolisthesis in Elderly Chinese Men and Women: A Year-4 Follow-up Study. Spine (Phila Pa 1976) 2016;41:1096-103.
93. Amato M, Totty WG, Gilula LA. Spondylolysis of the lumbar spine: demonstration of defects and laminal

fragmentation. Radiology 1984;153:627-9.
94. Libson E, Bloom RA, Dinari G. Symptomatic and asymptomatic spondylolysis and spondylolisthesis in young adults. Int Orthop 1982;6:259-61.
95. Schmid T, Heini P, Benneker L. A rare case of non-traumatic, multi-level, bilateral pedicle fractures of the lumbar spine in a 60-year-old patient. Eur Spine J 2017;26:197-201.
96. Hu SS, Tribus CB, Diab M, Ghanayem AJ. Spondylolisthesis and spondylolysis. J Bone Joint Surg Am 2008;90:656-71.
97. He LC, Wang YX, Gong JS, Griffith JF, Zeng XJ, Kwok AW, Leung JC, Kwok T, Ahuja AT, Leung PC. Prevalence and risk factors of lumbar spondylolisthesis in elderly Chinese men and women. Eur Radiol 2014;24:441-8.
98. Wang YXJ, Káplár Z, Deng M, Leung JCS. Lumbar degenerative spondylolisthesis epidemiology: A systematic review with a focus on gender-specific and age-specific prevalence. J Orthop Translat 2016;11:39-52.
99. Fon GT, Pitt MJ, Thies AC Jr. Thoracic kyphosis: range in normal subjects. AJR Am J Roentgenol 1980;134:979-83.
100. Vialle R, Levassor N, Rillardon L, Templier A, Skalli W, Guigui P. Radiographic analysis of the sagittal alignment and balance of the spine in asymptomatic subjects. J Bone Joint Surg Am 2005;87:260-7.
101. Jackson RP, McManus AC. Radiographic analysis of sagittal plane alignment and balance in standing volunteers and patients with low back pain matched for age, sex, and size: a prospective controlled clinical study. Spine (Phila Pa 1976) 1994;19:1611-8.
102. Boyle JJ, Milne N, Singer KP. Influence of age on cervicothoracic spinal curvature: an ex vivo radiographic survey. Clin Biomech (Bristol, Avon) 2002;17:361-7.
103. Kado DM, Prenovost K, Crandall C. Narrative review: hyperkyphosis in older persons. Ann Intern Med 2007;147:330-8.
104. Ohrt-Nissen S, Cheung JPY, Hallager DW, Gehrchen M, Kwan K, Dahl B, Cheung KMC, Samartzis D. Reproducibility of thoracic kyphosis measurements in patients with adolescent idiopathic scoliosis. Scoliosis Spinal Disord 2017;12:4.
105. Kyrölä KK, Salme J, Tuija J, Tero I, Eero K, Arja H. Intra- and Interrater Reliability of Sagittal Spinopelvic Parameters on Full-Spine Radiographs in Adults With Symptomatic Spinal Disorders. Neurospine 2018;15:175-81.
106. Sachs B, Bradford D, Winter R, Lonstein J, Moe J, Willson S. Scheuermann kyphosis. Follow-up of Milwaukee-brace treatment. J Bone Joint Surg Am 1987;69:50-7.
107. Sørensen KH. Scheuermann's juvenile kyphosis. København: Munksgaard 1964:222-4
108. Farsetti P, Tudisco C, Caterini R, Ippolito E. Juvenile and idiopathic kyphosis. Long-term follow-up of 20 cases. Arch Orthop Trauma Surg 1991;110:165-8.
109. Gaca AM, Barnhart HX, Bisset GS 3rd. Evaluation of wedging of lower thoracic and upper lumbar vertebral bodies in the pediatric population. AJR Am J Roentgenol 2010;194:516-20.
110. Masharawi Y, Salame K, Mirovsky Y, Peleg S, Dar G, Steinberg N, Hershkovitz I. Vertebral body shape variation in the thoracic and lumbar spine: characterization of its asymmetry and wedging. Clin Anat 2008;21:46-54.
111. Been E, Kalichman L. Lumbar lordosis. Spine J 2014;14:87-97.
112. Gelb DE, Lenke LG, Bridwell KH, Blanke K, McEnery KW. An analysis of sagittal spinal alignment in 100 asymptomatic middle and older aged volunteers. Spine (Phila Pa 1976) 1995;20:1351-8.
113. Kuntz C 4th, Levin LS, Ondra SL, Shaffrey CI, Morgan CJ. Neutral upright sagittal spinal alignment from the occiput to the pelvis in asymptomatic adults: a review and resynthesis of the literature. J Neurosurg Spine 2007;6:104-12.
114. Le Huec JC, Thompson W, Mohsinaly Y, Barrey C, Faundez A. Sagittal balance of the spine. Eur Spine J 2019;28:1889-905.
115. Diebo BG, Varghese JJ, Lafage R, Schwab FJ, Lafage V. Sagittal alignment of the spine: What do you need to know? Clin Neurol Neurosurg 2015;139:295-301.
116. Schwab F, Patel A, Ungar B, Farcy JP, Lafage V. Adult spinal deformity-postoperative standing imbalance: how much can you tolerate? An overview of key parameters in assessing alignment and planning corrective surgery. Spine (Phila Pa 1976) 2010;35:2224-31.
117. Glassman SD, Berven S, Bridwell K, Horton W, Dimar JR. Correlation of radiographic parameters and clinical symptoms in adult scoliosis. Spine (Phila Pa 1976) 2005;30:682-8.
118. Sud A, Tsirikos AI. Current concepts and controversies on adolescent idiopathic scoliosis: Part I. Indian J Orthop 2013;47:117-28.
119. Tanure MC, Pinheiro AP, Oliveira AS. Reliability assessment of Cobb angle measurements using manual and digital methods. Spine J 2010;10:769-74.
120. Gstoettner M, Sekyra K, Walochnik N, Winter P, Wachter R, Bach CM. Inter- and intraobserver reliability assessment

of the Cobb angle: manual versus digital measurement tools. Eur Spine J 2007;16:1587-92.
121. Lenke LG, Edwards CC 2nd, Bridwell KH. The Lenke classification of adolescent idiopathic scoliosis: how it organizes curve patterns as a template to perform selective fusions of the spine. Spine (Phila Pa 1976) 2003;28:S199-207.
122. Buchowski JM, Kuhns CA, Bridwell KH, Lenke LG. Surgical management of posttraumatic thoracolumbar kyphosis. Spine J 2008;8:666-77.
123. Lowe T, Berven SH, Schwab FJ, Bridwell KH. The SRS classification for adult spinal deformity: building on the King/Moe and Lenke classification systems. Spine (Phila Pa 1976) 2006;31:S119-25.
124. Bao H, Yan P, Qiu Y, Liu Z, Zhu F. Coronal imbalance in degenerative lumbar scoliosis: Prevalence and influence on surgical decision-making for spinal osteotomy. Bone Joint J 2016;98-B:1227-33.
125. Plais N, Bao H, Lafage R, Gupta M, Smith JS, Shaffrey C, Mundis G, Burton D, Ames C, Klineberg E, Bess S, Schwab F, Lafage V; International Spine Study Group. The clinical impact of global coronal malalignment is underestimated in adult patients with thoracolumbar scoliosis. Spine Deform 2020;8:105-13.
126. Jurik AG. Imaging the spine in arthritis-a pictorial review. Insights Imaging 2011;2:177-91.
127. Rudwaleit M, van der Heijde D, Landewé R, Listing J, Akkoc N, Brandt J, Braun J, Chou CT, Collantes-Estevez E, Dougados M, Huang F, Gu J, Khan MA, Kirazli Y, Maksymowych WP, Mielants H, Sørensen IJ, Ozgocmen S, Roussou E, Valle-Oñate R, Weber U, Wei J, Sieper J. The development of Assessment of SpondyloArthritis international Society classification criteria for axial spondyloarthritis (part II): validation and final selection. Ann Rheum Dis 2009;68:777-83.
128. Proft F, Poddubnyy D. Ankylosing spondylitis and axial spondyloarthritis: recent insights and impact of new classification criteria. Ther Adv Musculoskelet Dis 2018;10:129-39.
129. Tsoi C, Griffith JF, Lee RKK, Wong PCH, Tam LS. Imaging of sacroiliitis: Current status, limitations and pitfalls. Quant Imaging Med Surg 2019;9:318-35.
130. Malaviya AN, Rawat R, Agrawal N, Patil NS. The Nonradiographic Axial Spondyloarthritis, the Radiographic Axial Spondyloarthritis, and Ankylosing Spondylitis: The Tangled Skein of Rheumatology. Int J Rheumatol 2017;2017:1824794.
131. Braun J, Sieper J, Bollow M. Imaging of sacroiliitis. Clin Rheumatol 2000;19:51-7.
132. van Tubergen A, Heuft-Dorenbosch L, Schulpen G, Landewé R, Wijers R, van der Heijde D, van Engelshoven J, van der Linden S. Radiographic assessment of sacroiliitis by radiologists and rheumatologists: does training improve quality? Ann Rheum Dis 2003;62:519-25.
133. Guglielmi G, Scalzo G, Cascavilla A, Carotti M, Salaffi F, Grassi W. Imaging of the sacroiliac joint involvement in seronegative spondylarthropathies. Clin Rheumatol 2009;28:1007-19.
134. Muche B, Bollow M, François RJ, Sieper J, Hamm B, Braun J. Anatomic structures involved in early- and late-stage sacroiliitis in spondylarthritis: a detailed analysis by contrast-enhanced magnetic resonance imaging. Arthritis Rheum 2003;48:1374-84.
135. Helliwell PS, Hickling P, Wright V. Do the radiological changes of classic ankylosing spondylitis differ from the changes found in the spondylitis associated with inflammatory bowel disease, psoriasis, and reactive arthritis? Ann Rheum Dis 1998;57:135-40.
136. Park WM, Spencer DG, McCall IW, Ward J, Buchanan WW, Stephens WH. The detection of spinal pseudarthrosis in ankylosing spondylitis. Br J Radiol 1981;54:467-72.
137. Feldtkeller E, Vosse D, Geusens P, van der Linden S. Prevalence and annual incidence of vertebral fractures in patients with ankylosing spondylitis. Rheumatol Int 2006;26:234-9.
138. Ogdie A, Harter L, Shin D, Baker J, Takeshita J, Choi HK, Love TJ, Gelfand JM. The risk of fracture among patients with psoriatic arthritis and psoriasis: a population-based study. Ann Rheum Dis 2017;76:882-5.
139. Younes M, Belghali S, Kriâa S, Zrour S, Bejia I, Touzi M, Golli M, Gannouni A, Bergaoui N. Compared imaging of the rheumatoid cervical spine: prevalence study and associated factors. Joint Bone Spine 2009;76:361-8.
140. Varma R, Lander P, Assaf A. Imaging of pyogenic infectious spondylodiskitis. Radiol Clin North Am 2001;39:203-13.
141. Govender S. Spinal infections. J Bone Joint Surg Br 2005;87:1454-8.
142. Cheung WY, Luk KD. Pyogenic spondylitis. Int Orthop 2012;36:397-404.
143. Teh J, Imam A, Watts C. Imaging of back pain. Imaging 2005;17:171-207.
144. Rodallec MH, Feydy A, Larousserie F, Anract P, Campagna R, Babinet A, Zins M, Drapé JL. Diagnostic imaging of solitary tumors of the spine: what to do and say.

Radiographics 2008;28:1019-41.
145. Kamholtz R, Sze G. Current imaging in spinal metastatic disease. Semin Oncol 1991;18:158-69.
146. Jacobson AF, Stomper PC, Cronin EB, Kaplan WD. Bone scans with one or two new abnormalities in cancer patients with no known metastases: reliability of interpretation of initial correlative radiographs. Radiology 1990;174:503-7.
147. Algra PR, Heimans JJ, Valk J, Nauta JJ, Lachniet M, Van Kooten B. Do metastases in vertebrae begin in the body or the pedicles? Imaging study in 45 patients. AJR Am J Roentgenol 1992;158:1275-9.
148. Jacobs WB, Perrin RG. Evaluation and treatment of spinal metastases: an overview. Neurosurg Focus 20062001;11:e10.
149. Sham JS, Cheung YK, Chan FL, Choy D. Nasopharyngeal carcinoma: pattern of skeletal metastases. Br J Radiol 1990;63:202-5.
150. Goldman SM, Fajardo AA, Naraval RC, Madewell JE. Metastatic transitional cell carcinoma from the bladder: radiographic manifestions. AJR Am J Roentgenol 1979 ;132:419-25.
151. Kunkler IH, Merrick MV, Rodger A. Bone scintigraphy in breast cancer: a nine-year follow-up. Clin Radiol 1985;36:279-82.
152. Price HI, Batnitzky S. The computed tomographic findings in benign diseases of the vertebral column. Crit Rev Diagn Imaging 1985;24:39-89.
153. Murphey MD, Choi JJ, Kransdorf MJ, Flemming DJ, Gannon FH. Imaging of osteochondroma: variants and complications with radiologic-pathologic correlation. Radiographics 2000;20:1407-34.
154. Laredo JD, el Quessar A, Bossard P, Vuillemin-Bodaghi V. Vertebral tumors and pseudotumors. Radiol Clin North Am 2001;39:137-63, vi.
155. Hansford BG, Silbermann R. Advanced Imaging of Multiple Myeloma Bone Disease. Front Endocrinol (Lausanne) 2018;9:436.
156. Collins CD. Multiple myeloma. Cancer Imaging 2004;4 Spec No A:S47-53.
157. Lasocki A, Gaillard F, Harrison SJ. Multiple myeloma of the spine. Neuroradiol J 2017;30:259-68.
158. Lecouvet FE, Vande Berg BC, Michaux L, Jamart J, Maldague BE, Malghem J. Development of vertebral fractures in patients with multiple myeloma: does MRI enable recognition of vertebrae that will collapse? J Comput Assist Tomogr 1998;22:430-6.
159. Spiess JL, Adelstein DJ, Hines JD. Multiple myeloma presenting with spinal cord compression. Oncology 1988;45:88-92.

Cite this article as: Ruiz Santiago F, Láinez Ramos-Bossini AJ, Wáng YXJ, López Zúñiga D. The role of radiography in the study of spinal disorders. Quant Imaging Med Surg 2020;10(12):2322-2355. doi: 10.21037/qims-20-1014

TRABAJO 2: THE VALUE OF MAGNETIC RESONANCE IMAGING AND COMPUTED TOMOGRAPHY IN THE STUDY OF SPINAL DISORDERS.

Ruiz Santiago F, **Láinez Ramos-Bossini AJ**, Wáng YXJ, Martínez Barbero JP, García Espinosa J, Martínez Martínez A. The value of magnetic resonance imaging and computed tomography in the study of spinal disorders. Quant Imaging Med Surg. 2022;12(7):3947-3986. doi: 10.21037/qims-2022-04. PMID: 35782254. FI: 2,8. Q2 (T2).

Se trata de una revisión bibliográfica y pictórica que cubre los objetivos 1 y 2.

Review Article

The value of magnetic resonance imaging and computed tomography in the study of spinal disorders

Fernando Ruiz Santiago[1], Antonio Jesús Láinez Ramos-Bossini[2], Yì Xiáng J. Wáng[3], José Pablo Martínez Barbero[2], Jade García Espinosa[2], Alberto Martínez Martínez[2]

[1]Department of Radiology and Physical Medicine, University of Granada, Granada, Spain; [2]Department of Radiology and Physical Medicine, Hospital Virgen de las Nieves, University of Granada, Granada, Spain; [3]Department of Imaging and Interventional Radiology, the Chinese University of Hong Kong, Shatin, New Territories, Hong Kong, China

Contributions: (I) Conception and design: F Ruiz Santiago, AJ Láinez Ramos-Bossini, YXJ Wáng; (II) Administrative support: F Ruiz Santiago, AJ Láinez Ramos-Bossini, YXJ Wáng, A Martínez Martínez; (III) Provision of study materials or patients: F Ruiz Santiago, AJ Láinez Ramos-Bossini, YXJ Wáng, A Martínez Martínez; (IV) Collection and assembly of data: F Ruiz Santiago, AJ Láinez Ramos-Bossini, YXJ Wáng, JP Martínez Barbero, J García Espinosa, A Martínez Martínez; (V) Data analysis and interpretation: F Ruiz Santiago, AJ Láinez Ramos-Bossini, YXJ Wáng, A Martínez Martínez; (VI) Manuscript writing: All authors; (VII) Final approval of manuscript: All authors.

Correspondence to: Dr. Fernando Ruiz Santiago. C-Julio Verne 8, 7 B 18003 Granada, Spain. Email: ferusan12@gmail.com.

Abstract: Computed tomography (CT) and magnetic resonance imaging (MRI) have replaced conventional radiography in the study of many spinal conditions, it is essential to know when these techniques are indicated instead of or as complementary tests to radiography, which findings can be expected in different clinical settings, and their significance in the diagnosis of different spinal conditions. Proper use of CT and MRI in spinal disorders may facilitate diagnosis and management of spinal conditions. An adequate clinical approach, a good understanding of the pathological manifestations demonstrated by these imaging techniques and a comprehensive report based on a universally accepted nomenclature represent the indispensable tools to improve the diagnostic approach and the decision-making process in patients with spinal pain. Several guidelines are available to assist clinicians in ordering appropriate imaging techniques to achieve an accurate diagnosis and to ensure appropriate medical care that meets the efficacy and safety needs of patients. This article reviews the clinical indications of CT and MRI in different pathologic conditions affecting the spine, including congenital, traumatic, degenerative, inflammatory, infectious and tumor disorders, as well as their main imaging features. It is intended to be a pictorial guide to clinicians involved in the diagnosis and treatment of spinal disorders.

Keywords: Spine; computed tomography (CT); magnetic resonance imaging (MRI); back pain; spinal disorder; spinal diseases; osteoporotic fracture

Submitted Feb 16, 2022. Accepted for publication Apr 13, 2022.
doi: 10.21037/qims-2022-04
View this article at: https://dx.doi.org/10.21037/qims-2022-04

Introduction

The widespread use of computed tomography (CT) and magnetic resonance imaging (MRI) for imaging spinal disorders has led to a decrease in the use of radiography as the first imaging modality in many clinical settings. Several guidelines are available to assist clinicians in ordering appropriate imaging techniques to achieve an accurate diagnosis and to ensure appropriate medical care that meets the efficacy and safety needs of patients (1-5).

When advanced imaging of the lumbar spine is required, MRI is often recommended over CT, due to the higher soft tissue contrast of the former and the use of ionizing radiation of the latter (6,7). Nevertheless, CT is still a useful technique for the study of bone structure and the follow-up

of interventional procedures.

Because CT and MRI have replaced conventional radiography in the study of many spinal conditions, it is essential to know when these techniques are indicated instead of or as complementary tests to radiography, which findings can be expected in different clinical settings, and their significance in the diagnosis of different spinal conditions.

General indications for CT and MRI of the spine

The primary indications for CT of the spine mainly include the evaluation of congenital anomalies, alignment abnormalities, traumatic injuries, and postoperative evaluation, sometimes with the use of intrathecal contrast.

On the other hand, MRI is the technique of choice in patients with suspected spinal cord injury or compression, in the presence of warning signs such as cauda equina syndrome, neoplasia or infection, or in case of complicated low back pain (e.g., persistent for more than 6 weeks despite conservative treatment), either because the patient is a candidate for intervention or surgery or because there is no diagnostic certainty. Patients with recurrent pain after surgery should be studied using contrast-enhanced MRI (1-5).

CT and MRI in congenital conditions of the spine

Congenital alterations of the spine can be simple, when there is no associated spinal deformity or they have little or no clinical significance, or complex, when they are associated with severe deformities. Morphologically, congenital alterations of the spine can be classified as secondary to defects involving vertebral formation, vertebral segmentation, or both (8,9). In the first case, all or part of the vertebra is not well formed/developed, leading to deformities such as agenesis, hemivertebrae, wedged or butterfly vertebrae. In the second case, the embryonic vertebrae do not separate, resulting in congenital vertebral block when complete, or unsegmented bar formation when incomplete (*Figure 1*).

Congenital deformities can also be classified according to the pattern of curvature. Among patients with congenital spinal deformities, 80% had scoliosis, 14% had kyphoscoliosis, and 6% had pure kyphosis. Hemivertebra is the most common cause of congenital scoliosis followed by unilateral unsegmented bar. Segmented hemivertebra is the most frequent and dangerous form because, totally separated from its adjacent vertebrae, it grows and acts as a wedge that enlarges and leads to progressive scoliosis. A semi-segmented hemivertebra is synostosed to one of the neighbouring vertebrae, thus the potential of growing deformity is usually lower. Finally, incarcerated hemivertebrae are inserted in a niche of the spine with no significant disc spaces and, therefore, they show less growth potential and minor deformity (8) (*Figure 1*).

Anterior failure of vertebral body formation is the most common cause of congenital kyphosis or kyphoscoliosis, followed by segmentation failure and mixed abnormalities (8). It has been classified into posterolateral quadrant vertebra (35%), posterior hemivertebra (7%), butterfly vertebra (13%) and anterior wedge vertebrae (5%) (11) (*Figure 1*).

Vertebral malformations have also been classified according to the underlying embryopathy. When abnormalities occur in the early phase of notochord formation, the gastrulation phase in the first 2–3 weeks of embryo development, malformations may affect structures derived from the three germinal cell layers, including the neuroaxis and axial skeleton. Abnormalities during primary or secondary neurulation (3–6 weeks) can also contribute to these malformations. These congenital malformations of the spine and spinal cord are collectively referred to as spinal dysraphism. Depending on the presence or absence of overlying skin covering, spinal dysraphism is divided into open and closed types. Myelomeningocele account for 98% of open dysraphism in which both the neural placode and meningeal lining protrude through the bony and cutaneous defect in the midline. Closed spinal dysraphism can be further classified according to the presence or absence of a subcutaneous mass. In the presence of a subcutaneous mass, two main forms of closed dysraphism can be differentiated: lipomyelocele and lipomyelomeningocele. They can be differentiated based on the position of the neural placode-lipoma interface, which lies within and out of the limits of the spinal canal, respectively. When no subcutaneous mass is present, several simple dysraphic states can be distinguished, including intradural lipoma, filar lipoma, tight filum terminale, dermal sinus and persistent terminal ventricle. Finally, there are other complex dysraphic states such as dorsal enteric fistula, neuroenteric cyst, split notochord syndrome, split cord/diastematomyelia, caudal regression syndrome, and segmental spinal dysgenesis (12-14) (*Figure 2*).

Radiography is usually the first imaging method to study congenital vertebral anomalies and related deformities, allowing their classification, evaluation of severity, risk of deformity progression, and vertebral count (15). As

Quantitative Imaging in Medicine and Surgery, Vol 12, No 7 July 2022

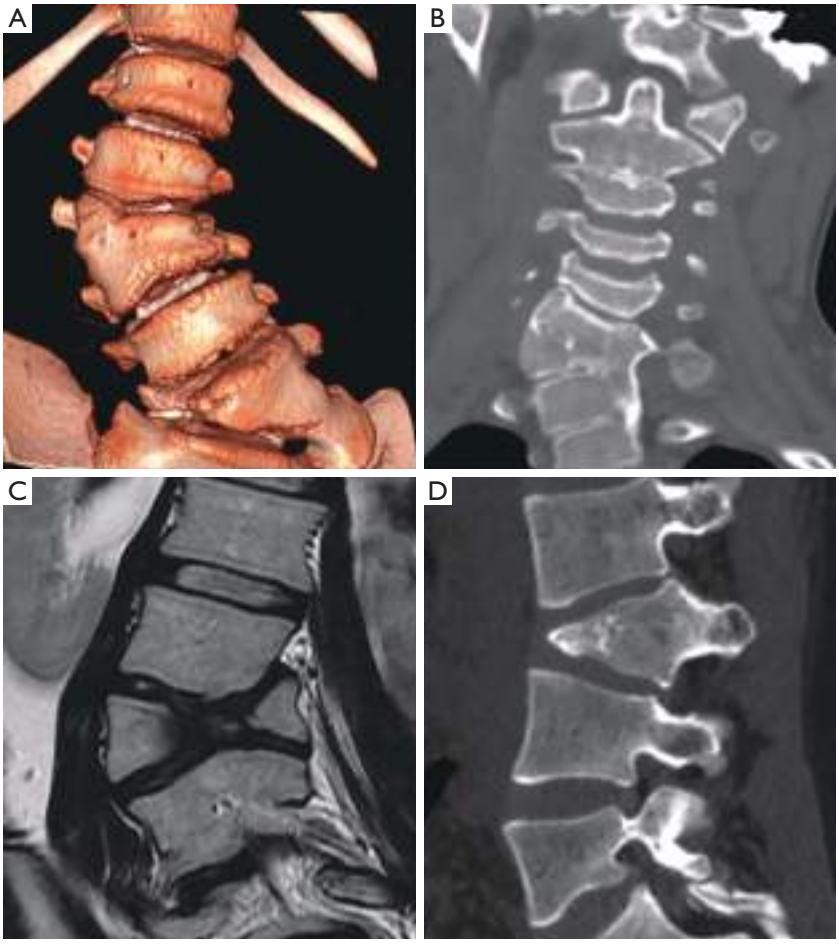

Figure 1 Congenital deformities. (A) Scoliosis secondary to a semi-segmented hemivertebra. (B) Klippel-Feil syndrome with formation and segmentation abnormalities. (C) Scoliosis secondary to asymmetric butterfly vertebra [from reference (10)]. (D) Kyphosis secondary to anterior failure of vertebral formation.

the number of bone malformations increases, there is a higher incidence of cord anomalies ranging from 20% to 58% (9,15,16), being higher in the presence of combined failures of segmentation and formation. Deformities in the sacrococcygeal area present the highest rate of spinal cord anomalies (16). MRI is the appropriate technique for complete evaluation of intraspinal abnormalities, including the presence of Chiari malformation or syrinxes, anomalies of the conus medullaris, or tethered cord syndrome (TCS). Filar thickness >2 mm measured at the L5-S1 level is considered abnormal. Proximal to this level, the stretched filum may falsely appear of normal thickness (17,18). CT may also be useful in defining the anatomy of vertebral deformities in pre-surgical planning (19). The information provided by imaging methods should be accurate, reporting the correct type of malformation is fundamentally important in the decision-making process (8,18).

Among simple congenital abnormalities, transitional vertebra is considered a developmental variant secondary to failed segmentation. The estimated mean prevalence is 7.5% for sacralization and 5.5% for lumbarization (20), ranging from 9.9% to 28.6% (21). The Castellvi classification is the most widely used to categorize lumbosacral transitional anomalies: type I refers to unilateral or bilateral enlarged transverse processes, type II includes unilateral or bilateral pseudo-articulation between the transverse process and

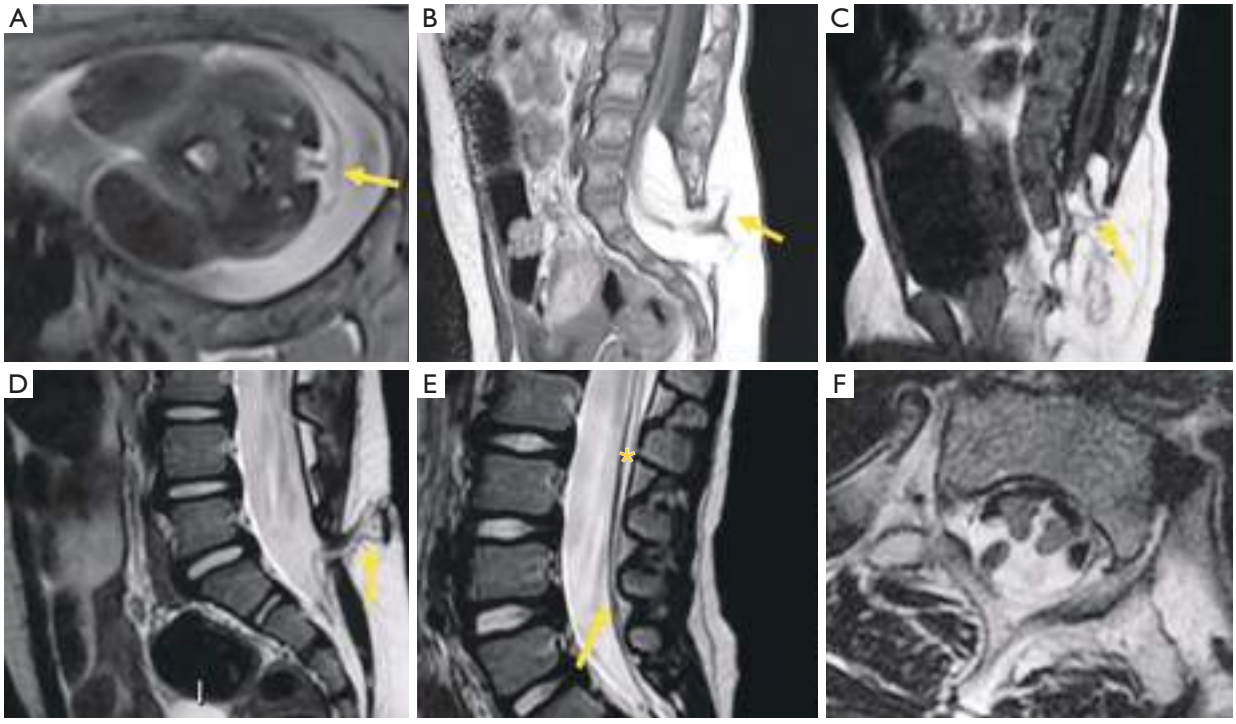

Figure 2 Spinal dysraphism. (A) Myelomeningocele in open dysraphism in intrauterine fetus showing the protruded placode (arrow). (B) Posterior closed dysraphism with lipomyelomeningocele. The lipoma/placode interface (arrow) is outside the spinal canal. (C) Lipomyelocele The lipoma/placode interface (arrow) is within the spinal canal. (D) Dermal sinus (arrow). (E) Tethered cord with filum terminale lipoma (*) and filar thickening (arrow). (F) Split cord/diastematomyelia.

the sacrum, type III refers to unilateral or bilateral fusion of the transverse process with the sacrum, and type IV is when there is unilateral fusion and contralateral pseudo-articulation. Types II and IV, in which a dysplastic transverse processes articulates with the sacrum, show a positive correlation with the presence of low back pain due to mechanical stress, or extraforaminal nerve compression at the transitional level (22-24) (*Figure 3*). Nevertheless, a recent study suggests that Castellvi type III seems to be associated with prolonged low back pain (21). Many authors consider that degenerative findings more commonly occur in transitional vertebrae above the transitional level (21,25).

Differentiating lumbarization from sacralization on MRI may be challenging when a complete vertebral count of the entire spine cannot be performed. Several methods have been described to identify the level of the vertebral body. The iliolumbar ligament is present in 85.7% of cases and extends from the L5 transverse process to the iliac wing in 96% (26). Other anatomical landmarks, such as the level of the conus medullaris, right renal artery, superior mesenteric artery, aortic bifurcation, or iliac crest height, are considered less accurate (27,28). More recently, identification of the nerve root of L5, with no proximal branching, has demonstrated 98% accuracy to identify the L5 vertebral body (29) (*Figure 4*).

Transitional anomalies can also be found at the cervicothoracic junction. Cervical ribs are the most frequent transitional abnormalities and have been described in association with lumbar sacralization. Another less known transitional anomaly is the elongation of the anterior tubercle of the cervical transverse process, which can lead to fusion of two vertebrae, typically C5 and C6 (30).

Traumatic pathologies

Conventional radiography has been largely superseded by CT for the assessment of traumatic spinal injury (2). The reported sensitivity values of the former are much lower compared to

Quantitative Imaging in Medicine and Surgery, Vol 12, No 7 July 2022

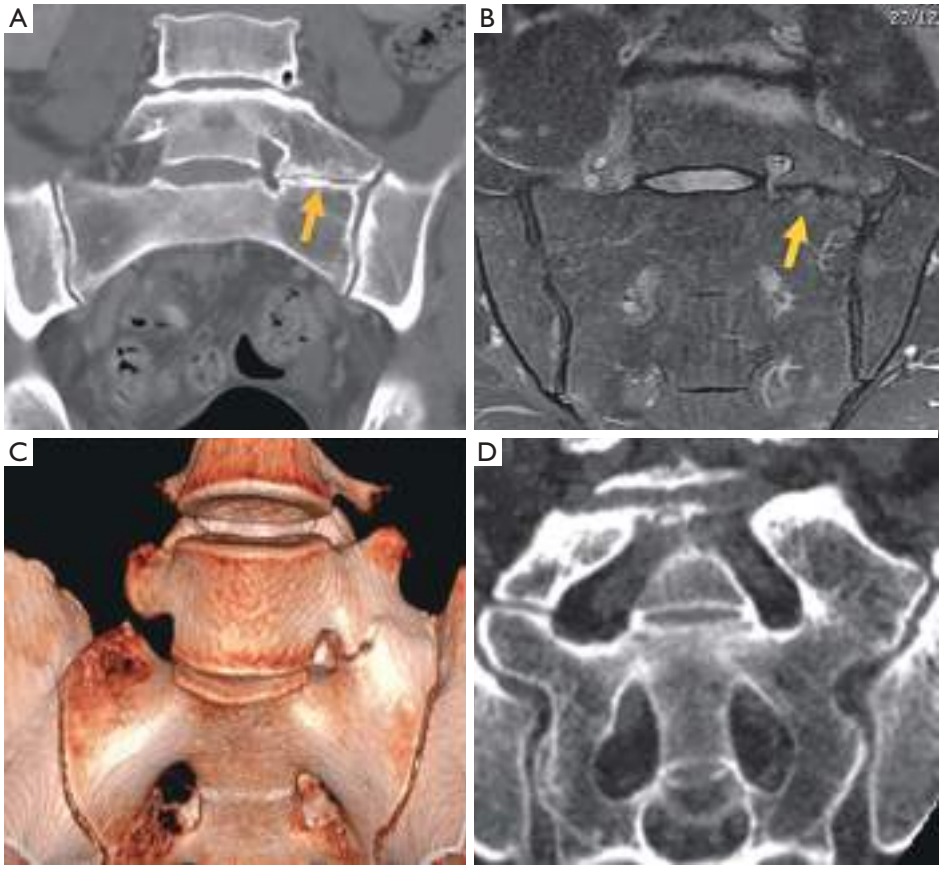

Figure 3 Castellvi types of transitional vertebra in three cases. Type II on CT depicting the neo articulation (arrow) (A) and MRI (B) showing the subchondral edema (arrow). (C) Type III on 3D CT. (D) Type IV on coronal CT. CT, computed tomography; MRI, magnetic resonance imaging.

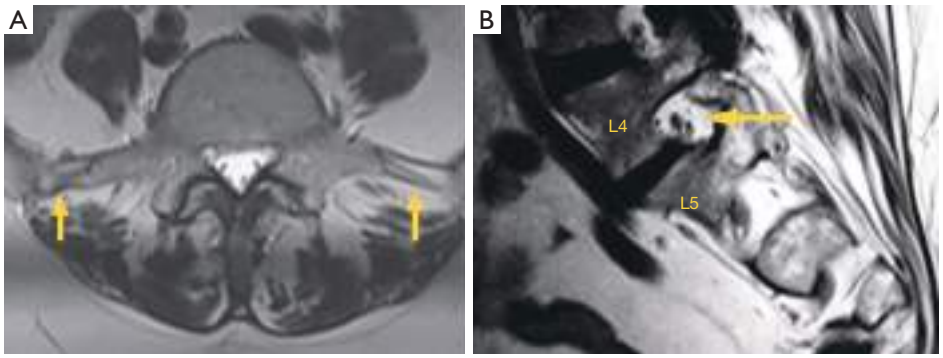

Figure 4 Transitional vertebral. (A) Iliolumbar ligament at L5 (arrows). (B) Splitting pattern of L4 (arrow) compared to L5 nerve root.

 Quant Imaging Med Surg 2022;12(7):3947-3986 | https://dx.doi.org/10.21037/qims-2022-04

Figure 5 AO-Spine thoracolumbar fracture classification score. (A) A0. Apophyseal fracture. (B) A1. Compression fracture without involvement of the posterior wall. (C) A2. Split fracture without involvement of the posterior wall. (D) A3. Burst fracture with involvement of one endplate. (E) A4. Burst fracture with involvement of both endplates. (F) B1. Trans osseous fracture. (G) B2. Posterior tension band injury fracture. (H) B3. Anterior tension band injury fracture (arrow). (I) Fracture dislocation injury type C. (J) MRI showing flavum (arrow), interspinous and supraspinous ligamentum tear. AO, Arbeitsgemeinschaft für Osteosynthesefragen; MRI, magnetic resonance imaging.

CT at the cervical and thoracolumbar spine, ranging from 36% to 65% in the former case (31,32), and from 49% to 82% in the latter (33-35). The most widely accepted classification system at present is mainly based on CT findings, either at the cervical (36) or thoracolumbar (37) level. The thoracolumbar fracture system scores include the morphology of the fracture (0–8 points) and the neurological status (0–4 points), but also other modifying variables such as the status of ligaments, which can tilt the balance between medical or surgical treatment. Three types of vertebral injuries based on morphological criteria have been described, with a total of 9 subgroups which are classified into three main categories: (I) compression injuries, (II) tension band injuries, and (III) translational injuries (*Figure 5*). The score strongly influences the therapeutic management. Injuries with a score of less than or equal to three points are treated non-surgically, those with more than five points are managed surgically, while both options are acceptable for scores of four and five points. Therefore, all B2, B3 and C type fractures must be managed surgically, unless there is a medical contraindication. Both surgical and non-surgical treatment can be applied to type A4 and B1 fractures. The remaining fracture subtypes can be managed conservatively, except when neurological or other clinical modifiers increase score severity (38). One of the modifiers included in this score is the status of the ligamentous complex, which adds 1 point when altered. Indirect signs of posterior ligamentous complex (PLC) injury include vertebral translation greater than 3.5 mm (39) and increased interspinous distance (40). Regarding the interspinous distance, variations of up to 7 mm can be normal, while 20% widening compared to adjacent levels is considered as an indirect sign of unstable PLC, that frequently results in surgical treatment (40).

MRI is primarily indicated when doubts about the most suitable treatment persist after CT evaluation of the fracture, as it allows quantification of spinal cord damage and assessment of the presence and severity of PLC injury (41). Ligament rupture on MRI is evidenced as a frank interruption of a normally dark ligament, which is replaced by fluid of high signal intensity on fluid sensitive MRI sequences. The accuracy of MRI has been reported to be higher for detecting injuries of the supraspinous ligament and ligamentum flavum, and slightly lower for injuries to the interspinous ligament and facet capsule (42) (*Figure 5*). The integrity of the PLC may imply a change in treatment strategy towards conservative therapy or minimally invasive surgery (43).

In terms of morphology, the classification is similar at the cervical and lumbar spine, except for subtle differences in individual scoring categories, and the fact that the ligaments are considered along with the disc complex, i.e., disco-ligamentous complex (DLC). Morphology score

Figure 6 AO-Spine subaxial fracture classification score. (A) Compression fracture; (B) burst fracture; (C) tension band injury fracture; (D) locked facets; (E) fracture dislocation; (F) sagittal T2 weighted images showing ligamentum flavum and supraspinous ligaments tear (arrow). AO, Arbeitsgemeinschaft für Osteosynthesefragen.

(0–4 points), DLC score (0–2 points) and neurologic status (0–4 points) are thus considered in the decision-making process; fractures with score ≤3 are managed conservatively and fractures with score ≥5 surgically, whereas in fractures with score 4 both options are acceptable (44) (*Figure 6*).

No morphometric abnormalities related to the trauma scores 0 point. Simple compression receives 1 point, whereas a burst fracture receives 2 points. Distraction injuries, including perched facets, receive 3 points. Rotation/translation injuries score 4 points (45).

The DLC consists of the intervertebral disc, anterior and posterior longitudinal ligaments, interspinous ligaments, facet capsules, and ligamentum flavum. Accordingly, DLC status can be scored as 0 (intact), 1 (indeterminate, isolated MRI signal change or isolated widening of the spinous process), and 2 (disrupted, widening of the disc, facet perch or locked) (46) (*Figure 6*).

Facet fractures are additionally classified as follows: *F1* fractures when non-displaced fractures present with fragments smaller than 1 cm or less than 40% involvement of the lateral mass; *F2* fractures are those that have the potential to be unstable (i.e., a fragment greater than 1 cm, involvement of more than 40% of the lateral mass, or presence of facet displacement). *F3* fractures consist of a floating lateral mass that occurs when the fracture of the pedicle and lamina isolate the lateral mass from the vertebral body. Finally, *F4* fractures include subluxation and/or facet lock. A 'bilateral modifying factor' applies when the same type of facet injury bilaterally affects the same vertebra.

Although the neurological status is usually assessed clinically, MRI allows correlating clinical neurological findings with the severity and extent of spinal cord damage. Therefore, MRI is useful in determining the exact location and extent of damage. Spinal cord injuries are classified into three types based on T2-weighted and/or T2*-gradient echo images: (I) represents cord hemorrhage, shows initial hypointensity on MRI and carries a poor prognosis; (II) represents cord edema, shows initial hyperintensity and bears the best prognosis; (III) is considered as a contusion

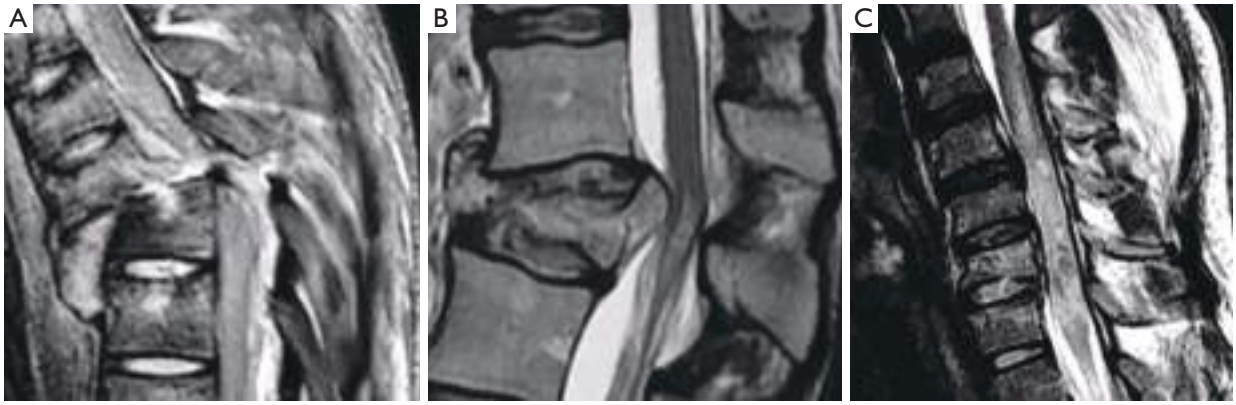

Figure 7 Traumatic spinal cord injury. (A) Type I, hemorrhagic lesion; (B) Type II, edematous injury; (C) Type III, mixed injury.

or small central hemorrhage surrounded by edema, shows a mixed pattern, and has an intermediate prognosis (47) (*Figure 7*).

Modifying factors at the cervical level include *M1*, which describes the existence of an incomplete injury to the PLC. *M2* includes the presence of a critical disc herniation protruding posteriorly to a line that continues the posterior border of the vertebra below the level of the fracture. It should be noted that the incidence of disc herniation in the setting of spinal trauma is low, around 0.4% (48). *M3* is a modifying factor that assesses the presence of a metabolic disease that stiffens the spine such as diffuse idiopathic skeletal hyperostosis (DISH), ankylosing spondylitis (AS), or ossifications of the posterior longitudinal ligament and ligamenta flava. Finally, the *M4* factor considers the presence of signs of vertebral artery injury.

MRI is considered inferior to CT in the identification and characterization of cortical fractures, but superior in the identification of soft tissue injuries and trabecular fractures of the vertebral bodies. MRI is indicated if there is suspicion of myelopathy or ligament instability, or if a hematoma or disc herniation needs to be ruled out before proceeding with closed reduction of locked cervical facets. Myelopathy can be compressive due to acute traumatic herniation or the presence of a bony fragment or extramedullary hematoma. Epidural hematomas usually show an iso-hyperintense signal on T1 weighted images and hyperintensity on T2 weighted images. The incidence of epidural hematomas after trauma has been estimated at about 2.5%, although 59% of them were associated with cord compression (49,50). Diffusion tensor imaging (DTI) with measurement of the apparent diffusion coefficient (ADC) and fractional anisotropy (FA), as well as tractography, allow quantitative data to be obtained on the axonal integrity of the spinal cord in traumatized patients (51).

Low energy vertebral fractures

The development of a vertebral fracture following minor trauma is a hallmark of osteoporosis. These fractures can be characterized and quantified by radiography or CT, but MRI is the best option for detecting edema, which is considered a sign of acute or unstable chronic fracture. In addition, the morphological changes that allow the diagnosis of osteoporotic fractures may take time to develop. Therefore, non-visualization of a vertebral fracture on plain radiography in an osteoporotic patient does not exclude its presence. MRI can detect fractures without vertebral deformity. In elderly patients with spinal trauma, in addition to the traumatic fracture, attention should be paid to screen whether other chronic osteoporotic vertebral fractures (OVF) or deformities (OVD) exist (*Figure 8*). Trauma signs on radiographs can be very subtle, and particular attention should be paid to buckling of the anterior vertebral cortex (52) (*Figure 9*).

On MRI, changes in vertebral signal intensity depend on the age of the fracture (*Figure 10*). Acute fractures usually show a band-like pattern of bone edema, located subchondral to the vertebral platform, with preservation of the normal signal intensity in the rest of the vertebral body. The linear image of the fracture can often be identified within the area of subchondral edema. The margin between the edema and the normal bone marrow is usually regular

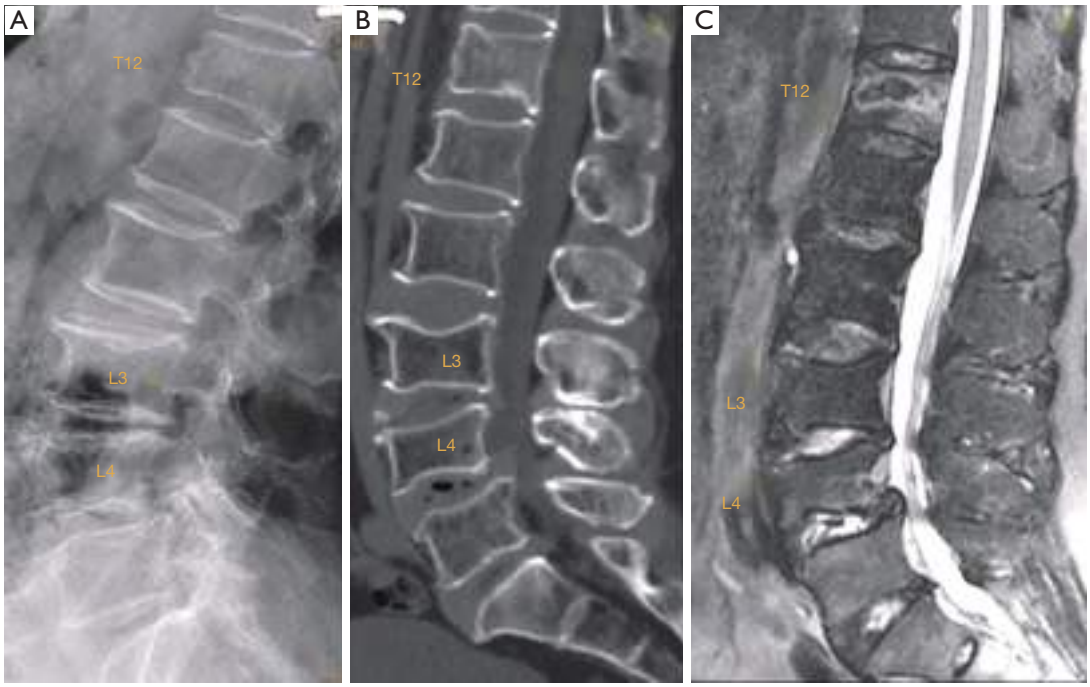

Figure 8 Elderly patient with spine trauma. (A) Radiograph; (B) sagittally reconstructed CT; (C) sagittal T2 weighted fat suppressed MRI. A T12 traumatic fracture, L3 chronic osteoporotic upper endplate fracture, and L4 chronic osteoporotic deformity (i.e., fracture) are detected. For T12, on radiograph, attention should be paid to the anterior cortex fracture and vertebral height loss, while on MRI apparent abnormal high signal is noted. Conversely, L3 and L4 show deformity, but no abnormal high signal is noted on MRI. CT, computed tomography; MRI, magnetic resonance imaging.

and well defined. Bone marrow oedema (BMO) usually resolves within 1 to 3 months, provided the fracture stabilizes. If it remains unstable, the edema can become chronic and be associated with sclerotic changes (10).

Fissures or cysts of air or fluid content may also form within the vertebral body. Their presence indicates intravertebral instability or lack of repair of the fracture site and are much more frequent in OVFs than in pathological fractures due to tumor involvement of the vertebral bodies (53,54). With the chronicity of the fracture, the fat signal from the vertebral bone marrow is recovered. Regarding morphology, the retropulsion of a bone fragment into the canal indicates a burst fracture and is considered a specific sign of benignity (*Figure 10C*,*10D*).

Finally, it should be noted that the age group with high prevalence of OVF also has a high prevalence of metastatic spinal tumors. Differentiating between OVD and metastatic deformity can be sometimes difficult using radiography alone. In such cases, MRI is the preferred imaging technique for differential diagnosis (10). Visualization of the convex posterior border of the vertebral body, extension into the posterior elements, and diffuse abnormal bone marrow signal are suggestive of pathologic fracture (55) (*Figure 11*).

The role of contrast agents in the differentiation between benign and malignant fractures has also been discussed in the literature. At the intraosseous level, benign fractures exhibit a gadolinium enhancement pattern equivalent to that of the adjacent normal vertebrae, with T1 signal intensity analogous to the normal appearance of non-fractured vertebrae. Conversely, gadolinium enhancement in malignant fractures is usually more heterogeneous and intense than in the adjacent normal vertebrae. However, in acute benign fractures with significant edema, vertebral enhancement can be so intense that it can mimic malignancy (56).

In-phase and out-of-phase T1 weighted chemical shift images have also been advocated for this differential

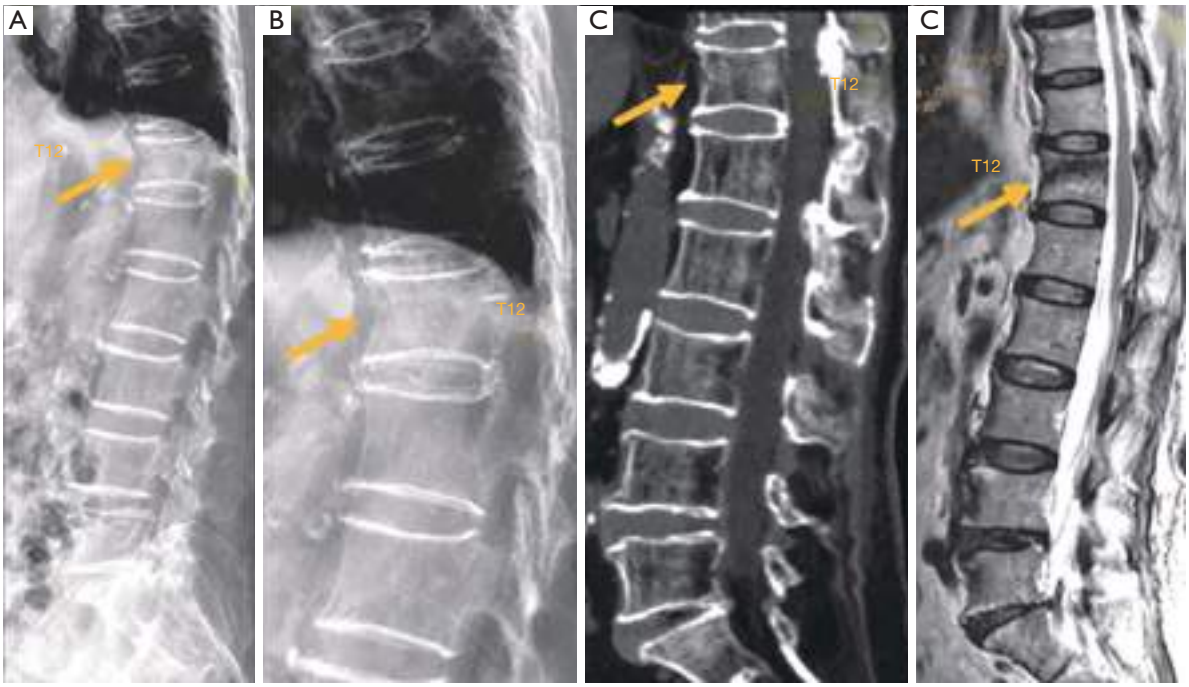

Figure 9 Subtle osteoporotic fracture after low energy trauma (arrow). (A) Radiograph; (B) radiograph magnified view for T12; (C) sagittally reconstructed CT; (D) T1 weighted MRI. On radiograph T12 vertebral anterior cortex buckling is noted. There is no apparent height loss of the vertebral body. CT confirms T12 fracture and vertebral anterior cortex break. MRI also confirms T12 fracture. CT, computed tomography; MRI, magnetic resonance imaging.

purpose. In in-phase images, water and fat contribute to the bone marrow signal. In out-phase images fat is subtracted from water, thus decreasing signal intensity. In the case of tumor infiltration, fat is replaced by neoplastic cells and, thus, this decrease in signal does not occur. A ratio of the out-of-phase to in-phase signal >0.8 is moderately sensitive and highly specific for malignancy (57) (*Figure 11*).

Degenerative pathologies

Degenerative pathology of the spine can affect several anatomical locations, including synovial joints, spinous processes, intervertebral discs, and ligaments and their insertions at the bone.

Synovial joints: atlanto-axial, facets, costovertebral and sacroiliac

The facet joints constitute the outer wall of the vertebral foramen. Since they are synovial joints, degenerative signs of osteoarthritis include joint space narrowing, subchondral cysts and/or sclerosis, vacuum phenomenon, and osteophyte formation. MRI allows the detection of intra-articular effusion and edematous changes in bone and soft tissues (58). These findings have been associated with instability of the involved segment and the presence of symptoms (58-60), and they have been described in at least 14% of patients with low back pain (61,62). Some authors consider the facet joint effusion of more than 1 mm in recumbent MRI is an indication to perform standing or dynamic radiograph to check for occult spondylolisthesis or instability (63).

These features are important for decision-making, since facet joint osteoarthritis has been described in 64–67% of asymptomatic patients in CT, and in 3–18% of asymptomatic patients in MRI (64-67) (*Figure 12*).

Spinous processes (Baastrup's disease)

Baastrup's disease (kissing spine syndrome) refers to interspinous degenerative changes associated with hyper-

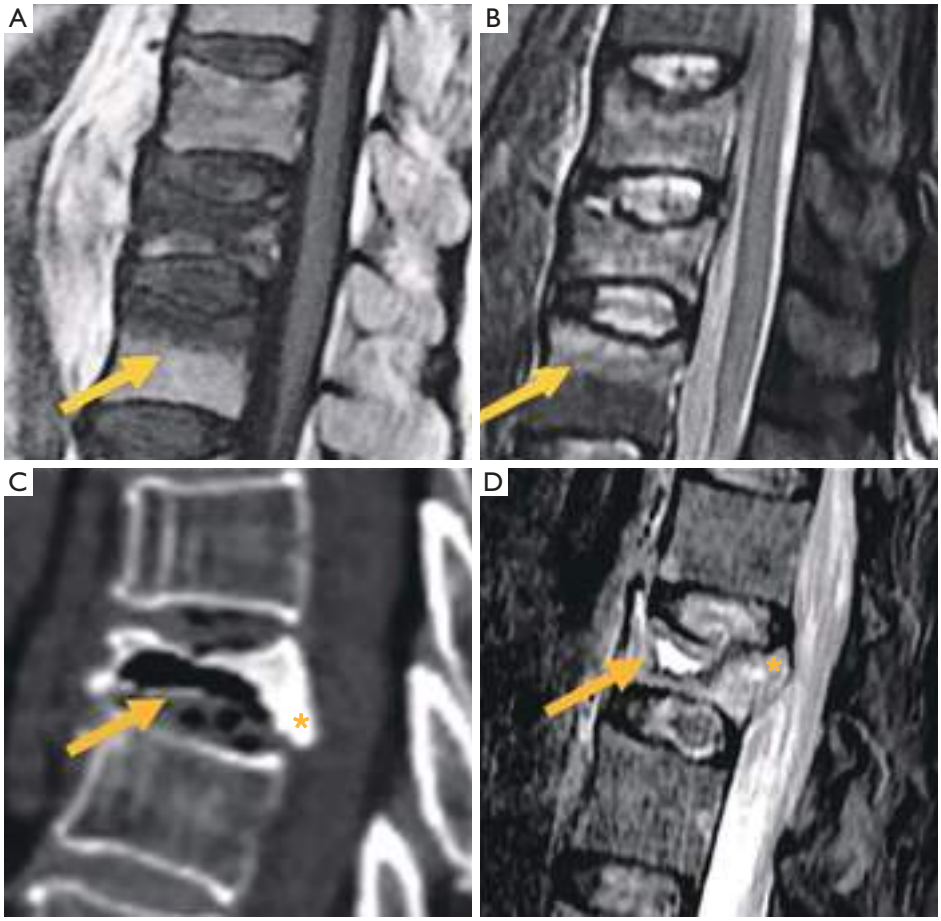

Figure 10 Osteoporotic fractures. Sagittal T1 (A) and STIR (B) showing the band like edema pattern (arrows). (C) Burst fracture with intravertebral vacuum cleft (arrow) and retropulsion of the posteroinferior margin (*). (D) Sagittal STIR with intravertebral liquid cleft (arrow) and retropulsion of posterosuperior margin (*). STIR, short tau inversion recovery.

lordosis and narrowing of the disc and facet joints interspace. The hallmark of the imaging findings is the close approximation and contact of adjacent spinous processes, with associated abnormalities including edema, bone cysts, sclerosis, flattening and enlargement of the articulating surfaces, bursitis and, occasionally, epidural cysts or midline epidural fibrotic masses (68). Interspinous bursitis and epidural cyst may communicate with the facet joints (*Figure 12*).

Intervertebral disc

MRI can accurately depict early or advanced changes of disc degeneration. Disc degeneration, whether physiological or pathological, is usually manifested by changes in signal intensity in the nucleus pulposus and annulus fibrosus. Fibrous transformation of the nucleus pulposus leads to formation of intranuclear clefts. It may be followed by varying degrees of loss of signal intensity in T2 weighted images and reduction in disc height. Several classifications have been published quantifying these changes into discrete, moderate, and severe (69,70). The Pfirrmann classification of disc degeneration was modified by Griffith for research purposes rather than clinical utility (71). Although these abnormalities are highly prevalent in asymptomatic subjects, mild changes are more common than moderate or severe changes (69,72).

Disc space narrowing is commonly considered a sign

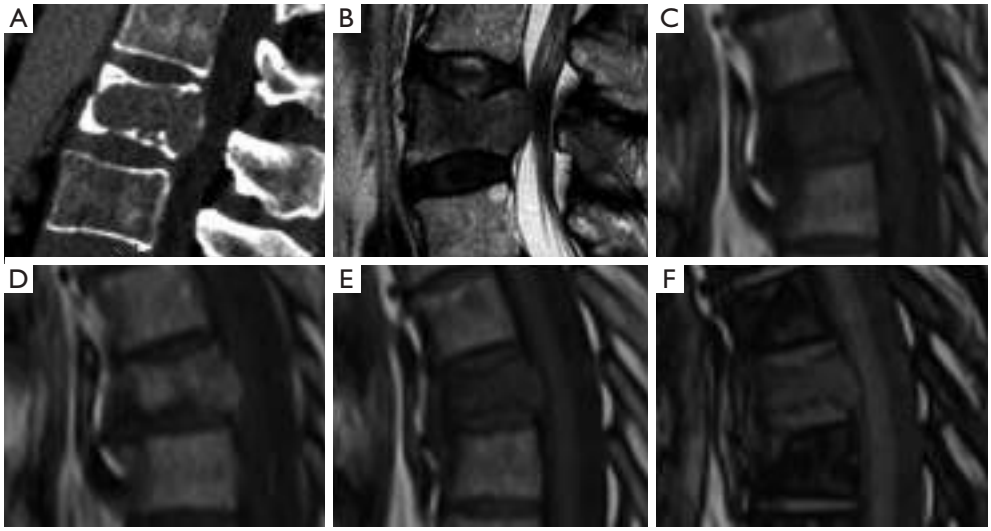

Figure 11 Pathologic fracture in several cases of metastatic lung cancer. Sagittal CT (A) and sagittal T2 weighted images (B) showing convex posterior border. Sagittal T1 weighted image without (C) and with (D) contrast in pathologic fracture. In phase (E) and out of phase (F) showing lack of fat in this metastatic vertebra, with a signal intensity out phase/phase ratio of 0.95. CT, computed tomography.

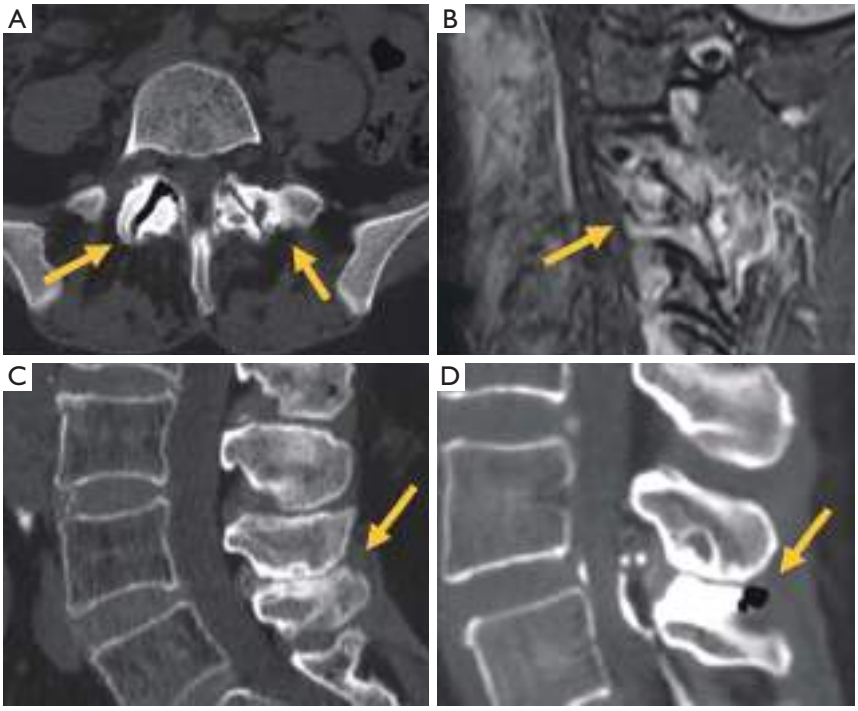

Figure 12 Osteoarthritis of the posterior elements. (A) Axial CT of facet joint osteoarthritis (arrows). (B) Sagittal STIR showing edema in cervical facet joint osteoarthritis (arrow). (C) Sagittal CT showing Baastrup's disease (arrow). (D) Interspinous bursitis (arrow) demonstrated during injection with dye and steroids of the facets joint. CT, computed tomography; STIR, short tau inversion recovery.

 Quant Imaging Med Surg 2022;12(7):3947-3986 | https://dx.doi.org/10.21037/qims-2022-04

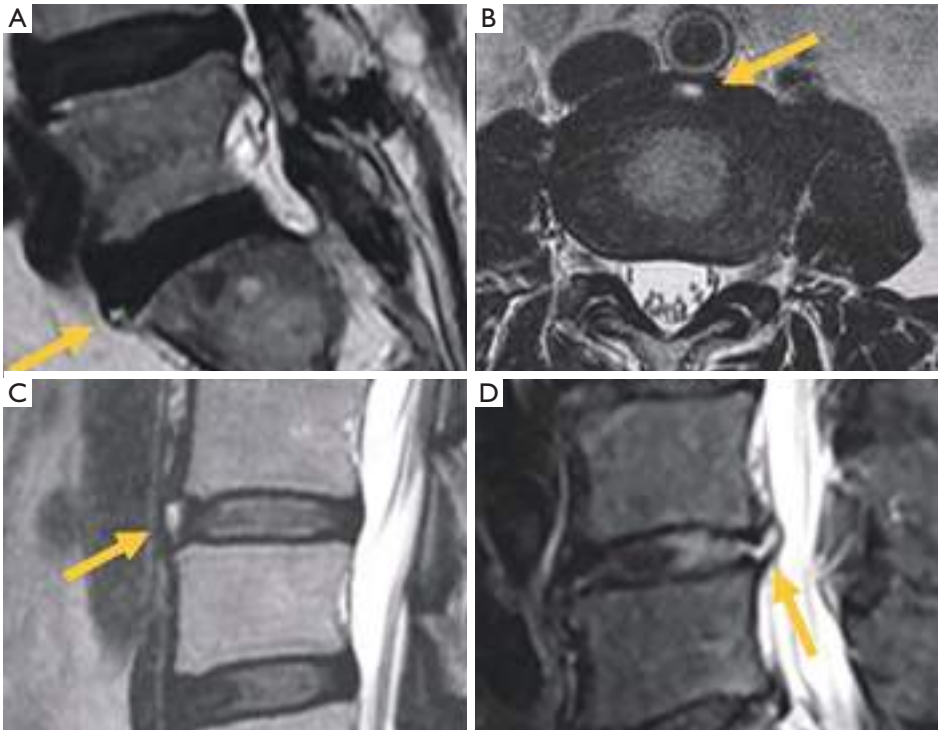

Figure 13 Annular tears on T2 weighted images. Sagittal (A) and axial (B) of transverse tears (arrow). (C) Concentric and radial (D) tears (arrows).

of disc degeneration. In common practice, applying both Pfirrmann 5-level grading and Griffith's 8-level grading schemes, a higher degree of disc space narrowing leads to higher disc degeneration scores. However, osteoporosis is associated with vertebral height loss, particularly vertebral middle height loss, which allows the expansion of the disc vertically (73,74). It has been noted that lower lumbar bone mineral density (osteopenia and osteoporosis) is associated with a decrease in lumbar disc anterior height and posterior height; however, the middle height of the discs was increased (therefore the disc biconvexity index was increased) (74). Thus, an osteoporotic spine is less likely graded as having disc space narrowing, and thereof, less likely graded as having disc degeneration (or would likely being graded as a lesser degree of disc degeneration). Therefore, Pfirrmann criteria for lumbar spine degeneration is less applicable in elderly subjects, particularly elderly female subjects among whom osteoporosis is very common (75). Moreover, loss of the bright signal on T2 weighted images can also be due to natural aging, rather than disc degeneration alone. The classification of "degenerated disc" according to Pfirrmann *et al.* and Griffith *et al.* does not compel the reader to differentiate the pathologic degeneration from the normal consequence of aging. Moreover, there are two types of disc degeneration (76). 'Endplate-driven' disc degeneration involves endplate defects and inwards collapse of the annulus, which has a high heritability, mostly affects discs in the upper lumbar and thoracic spine, and often starts to develop before age 30 years. 'Annulus-driven' disc degeneration involves a radial fissure and/or a disc prolapse, has a low heritability, mostly affects discs in the lower lumbar spine, and develops progressively after age 30 years.

Degenerative changes in the annulus fibrosus usually manifest as high intensity zones (HIZ) on T2 weighted images and have been found to be a diagnostic sign of painful intervertebral disc disease with a positive predictive value ranging from 53% to 95% (72,77,78). They are secondary to tears or fissures of the annulus fibrosus, which are classified as concentric, rim or transverse, and radial. Radial fissures have been associated to discogenic pain (*Figure 13*) (79). Nevertheless, concentric, and transverse

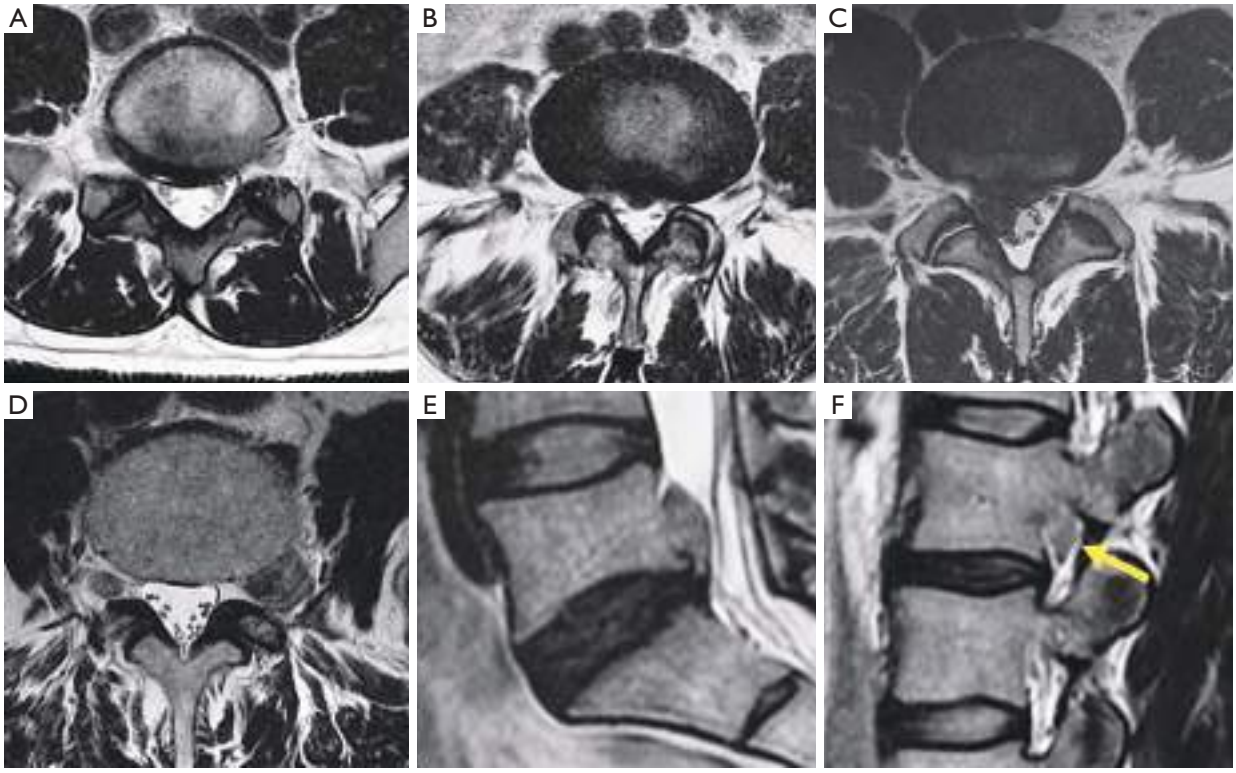

Figure 14 Disc displacement. (A) Diffuse bulge; (B) central protrusion; (C) right paracentral disc extrusion; (D) foraminal extrusion; (E) cranial migration of the disc extrusion; (F) sequestered fragment (arrow).

fissures have also been described in asymptomatic individuals, and their prevalence increases with age (70,80,81). Hyperintensity or contrast enhancement cannot be considered a sign of acuity because they may be apparent for long periods of time without being symptomatic all the time (80).

Disc displacement is currently classified as bulging or disc herniation based on the nomenclature agreement of the joint task forces of the North American Spine Society, the American Society of Spine Radiology, and the American Society of Neuroradiology (*Figure 14*) (82).

Disc bulging is defined as a disc protruding beyond the margins of the vertebral endplates by more than 25% of its circumference. It may be symmetric or asymmetric. It has been described in 15–81% of asymptomatic subjects (69,80).

A disc herniation is a focal protrusion of disc material affecting less than 25% of the disc circumference. Two types of herniations are considered. In the protrusion type, only a partial tear of the annulus fibrosus is present. On imaging, the base of the hernia is wider than the rest of dimensions of the protruded disc. In extrusion hernia, the whole thickness of the annulus fibrosus is torn. On imaging, the base of the extruded disc is smaller than the length of the extruded material. The prevalence of disc herniation in asymptomatic individuals is higher for the protrusion type (20–63%) than for the extrusion type (24%) (69,72,80,83,84).

The extruded disc may migrate upward or downward or lose contact with the parent disc as a sequestered fragment. Sequestration has not been described in asymptomatic subjects (72).

With respect to a transverse plane through the intervertebral disc, the location of lesions within the spinal canal can be described from medial to lateral as occupying the central area (including paracentral, more precisely, right central or left central), subarticular (including lateral recess), foraminal, extraforaminal and anterior. The term "paracentral", although less precise than right or left central, is useful in clinical practice because the base of the

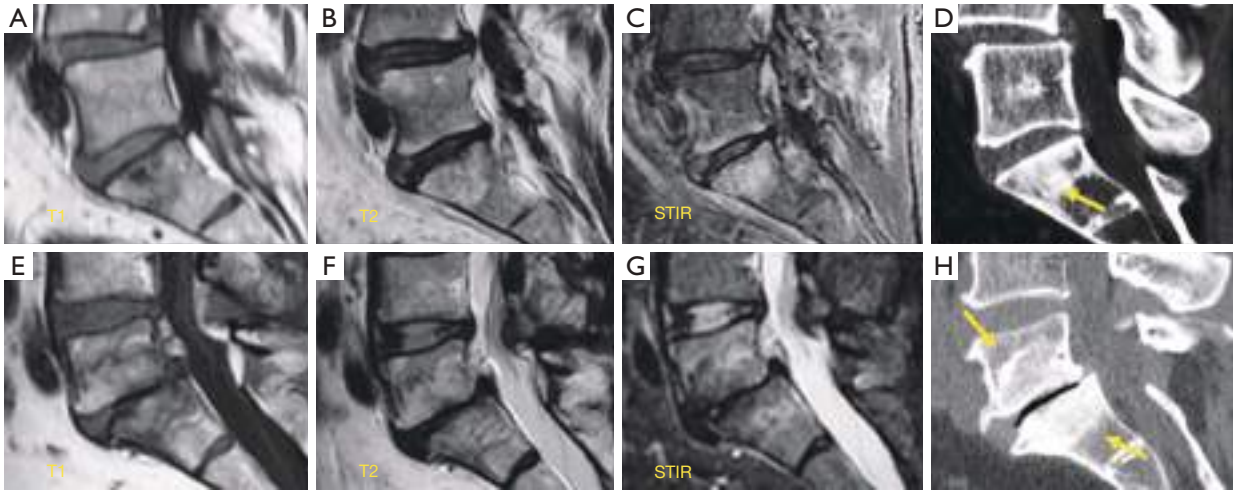

Figure 15 Modic changes. Sagittal T1 weighted image (A), T2 weighted image (B) and STIR sequence image (C) of Modic type I changes. Sclerosis (arrow) detected at S1 on CT (D) is barely visible on MRI. Sagittal T1 weighted image (E), T2 weighted image (F) and STIR image sequence (G) of Modic type II changes. Sclerosis (arrows) conspicuous on CT (H) is barely suspected on MRI. STIR, short tau inversion recovery; CT, computed tomography; MRI, magnetic resonance imaging.

herniation may affect the whole central area (82).

Discs may also herniate through the vertebral endplate (Schmorl's nodes). In the acute presentation, they may be surrounded by edema and be symptomatic. In the chronic form, they are surrounded by fat or sclerotic bone (85,86).

Vertebral endplate changes associated to degenerative disc disease have been described by Modic (*Figure 15*). Type I represents edema and can be stable, disappear or aggravate, or progress to type II. They manifest as hypointense on T1 weighted and hyperintense on fluid sensitive techniques. The positive predictive value for low back pain of type 1 Modic changes was 81% (87). Persistence or aggravation of Modic changes, associated loss of disc height and vertebral endplate irregularities are associated with persistence of pain. Modic I changes that regress or change to type II are associated with improvement of pain. Symptomatic Modic I changes tend to affect lower lumbar discs and have greater extension in height and backward in the vertebral endplate than asymptomatic Modic I changes which tend to be focally localized in the anterosuperior margin of the mid-column vertebral bodies. Posteriorly oriented Modic changes are more painful than anteriorly oriented Modic changes. Vertically larger Modic changes are more strongly associated with low back pain (88,89).

Type II Modic changes represent fat deposition and are usually considered stable, but sometimes can evolve to type I (90,91). They manifest as hyperintense on T1 and T2 sequences and hypointense on fat saturated images. Type III Modic changes represent subchondral sclerosis and are considered very rare (72), but this is probably due to the insensitivity of MRI to detect sclerotic bone (*Figure 15*). They manifest as low signal in all sequences. The prevalence of Modic changes increases with age and have been described in 0–13.5% of asymptomatic patients for Modic I and 3–25% for Modic II, respectively (72,80,84).

Ligaments and their insertions at the bone, resulting in DISH

DISH is a systemic condition, with an estimated prevalence of approximately 10% in people >50 years of age. The radiographic criterion proposed by Resnik for its diagnosis is the presence of large bridging osteophytes in at least four adjacent thoracic vertebrae. Patients with DISH are often asymptomatic, although can manifest clinically with back pain and stiffness, neurologic compromise from spinal stenosis, and dysphagia or airway obstruction from large anterior cervical bridging osteophytes (92). Spinal stiffness in the final stages of the disease implies increased spinal vulnerability to low energy trauma (93). On the other hand, the diagnostic criteria proposed by Utsinger reduced the threshold for spinal involvement to two contiguous

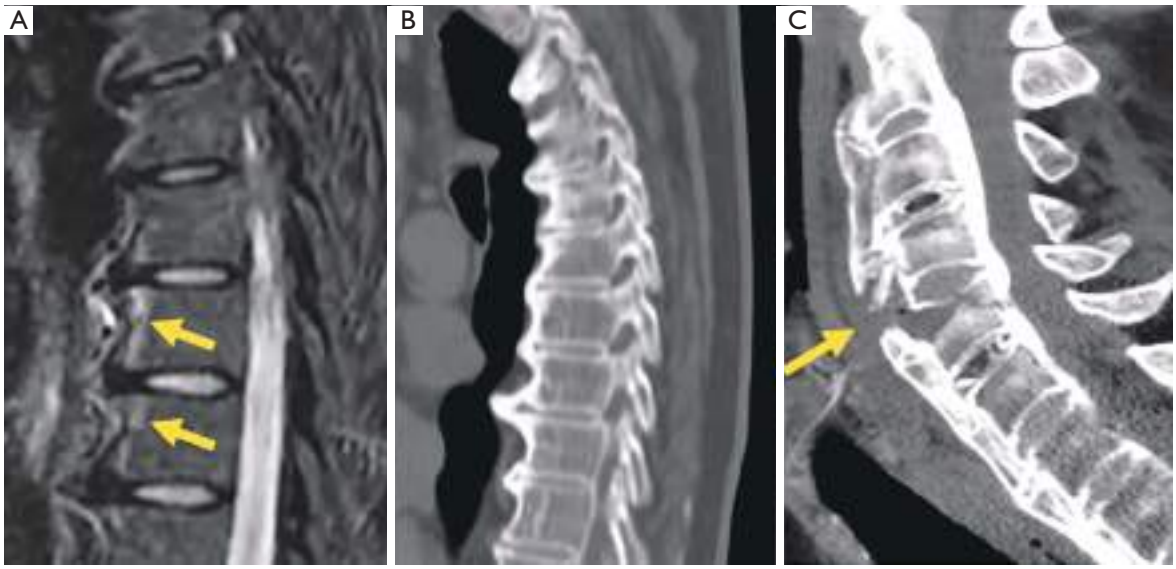

Figure 16 DISH. (A) Sagittal STIR showing subligamentous edema (arrows). (B) Sagittal reformatted CT showing bridging osteophytes. (C) Sagittal CT of low energy cervical fracture in a patient with DISH (arrow). DISH, diffuse idiopathic skeletal hyperostosis; STIR, short tau inversion recovery; CT, computed tomography.

vertebral bodies, but involvement of peripheral entheses was included for early diagnosis (94) (*Figure 16*).

Spinal stenosis

Degenerative disorders may lead to degenerative spinal stenosis. It may coexist with or be affected by a pre-existing congenital or developmental stenosis. MRI allows differentiating the two forms of spinal stenosis by assessing the morphology of the central and lateral canal, as well characterizing, and quantifying its severity. It may also be useful in identifying other causes of spinal stenosis in which the osseous architecture is unremarkable, such as epidural lipomatosis (95).

The criteria for defining developmental stenosis at lumbar level are not uniform in the literature (96), with the reported pathological values of sagittal diameter ranging from 9 to 14 mm at the lower lumbar level (97-101); however, the axial area of the thecal sac is considered a more effective parameter in the diagnosis of stenosis. In this regard, severe stenosis is defined by values <76 mm^2, while values ranging from 76 to 100 mm^2 indicate moderate stenosis (102). Park classified central stenosis based on nerve root aggregation of the cauda equina (103). According to this classification, grade 1 (mild stenosis) is present when the anterior cerebrospinal fluid (CSF) space is mildly obliterated with no nerve root aggregation. Grade 2 or moderate stenosis indicates cauda equina aggregation, while grade 3 implies severe stenosis, with the entire cauda equina appearing as a bundle (*Figure 17*).

In the lateral canal, stenosis may occur at the proximal entrance of the root (i.e., lateral recess), or at the exit (i.e., foramen). Nerve root involvement in the lateral recess ranges from contact of the disc with the nerve root to deviation and/or compression of the root between the disc and posterior osseous structures (101). Bartynski *et al.* (101) graded lateral recess stenosis as (104): grade 0, no stenosis; grade 1, mild stenosis with no repercussion on the nerve root; grade 2, moderate stenosis, with root flattening and partial obliteration of the CSF space; grade 3, severe stenosis in which there is severe root compression with complete obliteration of the CSF space.

According to Lee's classification of foraminal stenosis, perineural fat obliteration in either vertical or transverse direction is considered mild stenosis, and obliteration in both the vertical and transverse axes implies moderate stenosis. Severe stenosis shows morphological changes or collapse of the nerve root (105). Wildermuth's classification

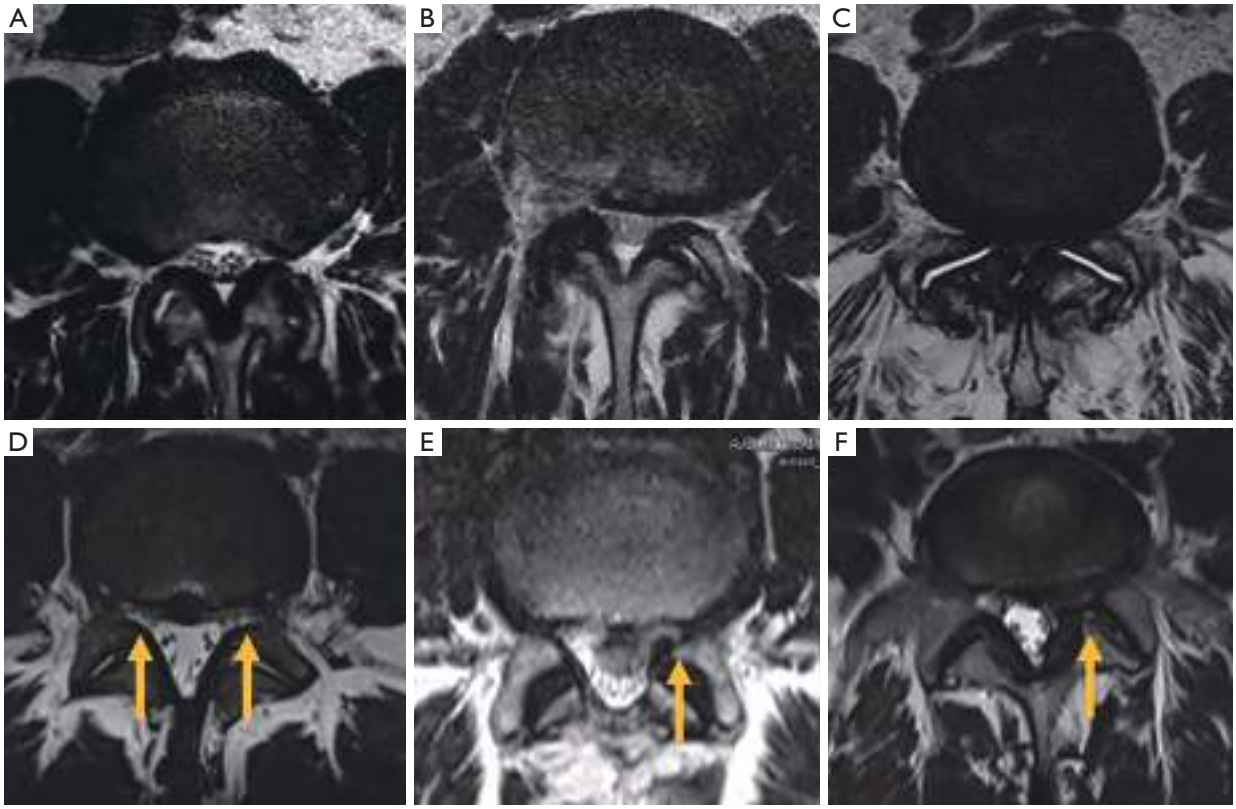

Figure 17 Lumbar canal stenosis. Axial T2 images of mild (A), moderate (B) and severe (C) central canal stenosis. (D) Mild bilateral lateral recess stenosis (arrows). Moderate (E) and severe (F) left foraminal stenosis (arrows).

considers grade 1 foraminal stenosis when there is only deformity of the epidural fat, moderate (grade 2) stenosis when epidural fat only partially surrounds the nerve root, and severe or advanced (grade 3) stenosis when there is complete obliteration of the foraminal epidural fat (106). Several parameters of the compressed nerve root have been associated with good response to foraminal injections, including increased nerve T2 signal intensity (107) and perineural fat effacement >25%, described as the "melting sign" (108) (*Figure 18*).

The estimated minimum sagittal diameter of the cervical spinal canal between C3 and C7 is 12 mm. Lower values increase the risk of degenerative spinal stenosis (109). In the foramen, uncovertebral arthrosis is the main cause of stenosis. Uncinate joints are found from C2-C3 to C6-C7, and they become hypertrophic because of the mechanical overload caused by disc impingement. Osteophytes may project into the foramen resulting in stenosis with radiculopathy (110).

Central canal stenosis at the cervical level was classified by Kang *et al.* in 4 grades (111): grade 0, absence of stenosis; grade 1, obliteration of the subarachnoid space greater than 50% without deformity of the spinal cord; grade 2, central canal stenosis with spinal cord deformity but without altered signal intensity in the spinal cord; grade 3, central canal stenosis with signs of compressive myelopathy (hyperintense T2-weighted intramedullary signal) (*Figure 19*).

Grading of cervical foraminal stenosis in clinical practice on MRI must be based on both sagittal and axial images to get a complete picture of the neural foramen. Park *et al.* (112) classified stenosis severity based on oblique sagittal views, although these are not routinely performed and need to be reconstructed, while Kim *et al.* (113) graded foraminal stenosis based on morphometric measurements on axial images, which can be time consuming. Therefore, most clinicians grade foraminal stenosis based on subjective terms

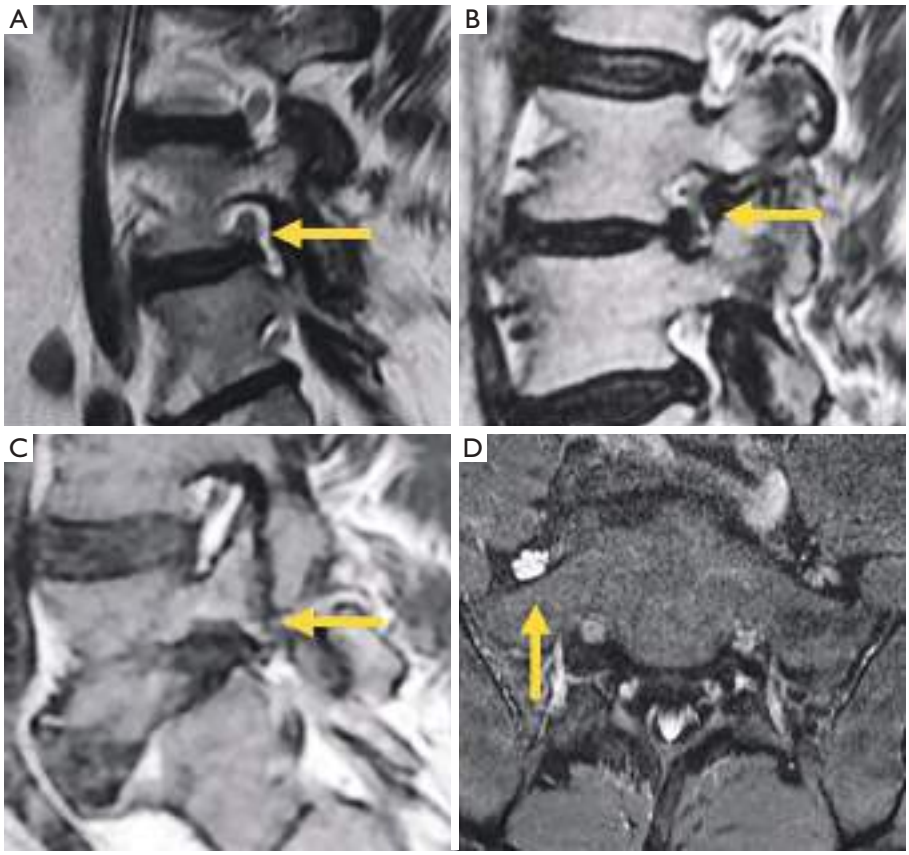

Figure 18 Lumbar foraminal stenosis. Sagittal T2 weighted images of mild (A), moderate (B) and severe (C) foraminal stenosis (arrow). (D) Axial intermediate weighted fat saturated image showing increased signal of L5 nerve root (arrow) in severe foraminal stenosis.

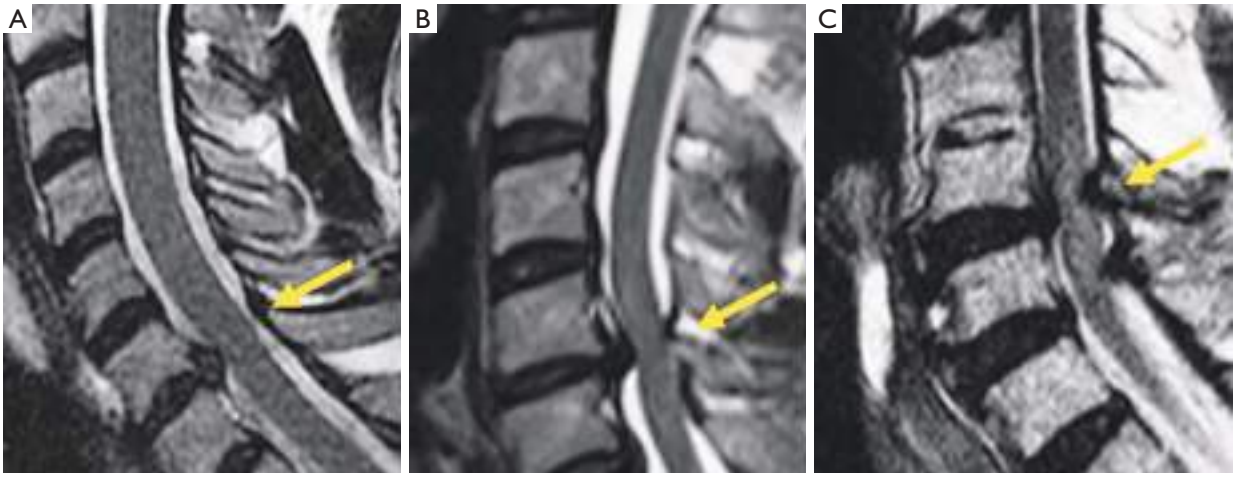

Figure 19 Cervical canal stenosis. Sagittal T2 weighted of mild (A), moderate (B) and severe (C) central canal stenosis (arrow).

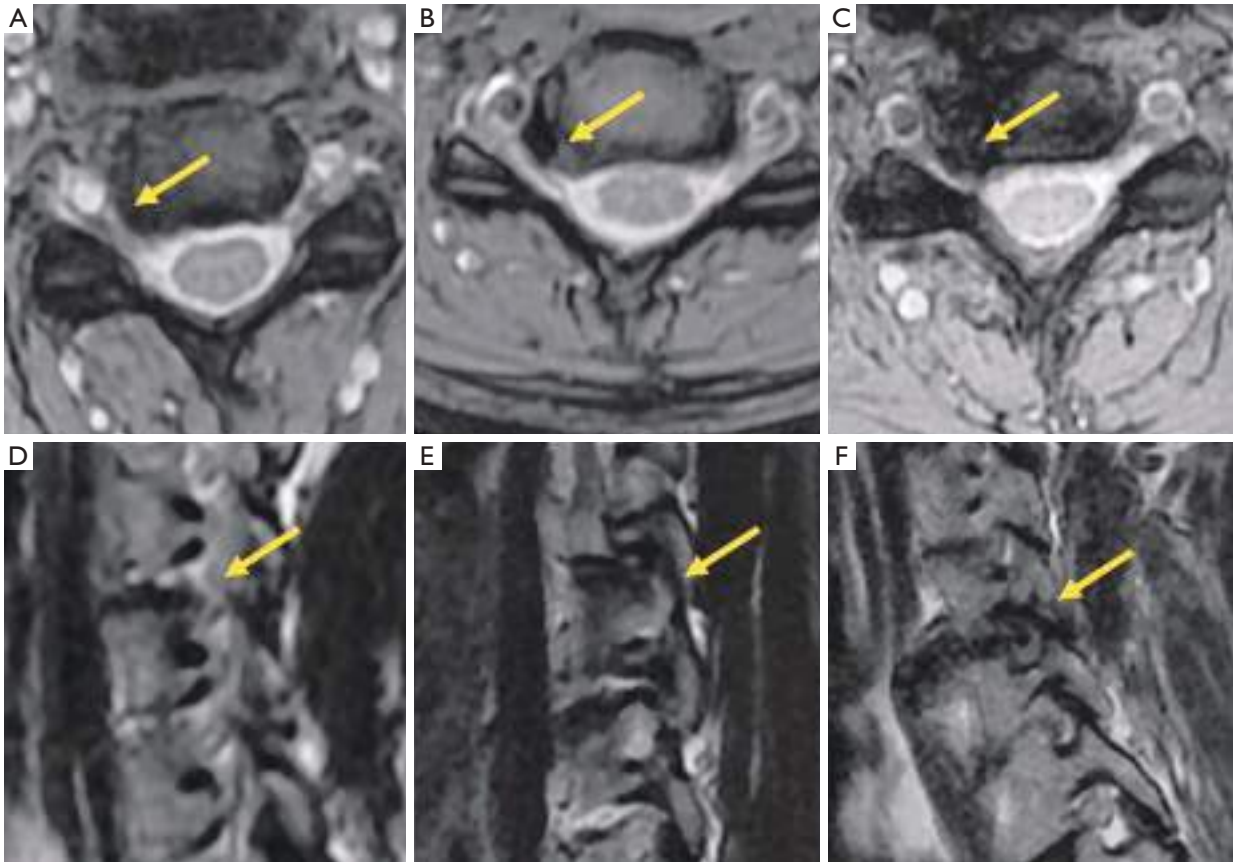

Figure 20 Cervical foraminal stenosis. Axial T2* weighted images of mild (A), moderate (B) and severe (C) foraminal stenosis (arrow). Sagittal T2 weighted images of mild (D), moderate (E) and severe (F) foraminal stenosis (arrow).

such as "mild", "moderate" and "severe" (114) (*Figure 20*). In the Park's classification system, mild foraminal stenosis shows partial perineural fat obliteration involving less than 50% of the nerve root circumference, moderate stenosis indicates perineural fat obliteration >50% of the nerve root circumference, and severe foraminal stenosis causes morphological changes in the nerve root (*Figure 20*). More severe grades are more likely related to clinical symptoms and are the target of treatment (115).

Alignment abnormalities

Six types of spondylolistheses have been described: congenital or dysplastic, isthmic, traumatic, pathologic, iatrogenic, and degenerative (pseudospondylolysis) (116).

Isthmic spondylolisthesis is the most frequent type of spondylolisthesis in young people and is generally secondary to a stress fracture in a previously normal bone. Direct visualization of the fracture on sagittal MRI may be difficult due to the small size of the isthmus. The sensitivity and specificity of this technique has been reported to be 81% (95% CI: 54–94%) and 99% (95% CI: 98–100%), respectively. Therefore, due to the absence of radiation, MRI is considered the first imaging exam to investigate spondylolisthesis, with CT being reserved for non-diagnostic or inconclusive cases (117). The use of isotropic volumetric MRI sequences, such as 3D-T1-VIBE (a T1-weighted, 3D gradient-echo MR sequence), has demonstrated greater diagnostic accuracy compared to CT. MRI achieved 100% accuracy in detecting complete fractures. For incomplete fractures, MRI sensitivity, specificity, and precision were 96.7%, 92.0%, and 94.6%, respectively (118). Early diagnosis is very important in young patients because it facilitates early treatment

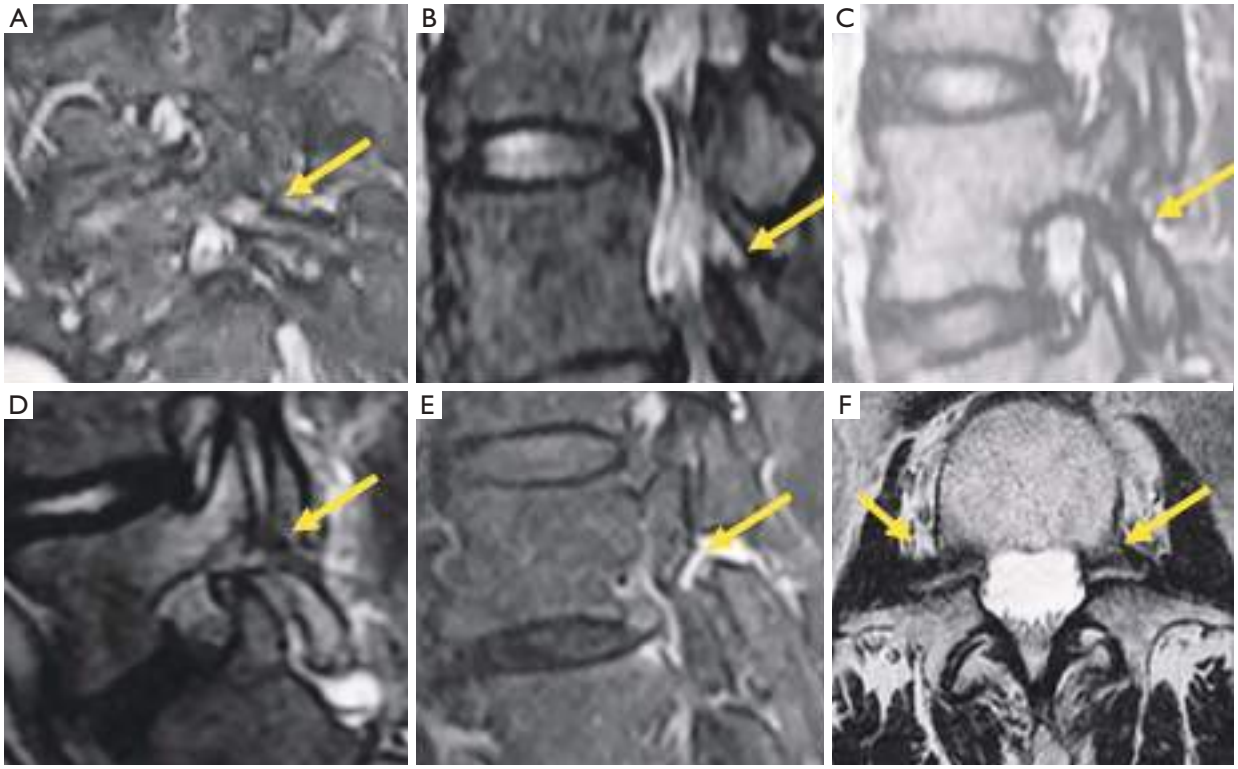

Figure 21 MRI of spondylolysis. (A) Sagittal STIR image of grade 1 spondylolysis showing edema without pars interarticularis defect (arrow). (B) Grade 2 spondylolysis, partial defect with edema (arrow). (C) Grade 2A spondylolysis, partial defect without edema (arrow). (D) Grade 3 spondylolysis, complete defect with edema (arrow). (E) Grade 4 spondylolysis, chronic defect without edema (arrow). (F) Bilateral pedicle spondylolysis (arrow). MRI, magnetic resonance imaging; STIR, short tau inversion recovery.

increasing the healing rate. The degree of edema on fluid-sensitive sequences (e.g., T2 weighted MRI or short tau inversion recovery (STIR) sequence) is associated with the severity of the stress injury. The Hollenberg's grading system includes 5 stages (119): grade 0 indicates a normal pars interarticularis with no MRI changes; grade 1 involves signal abnormalities in the pars interarticularis without fracture; grade 2 is defined by the presence of edema with incomplete fracture; grade 3 indicates the presence of complete fracture with edema; and grade 4 involves complete fracture without signal alterations, indicating chronic non-union. Other authors have added grade 0a, which implies cortical thickening with sclerosis but with no edema, as well as grade 2a, which indicates incomplete fracture without edema, probably denoting a healing fracture (*Figure 21*) (120). MRI is not particularly useful in follow-up because bone edema may persist in spite of clinical resolution of spondylolysis. It is also inferior to CT in the assessment of bony repair (121).

An indirect sign of L5 spondylolysis, even without spondylolisthesis, is the presence of epidural fat between the posterior dural layer and the anterior part of the spinous process of the vertebra in a median sagittal image, secondary to enlargement of the central canal. According to Sherif *et al.* (122), the specificity and sensitivity of this indirect sign are 96.7% and 78.8%, respectively. When spondylolisthesis develops there is usually widening of the central canal and narrowing of both foramina (*Figure 22*).

The second most common site of neural arch injury after the pars interarticularis is the vertebral pedicle. It may be associated with unilateral spondylolysis but has been also described without associated spondylolysis in some young athletes or even in osteoporotic patients (123).

Degenerative spondylolisthesis is secondary to facet and

Figure 22 MRI Indirect signs of spondylolysis and spondylolisthesis. (A) Epidural fat interposition between the thecal sac and the L5 spinous process in spondylolysis without spondylolisthesis. (B) Widening of the central canal (arrow) and foraminal stenosis (arrow) (C) in spondylolysis with spondylolisthesis. MRI, magnetic resonance imaging.

disc degeneration while the neural arch remains intact. As a result, the spinous process is anteriorly displaced along with the vertebral body, and the central canal usually becomes stenosed (*Figure 23*). It is the most frequent cause of spondylolisthesis in the elderly (124). A high proportion of degenerative spondylolisthesis can be asymptomatic and have no clinical consequence (125).

Traumatic spondylolisthesis is a rare injury defined as any acute fracture or dislocation of the posterior elements associated with vertebral spondylolisthesis. When it occurs at the C2 level, it is known as "hangman's fracture", with radiological signs analogous to isthmic spondylolisthesis. Of note, vertebral artery dissection has been found to be associated to this fracture type. Therefore, it is recommended to rule out this complication in patients with hangman's fracture and pay particular attention to the signal intensity of the vertebral artery in T2-weighted images, as loss of the normal flow-void signal is an indirect sign of artery dissection (126) (*Figure 23*).

Retrolisthesis is a manifestation of spondylolisthesis that consists of posterior shifting of a cephalad vertebra over a caudal vertebra. It is generally secondary to loss of disc material caused by intervertebral osteochondrosis or acute herniation of the nucleus pulposus (116).

Alterations in the spinal curvature

Scheuermann's disease or idiopathic kyphosis accounts for 90% of cases of juvenile kyphosis. Diagnostic criteria for this condition are kyphosis >45° and at least one vertebra with wedging >5°. Irregular endplates and Schmorl's nodes are associated findings (127) (*Figure 24*).

Scoliosis is defined as a lateral curvature of the spine >10° as measured by the Cobb method on a standing radiograph (128). Scoliosis can be classified as congenital, neuromuscular, degenerative, or idiopathic, the latter being the most common, usually painless, and diagnosed after excluding other potential etiologies.

MRI is indicated in children under 10 years of age who develop scoliosis (infantile and juvenile forms) because of its frequent association with neural axis anomalies (129). In general, tomographic imaging techniques are not indicated in adolescent idiopathic scoliosis (11 to 17 years), the most common type, except when painful or unusual symptoms are present, such as headache or neurological involvement (130). Presurgical screening in these patients has demonstrated a prevalence of neurological axis abnormalities of 7.9–12.6% (131-133). Bony causes of scoliosis include benign tumors such as osteoid osteoma or osteoblastoma (134) (*Figure 24*).

Inflammatory pathologies

Radiography is still useful as initial examination to rule out structural damage of the spine in suspected inflammatory spondyloarthritis (135). The main drawback of radiography is the lack of sensitivity in detecting early non-structural changes, such as BMO, synovitis, enthesitis, capsulitis, and intra-articular effusion, that may be indicative of active inflammatory changes. MRI is the dominant technique to depict early active changes (136). In fact, MRI can

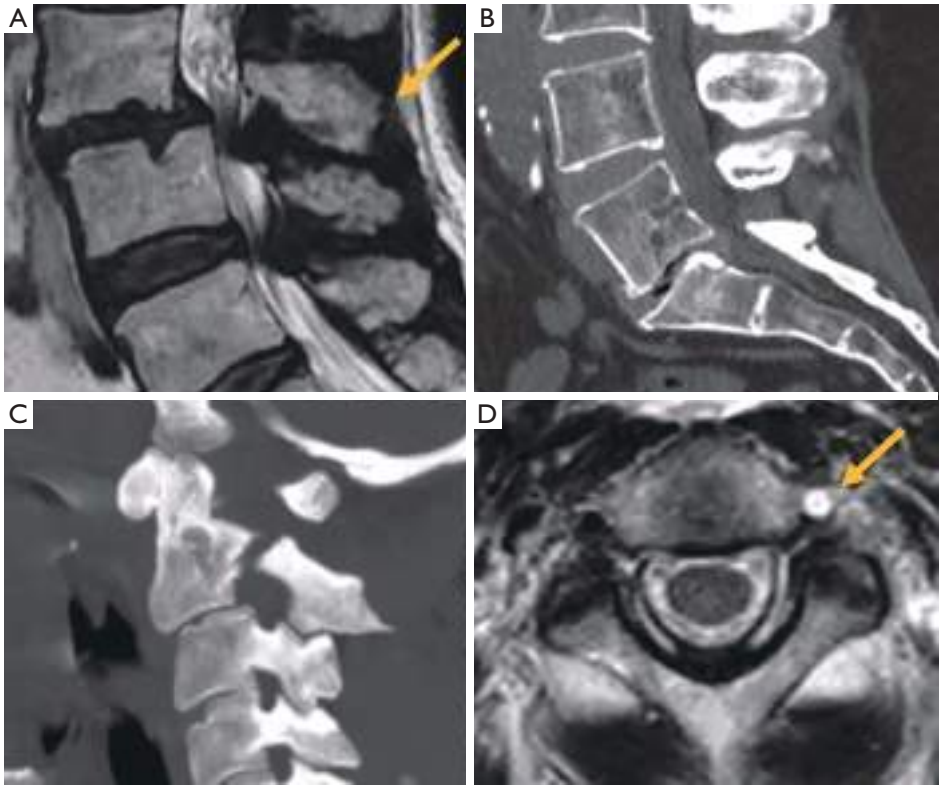

Figure 23 Alignment abnormalities in three patients. (A) Sagittal T2 weighted image of a patient with degenerative spondylolisthesis with narrowing of the central canal and anterior shifting of the spinous process (arrow). (B) Sagittal CT with retrolisthesis of L5. (C) CT with MIP reconstruction in Hangman's fracture. (D) Axial T2 of a hyperintense vertebral artery (arrow) secondary to arterial dissection in Hangman's fracture. CT, computed tomography; MIP, maximum intensity projection.

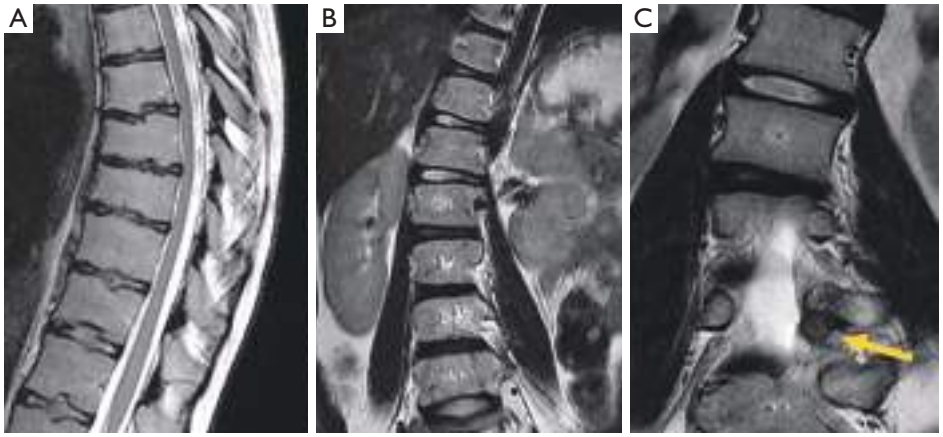

Figure 24 Alterations in spinal curvature. (A) Sagittal T2 weighted image of a case with Scheuermann's disease. (B) Coronal T2 weighted image of a case with neuromuscular scoliosis in Rett syndrome. (C) Coronal T2 weighted image of a patient with scoliosis secondary to osteoid osteoma (arrow).

 Quant Imaging Med Surg 2022;12(7):3947-3986 | https://dx.doi.org/10.21037/qims-2022-04

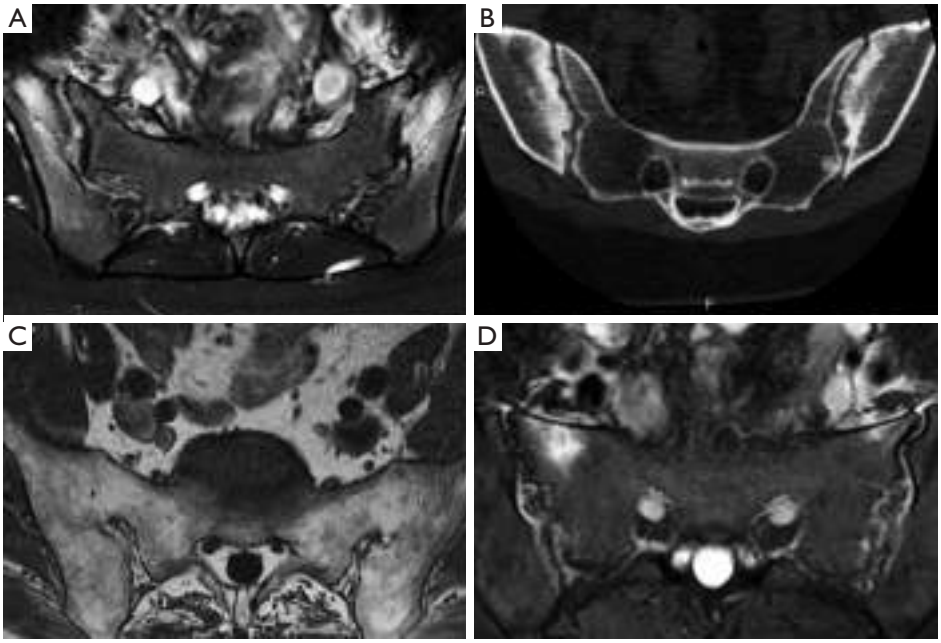

Figure 25 Sacroiliitis in four patients. (A) Axial STIR in active inflammatory spondyloarthropathy. (B) CT showing structural changes at the sacroiliac joints. (C) T2 weighted image of a patient with chronic sacroiliitis with fused joints. (D) Axial STIR sequence image of a patient with post-partum subchondral edema at both iliac wings. STIR, short tau inversion recovery; CT, computed tomography.

demonstrate signs of active sacroiliitis years before radiographic findings become evident (137).

Some authors differentiate between early non-radiographic AS, when no imaging abnormalities are seen on radiographs with or without inflammatory changes on MRI, and late radiographic AS, when signs of structural sacroiliitis are present on radiographs according to the New York classification criteria (138,139). These structural changes include erosions, sclerosis, bone fatty infiltration, fat deposition in an erosion cavity, and bone bridging or ankylosis, with being CT, the most accurate technique to depict most structural changes (137). CT findings of structural changes had a 58% sensitivity and 69% specificity for discerning which patients reported pain relief from an anesthetic injection (137) (*Figure 25*).

Currently, the Assessment in Spondyloarthritis International Society (ASAS) classification criteria for AS are the most widely used. These criteria cover patients with and without radiographic sacroiliitis and include a clinical and an imaging arm. Imaging findings consistent with sacroiliitis are the key criterion on the imaging arm and include definite radiographic sacroiliitis according to the modified New York criteria (NYC) or active sacroiliitis on MRI (138,140,141). The required MRI feature for sacroiliitis is the presence of BMO on either two consecutive slices, or multiple lesions on a single slice. Inflammation must be clearly present and in a typical anatomical location (subchondral bone) (142).

The two arms altogether have 82.9% sensitivity and 84.4% specificity and, for the 'imaging arm' alone, the reported sensitivity was 66.2% and specificity 97.3% (143,144). Of note, imaging cannot be assessed in isolation and needs to be interpreted in the light of clinical presentation and results of laboratory investigations. It must be considered that BMO can be present in asymptomatic individuals, may be related to sport activities and be present in other conditions like osteoarthritis or the post-partum period (135) (*Figure 25*).

Regarding spinal lesions, a new consensus will replace the previous agreement of the ASAS group (145,146). Vertebral corner BMO and corner fat lesions, known as Romanus lesions, were recorded if present on 2 slices; facet joint, lateral, and posterior inflammatory lesions were recorded if present on a single slice. The presence

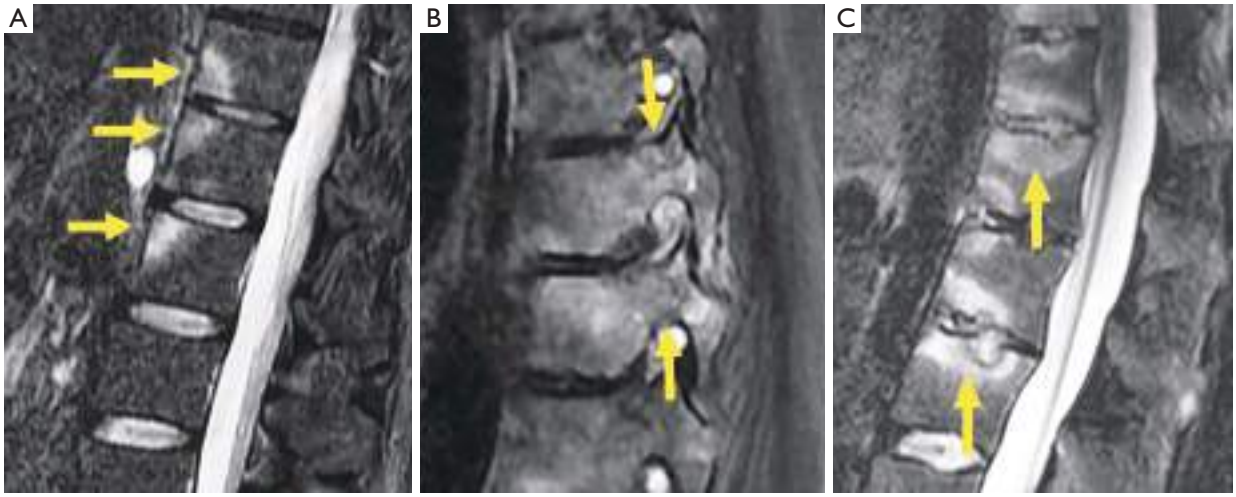

Figure 26 Spinal involvement in axial spondyloarthropathy. Sagittal STIR images showing Romanus lesions (arrows) (A), costovertebral joints inflammation (arrows) (B), and Andersson lesions (arrows) (C). STIR, short tau inversion recovery.

of ≥2 vertebral corner BMO had 90–95% specificity for axial spondyloarthropathy (147). Inflammatory changes in the vertebral endplate are known as Andersson lesions. Two theories about its pathogenesis consider that it may be either part of the inflammatory process of the disease or a pseudoarthrosis after minor trauma. It is important to differentiate them because the former may be treated medically and the latter usually require surgical management (147) (*Figure 26*).

Infectious pathologies

In suspected spinal infection, MRI is the preferred imaging technique due to its high sensitivity and specificity, which has been proved to be superior to radiographs and bone scans (148-151). MRI can detect osteomyelitis as early as 3–5 days after onset of infection with reported sensitivity, specificity, and accuracy values of 96%, 92% and 94%, respectively (149,152). In addition, it can detect the very earliest sign of spondylodiscitis, namely subtle subchondral endplate edema changes (153). Edema or fluid in the psoas musculature, termed MRI psoas sign, is another finding consistent with early spondylodiscitis, with sensitivity and specificity values around 92% (154,155). MRI can localize the sites of infection, such as disc, vertebral bodies, facet joints, paravertebral musculature, epidural space, meninges, or spinal cord. Intravenous gadolinium contrast administration helps to delineate abscess formation. Hyperparathyroidism, neuropathic arthropathy, acute Schmorl's nodes, synovitis, acne, pustulosis, hyperostosis, osteitis (SAPHO) syndrome, AS, Modic changes type I and tumors are non-infectious mimics that may resemble pyogenic spondylodiscitis (136,156,157).

Extension to paravertebral soft tissues or the epidural space can be in the form of a phlegmon, which shows homogeneous enhancement with no significant pus collection, or forming a liquid abscess that shows peripheral enhancement delimiting a fluid collection (156). Abscess usually shows high signal on diffusion weighted images and low ADC value indicating restricted diffusion (157).

The evolution of pyogenic infections is much faster compared with tuberculosis due to the release of proteolytic enzymes in the former group. Tuberculosis usually exhibits a more chronic pattern, and radiographic changes take longer to become apparent, usually between 8–12 weeks (158). Subligamentous spread of tuberculosis can occur before spreading to the intervertebral space. In this case, erosion or scalloping of the anterior vertebral wall can be detected on radiographs (159) (*Figure 27*). Some findings that favor the diagnosis of tuberculosis include larger collections, cold abscesses adjacent to the affected spine, thoracolumbar junction, no/scarce involvement of the disc space, skip lesions involving multiple locations due to subligamentous spread and whole vertebral body or posterior involvement (160,161) (*Figure 27*).

Brucellosis is an endemic zoonotic disease that may affect

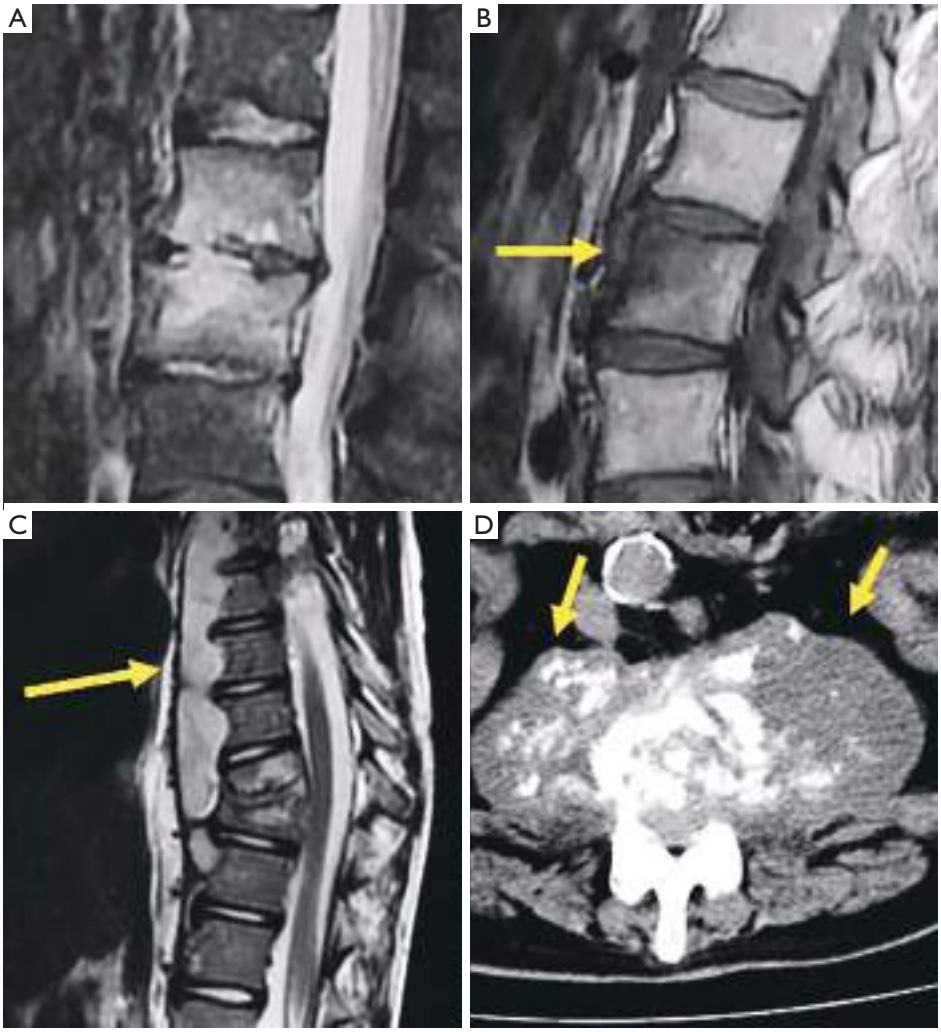

Figure 27 Infectious pathology of the spine. (A) Sagittal STIR image of a case of pseudomonas discitis. (B) Sagittal T1 weighted image of a case of brucella osteomyelitis (arrow). (C) Sagittal T2 weighted image of a case of tuberculous prevertebral subligamentous abscess (arrow). (D) Axial CT of a case of chronic bilateral psoas abscess showing muscle enlargement with fluid collection and small calcifications (arrows). STIR, short tau inversion recovery; CT, computed tomography.

the spinal column with a chronic course mimicking another disease, including spondylosis. It may present with a typical pattern of discitis, but most often shows inflammatory changes of the vertebral body (162) (*Figure 27*).

Tumor pathologies

Spinal tumors can be metastatic, primary benign or primary malignant. Approximately 90% of them are metastatic and 20% present with canal invasion and/ or cord compression (163). Due to the overlapping of bony structures of the spine, conventional radiography is often insufficient and further characterization with CT or MRI is needed (164). MRI is usually the most useful method for evaluating spinal tumors and has superior contrast to localize disease in various compartments (intramedullary,

intradural-extramedullary, extradural, intraosseous, paravertebral). Regarding primary bone tumors it has shown higher diagnostic accuracy than CT and radiography (165). Regarding bone metastases, MRI has shown better diagnostic performance than SPECT, positron emission tomography (PET) or CT (166,167). In myeloma, MRI has shown greater sensitivity than 18F-FDG-PET in staging, but inferior for evaluating response to treatment that is detected earlier on 18F-FDG-PET whereas it takes approximately 9–12 months for lesions to resolve on MRI (168,169).

Hemangiomas is the most frequent benign tumor lesions seen in the spine with an incidence ranging from 10% to 27% and related to increasing age (170,171). CT is more sensitive than radiography revealing a classic "corduroy cloth" on sagittal images or the polka dot sign on axial images (171,172). Typical hemangiomas are generally non-symptomatic and appear as hyperintense on T1 and T2 weighted MRI, due to the predominance of fatty tissue that is suppressed with fat suppression techniques (173). Hyperintensity is typically greater than that of fat on T2 images because of the water content, thereby differentiating hemangiomas from focal fat deposition (173). Atypical hemangiomas show iso-hypointense signal on T1 weighted sequences and hyperintense signal on T2 weighted and fat suppression sequences with variable extent of enhancement after gadolinium administration. CT can show the typical osseous remodelling of hemangiomas and the typical signs described above in up to 80% of the cases (174). Aggressive vertebral hemangiomas consist of a very rare subset of vertebral hemangiomas that enlarge, disrupting the cortex and extending to the soft tissues, even resulting in neural compression (170). Due to its aggressive appearance the final diagnosis may require CT guided biopsy (175) (*Figure 28*).

Other benign osteolytic tumors or pseudo-tumors involving the spine include eosinophilic granuloma (EG), osteoid osteoma, osteoblastoma, giant cell tumor (GCT), and aneurysmatic bone cyst (ABC). Extreme collapse of the vertebral body, vertebra plana or coin-on-edge vertebra is a typical feature of EG, a benign tumor-like disorder characterized by clonal proliferation of Langerhans cells. Spinal EG account for up to 15% of all EGs and most lesions affect children between 3 and 12 years. With healing, a reconstruction of the vertebra occurs and re-establishes an almost normal appearance (176) (*Figure 29*).

Osteoid osteoma and osteoblastoma share imaging and pathological features. The size of the radiolucent nidus is the only criterium to differentiate them, with osteoblastomas nidus greater than 2 cm and showing a more aggressive expansion pattern. Both show surrounding sclerosis and an edema pattern on MRI that may simulate a more sinister condition. GCT and ABC usually present as osteolytic expansile lesions that may have fluid-fluid levels. GCT is more frequent at the sacrum, while ABC tends to affect the posterior elements (176,177) (*Figure 30*).

Benign sclerotic tumors or pseudotumors include bone island (enostosis), sclerosis secondary to osteoid osteoma, or healed benign lesions such as cysts or fibromas. Bone island, or enostoma, is often considered a variant of normality. It appears when compact bone develops within bone marrow and typically shows an irregula and spiculated margin surrounded by normal trabecular bone. MRI shows low signal on T1 and T2 weighted images with no enhancement after contrast injection. Sometimes, it may be difficult to differentiate enostoma from malignant osteoblastic lesions. Biopsy should be considered if the lesion increases in diameter by more than 25% within 6 months or 50% within 1 year (172,176-178) (*Figure 31*).

Osteochondroma is a benign developmental exophytic lesion rather than an actual tumor. Spinal osteochondromas account for 1–4% and 9% of all solitary and multiple osteochondromas, respectively. Radiographically, osteochondroma is a bone exostosis protruding from the bone and showing varying degrees of chondroid calcification of the cartilaginous cap (176,178,179) (*Figure 31*).

Regarding primary malignant tumors, metastases, lymphoma, and multiple myeloma (MM) are the most frequent. Chordoma, plasmacytoma, osteosarcoma and primary lymphoma of the bone are rare. Osteosarcoma often presents with osteoid calcification of the tumor matrix, with marked mineralization originating in the vertebral body that may manifest as an "ivory vertebra". This sclerotic vertebra can also be seen in bone lymphoma (164).

Chordomas usually present with an osteolytic pattern and soft tissue mass. They usually appear in the sacrococcygeal region (50% of cases), followed by the spheno-occipital region (35%) and the vertebral bodies (15%). It should be differentiated from benign notochordal tumors that are contained within the

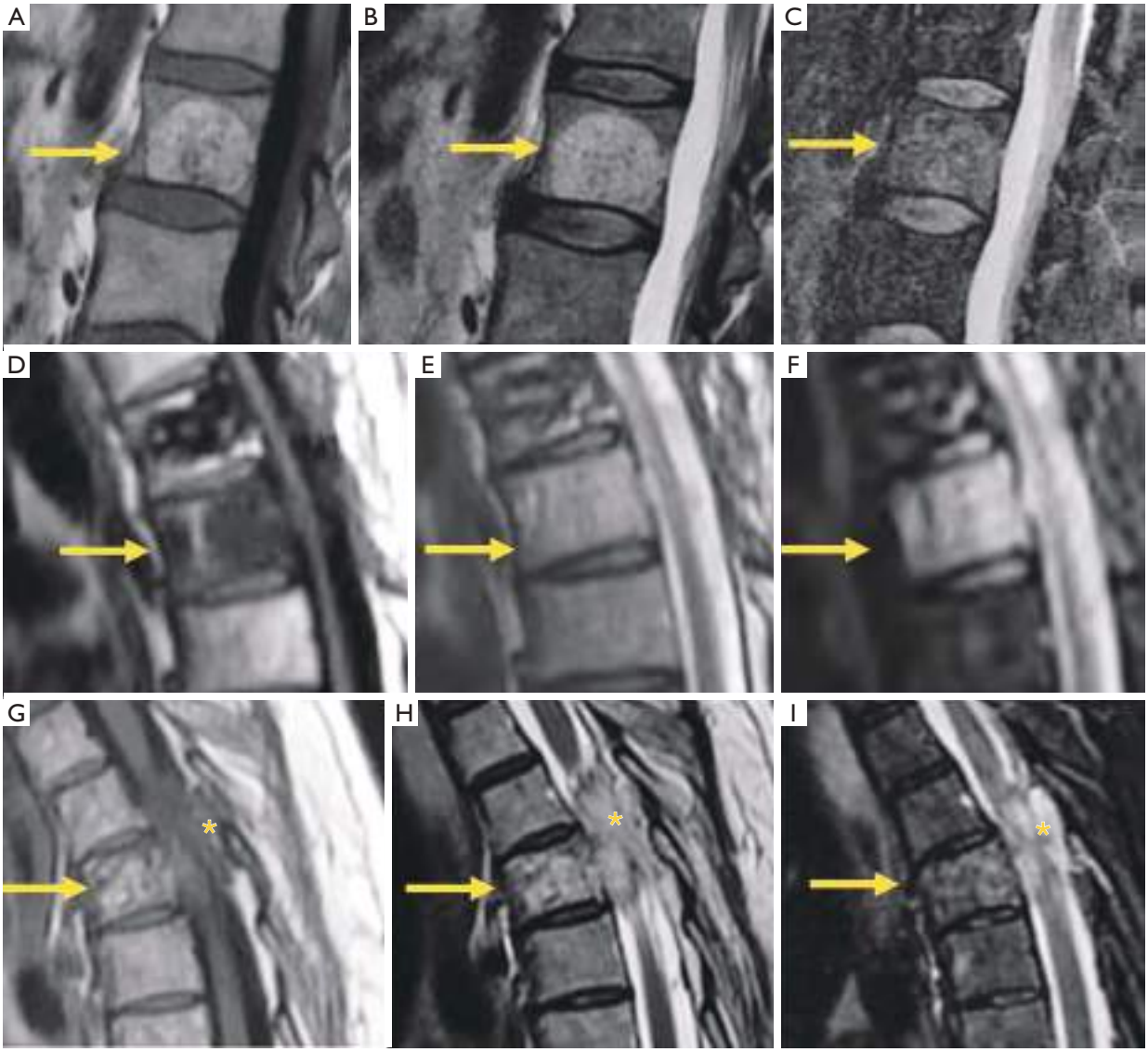

Figure 28 Vertebral hemangioma. Sagittal T1 weighted image (A), T2 weighted image (B), and STIR sequence image (C) of typical hemangioma (arrows), hyperintense on T1 and T2 due to fat content, remaining hyperintense on STIR only the vascular content. Sagittal T1 weighted image (D), T2 weighted image (E), and STIR image sequence (F) of atypical hemangioma (arrows), hypointense on T1 due to predominance of vascular component and scarce fat content. Sagittal T1 weighted image (G), T2 weighted image (H), and STIR image sequence (I) of aggressive hemangioma (arrows) extending to the spinal canal (*). STIR, short tau inversion recovery.

 Quant Imaging Med Surg 2022;12(7):3947-3986 | https://dx.doi.org/10.21037/qims-2022-04

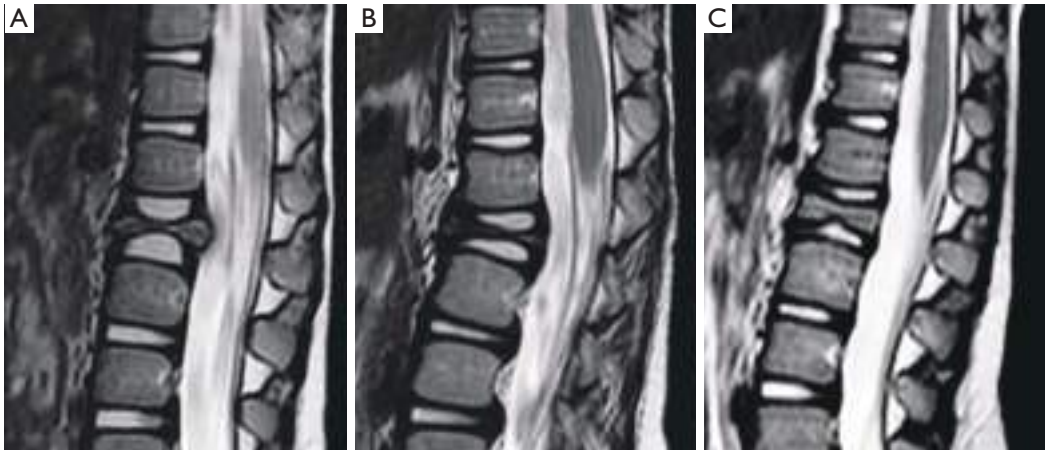

Figure 29 Eosinophilic granuloma. (A) Initial sagittal T2 weighted image that evolved to severe collapse of the vertebral body in 2 months (B). (C) Partial vertebral height recovery at 3 years follow-up.

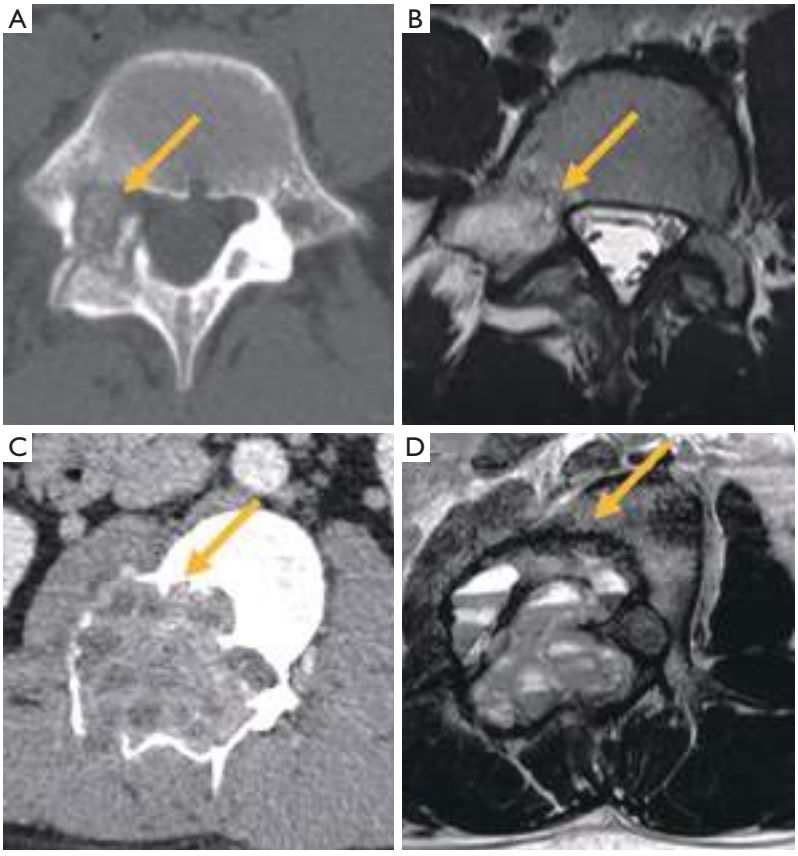

Figure 30 Osteolytic lesions of the spine. (A) Axial CT image of osteoblastoma showing the osteolytic lesion (arrow), and (B) edema pattern on MRI (arrow). (C) CT of aneurysmal bone cyst (arrow). (D) T2 weighted image showing fluid-fluid levels in the same case (arrow). CT, computed tomography; MRI, magnetic resonance imaging.

 Quant Imaging Med Surg 2022;12(7):3947-3986 | https://dx.doi.org/10.21037/qims-2022-04

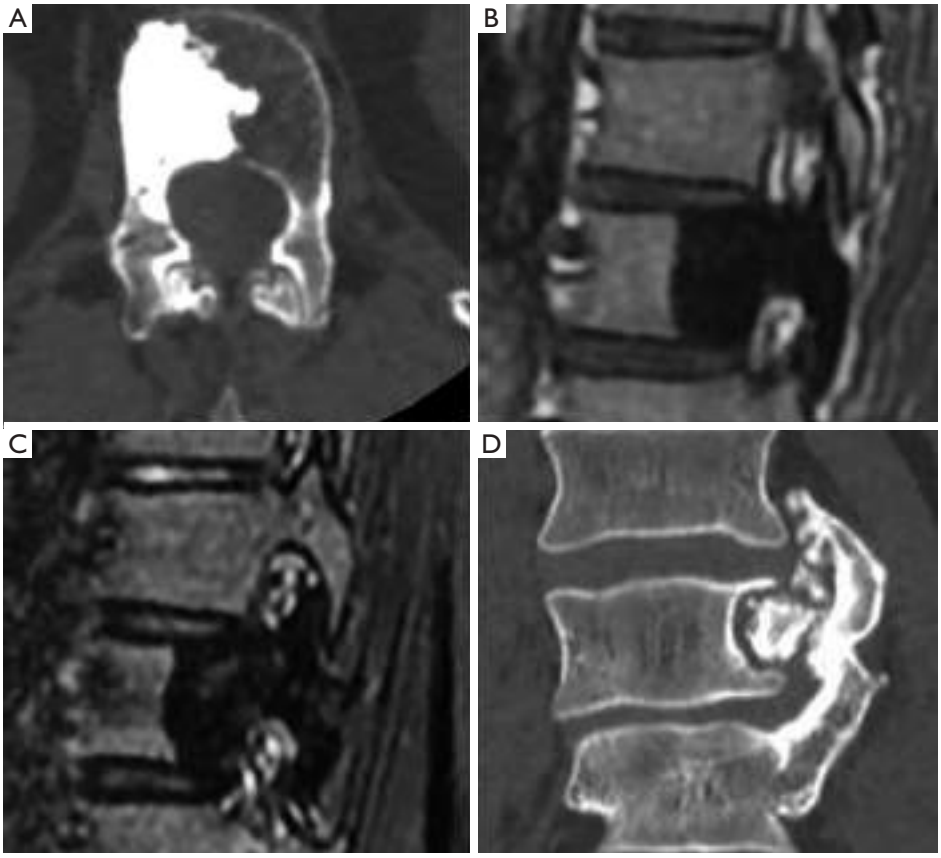

Figure 31 Benign tumors of the spine. (A) Axial CT image of enostoma; (B) sagittal T1 and STIR (C) images of enostoma; (D) coronal reformatted CT image of osteochondroma. CT, computed tomography; STIR, short tau inversion recovery.

vertebral bones, and usually behave as hypointense on T1 weighted images, hyperintense on T2 weighted images, with no significant contrast enhancement. They tend to be smaller (<30 mm) and mostly sclerotic (179). These may be managed by radiological surveillance, while for chordomas or atypical lesions, biopsy and/or surgical removal must be considered (180) (*Figure 32*).

Metastatic bone lesions can manifest on CT with an osteolytic, osteoblastic, or mixed pattern. Focal lytic metastases demonstrate decreased T1 weighted signal relative to the muscle or disc, and increased T2 weighted signal compared to normal bone marrow. Blastic lesions show decreased T1 weighted and T2 weighted signal. Enhancement after contrast administration is variable (181) (*Figure 33*).

Infiltration patterns in MM may range from normal bone marrow appearance to focal infiltration, diffuse disease, 'salt-and-pepper' like involvement, or combined involvement (*Figure 34*) (181-183). MM lesions show high contrast-enhancement due to neo-angiogenesis, with steep and rapid first-pass enhancement followed by washout. High signal on high b-value images indicates bone marrow infiltration. Of note, normal red bone marrow, which is usually more pronounced in young individuals, tends to exhibit the same signal intensity changes compared to MM-infiltrated bone marrow. Contrast enhancement curves may vary, usually with a less steep wash-in and wash-out than in MM (183).

Leukemia and lymphoma may also present as bone marrow infiltrative disorders. A diffuse infiltrative pattern is most frequent in patient with leukemia and a focal/patchy pattern is more prevalent in patients with lymphoma (184) (*Figure 35*).

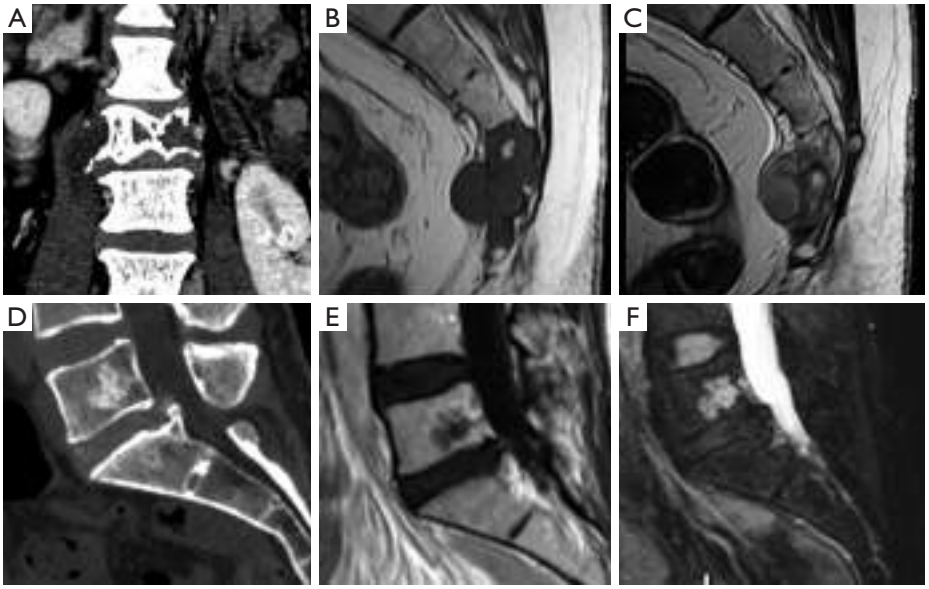

Figure 32 Notochordal tumors. (A) Coronal reformatted CT of a lumbar chordoma. (B) Sagittal T1 without and with contrast (C) of a sacral chordoma. Sagittal reformatted CT (D), T1 (E), and STIR images (F) of a benign notochordal tumor. CT, computed tomography; STIR, short tau inversion recovery.

Figure 33 Spinal metastases. (A) Sagittal CT reformation and Sagittal T2 weighted images (B) in a case of osteolytic lung cancer metastasis. (C) Sagittal CT reformation and sagittal T2 weighted image (D) in a case of osteoblastic breast carcinoma metastasis demonstrating increased density on CT scan and hypointensity on MRI. CT, computed tomography; MRI, magnetic resonance imaging.

 Quant Imaging Med Surg 2022;12(7):3947-3986 | https://dx.doi.org/10.21037/qims-2022-04

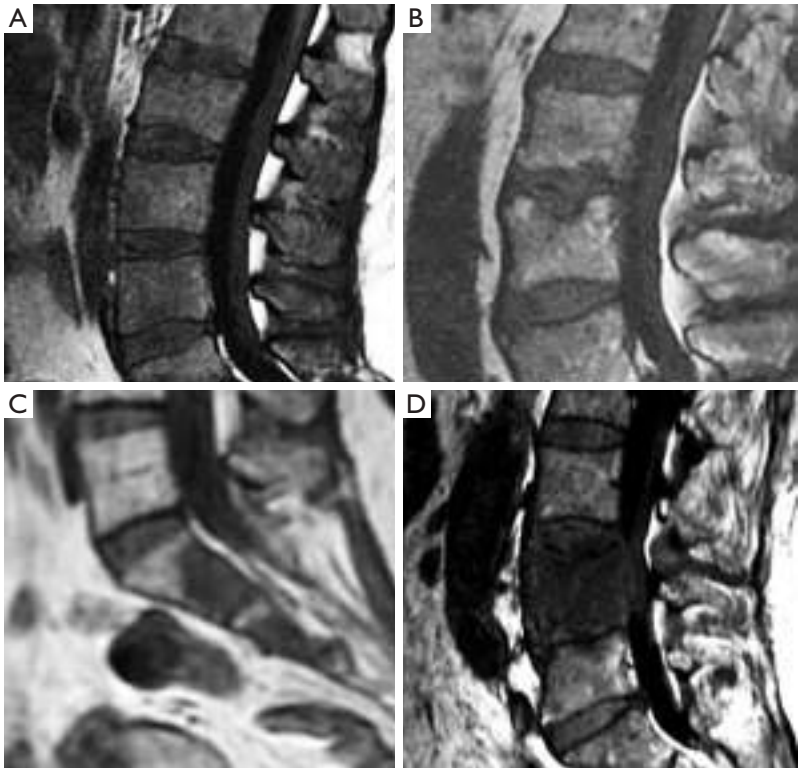

Figure 34 Patterns of spinal involvement in myeloma. Sagittal T1 weighted imaging shows diffuse (A) and salt and pepper (B) infiltration. (C) Focal and combined (D) involvement of the spine.

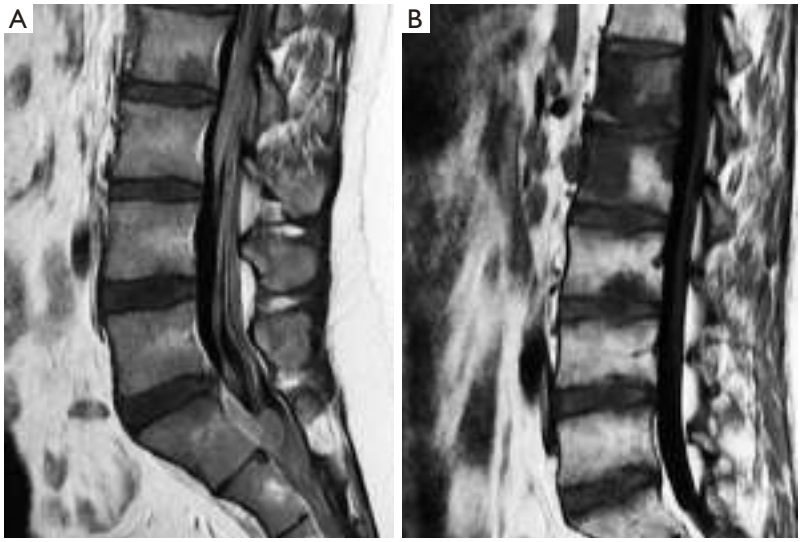

Figure 35 Infiltrative pattern in hematologic malignancies. (A) Sagittal T1 in diffuse infiltrative pattern in leukemia. (B) Patchy infiltrative pattern in Hodgkin's lymphoma.

 Quant Imaging Med Surg 2022;12(7):3947-3986 | https://dx.doi.org/10.21037/qims-2022-04

Conclusions

Proper use of CT and MRI in spinal disorders may facilitate the diagnosis and management of spinal conditions. An adequate clinical approach, an expert understanding of the pathological manifestations demonstrated by these imaging techniques and a comprehensive report based on a universally accepted nomenclature represent the indispensable tools to improve the diagnostic approach and the decision-making process in patients with spinal pain.

Acknowledgments

Funding: None.

Footnote

Conflicts of Interest: All authors have completed the ICMJE uniform disclosure form (available at https://qims.amegroups.com/article/view/10.21037/qims-2022-04/rc). YXJW serves as the Editor-in-Chief of *Quantitative Imaging in Medicine and Surgery*. The other authors have no conflicts of interest to declare.

Ethical Statement: The authors are accountable for all aspects of the work in ensuring that questions related to the accuracy or integrity of any part of the work are appropriately investigated and resolved.

References

1. ACR-ASNR-SCBT-MR practice guidelines for the performance of magnetic resonance imaging (MRI) of the adult spine. American College of Radiology. 2018. Available online: https://www.acr.org/-/media/ACR/Files/Practice-Parameters/MR-Adult-Spine.pdf?la=en. Accessed on March 28, 2022.
2. Beckmann NM, West OC, Nunez D Jr, Kirsch CFE, Aulino JM, Broder JS, Cassidy RC, Czuczman GJ, Demertzis JL, Johnson MM, Motamedi K, Reitman C, Shah LM, Than K, Ying-Kou Yung E, Beaman FD, Kransdorf MJ, Bykowski J. ACR Appropriateness Criteria® Suspected Spine Trauma. J Am Coll Radiol 2019;16:S264-85.
3. Patel ND, Broderick DF, Burns J, Deshmukh TK, Fries IB, Harvey HB, Holly L, Hunt CH, Jagadeesan BD, Kennedy TA, O'Toole JE, Perlmutter JS, Policeni B, Rosenow JM, Schroeder JW, Whitehead MT, Cornelius RS, Corey AS. ACR Appropriateness Criteria Low Back Pain. J Am Coll Radiol 2016;13:1069-78.
4. Booth TN, Iyer RS, Falcone RA Jr, Hayes LL, Jones JY, Kadom N, Kulkarni AV, Myseros JS, Partap S, Reitman C, Robertson RL, Ryan ME, Saigal G, Soares BP, Tekes-Brady A, Trout AT, Zumberge NA, Coley BD, Palasis S. ACR Appropriateness Criteria® Back Pain-Child. J Am Coll Radiol 2017;14:S13-24.
5. Jenkins HJ, Downie AS, Maher CG, Moloney NA, Magnussen JS, Hancock MJ. Imaging for low back pain: is clinical use consistent with guidelines? A systematic review and meta-analysis. Spine J 2018;18:2266-77.
6. Needham G, Grimshaw J. EU Radiation Protection 118: Referral Guidelines For Imaging. European Commission. 2007. Available online: https://www.sergas.es/docs/profesional/boapraticaclinica/rp118.pdf
7. Tahvonen P, Oikarinen H, Pääkkö E, Karttunen A, Blanco Sequeiros R, Tervonen O. Justification of CT examinations in young adults and children can be improved by education, guideline implementation and increased MRI capacity. Br J Radiol 2013;86:20130337.
8. McMaster MJ. Spinal growth and congenital deformity of the spine. Spine (Phila Pa 1976) 2006;31:2284-7.
9. Trenga AP, Singla A, Feger MA, Abel MF. Patterns of congenital bony spinal deformity and associated neural anomalies on X-ray and magnetic resonance imaging. J Child Orthop 2016;10:343-52.
10. Wáng YXJ, Santiago FR, Deng M, Nogueira-Barbosa MH. Identifying osteoporotic vertebral endplate and cortex fractures. Quant Imaging Med Surg 2017;7:555-91.
11. McMaster MJ, Singh H. Natural history of congenital kyphosis and kyphoscoliosis. A study of one hundred and twelve patients. J Bone Joint Surg Am 1999;81:1367-83.
12. Chaturvedi A, Klionsky NB, Nadarajah U, Chaturvedi A, Meyers SP. Malformed vertebrae: a clinical and imaging review. Insights Imaging 2018;9:343-55.
13. Rufener S, Ibrahim M, Parmar HA. Imaging of congenital spine and spinal cord malformations. Neuroimaging Clin N Am 2011;21:659-76, viii.

14. Kumar J, Afsal M, Garg A. Imaging spectrum of spinal dysraphism on magnetic resonance: A pictorial review. World J Radiol 2017;9:178-90.
15. Jones JY, Saigal G, Palasis S, Booth TN, Hayes LL, Iyer RS, Kadom N, Kulkarni AV, Milla SS, Myseros JS, Reitman C, Robertson RL, Ryan ME, Schulz J, Soares BP, Tekes A, Trout AT, Karmazyn B. ACR Appropriateness Criteria® Scoliosis-Child. J Am Coll Radiol 2019;16:S244-51.
16. Belmont PJ Jr, Kuklo TR, Taylor KF, Freedman BA, Prahinski JR, Kruse RW. Intraspinal anomalies associated with isolated congenital hemivertebra: the role of routine magnetic resonance imaging. J Bone Joint Surg Am 2004;86:1704-10.
17. Pinto FC, Fontes RB, Leonhardt Mde C, Amodio DT, Porro FF, Machado J. Anatomic study of the filum terminale and its correlations with the tethered cord syndrome. Neurosurgery 2002;51:725-9; discussion 729- 30.
18. Kumar I, Sachan A, Aggarwal P, Verma A, Shukla RC. Structured MRI reporting in spinal dysraphism. Acta Radiol 2020;61:1520-33.
19. Wu ZX, Huang LY, Sang HX, Ma ZS, Wan SY, Cui G, Lei W. Accuracy and safety assessment of pedicle screw placement using the rapid prototyping technique in severe congenital scoliosis. J Spinal Disord Tech 2011;24:444-50.
20. Bron JL, van Royen BJ, Wuisman PI. The clinical significance of lumbosacral transitional anomalies. Acta Orthop Belg 2007;73:687-95.
21. Hanhivaara J, Määttä JH, Karppinen J, Niinimäki J, Nevalainen MT. The Association of Lumbosacral Transitional Vertebrae with Low Back Pain and Lumbar Degenerative Findings in MRI: A Large Cohort Study. Spine (Phila Pa 1976) 2022;47:153-62.
22. Castellvi AE, Goldstein LA, Chan DP. Lumbosacral transitional vertebrae and their relationship with lumbar extradural defects. Spine (Phila Pa 1976) 1984;9:493-5.
23. Nardo L, Alizai H, Virayavanich W, Liu F, Hernandez A, Lynch JA, Nevitt MC, McCulloch CE, Lane NE, Link TM. Lumbosacral transitional vertebrae: association with low back pain. Radiology 2012;265:497-503.
24. Porter NA, Lalam RK, Tins BJ, Tyrrell PN, Singh J, Cassar-Pullicino VN. Prevalence of extraforaminal nerve root compression below lumbosacral transitional vertebrae. Skeletal Radiol 2014;43:55-60.
25. Elster AD. Bertolotti's syndrome revisited. Transitional vertebrae of the lumbar spine. Spine (Phila Pa 1976) 1989;14:1373-7.
26. Carrino JA, Campbell PD Jr, Lin DC, Morrison WB, Schweitzer ME, Flanders AE, Eng J, Vaccaro AR. Effect of spinal segment variants on numbering vertebral levels at lumbar MR imaging. Radiology 2011;259:196-202.
27. Farshad-Amacker NA, Aichmair A, Herzog RJ, Farshad M. Merits of different anatomical landmarks for correct numbering of the lumbar vertebrae in lumbosacral transitional anomalies. Eur Spine J 2015;24:600-8.
28. Tureli D, Ekinci G, Baltacioglu F. Is any landmark reliable in vertebral enumeration? A study of 3.0-Tesla lumbar MRI comparing skeletal, neural, and vascular markers. Clin Imaging 2014;38:792-6.
29. Peckham ME, Hutchins TA, Stilwill SE, Mills MK, Morrissey BJ, Joiner EAR, Sanders RK, Stoddard GJ, Shah LM. Localizing the L5 Vertebra Using Nerve Morphology on MRI: An Accurate and Reliable Technique. AJNR Am J Neuroradiol 2017;38:2008-14.
30. Ortega Herrera R, Ruiz Santiago F, Cañadillas Barea L, Galera L. Elongation of the anterior tubercle of the cervical vertebral transverse process. Radiologia 1999;41:531-3.
31. Bailitz J, Starr F, Beecroft M, Bankoff J, Roberts R, Bokhari F, Joseph K, Wiley D, Dennis A, Gilkey S, Erickson P, Raksin P, Nagy K. CT should replace three-view radiographs as the initial screening test in patients at high, moderate, and low risk for blunt cervical spine injury: a prospective comparison. J Trauma 2009;66:1605-9.
32. Griffen MM, Frykberg ER, Kerwin AJ, Schinco MA, Tepas JJ, Rowe K, Abboud J. Radiographic clearance of blunt cervical spine injury: plain radiograph or computed tomography scan? J Trauma 2003;55:222-6; discussion 226-7.
33. Karul M, Bannas P, Schoennagel BP, Hoffmann A, Wedegaertner U, Adam G, Yamamura J. Fractures of the thoracic spine in patients with minor trauma: comparison of diagnostic accuracy and dose of biplane radiography and MDCT. Eur J Radiol 2013;82:1273-7.
34. Rhea J, Sheridan R, Mullins M, Novelline R. Can chest and abdominal trauma CT eliminate the need for plain films of the spine? – Experience with 329 multiple trauma patients. Emerg Radiol 2001;8:99-104.
35. Sheridan R, Peralta R, Rhea J, Ptak T, Novelline R. Reformatted visceral protocol helical computed tomographic scanning allows conventional radiographs of the thoracic and lumbar spine to be eliminated in the evaluation of blunt trauma patients. J Trauma 2003;55:665-9.
36. Vaccaro AR, Koerner JD, Radcliff KE, Oner FC, Reinhold

M, Schnake KJ, Kandziora F, Fehlings MG, Dvorak MF, Aarabi B, Rajasekaran S, Schroeder GD, Kepler CK, Vialle LR. AOSpine subaxial cervical spine injury classification system. Eur Spine J 2016;25:2173-84.
37. Vaccaro AR, Schroeder GD, Kepler CK, Cumhur Oner F, Vialle LR, Kandziora F, Koerner JD, Kurd MF, Reinhold M, Schnake KJ, Chapman J, Aarabi B, Fehlings MG, Dvorak MF. The surgical algorithm for the AOSpine thoracolumbar spine injury classification system. Eur Spine J 2016;25:1087-94.
38. Ruiz Santiago F, Tomás Muñoz P, Moya Sánchez E, Revelles Paniza M, Martínez Martínez A, Pérez Abela AL. Classifying thoracolumbar fractures: role of quantitative imaging. Quant Imaging Med Surg 2016;6:772-84.
39. Radcliff K, Su BW, Kepler CK, Rubin T, Shimer AL, Rihn JA, Harrop JA, Albert TJ, Vaccaro AR. Correlation of posterior ligamentous complex injury and neurological injury to loss of vertebral body height, kyphosis, and canal compromise. Spine (Phila Pa 1976) 2012;37:1142-50.
40. Neumann P, Wang Y, Kärrholm J, Malchau H, Nordwall A. Determination of inter-spinous process distance in the lumbar spine. Evaluation of reference population to facilitate detection of severe trauma. Eur Spine J 1999;8:272-8.
41. Rajasekaran S, Vaccaro AR, Kanna RM, Schroeder GD, Oner FC, Vialle L, Chapman J, Dvorak M, Fehlings M, Shetty AP, Schnake K, Maheshwaran A, Kandziora F. The value of CT and MRI in the classification and surgical decision-making among spine surgeons in thoracolumbar spinal injuries. Eur Spine J 2017;26:1463-9.
42. Pizones J, Izquierdo E, Alvarez P, Sánchez-Mariscal F, Zúñiga L, Chimeno P, Benza E, Castillo E. Impact of magnetic resonance imaging on decision making for thoracolumbar traumatic fracture diagnosis and treatment. Eur Spine J 2011;20 Suppl 3:390-6.
43. Rajasekaran S, Kanna RM, Shetty AP. Management of thoracolumbar spine trauma: An overview. Indian J Orthop 2015;49:72-82.
44. Spitnale MJ, Grabowski G. Classification in Brief: Subaxial Cervical Spine Injury Classification and Severity Score System. Clin Orthop Relat Res 2020;478:2390-8.
45. Vaccaro AR, Hulbert RJ, Patel AA, Fisher C, Dvorak M, Lehman RA Jr, Anderson P, Harrop J, Oner FC, Arnold P, Fehlings M, Hedlund R, Madrazo I, Rechtine G, Aarabi B, Shainline M; Spine Trauma Study Group. The subaxial cervical spine injury classification system: a novel approach to recognize the importance of morphology, neurology, and integrity of the disco-ligamentous complex. Spine (Phila Pa 1976) 2007;32:2365-74.
46. Joaquim AF, Patel AA, Vaccaro AR. Cervical injuries scored according to the Subaxial Injury Classification system: An analysis of the literature. J Craniovertebr Junction Spine 2014;5:65-70.
47. Bondurant FJ, Cotler HB, Kulkarni MV, McArdle CB, Harris JH Jr. Acute spinal cord injury. A study using physical examination and magnetic resonance imaging. Spine (Phila Pa 1976) 1990;15:161-8.
48. Apple DF Jr, McDonald AP, Smith RA. Identification of herniated nucleus pulposis in spinal cord injury. Paraplegia 1987;25:78-85.
49. Ricart PA, Verma R, Fineberg SJ, Fink KY, Lucas PA, Lo Y, Asprinio DE, Amorosa LF. Post-traumatic cervical spine epidural hematoma: Incidence and risk factors. Injury 2017;48:2529-33.
50. Pierce JL, Donahue JH, Nacey NC, Quirk CR, Perry MT, Faulconer N, Falkowski GA, Maldonado MD, Shaeffer CA, Shen FH. Spinal Hematomas: What a Radiologist Needs to Know. Radiographics 2018;38:1516-35.
51. Vedantam A, Jirjis MB, Schmit BD, Wang MC, Ulmer JL, Kurpad SN. Diffusion tensor imaging of the spinal cord: insights from animal and human studies. Neurosurgery 2014;74:1-8; discussion 8; quiz 8.
52. Wáng YXJ, Che-Nordin N. Some radiographically 'occult' osteoporotic vertebral fractures can be evidential if we look carefully. Quant Imaging Med Surg 2019;9:1992-5.
53. Matzaroglou C, Georgiou CS, Panagopoulos A, Assimakopoulos K, Wilke HJ, Habermann B, Panos G, Kafchitsas K. Kümmell's Disease: Clarifying the Mechanisms and Patients' Inclusion Criteria. Open Orthop J 2014;8:288-97.
54. Venmans A, Klazen CA, Lohle PN, Mali WP, van Rooij WJ. Natural history of pain in patients with conservatively treated osteoporotic vertebral compression fractures: results from VERTOS II. AJNR Am J Neuroradiol 2012;33:519-21.
55. Jung HS, Jee WH, McCauley TR, Ha KY, Choi KH. Discrimination of metastatic from acute osteoporotic compression spinal fractures with MR imaging. Radiographics 2003;23:179-87.
56. Mauch JT, Carr CM, Cloft H, Diehn FE. Review of the Imaging Features of Benign Osteoporotic and Malignant Vertebral Compression Fractures. AJNR Am J Neuroradiol 2018;39:1584-92.
57. Erly WK, Oh ES, Outwater EK. The utility of in-phase/opposed-phase imaging in differentiating malignancy from acute benign compression fractures of the spine. AJNR

Am J Neuroradiol 2006;27:1183-8.
58. Borg B, Modic MT, Obuchowski N, Cheah G. Pedicle marrow signal hyperintensity on short tau inversion recovery- and t2-weighted images: prevalence and relationship to clinical symptoms. AJNR Am J Neuroradiol 2011;32:1624-31.
59. Perolat R, Kastler A, Nicot B, Pellat JM, Tahon F, Attye A, Heck O, Boubagra K, Grand S, Krainik A. Facet joint syndrome: from diagnosis to interventional management. Insights Imaging 2018;9:773-89.
60. Lakadamyali H, Tarhan NC, Ergun T, Cakir B, Agildere AM. STIR sequence for depiction of degenerative changes in posterior stabilizing elements in patients with lower back pain. AJR Am J Roentgenol 2008;191:973-9.
61. Rihn JA, Lee JY, Khan M, Ulibarri JA, Tannoury C, Donaldson WF 3rd, Kang JD. Does lumbar facet fluid detected on magnetic resonance imaging correlate with radiographic instability in patients with degenerative lumbar disease? Spine (Phila Pa 1976) 2007;32:1555-60.
62. Friedrich KM, Nemec S, Peloschek P, Pinker K, Weber M, Trattnig S. The prevalence of lumbar facet joint edema in patients with low back pain. Skeletal Radiol 2007;36:755-60.
63. Chaput C, Padon D, Rush J, Lenehan E, Rahm M. The significance of increased fluid signal on magnetic resonance imaging in lumbar facets in relationship to degenerative spondylolisthesis. Spine (Phila Pa 1976) 2007;32:1883-7.
64. Jensen MC, Brant-Zawadzki MN, Obuchowski N, Modic MT, Malkasian D, Ross JS. Magnetic resonance imaging of the lumbar spine in people without back pain. N Engl J Med 1994;331:69-73.
65. Weishaupt D, Zanetti M, Hodler J, Boos N. MR imaging of the lumbar spine: prevalence of intervertebral disk extrusion and sequestration, nerve root compression, end plate abnormalities, and osteoarthritis of the facet joints in asymptomatic volunteers. Radiology 1998;209:661-6.
66. Kalichman L, Li L, Kim DH, Guermazi A, Berkin V, O'Donnell CJ, Hoffmann U, Cole R, Hunter DJ. Facet joint osteoarthritis and low back pain in the community-based population. Spine (Phila Pa 1976) 2008;33:2560-5.
67. Suri P, Miyakoshi A, Hunter DJ, Jarvik JG, Rainville J, Guermazi A, Li L, Katz JN. Does lumbar spinal degeneration begin with the anterior structures? A study of the observed epidemiology in a community-based population. BMC Musculoskelet Disord 2011;12:202.
68. Filippiadis DK, Mazioti A, Argentos S, Anselmetti G, Papakonstantinou O, Kelekis N, Kelekis A. Baastrup's disease (kissing spines syndrome): a pictorial review. Insights Imaging 2015;6:123-8.
69. Stadnik TW, Lee RR, Coen HL, Neirynck EC, Buisseret TS, Osteaux MJ. Annular tears and disk herniation: prevalence and contrast enhancement on MR images in the absence of low back pain or sciatica. Radiology 1998;206:49-55.
70. Pfirrmann CW, Metzdorf A, Zanetti M, Hodler J, Boos N. Magnetic resonance classification of lumbar intervertebral disc degeneration. Spine (Phila Pa 1976) 2001;26:1873-8.
71. Griffith JF, Wang YX, Antonio GE, Choi KC, Yu A, Ahuja AT, Leung PC. Modified Pfirrmann grading system for lumbar intervertebral disc degeneration. Spine (Phila Pa 1976) 2007;32:E708-12.
72. Ract I, Meadeb JM, Mercy G, Cueff F, Husson JL, Guillin R. A review of the value of MRI signs in low back pain. Diagn Interv Imaging 2015;96:239-49.
73. Ravault PP, Meunier P, Sambin P, Cret R, Bianchi GS. An early sign of spinal osteoprosis: enlargement of lumbar disc spaces. Rev Lyon Med 1969;18:603-13.
74. Kwok AW, Wang YX, Griffith JF, Deng M, Leung JC, Ahuja AT, Leung PC. Morphological changes of lumbar vertebral bodies and intervertebral discs associated with decrease in bone mineral density of the spine: a cross-sectional study in elderly subjects. Spine (Phila Pa 1976) 2012;37:E1415-21.
75. Wang YXJ. Several concerns on grading lumbar disc degeneration on MR image with Pfirrmann criteria. J Orthop Translat 2022;32:101-2.
76. Adams MA, Dolan P. Intervertebral disc degeneration: evidence for two distinct phenotypes. J Anat 2012;221:497-506.
77. Aprill C, Bogduk N. High-intensity zone: a diagnostic sign of painful lumbar disc on magnetic resonance imaging. Br J Radiol 1992;65:361-9.
78. Schellhas KP, Pollei SR, Gundry CR, Heithoff KB. Lumbar disc high-intensity zone. Correlation of magnetic resonance imaging and discography. Spine (Phila Pa 1976) 1996;21:79-86.
79. Bogduk N, Aprill C, Derby R. Lumbar discogenic pain: state-of-the-art review. Pain Med 2013;14:813-36.
80. Chung CB, Vande Berg BC, Tavernier T, Cotten A, Laredo JD, Vallee C, Malghem J. End plate marrow changes in the asymptomatic lumbosacral spine: frequency, distribution and correlation with age and degenerative changes. Skeletal Radiol 2004;33:399-404.
81. Munter FM, Wasserman BA, Wu HM, Yousem DM. Serial MR Imaging of Annular Tears in Lumbar Intervertebral Disks. AJNR Am J Neuroradiol 2002;23:1105-9.

82. Fardon DF, Williams AL, Dohring EJ, Murtagh FR, Gabriel Rothman SL, Sze GK. Lumbar disc nomenclature: version 2.0: Recommendations of the combined task forces of the North American Spine Society, the American Society of Spine Radiology and the American Society of Neuroradiology. Spine J 2014;14:2525-45.
83. Boden SD, Davis DO, Dina TS, Patronas NJ, Wiesel SW. Abnormal magnetic-resonance scans of the lumbar spine in asymptomatic subjects. A prospective investigation. J Bone Joint Surg Am 1990;72:403-8.
84. Weishaupt D, Zanetti M, Hodler J, Min K, Fuchs B, Pfirrmann CW, Boos N. Painful Lumbar Disk Derangement: Relevance of Endplate Abnormalities at MR Imaging. Radiology 2001;218:420-7.
85. Amoretti N, Guinebert S, Kastler A, Torre F, Andreani O, Foti P, Cornelis F, Theumann N, Hauger O. Symptomatic Schmorl's nodes: role of percutaneous vertebroplasty. Open study on 52 patients. Neuroradiology 2019;61:405-10.
86. Wu HT, Morrison WB, Schweitzer ME. Edematous Schmorl's nodes on thoracolumbar MR imaging: characteristic patterns and changes over time. Skeletal Radiol 2006;35:212-9.
87. Luoma K, Vehmas T, Kerttula L, Grönblad M, Rinne E. Chronic low back pain in relation to Modic changes, bony endplate lesions, and disc degeneration in a prospective MRI study. Eur Spine J 2016;25:2873-81.
88. Määttä JH, Karppinen J, Paananen M, Bow C, Luk KDK, Cheung KMC, Samartzis D. Refined Phenotyping of Modic Changes: Imaging Biomarkers of Prolonged Severe Low Back Pain and Disability. Medicine (Baltimore) 2016;95:e3495.
89. Wáng YXJ, Wu AM, Ruiz Santiago F, Nogueira-Barbosa MH. Informed appropriate imaging for low back pain management: A narrative review. J Orthop Translat 2018;15:21-34.
90. Kerttula L, Luoma K, Vehmas T, Grönblad M, Kääpä E. Modic type I change may predict rapid progressive, deforming disc degeneration: a prospective 1-year follow-up study. Eur Spine J 2012;21:1135-42.
91. Kuisma M, Karppinen J, Niinimäki J, Kurunlahti M, Haapea M, Vanharanta H, Tervonen O. A three-year follow-up of lumbar spine endplate (Modic) changes. Spine (Phila Pa 1976) 2006;31:1714-8.
92. Le HV, Wick JB, Van BW, Klineberg EO. Diffuse Idiopathic Skeletal Hyperostosis of the Spine: Pathophysiology, Diagnosis, and Management. J Am Acad Orthop Surg 2021;29:1044-51.
93. Mader R, Verlaan JJ, Eshed I, Bruges-Armas J, Puttini PS, Atzeni F, Buskila D, Reinshtein E, Novofastovski I, Fawaz A, Kurt V, Baraliakos X. Diffuse idiopathic skeletal hyperostosis (DISH): where we are now and where to go next. RMD Open 2017;3:e000472.
94. Utsinger PD. Diffuse idiopathic skeletal hyperostosis. Clin Rheum Dis 1985;11:325-51.
95. Venkatanarasimha N, Parrish RW. Case 148: Thoracic epidural lipomatosis. Radiology 2009;252:618-22.
96. Lai MKL, Cheung PWH, Cheung JPY. A systematic review of developmental lumbar spinal stenosis. Eur Spine J 2020;29:2173-87.
97. Cheung JP, Samartzis D, Shigematsu H, Cheung KM. Defining clinically relevant values for developmental spinal stenosis: a large-scale magnetic resonance imaging study. Spine (Phila Pa 1976) 2014;39:1067-76.
98. Chatha DS, Schweitzer ME. MRI criteria of developmental lumbar spinal stenosis revisited. Bull NYU Hosp Jt Dis 2011;69:303-7.
99. Postacchini F, Pezzeri G. CT scanning versus myelography in the diagnosis of lumbar stenosis. A preliminary report. Int Orthop 1981;5:209-15.
100. Mrówka R, Pieniazek J. Developmental narrowing of the spinal canal in the lumbar region. Zentralbl Neurochir 1986;47:144-8.
101. Bartynski WS, Petropoulou KA. The MR imaging features and clinical correlates in low back pain-related syndromes. Magn Reson Imaging Clin N Am 2007;15:137-54, v.
102. Sirvanci M, Bhatia M, Ganiyusufoglu KA, Duran C, Tezer M, Ozturk C, Aydogan M, Hamzaoglu A. Degenerative lumbar spinal stenosis: correlation with Oswestry Disability Index and MR imaging. Eur Spine J 2008;17:679-85.
103. Park HJ, Kim SS, Lee YJ, Lee SY, Park NH, Choi YJ, Chung EC, Rho MH. Clinical correlation of a new practical MRI method for assessing central lumbar spinal stenosis. Br J Radiol 2013;86:20120180.
104. Bartynski WS, Lin L. Lumbar root compression in the lateral recess: MR imaging, conventional myelography, and CT myelography comparison with surgical confirmation. AJNR Am J Neuroradiol 2003;24:348-60.
105. Lee S, Lee JW, Yeom JS, Kim KJ, Kim HJ, Chung SK, Kang HS. A practical MRI grading system for lumbar foraminal stenosis. AJR Am J Roentgenol 2010;194:1095-8.
106. Wildermuth S, Zanetti M, Duewell S, Schmid MR, Romanowski B, Benini A, Böni T, Hodler J. Lumbar spine: quantitative and qualitative assessment of positional (upright flexion and extension) MR imaging and

myelography. Radiology 1998;207:391-8.
107. Kim YH, Kim HJ, Seo J, Chai JW, Song HG, Choi YH, Kim DH. Spinal nerve signal intensity on Dixon T2-weighted water-only sequence: an important outcome predictor after lumbar transforaminal epidural injection. Eur Radiol 2021;31:9459-67.
108. Farshad M, Sutter R, Hoch A. Severity of foraminal lumbar stenosis and the relation to clinical symptoms and response to periradicular infiltration-introduction of the "melting sign". Spine J 2018;18:294-9.
109. Cook C, Braga-Baiak A, Pietrobon R, Shah A, Neto AC, de Barros N. Observer agreement of spine stenosis on magnetic resonance imaging analysis of patients with cervical spine myelopathy. J Manipulative Physiol Ther 2008;31:271-6.
110. Yilmazlar S, Kocaeli H, Uz A, Tekdemir I. Clinical importance of ligamentous and osseous structures in the cervical uncovertebral foraminal region. Clin Anat 2003;16:404-10.
111. Kang Y, Lee JW, Koh YH, Hur S, Kim SJ, Chai JW, Kang HS. New MRI grading system for the cervical canal stenosis. AJR Am J Roentgenol 2011;197:W134-40.
112. Park HJ, Kim SS, Lee SY, Park NH, Chung EC, Rho MH, Kwon HJ, Kook SH. A practical MRI grading system for cervical foraminal stenosis based on oblique sagittal images. Br J Radiol 2013;86:20120515.
113. Kim S, Lee JW, Chai JW, Yoo HJ, Kang Y, Seo J, Ahn JM, Kang HS. A New MRI Grading System for Cervical Foraminal Stenosis Based on Axial T2-Weighted Images. Korean J Radiol 2015;16:1294-302.
114. Meacock J, Schramm M, Selvanathan S, Currie S, Stocken D, Jayne D, Thomson S. Systematic review of radiological cervical foraminal grading systems. Neuroradiology 2021;63:305-16.
115. Lee HD, Jeon CH, Chung NS, Yoon HS, Chung HW. Is the Severity of Cervical Foraminal Stenosis Related to the Severity and Sidedness of Symptoms? Healthcare (Basel) 2021;9:1743.
116. Gallucci M, Limbucci N, Paonessa A, Splendiani A. Degenerative disease of the spine. Neuroimaging Clin N Am 2007;17:87-103.
117. Dhouib A, Tabard-Fougere A, Hanquinet S, Dayer R. Diagnostic accuracy of MR imaging for direct visualization of lumbar pars defect in children and young adults: a systematic review and meta-analysis. Eur Spine J 2018;27:1058-66.
118. Ang EC, Robertson AF, Malara FA, O'Shea T, Roebert JK, Schneider ME, Rotstein AH. Diagnostic accuracy of 3-T magnetic resonance imaging with 3D T1 VIBE versus computer tomography in pars stress fracture of the lumbar spine. Skeletal Radiol 2016;45:1533-40.
119. Hollenberg GM, Beattie PF, Meyers SP, Weinberg EP, Adams MJ. Stress reactions of the lumbar pars interarticularis: the development of a new MRI classification system. Spine (Phila Pa 1976) 2002;27:181-6.
120. Cheung KK, Dhawan RT, Wilson LF, Peirce NS, Rajeswaran G. Pars interarticularis injury in elite athletes - The role of imaging in diagnosis and management. Eur J Radiol 2018;108:28-42.
121. Dunn AJ, Campbell RS, Mayor PE, Rees D. Radiological findings and healing patterns of incomplete stress fractures of the pars interarticularis. Skeletal Radiol 2008;37:443-50.
122. Sherif H, Mahfouz AE. Epidural fat interposition between dura mater and spinous process: a new sign for the diagnosis of spondylolysis on MR imaging of the lumbar spine. Eur Radiol 2004;14:970-3.
123. Schmid T, Heini P, Benneker L. A rare case of non-traumatic, multi-level, bilateral pedicle fractures of the lumbar spine in a 60-year-old patient. Eur Spine J 2017;26:197-201.
124. He LC, Wang YX, Gong JS, Griffith JF, Zeng XJ, Kwok AW, Leung JC, Kwok T, Ahuja AT, Leung PC. Prevalence and risk factors of lumbar spondylolisthesis in elderly Chinese men and women. Eur Radiol 2014;24:441-8.
125. Wang YXJ, Káplár Z, Deng M, Leung JCS. Lumbar degenerative spondylolisthesis epidemiology: A systematic review with a focus on gender-specific and age-specific prevalence. J Orthop Translat 2016;11:39-52.
126. Gupta P, Kumar A, Gamangatti S. Mechanism and patterns of cervical spine fractures-dislocations in vertebral artery injury. J Craniovertebr Junction Spine 2012;3:11-5.
127. Ruiz Santiago F, Moreno Gaya M, Suárez Boville I, López Milena G, Rodríguez Fernández, C Tristán Fernández J, Rodríguez Vacas J. Evolución clínica y radiológica de la cifosis juvenil. Rehabilitación 2003;37:11-6.
128. Khanna G. Role of imaging in scoliosis. Pediatr Radiol 2009;39 Suppl 2:S247-51.
129. Dobbs MB, Lenke LG, Szymanski DA, Morcuende JA, Weinstein SL, Bridwell KH, Sponseller PD. Prevalence of neural axis abnormalities in patients with infantile idiopathic scoliosis. J Bone Joint Surg Am 2002;84:2230-4.
130. Davies A, Saifuddin A. Imaging of painful scoliosis. Skeletal Radiol 2009;38:207-23.
131. Johnson MA, Gohel S, Mitchell SL, Flynn JJM, Baldwin KD. Entire-spine Magnetic Resonance Imaging Findings and Costs in Children With Presumed Adolescent

Idiopathic Scoliosis. J Pediatr Orthop 2021;41:585-90.
132. Swarup I, Silberman J, Blanco J, Widmann R. Incidence of Intraspinal and Extraspinal MRI Abnormalities in Patients With Adolescent Idiopathic Scoliosis. Spine Deform 2019;7:47-52.
133. de Oliveira RG, de Araújo AO, Gomes CR. Magnetic resonance imaging effectiveness in adolescent idiopathic scoliosis. Spine Deform 2021;9:67-73.
134. Ransford AO, Pozo JL, Hutton PA, Kirwan EO. The behaviour pattern of the scoliosis associated with osteoid osteoma or osteoblastoma of the spine. J Bone Joint Surg Br 1984;66:16-20.
135. Jurik AG. Imaging the spine in arthritis-a pictorial review. Insights Imaging 2011;2:177-91.
136. Caetano AP, Mascarenhas VV, Machado PM. Axial Spondyloarthritis: Mimics and Pitfalls of Imaging Assessment. Front Med (Lausanne) 2021;8:658538.
137. Haibel H, Rudwaleit M, Listing J, Heldmann F, Wong RL, Kupper H, Braun J, Sieper J. Efficacy of adalimumab in the treatment of axial spondylarthritis without radiographically defined sacroiliitis: results of a twelve-week randomized, double-blind, placebo-controlled trial followed by an open-label extension up to week fifty-two. Arthritis Rheum 2008;58:1981-91.
138. Rudwaleit M, van der Heijde D, Landewé R, Listing J, Akkoc N, Brandt J, et al. The development of Assessment of SpondyloArthritis international Society classification criteria for axial spondyloarthritis (part II): validation and final selection. Ann Rheum Dis 2009;68:777-83.
139. Malaviya AN, Rawat R, Agrawal N, Patil NS. The Nonradiographic Axial Spondyloarthritis, the Radiographic Axial Spondyloarthritis, and Ankylosing Spondylitis: The Tangled Skein of Rheumatology. Int J Rheumatol 2017;2017:1824794.
140. Elgafy H, Semaan HB, Ebraheim NA, Coombs RJ. Computed tomography findings in patients with sacroiliac pain. Clin Orthop Relat Res 2001;(382):112-8.
141. Proft F, Poddubnyy D. Ankylosing spondylitis and axial spondyloarthritis: recent insights and impact of new classification criteria. Ther Adv Musculoskelet Dis 2018;10:129-39.
142. Rudwaleit M, Jurik AG, Hermann KG, Landewé R, van der Heijde D, Baraliakos X, Marzo-Ortega H, Ostergaard M, Braun J, Sieper J. Defining active sacroiliitis on magnetic resonance imaging (MRI) for classification of axial spondyloarthritis: a consensual approach by the ASAS/OMERACT MRI group. Ann Rheum Dis 2009;68:1520-7.
143. Rudwaleit M, Landewé R, van der Heijde D, Listing J, Brandt J, Braun J, et al. The development of Assessment of SpondyloArthritis international Society classification criteria for axial spondyloarthritis (part I): classification of paper patients by expert opinion including uncertainty appraisal. Ann Rheum Dis 2009;68:770-6.
144. Akgul O, Ozgocmen S. Classification criteria for spondyloarthropathies. World J Orthop 2011;2:107-15.
145. Maksymowych WP, Eshed I, Machado PM, Juhl Pedersen SJ, Weber U, De Hooge M, Sieper J, Wichuk S, Poddubnyy D, Rudwaleit M, Van der Heijde D, Landewé RBM, Lambert RG, Østergaard M, Baraliakos X. Consensus definitions for MRI lesions in the spine of patients with axial spondyloarthritis: first analysis from the assessments in spondyloarthritis international society classification cohort (abstract). Ann Rheum Dis 2020;79:749-50.
146. Hermann KG, Baraliakos X, van der Heijde DM, Jurik AG, Landewé R, Marzo-Ortega H, Østergaard M, Rudwaleit M, Sieper J, Braun J; Assessment in SpondyloArthritis international Society (ASAS). Descriptions of spinal MRI lesions and definition of a positive MRI of the spine in axial spondyloarthritis: a consensual approach by the ASAS/OMERACT MRI study group. Ann Rheum Dis 2012;71:1278-88.
147. Park YS, Kim JH, Ryu JA, Kim TH. The Andersson lesion in ankylosing spondylitis: distinguishing between the inflammatory and traumatic subtypes. J Bone Joint Surg Br 2011;93:961-6.
148. Hong SH, Choi JY, Lee JW, Kim NR, Choi JA, Kang HS. MR imaging assessment of the spine: infection or an imitation? Radiographics 2009;29:599-612.
149. Modic MT, Feiglin DH, Piraino DW, Boumphrey F, Weinstein MA, Duchesneau PM, Rehm S. Vertebral osteomyelitis: assessment using MR. Radiology 1985;157:157-66.
150. Tali ET. Spinal infections. Eur J Radiol 2004;50:120-33.
151. Dagirmanjian A, Schils J, McHenry M, Modic MT. MR imaging of vertebral osteomyelitis revisited. AJR Am J Roentgenol 1996;167:1539-43.
152. Maiuri F, Iaconetta G, Gallicchio B, Manto A, Briganti F. Spondylodiscitis. Clinical and magnetic resonance diagnosis. Spine (Phila Pa 1976) 1997;22:1741-6.
153. Dunbar JA, Sandoe JA, Rao AS, Crimmins DW, Baig W, Rankine JJ. The MRI appearances of early vertebral osteomyelitis and discitis. Clin Radiol 2010;65:974-81.
154. Ledbetter LN, Salzman KL, Shah LM. Imaging Psoas Sign in Lumbar Spinal Infections: Evaluation of Diagnostic

Accuracy and Comparison with Established Imaging Characteristics. AJNR Am J Neuroradiol 2016;37:736-41.
155. Tetsuka S, Suzuki T, Ogawa T, Hashimoto R, Kato H. Spinal Epidural Abscess: A Review Highlighting Early Diagnosis and Management. JMA J 2020;3:29-40.
156. Moritani T, Kim J, Capizzano AA, Kirby P, Kademian J, Sato Y. Pyogenic and non-pyogenic spinal infections: emphasis on diffusion-weighted imaging for the detection of abscesses and pus collections. Br J Radiol 2014;87:20140011.
157. Laur O, Mandell JC, Titelbaum DS, Cho C, Smith SE, Khurana B. Acute Nontraumatic Back Pain: Infections and Mimics. Radiographics 2019;39:287-8.
158. Cheung WY, Luk KD. Pyogenic spondylitis. Int Orthop 2012;36:397-404.
159. Teh J, Imam A, Watts C. Imaging of back pain. Imaging 2005;17:171-207.
160. Diehn FE. Imaging of spine infection. Radiol Clin North Am 2012;50:777-98.
161. Afonso PD, Almeida A. Tuberculous spondilodiskitis: imaging features. Acta Med Port 2011;24:349-54.
162. Shen L, Jiang C, Jiang R, Fang W, Feng Q, Wang L, Wu C, Ma Z. Diagnosis and classification in MRI of brucellar spondylitis. Radiol Infect Dis 2017;4:102-7.
163. Mundy GR. Metastasis to bone: causes, consequences and therapeutic opportunities. Nat Rev Cancer 2002;2:584-93.
164. Rodallec MH, Feydy A, Larousserie F, Anract P, Campagna R, Babinet A, Zins M, Drapé JL. Diagnostic imaging of solitary tumors of the spine: what to do and say. Radiographics 2008;28:1019-41.
165. Yang L, Zhang S, Gu R, Peng C, Wu M. Imaging features of primary spinal osseous tumors and their value in clinical diagnosis. Oncol Lett 2019;17:1089-93.
166. Liu T, Wang S, Liu H, Meng B, Zhou F, He F, Shi X, Yang H. Detection of vertebral metastases: a meta-analysis comparing MRI, CT, PET, BS and BS with SPECT. J Cancer Res Clin Oncol 2017;143:457-65.
167. Zhou J, Gou Z, Wu R, Yuan Y, Yu G, Zhao Y. Comparison of PSMA-PET/CT, choline-PET/CT, NaF-PET/CT, MRI, and bone scintigraphy in the diagnosis of bone metastases in patients with prostate cancer: a systematic review and meta-analysis. Skeletal Radiol 2019;48:1915-24.
168. Lütje S, de Rooy JW, Croockewit S, Koedam E, Oyen WJ, Raymakers RA. Role of radiography, MRI and FDG-PET/CT in diagnosing, staging and therapeutical evaluation of patients with multiple myeloma. Ann Hematol 2009;88:1161-8.
169. Mesguich C, Hulin C, Latrabe V, Asselineau J, Bordenave L, Perez P, Hindie E, Marit G. Prospective Comparison of 18F-Choline Positron Emission Tomography/Computed Tomography (PET/CT) and 18F-Fluorodeoxyglucose (FDG) PET/CT in the Initial Workup of Multiple Myeloma: Study Protocol of a Prospective Imaging Trial. JMIR Res Protoc 2020;9:e17850.
170. Chen HI, Heuer GG, Zaghloul K, Simon SL, Weigele JB, Grady MS. Lumbar vertebral hemangioma presenting with the acute onset of neurological symptoms. Case report. J Neurosurg Spine 2007;7:80-5.
171. Gaudino S, Martucci M, Colantonio R, Lozupone E, Visconti E, Leone A, Colosimo C. A systematic approach to vertebral hemangioma. Skeletal Radiol 2015;44:25-36.
172. Price HI, Batnitzky S. The computed tomographic findings in benign diseases of the vertebral column. Crit Rev Diagn Imaging 1985;24:39-89.
173. Ross JS, Masaryk TJ, Modic MT, Carter JR, Mapstone T, Dengel FH. Vertebral hemangiomas: MR imaging. Radiology 1987;165:165-9.
174. Cross JJ, Antoun NM, Laing RJ, Xuereb J. Imaging of compressive vertebral haemangiomas. Eur Radiol 2000;10:997-1002.
175. Rimondi E, Rossi G, Bartalena T, Ciminari R, Alberghini M, Ruggieri P, Errani C, Angelini A, Calabrò T, Abati CN, Balladelli A, Tranfaglia C, Mavrogenis AF, Vanel D, Mercuri M. Percutaneous CT-guided biopsy of the musculoskeletal system: results of 2027 cases. Eur J Radiol 2011;77:34-42.
176. Garcia DAL, Aivazoglou LU, Garcia LAL, Ferreira FBMD, França SM, Guimarães JB, Fernandes ADRC. Diagnostic Imaging of Primary Bone Tumors of the Spine. Curr Radiol Rep 2017;5:1-13.
177. Orguc S, Arkun R. Primary tumors of the spine. Semin Musculoskelet Radiol 2014;18:280-99.
178. Greenspan A, Steiner G, Knutzon R. Bone island (enostosis): clinical significance and radiologic and pathologic correlations. Skeletal Radiol 1991;20:85-90.
179. Murphey MD, Choi JJ, Kransdorf MJ, Flemming DJ, Gannon FH. Imaging of osteochondroma: variants and complications with radiologic-pathologic correlation. Radiographics 2000;20:1407-34.
180. Usher I, Flanagan AM, Choi D. Systematic Review of Clinical, Radiologic, and Histologic Features of Benign Notochordal Cell Tumors: Implications for Patient Management. World Neurosurg 2019;130:13-23.
181. Hwang S, Panicek DM. Magnetic resonance imaging of bone marrow in oncology, Part 2. Skeletal Radiol 2007;36:1017-27.

 Quant Imaging Med Surg 2022;12(7):3947-3986 | https://dx.doi.org/10.21037/qims-2022-04

182. Ruiz Santiago F, Láinez Ramos-Bossini AJ, Wáng YXJ, López Zúñiga D. The role of radiography in the study of spinal disorders. Quant Imaging Med Surg 2020;10:2322-55.
183. Dutoit JC, Verstraete KL. MRI in multiple myeloma: a pictorial review of diagnostic and post-treatment findings. Insights Imaging 2016;7:553-69.
184. Nguyen JC, Davis KW, Arkader A, Guariento A, Sze A, Hong S, Jaramillo D. Pre-treatment MRI of leukaemia and lymphoma in children: are there differences in marrow replacement patterns on T1-weighted images? Eur Radiol 2021;31:7992-8000.

Cite this article as: Ruiz Santiago F, Láinez Ramos-Bossini AJ, Wáng YXJ, Martínez Barbero JP, García Espinosa J, Martínez Martínez A. The value of magnetic resonance imaging and computed tomography in the study of spinal disorders. Quant Imaging Med Surg 2022;12(7):3947-3986. doi: 10.21037/qims-2022-04

TRABAJO 3: RADIOGRAPHIC DIAGNOSIS OF OSTEOPOROTIC VERTEBRAL FRACTURES. AN UPDATED REVIEW (DIAGNÓSTICO RADIOLÓGICO DE LAS FRACTURAS VERTEBRALES OSTEOPORÓTICAS. UNA REVISIÓN ACTUALIZADA).

López Zúñiga D, **Láinez-Ramos-Bossini AJ**, Ruiz Santiago F. Radiographic diagnosis of osteoporotic vertebral fractures. An updated review. Med Clin (Barc). 2022;158(3):125-132. doi:10.1016/j.medcli.2021.06.019. FI: 3,9. Q2 (T2).

Se trata de una revisión bibliográfica y pictórica que cubre los objetivos 1 y 2.

Medicina Clínica 158 (2022) 125–132

MEDICINA CLINICA

www.elsevier.es/medicinaclinica

Review

Radiographic diagnosis of osteoporotic vertebral fractures. An updated review

Daniel López Zúñiga [a], Antonio Jesús Láinez-Ramos-Bossini [a,b], Fernando Ruiz Santiago [a,b,*]

[a] Department of Radiology, "Virgen de las Nieves" University Hospital, Granada, Spain
[b] Department of Radiology and Physical Medicine, University of Granada, Granada, Spain

ARTICLE INFO

Article history:
Received 20 March 2021
Accepted 1 June 2021
Available online 13 August 2021

Keywords:
Osteoporosis
Vertebral fracture
Conventional radiography
Radiological diagnosis

ABSTRACT

The radiological diagnosis of osteoporotic vertebral fractures (OVFs) is of major importance considering its therapeutic and prognostic implications. Both radiologists and clinicians have the opportunity to diagnose OVFs in daily clinical practice due to the widespread use of spine and chest radiography. However, several studies have reported an under-diagnosis of OVFs, particularly by a lack of consensus on the diagnostic criteria. Therefore, up-to-date knowledge of the most relevant approaches for the diagnosis of OVFs is necessary for many physicians. This article aims to review the most commonly used classification systems in the diagnosis of OVFs based on conventional radiography. We discuss their rationale, advantages and limitations, as well as their utility according to the context. This review will provide a concise yet useful understanding of the typology of OVFs, their clinical significance and prognosis. Finally, we include anatomical variations that can be confused with OVFs by non-experts.

Diagnóstico radiológico de las fracturas vertebrales osteoporóticas. Una revisión actualizada

Palabras clave:
Osteoporosis
Fractura vertebral
Radiografía simple
Diagnóstico radiológico

RESUMEN

El diagnóstico radiológico de las fracturas vertebrales osteoporóticas (FVO) es de gran importancia, considerando sus implicaciones terapéuticas y pronósticas. Tanto los radiólogos como los facultativos tienen la oportunidad de diagnosticar las FVO en la práctica clínica diaria debido al uso extendido de las radiografías de columna y tórax. Sin embargo, diversos estudios han reportado el infradiagnóstico de las FVO, particularmente debido a la falta de consenso sobre los criterios diagnósticos. Por tanto, es necesario actualizar el conocimiento de los enfoques más relevantes en cuanto al diagnóstico de las FVO de muchos médicos. El objetivo del presente artículo es revisar los sistemas de clasificación más comúnmente utilizados para diagnosticar las FVO sobre la base de la radiografía convencional. Debatimos sus fundamentos, ventajas y limitaciones, así como su utilidad con respecto al contexto. Esta revisión aportará una comprensión concisa y útil de la tipología de las FVO, su significación clínica y pronóstico. Por último, incluimos variaciones anatómicas que pueden ser confundidas con las FVO por los no expertos.

Introduction

Osteoporosis is characterised by the deterioration of bone mass and micro-architecture, which increases the risk of fragility fractures.[1] It is the most common metabolic bone disease in the world, representing a major health concern with 27.6 million people affected in the European Union.[2–4] Its prevalence is higher in women and increases with age, being 3–4 times more frequent above the age of 50.[3]

Vertebral fractures are the most frequent location in osteoporotic patients.[3] Detecting one or more osteoporotic vertebral fractures (OVFs) is sufficient to make the diagnosis of osteoporosis,

* Corresponding author.
E-mail address: ferusan12@gmail.com (F. Ruiz Santiago).

https://doi.org/10.1016/j.medcli.2021.06.019
0025-7753/

even in the absence of bone mineral density (BMD) determination.[2] Moreover, the presence of one or more OVFs significantly increases the risk of suffering other fractures in the future, regardless of the patient's BMD, and the associated morbidity and mortality are similar to osteoporotic hip fractures at 5 years.[1,3,5–8]

As highlighted by Lentle et al.,[6,9] OVFs are a special type of fracture due to several factors, including lack of consensus criteria on their definition, coexistence of bone consolidation and destruction with subsequent gradual fracture development, and paucity or even absence of symptoms. In fact, many OVFs are incidentally detected on imaging exams performed for unrelated reasons. It is estimated that only 30% of OVFs come to medical attention,[4] which has been attributed to various factors such as clinical focus on other findings of greater severity, lack of familiarity with OVFs[10] or ambiguous terminology in radiology reports.[11] However, an accurate diagnosis of OVFs is needed to initiate appropriate drug treatment and thus reduce the risk of future fractures.[10] Moreover, describing the severity of the OVF is essential because severe fractures are associated with greater deterioration of bone quality and higher risk of new fractures.[12]

Although radiologists have a central role in the diagnosis of OVFs, interpretation of chest and spine radiographs is a basic skill for all clinicians, thus recommendations for assessing OVFs should be known. However, with the development of more sophisticated imaging exams (e.g., CT, MRI), clinicians and even radiologists are losing interest in recognising the features and classification systems of OVFs on conventional radiography. The purpose of this article is to review the main radiographic approaches available regarding the diagnosis of OVFs, their advantages and limitations, as well as the anatomical variants that most frequently lead to diagnostic pitfalls.

Radiographic techniques to assess osteoporotic vertebral fractures

Conventional or plain radiography is a fast, widely available and inexpensive technique that involves relatively low effective radiation doses (0.3–0.7 mSv).[13] For these reasons, it is considered by some authors to be the best imaging technique to assess the presence of low-energy vertebral fractures.[14] Although spine radiographs are the optimal radiographic technique to make an accurate diagnosis of OVF, chest radiography also allows their detection, thus cautious examination of the spine should always be carried out, even in patients without pain.

Conventional spine radiography

Conventional radiography of the thoracolumbar spine, in both anterior–posterior (AP) and lateral projections, is the initial imaging exam of choice in patients with symptoms suggestive of low-energy vertebral fracture (localised pain, height reduction, or thoracic kyphosis), especially if there is associated trauma.[15,16]

Performing an adequate radiographic technique is necessary to avoid diagnostic errors due to incorrect positioning of the patient or inadequate acquisition parameters.[1] Parallel positioning of the patient's spine on the table and adequate centring, collimation and physical parameters must be ensured to avoid poor image quality.[17] The coverage should include the spinal segment between C7 and S1.[14]

Although specific projections centred at the thoracolumbar junction may be used,[18] the AP and lateral projections are usually sufficient for correct assessment of the height of vertebral bodies and for detection of fracture lines. Although assessment based on both projections increases diagnostic sensitivity, the AP projection is less sensitive, being the lateral projection the only one used in most epidemiological studies.[1] In this projection, the two main parameters to be assessed are vertebral height and the degree of kyphotic deformity. It should be stressed that the decrease in these parameters over time may allow the diagnosis of incident OVFs, thus radiographic follow-up is essential to spot new OVFs. On the other hand, Wáng et al.[19] suggest that the majority of moderate and severe vertebral fractures can be detected on AP projections in patients at high risk of osteoporosis.

Conventional chest radiography

Although not the initial imaging technique of choice, chest radiography is undoubtedly one of the most widely used imaging exams and generally covers all or part of the thoracolumbar junction in the lateral projection, allowing the diagnosis of OVFs both in symptomatic and asymptomatic patients. Therefore, this examination can be a valuable screening method for OVFs. However, it has been found that only one third of OVFs are described in radiologic reports of chest radiographs.[15] In general, the same technical quality requirements and measures as in spine radiography are applicable. Although few literature is available on the utility of the AP projection and further studies are needed to demonstrate its positive predictive value and cost-effectiveness in real-world practice, it opens up a great opportunity for the diagnosis of OVFs in patients with radiographs performed for other reasons (e.g. abdomen or chest radiography).

Classification systems used in the diagnosis of osteoporotic vertebral fractures on conventional radiography

For more than half a century, numerous classification systems have been developed with the aim to classify OVFs based on imaging features on conventional radiography. Nevertheless, only a few classifications have gained international acceptance, and the criteria for the diagnosis and classification of OVFs remain a subject of debate among experts.[20–22] In this sense, OVF has traditionally been considered to involve a loss of at least 20% of the vertebral height.[14] However, with progressive understanding of the pathophysiology of OVFs, many authors have recognised that this classic definition is neither necessary nor sufficient to diagnose OVFs,[1,23] because there are other signs that can be indicative of OVF in the absence of significant reduction of vertebral height. Accordingly, loss of parallelism between adjacent vertebrae or vertebral endplates (VEs), impaction of the VE on the vertebral body (VB), cortical discontinuities of the VB or VE, or indentation of vertebral surfaces, particularly in the anterior cortex, are currently considered signs of OVF in the appropriate clinical setting.[1,6,22]

A review of the literature on this topic reveals various radiographic diagnostic criteria for OVF, but all or most of them can be classified into three main categories: quantitative, qualitative and combined (semiquantitative) methods. Each of these approaches has certain advantages and limitations that must be known in order to apply the most appropriate one according to the clinical context.

Quantitative or morphometric methods

Quantitative or morphometric methods are based on the measurement of the anterior, medial and posterior vertebral height (AVH, MVH and PVH, respectively). The comparison of these measurements with reference values allows determining the presence of fracture. Other aspects such as vertebral morphology are not assessed directly, although some of them can be actually inferred from the ratios obtained. For instance, the relationship between the AVH and the PVH reflects the degree of fracture wedging (Fig. 1).[18,24] Numerous morphometric algorithms have been developed with different degrees of complexity. The Eastell-Melton

Fig. 1. Examples of morphometric measurements and their associated morphological parameters. (A) Anterior wedging; (b) posterior wedging; (c) biconcavity; (d) crush fracture. Red points mark the vertebral height which is decreased.

method[25] distinguishes three types of fractures (wedge, biconcavity, compression or crush fracture) depending on the vertebral height which is decreased, while the McCloskey-Kanis method further classifies the wedge type into anterior and posterior. Posterior wedge includes loss of PVH and MVH. Of note, isolated loss of the PVH was considered a variant which typically occurs at L5.[26]

One of the main advantages of quantitative methods is that they are based on objective and reproducible measurements, particularly in healthy individuals.[24] In addition, the agreement with semi-quantitative methods is very high for intermediate and severe OVFs. Moreover, because of their simplicity, most of these methods can be applied by inexperienced observers, which is of particular interest to clinicians with little experience, or even to non-physicians in the research field. Furthermore, they can be used to implement ad hoc software and evaluate the efficiency of automated diagnostic algorithms using different methods (e.g., based on statistics or artificial intelligence).

One of the main limitations of these methods is that they do not consider morphological alterations that may indicate OVF in the absence of vertebral height loss. In addition, it is not possible to ascertain whether the vertebral height loss is due to OVFs or other non-fracture causes, resulting in a high number of false positives. Moreover, there is low agreement with the semi-quantitative methods for mild or low-grade OVFs, with a higher rate of false positives using morphometric methods. Finally, these methods are time consuming for clinical practice and show a relatively high inter- and intra-observer variability.[14] In particular, the selected points for the measurement of each vertebral height (mainly the MVH) are quite subjective, particularly in cases of poor quality radiographs, spinal rotation or blurred vertebral edges.[27]

Qualitative methods

Classification of osteoporotic vertebral fractures proposed by Jiang et al.

Some OVFs do not display significant alterations of vertebral height or area, thus morphometric and combined methods are not appropriate.[1,28] To diagnose these OVFs, several methods have been developed based on a step-by-step analysis focused on abnormalities of the VE. The main approach within this group is the algorithm-based qualitative (ABQ) method and its modified versions proposed by Jiang et al.[27,28], although this consideration has been overlooked in some clinical guidelines[29].

The ABQ method is designed to detect alterations in the VEs that are present in OVFs and exclude other potential causes for such alterations, (e.g. anatomical variants, diseases or poor radiographic technique). The steps of this algorithm lead to one of the following conclusions: (a) normal vertebra, (b) OVF (VE depression ± loss of vertebral height), or (c) non-osteoporotic deformity (>15% loss of vertebral height without VE depression).

Classification of osteoporotic vertebral fractures proposed by Sugita et al.

According to this classification,[30] five types of OVF are distinguished based on the morphology of the VB in the lateral projection (performed in an acute setting) (Fig. 2): type I (swelled-front): >50% bulge of the anterior wall; type II (bow-shaped): focal depression of the anterior wall and upper VE; type III (projecting): focal prominence < 50% of the anterior wall; type IV (concave): depression of the upper VE without affecting the anterior wall; and type V (indented): indentation of the centre of the anterior wall with fracture line.

Types I, II and III have a worse prognosis and are associated with higher incidence of late vertebral collapse, while types IV and V have a better prognosis. The former group frequently show an intravertebral cleft that can be detected in radiographs as an intravertebral vacuum phenomenon. This observation has been partially supported by the work of Ha et al.,[31] who developed a simplified classification of OVFs with two groups: end plate or midportion types. In the endplate type fracture, cortical disruption of the VB is located at the endplate area or the anterior cortex adjacent to the endplate with confined signal changes on MRI around the endplate. In the mid-portion type, cortical disruptions of the VB and signal changes on MRI occur around the mid-portion of the vertebra. The authors noted that mid-portion type fractures and injury to the posterior vertebral wall are relative risk factors for progressive collapse following the acute fracture event.

The main advantage of qualitative methods is that they allow the diagnosis of OVF without significant loss of vertebral height. In addition, prospective studies with large sample sizes have recently demonstrated an inverse correlation between OVFs diagnosed with qualitative methods and BMD, which is significantly higher compared to that of morphometric methods.[32] The main limitation of qualitative methods lies in the need for qualified observers who can discern among the possible causes of an abnormal VE morphology.[32] Furthermore, in cases of old fractures, remodelling of the VE over time can make discontinuities or depression of the VE unidentifiable, resulting in an increased number of false negatives.[27]

Combined methods

Combined methods are based on both the description of the vertebral morphology and the quantification of height or surface loss. Although several classification systems have been reported, those proposed by Genant et al.,[33] and the German Society for Orthopaedics and Trauma (DGOU)[20] will be described because of their interest and applicability.

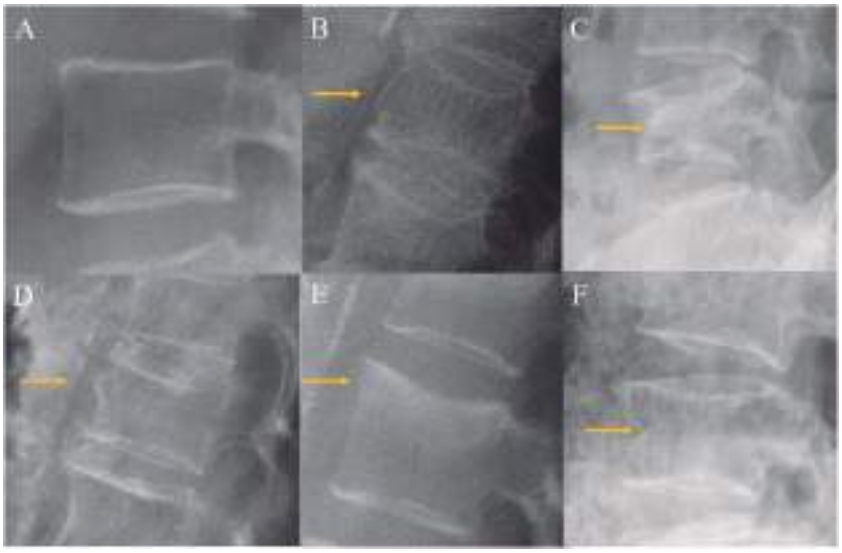

Fig. 2. Examples of OVF (osteoporotic vertebral fracture) according to the classification proposed by Sugita et al.[31]. (A) Normal vertebra. (B) Type I (swelled-front fracture). C) Type II (bow-shaped fracture). (D) Type III (projecting fracture). (E) Type IV (concave fracture). (F) Type V (indented fracture).

Classification of osteoporotic vertebral fractures proposed by Genant et al.

This is one of the most widely used systems for the diagnosis of OVFs based on conventional radiography in epidemiological studies.[34] It is based on the determination of vertebral height or surface loss (degrees 0–3) and the morphology of the vertebra, depending on the vertebral body height affected (anterior, middle or posterior). The estimation of height loss is based on visual assessment instead of direct measurements of the VB. The observer must then compare the actual vertebral height with the theoretical height that the vertebra should have, which requires previous experience.[14,27] In fact, the inter-observer agreement for osteoporotic vertebral deformity according to Genant's grading system may show disparities.[34]

Depending on the percentage of height and/or surface loss, the following degrees of deformity are established: grade 0 or normal vertebra (height loss < 20% and surface loss < 10%); grade 0.5 or borderline deformity (height loss 15–20%); grade 1 or mild deformity (height loss 20–25% and surface loss 10–20%); grade 2 or moderate deformity (height loss 25–40% and surface loss 20–40%) and grade 3 or severe deformity (height and surface loss > 40%).

Depending on the morphology of the vertebra, the following OVF types are distinguished: wedge fracture (involvement of the anterior wall); biconcave fracture (involvement of the middle wall; and crush fracture (involvement of the posterior wall).

Other morphological changes such as VE deformities or disruption of the cortical outline must be considered as defining criteria for OVF. Recently, Wang et al.,[35] emphasized the importance of recognising the presence of endplate and/or cortex fracture (ECF), and proposed an expanded semi-quantitative (eSQ) OVF classification into six degrees for a more accurate reporting in follow-up research studies. Accordingly, the eSQ considers Genant's borderline deformity as grade I or minimal. This grade may be important when there is associated ECF. Genant's grade I deformity is equivalent to eSQ mild grade (grade 2); Genant's moderate grade (grade 2) is subdivided into eSQ grade 3 OVF (moderate, >25%–<1/3 height loss) and eSQ grade 4 OVF (moderately-severe, >1/3–<40% height loss). The rationale for this division is that OVFs with >1/3 height loss are always associated with positive ECF sign radiographically,[36] and that the presence of ECF is associated with further vertebral collapse and risk of new fractures.[37] Finally, Genant's severe grade 3 is subdivided into eSQ grade 5 (severe, >40%–<2/3 height loss) and eSQ grade 6 (collapsed, >2/3 height loss) (Fig. 3). Nevertheless, for daily clinical practice, Wang also proposed to simplify Genant's classification into three categories: <1/5 vertebral height loss, 1/5–1/3 vertebral height loss and >1/3 vertebral height loss. OVFs of >1/3 of height loss are always associated with ECF.[38,39]

In general, combined methods can be easily applied in clinical practice and research, showing excellent inter-observer agreement.[14] In addition, the spinal deformity index proposed by Minne et al.,[40] which is obtained by adding up the degrees of the fractures present in the T4-L4 segment, has demonstrated prognostic value in estimating the severity of OVFs using the Genant's method.[33] One of the main advantages of the latter system over qualitative methods lies in the possibility of grading fractures by quantifying height loss, which allows a more accurate estimation of the patient's prognosis.

The Genant's classification is insufficiently sensitive to detect OVFs that do not exceed 15–20% height loss (false negatives). In addition, slight vertebral height loss can be secondary to alterations other than osteoporosis (e.g. developmental abnormalities, normal aging, postural changes) especially in men (false positives).[1,6] On the other hand, the correlation between Genant's grade I deformities and the development of OVFs is low.[41] In comparison with Sugita's classification, it is more focused on the degree of vertebral height loss. Conversely, Sugita's classification focuses on the shape of vertebral deformity, although it does not consider the involvement of the posterior wall.

Classification of osteoporotic vertebral fracture proposed by the Spine Section of the German Society for Orthopaedics and Trauma (DGOU)

This classification aims to be a reliable and simple approach to be implemented in daily clinical practice, facilitating decision-making on the most appropriate treatment for vertebral fractures.[20,42] This classification considers both the morphological pattern and the biomechanical stability of the fracture. It is not exclusively based on radiography, but also on CT and MRI. This system divides vertebral fractures into the following types (Fig. 4): type 1: no vertebral deformity, exclusively oedema in the VB (detected by MRI); type 2: deformity without or with < 1/5 involvement of the posterior ver-

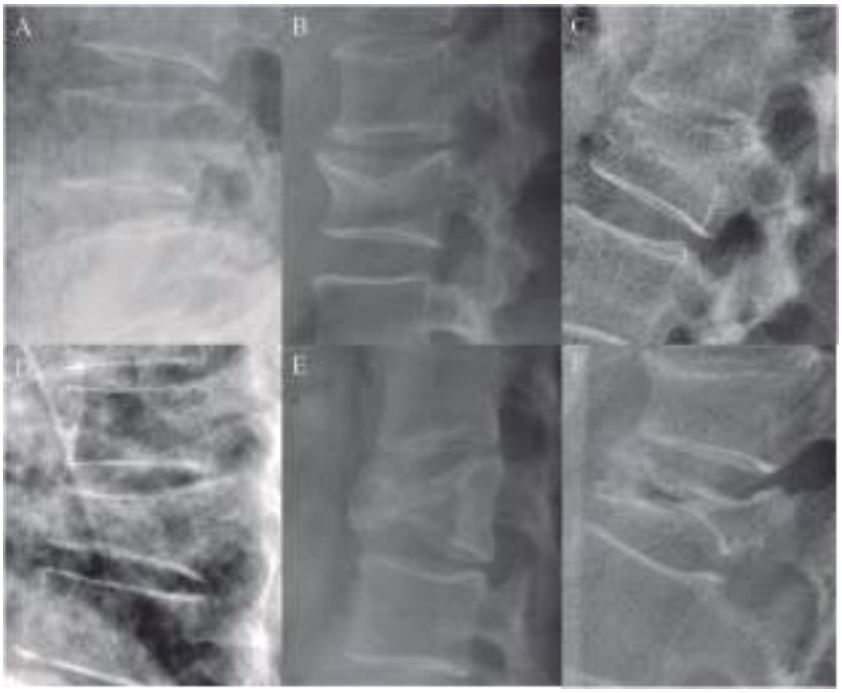

Fig. 3. Examples of expanded semi-quantitative (eSQ) OVF (osteoporotic vertebral fracture) classification by Wang et al.[35] (A) Grade I, minimal; (B) Grade II, mild; (C) Grade III, moderate; (D) Grade IV, moderate-severe; (E) Grade V, severe; (F) Grade VI, collapsed.

tebral wall; type 3: deformity with involvement of the posterior vertebral wall; type 4: loss of integrity of the VB, collapse of the VB or "pincer" type fracture; and type 5: injuries with rotation or distraction.

The main advantage of this classification lies in its simplicity, which facilitates its use in daily clinical practice. In addition, it includes recommendations on the appropriate treatment for each type of fracture (i.e., conservative vs. surgical). Regarding the limitations of this classification, no proper validation has been performed so far and, as stated above, a major drawback for non-radiologists is the need for an MRI exam to diagnose type 1 fractures. Furthermore, it does not take into consideration that height loss or deformities can be secondary to causes other than fractures.

Compared to the classification by Ha et al.,[31] the DGOU's system (similarly to that proposed by Wang et al.[35]) is relatively complex. Therefore, further research is still required to develop a

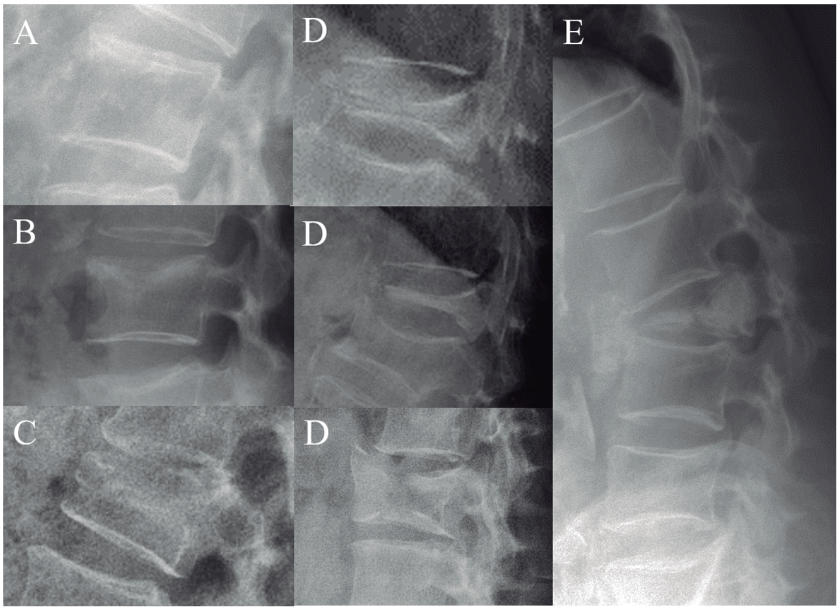

Fig. 4. Examples of OVFs (osteoporotic vertebral fractures) according to the DGOU's classification: (A) Type 1. (B) Type 2. (C) Type 3. (D) Types 4. (E) Type 5. Adapted from Schnake KJ et al.[20]

Table 1
Summary of the main classification methods for the diagnosis of osteoporotic vertebral fractures (OVF).

	Quantitative methods	Qualitative methods	Combined methods
Main characteristics	Measurement of height or surface without assessment of vertebral morphology	Exclusion of VE abnormalities caused by conditions other than OVF	Estimation of height loss combined with vertebral morphology
Advantages	Reproducibility (healthy subjects), Objective, Automatization	Excludes potential confounders (anatomical variants, other conditions). Better correlation with BMI and incidence of new OVFs.	Traditionally considered the best method due to its simplicity. High inter and intra-observer agreement.
Limitations	False positives (height loss due to non-fracture causes), False negatives (OVF without height loss)	Need for highly-trained or expert observers	Confusion with anatomical variants and other conditions. It requires training and experience
Applicability	Automated diagnosis, research	Daily clinical practice	Daily clinical practice, research
Examples	Eastell et al.,[25] McCloskey et al.[26]	Jiang et al.,[23] Sugita et al.[30]	Genant et al.,[33] DGOU[20]

VE: vertebral endplate; BMI: bone mass index.

classification that optimizes both simplicity and clinical efficiency, with relevant clues that ensure the most appropriate management and prognosis for OVFs.

A summary of the main classification methods for the diagnosis of osteoporotic vertebral fractures (OVF) is shown in Table 1.

Imaging findings that can be mistaken for osteoporotic vertebral fractures

There are several causes other than OVF that can lead to reduced vertebral height and they should be known to avoid diagnostic errors. The most relevant ones[14,43] are described below with some illustrative examples shown in Fig. 5.

- **Physiological wedging**: In normal children and adults, the VB is anteriorly wedged from T1 through L2 (peak at T7), non-wedged at L3, and posteriorly wedged at L4–L5 (peak at L5). In physiologic vertebral wedging thoracic kyphosis values are within the normal range and Schmorl's nodes are absent.[44]
- **Short vertebral height**: term introduced by Jiang et al.,[23] to explain the low percentage of fractures found when applying the ABQ method in comparison with morphometric methods. It consists of abnormal morphometric measurements, i.e. reduced vertebral height, without alterations of the VE.[45] Up to 20% of height loss can be normal with aging, but it may be difficult to differentiate it from mild vertebral fractures.
- **Cupid's bow deformity**: This is a developmental variant characterised by a focal defect of the parasagittal cartilage of the VE, normally affecting the lower endplate of L4 and L5.[46] In the lateral projection it is observed as an indentation of the posterior region of the lower endplate, simulating a VE depression fracture.[14]
- **Scheuermann's disease**: This is a rare disease which predominantly affects young males. It is characterised by alterations of the thoracolumbar spine coexisting with a height reduction of the intervertebral space and increased AP diameter. The most frequently used diagnostic criterion in clinical practice is the presence of a kyphotic angulation of at least 5° in three or more adjacent VBs.[47]

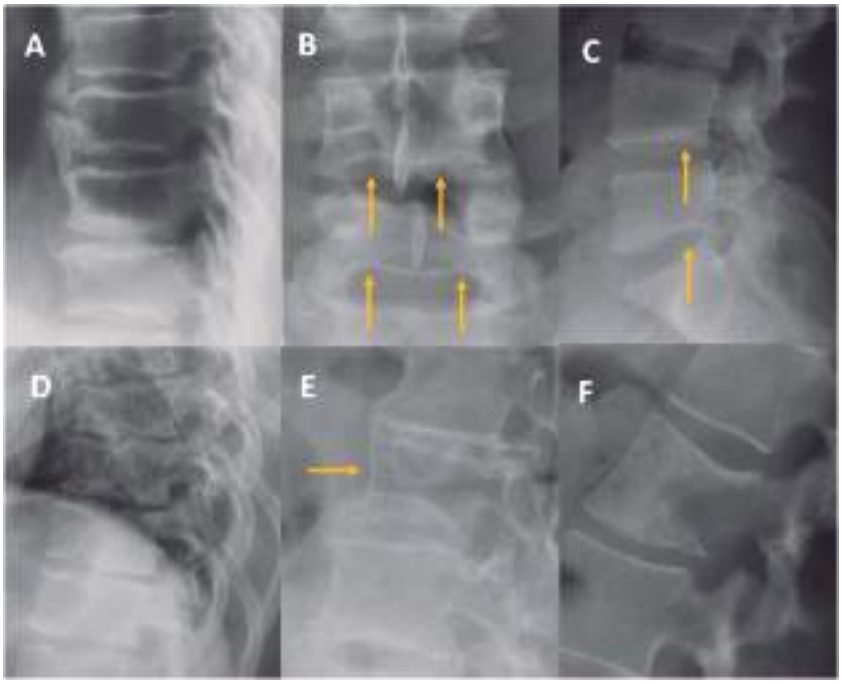

Fig. 5. Examples of non-osteoporotic vertebral height loss (A) Short vertebral height. (B and C) Cupid's bow deformity which causes indentation of the vertebral endplate in the lateral projection (arrows). (D) Scheuermann's disease. (E) Wedging and sclerosis in degenerative scoliosis. (F) Pathologic fracture in osteolytic metastasis.

- **Schmorl's nodes or intraspongeal disc herniations:** These represent a common finding, especially in patients with a degenerative spine, such as those with Scheuermann's disease. Schmorl's nodes are focal depressions of the VE due to weakness of the intervertebral disc, usually by degenerative phenomena. Although usually small in size, they are sometimes larger and can simulate OVFs. In these cases, it should be remembered that Schmorl's nodes have well-defined, rounded, sclerotic contours and do not extend through the entire endplate.[14]
- **Degenerative scoliosis**: Due to the rotational effect of scoliosis on the VBs, these may acquire a biconcave appearance and be misinterpreted as an OVF. The AP projection allows to verify the presence of scoliosis, specifically the incurvation of the spinal axis and the decrease in size of the VBs in the concavity of the curve in comparison with the convexity.
- **Pathological vertebral fracture:** Most of the literature aimed at differentiating benign osteoporotic from pathological vertebral fractures secondary to metastases or primary tumours is based on MRI findings. Nevertheless, although less sensitive, there are several plain radiograph signs that may orientate in this challenging differential diagnosis. As stated above, OVFs usually present 3 morphologic patterns, namely wedge, concave (fish vertebra or diabolo-shaped vertebra) and, in advanced cases, crush. Involvement of the posterior vertebral wall in crush fractures appears as retropulsion of the posterior margin, either superior or inferior, of the vertebral body (VB). The presence of gas collections within the latter is considered a sign of vertebral necrosis and/or intravertebral instability and suggests benign osteoporotic fracture.[48,49]

In pathological fractures, the osteolytic pattern in the VB can be detected, although 30–50% of bone loss is usually required for this pattern to be visible on plain-film radiography.[50,51] Expansion of the cortex due to tumour growth inside the fractured body manifests as a convex wall while extension of the tumour to the paravertebral space can be detected as a paravertebral mass. Finally, unilateral destruction of the pedicle is usually responsible for the "winking owl" or "one-eyed vertebra" sign. Occasionally, destruction of both pedicles may lead to the "blind vertebra sign" in which there is no rounded shape of any of the pedicles in the AP view.[52]

Conclusions

We have reviewed the three main different approaches for classifying OVFs using conventional radiography. Quantitative or morphometric methods offer high reproducibility and objectivity but have low sensitivity for the detection of fractures characterised by subtle morphological alterations in which there is no significant vertebral height loss. Qualitative methods offer greater sensitivity for the diagnosis of OVFs that do not have significant vertebral height loss, but they require highly trained observers capable of discriminating the specific and sometimes very subtle imaging findings. Combined methods consider both loss of vertebral height or surface and vertebral morphology. The most suitable approach depends on context, familiarity and ease of use for the reader. Finally, it is important to acknowledge the most frequent non-fracture causes for vertebral abnormalities that can be mistaken for vertebral fractures on conventional radiography.

Conflict of interest

Nothing to declare.

References

1. Wáng YXJ, Santiago FR, Deng M, Nogueira-Barbosa MH. Identifying osteoporotic vertebral endplate and cortex fractures. Quant Imaging Med Surg. 2017;7:555–91.
2. Cosman F, de Beur SJ, LeBoff MS, Lewiecki EM, Tanner B, Randall S, et al. Clinician's guide to prevention and treatment of osteoporosis. Osteoporos Int. 2014;25:2359–81.
3. Hernlund E, Svedbom A, Ivergård M, Compston J, Cooper C, Stenmark J, et al. Osteoporosis in the European Union: medical management, epidemiology and economic burden. Arch Osteoporos. 2013;8:136.
4. Williams AL, Al-Busaidi A, Sparrow PJ, Adams JE, Whitehouse RW. Under-reporting of osteoporotic vertebral fractures on computed tomography. Eur J Radiol. 2009;69:179–83.
5. Ross PD. Clinical consequences of vertebral fractures. Am J Med. 1997;103:S30–43.
6. Lentle B, Trollip J, Lian K. The radiology of osteoporotic vertebral fractures redux. J Clin Densitom. 2016;19:40–7.
7. Kanis JA, Oden A, Johnell O, De Laet C, Jonsson B. Excess mortality after hospitalisation for vertebral fracture. Osteoporos Int. 2004;15:108–12.
8. Cooper C, Atkinson EJ, Jacobsen SJ, O'fallon WM, Melton LJ. Population-based study of survival after osteoporotic fractures. Am J Epidemiol. 1993;137:1001–5.
9. Lentle BC, Hammond I, Firth GB, Sutton RAL. Imaging of osteoporotic fractures on XR CT, and MR. Curr Radiol Rep. 2014;2:32.
10. Li Y, Yan L, Cai S, Wang P, Zhuang H, Yu H. The prevalence and underdiagnosis of vertebral fractures on chest radiograph. BMC Musculoskelet Disord. 2018;19:235.
11. Delmas PD, van de Langerijt L, Watts NB, Eastell R, Genant H, Grauer A, et al. Underdiagnosis of vertebral fractures is a worldwide problem: the IMPACT study. J Bone Miner Res. 2004;20:557–63.
12. Genant HK, Delmas PD, Chen P, Jiang Y, Eriksen EF, Dalsky GP, et al. Severity of vertebral fracture reflects deterioration of bone microarchitecture. Osteoporos Int. 2007;18:69–76.
13. Damilakis J, Adams JE, Guglielmi G, Link TM. Radiation exposure in X-ray-based imaging techniques used in osteoporosis. Eur Radiol. 2010;20:2707–14.
14. Griffith JF. Identifying osteoporotic vertebral fracture. Quant Imaging Med Surg. 2015;5:592–602.
15. Gruber M, Dinges J, Müller D, Baum T, Rummeny E, Bauer J. Impact of specific training in detecting osteoporotic vertebral fractures on routine chest radiographs. RöFo – Fortschritte auf dem Gebiet der Röntgenstrahlen und der Bildgeb Verfahren. 2013;185:1074–80.
16. Rajasekaran S, Kanna RM, Schnake KJ, Vaccaro AR, Schroeder GD, Sadiqi S, et al. Osteoporotic thoracolumbar fractures—how are they different?—Classification and treatment algorithm. J Orthop Trauma. 2017;31:S49–56.
17. Almén A, Tingberg A, Besjakov J, Mattsson S. The use of reference image criteria in X-ray diagnostics: an application for the optimisation of lumbar spine radiographs. Eur Radiol. 2004:14, http://dx.doi.org/10.1007/s00330-004-2320-6.
18. Oei L, Rivadeneira F, Ly F, Breda SJ, Zillikens MC, Hofman A, et al. Review of radiological scoring methods of osteoporotic vertebral fractures for clinical and research settings. Eur Radiol. 2013;23:476–86.
19. Wáng YXJ, Du MM, Che-Nordin N, Ye PP, Qiu SW, Griffith JF, et al. Recognizing osteoporotic vertebral deformity on frontal view radiograph: a cohort analysis and a pictorial review. Arch Osteoporos. 2020:15, http://dx.doi.org/10.1007/s11657-020-00716-5.
20. Schnake KJ, Blattert TR, Hahn P, Franck A, Hartmann F, Ullrich B, et al. Classification of osteoporotic thoracolumbar spine fractures: recommendations of the spine section of the German Society for Orthopaedics and Trauma (DGOU). Glob Spine J. 2018;8:46S–9S.
21. Link TM, Guglielmi G, van Kuijk C, Adams JE. Radiologic assessment of osteoporotic vertebral fractures: diagnostic and prognostic implications. Eur Radiol. 2005;15:1521–32.
22. Wáng YXJ, Deng M, He L-C, Che-Nordin N, Santiago FR. Osteoporotic vertebral endplate and cortex fractures: a pictorial review. J Orthop Transl. 2018;15:35–49.
23. Jiang G, Eastell R, Barrington NA, Ferrar L. Comparison of methods for the visual identification of prevalent vertebral fracture in osteoporosis. Osteoporos Int. 2004;15:887–96.
24. Grados F, Fechtenbaum J, Flipon E, Kolta S, Roux C, Fardellone P. Radiographic methods for evaluating osteoporotic vertebral fractures. Jt Bone Spine. 2009;76:241–7.
25. Eastell R, Cedel SL, Wahner HW, Riggs BL, Melton LJ. Classification of vertebral fractures. J Bone Miner Res. 1991;6:207–15.
26. McCloskey EV, Spector TD, Eyres KS, Fern ED, O'Rourke N, Vasikaran S, et al. The assessment of vertebral deformity: a method for use in population studies and clinical trials. Osteoporos Int. 1993;3:138–47.
27. Szulc P. Vertebral fracture: diagnostic difficulties of a major medical problem. J Bone Miner Res. 2018;33:553–9.
28. McKiernan FE. The broadening spectrum of osteoporotic vertebral fracture. Skeletal Radiol. 2009;38:303–8.
29. Lentle B, Cheung AM, Hanley DA, Leslie WD, Lyons D, Papaioannou A, et al. Osteoporosis Canada 2010 guidelines for the assessment of fracture risk. Can Assoc Radiol J. 2011;62:243–50.
30. Sugita M, Watanabe N, Mikami Y, Hase H, Kubo T. Classification of vertebral compression fractures in the osteoporotic spine. J Spinal Disord Tech. 2005;18:376–81, http://dx.doi.org/10.1097/01.bsd.0000168716.23440.61.

31. Ha KY, Kim YH. Risk factors affecting progressive collapse of acute osteoporotic spinal fractures. Osteoporos Int. 2013;24:1207–13.
32. Lentle B, Koromani F, Brown JP, Oei L, Ward L, Goltzman D, et al. The radiology of osteoporotic vertebral fractures revisited. J Bone Miner Res. 2019;34:e3669.
33. Genant HK, Wu CY, van Kuijk C, Nevitt MC. Vertebral fracture assessment using a semiquantitative technique. J Bone Miner Res. 1993;8:1137–48.
34. Fechtenbaum J, Briot K, Paternotte S, Audran M, Breuil V, Cortet B, et al. Difficulties in the diagnosis of vertebral fracture in men: agreement between doctors. Jt Bone Spine. 2014;81:169–74.
35. Wáng YXJ, Diacinti D, Yu W, Cheng X-G, Nogueira-Barbosa MH, Che-Nordin N, et al. Semi-quantitative grading and extended semi-quantitative grading for osteoporotic vertebral deformity: a radiographic image database for education and calibration. Ann Transl Med. 2020;8, 398-398.
36. Deng M, Kwok TCY, Leung JCS, Leung PC, Wáng YXJ. All osteoporotically deformed vertebrae with > 34% height loss have radiographically identifiable endplate/cortex fracture. J Orthop Transl. 2018;14:63–6.
37. Wáng YXJ, Che-Nordin N, Deng M, Leung JCS, Kwok AWL, He LC, et al. Osteoporotic vertebral deformity with endplate/cortex fracture is associated with higher further vertebral fracture risk: the Ms OS (Hong Kong) study results. Osteoporos Int. 2019;30:897–905.
38. Wáng YXJ. A modified semi-quantitative (mSQ) grading scheme for osteoporotic vertebral fracture in elderly women. Quant Imaging Med Surg. 2019;9:146–50.
39. Ruiz Santiago F, Láinez Ramos-Bossini AJ, Wáng YXJ, López Zúñiga D. The role of radiography in the study of spinal disorders. Quant Imaging Med Surg. 2020;10:2322–55.
40. Minne HW, Leidig G, Wüster C, Siromachkostov L, Baldauf G, Bickel R, et al. A newly developed spine deformity index (SDI) to quantitate vertebral crush fractures in patients with osteoporosis. Bone Miner. 1988;3:335–49.
41. Johansson H, Odén A, McCloskey EV, Kanis JA. Mild morphometric vertebral fractures predict vertebral fractures but not non-vertebral fractures. Osteoporos Int. 2014;25:235–41.
42. Blattert TR, Schnake KJ, Gonschorek O, Gercek E, Hartmann F, Katscher S, et al. Nonsurgical and surgical management of osteoporotic vertebral body fractures: recommendations of the spine Section of the German Society for Orthopaedics and Trauma (DGOU). Glob Spine J. 2018;8:50S–5S.
43. Ruiz Santiago F, Tomás Muñoz P, Moya Sánchez E, Revelles Paniza M, Martínez Martínez A, Pérez Abela AL. Classifying thoracolumbar fractures: role of quantitative imaging. Quant Imaging Med Surg. 2016;6:772–84.
44. Masharawi Y, Salame K, Mirovsky Y, Peleg S, Dar G, Steinberg N, et al. Vertebral body shape variation in the thoracic and lumbar spine: Characterization of its asymmetry and wedging. Clin Anat. 2008;21:46–54.
45. Ferrar L, Jiang G, Armbrecht G, Reid DM, Roux C, Glüer CC, et al. Is short vertebral height always an osteoporotic fracture? The Osteoporosis and Ultrasound Study (OPUS). Bone. 2007;41:5–12.
46. Chan KK, Sartoris DJ, Haghighi P, Sledge P, Barrett-Connor E, Trudell DT, et al. Cupid's bow contour of the vertebral body: Evaluation of pathogenesis with bone densitometry and imaging-histopathologic correlation. Radiology. 1997;202:253–6.
47. Bezalel T, Carmeli E, Been E, Kalichman L. Scheuermann's disease: current diagnosis and treatment approach. J Back Musculoskelet Rehabil. 2014;27:383–90.
48. Cho JH, Shin SI, Lee JH, Yeom JS, Chang BS, Lee CK. Usefulness of prone crosstable lateral radiographs in vertebral compression fractures. Clin Orthop Surg. 2013;5:195–201.
49. Ruiz Santiago F, Guzmán Alvarez L, Tello Moreno M, Navarrete González PJ. Plain-film radiography in the study of spinal pain. Radiologia. 2010;52:126–37.
50. Kamholtz R, Sze G. Current imaging in spinal metastatic disease. Semin Oncol. 1991;18:158–9.
51. Jacobson AF, Stomper PC, Cronin EB, Kaplan WD. Bone scans with one or two new abnormalities in cancer patients with no known metastases: reliability of interpretation of initial correlative radiographs. Radiology. 1990;174:503–7.
52. Jacobs WB, Perrin RG. Evaluation and treatment of spinal metastases: an overview. Neurosurg Focus. 2001;11:e10.

TRABAJO 4: IMAGING OF LOW-ENERGY VERTEBRAL FRACTURES (DIAGNÓSTICO POR IMAGEN DE LAS FRACTURAS VERTEBRALES DE BAJA ENERGÍA).

Láinez Ramos-Bossini AJ, Ruiz Santiago F, Moraleda Cabrera B, López Zúñiga D, Ariza Sánchez A. Imaging of low-energy vertebral fractures. Radiologia (Engl Ed). 2023;65(3):239-250. doi: 10.1016/j.rxeng.2023.01.006. Epub 2023 May 11. PMID: 37268366. FI: 1,3 (cuartil no asignado, primer año con FI).

Se trata de una revisión pictórica que cubre el objetivo 2 y la parte correspondiente a la radiografía simple del objetivo 1.

Radiología 65 (2023) 239–250

RADIOLOGÍA

www.elsevier.es/rx

ACTUALIZACIÓN

Diagnóstico por imagen de las fracturas vertebrales de baja energía

A.J. Láinez Ramos-Bossini[a,b,c,d], **F. Ruiz Santiago**[a,b,e,*], **B. Moraleda Cabrera**[a,b], **D. López Zúñiga**[a,b] y **A. Ariza Sánchez**[a,b]

[a] *Sección de Radiología Musculoesquelética, Servicio de Radiodiagnóstico, Hospital Universitario Virgen de las Nieves, Granada, España*
[b] *Instituto Biosanitario de Granada (ibs.GRANADA), Granada, España*
[c] *Programa de doctorado en Medicina Clínica y Salud Pública, Universidad de Granada, Granada, España*
[d] *Departamento de Psiquiatría, Facultad de Medicina, Universidad de Granada, Granada, España*
[e] *Departamento de Medicina Física y Rehabilitación, Facultad de Medicina, Universidad de Granada, Granada, España*

Recibido el 6 de octubre de 2022; aceptado el 1 de enero de 2023
Disponible en Internet el 10 de febrero de 2023

PALABRAS CLAVE
Cuerpo vertebral;
Fractura por compresión;
Osteoporosis;
Radiología convencional;
Diagnóstico radiológico;
Tomografía computarizada;
Resonancia magnética;
Difusión;
Valor ADC

Resumen Las fracturas vertebrales de baja energía suponen un reto diagnóstico para el radiólogo debido a su naturaleza, frecuentemente inadvertida, y a su semiología en imagen, a menudo sutil. Sin embargo, el diagnóstico de este tipo de fracturas puede resultar determinante, no solo por permitir realizar un tratamiento dirigido que evite complicaciones, sino también por la posibilidad de diagnosticar patologías sistémicas como la osteoporosis o la enfermedad metastásica. El tratamiento farmacológico en el primer caso ha demostrado evitar el desarrollo de otras fracturas y complicaciones, mientras que los tratamientos percutáneos y las diversas terapias oncológicas pueden ser una alternativa en el segundo caso. Por lo tanto, es preciso conocer la epidemiología y los hallazgos por imagen de este tipo de fracturas. El objetivo de este trabajo es revisar el diagnóstico por imagen de las fracturas de baja energía, con especial énfasis en las características que deben reseñarse en el informe radiológico para orientar a un diagnóstico específico que favorezca y optimice el tratamiento de los pacientes que padecen este tipo de fracturas.

* Autor para correspondencia.
Correo electrónico: ferusan12@gmail.com (F. Ruiz Santiago).

https://doi.org/10.1016/j.rx.2023.01.003

KEYWORDS
Vertebral body;
Compression fracture;
Osteoporosis;
Conventional radiography;
Radiological diagnosis;
Computed tomography;
Magnetic resonance imaging;
Diffusion weighted;
ADC value

Imaging of low-energy vertebral fractures

Abstract Low-energy vertebral fractures pose a diagnostic challenge for the radiologist due to their often-inadvertent nature and often subtle imaging semiology. However, the diagnosis of this type of fractures can be decisive, not only because it allows targeted treatment to prevent complications, but also because of the possibility of diagnosing systemic pathologies such as osteoporosis or metastatic disease. Pharmacological treatment in the first case has been shown to prevent the development of other fractures and complications, while percutaneous treatments and various oncological therapies can be an alternative in the second case. Therefore, it is necessary to know the epidemiology and typical imaging findings of this type of fractures. The objective of this work is to review the imaging diagnosis of low-energy fractures, with special emphasis on the characteristics that should be outlined in the radiological report to guide a specific diagnosis that favours and optimizes the treatment of patients suffering of low energy fractures.

Introducción

Las fracturas vertebrales secundarias a traumatismos de baja energía (FVBE) se definen como aquellas que tienen lugar sin un antecedente traumático conocido o son secundarias a caídas desde la propia altura del paciente. Las FVBE conllevan una significativa morbimortalidad que se incrementa de forma notable con la edad, representando una proporción elevada de los pacientes hospitalizados por traumatismo[1,2]. Con frecuencia, las FVBE ocurren en el contexto de una pérdida de la masa y de la arquitectura ósea normales (osteoporosis). La osteoporosis es la enfermad metabólica más común y afecta a más de 200 millones de personas en el mundo, estimándose que del 30 al 50% de las mujeres y del 20 al 30% de los hombres tendrán fracturas vertebrales por esta causa[3]. Estas fracturas pueden ser relativamente asintomáticas y detectarse en estudios radiológicos como hallazgo incidental. En otros casos pueden presentarse con dolor localizado después de una actividad cotidiana (levantarse, toser, etc.) o tras una caída desde la propia altura. Otra causa importante son las fracturas patológicas secundarias a tumores primarios o a metástasis. No obstante, se estima que hasta un tercio de las fracturas en pacientes oncológicos no son de causa tumoral, sino de causa osteoporótica[4]. De ahí la importancia de los métodos de imagen en su diagnóstico diferencial. En ambos casos, la semiología radiológica puede orientar adecuadamente el diagnóstico y la clasificación de las FVBE, condicionando un manejo óptimo del paciente[5]. Por lo tanto, es preciso conocer las características que permiten identificar y clasificar las FVBE en las distintas técnicas de imagen radiológicas, así como el papel de estas atendiendo al escenario clínico y al grado de sospecha.

El objetivo del presente trabajo es revisar los signos que permiten diagnosticar con diferentes técnicas de imagen las fracturas de baja energía de la columna vertebral y permiten diferenciar las fracturas por insuficiencia de las fracturas patológicas.

Diagnóstico por imagen de las FVBE

Desde el punto de vista radiológico, las FVBE pueden detectarse y cuantificarse mediante distintas modalidades de imagen. Las más relevantes en la práctica clínica son la absorciometría con rayos X de doble energía (DXA), la radiografía simple, la tomografía computarizada (TC) y la resonancia magnética (RM). En la tabla 1 se describen las indicaciones y las principales ventajas y limitaciones de cada técnica.

Radiografía simple

La radiografía simple es la primera técnica de elección para el diagnóstico de FVBE[6]. Sin embargo, su rendimiento diagnóstico es limitado. En el caso de las FVBE torácicas, los valores de sensibilidad en la detección de las fracturas oscilan entre el 40,0[7] y el 49,2%[8], mientras que para las FVBE lumbares se ha estimado en torno al 57,8%[5]. En este sentido, es necesario recordar que los signos radiográficos de una FBVE pueden ser sutiles, y que los cambios morfológicos que identificamos en la radiografía pueden necesitar tiempo para desarrollarse. Por estos motivos, el hecho de no identificar con claridad signos de fractura vertebral mediante radiografía simple no excluye su presencia, siendo recomendable complementar el estudio con técnicas más sensibles en el caso de pacientes osteoporóticos con alta sospecha clínica[9]. Son muchos los métodos que se utilizan para clasificar y cuantificar la severidad de las fracturas osteoporóticas[10], incluyendo métodos cuantitativos como los propuestos por Eastell et al.[11] o McCloskey et al.[12], cualitativos como el abordaje basado en algoritmo de Jiang et al.[13] o el método de Sugita et al.[14], o combinados o semicuantitativos, como los de Genant et al.[15], Wáng et al.[16], o el de la *German Society for Orthopaedics and Trauma* (DGOU)[17]. Sus ventajas e inconvenientes se han descrito en trabajos previos[10,18], pero básicamente los métodos cuantitativos son los más objetivos al basarse en la

Radiología 65 (2023) 239–250

Tabla 1 Indicaciones, ventajas y limitaciones de las diferentes técnicas de imagen utilizadas en la evaluación de fracturas vertebrales de baja energía

	Indicación	Ventajas	Limitaciones
Absorciometría con rayos X de doble energía	Cribado de fractura vertebral subclínica	Mínima radiación, rapidez	Baja resolución espacial, baja accesibilidad
Radiografía simple	Evaluación inicial en urgencias	Rapidez, accesibilidad, escasa radiación	Baja resolución espacial Radiación ionizante
Tomografía computarizada	Fractura vertebral no caracterizable en RX Sospecha de fractura vertebral no visible en RX	Rapidez, alta resolución espacial	Radiación ionizante
Resonancia magnética	Fractura vertebral oculta	Alta resolución tisular, ausencia de radiación ionizante	Lentitud

Figura 1 Ejemplos de fractura vertebral según su patrón morfológico en radiografía simple. A) Fractura con deformidad en cuña anterior. B) Fractura con deformidad bicóncava, de pez o en diábolo. C) Fractura con deformidad en estallido. Nótese la retropulsión del margen posterosuperior de la vértebra (flecha).

medición de la altura vertebral, que puede hacerse manual o automáticamente, aunque pueden tener falsos positivos al diagnosticar como fracturas pérdidas de altura secundarias a otras causas y falsos negativos en fracturas sin pérdida de altura. Con respecto a los métodos cualitativos, el método ABQ *(algorithm-based qualitative method)* requiere evaluadores expertos para identificar las fracturas y diferenciarlas de deformidades vertebrales secundarias a otras causas (alteraciones del desarrollo, enfermedad de Scheuermann, escoliosis, etc.). Por último, los métodos semicuantitativos se usan en estudios epidemiológicos, por ejemplo el de Genant et al., pero también tienen aplicaciones en la práctica diaria para decidir el tipo de tratamiento, como el DGOU.

En cualquiera de los casos, los patrones morfológicos más frecuentes de las fracturas osteoporóticas son la deformidad en cuña anterior o posterior (esta última muy infrecuente), cóncava o bicóncava (en vértebra de pez o diábolo) y en estallido (fig. 1). En el caso de las fracturas en estallido puede existir retropulsión del margen posterosuperior o posteroinferior de la vértebra como signo que refuerza el diagnóstico de fractura no tumoral. La presencia de fenómenos de vacío intravertebral también se encuentra asociada con mayor frecuencia a fracturas no tumorales y se considera un signo de necrosis, falta de consolidación de las trabéculas óseas o inestabilidad intravertebral[19,20].

En el caso de sospecha de fractura patológica secundaria a neoplasia, la radiografía simple suele ser poco sensible a la destrucción o infiltración medular, requiriendo entre el 30 y el 50% de destrucción ósea para ser detectada[21,22]. La expansión del córtex vertebral debido al crecimiento del tumor dentro del cuerpo fracturado se manifiesta como una convexidad de las paredes vertebrales, mientras que la extensión del tumor al espacio paravertebral se puede detectar como una masa paravertebral. La osteólisis puede ser también evidente como destrucción de las paredes vertebrales y, cuando afecta al pedículo o pedículos, puede manifestarse con el signo de la vértebra tuerta o ciega, respectivamente[23] (fig. 2). Del mismo modo, en el mieloma múltiple las fracturas y deformidades óseas pueden simular fracturas secundarias a osteoporosis, tanto en su morfología como en su localización. Estas fracturas pueden presentarse en el 50 al 70% de los pacientes con mieloma múltiple[24,25]. La resorción ósea excesiva es responsable de la apariencia radiolúcida de los huesos. En la radiografía convencional pueden presentarse, por separado o en asociación, la osteopenia y las lesiones líticas (fig. 2).

Tomografía computarizada (TC)

La TC es la prueba de elección cuando los hallazgos en la radiografía simple son equívocos, aunque algunos autores hacen especial énfasis en la necesidad de generar evidencia de calidad sobre su conveniencia como técnica de primera elección, considerando las limitaciones de la radiografía simple[4]. Es importante reseñar que siempre debe realizarse radiografía previamente, pues la TC implica dosis de radiación entre 13 y 55 veces mayor que la radiografía simple, en función del segmento de columna evaluado[6-8]. A pesar de su mayor capacidad, frente a la radiología simple, para detectar las lesiones o las fracturas corticales, en los pacientes osteoporóticos las líneas de fractura pueden ser muy sutiles

Figura 2 Ejemplos de fractura vertebral metastásica en radiografía simple. A) Fractura vertebral metastásica (asterisco) que condiciona una deformidad en cuña posterior. B) Signo de la vértebra tuerta por lisis del pedículo derecho (flecha). C) Fractura metastásica con morfología «en estallido» en mieloma múltiple (flecha). Nótese la alteración difusa de la radiolucencia normal del cuerpo vertebral fracturado, así como de las vértebras adyacentes debido a la infiltración tumoral.

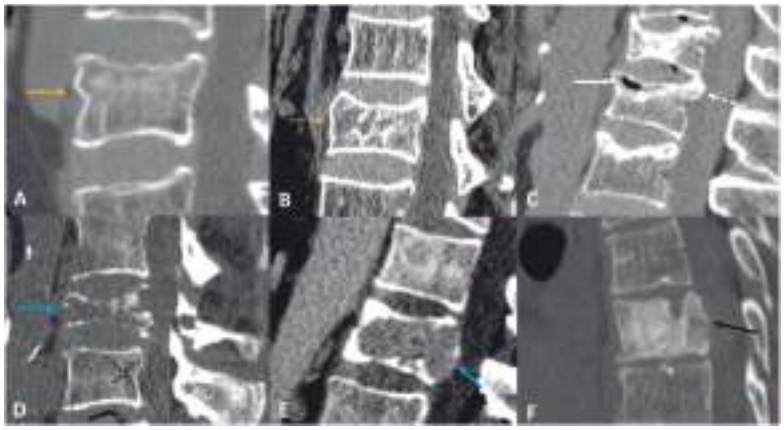

Figura 3 Ejemplos de fractura vertebral en tomografía computarizada. A) Fractura osteoporótica con abombamiento cortical anterior (flecha naranja). B) Fractura osteoporótica con discontinuidad cortical de la plataforma superior y quiste intravertebral (flecha naranja discontinua). C) Fractura osteoporótica con bandas de esclerosis y hendidura intravertebral con gas en su interior (fenómeno de vacío intrasomático, flecha blanca) y retropulsión del margen vertebral posterosuperior (flecha blanca discontinua). D) Fractura secundaria a metástasis lítica, con fenómenos de destrucción cortical y trabecular (flecha azul discontinua). E) Fractura patológica con lesión expansiva intrasomática que abomba la pared posterior (flecha azul). F) Fractura patológica en una metástasis osteoblástica.

y pasar desapercibidas para radiólogos poco expertos. Hay que prestar especial atención a las disrupciones corticales y al abombamiento o depresión de las plataformas o cortical de los cuerpos vertebrales. La compresión del hueso trabecular también puede dar lugar a imágenes lineales de aumento de densidad[26] (fig. 3).

La TC también permite identificar con más detalle que la radiografía simple los signos que se asocian a fracturas osteoporóticas, como el fenómeno de vacío intravertebral o la retropulsión de los márgenes vertebrales en el caso de fracturas en estallido. Igualmente, en el caso de fracturas patológicas, la TC es capaz de detectar con mayor sensibilidad las lesiones osteolíticas y las osteoblásticas, así como la convexidad de las paredes del cuerpo vertebral y la extensión a las partes blandas de la masa tumoral[27] (fig. 3).

Resonancia magnética (RM)

La RM es la técnica más sensible para detectar edema vertebral, signo que traduce una fractura aguda o inestable y puede evidenciarse aun en ausencia de los cambios morfológicos vertebrales descritos en los apartados previos[9]. Los hallazgos de imagen en relación con el edema vertebral son dinámicos en función de la cronología de la fractura. Así, las fracturas agudas osteoporóticas suelen mostrar un patrón de edema óseo en banda que recorre el trazo de fractura, muchas veces identificable, paralelo a las plataformas vertebrales y de localización subcondral, respetando la intensidad de señal del resto del cuerpo vertebral. El límite entre el hueso sano y el foco de edema por fractura suele ser regular y bien definido. Cuando la fractura se estabiliza, el edema suele desaparecer en un periodo inferior a tres semanas. Sin embargo, en el caso de fracturas inestables, el edema tiende a cronificarse y se suele asociar a cambios escleróticos y a alteraciones morfológicas del cuerpo vertebral, acuñamiento o pérdida de altura más marcados en bipedestación y reversibles en diferente grado en decúbito supino o prono. Por el contrario, la fractura crónica reparada se caracteriza por una recuperación de la intensidad de señal grasa normal del cuerpo vertebral, a pesar de que permanezca, también estable, la deformidad provocada por la fractura. La presencia de quistes de aire o de líquido en el interior del cuerpo vertebral suele indicar falta de consolidación de la fractura y su persistencia en el tiempo implica inestabilidad secundaria a la falta de consolidación del foco de fractura. Estos *cleft* o hendiduras son mucho más frecuentes en las FVBE osteoporóticas que en las fracturas metastásicas (fig. 4).

Radiología 65 (2023) 239–250

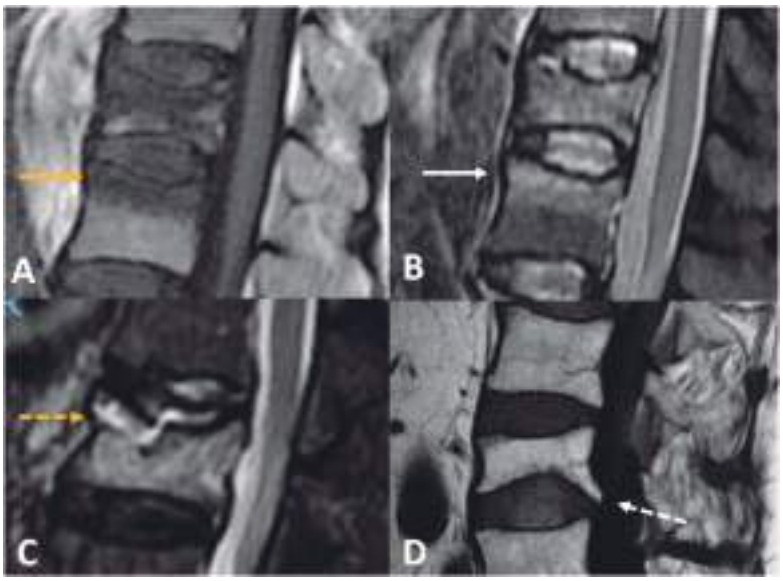

Figura 4 Ejemplos de fractura vertebral osteoporótica en resonancia magnética. A) Imagen T1 TSE sagital. Fractura aguda con bandas hipointensas paralelas a la plataforma vertebral superior. Puede identificarse la línea de fractura, de menor intensidad (flecha naranja). B) Imagen STIR sagital de la misma fractura, donde se evidencia el aumento de intensidad en banda correspondiente al edema perifractuario (flecha blanca). C) Imagen STIR sagital. Fractura con hendidura o *cleft* subcondral en la parte superior que traduce inestabilidad del foco de fractura (flecha naranja discontinua). D) Imagen T1 TSE sagital. Fractura crónica en estallido con retropulsión del margen vertebral posteroinferior en la que se ha recuperado la intensidad de señal grasa vertebral tras su consolidación (flecha blanca discontinua).

El diagnóstico diferencial más importante de la fractura vertebral osteoporótica son las fracturas patológicas secundarias a lesiones localizadas en las vértebras, ya sean malignas, como metástasis, mieloma, leucemia, linfoma, o bien tumores-pseudotumores primitivos de columna benignos o malignos, como el hemangioma (malformación vascular intraósea), el tumor de células gigantes, el quiste óseo aneurismático, el cordoma, etc. En este caso suele estar indicada la RM sin y con contraste[28]. Es sabido que las fracturas vertebrales osteoporóticas pueden presentarse hasta en un tercio de los pacientes oncológicos, por lo que las fracturas en estos pacientes no siempre son sinónimo de metástasis[4,29].

Las fracturas patológicas metastásicas pueden mostrar la sustitución completa de la médula ósea normal del cuerpo vertebral por una intensidad de seña anómala, o, cuando la sustitución es incompleta, mostrar un patrón nodular o parcheado, o con un margen irregular entre las áreas de señal alterada y las de señal conservada. Los signos morfológicos son un borde vertebral convexo, debido a la expansión provocada por el crecimiento tumoral, y la presencia de masa paravertebral asimétrica o lobulada[30] (fig. 5). Una causa de error puede ser la presencia de edema y/o hemorragia perivertebral en las fracturas vertebrales benignas, que se muestra como un engrosamiento de partes blandas más simétrico y liso que el aspecto de masa tumoral asimétrica de las fracturas malignas.

La afectación del pedículo puede verse tanto en fracturas metastásicas como en fracturas osteoporóticas y no es un criterio válido para su diferenciación. Sí es más indicativo de metástasis la afectación parcheada de otros elementos del arco posterior, como las apófisis espinosas o las láminas[31].

Las fracturas vertebrales ocurren entre el 50 y el 70% de los pacientes con mieloma múltiple. Pueden dar lugar a compresión de la médula espinal hasta en el 15% de los casos[24,25]. En la RM el mieloma puede presentar varios patrones de afectación que abarcan desde una intensidad de señal normal de los cuerpos vertebrales (28%) hasta una alteración difusa de la señal (29%), una alteración focal (30%), una alteración combinada focal y difusa (11%) y, finalmente, un patrón moteado en sal y pimienta (3%)[32,33]. En casos típicos de mieloma múltiple las vértebras muestran múltiples lesiones líticas junto con un patrón parcheado e infiltrativo y las fracturas vertebrales pueden mostrar un componente de tejido blando (fig. 6).

Muchas fracturas por compresión vertebral en pacientes con mieloma múltiple parecen benignas en la RM. La distribución topográfica es similar a la de las fracturas vertebrales por compresión en pacientes con osteoporosis. Por eso, la apariencia del mieloma múltiple puede ser engañosa, simulando una fractura vertebral por compresión osteoporótica en aproximadamente el 67% de los casos, con presencia de fracturas en diferentes estadios de evolución. Hasta el 38% de los pacientes con mieloma pueden presentar solo fracturas de apariencia benigna[34].

En la tabla 2 se resumen los criterios morfológicos y de señal que permiten diferenciar las fracturas benignas de las malignas, así como el comportamiento típico con contraste y en difusión.

El papel del contraste en la diferenciación entre fracturas de etiología benigna y maligna también ha sido discutido

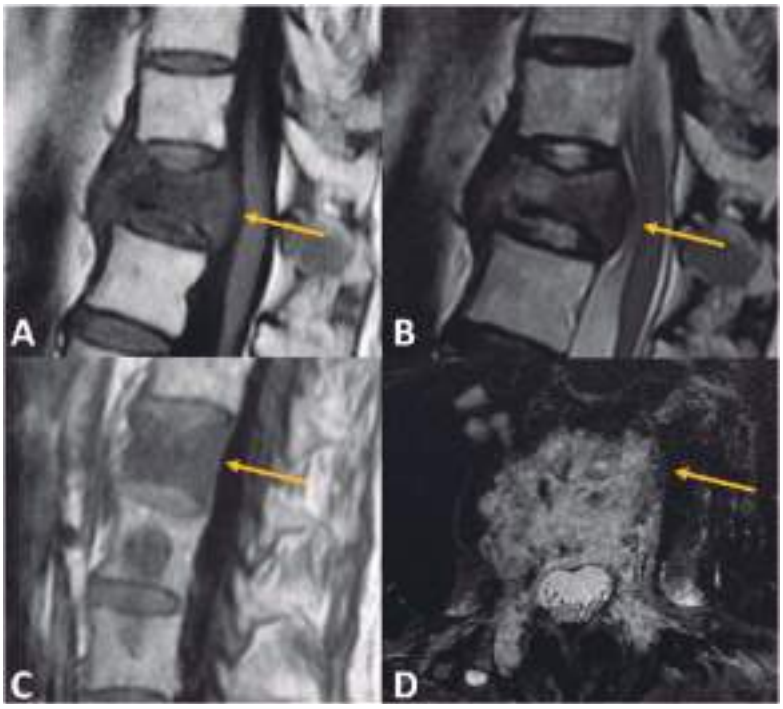

Figura 5 Ejemplos de fractura vertebral patológica en resonancia magnética. A,B) Imágenes T1 flair y T2 TSE sagitales en un paciente con cáncer de pulmón que muestran el borde convexo posterior del cuerpo vertebral (flecha). C) Imagen T1 flair sagital de fractura patológica con afectación difusa de la señal del cuerpo vertebral (flecha) en un paciente con linfoma. La vértebra inferior muestra una afectación parcheada. D) Imagen T2 TSE axial con supresión grasa de fractura patológica con afectación de ambos pedículos y extensión asimétrica a las partes blandas (flecha).

Tabla 2 Criterios de imagen para la diferenciación de las fracturas benignas y malignas

Criterio	Fracturas benignas	Fracturas malignas
Morfología	Retropulsión del margen posterior	Borde convexo
	Masa paravertebral fina y simétrica	Masa paravertebral grande o asimétrica
Señal	Señal ósea normal en fase crónica	
	Patrón de edema en banda	Afectación difusa de toda la médula
	Hendidura o *cleft* vertebral	Afectación parcheada de la médula
	Áreas de respeto de señal	Margen irregular entre edema y médula ósea normal
	Margen definido entre edema y médula ósea normal	
	Mayor contenido graso	Menor contenido o ausencia de grasa
Realce	Retorno a la señal medular normal de las vértebras adyacentes	Más intenso que las vértebras adyacentes
Difusión	Baja señal en difusión	Alta señal en difusión
	Alta señal en mapa ADC	Baja señal en mapa ADC
	ADC entre 1,2 y 2×10^{-3} mm^2/s	ADC entre 0,7 y $1,3 \times 10^{-3}$ mm^2/s

en la literatura. A nivel intraóseo las fracturas benignas tendrán un realce equivalente a las vértebras normales adyacentes, desapareciendo la baja señal de la secuencia T1 sin contraste, mostrando la vértebra fracturada una intensidad de señal similar a las de las vértebras no fracturadas. El realce en las fracturas malignas suele ser más heterogéneo y más intenso que las vértebras normales adyacentes. No obstante, en fracturas agudas benignas con importante edema el realce puede ser tan intenso que puede simular malignidad[30]. En estos casos el dilema es plantear un control a corto plazo (1-2 meses) para ver la disminución de los cambios inflamatorios en las fracturas benignas, o bien optar por la biopsia guiada por técnicas de imagen (fig. 7). En cuanto a los estudios de perfusión, son las curvas tipo III a V las que suelen estar presentes en caso de afectación tumoral[33], y los parámetros de perfusión suelen ser más elevados, aunque existe superposición tanto en el tipo de curva como en los parámetros de perfusión con las fracturas benignas agudas[35,36].

Radiología 65 (2023) 239–250

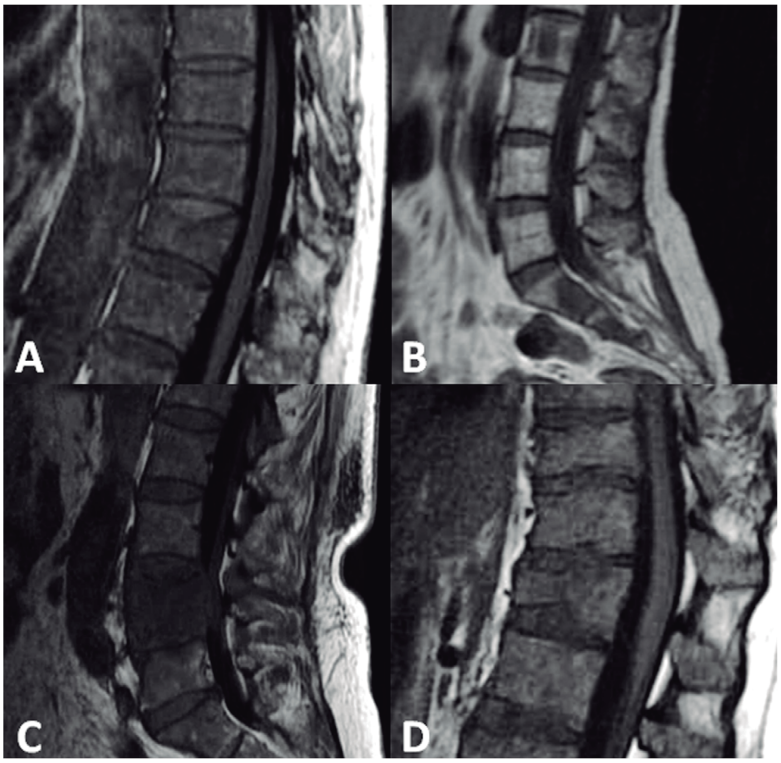

Figura 6 Ejemplos de afectación vertebral por mieloma en resonancia magnética. Las imágenes T1 flair (A,C,D) y TSE (B) sagitales muestran un patrón difuso (A), focal (B), mixto (difuso y focal) (C) y «en sal y pimienta» (D).

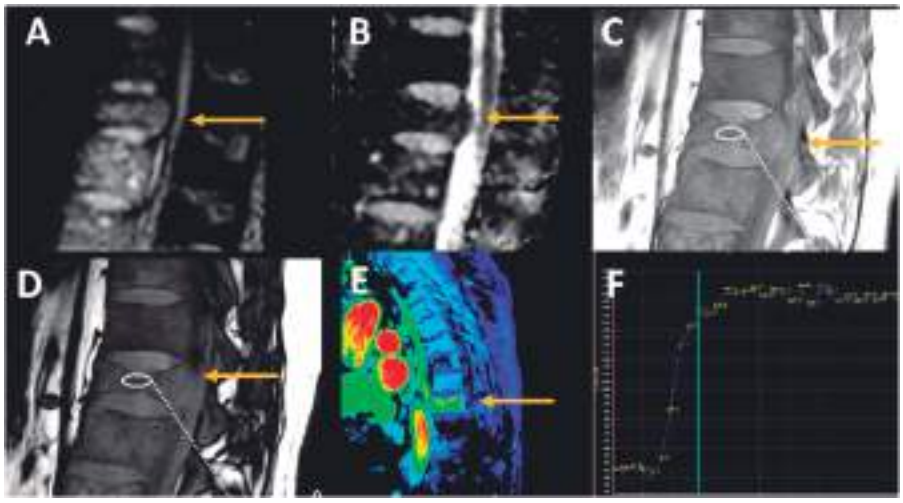

Figura 7 Diferenciación entre fracturas benignas y malignas por resonancia magnética mediante secuencias avanzadas. A) Imagen sagital potenciada en difusión y correspondiente al mapa ADC (B) en una fractura patológica por cáncer de próstata con restricción de la difusión ($0{,}7 \times 10^{-3}$ mm^2/s) (flechas). C) Secuencia fase y fuera de fase (D) con cociente entre la intensidad de señal de 0,85. E) Secuencia Thrive dinámica tras contraste y curva tipo III (F) en una fractura osteoporótica aguda.

También la imagen ponderada por difusión puede ser útil en la diferenciación entre las fracturas de causa benigna y maligna, mostrando restricción de la difusión en fracturas patológicas malignas. Esto ha sido atribuido a la alta celularidad y a la alta relación núcleo-citoplasma en células tumorales de división rápida. Producirán por tanto una señal elevada en difusión con una señal baja en el mapa ADC *(apparent diffusion coefficient)*. En cambio, en las fracturas de causa osteoporótica la difusión es mayor debido al edema, por lo que producirán una imagen hipo o

isointensa en difusión y señal más elevada en el mapa ADC (fig. 7)[37].

En el adulto la médula ósea normal tiene mayor contenido de grasa que de agua y componente celular; por tanto, la médula ósea normal muestra baja señal en difusión y bajo valor ADC, que normalmente oscila entre 0,2 y $0,6 \times 10^{-3}$ mm^2/s. La presencia de células grasas limita la presencia de agua extracelular por su naturaleza hidrofóbica. Por el contrario, la médula ósea roja, más abundante en pacientes jóvenes y niños, muestra mayor intensidad de señal en difusión y mayores valores ADC. Esto es debido a su mayor celularidad y contenido de agua extracelular. Algunos autores han referido el punto de corte en el valor ADC que permite diferenciar la médula ósea normal de una vértebra afectada por lesión tumoral, oscilando entre 0,655 y $0,774 \times 10^{-3}$ mm^2/s[37,38]. Cifras superiores sugieren una lesión maligna, cuyos valores oscilan entre 0,7 y $1,3 \times 10^{-3}$ mm^2/s. En el caso de las fracturas osteoporóticas la presencia de edema hace que los valores ADC sean superiores a los de las fracturas malignas, oscilando entre 1,2 y 2×10^{-3} mm^2/s. Las lesiones inflamatorias o infecciosas suelen mostrar un valor ADC intermedio entre las fracturas benignas y malignas: $1,2 \times 10^{-3}$ mm^2/s[39]. En cualquier caso, hay que recordar que los valores ADC se ven afectados por diversos factores, lo que dificulta la estandarización de unos valores de corte. Estos factores incluyen la fuerza del campo magnético, el tipo de imán, los diferentes tipos de secuencias de pulsos, el área de interés seleccionada o los parámetros de adquisición, incluyendo el valor de b, que pueden modificar la sensibilidad a otras causas de movimiento incoherente y afectar los valores ADC. En el caso de las fracturas vertebrales, factores derivados de la presencia de sangre (en sus distintos estadios evolutivos) o de gas pueden condicionar heterogeneidad local del campo magnético que deriva en artefactos por susceptibilidad magnética, provocando errores tanto en la interpretación de las imágenes de valor b alto como en la medida y la reproducibilidad de los valores de ADC[40,41].

Las imágenes de desplazamiento químico de fase (señal agua + grasa) y fuera de fase (señal agua − grasa) también se han utilizado con este propósito diferencial. En las secuencias en fase el agua y la grasa contribuyen a la señal de la médula ósea. En la fase opuesta se resta la señal de la grasa de la señal del agua, lo que resulta en una disminución de señal mayor cuanto más contenido de grasa existe en la lesión. En caso de infiltración tumoral no se produce esta disminución de señal, al no haber contenido graso. Un cociente entre la señal fuera de fase con respecto a la señal en fase > 0,9 permitió clasificar correctamente el 84,3% de los casos en benignos o malignos[42]. Es decir, con el menor contenido graso de la lesión aumenta la probabilidad de ser maligna. También se puede calcular la proporción de grasa relativa dividiendo la señal de la imagen de solo grasa por la señal de la imagen en fase (agua + grasa). Esta fracción de grasa será generalmente menor del 20% en las lesiones malignas[43].

Inteligencia artificial e impresión 3D en las fracturas vertebrales de baja energía

En los últimos años se están desarrollando sistemas de diagnóstico automatizado basados en inteligencia artificial con resultados prometedores. La inteligencia artificial es el conjunto de técnicas que posibilitan el desempeño de funciones propias de la inteligencia humana mediante sistemas automatizados. Las diferentes áreas y metodologías incluidas dentro de la misma escapan al objetivo del presente artículo, pero merece la pena reseñar que, en los últimos años, vienen desarrollándose sistemas de diagnóstico automatizado basados en inteligencia artificial con resultados prometedores. Por ejemplo, Petraikin et al.[44] han desarrollado recientemente un modelo (Comprise-G) capaz de detectar fracturas vertebrales grado 2 y 3 en TC con una sensibilidad y especificidad del 83,2% y del 90% en el conjunto de datos de prueba. También se están explorando diferentes aproximaciones para ayudar en el diagnóstico diferencial entre fracturas osteoporóticas y metastásicas[45]. Sin embargo, el entrenamiento y la implementación de los modelos de inteligencia artificial requieren la resolución de diferentes limitaciones que se encuentran frecuentemente en este contexto, como la asimetría de los conjuntos de datos, las imágenes no etiquetadas, la heterogeneidad en la calidad de las imágenes o las dificultades a la hora de extrapolar a la práctica los resultados obtenidos en contextos de investigación[46]. A pesar de que aún existen importantes limitaciones en términos de validación externa, es probable que contemos con herramientas potentes para el diagnóstico automatizado de este tipo de fracturas en los próximos años, por lo que deben conocerse las posibilidades y el estado del arte de la inteligencia artificial.

Por otra parte, las tecnologías de impresión 3D están implementándose de forma progresiva en diferentes instituciones, y ofrecen diversas posibilidades para una mejor comprensión y abordaje terapéutico de las fracturas vertebrales, permitiendo obtener réplicas fidedignas de la columna vertebral del paciente con fines diagnósticos, educativos y de gran utilidad para la planificación quirúrgica e intervencionista[47,48]. La principal desventaja es la necesidad de disponer de un espacio habilitado con adecuado equipamiento y de dominar diferentes etapas del proceso (conocimiento del *hardware* y del *software*), pero actualmente resulta sencillo generar modelos 3D impresos a partir de reconstrucciones volumétricas con programas como 3D Slicer[49], MeshMixer[50], Ultimaker Cura[51] o ChituBox[52] (figs. 8 y 9).

Fracturas vertebrales tras traumatismo de baja energía en la columna vertebral anquilosada

Espondilitis anquilosante

Los pacientes con espondilitis anquilosante presentan un riesgo significativamente aumentado (hasta 4 veces) de sufrir FVBE[53]. Desde el punto de vista clínico, existe un riesgo aumentado de pasar por alto las fracturas vertebrales en estos pacientes, debido a que suelen confundirlas con el dolor propio de su enfermedad de base[54]. Las fracturas de las vértebras pueden afectar a los puentes ligamentosos y se han descrito en el 6% de los pacientes con espondilitis anquilosante, especialmente en pacientes con enfermedad de larga duración[55]. La radiografía simple, la RM sin contraste intravenoso o la TC del área de la columna vertebral sin contraste intravenoso son técnicas apropiadas como

Radiología 65 (2023) 239–250

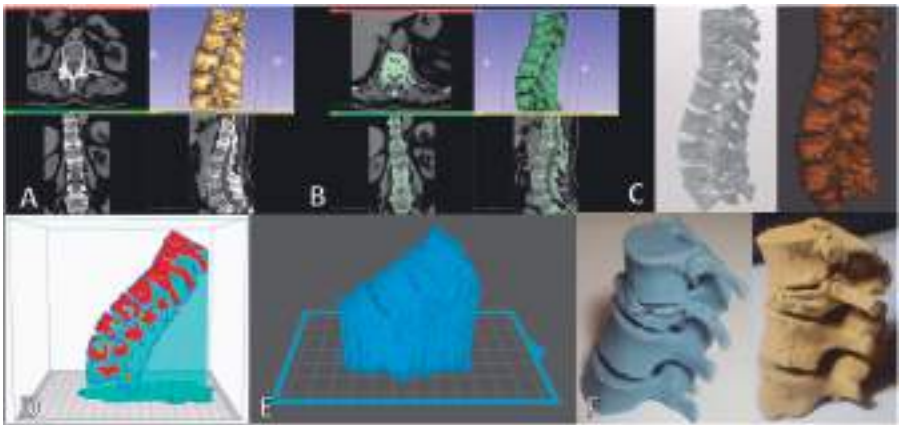

Figura 8 Generación de modelos de fractura vertebral impresos en 3D. A) Visualización del archivo DICOM en 3D Slicer®. B) Segmentación anatómica de la región de interés en 3D Slicer. C) Modelado 3D de la pieza segmentada con el software 3D Builder® (izquierda) y MeshMixer® (derecha). Nótese la malla tridimensional en esta última. D) Preparación para impresión 3D del modelo con soportes para equipos con tecnologías tipo FDM *(fused deposition modeling)* en Ultimaker Cura®. E) Preparación para impresión 3D del modelo con soportes para equipos con tecnologías de estereolitografía (SLA) en ChituBox®. F) Modelo impreso con tecnología SLA tras la retirada de soportes (izquierda) y pintura manual con aerógrafo (derecha).

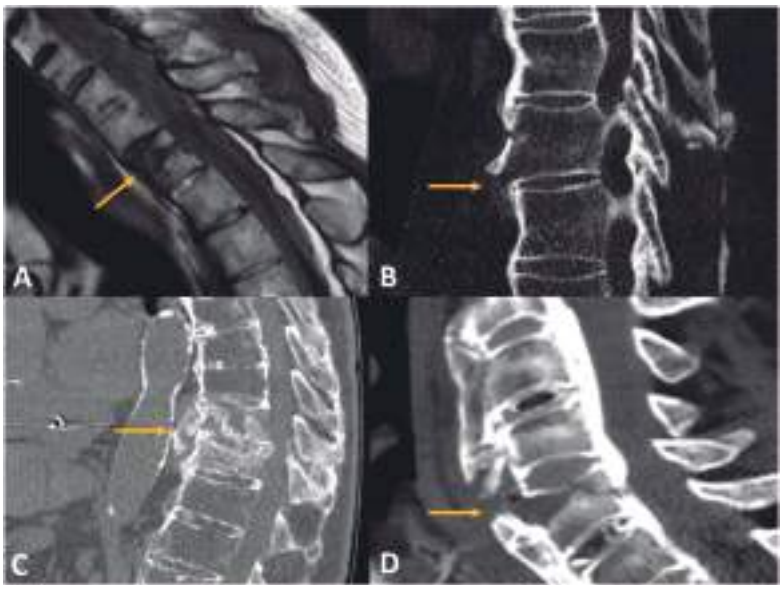

Figura 9 Fracturas vertebrales en pacientes con espondiloartropatía. A) Imagen T1 TSE sagital. Fractura de T1 en paciente con espondilitis anquilosante (flecha). B) TC de columna torácica, imagen sagital (algoritmo de reconstrucción ósea). Fractura aguda dorsal que afecta a la cortical anterior y al ligamento longitudinal anterior calcificado en paciente con espondilitis anquilosante (tipo B3 de la AO). C) TC de fractura torácica baja crónica con afectación transdiscal en paciente con espondilitis anquilosante. D) TC de fractura vertebral cervical baja en paciente con hiperostosis esquelética idiopática difusa.

imágenes iniciales para la sospecha de fractura en pacientes con anquilosis de la columna[56]. La radiografía puede ser la técnica inicial ante la sospecha de fractura, aunque factores como la osteoporosis o la localización anatómica (p. ej., cervicodorsal) pueden dificultar el diagnóstico[57]. Por tanto, si las radiografías son negativas, debe realizarse una técnica tomográfica, RM o TC. La sensibilidad de ambas técnicas es equivalente, siendo algunas mejor detectadas en RM y otras en TC, lo que sugiere que ambas aportan información complementaria. La TC se considera la técnica de referencia para valorar los detalles óseos en pacientes con espondilitis anquilosante y fractura vertebral. Los actuales equipos con capacidad multiplanar isotrópica permiten evaluar con gran detalle la anatomía ósea y obtener reconstrucciones volumétricas muy precisas, permitiendo visualizar la localización, la extensión y las características de las fracturas vertebrales[58]. Otra gran ventaja de esta técnica es la rapidez en la adquisición de imágenes. La TC permite visualizar

el signo más típico de las fracturas transdiscales, que es el ensanchamiento del espacio intervertebral. Igualmente permite visualizar las líneas de baja densidad que recorren el cuerpo vertebral en las fracturas transvertebrales. La principal desventaja de la TC es la baja resolución tisular para evaluar las partes blandas, la médula y las raíces nerviosas. La RM presenta evidentes ventajas en este sentido, siendo la técnica de elección para detectar lesiones de partes blandas, discoligamentarias y edema óseo, y es una técnica excelente para evaluar estructuras nerviosas[59].

Es importante diferenciar estas fracturas de las lesiones inflamatorias de los platillos vertebrales o lesiones de Anderson, que se tratan médicamente. Sin embargo, las fracturas vertebrales en estos pacientes son con frecuencia del tipo B3 de la clasificación de la Arbeitsgemeinschaft für Osteosynthesefragen (AO). Es decir, afectan a la banda de tensión o ligamento longitudinal anterior, dando lugar a pseudoartrosis que requerirán tratamiento quirúrgico[60,61].

Hiperostosis esquelética idiopática difusa (HEID)

La HEID, o enfermedad de Forestier-Rotes-Quirol, es una patología sistémica caracterizada por una osificación progresiva de los ligamentos y entesis, particularmente en el esqueleto axial (con clara predominancia de la columna torácica) y las articulaciones periféricas[62]. El diagnóstico de esta enfermedad se basa en la detección de puentes óseos osteofitarios en cuatro o más vértebras torácicas adyacentes[63]. Al igual que ocurre en el caso de la espondilitis anquilosante, los pacientes con HEID presentan un mayor riesgo de FVBE debido a la rigidez de la columna vertebral, que conlleva una disminución ostensible en la capacidad para absorber fuerzas de tracción[64]. Debido a este mecanismo fisiopatológico común, las fracturas vertebrales en pacientes con HEID presentan características similares a las descritas en pacientes con espondilitis anquilosante, aunque se ha encontrado que las fracturas vertebrales transvertebrales son más frecuentes que las transdiscales en la HEID (ocurre lo contrario en la espondilitis anquilosante) y que la mortalidad asociada a las fracturas vertebrales en la HEID es mayor que en pacientes con espondilitis anquilosante[47]. En estos pacientes la TC resulta de especial utilidad para identificar FVBE que afectan a los elementos posteriores[65].

Conclusiones

El diagnóstico por imagen de las FVBE supone con frecuencia un reto para el radiólogo, siendo necesario un adecuado conocimiento del papel de la radiografía simple, de la TC y de la RM. En este trabajo se ha revisado el papel de las distintas pruebas de imagen, así como las características principales que deben evaluarse para realizar un diagnóstico preciso y útil de fractura vertebral. No debe olvidarse la importancia de las patologías previas del paciente (p.ej., antecedentes oncológicos, espondiloartropatías) y la orientación clínica, pues existe un riesgo no desdeñable de sobrediagnóstico si las pruebas de imagen se utilizan indiscriminadamente.

Financiación

No se ha recibido ningún tipo de financiación para la realización de este trabajo.

Autoría

1. Responsables de la integridad del estudio: FRS, AJLRB.
2. Concepción del estudio: FRS, AJLRB.
3. Diseño del estudio: FRS, AJLRB.
4. Obtención de los datos: todos los autores.
5. Análisis e interpretación de los datos: todos los autores.
6. Tratamiento estadístico: no aplicable.
7. Búsqueda bibliográfica: todos los autores.
8. Redacción del trabajo: FRS, AJLRB, DLZ.
9. Revisión crítica del manuscrito con aportaciones intelectualmente relevantes: todos los autores.
10. Aprobación de la versión final: todos los autores.

Conflicto de intereses

Los autores declaran no presentar conflictos de intereses.

Agradecimientos

Los autores agradecen la ayuda prestada por David López Cornejo y a 3D Translation S.L. por el asesoramiento en la preparación de los modelos impresos en 3D.

Anexo. Material adicional

Se puede consultar material adicional a este artículo en su versión electrónica disponible en doi:10.1016/j.rx.2023.01.003.

Bibliografía

1. Bhattacharya B, Maung A, Schuster K, Davis KA. The older they are the harder they fall: Injury patterns and outcomes by age after ground level falls. Injury. 2016;47:1955–9, http://dx.doi.org/10.2214/ajr.162.4.8141015.
2. Spaniolas K, Cheng JD, Gestring ML, Sangosanya A, Stassen NA, Bankey PE. Ground level falls are associated with significant mortality in elderly patients. J Trauma. 2010;69:821–4, http://dx.doi.org/10.1097/ta.0b013e3181efc6c6.
3. Wang YX, Ruiz Santiago F, Deng M, Nogueira-Barbosa MH. Identifying osteoporotic vertebral endplate and cortex fractures. Quant Imaging Med Surg. 2017;7:555–91, http://dx.doi.org/10.21037/qims.2017.10.05.
4. Tann SB, Kozak JA, Mawad ME. The limitations of magnetic resonance imaging in the diagnosis of pathologic vertebral fractures. Spine. 1991;16:919–23, http://dx.doi.org/10.1097/00007632-199108000-00009.
5. Rajasekaran S, Vaccaro AR, Kanna RM, Schroeder GD, Oner FC, Vialle L, et al. The value of CT and MRI in the classification and surgical decision-making among spine surgeons in thoracolumbar spinal injuries. Eur Spine J. 2017;26:1463–9, http://dx.doi.org/10.1007/s00586-016-4623-0.
6. Pedersen V, Lampart A, Bingisser R, Nickel CH. Accuracy of plain radiography in detecting fractures in older individuals after low-energy falls: current evidence.

Trauma Surg Acute Care Open. 2020;5:e000560, http://dx.doi.org/10.1136/tsaco-2020-000560.
7. Lampart A, Arnold I, Mäder N, Niedermeier S, Escher A, Stahl R, et al. Prevalence of fractures and diagnostic accuracy of emergency X-ray in older adults sustaining a low-energy fall: A retrospective study. J Clin Med. 2019;9:97, http://dx.doi.org/10.3390/jcm9010097.
8. Karul M, Bannas P, Schoennagel BP, Hoffmann A, Wedegaertner U, Adam G, et al. Fractures of the thoracic spine in patients with minor trauma: Comparison of diagnostic accuracy and dose of biplane radiography and MDCT. Eur J Radiol. 2013;82:1273–7, http://dx.doi.org/10.1016/j.ejrad.2013.01.016.
9. Ruiz Santiago F, Láinez Ramos-Bossini A, Wáng YXJ, Martínez Barbero J, García Espinosa J, Martínez Martínez A. The value of magnetic resonance imaging and computed tomography in the study of spinal disorders. Quant Imaging Med Surg. 2022;12:3947–86, http://dx.doi.org/10.21037/qims-2022-04.
10. López Zúñiga D, Láinez-Ramos-Bossini AJ, Ruiz Santiago F. Radiographic diagnosis of osteoporotic vertebral fractures. An updated review. Med Clin (Barc). 2022;158:125–32, http://dx.doi.org/10.1016/j.medcli.2021.06.019.
11. Eastell R, Cedel SL, Wahner HW, Riggs BL, Melton LJ. Classification of vertebral fractures. J Bone Miner Res. 1991;6:207–15, http://dx.doi.org/10.1002/jbmr.5650060302.
12. McCloskey EV, Spector TD, Eyres KS, Fern ED, O'Rourke N, Vasikaran S, et al. The assessment of vertebral deformity: A method for use in population studies and clinical trials. Osteoporos Int. 1993;3:138–47, http://dx.doi.org/10.1007/bf01623275.
13. Jiang G, Eastell R, Barrington NA, Ferrar L. Comparison of methods for the visual identification of prevalent vertebral fracture in osteoporosis. Osteoporos Int. 2004;15:887–96, http://dx.doi.org/10.1007/s00198-004-1626-1.
14. Sugita M, Watanabe N, Mikami Y, Hase H, Kubo T. Classification of vertebral compression fractures in the osteoporotic spine. J Spinal Disord Tech. 2005;18:376–81, http://dx.doi.org/10.1097/01.bsd.0000168716.23440.61.
15. Genant HK, Wu CY, van Kuijk C, Nevitt MC. Vertebral fracture assessment using a semiquantitative technique. J Bone Miner Res. 1993;8:1137–48, http://dx.doi.org/10.1002/jbmr.5650080915.
16. Wáng YXJ, Diacinti D, Yu W, Cheng X-G, Nogueira-Barbosa MH, Che-Nordin N, et al. Semi-quantitative grading and extended semi-quantitative grading for osteoporotic vertebral deformity: A radiographic image database for education and calibration. Ann Transl Med. 2020;8:398, http://dx.doi.org/10.21037/atm.2020.02.23.
17. Schnake KJ, Blattert TR, Hahn P, Franck A, Hartmann F, Ullrich B, et al. Classification of osteoporotic thoracolumbar spine fractures: Recommendations of the Spine Section of the German Society for Orthopaedics and Trauma (DGOU). Glob Spine J. 2018;8:9S–46S, http://dx.doi.org/10.1177/2192568217717972.
18. Ruiz Santiago F, Láinez Ramos-Bossini AJ, Wáng YXJ, López Zúñiga D. The role of radiography in the study of spinal disorders. Quant Imaging Med Surg. 2020;10:2322–55, http://dx.doi.org/10.21037/qims-20-1014.
19. Ruiz Santiago F, GuzmánÁlvare ZL, TelloMoren OM, NavarreteGonzále ZPJ. [Plain-film radiography in the study of spinal pain]. Radiologia. 2010;52:126–37, http://dx.doi.org/10.1016/j.rx.2009.12.010.
20. Cho JH, Shin SI, Lee JH, Yeom JS, Chang BS, Lee CK. Usefulness of prone cross-table lateral radiographs in vertebral compression fractures. Clin Orthop Surg. 2013;5:195–201, http://dx.doi.org/10.4055/cios.2013.5.3.195.
21. Kamholt R, Sze G. Current imaging in spinal metastatic disease. Semin Oncol. 1991;18:158–69. PMID: 2014400.
22. Jacobson AF, Stomper PC, Cronin EB, Kaplan WD. Bone scans with one or two new abnormalities in cancer patients with no known metastases: Reliability of interpretation of initial correlative radiographs. Radiology. 1990;174:503–7, http://dx.doi.org/10.1148/radiology.174.2.2296659.
23. Jacobs WB, Perrin RG. Evaluation and treatment of spinal metastases: an overview. Neurosurg Focus. 2001;11:1–11, http://dx.doi.org/10.3171/foc.2001.11.6.11.
24. Lecouvet FE, Vande Berg BC, Michaux L, Jamart J, Maldague BE, Malghem J. Development of vertebral fractures in patients with multiple myeloma: Does MRI enable recognition of vertebrae that will collapse? J Comput Assist Tomogr. 1998;22:430–6, http://dx.doi.org/10.1097/00004728-199805000-00016.
25. Spiess JL, Adelstein DJ, Hines JD. Multiple myeloma presenting with spinal cord compression. Oncology. 1988;45:88–92, http://dx.doi.org/10.1159/000226539.
26. Ruiz Santiago F, Castellano García MM, Guzmán Álvarez L, Tello Moreno M. [Computed tomography and magnetic resonance imaging for painful spinal column: contributions and controversies]. Radiologia. 2011;53:116–33, http://dx.doi.org/10.1016/j.rx.2010.10.003.
27. Laredo JD, Lakhdari K, Bellaïche L, Hamze B, Janklewicz P, Tubiana JM. Acute vertebral collapse: CT findings in benign and malignant nontraumatic cases. Radiology. 1995;194:41–8, http://dx.doi.org/10.1148/radiology.194.1.7997579.
28. Shah LM, Jennings JW, Kirsch CFE, Hohenwalter EJ, Beaman FD, Cassidy RC, et al. ACR Appropriateness Criteria® Management of Vertebral Compression Fractures. J Am Coll Radiol. 2018;15:S347–64, http://dx.doi.org/10.1016/j.jacr.2018.09.019.
29. Wáng YXJ, Wu AM, Ruiz Santiago F, Nogueira-Barbosa MH. Informed appropriate imaging for low back pain management: A narrative review. J Orthop Translat. 2018;15:21–34, http://dx.doi.org/10.1016/j.jot.2018.07.009.
30. Mauch JT, Carr CM, Cloft H, Diehn FE. Review of the imaging features of benign osteoporotic and malignant vertebral compression fractures. AJNR Am J Neuroradiol. 2018;39:1584–92, http://dx.doi.org/10.3174/ajnr.a5528.
31. Ishiyama M, Fuwa S, Numaguchi Y, Kobayashi N, Saida Y. Pedicle involvement on MR imaging is common in osteoporotic compression fractures. AJNR Am J Neuroradiol. 2010;31:668–73, http://dx.doi.org/10.3174/ajnr.a1905.
32. Hwang S, Panicek DM. Magnetic resonance imaging of bone marrow in oncology. Part 2. Skeletal Radiol. 2007;36:1017–27, http://dx.doi.org/10.1007/s00256-007-0308-4.
33. Dutoit JC, Verstraete KL. MRI in multiple myeloma: A pictorial review of diagnostic and post-treatment findings. Insights Imaging. 2016;7:553–69, http://dx.doi.org/10.1007/s13244-016-0492-7.
34. Lecouvet FE, Vande Berg BC, Maldague BE, Michaux L, Laterre E, Michaux JL, et al. Vertebral compression fractures in multiple myeloma. Part I. Distribution and appearance at MR imaging. Radiology. 1997;204:195–9, http://dx.doi.org/10.1148/radiology.204.1.9205246.
35. Li K, Huang L, Lang Z, Ni L, Du J, Yang H. Reliability and validity of different MRI sequences in improving the accuracy of differential diagnosis of benign and malignant vertebral fractures: A meta-analysis. AJR Am J Roentgenol. 2019;213:427–36, http://dx.doi.org/10.2214/AJR.18.20560.
36. Arevalo-Perez J, Peck KK, Lyo JK, Holodny AI, Lis E, Karimi S. Differentiating benign from malignant vertebral fractures using T1-weighted dynamic contrast-enhanced MRI. J Magn Reson Imaging. 2015;42:1039–47, http://dx.doi.org/10.1002/jmri.24863.
37. Eiber M, Holzapfel K, Ganter C, Epple K, Metz S, Geinitz H, et al. Whole-body MRI including diffusion-weighted imaging (DWI) for patients with recurring prostate cancer: Technical feasibility and assessment of lesion conspicuity in DWI. J Magn Reson Imaging. 2011;33:1160–70, http://dx.doi.org/10.1002/jmri.22542.

38. Messiou C, Collins DJ, Morgan VA, Desouza NM. Optimising diffusion weighted MRI for imaging metastatic and myeloma bone disease and assessing reproducibility. Eur Radiol. 2011;21:1713–8, http://dx.doi.org/10.1007/s00330-011-2116-4.
39. Dietrich O, Geith T, Reiser MF, Baur-Melnyk A. Diffusion imaging of the vertebral bone marrow. NMR Biomed. 2017;30:e3333, http://dx.doi.org/10.1002/nbm.3333.
40. Bickel H, Pinker K, Polanec S, Magometschnigg H, Wengert G, Spick C, et al. Diffusion-weighted imaging of breast lesions: Region-of-interest placement and different ADC parameters influence apparent diffusion coefficient values. Eur Radiol. 2017;27:1883–92, http://dx.doi.org/10.1007/s00330-016-4564-3.
41. Luo Z, Litao L, Gu S, Luo X, Li D, Yu L, et al. Standard-b-value vs low-b-value DWI for differentiation of benign and malignant vertebral fractures: A meta-analysis. Br J Radiol. 2016;89:20150384, http://dx.doi.org/10.1259/bjr. 20160224.
42. Rathore R, Parihar A, Dwivedi DK, Dwivedi AK, Kohli N, Garg RK, et al. Predictive models in differentiating vertebral lesions using multiparametric MRI. AJNR Am J Neuroradiol. 2017;38:2391–8, http://dx.doi.org/10.3174/ajnr.A5411.
43. Donners R, Figueiredo I, Tunariu N, Blackledge M, Koh DM, Fenor de la Maza MD, et al. Multiparametric bone MRI can improve CT-guided bone biopsy target selection in cancer patients and increase diagnostic yield and feasibility of next-generation tumour sequencing. Eur Radiol. 2022;32:4647–56, http://dx.doi.org/10.1007/s00330-022-08536-6.
44. Petraikin AV, Belaya ZE, Kiseleva AN, Artyukova ZR, Belyaev MG, Kondratenko VA, et al. Artificial intelligence technology for recognition of vertebral compression fractures using a morphometric analysis model based on convolutional neural networks. Probl Endokrinol (Mosk). 2020;66:48–60, http://dx.doi.org/10.14341/probl12605.
45. Musa Aguiar P, Zarantonello P, Aparisi Gómez MP. Differentiation between osteoporotic and neoplastic vertebral fractures: State of the art and future perspectives. Curr Med Imaging. 2021;18:187–207, http://dx.doi.org/10.2174/1573405617666210412142758.
46. Redruello-Guerrero P, Jiménez-Gutiérrez C, Láinez Ramos-Bossini AJ, Jiménez-Gutiérrez PM, Rivera-Izquierdo M, Benítez Sánchez JM. Artificial intelligence for the triage of COVID-19 patients at the emergency department: A systematic review. Signa Vitae. 2022;18:17–26, http://dx.doi.org/10.22514/sv.2022.069.
47. Láinez Ramos AJ, Láinez Millán B, Redruello Guerrero P, Prados Salazar JC. Implementation of novel technologies for teaching and learning normal and pathological anatomy of the spine: From medical imaging to 3D printing. En: Vico-Bosch A, Vega-Caro L, Buzón-García O, editores. Entornos virtuales para la educación en tiempos de pandemia: Perspectivas metodológicas. Madrid: Dykinson S.L.; 2021. p. 944–6, https://dialnet.unirioja.es/servlet/articulo?codigo=8265907.
48. Cai H, Liu Z, Wei F, Yu M, Xu N, Li Z. 3D printing in spine surgery. Adv Exp Med Biol. 2018;1093:345–59, http://dx.doi.org/10.1007/978-981-13-1396-7_27.
49. Fedorov A, Beichel R, Kalpathy-Cramer J, Finet J, Fillion-Robin JC, Pujol S, et al. 3D slicer as an image computing platform for the quantitative imaging network. Magn Reson Imaging. 2012;30:1323–41, http://dx.doi.org/10.1016/j.mri.2012.05.001.
50. Autodesk Meshmixer free software for making awesome stuff, 2022 [consultado 11 Dic 2022]. Disponible en: https://meshmixer.com/.
51. Software de impresión 3D para un flujo de trabajo de producción avanzado, 2022 [consultado 11 Dic 2022]. Disponible en: https://ultimaker.com/es/software.
52. CHITUBOX Software. A powerful and easy way to prepare for SLA/DLP/LCD 3D printing, 2022 [consultado 11 Dic 2022]. Disponible en: https://www.chitubox.com/en/index.
53. Westerveld LA, Verlaan JJ, Oner FC. Spinal fractures in patients with ankylosing spinal disorders: A systematic review of the literature on treatment, neurological status and complications. Eur Spine J. 2009;18:145–56, http://dx.doi.org/10.1007/s00586-008-0764-0.
54. Waldman SK, Brown C, Lopez de Heredia L, Hughes RJ. Diagnosing and managing spinal injury in patients with ankylosing spondylitis. J Emerg Med. 2013;44:e315–9, http://dx.doi.org/10.1016/j.jemermed.2012.11.002.
55. Finkelstein JA, Chapman JR, Mirza S. Occult vertebral fractures in ankylosing spondylitis. Spinal Cord. 1999;37:444–7, http://dx.doi.org/10.1038/sj.sc.3100837.
56. Czuczman GJ, Mandell JC, Wessell DE, Lenchik L, Ahlawat S, Baker JC, et al., Expert Panel on Musculoskeletal Imaging. ACR Appropriateness Criteria® Inflammatory Back Pain: Known or suspected axial spondyloarthritis: 2021 update. J Am Coll Radiol. 2021;18 11 Suppl:S340–60, http://dx.doi.org/10.1016/j.jacr.2021.08.003.
57. Mandl P, Navarro-Compan V, Terslev L, Aegerter P, van der Heijde D, d'Agostino MA, et al. EULAR recommendations for the use of imaging in the diagnosis and management of spondyloarthritis in clinical practice. Ann Rheum Dis. 2015;74:1327–39, http://dx.doi.org/10.1136/annrheumdis-2014-206971.
58. Koivikko MP, Kluru MJ, Koskinen SK. Multidetector computed tomography of cervical spine fractures in ankylosing spondylitis. Acta Radiol. 2004;45:751–9, http://dx.doi.org/10.1080/02841850410001330.
59. Thumbikat P, Hariharan RP, Ravichandran G, McClelland MR, Mathew KM. Spinal cord injury in patients with ankylosing spondylitis: A 10-year review. Spine (Phila Pa 1976). 2007;32:2989–95, http://dx.doi.org/10.1097/BRS.0b013e31815cddfc.
60. Park YS, Kim JH, Ryu JA, Kim TH. The Andersson lesion in ankylosing spondylitis: Distinguishing between the inflammatory and traumatic subtypes. J Bone Joint Surg Br. 2011;93:961–6, http://dx.doi.org/10.1302/0301-620X.93B7.26337.
61. Ruiz Santiago F, Tomás Muñoz P, Moya Sánchez E, Revelles Paniza M, Martínez Martínez A, Pérez Abela AL. Classifying thoracolumbar fractures: Role of quantitative imaging. Quant Imaging Med Surg. 2016;6:772–84, http://dx.doi.org/10.21037/qims.2016.12.04.
62. Mader R, Verlaan J-J, Eshed I, Bruges-Armas J, Sarzi Puttini P, Atzeni F, et al. Diffuse idiopathic skeletal hyperostosis (DISH): Where we are now and where to go next. RMD Open. 2022;3:e000472, http://dx.doi.org/10.1136/rmdopen-2017-000472.
63. Resnick D, Niwayama G. Radiographic and pathologic features of spinal involvement in diffuse idiopathic skeletal hyperostosis (DISH). Radiology. 1976;119:559–68, http://dx.doi.org/10.1148/119.3.559.
64. Caron T, Bransford R, Nguyen Q, Agel J, Chapman J, Bellabarba C. Spine fractures in patients with ankylosing spinal disordes. Spine (Phila Pa 1976). 2010;35:E458–64, http://dx.doi.org/10.1097/BRS.0B013E3181CC764F.
65. Hendrix RW, Melany M, Miller F, Rogers LF. Fracture of the spine in patients with ankylosis due to diffuse skeletal hyperostosis: clinical and imaging findings. AJR Am J Roentgenol. 1994;162:899–904, http://dx.doi.org/10.2214/ajr.162.4.8141015.

TRABAJO 5: VERTEBRAL ARTERY DISSECTION SECONDARY TO HANGMAN'S FRACTURE (DISECCIÓN DE ARTERIA VERTEBRAL SECUNDARIA A FRACTURA TIPO HANGMAN)

Láinez Ramos-Bossini AJ, Gálvez López R, Pastor Rull J. Vertebral artery dissection secondary to hangman's fracture. Med Clin (Barc). 2020;154(5):195-196. English, Spanish. doi: 10.1016/j.medcli.2019.02.008. Epub 2019 Apr 4. PMID: 30954291. FI: 1,725. Q3 (T2).

Se trata de una carta al editor que cubre parte del objetivo 1.

Cartas al Editor / Med Clin (Barc). 2020;**154(5)**:194–196

Disección de arteria vertebral secundaria a fractura tipo *hangman*

Vertebral artery dissection secondary to hangman's fracture

Sr. Editor:

La disección de la arteria vertebral (DAV) es una entidad rara[1], con una incidencia anual estimada de un caso por 100.000 habitantes, aunque se considera infradiagnosticada[2]. Afecta a todos los grupos de edad, con un pico de incidencia en la quinta década de la vida[3], y supone hasta el 25% de los accidentes cerebrovasculares (ACV) en pacientes jóvenes y de mediana edad[1,3]. Presentamos el caso de un paciente que acude a Urgencias por dolor cervical tras una caída accidental en su domicilio, en el que se diagnostica fractura cervical tipo *hangman* y DAV postraumática.

Se trata de un paciente varón de 67 años, con antecedentes de EPOC grado 2 y estenosis del canal lumbar, que acudió a Urgencias tras sufrir una caída accidental en su domicilio, sin pérdida de conciencia. La exploración física fue normal y el paciente se encontraba estable clínica y hemodinámicamente, pero manifiestaba un intenso dolor cervical. Se solicitaron radiografías cervicales y se pautó tratamiento analgésico intravenoso.

En la radiografía cervical lateral se apreció una espondilolistesis de C2 sobre C3, por lo que se decidió realizar una TC de columna cervical, en la que se apreció una fractura del anillo del axis tipo II («fractura del ahorcado» o tipo *hangman*).

Ante este hallazgo, se decidió la inmovilización cervical con collarín y el ingreso en planta de Neurocirugía. Se solicitó resonancia magnética de columna cervical, en la que se descartó lesión traumática medular o rotura del ligamento transverso del atlas. Sin embargo, se apreció hiperintensidad de señal de la arteria vertebral derecha (AVD) en secuencias T1 y T2 en los segmentos V2, V3 y V4, lo que evidenció una oclusión o flujo muy lento de la misma (fig. 1).

Dada la alta sospecha de disección traumática de la AVD, se decidió realizar una angiotomografía computarizada, en la que se confirmó la oclusión de dicha arteria desde la porción distal de V2 hasta la porción media de V3. Tras el diagnóstico de DAV, se pautó tratamiento con heparina de bajo peso molecular y acenocumarol oral posteriormente. El paciente evolucionó favorablemente y fue dado de alta.

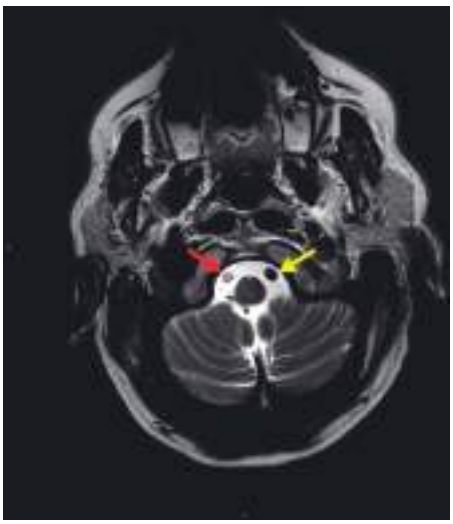

Figura 1. Imagen axial de resonancia magnética de columna cervical en secuencia potenciada en T2 TSE. Se aprecia un aumento de la señal de la arteria vertebral derecha (flecha roja) respecto a la contralateral (flecha amarilla), lo que apunta a una posible disección de la primera.

Clásicamente, la DAV se ha considerado asociada a traumatismos de alta energía, pero cada vez se halla con mayor frecuencia tras traumatismos leves[4]. Las fracturas de columna cervical alta y las que afectan al foramen transverso se asocian de manera específica a DAV, pero también se han descrito DAV asociadas a fracturas mínimas[4]. Hasta la mitad de las DAV postraumáticas presentan una fractura cervical asociada[5].

El problema principal de las DAV es que se suelen manifestar con síntomas poco específicos, fundamentalmente dolor cervical o de cabeza, y a menudo quedan enmascaradas por el propio traumatismo cervical[2]. Sin embargo, en su desarrollo pueden dar lugar a ACV secundarios. Es frecuente que exista un intervalo libre de síntomas, que se explica por la compensación de flujo a través de la arteria contralateral.

La mayor parte de las disecciones se resuelven de manera espontánea y los resultados a largo plazo son favorables. Más de dos tercios de las oclusiones y hasta el 90% de las estenosis acaban por recanalizarse[3]. Sin embargo, el pronóstico es variable. Entre las complicaciones de la DAV a medio y largo plazo se encuentra la cefalea crónica, la disección recidivante y las secuelas de ACV[3]. La mortalidad atribuida a las disecciones de carótida y vertebral es menor del 5% y los pacientes que experimentan un ACV secundario a esta afección presentan una buena recuperación funcional en un 75%[3].

Se recomienda el cribado de DAV en pacientes tras un accidente de tráfico grave aunque se encuentren asintomáticos, ya que la administración de anticoagulación ha demostrado eficacia en la prevención de ictus isquémico por embolización de fragmentos trombóticos desde la arteria afectada[5].

Los autores queremos reseñar la dificultad diagnóstica que reviste la DAV, ya que puede ser enmascarada por la propia clínica de la lesión traumática, y la importancia de mantener una actitud suspicaz incluso ante traumatismos mínimos. Además, se plantea la necesidad de valorar de manera adecuada la posible existencia de fracturas cervicales en pacientes de cierta edad, aun ante traumatismos de baja energía. La instauración de tratamiento anticoagulante de manera precoz ha demostrado una disminución significativa del riesgo de ACV secundario a disección arterial cervical.

Bibliografía

1. Lee WJ, Jung KH, Moon J, Lee ST, Chu K, Lee SK, et al. Prognosis of spontaneous cervical artery dissection and transcranial Doppler findings associated with clinical outcomes. Eur Radiol. 2016;26:1284–91, http://dx.doi.org/10.1007/s00330-015-3944-4
2. Schellinger PD, Schwab S, Krieger D, Fiebach JB, Steiner T, Hund EF, et al. Masking of vertebral artery dissection by severe trauma to the cervical spine. Spine. 2001;26:314–9, http://dx.doi.org/10.1097/00007632-200102010-00019
3. Schievink WI. Spontaneous dissection of the carotid and vertebral arteries. N Engl J Med. 2001;344:898–906, http://dx.doi.org/10.1056/NEJM200103223441206
4. Tabuchi S, Nakayasu H. Traumatic vertebral artery dissection and cerebral infarction following head and neck injury with a lucid interval. Acute Med Surg. 2015;2:127–30, http://dx.doi.org/10.1002/ams2.75
5. Sporns PB, Niederstadt T, Heindel W, Raschke MJ, Hartensuer R, Dittrich R, et al. Imaging of spontaneous and traumatic cervical artery dissection. Clin Neuroradiol. 2018, http://dx.doi.org/10.1007/s00062-018-0666-4 [Publicación electrónica].

RESULTADOS

Trabajo 5: Vertebral artery dissection secondary to hangman's fracture.

Antonio Jesús Láinez Ramos-Bossini[a,*], Regina Gálvez López[b] y Jorge Pastor Rull[a]

[a] *Servicio de Radiodiagnóstico, Hospital Virgen de las Nieves, Granada, España*
[b] *Servicio de Urgencias, Hospital Virgen de las Nieves, Granada, España*

* Autor para correspondencia.
Correo electrónico: ajbossini@ugr.es (A.J. Láinez Ramos-Bossini).

https://doi.org/10.1016/j.medcli.2019.02.008

TRABAJO 6: FACTORS INFLUENCING VERTEBRAL COLLAPSE IN OSTEOPOROTIC VERTEBRAL FRACTURES.

Ruiz Santiago F, **Láinez Ramos-Bossini AJ**, Moraleda-Cabrera B. Factors influencing vertebral collapse in osteoporotic vertebral fractures.

Se trata de un estudio de investigación original retrospectivo que cubre el objetivo 2.

Trabajo no publicado en el momento del depósito de la Tesis Doctoral.

Factors influencing vertebral collapse in osteoporotic vertebral fractures. A case-control study

Ruiz Santiago F[1,2,3], Láinez Ramos-Bossini AJ[1,2,4], Moraleda-Cabrera B[1,2]

1. Section of Musculoskeletal Radiology. Department of Radiology. Hospital Universitario Virgen de las Nieves. 18014 Granada, Spain

2. Biosanitary Institute of Granada (ibs.GRANADA). 18016 Granada, Spain

3. Department of Radiology and Physical Medicine. Faculty of Medicine. University of Granada. 18016 Granada, Spain

4. PhD Programme of Clinical Medicine and Public Health. University of Granada. 18014 Granada, Spain

*Corresponding author:

Antonio Jesús Láinez Ramos-Bossini

Department of Radiology.

Hospital Universitario Virgen de las Nieves.

Avda Fuerzas Armadas, 2

18014 Granada, Spain

E-mail: ajbossini@ugr.es

ABSTRACT

OBJECTIVES

To identify risk factors for collapse of osteoporotic vertebral fractures (OVF) on computed tomography (CT) and conventional radiography (CR).

METHODS AND MATERIALS

This is a retrospective case-control study including a consecutive series of patients with OVF diagnosed in our institution from January to September 2019. Inclusion criteria were to have standing CR and supine CT within 2 weeks after the diagnosis of OVF and a follow-up CR at 6 months or later. We evaluated vertebral height loss, local kyphosis, vertebral density, and fracture type according to the grading systems of Genant, Sugita, Association of Osteosynthesis (AO) Spine, and the German Society for Orthopaedics and Trauma. Vertebral collapse was defined as loss of ≥50% of vertebral area or height.

RESULTS

Fifty-six patients were included in the study, with a mean age of 72.6±1.2 years, including 48 women. Twenty-five (44.6%) OVFs developed collapse on follow-up. None of the fracture classification systems were found to be predictive of collapse. Multivariate analysis showed that older age, increased density ratio (≥2) between the fractured and non-fractured vertebral bodies, and a ≥6% difference in posterior vertebral height (PVH) loss between standing CR and supine CT exhibited 88% discriminative power in predicting vertebral collapse.

CONCLUSION

Age over 72.5 years, a density ratio ≥2 between the fractured and non-fractured vertebral bodies, and a difference equal to or higher than 6% in PVH loss between standing CR and supine CT, are risk factors for developing vertebral collapse after OVF.

KEYWORDS: spinal fractures, osteoporosis, computed tomography, radiography, risk factors, osteoporotic fracture.

INTRODUCTION

Osteoporotic vertebral fractures (OVFs) are the most frequent osteoporotic fractures [1], and their detection is sufficient to make the diagnosis of osteoporosis even in the absence of bone mineral density studies [2]. Ninety percent of all vertebral fractures are osteoporotic and may occur without any noticeable trauma or following a low-energy injury such as falling to the ground [3]. One of the main current challenges in radiology regarding OVFs is to correctly classify them and to identify the imaging features that imply a risk of collapse or increased local vertebral kyphosis. These complications may adversely affect the clinical and functional recovery of the patient. In fact, loss of sagittal balance due to increased kyphosis seems to be the main cause of persistent pain and gait disturbances [4].

Conventional radiography (CR) is still considered the initial screening examination to detect OVFs [5], although its reported sensitivity in vertebral fracture detection is lower compared to CT or MRI [6-8], depending on different factors such as anatomical location, technical parameters, or bone density quality.

Computed tomography (CT) has diagnostic advantages compared with CR, allowing the identification of more subtle signs of vertebral fracture [3] such as discontinuity or buckling of the cortex and impaction of the fractured trabeculae. In addition, several studies have found that Hounsfield unit (HU) values of the vertebral marrow (trabecular bone) correlate with bone mineral density, and that routine CT examination can be used to identify patients with osteoporosis [9, 10]. Normal HU values at the vertebral bone marrow range from 256.7±41.8 (mean ± standard deviation) in the second decade of life to 90.0±25.5 in the ninth decade of life in men, and from 253.5±29.6 to 67.3±41.2 in women, respectively [11]. Lower HU values are suggestive of osteoporosis, which increases the risk of developing more severe OVFs [12].

On magnetic resonance imaging (MRI), several findings have been associated with absence of consolidation and persistence of pain, including the presence of an intravertebral cleft, location at the thoracolumbar transition, or a diffuse area of low T2 signal intensity probably secondary to fibrosis and impaction of trabeculae [13].

Several classification systems have been developed to categorize and quantify the severity of OVFs. However, there is no universal agreement on which of these systems is the most useful for appropriate patient management. For instance, the semiquantitative Genant's classification is mainly used in epidemiological studies. This classification categorizes vertebral fractures based on the morphology and degree of area and height loss, but it does not provide indications for

clinical management [14]. On the other hand, Sugita et al. classified fractures into 5 morphological types based on radiographic findings, with swelled, bow-shaped and projecting types being frequently associated with the presence of intravertebral cleft and late collapse, as well as with worse prognosis [15].

Recently, the German Society for Orthopaedics and Trauma proposed a classification system for OVFs that offers a comprehensive score based on the type of fracture and clinical factors to decide between surgical or medical management [16, 17]. This classification scores bone density and progressive fracture sintering, among other factors. Preliminary results suggest that this score is an appropriate tool for the preoperative assessment of OVFs [18].

Different risk factors for the development of collapse in the case of traumatic vertebral fractures have been published in the literature, including burst fractures, location in the thoracolumbar transition (T12-L1), and age over 50 years [19, 20]. Osteoporosis is also a risk factor for vertebral collapse, although most OVFs heal well with conservative treatment. Nevertheless, between 8.9% and 20% of cases may develop painful non-union or pseudoarthrosis, progressive kyphosis and neurological damage [21-23]. Vertebral pseudoarthrosis usually presents with intravertebral cysts or clefts and injury of the posterior vertebral wall [23].

The aim of this study was to identify risk factors related to the development of vertebral collapse of OVFs based on radiological findings in CR and CT.

MATERIALS AND METHODS

Study design and participants

This study was approved by our Institutional Review Board (code TFG-FX-2019). The Strengthening the Reporting of Observational Studies in Epidemiology (STROBE) guidelines [24] were followed when designing and reporting this study. We designed a retrospective single-centre case-control study including a consecutive series of patients with acute OVF of the thoracolumbar spine diagnosed by imaging studies performed at the emergency department in our institution from January to September 2019. The following inclusion criteria were established:

1. Patients diagnosed with acute OVF by standing CR and supine CT.
2. Patients with imaging follow-up of their fracture at least 6 months after diagnosis by standing CR to exclude delayed vertebral body collapse.

3. Type A fractures of the AO classification.
4. Management with conservative medical treatment.

The exclusion criteria were:

1. Fracture with vertebral collapse (more than 50% of vertebral area or height loss) at initial diagnosis.
2. Lack of follow-up CR at least 6 months after initial diagnosis.
3. More than 1 acute OVF.
4. Patients treated by surgery or vertebral augmentation.
5. Patients with poor quality of images, such as rotated, non-parallel radiographs.

Eighty-four patients with OVF were initially included. Of them, 28 were excluded (11 due to vertebral collapse at the time of initial diagnosis, 6 due to the presence of more than one acute vertebral fracture, and 11 due to lack of follow-up CR 6 months after the fracture). Therefore, a total of 56 cases were analysed in the study.

Variables of the study

The dependent variable was vertebral collapse, defined as the presence of >50% loss of vertebral body area or height at the end of follow-up:

The qualitative independent variables included were sex, vertebral fracture location, cause (spontaneous, exertion, fall), presence of cleft, fracture of lateral walls (absent, unilateral, bilateral), involvement of vertebral endplates (absent, superior, inferior, both), and involvement of anterior and posterior walls (absent, anterior, posterior, both).

We assessed several qualitative variables related to the type of fracture at the time of initial diagnosis and at the end of follow-up based on the following grading systems:
1. Genant's morphological (wedge, biconcave, crush) and quantitative (grade 0, 1, 2, 3) classifications.
2. Classification of the German Society for Orthopaedics and Trauma (OF1, OF2, OF3, OF4, OF5).
3. The AO Spine classification (A1 to A4), which was only used at the initial evaluation because it does not allow to quantify fracture progression.

4. Sugita's classification (swelled-front, bow-shaped, projecting, concave, dented), which was also used only at the initial assessment because it is not applicable when severe posterior height loss or wall damage develops.

Quantitative variables included patient age, local kyphosis, and percentage loss of vertebral area, anterior, middle, and posterior height in standing CR and supine CT images (Figure 1). To calculate the percentage loss of vertebral area and height in CR and CT, measurements of the fractured vertebral body were divided by the mean of measurements made at the normal cephalad and caudal vertebrae. To compare the variability between standing measurements on radiography and supine measurements on CT, we calculated the differences in height and area loss as well as in local kyphosis obtained in both imaging techniques.

HU values were measured with oval region of interest (ROI) areas of approximately 1.5-2 cm^2 at two different levels of the trabecular bone of the fractured vertebra, the adjacent upper and lower normal vertebrae, and the aortic lumen. The mean value of these measurements was used as the final density value of the fractured vertebra, the normal vertebra, and the aorta (Figure 2). For measurements on the fractured vertebra, care was taken to avoid cystic cavities or sclerotic fracture impaction lines in the ROI area. The aorta showed an almost constant density in all patients and was chosen as the internal reference standard.

All CT examinations were performed on 16-slice Brightspeed or 64-slice Lightspeed CT scanners. Helical CT images with 0.63-1.25 mm thickness and 0.63-1.25 mm interval reconstructions were obtained. Two radiologists (FRS and AJLRB) with 30 and 5 years of experience independently performed measurements using an on-screen digital pointer with the Carestream Vue Picture Archiving and Communication System. For the sake of consistency, mean values of both measurements were used as final values. Fracture classification was also performed by both radiologists independently. In case of disagreement, the case was revised and discussed until agreement was reached.

Statistical analysis

We performed a descriptive analysis of the frequency of the qualitative categorical variables, as well as a numerical analysis of the continuous variables. The Kolmogorov-Smirnov test was applied to verify the normal distribution of the quantitative variables. In the bivariate analysis, quantitative variables were compared using Student's t test for independent variables and the chi-square test for qualitative variables. Then, we performed a multivariate analysis based on a binary

logistic regression model. Goodness-of-fit was calculated using the Hosmer-Lemeshow test. Finally, Receiver operating characteristic (ROC) curves were used for discriminant analysis.

All data were collected and analyzed using SPSS v.20 software, with a p value of less than 0.05 deemed as statistically as significant.

RESULTS

Of the 56 patients included in the study, 8 (14.3%) were men and 48 (85.7%) were women. The mean age was 72.6 ± 1.2 years. The fracture was spontaneous or after exertion in 6 cases (10.7%), and after falling to the ground from a standing position in 50 cases (89.3%). Figure 3 shows the number of fractures identified and the vertebral endplates and walls affected. Both endplates were fractured in 6 cases (10.7%) and none of the endplates was involved in only 1 case (1.8%). Both anterior and posterior walls were fractured in 21 cases (37.5%), and none of the walls were involved in 4 cases (7.1%). Lateral wall fracture was absent in 12 cases (21.4%). At the time of initial diagnosis, 25 fractures (44.6%) showed an intravertebral cleft.

Twenty-five OVFs (44.6%) developed vertebral collapse on follow-up. Vertebral collapse was associated with fracture of the inferior (3/3 cases, 100%; p = 0.040) and both endplates (5/6 cases, 83.3%; p = 0.044).

Tables 1 and 2 show the quantitative and qualitative variables at the time of initial diagnosis of the patients, respectively.

Numerical variables associated with vertebral collapse were older age, initial percentage of posterior vertebral height (PVH), and area loss on standing CR, low density of the non-fractured vertebral body, hight density of the fractured body, and the ratio between the density of the fractured body and the aorta. The density ratio of the fractured versus non-fractured vertebral body, as well as the difference between the percentage of vertebral area and PVH loss on CR versus CT were also significantly associated with vertebral collapse.

No fracture classification was predictive of vertebral collapse.

The results of logistic regression are shown in Table 3. The model showed that age, fractured/non-fractured body density ratio, and the difference in the percentage of PVH loss between CR and CT were positively correlated with the development of vertebral collapse (Figure 4). This model correctly classified 89.8% of the cases and predicted collapse with a sensitivity of 79% and a specificity of 81% (Figure 5).

The discriminative power to correctly classify the collapse of OVFs was 72.5% for age, 75.5%

for the fractured/non-fractured body density ratio, and 67.8% for the difference of percentage loss of PVH on CR versus CT. For predicting vertebral collapse, a cut-off value of 72.5 years showed a sensitivity of 72% and specificity of 58.1%, a ratio >2 for the fractured/non-fractured body density ratio showed a sensitivity of 40% and specificity of 90.3%, and a cut-off value of 6% for the difference in the percentage of PVH loss between CR and CT showed a sensitivity of 40% and specificity of 87.1%.

DISCUSSION

Vertebral fractures are the most common type of osteoporotic fractures. Inappropriate or insufficient treatment of OVFs may lead to progressive collapse of the vertebral body with increased kyphotic deformity, which has been associated with impaired quality of life and even higher mortality rates due to cardiopulmonary complications [25].

Several classification systems can be used to guide the management of OVFs. The AO Spine classification system was developed to evaluate traumatic fractures and considers osteoporosis as a modifier that may preclude surgery due to poor bone quality [22, 23]. Therefore, specific classifications for OVFs may be considered more appropriate in this setting if they can provide useful guidance to choose the correct treatment, avoiding the progressive sintering of the vertebral body and clinically meaningful kyphotic deformity. Genant's classification was devised for epidemiological purposes, with no prognostic implications [14]. Sugita's morphological classification (mainly the projecting, swelling and bow-shaped fracture types) was reported to have predictive value for vertebral collapse [15]. However, this has not been supported in posterior works [13, 24], including ours. Although a recent study reported that the classification proposed by the German Society for Orthopaedics and Trauma is useful for selecting patients for kyphoplasty [18], there is no current evidence demonstrating its predictive value for vertebral collapse, and this has not been supported in our present study either.

According to the AO Spine classification system, 5 out 6 A4 fractures (fracture of posterior wall and both endplates) collapsed in our series, and therefore would have required interventional treatment (percutaneous or open) shortly after diagnosis instead of conservative management. Nevertheless, the rate of collapse in A3 fractures (fracture of the posterior wall with only one fractured endplate) was found to be only slightly higher than in A1 fractures (42.1% versus 35.5%, respectively). This emphasizes the difficulty of choosing an appropriate and standardized treatment in osteoporotic burst fractures (i.e., A3 and A4). In a previous survey, 96.2% of A3 factures were operated in Germany compared to 41.2% in the Netherlands [25]. Another study

reported that 50% of A3/A4 fractures were operated due to progressive kyphosis and persistent pain [26].

Therefore, factors other than the type of fracture need to be considered to standardize the most appropriate treatment. Fracture of the inferior endplate was found in our work to be associated with vertebral collapse in the bivariate analysis, with high specificity. Nevertheless, is an infrequent finding in traumatic (1.5%) and osteoporotic fractures (9.8-17.4%) [27]. In our series, it was present only in 9 out 56 cases (16.1%), precluding its inclusion in the multivariate analysis.

Imaging plays an important role in defining factors predictive of vertebral non-union and collapse. Most of these factors have been studied in MRI and include mid-portion type fracture [24], middle-column injury, and confined high-intensity or diffuse low-intensity areas in the fractured vertebra on T2-weighted images [13, 28]. However, as our work demonstrates, information predictive of vertebral collapse can also be obtained from measurements on standing CR and supine CT. Differences in measurements between both techniques may be explained by the fact that vertebral height and area tend to recover from compression in supine position, especially in the most unstable vertebral fractures. These differences, mainly in PVH, showed predictive value for vertebral collapse in our study.

Previous studies have suggested that pseudoarthrosis, manifested as the presence of intravertebral clefts or cysts, are risk factors to consider as they indicate lack of consolidation with probable instability [29, 30]. Dynamic instability and consequent hypermobility at the fracture site can lead to collapse and retropulsion of the bone fragments into the spinal canal [31, 32]. This factor was not statistically significant in our study despite the higher percentage of collapse in fractures with intravertebral cleft or cyst (53.8% versus 33.3%). Other authors have noted that this instability may be demonstrated by determining the differences of local kyphosis in standing and supine spine images [33, 34]. In our work, the difference in the percentage of PVH loss between standing CR and supine CT reached statistical significance and should therefore be considered in the decision-making process.

Of great interest was the association between the low density of the non-fractured vertebra as well as the fractured/non-fractured vertebral body density ratio with vertebral collapse. Previous studies have reported low vertebral body density values in patients with OVFs [12, 35], in agreement with our findings. However, the novelty of our work lies in demonstrating that an increased ratio density of the fractured vertebral body versus the non-fractured osteoporotic vertebral body is a risk factor for vertebral collapse, with a ratio of 2 showing 90.3 of specificity. We hypothesize that this is the homologous finding on CT of the low signal intensity of fractured vertebra on MRI described in previous works as a predictive sign of vertebral collapse [13, 28], resulting from impaction of the trabeculae.

Finally, patient age also needs to be considered in the decision-making process. The relationship between age with osteoporosis and low bone density on CT has been clearly established in the literature [36]. In our work, age over 72.5 years showed the highest discriminative power value for predicting vertebral collapse. Therefore, older patients with other factors predictive of vertebral collapse on CT and CR should be selected for early non-conservative treatment.

The main limitations of our study are its retrospective, single-centre nature, and the limited sample size, which calls for further studies to verify our findings.

CONCLUSION

Our work strongly suggests that there is an increased risk of vertebral collapse in fractures with differences of more than 6% in PVH loss between standing CR and supine CT, a CT density ratio between the fractured and non-fractured vertebral body >2, and age over 72.5 years. Accordingly, non-conservative management (i.e., surgery or percutaneous augmentation) of OVFs must be considered when these findings are present.

REFERENCES

1. Diacinti D, Guglielmi G. How to define an osteoporotic vertebral fracture? Quant Imaging Med Surg 2019;9(9):1485-1494. doi: 10.21037/qims.2019.09.10

2. LeBoff MS, Greenspan SL, Insogna KL, Lewiecki EM, Saag KG, Singer AJ, Siris ES. The clinician's guide to prevention and treatment of osteoporosis. Osteoporos Int. 2022 Oct;33(10):2049-2102. doi: 10.1007/s00198-021-05900-y

3. Wáng YXJ, Santiago FR, Deng M, Nogueira-Barbosa MH (2017) Identifying osteoporotic vertebral endplate and cortex fractures. Quant Imaging Med Surg 7:555–591. https://doi.org/10.21037/QIMS.2017.10.05

4. Le Huec JC, Thompson W, Mohsinaly Y, et al (2019) Sagittal balance of the spine. Eur Spine J 28:1889–1905. https://doi.org/10.1007/S00586-019-06083-1

5. Oei, L., Rivadeneira, F., Ly, F. et al. Review of radiological scoring methods of osteoporotic vertebral fractures for clinical and research settings. Eur Radiol 23, 476–486 (2013). https://doi.org/10.1007/s00330-012-2622-z

6. Karul M, Bannas P, Schoennagel BP, Hoffmann A, Wedegaertner U, Adam G, Yamamura J. Fractures of the thoracic spine in patients with minor trauma: comparison of diagnostic accuracy and dose of biplane radiography and MDCT. Eur J Radiol. 2013 Aug;82(8):1273-7. doi: 10.1016/j.ejrad.2013.01.016.

7. Jung CW, Lee J, Ham DW, Kang H, Chang DG, Kim YB, Ahn YJ, Shim JH, Song KS. Forward Bending in Supine Test: Diagnostic Accuracy for Acute Vertebral Fragility Fracture. Healthcare (Basel). 2022 Jun 29;10(7):1215. doi: 10.3390/healthcare10071215.

8. Lentle B, Trollip J, Lian K (2016) The Radiology of Osteoporotic Vertebral Fractures Redux. J Clin Densitom 19:40–47. https://doi.org/10.1016/J.JOCD.2015.08.009

9. Pickhardt PJ, Lee LJ, Muñoz Del Rio A, et al (2011) Simultaneous screening for osteoporosis at CT colonography: bone mineral density assessment using MDCT attenuation techniques compared with the DXA reference standard. J Bone Miner Res 26:2194–2203. https://doi.org/10.1002/JBMR.428

10. Pickhardt PJ, Pooler BD, Lauder T, et al (2013) Opportunistic screening for osteoporosis using abdominal computed tomography scans obtained for other indications. Ann Intern Med 158:588–595. https://doi.org/10.7326/0003-4819-158-8-201304160-00003

11. Schreiber JJ, Anderson PA, Rosas HG, Buchholz AL, Au AG. Hounsfield units for assessing bone mineral density and strength: a tool for osteoporosis management. J Bone Joint Surg Am. 2011 Jun 1;93(11):1057-63. doi: 10.2106/JBJS.J.00160. PMID: 21655899.

12. Zou D, Ye K, Tian Y, et al (2020) Characteristics of vertebral CT Hounsfield units in elderly patients with acute vertebral fragility fractures. Eur Spine J 29:1092–1097. https://doi.org/10.1007/S00586-020-06363-1

13. Tsujio T, Nakamura H, Terai H, et al (2011) Characteristic radiographic or magnetic resonance images of fresh osteoporotic vertebral fractures predicting potential risk for nonunion: a prospective multicenter study. Spine (Phila Pa 1976) 36:1229–1235. https://doi.org/10.1097/BRS.0B013E3181F29E8D

14. Genant HK, Wu CY, van Kuijk C, Nevitt MC (1993) Vertebral fracture assessment using a semiquantitative technique. J Bone Miner Res 8:1137–1148. https://doi.org/10.1002/JBMR.5650080915

15. Sugita M, Watanabe N, Mikami Y, et al (2005) Classification of vertebral compression fractures in the osteoporotic spine. J Spinal Disord Tech 18:376–381. https://doi.org/10.1097/01.BSD.0000168716.23440.61

16. Schnake KJ, Blattert TR, Hahn P, et al (2018) Classification of Osteoporotic Thoracolumbar Spine Fractures: Recommendations of the Spine Section of the German Society for Orthopaedics and Trauma (DGOU). Glob spine J 8:46S-49S. https://doi.org/10.1177/2192568217717972

17. Blattert TR, Schnake KJ, Gonschorek O, et al (2018) Nonsurgical and Surgical Management of Osteoporotic Vertebral Body Fractures: Recommendations of the Spine Section of the German Society for Orthopaedics and Trauma (DGOU). Glob spine J 8:50S-55S. https://doi.org/10.1177/2192568217745823

18. Palmowski Y, Balmer S, Hu Z, et al (2022) Relationship Between the OF Classification and Radiological Outcome of Osteoporotic Vertebral Fractures After Kyphoplasty. Glob spine J 12:646–653. https://doi.org/10.1177/2192568220964051

19. Yaman O, Zileli M, Şentürk S, et al (2021) Kyphosis After Thoracolumbar Spine Fractures: WFNS Spine Committee Recommendations. Neurospine 18:681–692. https://doi.org/10.14245/NS.2142340.170

20. Curfs I, Grimm B, Linde M van der, et al (2016) Radiological Prediction of Posttraumatic Kyphosis After Thoracolumbar Fracture. Open Orthop J 10:135–142. https://doi.org/10.2174/1874325001610010135

21. Viswanathan VK, Shetty AP, Sindhiya N, et al (2022) Prospective Study to Identify the Clinical and Radiologic Factors Predictive of Pseudarthrosis Development in Patients with Osteoporotic Vertebral Fractures. World Neurosurg 167:e350–e359. https://doi.org/10.1016/J.WNEU.2022.08.011

22. Inose H, Kato T, Ichimura S, Nakamura H, Hoshino M, Togawa D, Hirano T, Tokuhashi Y, Ohba T, Haro H, Tsuji T, Sato K, Sasao Y, Takahata M, Otani K, Momoshima S, Yuasa M, Hirai T, Yoshii T, Okawa A. Risk Factors of Nonunion After Acute Osteoporotic Vertebral Fractures: A Prospective Multicenter Cohort Study. Spine (Phila Pa 1976). 2020 Jul 1;45(13):895-902. doi: 10.1097/BRS.0000000000003413.

23. Wakao N, Sakai Y, Watanabe T, Osada N, Sugiura T, Iida H, Ozawa Y, Murotani K. Spinal pseudoarthrosis following osteoporotic vertebral fracture: prevalence, risk factors, and influence on patients' activities of daily living 1 year after injury. Arch Osteoporos. 2023 Mar 29;18(1):45. doi: 10.1007/s11657-023-01236-8

24. von Elm E, Altman DG, Egger M, et al (2008) The Strengthening the Reporting of Observational Studies in Epidemiology (STROBE) statement: guidelines for reporting observational studies. J Clin Epidemiol 61:344–349. https://doi.org/10.1016/J.JCLINEPI.2007.11.008

25. Hinde K, Maingard J, Hirsch JA, et al (2020) Mortality Outcomes of Vertebral Augmentation (Vertebroplasty and/or Balloon Kyphoplasty) for Osteoporotic Vertebral Compression Fractures: A Systematic Review and Meta-Analysis. Radiology 295:96–103. https://doi.org/10.1148/RADIOL.2020191294

22. Vaccaro AR, Oner C, Kepler CK, et al (2013) AOSpine thoracolumbar spine injury classification system: fracture description, neurological status, and key modifiers. Spine (Phila Pa 1976) 38:2028–2037. https://doi.org/10.1097/BRS.0B013E3182A8A381

23. Santiago FR, Muñoz PT, Sánchez EM, et al (2016) Classifying thoracolumbar fractures: role of quantitative imaging. Quant Imaging Med Surg 6:772–784. https://doi.org/10.21037/QIMS.2016.12.04

24. Ha KY, Kim YH (2013) Risk factors affecting progressive collapse of acute osteoporotic spinal fractures. Osteoporos Int 24:1207–1213. https://doi.org/10.1007/S00198-012-2065-Z

25. Pishnamaz M, Curfs I, Balosu S, et al (2015) Two-Nation Comparison of Classification and Treatment of Thoracolumbar Fractures: An Internet-Based Multicenter Study Among Spine Surgeons. Spine (Phila Pa 1976) 40:1749–1756. https://doi.org/10.1097/BRS.0000000000001143

26. Joaquim AF, Daubs MD, Lawrence BD, et al (2013) Retrospective evaluation of the validity of the Thoracolumbar Injury Classification System in 458 consecutively treated patients. Spine J 13:1760–1765. https://doi.org/10.1016/J.SPINEE.2013.03.014

27. Wáng YXJ. An update of our understanding of radiographic diagnostics for prevalent osteoporotic vertebral fracture in elderly women. Quant Imaging Med Surg. 2022 Jul;12(7):3495-3514. doi: 10.21037/qims-22-360. PMID: 35782246; PMCID: PMC9246755

28. Kanchiku T, Imajo Y, Suzuki H, et al (2014) Usefulness of an early MRI-based classification system for predicting vertebral collapse and pseudoarthrosis after osteoporotic vertebral fractures. J Spinal Disord Tech 27:. https://doi.org/10.1097/BSD.0B013E318292B509

29. Kim DY, Lee SH, Jang JS, et al (2004) Intravertebral vacuum phenomenon in osteoporotic compression fracture: report of 67 cases with quantitative evaluation of intravertebral instability. J Neurosurg 100:24–31. https://doi.org/10.3171/SPI.2004.100.1.0024

30. Peh WCG, Gelbart MS, Gilula LA, Peck DD (2003) Percutaneous vertebroplasty: treatment of painful vertebral compression fractures with intraosseous vacuum phenomena. AJR Am J Roentgenol 180:1411–1417. https://doi.org/10.2214/AJR.180.5.1801411

31. Kaneda K, Asano S, Hashimoto T, et al (1992) The treatment of osteoporotic-posttraumatic vertebral collapse using the Kaneda device and a bioactive ceramic vertebral prosthesis. Spine (Phila Pa 1976) 17:295–303. https://doi.org/10.1097/00007632-199208001-00015

32. Baba H, Maezawa Y, Kamitani K, et al (1995) Osteoporotic vertebral collapse with late neurological complications. Paraplegia 33:281–289. https://doi.org/10.1038/SC.1995.64

33. Cho JH, Shin SI, Lee JH, et al (2013) Usefulness of prone cross-table lateral radiographs in vertebral compression fractures. Clin Orthop Surg 5:195–201. https://doi.org/10.4055/CIOS.2013.5.3.195

34. McKiernan F, Jensen R, Faciszewski T (2003) The dynamic mobility of vertebral compression fractures. J Bone Miner Res 18:24–29. https://doi.org/10.1359/JBMR.2003.18.1.24

35. Lee SJ, Binkley N, Lubner MG, et al (2016) Opportunistic screening for osteoporosis using the sagittal reconstruction from routine abdominal CT for combined assessment of vertebral fractures and density. Osteoporos Int 27:1131–1136. https://doi.org/10.1007/S00198-015-3318-4

36. Emohare O, Cagan A, Morgan R, et al (2014) The use of computed tomography attenuation to evaluate osteoporosis following acute fractures of the thoracic and lumbar vertebra. Geriatr Orthop Surg Rehabil 5:50–55. https://doi.org/10.1177/2151458514525042

TABLES

	MEAN ± SEM	COLLAPSE	NO COLLAPSE	SIGNIFICANCE
AGE	72.6 ± 1.2	76.6 ± 1.5	69.3 ± 1.6	p = 0.003
HU AORTA	39.3 ± 0.6	38.7 ± 0.9	39.9 ± 0.9	NS
HU FRACTURED VERTEBRA	125.4 ± 5.6	138.9 ± 10.0	114.4 ± 5.5	P=0.039
HU NON-FRACTURED VERTEBRA	87.4 ± 4.6	76.4 ± 6.0	96.2 ± 6.4	p = 0.031
HU RATIO FRACTURED VERTEBRA/AORTA	3.1 ± 0.1	3.7 ± 0.3	2.9 ± 0.1	P=0.27
HU RATIO NON-FRACTURED V/AORTA	2.3 ± 0.1	2.0 ± 0.1	2.4 ± 0.1	NS
HU RATIO FRACTURED V/ NON-FRACTURED V	1.7 ± 0.1	2.1 ± 0.3	1.3 ± 0.9	p = 0.022
AREA LOSS (CR) (%)	21.1 ± 1.3	24.1 ± 2.4	18.6 ± 1.3	p = 0.048
AVH LOSS (CR) (%)	23.9 ± 1.6	26.5 ± 2.9	21.8 ± 1.5	NS
MVH LOSS (CR) (%)	26.7 ± 1.3	29.1 ± 2.5	24.7 ± 1.3	NS
PVH LOSS (CR) (%)	7.9 ± 1.1	10.8± 2.0	5.6. ± 0.9	p = 0.023
LOCAL KYPHOSIS (CR)	10.8 ± 0.7	11.1 ± 0.9	10.6 ± 0.9	NS
AREA LOSS (CT) (%)	13.3 ± 1.2	13.5 ± 2.1	13.0 ± 1.5	NS
LOSS OF AVH (CT) (%)	15.8 ± 1.2	16.5 ± 1.9	15.2 ± 1.6	NS
LOSS OF MVH (CT) (%)	21.6 ± 1.3	22.1 ± 2.0	21.2 ± 1.7	NS
LOSS OF PVH (CT) (%)	5.2 ± 0.6	5.5 ± 1.1	5.0 ± 0.7	NS
LOCAL KYPHOSIS (CT)	6.8 ± 0.6	6.6 ± 0.7	7.0 ± 0.9	NS
D. AREA LOSS (CR-CT) (%)	7.8 ± 1.1	10.6 ± 2.0	5.5 ± 1.1	p = 0.037
D. AVH LOSS (CR-CT) (%)	8.1 ± 1.2	10.0 ± 2.2	6.6 ± 1.3	NS
D. MVH LOSS (CR-CT) (%)	5.1 ± 1.0	7.0 ± 1.7	3.5 ± 1.1	NS
D. PVH LOSS (CR-CT) (%)	2.7 ± 0.9	5.3 ± 1.4	0.6 ± 0.9	p = 0.005
D. LOCAL KYPHOSIS (CR-CT)	4.0 ± 0.5	4.4 ± 0.8	3.6 ± 0.6	NS

Table 1. Association of numeric variables with vertebral collapse. Values are expressed as mean ± standard error of the mean (SEM). HU, Hounsfield units. V, vertebra. NS, not significant. AVH, anterior vertebral height. MVH, middle vertebral height. PVH, posterior vertebral height. D, Difference.

	INITIAL		COLLAPSE	SIGNIFICANCE
CLEFT	NO	31 (55.4%)	11 (35.5%)	NS
	YES	25 (44.6%)	14 (56.0%)	
FRACTURED VERTEBRA	T7	2 (3.6%)	1 (50%)	NS
	T11	4 (7.1%)	2 (50%)	
	T12	9 (16.1%)	4 (44.4%)	
	L1	27 (48.2%)	10 (37.0%)	
	L2	8 (14.3%)	3 (37.5%)	
	L3	2 (3.6%)	0 (0%)	
	L4	4 (7.1%)	2 (50%)	
AO CLASSIFICATION	A1	32 (57.1%)	11 (34.4%)	NS
	A3	18 (32.1%)	8 (44.4%)	
	A4	6 (10.7%)	5 (83.3%)	
GENANT QUANTITATIVE	0	27 (48.2%)	11 (40.7%)	NS
	1	13 (23.2%)	6 (46.2%)	
	2	16 (28.6%)	8 (50%)	
GENANT QUALITATIVE	NORMAL	1 (1.8%)	0 (0%)	NS
	BICONCAVE	28 (50.0%)	14 (50.0%)	
	WEDGE	26 (46.4%)	10 (38.5%)	
	CRUSH	1 (1.8%)	1 (100%)	

DGOU CLASSIFICATION	OF1 OF2 OF3	3 (5.4%) 41 (73.2%) 12 (21.4%)	1 (33.3%) 16 (39.0%) 8 (66.7%)	NS
SUGITA CLASSIFICATION	SWELLED BOWSHAPED PROJECTING CONCAVE DENTED	9 (16.1%) 33 (58.9%) 8 (14.3%) 3 (5.4%) 3 (5.4%)	5 (55.6%) 12 (36.4%) 5 (62.5%) 2 (66.7%) 1 (33.3%)	NS
ENPLATE FRACTURE	NO SUPERIOR INFERIOR BOTH	1 (1.8%) 46 (82.1%) 3 (5.4%) 6 (10.7%)	0 (0%) 17 (37.0%) 3 (100%) 5 (83.3%)	p = 0.026
SUPERIOR ENDPLATE	NO YES	4 (7.1%) 52 (92.9%)	3 (75.0%) 22 (42.3%)	NS
INFERIOR ENDPLATE	NO YES	47 (83.9%) 9 (16.1%)	17 (36.2%) 8 (88.9%)	p = 0.040
BOTH ENDPLATES	NO YES	50 (89.3%) 6 (10.7%)	20 (40%) 5 (83.3%)	p = 0.044
ANTERIOR/POSTERIOR WALL	NO ANTERIOR POSTERIOR BOTH	4 (7.1%) 28 (50%) 3 (5.4%) 21 (37.5%)	1 (25%) 11 (39.3%) 2 (66.7%) 11 (52.4%)	NS
ANTERIOR WALL	NO YES	7 (12.5%) 49 (87.5%)	3 (42.9%) 22 (44.9%)	NS
POSTERIOR WALL	NO YES	32 (57.1%) 24 (42.9%)	12 (37.5%) 13 (54.2%)	NS
ANTERIOR AND POSTERIOR WALLS	NO YES	35 (62.5%) 21 (37.5%)	14 (40%) 11 (52.4%)	NS
LATERAL WALLS	NO UNILATERAL BILATERAL	12 (21.4%) 13 (23.2%) 31 (55.4%)	5 (41.7%) 4 (30.8%) 16 (51.6%)	NS

Table 2. Association of categorical variables with vertebral collapse. Comparison is made between the first column (initial values) and the development or not of vertebral collapse. V, vertebra. NA, not applicable. NS, not significant. DGOU, German Society for Orthopaedics and Trauma.

VARIABLE	B	SIGNIFICANCE	OR	95% CI
AGE	0.114	p = 0.014	1.122	1.02 - 1.22
HU FRACTURED/ NON FRACTURED VERTEBRA	2.415	p = 0.006	11.18	1.97 - 63.40
DIFFERENCE PVH LOSS CR-CT (%)	0.303	p = 0.003	1.306	1.10 - 1.65

Table 3. Multivariate analysis. Results of logistic regression. PVH, posterior vertebral height. CR, conventional radiography. CT, computed tomography. OR, odds ratio. CI, confidence interval. HU. Hounsfield units.

VARIABLE	AUC	CUT-OFF VALUE	SENSITIVITY	SPECIFICITY
AGE	0.725	72.5	72%	58.1%
HU RATIO FRACTURED/ NON FRACTURE VB	0.783	2	40%	90.3%
DIFFERENCE PVH LOSS CR-CT (%)	0.678	6%	40%	87.1%
ALL VARIABLES	0.898	NA	79%	81 %

Table 4. Discriminative power to predict vertebral fracture collapse with the selected variables. AVH, anterior vertebral height. CR, conventional radiography. CT, computed tomography. NA, not applicable.

FIGURES

Figure 1. Measurements on computed tomography (CT) and conventional radiography (CR). A. Example of area measurement on CT. B. Example of measurement of the anterior, middle, and posterior vertebral height on standing CR. C. Example of local kyphosis measurement on CR. D. Example of local kyphosis measurement on CT.

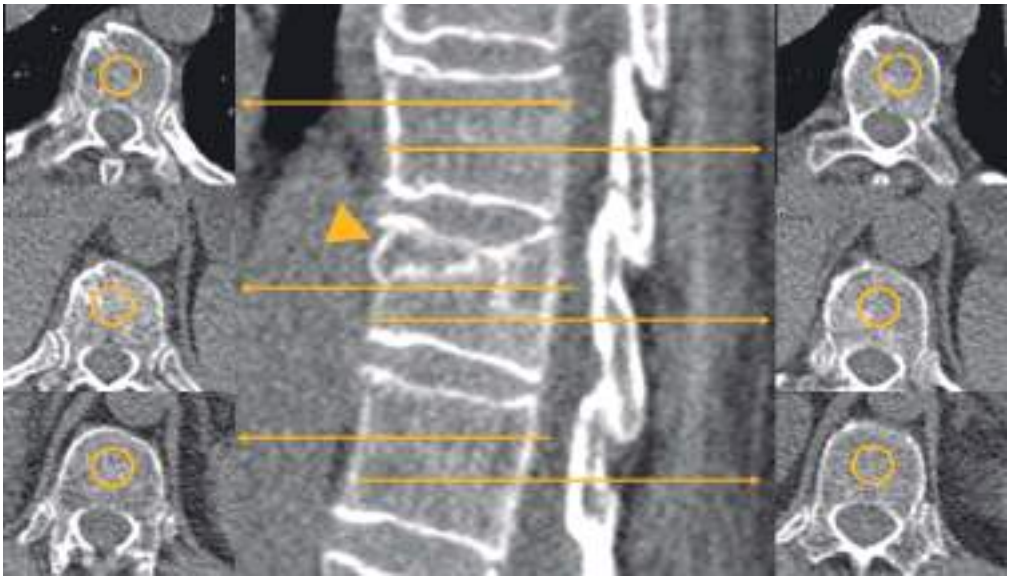

Figure 2. Example of HU measurements in the fractured and non-fractured vertebrae. Note that the intravertebral cleft/cyst was avoided for measurement in the fractured vertebral body (arrowhead).

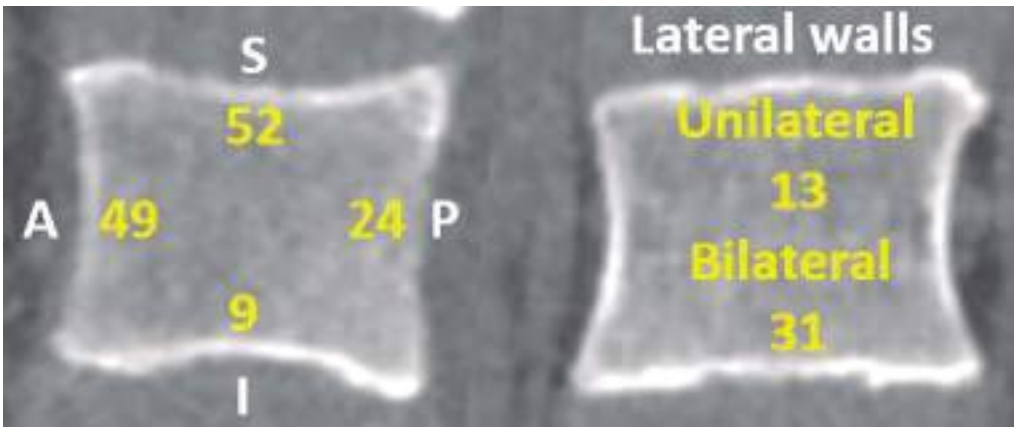

Figure 3. Frequency of vertebral endplates and walls involvement in our series. A. Sagittal CT image. B. Coronal CT image. A, Anterior vertebral wall. P, Posterior vertebral wall. S, Superior endplate. I, Inferior endplate.

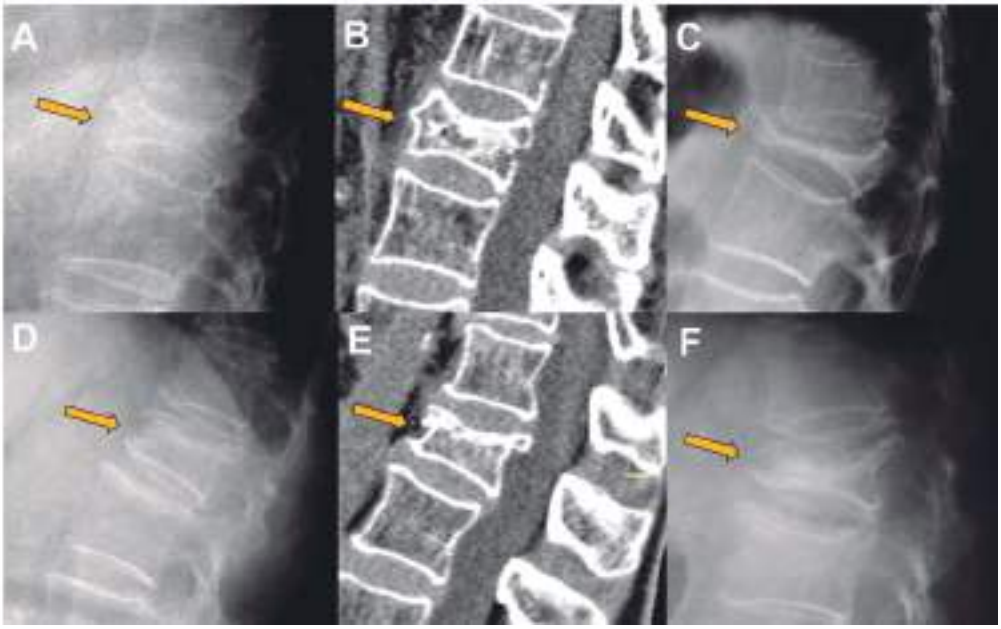

Figure 4. Two cases of vertebral collapse. Case 1 :Fracture of the L1 vertebral body (arrow) in a 74-year-old patient who fell from a standing position. A. Standing radiography showed 16% posterior vertebra height (PVH) loss compared to CT (B). The CT density ratio between the fractured vertebral body versus the non-fractured vertebra was 2.2. C Follow-up radiography revealed collapse of the vertebral body. Case 2: Fracture of the T12 vertebral body (arrow) in a 73-year-old patient. D. Standing radiography showed 6% PVH loss compared to CT (E). The CT density ratio between the fractured vertebral body versus the non-fractured vertebra was 3.2. F. Follow-up radiography revealed collapse of the vertebral body.

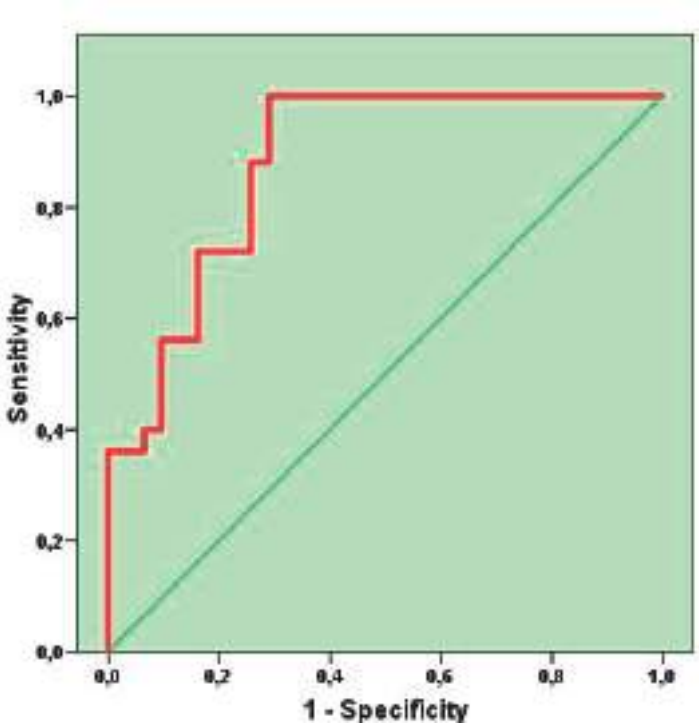

Figure 5. Receiver operating characteristic (ROC) curve of the selected model to predict vertebral collapse. Area under the curve of 89.8%.

TRABAJO 7: PERCUTANEOUS VERTEBROPLASTY VERSUS CONSERVATIVE TREATMENT AND PLACEBO IN OSTEOPOROTIC VERTEBRAL FRACTURES: META-ANALYSIS AND CRITICAL REVIEW OF THE LITERATURE.

Láinez Ramos-Bossini AJ, López Zúñiga D, Ruiz Santiago F. Percutaneous vertebroplasty versus conservative treatment and placebo in osteoporotic vertebral fractures: meta-analysis and critical review of the literature. Eur Radiol. 2021;31(11):8542-8553. doi:10.1007/s00330-021-08018-1. FI: 7,034. Q1 (T1).

Se trata de una revisión sistemática y meta-análisis que cubre el objetivo 3.

European Radiology (2021) 31:8542–8553
https://doi.org/10.1007/s00330-021-08018-1

MUSCULOSKELETAL

Percutaneous vertebroplasty versus conservative treatment and placebo in osteoporotic vertebral fractures: meta-analysis and critical review of the literature

A. J. Láinez Ramos-Bossini[1,2,3] · D. López Zúñiga[1] · F. Ruiz Santiago[1,2]

Received: 30 December 2020 / Revised: 23 February 2021 / Accepted: 27 April 2021 / Published online: 7 May 2021

Abstract

Objectives To assess the current evidence regarding the efficacy of percutaneous vertebroplasty (PVP) over conservative treatment (CT) and placebo in osteoporotic vertebral fractures (OVFs) by performing a meta-analysis of randomized controlled trials (RCTs).

Materials and methods A systematic search was conducted on PubMed, EMBASE, and Cochrane databases. The main outcomes were pain relief, improvement of functional disability, and quality of life at different time points: short-term (1–2 weeks), medium-term (1–3 months), and long-term (≥ 6 months). Subgroup analyses based on time from fracture onset and sham procedure were also performed.

Results A total of 14 RCTs were included in the meta-analysis. PVP showed significant benefits over CT in all outcomes, but slight-to-none clear differences over placebo. Subgroup analyses revealed that PVP performed in fractures < 6 weeks provided superior short-term pain relief than the control group ($p = .02$), and better quality of life in the medium-term ($p = .03$) and long-term ($p = .006$). Placebo based on infiltrating the skin alone was significantly inferior to PVP at most time points in all outcomes, but no significant differences between PVP and placebo were found when the sham procedure consisted of infiltrating both the skin and periosteum.

Conclusions PVP showed significant advantages over CT in terms of efficacy, but benefits were more limited when compared to placebo. In addition, benefits of PVP are more prominent in recent OVFs. Differences in the sham procedure or criteria regarding patient's selection/allocation seem to be the main causes of disparity in previous RCTs.

Key Points

- *Previous RCTs showed significant advantages of PVP over CT in terms of efficacy, but benefits were more limited when compared to placebo.*
- *Differences in patient allocation or in the sham procedure might explain the lack of benefits of PVP versus placebo found in previous RCTs.*
- *Despite controversial opinions, PVP should be offered to patients with OVFs as an alternative option to conservative treatment.*

Keywords Osteoporosis · Vertebral fracture · Percutaneous vertebroplasty · Conservative treatment · Placebo

✉ A. J. Láinez Ramos-Bossini
ajbossini@ugr.es

[1] Department of Radiology, Virgen de las Nieves University Hospital, Fuerzas Armadas Av. 2, 18014 Granada, Spain

[2] Department of Radiology, Faculty of Medicine, University of Granada, Granada, Spain

[3] Programme in Clinical Medicine and Public Health, University of Granada, Granada, Spain

Abbreviations

CT	Conservative treatment
OVF	Osteoporotic vertebral fracture
PVP	Percutaneous vertebroplasty
RCT	Randomized controlled trial

Introduction

There is extensive literature suggesting that percutaneous vertebroplasty (PVP) relieves pain to a greater extent than

Eur Radiol (2021) 31:8542–8553

CT (e.g., oral analgesics, rehabilitation exercise, anti-osteoporotic drugs, spinal orthotics, and multimodal therapy), showing better results in terms of pain relief, functional disability, and quality of life [1–3]. Nevertheless, the results of studies comparing PVP versus placebo are not straightforward [4, 5]. This critical review and meta-analysis aims to examine previous randomized controlled trials (RCTs) comparing PVP versus placebo or CT and to explain the potential causes of discrepancies. These may include the time elapsed between the onset of the fracture, and the method used as placebo, which might represent a form of treatment instead. We also theorize that one of the main problems of previous RCTs is to consider all OVFs similar in the randomized allocation. Our hypothesis is that all OVFs, like traumatic fractures, are not equal and, therefore, comparisons of different treatments for OVFs should consider the type of fracture as a co-variate, avoiding to draw general conclusions that may hamper the use of the most appropriate treatment.

Materials and methods

Eligibility criteria

The design of the meta-analysis and the selection criteria were based on the PICO search strategy. The population was formed by patients with symptomatic OVF susceptible of PVP or CT; the intervention was PVP; the comparators were CT or placebo; and the outcomes included pain relief, improvement in functional disability, and improvement in quality of life. The Preferred Reporting Items for Systematic Reviews and Meta-Analyses (PRISMA) guidelines were followed.

Accordingly, the inclusion criteria were the following: published RCTs on PVP versus CT or placebo for OVF which included quantitative results on at least one of the primary outcomes on both arms. The exclusion criteria were studies with vertebral fractures of non-osteoporotic etiology, quasi-experimental designs, letters, abstracts, or conference proceedings.

Information sources and search strategy

Two authors (A.J.L.R.B. and D.L.Z.) searched the PubMed, EMBASE, and Cochrane Central Register of Controlled Trials databases. Different search strategies were used to optimize the number of relevant outcomes, including keywords such as “osteoporosis”, “spine fracture”, and “vertebroplasty” (Supplementary Files 1–3). No date or language restrictions were established. The search was updated to July 31, 2020.

All titles and abstracts of interest were screened and those which did not meet the eligibility criteria were excluded. Subsequently, the screened studies were fully read to assess whether they met all eligibility criteria. Figure 1 shows the flow diagram of the study.

Variables and instruments

The variables of the meta-analysis can be classified based on whether they are related to the primary outcomes or to patient selection/allocation.

Outcomes related to treatment effect

As mentioned above, the primary outcomes were the following:

1. Pain relief, measured by the Visual Analogue Scale (VAS) or other quantitative scales (e.g., Numeric Rating Scale, NRS).
2. Improvement in functional disability measured by the Roland-Morris Disability Questionnaire (RMDQ) [6] and the Oswestry Disability Index (ODI) [7].
3. Improvement in quality of life assessed by the Quality of Life Questionnaire of the European Foundation for Osteoporosis (QUALEFFO) [8]. Other questionnaires for this outcome were excluded due to lower specificity in this population.

These variables were grouped according to the time at which they were measured as follows: short-term (1–4 weeks), medium-term (1–6 months), and long-term (≥ 6 months).

Variables related to patient selection or allocation

We performed subgroup analyses for the next two variables:

1. Time from fracture onset, dichotomized in trials with OVFs ≤ 6 weeks and > 6 weeks.
2. Sham procedure. Within the placebo groups, we stratified groups based on the infiltration of subcutaneous tissue only or infiltration of skin and vertebral pedicle/lamina.

Data extraction

Two authors (A.J.L.R.B. and D.L.Z.) independently extracted the data from the selected articles and the third author (F.R.S.) reviewed the data and solved any discrepancies. If there were several publications on the same RCT that met these criteria, those with data covering the longest follow-up period were selected. All data were stored using a spreadsheet designed for such purpose and Review Manager 5.3 for Windows. Data that were only available in graphs were manually extracted

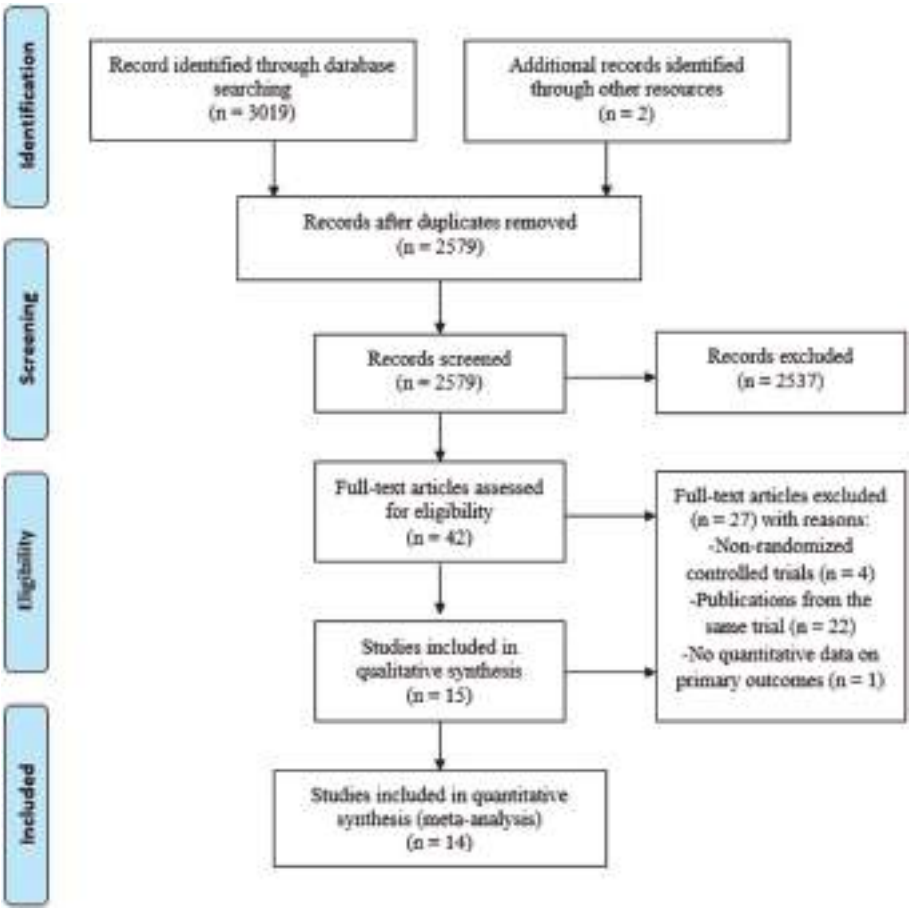

Fig. 1 Flow diagram of the study

using the free version of Plot Digitizer (http://plotdigitizer.sourceforge.net/).

Risk of bias and publication bias

The Cochrane Risk of Bias Tool v. 2 [9] was used to systematically assess the existence of potential biases. For each RCT, two authors (A.J.L.R.B. and D.L.Z.) classified the risk of bias as low, intermediate, or high. In case of discrepancy, the third author was consulted to reach consensus. Absence of blinding regarding the radiological detection of OVFs was not deemed to be sufficient reason for labelling a study as having a high risk of detection bias because blinding was prevented in PVP patients and this variable did not affect the primary outcomes. The publication bias was analyzed by means of funnel plots.

Statistical analysis

If the same instrument of measure was used (e.g., QUALEFFO questionnaire), quantitative variables were expressed as mean differences (MDs) with 95% confidence intervals (CIs). For variables using different scores (e.g., pain as 0 – 10 VAS or 1 – 10 NRS, functional disability), standardized mean differences (SMDs) with 95% CIs were calculated.

When standard deviations (SDs) were not available for a given variable, they were calculated from standard errors (SEs) using the formula $SD = SE \cdot \sqrt{N}$; from 95% CIs using the formula $SD = \sqrt{N} . \frac{(U_L - L_L)}{3.92}$ for sample sizes over 70 patients, or $SD = \sqrt{N} . \frac{(U_L - L_L)}{4.13}$ otherwise (with U_L and L_L being the upper and lower limits, respectively) according to the Cochrane's recommendations [10]; or from the range values using the formula $SD = f \cdot$ range, where f is a conversion factor for a given sample size, as described in [11]. If SEs or 95% CIs were not available, values for SDs were imputed based on the median of SDs across all studies in the same group [12].

We applied the inverse-variance weighting method with a random effects model, using the I^2 statistic to assess heterogeneity among studies with non-relevant, moderate, and considerable cut-off values set at $I^2 < 40\%$, $40\% < I^2 < 75\%$, and $I^2 > 75\%$, respectively [13]. Sensitivity analyses were carried out in the cases of significant heterogeneity ($I^2 > 40\%$) by consecutive elimination of each study in order to estimate its contribution to the pooled estimates.

Table 1 Baseline characteristics of patients in the included studies. Control groups are highlighted in gray color. *PVP* percutaneous vertebroplasty, *CT* conservative treatment, *M* male, *F* female, *VAS* Visual Analogue Scale, *ODI* Oswestry Disability Index, *RMDQ* Roland-Morris Disability Questionnaire, *QUALEFFO* Quality of Life Questionnaire of the European Foundation for Osteoporosis, *OVF* osteoporotic vertebral fracture, *MD* mean difference, *W* weeks

RCT	Group	*N*	Age	M/F ratio	OVF duration[a]	Follow-up[b]	Baseline VAS	Baseline RMDQ	Baseline QUALEFFO
Voormolen (2007)	PVP	18	72 (59–84)	4/14	85 (47–138)	2 W	7.1 (5–9)	15.7 (8–22)	60 (37–86)
	CT	16	74 (55–88)	2/14	76 (46–141)	2 W	7.6 (5–10)	17.8 (9–24)	67 (38–86)
Rousing (2009)	PVP	25	80 (65–96)	6/19	8.4 (3.7–13)	12	7.5 (6.6–8.4)	-	-
	CT	24	80 (71–93)	3/21	6.7 (2.1–11.4)	12	8.8 (8.2–9.3)	-	-
Kallmes (2009)	PVP	68	73.4 (9.4)	15/53	16 (10–36)[c] W	1	6.9 (2.0)	16.6 (3.8)	-
	Placebo	63	74.3 (9.6)	17/46	20 (8–38)[c] W	1	7.2 (1.8)	17.5 (4.1)	-
Buchbinder (2009)	PVP	38	74.2 (14)	7/31	9 (3.8–13)[c] W	24	7.4 (2.1)	17.3 (2.8)	56.9 (13.4)
	Placebo	40	78.9 (9.5)	9/31	9.5 (3–17)[c] W	24	7.1 (2.3)	17.3 (2.9)	59.6 (17.1)
Chen (2010)	PVP	18	77.5 (0.8)	4/14	< 6 W	3	7.8 (1.2)	-	-
	CT	22	76.3 (0.5)	6/16	< 6 W	3	8.1 (0.8)	-	-
Klazen (2010)	PVP	101	75.2 (9.8)	31/70	29.3 (17.1)	12	7.8 (1.5)	18.6 (3.6)	58.7 (13.5)
	CT	101	75.4 (8.4)	31/70	26.8 (16.0)	12	7.5 (1.6)	17.2 (4.2)	54.7 (14.4)
Farrokhi (2011)	PVP	40	72 (59–90)	10/30	27 (4–50) W	36	8.4 (1.6)	51.2 (2.2)[d]	-
	CT	42	74 (55–87)	12/30	30 (6–54) W	36	7.2 (1.7)	47.1 (2.8)[d]	-
Blasco (2012)	PVP	64	71.3 (10)	17/47	140.3 (96.1)	12	7.21 (0.3)	-	65.2 (2.2)
	CT	61	75.3 (8.5)	11/50	143.1 (130.3)	12	6.3 (0.4)	-	59.2 (2.2)
Chen (2014)	PVP	46	64.6 (9.1)	14/32	7.1 (3)	12	6.5 (0.9)	18.6 (1.8)	-
	CT	47	66.5 (9.1)	13/30	6.8 (2.5)	12	6.4 (0.9)	16.7 (1.3)	-
Chen (2015)	PVP	42	67 (8.4)	18/24	-	34.7	7.3 (1.0)	48.8 (6.8)	
	CT	42	66.1 (8.7)	19/23	-	34.7	7.5 (0.8)	48.9 (7.3)	
Hansen (2016)	PVP	22	70.6 (54–90)	4/18	74.7 (4.6)	12	5.3 (0.4)	-	-
	Placebo	24	69.3 (53–84)	2/22	76.1 (4.4)	12	4.6 (0.46)	-	-
Yang (2016)	PVP	56	77.1 (6.0)	20/36	5.5 (3.9)	12	7.5 (1.1)	80.2 (9.9)[d]	78.1 (8.1)
	CT	51	76.2 (5.6)	18/33	5.6 (3.8)	12	7.7 (1.1)	81.5 (9.7)[d]	77.5 (8.6)
Clark (2016)	PVP	61	80 (7)	13/48	2.8 (1.6) W	6	8.1 (1.8)	19.5 (3.5)	65.4 (11.4)
	Placebo	59	81 (7)	19/40	2.4 (1.4) W	6	8.2 (1.5)	19.8 (3.7)	67.7 (11.2)
Firanescu (2018)	PVP	90	74.7 (10.7)	23/67	43 (29–52)	12	7.7 (1.4)	18.0 (4.5)	68.4 (17.1)
	Placebo	86	76.9 (8.1)	20/66	36 (24–51)	12	7.9 (1.6)	17.8 (4.7)	69.7 (17.9)

[a] Maximum follow-up (in days if not otherwise specified). [b] In months if not otherwise specified. [c] Interquartile range values between brackets. [d] ODI instead of RMDQ

Two-tailed tests were performed with significant values set at $p < .05$. The statistical analyses were carried out with the Cochrane's software Review Manager 5.3 for Windows.

Results

Baseline characteristics of patients

The RCTs included in the meta-analysis encompassed data from 1367 patients, of which 689 were in the PVP group and 678 in the control group (272 and 406 in the placebo and CT groups, respectively). The RCT with a lowest sample size included 34 patients [14] and the largest one included 202 patients [15]. Of the 14 RCTs, 9 compared PVP versus CT [14–22] and 5 compared PVP versus placebo [4, 5, 23–25]. Table 1 summarizes the baseline characteristics of participants in each study.

Pain relief (Fig. 2)

1. Vertebroplasty versus placebo: The 5 RCTs comparing PVP versus placebo included results regarding pain relief,

Fig. 2 Forest plot for the outcome pain in the comparisons PVP versus placebo (top) and PVP versus CT (bottom) in the short- (1–2 weeks), medium- (1–3 months), and long-term (≥ 6 months)

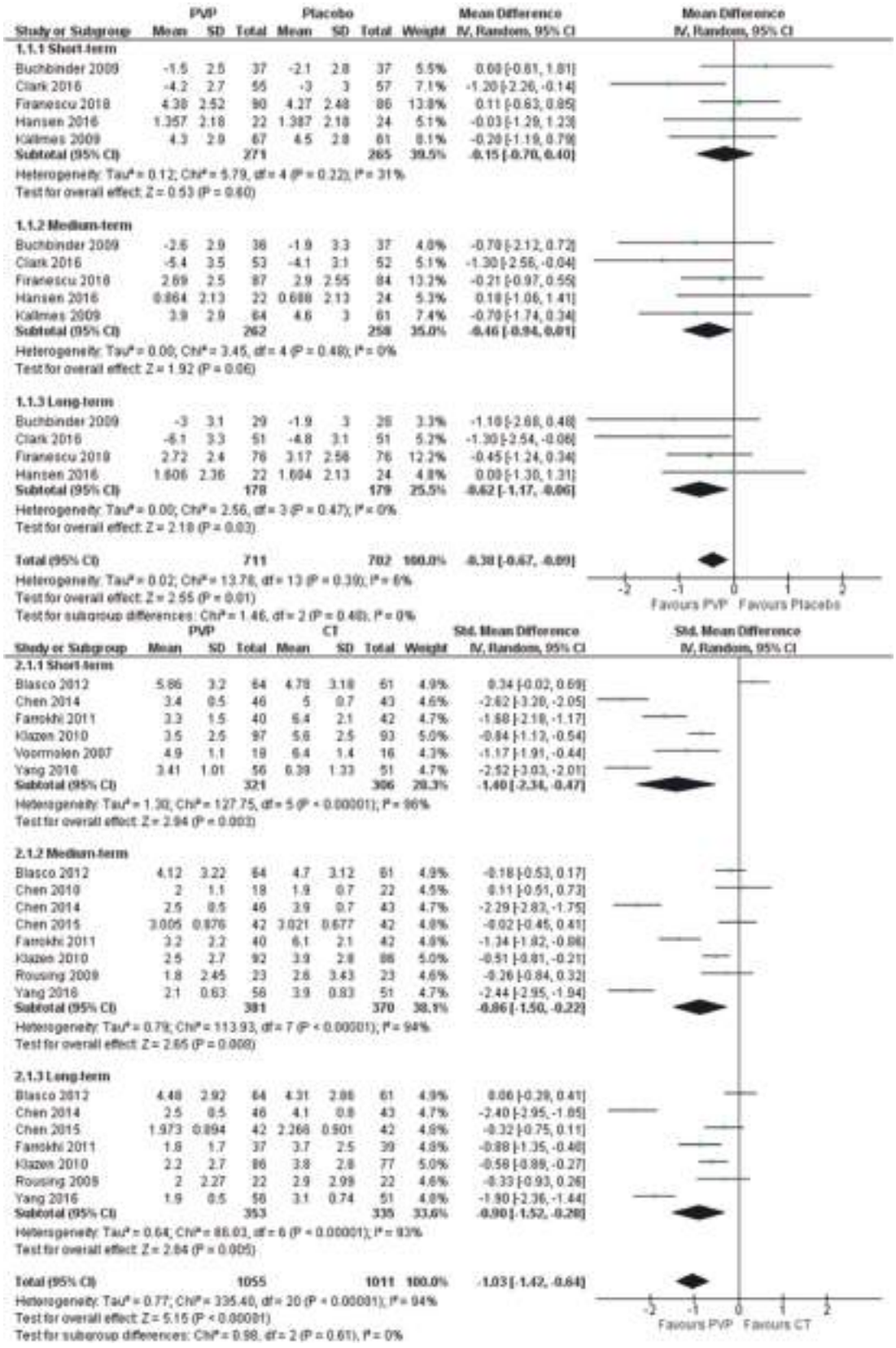
PVP
Placebo
Mean Difference
Mean Difference
Study or Subgroup Mean SD Total Mean SD Total Weight IV, Random, 95% CI
IV, Random, 95% CI
1.1.1 Short-term
Buchbinder 2009 -1.5 2.5 37 -2.1 2.8 37 5.5% 0.60 [-0.61, 1.81]
Clark 2016 -4.2 2.7 55 -3 3 57 7.1% -1.20 [-2.26, -0.14]
Firanescu 2018 4.38 2.52 80 4.27 2.48 86 13.8% 0.11 [-0.63, 0.85]
Hansen 2016 1.357 2.18 22 1.387 2.18 24 5.1% -0.03 [-1.29, 1.23]
Kallmes 2009 4.3 2.9 67 4.5 2.8 61 8.1% -0.20 [-1.19, 0.79]
Subtotal (95% CI) 271 265 39.5% -0.15 [-0.70, 0.40]
Heterogeneity: Tau² = 0.12; Chi² = 5.79, df = 4 (P = 0.22); I² = 31%
Test for overall effect: Z = 0.53 (P = 0.60)
1.1.2 Medium-term
Buchbinder 2009 -2.6 2.9 36 -1.9 3.3 37 4.8% -0.70 [-2.12, 0.72]
Clark 2016 -5.4 3.5 53 -4.1 3.1 52 5.1% -1.30 [-2.56, -0.04]
Firanescu 2018 2.69 2.5 87 2.9 2.55 84 13.2% -0.21 [-0.97, 0.55]
Hansen 2016 0.864 2.13 22 0.688 2.13 24 5.3% 0.18 [-1.06, 1.41]
Kallmes 2009 3.9 2.9 64 4.6 3 61 7.4% -0.70 [-1.74, 0.34]
Subtotal (95% CI) 262 258 35.0% -0.46 [-0.94, 0.01]
Heterogeneity: Tau² = 0.00; Chi² = 3.45, df = 4 (P = 0.48); I² = 0%
Test for overall effect: Z = 1.92 (P = 0.06)
1.1.3 Long-term
Buchbinder 2009 -3 3.1 29 -1.9 3 26 3.3% -1.10 [-2.68, 0.48]
Clark 2016 -6.1 3.3 51 -4.8 3.1 51 5.2% -1.30 [-2.54, -0.06]
Firanescu 2018 2.72 2.4 76 3.17 2.56 76 12.2% -0.45 [-1.24, 0.34]
Hansen 2016 1.606 2.36 22 1.604 2.13 24 4.8% 0.00 [-1.30, 1.31]
Subtotal (95% CI) 178 179 25.5% -0.62 [-1.17, -0.06]
Heterogeneity: Tau² = 0.00; Chi² = 2.56, df = 3 (P = 0.47); I² = 0%
Test for overall effect: Z = 2.18 (P = 0.03)
Total (95% CI) 711 702 100.0% -0.38 [-0.67, -0.09]
Heterogeneity: Tau² = 0.02; Chi² = 13.78, df = 13 (P = 0.39); I² = 6%
Test for overall effect: Z = 2.55 (P = 0.01)
Test for subgroup differences: Chi² = 1.46, df = 2 (P = 0.48), I² = 0%
-2 -1 0 1 2
Favours PVP Favours Placebo
PVP
CT
Std. Mean Difference
Std. Mean Difference
Study or Subgroup Mean SD Total Mean SD Total Weight IV, Random, 95% CI
IV, Random, 95% CI
2.1.1 Short-term
Blasco 2012 5.86 3.2 64 4.78 3.18 61 4.9% 0.34 [-0.02, 0.69]
Chen 2014 3.4 0.5 46 5 0.7 43 4.6% -2.62 [-3.20, -2.05]
Farrokhi 2011 3.3 1.5 40 5.4 2.1 42 4.7% -1.68 [-2.18, -1.17]
Klazen 2010 3.5 2.5 97 5.6 2.5 93 5.0% -0.84 [-1.12, -0.54]
Voormolen 2007 4.9 1.1 18 6.4 1.4 16 4.3% -1.17 [-1.91, -0.44]
Yang 2016 3.41 1.01 56 6.39 1.33 51 4.7% -2.52 [-3.03, -2.01]
Subtotal (95% CI) 321 306 28.3% -1.40 [-2.34, -0.47]
Heterogeneity: Tau² = 1.30; Chi² = 127.75, df = 5 (P < 0.00001); I² = 96%
Test for overall effect: Z = 2.94 (P = 0.003)
2.1.2 Medium-term
Blasco 2012 4.12 3.22 64 4.7 3.12 61 4.9% -0.18 [-0.53, 0.17]
Chen 2010 2 1.1 18 1.9 0.7 22 4.5% 0.11 [-0.51, 0.73]
Chen 2014 2.5 0.5 46 3.9 0.7 43 4.7% -2.29 [-2.83, -1.75]
Chen 2015 3.005 0.876 42 3.021 0.677 42 4.8% -0.02 [-0.45, 0.41]
Farrokhi 2011 3.2 2.2 40 6.1 2.1 42 4.8% -1.34 [-1.82, -0.86]
Klazen 2010 2.5 2.7 92 3.9 2.8 86 5.0% -0.51 [-0.81, -0.21]
Rousing 2009 1.8 2.45 23 2.6 3.43 23 4.6% -0.26 [-0.84, 0.32]
Yang 2016 2.1 0.63 56 3.9 0.83 51 4.7% -2.44 [-2.95, -1.94]
Subtotal (95% CI) 381 370 38.1% -0.86 [-1.50, -0.22]
Heterogeneity: Tau² = 0.79; Chi² = 113.93, df = 7 (P < 0.00001); I² = 94%
Test for overall effect: Z = 2.65 (P = 0.008)
2.1.3 Long-term
Blasco 2012 4.48 2.92 64 4.31 2.88 61 4.9% 0.06 [-0.29, 0.41]
Chen 2014 2.5 0.5 46 4.1 0.8 43 4.7% -2.40 [-2.95, -1.85]
Chen 2015 1.973 0.894 42 2.266 0.901 42 4.9% -0.32 [-0.75, 0.11]
Farrokhi 2011 1.8 1.7 37 3.7 2.5 39 4.8% -0.88 [-1.35, -0.40]
Klazen 2010 2.2 2.7 86 3.8 2.8 77 5.0% -0.58 [-0.89, -0.27]
Rousing 2009 2 2.27 22 2.9 2.99 22 4.6% -0.33 [-0.93, 0.26]
Yang 2016 1.9 0.5 56 3.1 0.74 51 4.8% -1.90 [-2.36, -1.44]
Subtotal (95% CI) 353 335 33.6% -0.90 [-1.52, -0.28]
Heterogeneity: Tau² = 0.64; Chi² = 86.03, df = 6 (P < 0.00001); I² = 93%
Test for overall effect: Z = 2.84 (P = 0.005)
Total (95% CI) 1055 1011 100.0% -1.03 [-1.42, -0.64]
Heterogeneity: Tau² = 0.77; Chi² = 335.40, df = 20 (P < 0.00001); I² = 94%
Test for overall effect: Z = 5.15 (P < 0.00001)
Test for subgroup differences: Chi² = 0.98, df = 2 (P = 0.61), I² = 0%
-2 -1 0 1 2
Favours PVP Favours CT

Trabajo 7: Percutaneous vertebroplasty versus conservative treatment and placebo in osteoporotic vertebral fractures: meta-analysis and critical review of the literature.

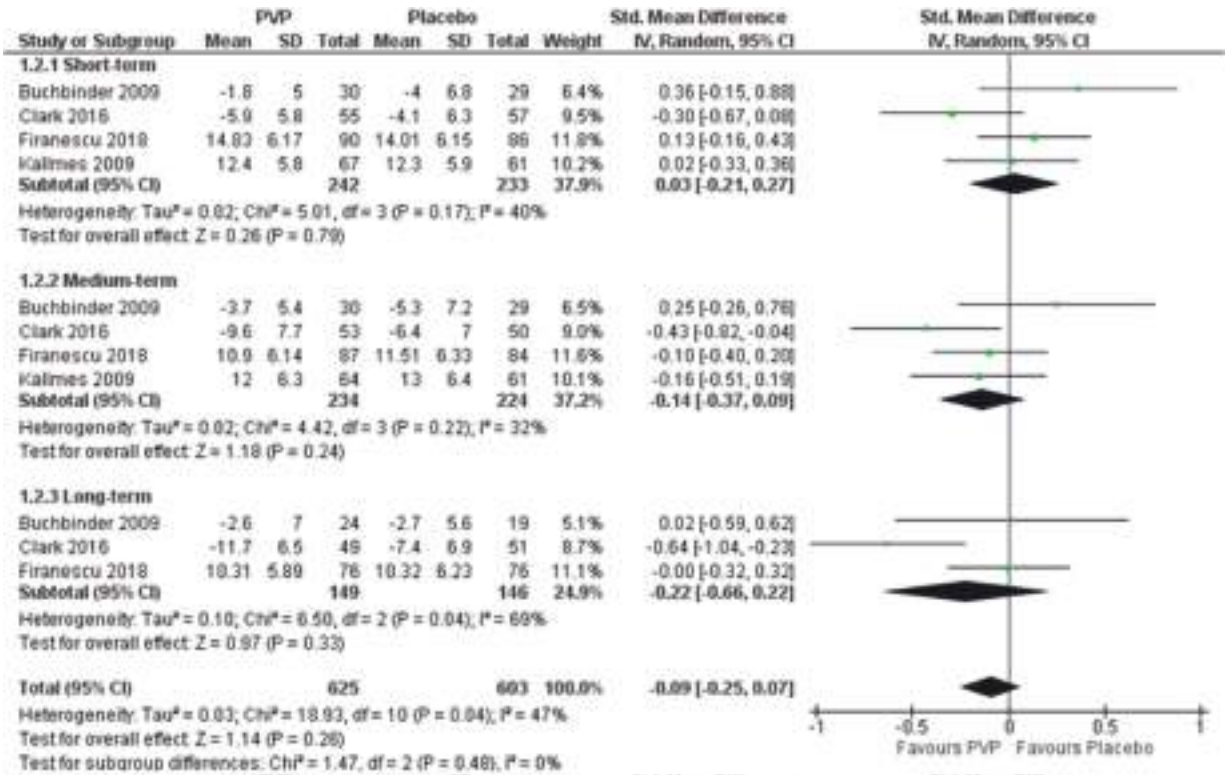

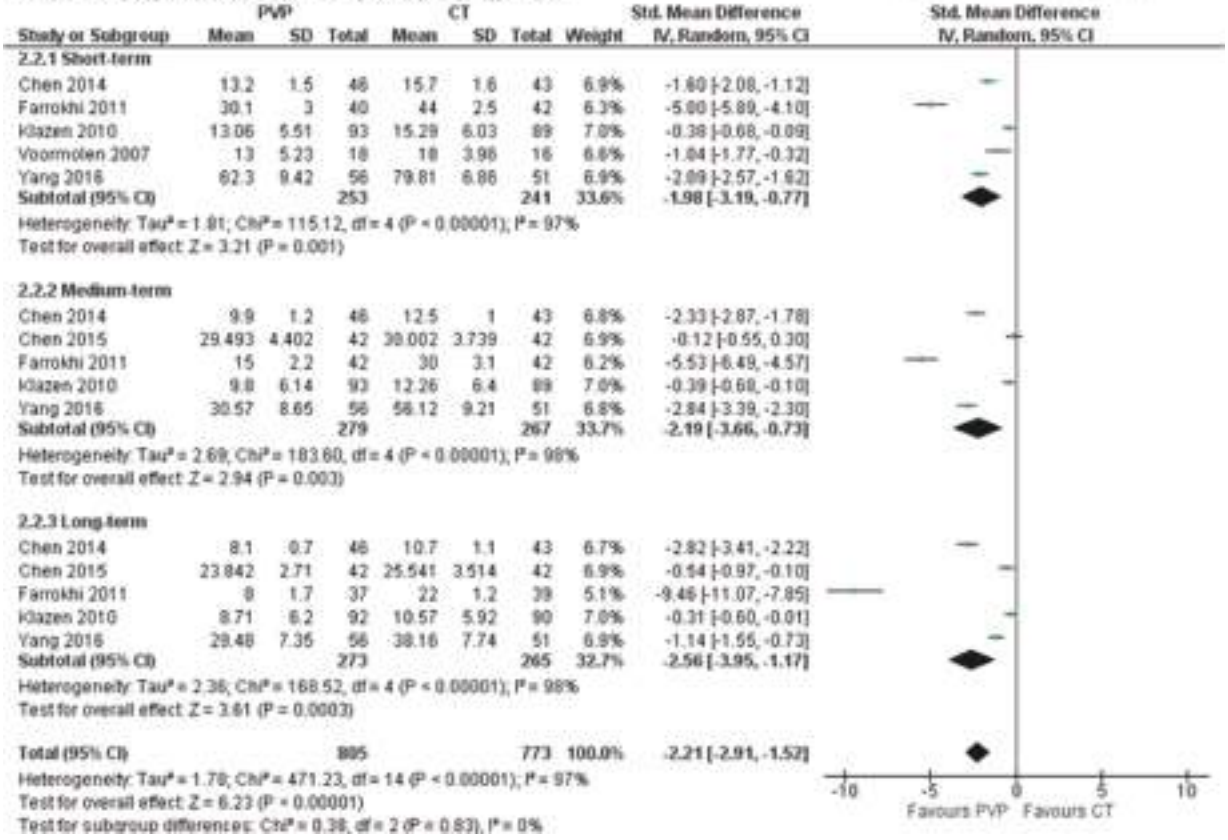

◀ **Fig. 3** Forest plot for the outcome disability in the comparisons PVP versus placebo (top) and PVP versus CT (bottom) in the short- (1–2 weeks), medium- (1–3 months), and long-term (≥ 6 months)

showing significant benefits favoring PVP in the long-term (MD: −0.62, 95% CI: −1.17 to −0.06) and in the overall analysis (MD: −0.38; 95% CI: −0.67 to −0.09),

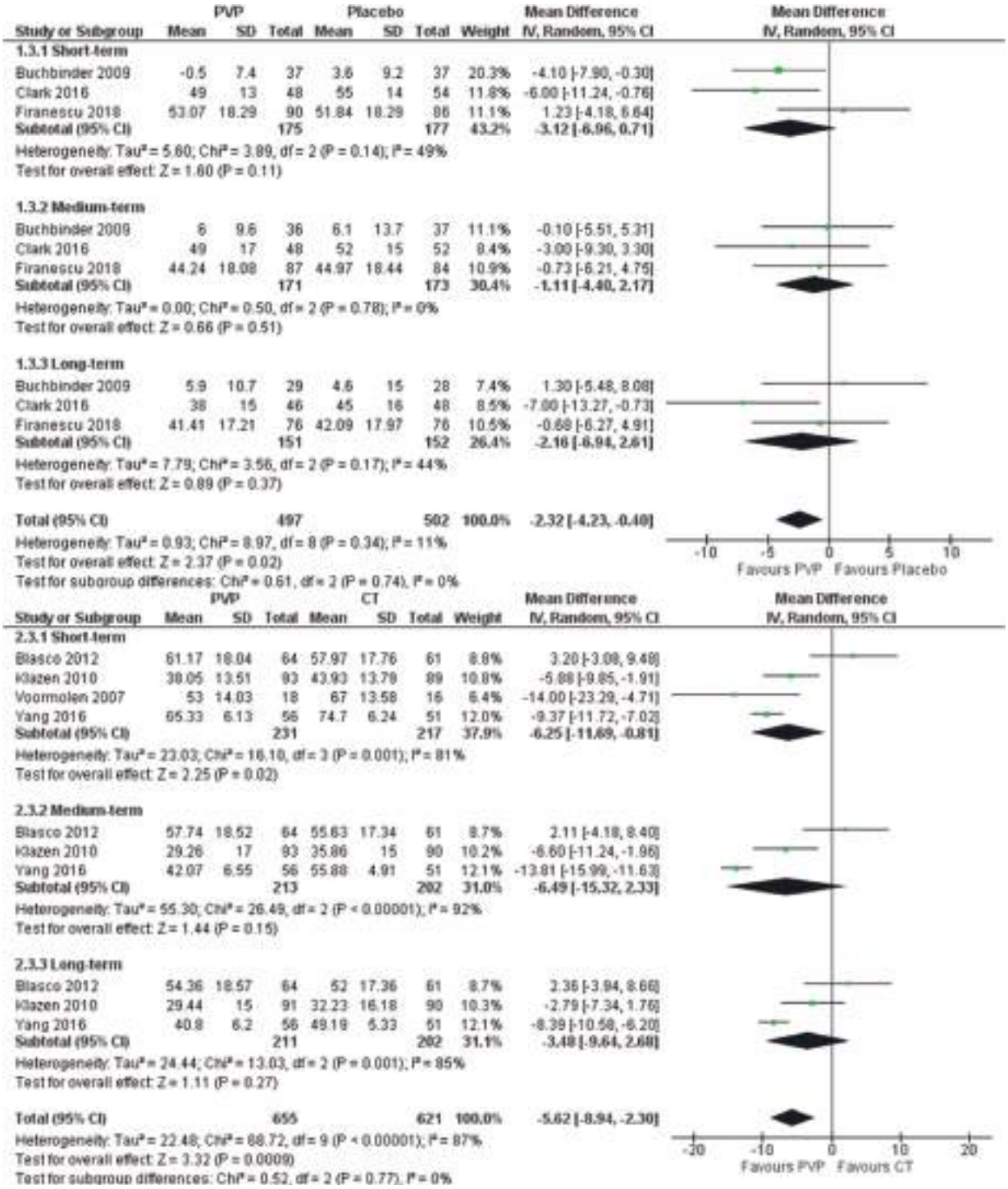

Fig. 4 Forest plot for the outcome quality of life in the comparison PVP versus placebo (top) and PVP versus CT (bottom) in the short- (1–2 weeks), medium- (1–3 months), and long-term (≥ 6 months)

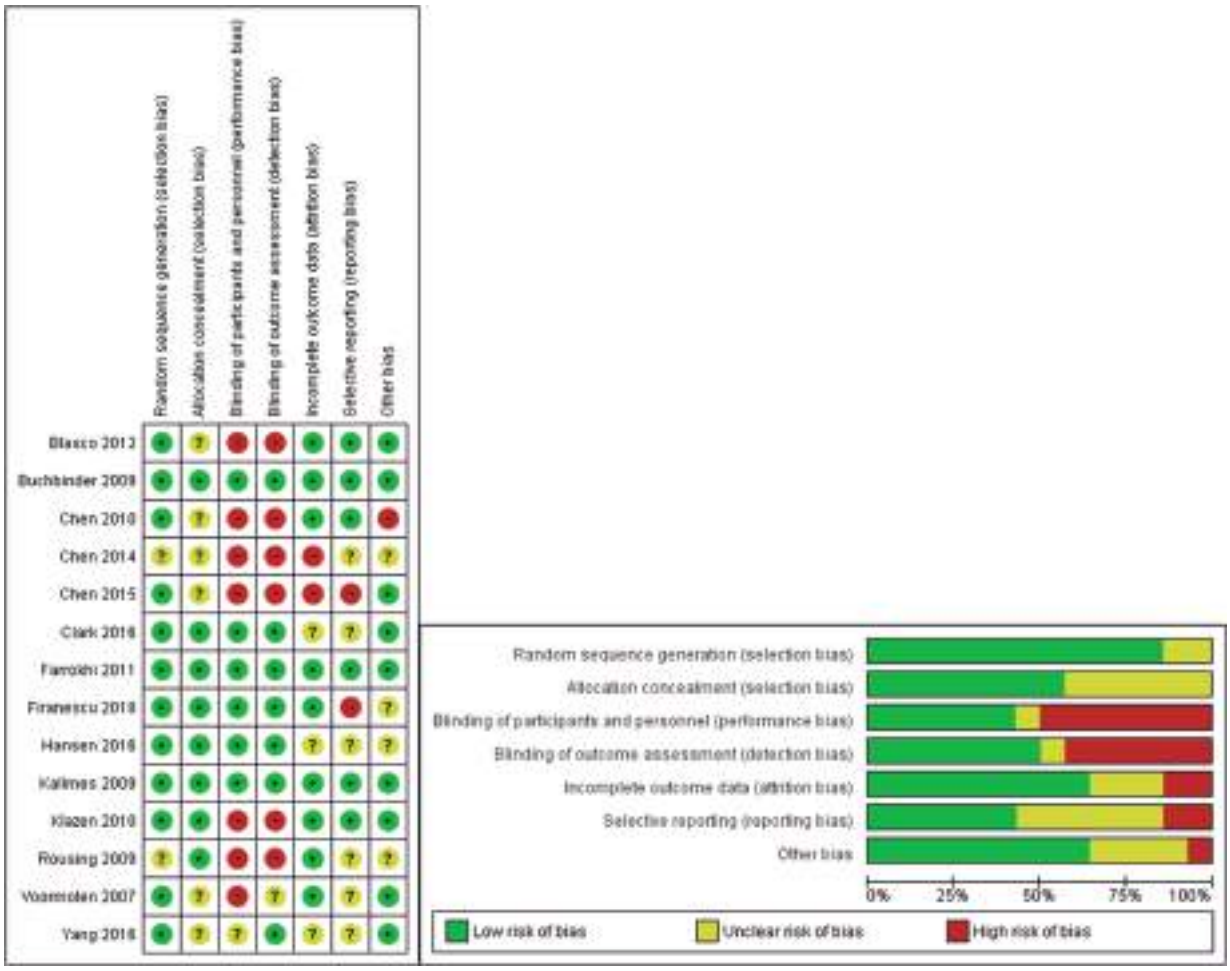

Fig. 5 Summary of risk of bias (left) and graph of risk of bias (right) of the trials included in the meta-analysis. For each of the items evaluated, "+" indicates low risk of bias, "?" indicates unclear risk, and "-" indicates high risk

and a trend toward significance ($p = .06$) in the medium-term (MD: −0.46; 95% CI: −0.94 to 0.01). No significant differences between groups were observed in the short-term.

2. Vertebroplasty versus conservative treatment: All 9 RCTs comparing PVP versus CT included results regarding pain relief. The results show significantly greater pain reduction in the PVP group in the short-term (SMD: −1.40; 95% CI: −2.34 to −0.47), medium-term (SMD: −0.86; 95% CI: −1.50 to −0.22), and long-term (SMD: −0.90; 95% CI: −1.52 to −0.28), in addition to the overall analysis (SMD: −1.03; 95% CI: −1.42 to −0.64).

Improvement of functional disability (Fig. 3)

1. Vertebroplasty versus placebo: Four RCTs included results regarding functional disability improvement according to the RMDQ or ODI questionnaire. The results showed no significant improvement at any time point.

2. Vertebroplasty versus conservative treatment: Six RCTs included results regarding functional disability improvement. The results show significant improvement in functional scores in the PVP group in the short-term (SMD: −1.98; 95% CI: −3.19 to −0.77), medium-term (SMD: −2.19; 95% CI: −3.66 to −0.73), and long-term (SMD: −2.56; 95% CI: −3.95 to −1.17), in addition to the overall analysis (SMD: −2.21; 95% CI: −2.91 to −1.52).

Improvement of quality of life (Fig. 4)

1. Vertebroplasty versus placebo: Three RCTs included results regarding improved quality of life according to the QUALEFFO questionnaire. The results show a trend toward significance ($p = .11$) in favor of PVP in the short-term (MD: −3.12; 95% CI: −6.96 to 0.71), and no significant differences in the medium- or long-term. The overall

analysis showed significant differences in favor of PVP (MD: −2.32; 95% CI: −4.23 to −0.40).

2. Vertebroplasty versus conservative treatment: Four RCTs included results regarding improved quality of life according to the QUALEFFO questionnaire. The results showed a significant improvement in the PVP group in the short-term (MD: −6.25; 95% CI: −11.69 to −0.81), but no significant benefit in the medium- or long-term. The overall analysis showed significant differences in favor of PVP (MD: −5.62; 95% CI: −8.94 to −2.30).

Subgroup analyses

1. Time from fracture onset: Pain relief was superior in the PVP group in fractures treated within 6 weeks in the short-term (MD: −2.18; 95% CI: −3.16 to −1.21), while no significant differences between PVP and control were observed in trials including OVFs of more than 6-week duration (test for subgroup differences: $p = .02$). Analogously, in the case of quality of life, significant between-group differences favoring PVP in the group of OVFs of < 6-week duration were found in the medium-term ($p = .03$) and long-term ($p = .006$), and a trend toward significance was observed in the short-term ($p = .11$). No significant between-group differences were found regarding disability at any time point. The corresponding forest plots can be consulted in the Supplementary Material (Supplementary Figures 1–9).
2. Sham procedure: In those RCTs in which placebo consisted of both infiltration of the skin and periosteum [4, 5, 23, 25], no significant differences between PVP and placebo were observed at any time point regarding pain, disability, or quality of life. Conversely, the RCT in which placebo consisted of infiltration of the skin alone [24] showed significant differences favoring PVP over placebo regarding pain in the short-term ($p = .03$), medium-term ($p = .04$), and long-term ($p = .04$). In addition, statistically significant differences favoring PVP were also found in this trial regarding disability in the medium-term ($p = .03$) and long-term ($p = .002$), and regarding quality of life in the short-term ($p = .02$) and long-term ($p = .03$). The corresponding forest plots can be consulted in the Supplementary Material (Supplementary Figures 10–18).

Risk of bias and publication bias

High risk of bias was judged in different trials, specifically performance bias ($n = 7$), detection bias ($n = 6$), attrition bias ($n = 2$), reporting bias ($n = 2$), and other bias ($n = 1$). In addition, several RCTs were judged to have an unclear risk of bias due to insufficient information on obtaining the sequence of randomization ($n = 2$), allocation concealment ($n = 6$), performance bias ($n = 1$), detection bias ($n = 1$), attrition ($n = 3$), or reporting bias ($n = 6$). The remainder were judged to have low risk of bias. Figure 5 summarizes the assessment of the risk of bias in the RCTs included in the meta-analysis.

Regarding publication bias, the shape of funnel plots indicated no significant biases, except in the case of functional disability in the comparison of PVP versus CT, in which lack of low-quality studies with favorable outcomes for CT was observed. Supplementary Figures 19–24 include the corresponding funnel plots.

Sensitivity analyses

See the Supplementary Material.

Discussion

Several RCTs comparing PVP versus CT or placebo have been published and pooled in meta-analyses which support the evidence that PVP provides more benefits than CT, despite the limited methodological quality and relatively high heterogeneity of the included studies [26–29]. For instance, Zuo et al (2019) [26] found that PVP showed better performance in pain relief compared to CT in acute/subacute OVFs. Similarly, Zhu et al (2019) [28] reported that PVP outperformed non-surgical treatment in terms of pain and functional disability. Moreover, Lou et al (2019) [27] concluded that, despite variability in outcomes, PVP showed benefits in patients with acute and severe OVFs. These results are in concordance with our findings. The recent meta-analysis by Sanli et al [29] also found significant differences favoring PVP over CT. However, the authors did not find significant differences between PVP and placebo. This is consistent with a previous exhaustive meta-analysis performed by Buchbinder et al for the Cochrane collaboration [30]. The authors concluded that there is moderate- to high-quality evidence that PVP has no significant benefits over placebo in OVFs, and that RCTs comparing PVP versus CT likely overestimated any benefit of PVP. However, authors such as Clark et al (2019) [31] strongly criticized the meta-analysis, highlighting the existence of biases in inclusion criteria, statistical analyses, and potential conflicts of interest.

Differences in inclusion criteria between RCTs might be an explanatory factor for discrepancies between studies using placebo versus CT as comparators. According to our subgroup analyses, RCTs in which fracture duration before treatment was less than 6 weeks favored PVP over placebo and CT regarding pain relief in the short-term. Conversely, trials in which patients with OVFs of more than 6-week duration were

included showed no significant differences between PVP and placebo or CT. These results have been supported by the meta-analysis by Lou et al [27]. These findings indicate that early application of PVP could optimize its beneficial effects and thus should be encouraged.

In relation to the sham procedure, it has been suggested that placebo performed with anesthetic blocking of the periosteum should be considered an intervention itself, since infiltration of anesthetics into the sensitive vertebral branches can have an analgesic effect and mask the differences in pain perception with respect to PVP, at least in the short-term. In fact, it has been found that up to a third of patients with OVFs responded to facet block, suggesting that PVP should be offered only to those who did not respond to the block [32]. In addition, PVP associated with facet block outperformed the results of PVP alone in the short-term [33]. This hypothesis is reinforced by our subgroup analysis, which showed that trials in which the periosteum of the vertebra was infiltrated during the sham procedure did not favor PVP over placebo [4, 5, 23, 25]. Conversely, the VAPOUR trial [24], in which only the subcutaneous tissue was infiltrated, showed significant benefits of PVP over placebo on pain relief, disability, and quality of life. These results are also endorsed by the meta-analysis of Lou et al (2019) [27]. Patients with OVF commonly have pain generated in the facet joints that may be reinforced by vertebral deformity secondary to biomechanical changes [34]. Therefore, persistent pain after PVP may not be due to failure of the procedure, but to other more common causes of back pain associated with degenerative spine changes. Facet joint interventions provide the most specific way of treating this residual pain [35].

Another issue not thoroughly analyzed in previous RCTs and which needs to be further addressed concerns the type of OVF and the degree of kyphosis or collapse. This is, in our opinion, one of the main potentially critical confounding factors in previous RCTs. As some authors have suggested [36], randomization and decision-making should be guided by classification scores that allow to compare treatments in patients with a similar degree and type of fracture, as is the case with traumatic fractures. Some RCTs included in this meta-analysis used the Genant's semi-quantitative grading system [37] to classify OVFs [4, 14, 15, 22, 24, 25], but none of them reported primary outcomes for each OVF subgroup, and the effect of the proportion of baseline moderate/severe OVF collapse in the outcome could not be analyzed as an independent variable, despite being a potential confounding factor in all previous RCTs. Further research is needed to determine which classification systems for OVFs should be used to indicate PVP or other alternative treatment. Candidates include the Genant's semi-quantitative grading system, the Sugita's classification, and the score of the German Society for Orthopaedics and Trauma. None of them has been validated for treatment purposes yet.

Progressive loss of vertebral height might also be a contributing factor to pain persistence following OVFs due to increased local kyphotic angle and/or positive sagittal imbalance. No vertebral height restoration can be expected from conservative treatment or placebo compared to augmentation techniques, namely PVP [25, 38] or kyphoplasty [39, 40]. Final vertebral height after OVF is also influenced by the time from fracture onset at the moment of treatment [41], with early percutaneous augmentation achieving not only higher percentages of vertebral height restoration but also preventing further collapse [38, 42].

The main strengths of this meta-analysis are the specific inclusion of RCTs, which reduces potential biases compared to other trial modalities and study designs, providing reliable evidence, and the number of trials analyzed, which makes up the largest meta-analysis of RCTs comparing PVP versus CT or placebo, to our knowledge. This was achieved by including two RCTs published in Chinese journals [18, 20], which were included in two previous meta-analyses [28, 43]. Among the limitations of the study, it is worth noting the significant heterogeneity and moderate-quality evidence of the included RCTs, the difficulty to translate some statistically significant advantages into clinically relevant benefits, and the non-inclusion of questionnaires other than QUALEFFO to assess quality of life. Moreover, studies with a longer follow-up and sufficient sample sizes are required to precisely determine the long-term therapeutic effects of PVP. But the most important limitation, which should be addressed in future studies, concerns the limited information on the type and severity of OVFs, as stated above.

Conclusions

In sum, this meta-analysis shows that PVP outperforms CT in terms of pain, functional disability, and quality of life at almost all time points. When compared with placebo, these advantages are not so clear, yet there seems to be slight benefits in terms of pain in the long-term. This could be explained by differences in the sham procedure and the time from OVF onset to intervention, with better results in fractures of less than 6-week duration.

Supplementary Information The online version contains supplementary material available at https://doi.org/10.1007/s00330-021-08018-1.

Acknowledgements The authors wish to express their gratitude to professor García-Noblejas from the Faculty of Translation and Interpreting of the University of Granada for his help in translating some Chinese manuscripts used in the study.

Funding The authors state that this work has not received any funding.

Declarations

Guarantor The scientific guarantor of this publication is Dr. Ruiz Santiago.

Conflict of interest The authors of this manuscript declare no relationships with any companies whose products or services may be related to the subject matter of the article.

Statistics and biometry One of the authors (Dr. Láinez Ramos-Bossini) has significant statistical expertise.

Informed consent No informed consent was required given the nature of this article.

Ethical approval Institutional Review Board approval was not required because of the nature of this article.

Methodology
- Meta-analysis
- Review of the literature

References

1. Hoyt D, Urits I, Orhurhu V et al (2020) Current concepts in the management of vertebral compression fractures. Curr Pain Headache Rep 24:1–10. https://doi.org/10.1007/s11916-020-00849-9
2. Hinde K, Maingard J, Hirsch JA et al (2020) Mortality outcomes of vertebral augmentation (vertebroplasty and/or balloon kyphoplasty) for osteoporotic vertebral compression fractures: a systematic review and meta-analysis. Radiology 295:96–103. https://doi.org/10.1148/radiol.2020191294
3. Edidin AA, Ong KL, Lau E, Kurtz SM (2015) Morbidity and mortality after vertebral fractures: comparison of vertebral augmentation and nonoperative management in the Medicare population. Spine (Phila Pa 1976) 40:1228–1241. https://doi.org/10.1097/BRS.0000000000000992
4. Buchbinder R, Osborne RH, Ebeling PR et al (2009) A randomized trial of vertebroplasty for painful osteoporotic vertebral fractures. N Engl J Med 361:557–568. https://doi.org/10.1056/NEJMoa0900429
5. Kallmes DF, Comstock BA, Heagerty PJ et al (2009) A randomized trial of vertebroplasty for osteoporotic spinal fractures. N Engl J Med 361:569–579. https://doi.org/10.1056/NEJMoa0900563
6. Roland M, Morris R (1983) A study of the natural history of back pain. Part I. Development of a reliable and sensitive measure of disability in low-back pain. Spine (Phila Pa 1976) 8:141–144. https://doi.org/10.1097/00007632-198303000-00004
7. Fairbank JC, Couper J, Davies JB, O'Brien JP (1980) The Oswestry Low Back Pain Disability Questionnaire. Physiotherapy 66:271–273
8. Lips P, Cooper C, Agnusdei D et al (1997) Quality of life as outcome in the treatment of osteoporosis: the development of a questionnaire for quality of life by the European Foundation for Osteoporosis. Osteoporos Int 7:36–38. https://doi.org/10.1007/BF01623457
9. Sterne JAC, Savović J, Page MJ et al (2019) RoB 2: a revised tool for assessing risk of bias in randomised trials. BMJ 366:l4898. https://doi.org/10.1136/bmj.l4898
10. Higgins J, Li T, Deeks J (2020) Chapter 6: Choosing effect measures and computing estimates of effect. In: Higgins J, Thomas J, Chandler J, et al (eds) Cochrane handbook for systematic reviews of interventions version 6.1
11. Walter SD, Yao X (2007) Effect sizes can be calculated for studies reporting ranges for outcome variables in systematic reviews. J Clin Epidemiol 60:849–852. https://doi.org/10.1016/j.jclinepi.2006.11.003
12. Ebrahim S, Johnston BC, Akl EA et al (2014) Addressing continuous data measured with different instruments for participants excluded from trial analysis: a guide for systematic reviewers. J Clin Epidemiol 67:560–570. https://doi.org/10.1016/j.jclinepi.2013.11.014
13. Deeks J, Higgins J, Altman D (2020) Chapter 10: Analysing data and undertaking meta-analyses. In: Cochrane handbook for systematic reviews of interventions version 6.1.
14. Voormolen MHJ, Mali WPTM, Lohle PNM et al (2007) Percutaneous vertebroplasty compared with optimal pain medication treatment: short-term clinical outcome of patients with subacute or chronic painful osteoporotic vertebral compression fractures. The VERTOS study. AJNR Am J Neuroradiol 28:555–560
15. Klazen CAHH, Lohle PNMM, De Vries J et al (2010) Vertebroplasty versus conservative treatment in acute osteoporotic vertebral compression fractures (Vertos II): an open-label randomised trial. Lancet 376:1085–1092. https://doi.org/10.1016/S0140-6736(10)60954-3
16. Rousing R, Andersen MO, Jespersen SM et al (2009) Percutaneous vertebroplasty compared to conservative treatment in patients with painful acute or subacute osteoporotic vertebral fractures: three-months follow-up in a clinical randomized study. Spine (Phila Pa 1976) 34:1349–1354. https://doi.org/10.1097/BRS.0b013e3181a4e628
17. Blasco J, Martinez-Ferrer A, MacHo J et al (2012) Effect of vertebroplasty on pain relief, quality of life, and the incidence of new vertebral fractures: a 12-month randomized follow-up, controlled trial. J Bone Miner Res 27:1159–1166. https://doi.org/10.1002/jbmr.1564
18. Chen G, Zhang S, Liu Y et al (2010) Percutaneous vertebroplasty compared to conservative treatment in patients with osteoporotic vertebral compression fractures. J Cervicodynia Lumbodynia 31:323–326
19. Chen D, An ZQ, Song S et al (2014) Percutaneous vertebroplasty compared with conservative treatment in patients with chronic painful osteoporotic spinal fractures. J Clin Neurosci 21:473–477. https://doi.org/10.1016/j.jocn.2013.05.017
20. Chen J, Qi X, Li S et al (2015) Bone cement injection as vertebral augmentation therapy for osteoporotic vertebral compression fractures. Chinese J Tissue Eng Res 19:3292–3296. https://doi.org/10.3969/j.issn.2095-4344.2015.21.003
21. Yang E-Z, Xu J-G, Huang G-Z et al (2016) Percutaneous vertebroplasty versus conservative treatment in aged patients with acute osteoporotic vertebral compression fractures: a prospective randomized controlled clinical study. Spine (Phila Pa 1976) 41:653–660. https://doi.org/10.1097/BRS.0000000000001298
22. Farrokhi MR, Alibai E, Maghami Z (2011) Randomized controlled trial of percutaneous vertebroplasty versus optimal medical management for the relief of pain and disability in acute osteoporotic vertebral compression fractures: clinical article. J Neurosurg Spine 14:561–569. https://doi.org/10.3171/2010.12.SPINE10286
23. Hansen EJ, Simony A, Rousing R et al (2016) Double blind placebo-controlled trial of percutaneous vertebroplasty (VOPE). Glob Spine J 6:s-0036-158-s-0036-158
24. Clark W, Bird P, Gonski P et al (2016) Safety and efficacy of vertebroplasty for acute painful osteoporotic fractures (VAPOUR): a multicentre, randomised, double-blind, placebo-controlled trial. Lancet 388:1408–1416. https://doi.org/10.1016/S0140-6736(16)31341-1

25. Firanescu CE, De Vries J, Lodder P et al (2018) Vertebroplasty versus sham procedure for painful acute osteoporotic vertebral compression fractures (VERTOS IV): randomised sham controlled clinical trial. BMJ 361:k1551. https://doi.org/10.1136/bmj.k1551
26. Zuo XH, Zhu XP, Bao HG et al (2018) Network meta-analysis of percutaneous vertebroplasty, percutaneous kyphoplasty, nerve block, and conservative treatment for nonsurgery options of acute/subacute and chronic osteoporotic vertebral compression fractures (OVCFs) in short-term and long-term effects. Medicine (Baltimore) 97:e11544. https://doi.org/10.1097/MD.0000000000011544
27. Lou S, Shi X, Zhang X et al (2019) Percutaneous vertebroplasty versus non-operative treatment for osteoporotic vertebral compression fractures: a meta-analysis of randomized controlled trials. Osteoporos Int 30:2369–2380. https://doi.org/10.1007/s00198-019-05101-8
28. Kamalian S, Bordia R, Ortiz AO (2012) Post–vertebral augmentation back pain: evaluation and management. AJNR Am J Neuroradiol 33:370–375. https://doi.org/10.3174/ajnr.A2775
29. Hatgis J, Granville M, Jacobson RE (2017) Evaluation and interventional management of pain after vertebral augmentation procedures. Cureus. 9:e1061. https://doi.org/10.7759/cureus.1061
30. Zhu R-SS, Kan S-LL, Ning G-ZZ et al (2019) Which is the best treatment of osteoporotic vertebral compression fractures: balloon kyphoplasty, percutaneous vertebroplasty, or non-surgical treatment? A Bayesian network meta-analysis. Osteoporos Int 30:287–298. https://doi.org/10.1007/s00198-018-4804-2
31. Sanli I, van Kuijk SMJ, de Bie RA et al (2020) Percutaneous cement augmentation in the treatment of osteoporotic vertebral fractures (OVFs) in the elderly: a systematic review. Eur Spine J 29:1553–1572. https://doi.org/10.1007/s00586-020-06391-x
32. Buchbinder R, Johnston RV, Rischin KJ et al (2018) Percutaneous vertebroplasty for osteoporotic vertebral compression fracture. Cochrane Database Syst Rev. https://doi.org/10.1002/14651858.CD006349.pub3
33. Clark W, Bird P, Diamond T et al (2019) Cochrane vertebroplasty review misrepresented evidence for vertebroplasty with early intervention in severely affected patients. BMJ Evid-Based Med 25:85–89. https://doi.org/10.1136/bmjebm-2019-111171
34. Wilson DJ, Owen S, Corkill RA (2011) Facet joint injections as a means of reducing the need for vertebroplasty in insufficiency fractures of the spine. Eur Radiol 21:1772–1778. https://doi.org/10.1007/s00330-011-2115-5
35. Cheng Y, Wu X, Shi J et al (2020) Percutaneous vertebroplasty and facet blocking for treating back pain caused by osteoporotic vertebral compression fracture. Pain Res Manag. https://doi.org/10.1155/2020/5825317
36. Piazzolla A, Bizzoca D, Solarino G et al (2020) Vertebral fragility fractures: clinical and radiological results of augmentation and fixation-a systematic review of randomized controlled clinical trials. Aging Clin Exp Res 32:1219–1232. https://doi.org/10.1007/s40520-019-01289-1
37. Genant HK, Wu CY, van Kuijk C, Nevitt MC (1993) Vertebral fracture assessment using a semiquantitative technique. J Bone Miner Res 8:1137–1148. https://doi.org/10.1002/jbmr.5650080915
38. Nakano M, Hirano N, Ishihara H, Kawaguchi Y, Watanabe H, Matsuura K (2006) Calcium phosphate cement-based vertebroplasty compared with conservative treatment for osteoporotic compression fractures: a matched case-control study. J Neurosurg Spine 4:110–117
39. Li Y, Zhu J, Xie C (2017) A comparative study of percutaneous kyphoplasty and conservative therapy on vertebral osteoporotic compression fractures in elderly patients. Int J Clin Exp Med 10:8139–8145
40. Iida K, Harimaya K, Tarukado K, Tono O, Matsumoto Y, Nakashima Y (2019) Kyphosis progression after balloon kyphoplasty compared with conservative treatment. Asian Spine J 13:928–935. https://doi.org/10.31616/asj.2018.0329
41. Pumberger M, Schitz F, Burger J, Schomig F, Putzier M, Palmowski Y (2020) Kyphoplasty restores the global sagittal balance of the spine independently from pain reduction. Sci Rep 10:8894
42. Van Meirhaeghe J, Bastian L, Boonen S et al (2013) A randomized trial of balloon kyphoplasty and non-surgical management for treating acute vertebral compression fractures: vertebral body kyphosis correction and surgical parameters. Spine (Phila Pa 1976) 38:971–983. https://doi.org/10.1097/BRS.0b013e31828e8e22
43. Guo J-B, Zhu Y, Chen B-L et al (2015) Surgical versus non-surgical treatment for vertebral compression fracture with osteopenia: a systematic review and meta-analysis. PLoS One 10:e0127145. https://doi.org/10.1371/journal.pone.0127145

DISCUSIÓN

VII. DISCUSIÓN

La presente tesis doctoral aborda diversos avances en el diagnóstico y tratamiento de las FVO desde la radiología. De acuerdo con los resultados presentados en los trabajos de la tesis, la investigación desarrollada ha permitido dar respuesta a los objetivos planteados de partida, a saber:

A. Objetivo general: revisar y profundizar en los avances radiológicos relativos al diagnóstico y tratamiento las fracturas vertebrales de naturaleza osteoporótica.

B. Objetivos específicos:

1. Revisar los hallazgos de imagen en RC, TC y RM de las principales patologías de la columna vertebral, y particularmente aquellas que pueden incluirse en el diagnóstico diferencial de las FVO.
2. Determinar qué factores tienen influencia en la evolución clínica y radiológica de las FVO, destacando el tipo de fractura según los diferentes sistemas de clasificación, los parámetros cuantitativos y cualitativos identificables en las pruebas de imagen, y la anatomía de la fractura.
3. Determinar si la vertebroplastia percutánea en las FVO es superior al placebo y al tratamiento conservador, y las potenciales causas de las controversias sobre su eficacia existentes en la literatura científica.

Además, ha sido posible dar respuesta a las hipótesis de trabajo que sustentan la línea de investigación de la tesis:

4. El diagnóstico radiológico de las FVO ha experimentado cambios significativos en los últimos años y no existe consenso sobre los sistemas de clasificación más útiles desde el punto de vista clínico y radiológico.
5. La mejor comprensión de la fisiopatología de las FVO permite establecer criterios diagnósticos cualitativos, cuantitativos y semicuantitativos.
6. Es posible determinar factores de riesgo en la evolución de las FVO a partir de hallazgos de imagen en las pruebas radiológicas empleadas de forma rutinaria en la práctica clínica.

7. El tratamiento intervencionista precoz de las FVO en pacientes seleccionados ofrece resultados superiores al tratamiento conservador

En esta sección se discutirán de forma ordenada e integrada los resultados obtenidos en los siete trabajos incluidos en la tesis doctoral, destacando los aspectos de mayor relevancia para la práctica clínica y para las futuras investigaciones en el área. Posteriormente trataremos las limitaciones de los trabajos y, finalmente, las necesidades actuales y perspectivas futuras en este ámbito de investigación, planteando potenciales líneas de trabajo que den continuidad a esta tesis doctoral.

1. Discusión de los principales resultados

Los principales resultados de la tesis pueden desglosarse en tres grandes bloques. El primero de ellos corresponde a una revisión actualizada de los avances en el diagnóstico de las fracturas vertebrales, en general, y osteoporóticas, en particular, mediante las diferentes técnicas de imagen utilizadas en radiología. Este bloque está conformado por los trabajos 1 a 5. Los trabajos 1 y 2 son revisiones narrativas y pictóricas extensas sobre el papel de la RC (trabajo 1) y de la TC y RM (trabajos 2 y 3) en el diagnóstico de las patologías de la columna vertebral. Los trabajos 3 y 4 son revisiones narrativas y pictóricas de menor extensión pero específicamente centradas en las FVO; la primera de ellas se ocupa del diagnóstico mediante RC, y la segunda está focalizada en los avances tecnológicos y de imagen radiológicos multimodales, incluyendo impresión 3D e IA. Finalmente, el trabajo 5 es una carta al editor que ilustra un caso particular de fractura vertebral cervical tras traumatismo de baja energía con una complicación infrecuente (disección de arteria vertebral) que pasó inadvertida clínicamente y se detectó mediante RM, lo que ejemplifica la utilidad de esta prueba de imagen en el diagnóstico de las fracturas vertebrales y sus complicaciones.

El segundo bloque corresponde al trabajo 6; es un estudio de investigación original retrospectivo del que se desprenden resultados interesantes sobre factores pronósticos para el colapso de las FVO que pueden detectarse en RC y TC en el momento del diagnóstico. Este trabajo reviste un gran interés desde el punto de vista clínico y radiológico, pues hemos identificado medidas y puntos de corte específicos con importante capacidad predictiva para el colapso de las FVO, lo que permite seleccionar pacientes para tratamientos conservadores o invasivos. Aunque será preciso validar estos

hallazgos mediante estudios prospectivos más amplios debido a las limitaciones intrínsecas del trabajo, los resultados son prometedores.

El último bloque, correspondiente al trabajo 7, está focalizado en el tratamiento de las FVO, específicamente en la VP, técnica empleada desde los años 80 y cuya eficacia se puso en tela de juicio a raíz de la publicación de dos ensayos clínicos comparados con placebo publicados en la prestigiosa revista *New England Journal of Medicine* en 2009 (Buchbinder et al., 2009; Kallmes et al., 2009) y por un posterior meta-análisis del grupo *Cochrane* (Buchbinder et al., 2018). Los resultados de nuestro meta-análisis ponen de manifiesto que sí existen datos estadística y clínicamente significativos a favor de este tratamiento, y ahonda mediante el análisis de subgrupos en algunas potenciales causas que han influido en los trabajos previos que no han encontrado tales beneficios, lo que puede ser de gran ayuda en futuras investigaciones.

A continuación, se discuten los resultados principales de la tesis doctoral. Con fines expositivos y de clarificación, se ha decidido agruparlos siguiendo la lógica de estos tres grandes bloques, con varios subapartados pertinentes para el primero de ellos debido a su extenso contenido.

1.1. La radiología en el diagnóstico de la patología de la columna vertebral

Como se ha descrito en la introducción de esta tesis, el conocimiento exhaustivo de los hallazgos radiológicos de la columna vertebral normal, de las variantes anatómicas más frecuentes y de la columna vertebral patológica parece a todas luces necesario para realizar un correcto diagnóstico de las FVO. Los trabajos 1 a 5 de esta tesis doctoral demuestran la importancia fundamental de este conocimiento, especialmente en el caso de la RC (trabajos 1 y 3). Por otra parte, se ha reseñado también la relevancia de ordenar este complejo conocimiento sobre la patología de la columna para hacerlo más accesible a los radiólogos y otros especialistas interesados en la utilidad y avances de las pruebas de imagen en el diagnóstico de las FVO. Por ello, los resultados de investigación derivados de estos trabajos de revisión han sido estructurados con una doble finalidad, científica (actualización y síntesis de la literatura) y educativa (agrupación y ordenamiento de contenidos complejos), lo que refuerza su utilidad práctica (Busetti et al., 2007). Se discuten a continuación los principales aspectos derivados de estos cinco trabajos.

1.1.1. Indicaciones, ventajas y limitaciones de las pruebas de imagen

En los trabajos 1 a 4 se revisan diversas cuestiones relativas a las indicaciones, ventajas y limitaciones de la RC, TC y RM en el diagnóstico de la patología de la columna. Un primer aspecto a reseñar es que, aunque la RC es la técnica fundacional de la radiología, sigue siendo una herramienta esencial en la práctica clínica diaria pues, a pesar de sus limitaciones, puede proporcionar una gran cantidad de información diagnóstica (Renner, 2009) y tiene la ventaja de ser una técnica rápida y de fácil acceso, lo que la hace especialmente útil en situaciones de urgencia. Sin embargo, en los últimos años, se ha observado una disminución en el interés de muchos médicos por la interpretación de la RC, a favor de la TC y RM, más costosas y no disponibles en todos los escenarios asistenciales. Esta tendencia es clara y concuerda con nuestra experiencia en la práctica clínica, trascendiendo el ámbito de la patología de la columna vertebral.

Esta situación conlleva varios problemas desde el punto de vista de la gestión de recursos, entre los que puede destacarse el sobrecoste derivado de requerir equipos más caros, la necesidad de especialistas en imagen disponibles las 24 horas del día, la sobreutilización de pruebas diagnósticas y la sobreexposición a radiación ionizante en la población. Por otra parte, cuanto menor es el uso de una técnica de imagen, peor es la pericia en su interpretación (Bodestedt, 2010); de ahí que cada vez comprobemos que existe un mayor desconocimiento de la semiología radiológica en RC por parte de muchos clínicos, e incluso radiólogos. Desde luego no debe caerse en la inferencia reduccionista de culpar al médico que solicita las pruebas de imagen avanzadas, pues debe entenderse que existe un complejo entramado de factores que han llevado a esta situación: mayor demanda y exigencia por parte de los pacientes, tendencia creciente hacia la medicina defensiva, sobrecarga burocrática, introducción de nuevas pruebas diagnósticas y terapéuticas más accesibles que puede usar el propio clínico como la ecografía (Frei, 2015). A ello también debemos añadir, en el caso particular de las FVO, las dificultades diagnósticas derivadas de la falta de criterios de consenso, los hallazgos de imagen que se prestan a confusión, y la dificultad intrínseca de diagnosticar FVO mínimas. También debe tenerse en cuenta la falta de correlación unívoca entre los hallazgos de imagen y la clínica, lo que complica aún más esta cuestión (Fortin, 2002). El trabajo 3 parte de las consideraciones referidas sobre esta compleja realidad y está concebido y dirigido a diversos especialistas, sean o no radiólogos, con la finalidad de revisar y sintetizar los aspectos clave para el diagnóstico de las FVO mediante RC.

En la línea de homogeneizar y asentar criterios de consenso para el uso racional de recursos en el contexto de la imagen médica, una cuestión tratada en la introducción de los trabajos de revisión realizados concierne a la síntesis de las principales indicaciones para realizar una RC de la columna vertebral, un aspecto crucial en la práctica clínica y en la toma de decisiones diagnósticas y terapéuticas (Flynn et al., 2011). Aunque pueda parecer ilógico, lo cierto es que actualmente faltan criterios de consenso universal en cuanto a las indicaciones de las pruebas de imagen ante la sospecha de patología de columna. Sin embargo, existen varias pautas disponibles para ayudar a los médicos en la solicitud de técnicas de imagen apropiadas para lograr un diagnóstico preciso y garantizar una atención médica adecuada que cumpla con las necesidades de eficacia y seguridad de los pacientes.

La indicación más frecuente para realizar una prueba de imagen en la columna es el dolor que no puede ser atribuido a una causa específica después de una evaluación clínica inicial (Balzano and Guglielmi, 2019). Aunque la mayoría de estos casos son autolimitados y se resuelven con el tiempo, la RC puede ser útil para identificar anomalías estructurales que pueda estar contribuyendo al dolor. Sin embargo, es importante tener en cuenta que la RC no siempre es necesaria en estos casos, y su uso debe ser considerado cuidadosamente para evitar la exposición innecesaria a la radiación. El dolor de espalda mecánico es otro motivo común para la realización de RC de columna vertebral (Chien and Bajwa, 2008). Se caracteriza por su relación con el movimiento o la postura y la radiología simple también puede ayudar a identificar sus causas, como las alteraciones de la alineación vertebral, las fracturas por compresión o las enfermedades degenerativas de la columna vertebral.

En el caso de las patologías traumáticas, aunque la TC ha reemplazado en gran medida a las RC, esta es apropiada en algunos escenarios clínicos como traumatismos de baja energía o pacientes de bajo riesgo donde la sospecha de fractura es baja. Existen diversas guías de referencia para ayudar en la toma de decisiones que los radiólogos y otros especialistas deben conocer, como las guías NEXUS y la regla C-Spine, específicamente orientadas a la selección de los pacientes en los que es apropiado realizar una prueba de imagen cuando se sospecha patología traumática cervical (Blackmore, 2003). En el caso de las patologías inflamatorias, infecciosas y tumorales, la RC tiene un papel mucho más limitado, particularmente en los dos primeros grupos, donde los hallazgos suelen ser aparentes solamente en casos avanzados y no es posible detectar edema óseo, sinovitis,

entesitis, capsulitis o derrame intraarticular, que pueden indicar cambios inflamatorios activos. En estas situaciones, la TC y, sobre todo, la RM, han reemplazado o complementan de forma necesaria a la RC, de ahí la importancia de conocer las indicaciones apropiadas para estas técnicas (Kumar and Hayashi, 2016).

Por último, cabe destacar que la RM es la técnica de elección en pacientes con sospecha de lesión o compresión de la médula espinal, en presencia de signos de alarma como el síndrome de cauda equina, neoplasia o infección (Schmalstieg and Weinshenker, 2012). De hecho, este es uno de los pocos casos en los que la RM está indicada de forma urgente (Laur et al., 2019), ya que la sensibilidad y especificidad de la RC y TC para la detección de compresión medular es limitada en varias patologías. Finalmente, es preciso que el radiólogo sepa en qué escenarios clínicos la administración de contraste intravenoso aportará información relevante, siendo este el caso en el diagnóstico y caracterización de la patologías inflamatorias, infecciosas y tumorales, además de las sospechas de complicación en la columna posquirúrgica (Husband et al., 2014).

1.1.2. La radiología en el diagnóstico de la patología congénita

La patología congénita de la columna vertebral es un tema de gran relevancia en el ámbito de la radiología y la medicina en general. En los trabajos 1 y 2 se examinan en detalle las alteraciones congénitas de la columna. El radiólogo debe conocer la clasificación general de las mismas: pueden ser simples, cuando no hay deformidad espinal asociada o escasa trascendencia clínica, o complejas, cuando están asociadas con deformidades graves o tienen implicaciones neurológicas. Por otra parte, pueden ser secundarias a defectos en la formación vertebral y dan lugar a agenesia, hemivértebras, vértebras en cuña o en mariposa, en la segmentación vertebral (p.ej., bloque vertebral) o ambas. En ocasiones puede realizarse un correcto diagnóstico diferencial entre los bloques vertebrales congénitos y adquiridos mediante la identificación de signos como el de la cintura de avispa (Ridley et al., 2018). Además, existen síndromes congénitos complejos como Klippel-Feil, Jarcho-Levin, o Goldenhar, en los que el informe radiológico suele ser de gran ayuda para el diagnóstico y toma de decisiones terapéuticas.

Las deformidades espinales congénitas, como la escoliosis, constituyen anomalías de relevancia clínica que requieren una evaluación precisa por parte de los radiólogos (Suh et al., 2001). La hemivértebra y la barra no segmentada unilateral son las causas más comunes de escoliosis congénita, mientras que los defectos anteriores en la formación del

cuerpo vertebral son la causa más común de cifosis congénita o cifoescoliosis. La presencia de malformaciones óseas también se asocia con una mayor incidencia de anomalías estructurales de la médula espinal, particularmente en casos de fallos combinados de segmentación y formación.

En la práctica clínica, se utilizan radiografías de columna vertebral completas (telerradiografías) para contar las vértebras, pues a correcta identificación de los niveles vertebrales es crucial para la planificación de la cirugía de columna. La radiografías de columna completa permiten detectar anomalías de transición, como costillas hipoplásicas o supernumerarias en la charnela toracolumbar (Kuklo, 2007). Se ha observado que las anomalías de transición lumbosacra, como la sacralización de L5 y la lumbarización de S1, están presentes en una proporción significativa de la población, y pueden estar relacionadas con el síndrome de Bertolotti y cambios degenerativos en los niveles adyacentes (Bron et al., 2007). Sin embargo, diferenciar entre lumbarización y sacralización puede resultar difícil cuando no se puede realizar un recuento vertebral completo, cosa que ocurre con cierta frecuencia en la práctica clínica, sobre todo en los estudios de RM (Adibatti and Asha, 2015). Aunque se han propuesto varios métodos para identificar el nivel del cuerpo vertebral como la localización del ligamento iliolumbar o la identificación de la raíz nerviosa de L5 sin ramificación proximal, su fiabilidad es limitada (Jagannathan et al., 2017) y en la práctica no es infrecuente tener que designar arbitrariamente una vértebra de referencia en el informe radiológico para describir los niveles vertebrales cuando existen dudas.

En resumen, las revisiones de los trabajos 1 y 2 resaltan la importancia de la evaluación radiológica precisa en pacientes con patologías congénitas de la columna. Tanto la RC como la TC y la RM desempeñan un papel crucial en la clasificación, evaluación de la gravedad y planificación del tratamiento. Los radiólogos deben estar familiarizados con las anomalías de transición y con los métodos para identificar los niveles vertebrales con precisión para garantizar la correlación clínicorradiológica y evitar problemas derivados de abordar un nivel vertebral incorrecto en el caso de tratamientos invasivos.

1.1.3. La radiología en el diagnóstico de la patología traumática

La patología traumática de la columna vertebral es otro tema ampliamente discutido en los trabajos 1 y 2. En primer lugar, la interpretación de la RC en el contexto de la columna cervical postraumática sigue siendo importante para los radiólogos, y la proyección lateral

es la más importante en este contexto. En el caso de las fracturas traumáticas toracolumbares, la sensibilidad de la RC es baja y su gravedad puede ser subestimada, especialmente las fracturas en estallido. Por lo tanto, la TC debe realizarse incluso después de la detección de una fractura vertebral en las RCs para una clasificación adecuada (véase el trabajo 6). Las lesiones traumáticas por excelencia en la columna son las fracturas vertebrales, que se tratarán en el apartado siguiente. No obstante, cabe reseñar la importancia de la variedad de sistemas de clasificación de fracturas desarrollados a lo largo del tiempo para estandarizar y facilitar la comunicación entre radiólogos y cirujanos, entre los que cabe reseñar el de la AO Spine. La práctica totalidad de FVO son del grupo A de esta clasificación, pero en el caso de fracturas traumáticas de alta energía resulta fundamental disponer de criterios de consenso que faciliten el manejo. La gran ventaja de la clasificación AO Spine es que incorpora elementos específicos identificables por imagen y otros elementos clínicos, que además varían en función del segmento de columna afectado, y otorga una puntuación objetiva a elementos concretos. Ello supone grandes ventajas para el manejo de los pacientes y permite una toma de decisiones óptima. Otro aspecto de gran relevancia es la concordancia intra e interobservadores, que en la clasificación AO Spine está demostrando muy buenos resultados (Urrutia et al., 2017). Nosotros utilizamos este sistema en la práctica clínica.

La RM se indica principalmente cuando persisten dudas sobre el tratamiento más adecuado después de la evaluación con TC, ya que permite cuantificar el daño a la médula espinal y evaluar la presencia y gravedad de la lesión del complejo ligamentario posterior (CLP), cuya integridad puede implicar un cambio en la estrategia de tratamiento hacia una terapia conservadora o una cirugía mínimamente invasiva. Además, aunque el estado neurológico generalmente se evalúa clínicamente, la RM permite correlacionar los hallazgos neurológicos con la gravedad y extensión del daño a la médula espinal, y es útil para determinar la ubicación exacta y la extensión de las lesiones, permitiendo su clasificación atendiendo a la presencia de hemorragia o edema.

En términos de identificación y caracterización de fracturas corticales, la RM es inferior a la TC, pero es superior en la detección de lesiones de tejidos blandos y fracturas trabeculares de los cuerpos vertebrales. Por lo tanto, la RM estará indicada siempre que se sospeche mielopatía o inestabilidad ligamentaria, o cuando se necesita descartar un hematoma o una hernia discal antes de proceder a la reducción cerrada de las facetas cervicales bloqueadas. La mielopatía puede ser compresiva debido a una hernia

traumática aguda, a la presencia de un fragmento óseo o a un hematoma extramedular. Los estudios actuales sobre imagen de tensor de difusión (DTI) con la medición del coeficiente de difusión aparente, anisotropía fraccional y tractografía, permiten obtener datos cuantitativos sobre la integridad axonal de la médula espinal en pacientes traumatizados y posiblemente se introduzcan en la práctica clínica en el futuro para facilitar la toma de decisioens.

1.1.4. La radiología en el diagnóstico de la patología degenerativa

En los trabajos de revisión hemos incluido apartados específicos extensos dedicados al papel de la imagen en la patología degenerativa de la columna vertebral, que puede afectar a diferentes estructuras anatómicas como las articulaciones sinoviales, los procesos espinosos, los discos intervertebrales y los ligamentos. Las articulaciones sinoviales (atlanto-axial, facetarias, costovertebrales y sacroilíacas) muestran signos degenerativos como el estrechamiento del espacio articular, quistes y/o esclerosis subcondral, fenómenos de vacío y formación de osteofitos. En este caso, la prueba más sensible para una valoración conjunta de los hallazgos es la RM, donde cabe destacar su capacidad para detectar derrame intraarticular y cambios edematosos en el hueso y tejidos blandos adyacentes, hallazgos asociados a inestabilidad segmentaria y frecuentemente sintomáticos, aunque debe tenerse en cuenta que también pueden estar presentes en pacientes asintomáticos.

La artrosis facetaria, sumamente frecuente, se ha descrito en un porcentaje significativo de pacientes con dolor lumbar, y la presencia de derrame articular de más de 1 mm en RM puede requerir la realización de RC o exploraciones dinámicas para descartar espondilolistesis oculta o inestabilidad. Aunque queda fuera de los objetivos de esta tesis doctoral, merece la pena mencionar el importante papel que juega la radiología intervencionista en el tratamiento del síndrome facetario mediante el bloqueo anestésico y radiofrecuencia del ramo intermedio de la raíz dorsal, ya que existen algunas controversias sobre su eficacia (Li et al., 2022; Wardhana et al., 2022). En el **Apéndice 5** puede consultarse un meta-análisis actualizado sobre este tema, aún no publicado.

Las alteraciones degenerativas de las apófisis espinosas (fenómeno o enfermedad de Baastrup, dependiendo de si es o no sintomática), se caracterizan por cambios degenerativos interespinosos asociados a hiperlordosis y estrechamiento del espacio intervertebral de los discos y las articulaciones facetarias. Los hallazgos de imagen

incluyen la aproximación y contacto estrecho de los procesos espinosos adyacentes, edema, quistes óseos, esclerosis, aplanamiento y agrandamiento de las superficies articulares, bursitis y, ocasionalmente, quistes epidurales o masas fibrosas epidurales en la línea media.

Otro aspecto fundamental relativo a la patología degenerativa de la columna tiene que ver con los cambios degenerativos del disco intervertebral, que se pueden evidenciar en la RM como cambios en la intensidad de señal, reducción de la altura discal, fisuras del anillo fibroso, o abombamientos discales. Se ha demostrado que la presencia de estos hallazgos (excepto las fisuras del anillo) es más prevalente en pacientes sintomáticos que en controles (Kallmes et al., 2015). Existen algunas clasificaciones que pueden resultar de utilidad como la de Pfirrmann (Pfirrmann et al., 2001), aunque su empleo en la práctica clínica puede resultar tedioso.

Por último, en los trabajos 2 y 3 se hace hincapié en los hallazgos de imagen en la hiperostosis esquelética difusa (DISH), una patología sistémica que se caracteriza por la presencia de grandes osteofitos y puentes óseos en al menos cuatro vértebras torácicas adyacentes que, por un lado, pueden experimentar sintomatología asociada a la enfermedad (dolor lumbar y rigidez, compresión neurológica debido a estenosis del canal, e incluso disfagia u obstrucción de las vías respiratorias debido a grandes osteofitos anteriores cervicales) y, por otro, se encuentran en mayor riesgo de sufrir fracturas vertebrales transdiscales o transvertebrales tras traumatismos de baja energía. Por ello, resulta fundamental para el radiólogo revisar exhaustivamente las pruebas de imagen, que frecuentemente plantean problemas diagnósticos, especialmente en el caso de la radiografía simple.

1.1.5. La radiología en el diagnóstico de la patología inflamatoria, infecciosa y tumoral

Como se ha referido previamente, la RM es la prueba de imagen idónea para el diagnóstico de este grupo de enfermedades. En la patología inflamatoria, el trabajo 2 refleja la importancia de la RM como técnica prínceps para el diagnóstico, especialmente en patologías como la sacroiliitis activa, ya que es capaz de detectar alteraciones años antes de que los hallazgos radiográficos sean evidentes y actualmente se incluye en los criterios ASAS en el brazo de imagen para el diagnóstico de espondilitis anquilosante. Lo mismo ocurre en la patología infecciosa, donde es la técnica de referencia debido a su alta

sensibilidad y especificidad, superando claramente a la RC y a las gammagrafías óseas, especialmente para detectar espondilodiscitis y osteomielitis. En el trabajo 2 se describen con detalle los signos más importantes que el radiólogo debe tener en cuenta a la hora de establecer un diagnóstico de sospecha, como el signo del psoas en la espondilodiscitis. Otro aspecto de gran importancia es el conocimiento de las ventajas que ofrece la administración intravenosa de contraste de gadolinio, particularmente para diagnosticar y delimitar la presencia de abscesos, una complicación relativamente frecuente de los procesos infecciosos de la columna.

Para la evaluación de tumores o metástasis, la RM es generalmente la técnica más útil dada su mayor resolución de contraste tisular. En el caso de metástasis, la RM ha mostrado mejor rendimiento diagnóstico en comparación con la gammagrafía ósea, la PET-TC y la TC, mientras que en el mieloma múltiple ha demostrado una mayor sensibilidad que la PET en la estadificación, pero es inferior para evaluar la respuesta al tratamiento. En cuanto a los tumores benignos, como los hemangiomas vertebrales, la TC puede ser útil para mostrar características como el signo del panal de abeja en imágenes sagitales o el signo de los lunares (*polka dot sign*) en imágenes axiales. Sin embargo, la RM sigue siendo importante para evaluar la extensión local. Como aspecto a reseñar, debe tenerse en cuenta el potencial impacto de las descripciones semiológicas en el informe radiológico, como es el caso del "hemangioma atípico" que característicamente muestra hiperintensidad STIR y T2 e hipointensidad T1, ya que puede generar alarmas innecesarias para el clínico. Por este motivo, es preferible optar por otros términos como "hemangioma de predominio vascular".

1.2. Avances en el diagnóstico radiológico de las fracturas vertebrales osteoporóticas

Entre las fundamentaciones principales de este trabajo destaca el impacto de las FVO en la salud y calidad de vida de los pacientes, lo que implica la consecuente necesidad de un diagnóstico preciso y precoz pues estas fracturas son una causa común de morbilidad y mortalidad, especialmente en la población anciana (Truumees, 2003). Por ello, para el radiólogo resulta indispensable disponer de conocimientos actualizados sobre el diagnóstico de las FVO (Lenchik et al., 2004). Cabe recordar que la FVO es una manifestación común de la osteoporosis y su detección es condición suficiente para establecer el diagnóstico de osteoporosis, incluso en ausencia de densitometría ósea. En

los trabajos realizados se ha hecho hincapié en que uno de los principales obstáculos para la detección de FVO es que estas pueden ser asintomáticas y pasar inadvertidas clínica y radiográficamente. En este sentido, el radiólogo debe saber que el sitio más frecuente de afectación de la FVO es la unión toracolumbar, seguido de la columna torácica media, y que puede ocurrir en tres posibles escenarios: traumatismo de energía mínima que pasa inadvertido por los pacientes, traumatismo de baja energía (caída desde la propia altura o menos), y traumatismo de alta energía. En los traumatismos de alta energía, la vértebra se fracturará incluso en ausencia de osteoporosis, pero la deformidad inducida será más extensa, y pueden coexistir otras fracturas vertebrales menos llamativas alejadas del epicentro del traumatismo.

Tal y como se desprende de los trabajos 1, 3 y 4, el papel de la RC en las FVO ha experimentado cambios a lo largo de los años, fruto de una mejor comprensión de la fisiopatología y correlación con otras pruebas de imagen. A pesar de estos avances, actualmente sigue existiendo una falta de consenso universal en cuanto a los criterios diagnósticos de FVO, lo que ha dado pie a una heterogénea variedad de clasificaciones principalmente basadas en los hallazgos en RC (aunque algunas como la propuesta por la DGOU utilizan la RM para algunas categorías). Uno de los aspectos más útiles de la tesis radica en la síntesis de las principales clasificaciones de FVO existentes en función de si son métodos cualitativos, cuantitativos o semicuantitativos. Ello permite no solamente ahondar en la comprensión de los déficits de las técnicas de imagen y de los propios evaluadores (radiólogos), sino ubicar futuras clasificaciones, cuya potencial utilidad puede estar determinada por esta naturaleza cualitativa, cuantitativa o semicuantitativa. Por ejemplo, si se desean implementar o comparar la precisión de diferentes métodos implementables por técnicas de IA o visión computacional, puede ser de especial interés centrarse en los métodos cuantitativos. De manera resumida, merece la pena reseñar los aspectos principales de cada una de las clasificaciones recogidas en el trabajo y sus ventajas e inconvenientes.

En primer lugar, los métodos cuantitativos o morfométricos se basan en mediciones precisas de las dimensiones vertebrales y la evaluación de la pérdida de altura vertebral. Aunque estos métodos ofrecen una alta reproducibilidad y objetividad, su sensibilidad para la detección de fracturas caracterizadas por alteraciones morfológicas sutiles puede ser baja. Por ejemplo, el método Eastell-Melton, que se basa en la comparación de las medidas de las alturas anterior, media y posterior de las vértebras en RC, puede dar lugar

a falsos positivos, especialmente en el caso de las FVO leves. Además, los métodos cuantitativos pueden requerir excesivo tiempo para la práctica clínica y muestran una variabilidad inter e intraobservador relativamente alta, lo que puede afectar a la precisión diagnóstica. A pesar de estas limitaciones, pueden ser útiles para el seguimiento longitudinal de los pacientes y la evaluación de la progresión de la enfermedad.

En cuanto a los métodos semicuantitativos, destacan los propuestos por Genant et al. y por la Sociedad Alemana de Ortopedia y Traumatología (DGOU). Resultan particularmente útiles debido a su simplicidad y aplicabilidad, incluso para observadores inexpertos. El método de Genant et al. es uno de los más utilizados en la práctica clínica y en la investigación. Este método clasifica las FVO en tres grados (leve, moderado y grave) basándose en la pérdida de altura vertebral estimada visualmente, y adjudica una categoría morfológica (en cuña, diábolo o estallido) atendiendo a la afectación predominante de una de las tres columnas del cuerpo vertebral. Una de las principales ventajas de este sistema es la posibilidad de graduar las fracturas cuantificando la pérdida de altura, lo que permite una estimación más precisa de su gravedad, y monitorizar su progresión evolutiva en función de los tratamientos aplicados. Además, este método ha demostrado tener valor pronóstico en algunos estudios. Por otro lado, el método de la DGOU es más novedoso y representa una clasificación muy útil para las FVO, no solo desde el punto de vista radiológico sino clínico, al estar pensada particularmente para la comunicación entre radiólogos y traumatólogos, de manera que ayude a la toma de decisiones clínicas de forma óptima. Aunque los métodos semicuantitativos pueden ser aplicados con relativa precisión por observadores inexpertos, la interpretación precisa de la RC y la clasificación correcta de las FVO requieren un conocimiento radiológico avanzado, y existen algunas limitaciones que deben considerarse, principalmente el bajo acuerdo entre observadores para las FVO con leve pérdida de altura, que en muchas ocasiones requieren de otros criterios (cualitativos) para su diagnóstico.

A diferencia de los métodos cuantitativos y semicuantitativos, los métodos cualitativos se centran exclusivamente en la evaluación de las características morfológicas de las vértebras para identificar cambios patológicos. Estos métodos requieren un alto nivel de habilidad y experiencia, ya que, en numerosas ocasiones, implican la capacidad de identificar cambios sutiles que pueden indicar la presencia de una FVO. Estos métodos son particularmente útiles para diferenciar las FVO de otras patologías o variantes anatómicas de la normalidad que pueden causar cambios en la morfología vertebral, como

la espondilosis degenerativa o las deformidades congénitas. A pesar de su utilidad, los métodos cualitativos también tienen sus limitaciones. Una de las principales es la necesidad de observadores experimentados y cualificados, y también existe una variabilidad entre observadores.

Un aspecto relevante del trabajo 3 radica en la distinción de las FVO de otros hallazgos de imagen similares derivados de variantes anatómicas u otras patologías vertebrales. Resulta evidente la trascendencia clínica de esta distinción, particularmente en pacientes sintomáticos, que pueden requerir de un tratamiento diferente o de pruebas complementarias para alcanzar un diagnóstico definitivo. Existen varias causas que pueden provocar una disminución de la altura vertebral y que pueden confundirse con las FVO en RC, como las deformidades vertebrales congénitas, las alteraciones degenerativas de la columna vertebral y las fracturas vertebrales patológicas secundarias a metástasis o tumores primarios. En los trabajos de revisión se han destacado varios patrones de imagen que deben ser tenidos en consideración para un adecuado diagnóstico diferencial en este sentido. Así, las alteraciones degenerativas de la columna vertebral suelen estar asociadas con otros hallazgos degenerativos como la presencia de osteofito o la disminución del espacio discal. Las fracturas vertebrales patológicas secundarias a metástasis o tumores primarios pueden ser particularmente difíciles de diferenciar de las FVO y requerirán en muchos casos el concurso de pruebas complementarias, particularmente RM, gammagrafía o PET-TC. Sin embargo, existen varios signos en las RCs simples que pueden orientar en este desafío diagnóstico, como la presencia de una lesión lítica o blástica, la destrucción del pedículo vertebral o la presencia de efectos expansivos locorregionales. Es importante prestar atención a hallazgos radiográficos, en ocasiones sutiles, que sugieran el diagnóstico de fractura patológica, tal y como se ha reseñado e ilustrado en los trabajos 1 a 4 (p.je., el signo del búho guiñando). Además, algunos signos pueden ser muy sutiles y se debe prestar especial atención a las discontinuidades del córtex de la pared anterior del cuerpo vertebral, que pasan frecuentemente inadvertidas (Telera et al., 2021).

Aunque la RC y TC juegan un importante papel en el diagnóstico de las FVO, la RM es la mejor opción para detectar edema, un signo de fractura aguda o crónica inestable, que además permite detectar FVO sin deformidad vertebral significativa asociada. Los cambios en la intensidad de la señal en RM del cuerpo vertebral dependen del tiempo de evolución de la fractura. Así, las fracturas agudas suelen mostrar un patrón de edema óseo

en forma de banda, con extensión subcondral transversal y preservación de la intensidad de señal normal en el resto del cuerpo vertebral. La imagen lineal del trazo de fractura a menudo se puede identificar en el interior del edema subcondral. El edema de la médula ósea generalmente se resuelve en 1 a 3 meses, siempre que la fractura se estabilice, pero si el foco de fractura permanece inestable, el edema puede volverse crónico y asociarse con cambios escleróticos (Piazzolla et al., 2015). En este sentido, las fisuras o quistes con gas o líquido también pueden formarse dentro del cuerpo vertebral y su presencia indica inestabilidad intravertebral o ausencia de reparación del foco de fractura y son mucho más frecuentes en FVO que en fracturas patológicas (Cianci et al., 2021). Con la cronicidad de la fractura, se recupera la intensidad de señal grasa propia de la médula ósea vertebral normal. En cuanto a la morfología, la retropulsión de un fragmento óseo hacia el canal indica una fractura en estallido y se considera un signo específico de benignidad.

Finalmente, cabe destacar que el grupo de edad con mayor prevalencia de FVO también presenta una prevalencia relativamente alta de metástasis en la columna vertebral, y la diferenciación entre deformidad osteoporótica vertebral y deformidad metastásica suele ser difícil en RC. En tales casos, la RM es la técnica de imagen de referencia para el diagnóstico diferencial (Cicala et al., 2013). La convexidad del borde posterior del cuerpo vertebral, la extensión hacia los elementos posteriores y la señal anormal difusa de la médula ósea son sugerentes de fractura patológica (Torres and Hammond, 2016). El uso de secuencias T1 poscontraste en la diferenciación entre fracturas benignas y malignas también se ha discutido en la literatura. Las fracturas benignas muestran un realce con gadolinio similar al de las vértebras adyacentes normales. Por el contrario, el realce en fracturas malignas suele ser más heterogéneo e intenso que en las vértebras adyacentes normales. Sin embargo, en fracturas benignas agudas con edema significativo, el realce vertebral puede ser más intenso y simular malignidad, habiéndose descrito algunos signos específicos para ayudar a su diferenciación en estos casos como el “see-through sign” (Lee et al., 2016). También se ha propuesto el uso de imágenes ponderadas en T1 con desplazamiento químico en fase y fuera de fase para este propósito diferencial. En las imágenes en fase, el agua y la grasa contribuyen a la señal de la médula ósea. En las imágenes fuera de fase, la grasa se sustrae del agua, disminuyendo así la intensidad de la señal. En el caso de la infiltración tumoral, la grasa es reemplazada por células neoplásicas y, por lo tanto, esta disminución de la señal no ocurre. Una relación de señal

fuera de fase/en fase >0,8 es moderadamente sensible y altamente específica para malignidad (Erly et al., 2006). Por último, las secuencias potenciadas en difusión también han mostrado potencial utilidad en la diferenciación entre fracturas benignas y malignas, encontrándose puntos de corte para valores de ADC con sensibilidad y especificidad relativamente altas (Bhugaloo et al., 2006).

En el trabajo 4 se revisan y sintetizan los hallazgos de imagen e innovaciones relacionadas con el diagnóstico de las FVO, destacando entre otros aspectos el papel de la impresión 3D y de la IA, tecnologías novedosas que ofrecen nuevas oportunidades para mejorar el diagnóstico, la planificación del tratamiento y la comunicación con el paciente. La IA se utiliza en el diagnóstico de fracturas vertebrales a través de algoritmos de aprendizaje automático que posibilitan analizar grandes conjuntos de imágenes y extraer características relevantes para identificar y clasificar las fracturas. Se han desarrollado sistemas basados en estos métodos que pueden detectar automáticamente fracturas vertebrales en RC y TC, mejorando la precisión y la eficiencia del diagnóstico y ayudando a los radiólogos a identificar fracturas de manera más rápida y precisa, lo que a su vez puede llevar a un tratamiento más precoz y efectivo. Aunque ya existen herramientas preparadas para uso clínico, en la práctica aún no se han instaurado; es probable que en pocos años dispongamos de este tipo de herramientas incorporados a los visualizadores DICOM aprobados para uso clínico.

En cuanto a la impresión 3D, se ha utilizado para la planificación preoperatoria y la fabricación de implantes personalizados en el tratamiento de las fracturas vertebrales. Con la ayuda de la TC, se puede obtener una reconstrucción tridimensional precisa de la columna vertebral del paciente. Esta información se utiliza para diseñar y fabricar implantes a medida que se adapten perfectamente a la anatomía del paciente y mejoran la estabilidad y la eficacia del tratamiento quirúrgico de las fracturas vertebrales. Además, como se ejemplifica en el trabajo 4, la impresión 3D se puede utilizar para crear modelos físicos de las vértebras fracturadas que pueden ser útiles para los cirujanos al planificar la estrategia quirúrgica y practicar la colocación de implantes antes de la cirugía, lo que se traduce en una mayor precisión y reducción de los tiempos quirúrgicos. Por último, cabe destacar el papel de la impresión 3D en la enseñanza médica; en el **Apéndice 3** puede consultarse un trabajo propio en el que demostramos las ventajas de utilizar estos modelos para el estudio de la anatomía normal y patológica de la columna vertebral en comparación con la enseñanza tradicional. En España ya existen algunas unidades

clínicas de impresión 3D, y su uso está instaurándose paulatinamente. No obstante, aún existen limitaciones que es preciso superar para su definitiva implantación, como la necesidad de personal entrenado y un equipo multdisciplinar, la escasez de estudios de calidad que demuestren la utilidad clínica y la eficacia de la impresión 3D en la práctica,

1.3. El papel de la radiología en el pronóstico de las FVO

El penúltimo trabajo de la tesis doctoral se centra en la predicción del colapso de las FVO a partir de los hallazgos de imagen en la RC y TC realizadas en el diagnóstico inicial, particularmente las diferencias en altura entre la RC y TC, las medidas de densidad de la vértebra fracturada y el tipo de FVO según distintas clasificaciones (Genant, Sugita, AO Spine). Los resultados de este estudio sugieren hipótesis que pueden tener importantes implicaciones clínicas en el manejo de las FVO, ya que la detección temprana de factores de riesgo para el colapso vertebral es crucial para identificar aquellos pacientes que pueden beneficiarse de un tratamiento intervencionista o quirúrgico.

En primer lugar, este estudio destaca la importancia de la RC y la TC en la evaluación inicial de las FVO. Aunque la CR es la prueba inicial de detección de las fracturas vertebrales, se ha demostrado que la CT tiene ventajas diagnósticas sobre la CR al permitir la identificación de signos sutiles de fractura vertebral y proporcionar mediciones más precisas de la pérdida de altura vertebral. Un aspecto esencial a tener en cuenta es que, en el proceso diagnóstico de las FVO, se solicita inicialmente una RC y, en función de los hallazgos y el grado de sospecha, el estudio se completa con una TC; es decir, cuando se detecta una fractura en RC pero se necesita valorar aspectos como la retropulsión del muro posterior, y en aquellos casos donde la fractura no es evidente en RC pero existe un alto grado de sospecha clínica. Desde un punto de vista técnico, el paciente se sitúa de pie en el caso de la RC y en decúbito supino en la TC, lo que se suele traducir en diferencias en la altura vertebral debido al efecto de la gravedad. En el estudio hemos encontrado que una diferencia de más del 6% en la pérdida de altura vertebral posterior entre la RC y la CT es un factor de riesgo significativo para el colapso vertebral en las FVO. Esto podría explicarse fisiopatológicamente basándose en que un mayor grado de pérdida de altura en el momento inicial de la fractura indica una mayor debilidad e inestabilidad de las trabéculas, que tenderán a colapsar con el tiempo por la propia carga axial de la columna. También indica la importancia que tiene la afectación de la pared

posterior en la gravedad de la fractura. Su afectación implica un aumento en el escalón de gravedad de las clasificaciones de la AO.

Por otra parte, tal y como se mencionó en la introducción de la tesis, una de las ventajas más significativas de la TC es que permite obtener mediciones cuantitativas absolutas y relativas de la densidad de los tejidos del cuerpo, así como medidas subrogadas que permitan comparar valores entre individuos o entre estructuras anatómicas similares normales y patológicas en un mismo paciente. En el estudio encontramos que una ratio de densidad (>2) entre el cuerpo vertebral fracturado y las vértebras adyacentes no fracturadas es un factor de riesgo para el colapso vertebral en las FVO. La principal hipótesis fisiopatológica que subyace a este hallazgo radica en que la mayor densidad en el cuerpo vertebral fracturado puede ser un indicador de esclerosis ósea y sugiere una mayor fragilidad del hueso, lo que aumenta el riesgo de colapso. Estos hallazgos resaltan la importancia de evaluar la densidad ósea mediante mediciones de unidades Hounsfield en la TC, ya que puede proporcionar información pronóstica adicional sobre el riesgo de colapso vertebral en pacientes con FVO.

La edad también se identificó como un factor de riesgo independiente para el colapso vertebral en las FVO. Los pacientes con edad igual o superior a 72,5 años presentaron un mayor riesgo de desarrollar colapso vertebral. La relación entre la edad y la osteoporosis, así como la disminución de la densidad ósea, ha sido previamente establecida en otros estudios, por lo que nuestros hallazgos refuerzan la importancia de considerar la edad como un factor determinante en la toma de decisiones clínicas en los pacientes con FVO; los pacientes de mayor edad con otros factores de riesgo radiológicos deben ser considerados para recibir un tratamiento más agresivo.

1.4. La radiología en el tratamiento de las FVO: eficacia de la vertebroplastia percutánea

La VP se ha utilizado como un abordaje terapéutico para aliviar el dolor y mejorar los resultados funcionales en pacientes con FVO. Sin embargo, la eficacia de la VP en comparación con el tratamiento conservador (CT) y el placebo no ha sido claramente establecida debido a los resultados contradictorios de estudios previos. Además, los estudios existentes no han considerado adecuadamente la heterogeneidad de las FVO y los posibles sesgos en la asignación aleatoria.

El metaanálisis y revisión sistemática de ensayos clínicos controlados y aleatorizados llevado a cabo demuestra que la VP proporciona un alivio del dolor, funcionalidad y calidad de vida significativamente mayor en comparación con el tratamiento conservador en el corto, mediano y largo plazo, aunque debe tenerse en cuenta que el manejo conservador puede ser una opción adecuada para algunos pacientes, especialmente aquellos con FVO asintomáticas o con baja carga sintomática. Por otro lado, al comparar la VP con el placebo, los resultados fueron menos concluyentes. Aunque se observaron beneficios leves en el alivio del dolor a largo plazo, no se encontraron diferencias significativas en la discapacidad funcional y la calidad de vida. Estos hallazgos son concordantes con otras revisiones de la literatura, algunas de ellas muy recientes (Jang et al., 2022; Noguchi et al., 2023), que han hecho evidente las incongruencias de las conclusiones de la revisión *Cochrane* de Buchbinder et al. (Buchbinder et al., 2018)

La heterogeneidad entre los estudios y los posibles sesgos de los ensayos clínicos suponen limitaciones clave de este metaanálisis. Las diferencias en la inclusión de los criterios entre los estudios podrían explicar las discrepancias observadas. La duración de la fractura antes del tratamiento y el tipo de placebo utilizado pueden ser factores críticos a tener en cuenta en la selección de pacientes, pues los análisis de subgrupos realizados muestran que los resultados de los ensayos clínicos pueden variar dependiendo de estos factores, y comprender su influencia puede ayudar a determinar qué pacientes son los más adecuados para recibir tratamiento con VP. Por otra parte, es necesario emplear clasificaciones apropiadas y lo más homogéneas posibles de las FVO, así como el grado de colapso vertebral, aspectos que también pueden influir en los resultados del tratamiento. La inclusión de estas variables en la asignación aleatoria y el análisis de subgrupos permitiría identificar qué pacientes se beneficiarían más de la VP en función de la gravedad y el tipo de fractura vertebral. Finalmente, otros factores como la edad del paciente, la presencia de comorbilidades, la expectativa de vida y las preferencias del paciente deben tenerse en cuenta al determinar el tratamiento más apropiado. Subrayamos la necesidad de realizar estudios con un seguimiento a largo plazo y muestras más grandes.

2. Limitaciones de la tesis doctoral

La tesis presentada presenta varias limitaciones que deben ser tenidas en cuenta a la hora de interpretar los resultados obtenidos y que derivan de la naturaleza de las diferentes

modalidades de trabajos desarrollados así como de otros factores metodológicos y contextuales. Así, respecto a los trabajos 1 a 4, caben destacar, en primer lugar, las limitaciones metodológicas propias de una revisión narrativa, que pueden estar sujetas a sesgos del revisor, ya que la selección y la interpretación de los estudios pueden ser influenciadas por las creencias y expectativas personales del revisor. Además, la falta de un enfoque metodológico estándar puede llevar a variabilidad en la calidad de las revisiones narrativas. Por último, es posible que las revisiones narrativas no identifiquen todos los estudios relevantes, especialmente si se limitan a ciertas bases de datos o términos de búsqueda. Las revisiones pictóricas también presentan estas limitaciones y la presentación de las imágenes es dependiente de la subjetividad del autor. En los trabajos presentados, la revisión conjunta de las figuras por parte de todos los autores resultó de gran utilidad para minimizar este tipo de sesgos subjetivos.

El trabajo 5 es un informe de caso, por lo que sus limitaciones son evidentes y notorias. Debido a su naturaleza descriptiva y no experimental, el nivel de evidencia que se puede derivar del mismo es mínimo, aunque como se ha comentado en la discusión, este no era su propósito. Además, al basarse en casos individuales, existe el riesgo de sesgos y generalizaciones inapropiadas. Por otro lado, la publicación de informes de caso puede estar sujeta a sesgos de publicación, ya que se tiende a reportar más frecuentemente los casos excepcionales o con resultados positivos, dejando de lado aquellos con resultados negativos o menos impactantes.

Respecto al trabajo 6, es importante tener en cuenta que este estudio se basa en una cohorte retrospectiva y presenta limitaciones inherentes, como el tamaño de la muestra y la posibilidad de sesgo de selección, lo que justifica la necesidad de estudios prospectivos, idealmente multicéntricos, para confirmar estos hallazgos y evaluar aún más la utilidad clínica de estos factores de riesgo radiológicos en la predicción del colapso vertebral en las FVO. Además, es importante destacar que la predicción del colapso vertebral en las FVO no se limita únicamente a los factores radiológicos evaluados en este estudio. Otros factores clínicos y biológicos, como la fragilidad ósea, la presencia de comorbilidades y la respuesta al tratamiento, también pueden influir en la evolución de las FVO y deben ser considerados en la toma de decisiones clínicas. Se necesita una aproximación integral y multidisciplinaria que incluya la evaluación de múltiples factores para una gestión óptima de las FVO.

Por último, el meta-análisis y la revisión sistemática realizados en el trabajo 7 tienen algunas limitaciones reseñables, entre las que cabe destacar la importante heterogeneidad entre los ensayos clínicos, la dificultad de traducir algunas diferencias estadísticamente significativas en resultados clínicamente relevantes, el reducido número de estudios con seguimiento a largo plazo y, sobre todo, la escasa información sobre el tipo y la gravedad de las FVO. Además, existen estudios en los que se han encontrado resultados similares entre la VP, la cifoplastia y la vesselplastia en términos de alivio del dolor, funcionalidad y mejoría de la calidad de vida en algunos estudios. Sin embargo, la evidencia disponible es limitada y se requieren más estudios comparativos directos para establecer conclusiones definitivas sobre la eficacia relativa de estas técnicas.

3. Utilidad práctica de los resultados obtenidos

Los trabajos 1 a 5 presentan una gran utilidad práctica y creemos que, a pesar de las limitaciones propias de su naturaleza, ya referidas, representan recursos de indudable valor para radiólogos y otros especialistas interesados en profundizar en el conocimiento radiológico de la patología de la columna vertebral y, particularmente, de las FVO. Los especialistas en radiología somos plenamente conscientes de la importancia de disponer de estudios que aúnen la síntesis de evidencia científica actualizada con la descripción visual de los hallazgos, y en la literatura existen limitaciones en los recursos disponibles, tal y como se ha señalado previamente. Además, la forma en que se han ordenado y dispuesto los contenidos en la estructura interna de cada artículo, y la dedicación de trabajos específicos en función de las técnicas y de la patología abordada (patología de la columna, en general, y de las FVO, en particular), facilitan su utilización en la práctica clínica y la asimilación de contenidos difícilmente abordables mediante otros formatos, no solo desde un punto de vista científico sino también educativo (Busetti et al., 2007).

De este modo, los trabajos de revisión 1 y 2 sirven referencia para cualquier radiólogo interesado en especializarse en la radiología musculoesquelética o en neurorradiología, ya que ofrecen una síntesis pictórica sustancialmente extensa de la patología de la columna en RC (trabajo 1), TC y RM (trabajo 2) con un soporte bibliográfico riguroso que apoya los hallazgos por imagen ilustrados en el artículo, particularmente los rangos de normalidad y patológicos para las alteraciones principales que debe conocerse en este ámbito radiológico.

Particular interés reviste el trabajo 3, pues, como hemos mencionado en el cuerpo de la tesis, está dirigido específicamente a médicos con menor experiencia en el diagnóstico por imagen de FVO, como especialistas en Medicina de Familia que trabajan en servicios de Atención Primaria o Urgencias, así como otros especialistas (reumatólogos, endocrinólogos, anestesistas, especialistas en medicina interna, etc.) que solicitan asiduamente RC para la valoración de dolor de espalda crónico y deben enfrentarse al diagnóstico de las FVO, en ocasiones muy difícil, como se ha podido comprobar en esta tesis. La síntesis de los hallazgos de imagen, controversias existentes y sistemas de clasificación más empleados para las FVO, con sus respectivas ventajas y limitaciones, sin duda puede resultar de gran ayuda para estos especialistas.

El trabajo 4 cumple una doble función práctica. Por un lado, sirve como artículo de referencia para el radiólogo general, que debe conocer las características de las FVO en las diferentes técnicas de imagen y los sistemas de clasificación existentes, con especial énfasis en los que resultan útiles para el informe radiológico y la comunicación con el clínico. Por otro lado, la inclusión de avances diagnósticos como la impresión 3D y la IA ayudan a actualizar conocimientos y a estar al tanto de la evolución de nuestra especialidad, cuya naturaleza exige una constante actualización e incorporación de nuevas tecnologías. El hecho de que se haya publicado en la revista oficial de Radiología de España es otro factor a considerar, teniendo en cuenta la necesidad de generar conocimiento útil para la práctica en nuestro propio entorno.

El trabajo 5 tiene una utilidad práctica más limitada que los anteriores tanto por su breve extensión como por su naturaleza. Sin embargo, supone una aportación útil porque destaca la importancia de descartar complicaciones asociadas a las fracturas de baja energía, en particular la disección de las arterias vertebrales en las fracturas cervicales, y la utilidad de la RM para su detección, con una imagen muy ilustrativa. Además, el tipo de publicación seleccionado y el contenido del artículo permiten enfatizar aspectos relacionados de trascendencia clínica, que en el caso presentado atañe a la falta de consenso existente sobre el tratamiento conservador de la disección de arteria vertebral asociada a la fractura del ahorcado.

En cuanto a las implicaciones prácticas del trabajo 6, los resultados sugieren que los pacientes con FVO que presentan una diferencia significativa en la pérdida de altura vertebral posterior entre la RC y la TC, una alta relación de densidad entre el cuerpo

vertebral fracturado y el no fracturado, y una edad avanzada, deben ser evaluados cuidadosamente y considerados para un tratamiento más agresivo, como la cirugía o cementación vertebral. Estos resultados, que deberán ser validados mediante estudios prospectivos más amplios, pueden ayudar a guiar la toma de decisiones clínicas y personalizar el enfoque terapéutico para maximizar los beneficios terapéuticos en pacientes con FVO.

Respecto al trabajo 7, supone una importante contribución al conocimiento sobre la eficacia de la VP. En primer lugar, por tratarse de un meta-análisis de ensayos clínicos aleatorizados, lo que otorga un alto nivel de evidencia científica al estudio. En segundo lugar, porque apoya la utilización de una técnica mínimamente invasiva que ha sido puesta en entredicho, a pesar de los numerosos estudios sobre su eficacia y su empleo en la práctica clínica desde hace cuatro décadas. En tercer lugar, porque el análisis de subgrupos permite hacer hipótesis sobre los motivos que pueden explicar las incongruencias sobre los beneficios de esta técnica en la literatura científica, lo que en la práctica clínica se traducirá en un mayor énfasis por la adecuada selección de pacientes, y en la práctica científica, en una mayor rigurosidad en los futuros ensayos y trabajos clínicos sobre la VP.

En resumen, la utilidad práctica de la investigación llevada a cabo en esta tesis doctoral se puede resumir en los siguientes aspectos: revisión actualizada de las patologías de la columna vertebral en las principales pruebas radiológicas empleadas en su evaluación, con un alto componente pictórico que aporta una elevada representatividad; síntesis del conocimiento relativo al diagnóstico radiológico de las FVO con enfoques dirigidos a radiólogos y a otros especialistas, destacando los sistemas de clasificación y su utilidad en la práctica clínica; identificación de potenciales factores predictivos para el colapso de las FVO, algunos no identificados hasta la fecha y cuya precisión deberá ser comprobada prospectivamente; y síntesis con el máximo nivel de evidencia (meta-análisis de ensayos clínicos aleatorizados y revisión sistemática) de la eficacia de la VP, la modalidad de cementoplastia más empleada en el tratamiento radiológico de las FVO.

4. Perspectivas futuras

La línea de investigación trazada en esta tesis solo supone el punto de partida de un largo camino. La constante y rápida evolución de la radiología está transformando el diagnóstico y tratamiento de un amplísimo espectro de patologías, y las FVO representan

una de las más propensas a mejorar en un futuro próximo. Aunque el paradigma que está modificando de forma más resonada esta especialidad es el de la IA, los avances en los equipos de imagen médica y herramientas informáticas de posprocesamiento, particularmente en el caso de RM, también hacen lógico pensar que en los próximos años dispondremos de métodos más rápidos y precisos para identificar precozmente las FVO y predecir su evolución basándonos en los hallazgos por imagen.

Por otra parte, el advenimiento e implantación cada vez más generalizada de los equipos de impresión 3D en la práctica clínica, implementados en unidades de impresión 3D clínicas al amparo de los servicios de radiodiagnóstico y bajo la supervisión de radiólogos entrenados, suponen otro hito que previsiblemente se implantará de forma rutinaria en los hospitales de tercer nivel. Aún queda por demostrar la utilidad real y definir los escenarios médico-quirúrgicos de esta tecnología, delimitar el perfil ideal de expertos y especialistas que deben integrar los equipos multidisciplinares al cargo de las unidades, y analizar la relación coste-efectividad desde el punto de vista de la gestión sanitaria. Todos estos aspectos exigen necesariamente el diseño adecuado de estudios que deberán realizarse en el futuro, minimizando los sesgos derivados de la heterogeneidad de sistemas de impresión 3D, patologías tratadas y uso clínico (educación de pacientes y familiares, enseñanza médica, planificación prequirúrgica, diseño de implantes y dispositivos personalizados, etc.). En el caso de la patología de columna y, en concreto, de las FVO, ya se han publicado trabajos interesantes en muchas de estas áreas, pero aún queda mucho por explorar.

Finalmente, el tratamiento de las FVO mediante técnicas intervencionistas llevadas a cabo por radiólogos es otro campo en expansión. El desarrollo de nuevos materiales y cementos biológicos, dispositivos como guías, agujas y equipos de imagen, es incesante, tal y como puede comprobarse en la literatura científica. Por otra parte, las indicaciones clínicas para la selección de pacientes candidatos a los distintos tratamientos disponibles sigue siendo un tema sin resolver, a pesar de los evidentes avances de los últimos años. El desarrollo de marcadores de imagen predictivos de la evolución de las FVO, el diseño de ensayos clínicos con criterios de inclusión y exclusión más refinados, y el consenso sobre las modalidades de cementación más eficaces en función del tipo de fractura y perfil del paciente, constituyen aspectos de potencial mejora sobre los que se debe continuar trabajando en el futuro.

CONCLUSIONES

VIII. CONCLUSIONES

De conformidad con los objetivos establecidos en esta tesis doctoral, los resultados obtenidos en los siete trabajos que la integran permiten establecer las siguientes conclusiones:

1. El conocimiento de los hallazgos radiológicos de la columna vertebral normal y patológica en RC, TC y RM resulta fundamental para realizar un correcto diagnóstico de las FVO. Deben considerarse las indicaciones, ventajas y limitaciones de estas pruebas de imagen en función de la etiología que se sospeche (traumática, degenerativa, inflamatoria, infecciosa o tumoral).

2. Es preciso conocer los diferentes sistemas de clasificación utilizados en el diagnóstico de las FVO, sus ventajas e inconvenientes, y su utilidad en la práctica clínica. La distinción entre sistemas de clasificación cualitativos, cuantitativos y semicuantitativos es útil para este propósito.

3. Las tecnologías de impresión 3D y los sistemas basados en IA representan áreas emergentes con aplicaciones útiles en el diagnóstico y tratamiento de las FVO. Su implementación clínica se está instaurando progresivamente en los últimos años, por lo que el radiólogo debe familiarizarse con ellas y conocer sus ventajas y limitaciones.

4. Una diferencia significativa en la pérdida de altura vertebral posterior entre la RC y la TC, una alta relación de densidad entre el cuerpo vertebral fracturado y los no fracturados, y una edad avanzada se asocian con un mayor riesgo de colapso vertebral en las FVO. Es necesario validar estos hallazgos mediante series más amplias, idealmente prospectivas y multicéntricas.

5. La VP ofrece ventajas significativas en el alivio del dolor, mejora en la funcionalidad y calidad de vida en comparación con el placebo y con el tratamiento conservador. La adecuada selección de pacientes candidatos a este tratamiento resulta fundamental para obtener los máximos beneficios clínicos.

BIBLIOGRAFÍA

IX. BIBLIOGRAFÍA

Adibatti M, Asha K. Lumbarisation of the First Sacral Vertebra a Rare Form of Lumbosacral Transitional Vertebra. Int J Morphol 2015;33:48–50. https://doi.org/10.4067/S0717-95022015000100007.

Alesandrini KL, Rigney JW. Pictorial presentation and review strategies in science learning. J Res Sci Teach 1981;18:465–74. https://doi.org/10.1002/TEA.3660180509.

Ameis A, Randhawa K, Yu H, Côté P, Haldeman S, Chou R, et al. The Global Spine Care Initiative: a review of reviews and recommendations for the non-invasive management of acute osteoporotic vertebral compression fracture pain in low- and middle-income communities. Eur Spine J 2018;27:861–9. https://doi.org/10.1007/S00586-017-5273-6/METRICS.

Balzano RF, Guglielmi G. Imaging of spine pain. Pain Imaging A Clin Approach to Pain Diagnosis 2019:135–58. https://doi.org/10.1007/978-3-319-99822-0_8/COVER.

Barbour V, Irfan M, Poff D, Wise M. Journals' Best Practices for Ensuring Consent for Publishing Medical Case Reports 2016. https://doi.org/10.24318/COPE.2019.1.6.

Bastawrous S, Wake N, Levin D, Ripley B. Principles of three-dimensional printing and clinical applications within the abdomen and pelvis. Abdom Radiol 2018;43:2809–22. https://doi.org/10.1007/S00261-018-1554-8/METRICS.

van de Belt TH, Nijmeijer H, Grim D, Engelen LJLPG, Vreeken R, van Gelder MMHJ, et al. Patient-Specific Actual-Size Three-Dimensional Printed Models for Patient Education in Glioma Treatment: First Experiences. World Neurosurg 2018;117:e99–105. https://doi.org/10.1016/J.WNEU.2018.05.190.

Bhugaloo AA, Abdullah BJJ, Siow YS, Ng KH. Diffusion weighted MR imaging in acute vertebral compression fractures: Differentiation between malignant and benign causes. Biomed Imaging Interv J 2006;2. https://doi.org/10.2349/BIIJ.2.2.E12.

Blackmore CC. Evidence-based imaging evaluation of the cervical spine in trauma. Neuroimaging Clin N Am 2003;13:283–91. https://doi.org/10.1016/S1052-5149(03)00024-8.

Blanch J, Nogués X, Moro MJ, Valero MC, del Pino-Montes D, Canals L, et al. Medical care circuits for postmenopausal patients in Spain. Rev Osteoporos y Metab Miner 2017;9:62–71. https://doi.org/10.4321/S1889-836X2017000200003.

Bodestedt Å. Interpretation of Relevant Imaging. In: Anniko M, Bernal-Sprekelsen M, Bonkowsky V, Bradley PJ, Iurato S, editors. Otorhinolaryngol. Head Neck Surg., Berlin, Heidelberg: Springer Berlin Heidelberg; 2010, p. 653–70. https://doi.org/10.1007/978-3-540-68940-9_75.

Bouza C, López T, Palma M, Amate JM. Hospitalised osteoporotic vertebral fractures in Spain: Analysis of the national hospital discharge registry. Osteoporos Int 2007;18:649–57. https://doi.org/10.1007/s00198-006-0292-x.

Broder J. Imaging the Chest: The Chest Radiograph. Diagnostic Imaging Emerg Physician 2011:185. https://doi.org/10.1016/B978-1-4160-6113-7.10005-5.

Bron JL, van Royen BJ, Wuisman PIJM. The clinical significance of lumbosacral transitional anomalies. Acta Orthop Belg 2007;73:687–95.

Buchbinder R, Johnston R V., Rischin KJ, Homik J, Jones CA, Golmohammadi K, et al. Percutaneous vertebroplasty for osteoporotic vertebral compression fracture. Cochrane Database Syst Rev 2018;2018. https://doi.org/10.1002/14651858.CD006349.PUB3/MEDIA/CDSR/CD006349/REL0003/CD006349/IMAGE_N/NCD006349-CMP-009-06.PNG.

Buchbinder R, Osborne RH, Ebeling PR, Wark JD, Mitchell P, Wriedt C, et al. A Randomized Trial of Vertebroplasty for Painful Osteoporotic Vertebral Fractures. N Engl J Med 2009;361:557–68. https://doi.org/10.1056/NEJMOA0900429/SUPPL_FILE/NEJM_BUCHBINDER_557SA1.PDF.

Busetti E, Dettori G, Forcheri P, Ierardi MG. A Pedagogical Approach to the Design of Learning Objects for Complex Domains. Int J Distance Educ Technol 2007;5:1–17. https://doi.org/10.4018/JDET.2007040101.

Butt WP. Conventional Radiography of the Axial Skeleton. Imaging Tech Orthop 1989:51–75. https://doi.org/10.1007/978-1-4471-1640-0_4.

Bydder GM. Principles of Magnetic Resonance Imaging. Imaging Tech CNS Neonates 1991:1–16. https://doi.org/10.1007/978-3-642-76488-2_1.

Cai H, Liu Z, Wei F, Yu M, Xu N, Li Z. 3D Printing in Spine Surgery. Adv Exp Med Biol 2018;1093:345–59. https://doi.org/10.1007/978-981-13-1396-7_27.

Caverly RH. MRI Fundamentals: RF Aspects of Magnetic Resonance Imaging (MRI). IEEE Microw Mag 2015;16:20–33. https://doi.org/10.1109/MMM.2015.2419753.

Celenk C, Celenk P. Bone Density Measurement Using Computed Tomography. In: Saba L, editor. Comput. Tomogr., Rijeka: IntechOpen; 2012. https://doi.org/10.5772/22884.

Chien JJ, Bajwa ZH. What is mechanical back pain and how best to treat it? Curr Pain Headache Rep 2008;12:406–11. https://doi.org/10.1007/S11916-008-0069-3/METRICS.

Cholaquidis A, Fraiman R, Sued M. On semi-supervised learning. Test 2018;29:914–37. https://doi.org/10.1007/s11749-019-00690-2.

Cianci F, Ferraccioli G, Ferraccioli ES, Gremese E. Comprehensive review on intravertebral intraspinal, intrajoint, and intradiscal vacuum phenomenon: From anatomy and physiology to pathology. Mod Rheumatol 2021;31:303–11. https://doi.org/10.1080/14397595.2020.1764744.

Cicala D, Briganti F, Casale L, Rossi C, Cagini L, Cesarano E, et al. Atraumatic vertebral compression fractures: Differential diagnosis between benign osteoporotic and malignant fractures by MRI. Musculoskelet Surg 2013;97:169–79. https://doi.org/10.1007/S12306-013-0277-9/METRICS.

Cosman F, de Beur SJ, LeBoff MS, Lewiecki EM, Tanner B, Randall S, et al. Clinician's Guide to Prevention and Treatment of Osteoporosis. Osteoporos Int 2014;25:2359–81. https://doi.org/10.1007/S00198-014-2794-2.

Curfs I, Schotanus M, Van Hemert W, Heijmans M, De Bie R, Van Rhijn L, et al. Reliability and Clinical Usefulness of Current Classifications in Traumatic Thoracolumbar Fractures: A Systematic Review of the Literature. Int J Spine Surg 2020;14:956–69. https://doi.org/10.14444/7145.

D'Août K. Evolution of the vertebral column. Surg Spine Spinal Cord A Neurosurg Approach 2016:5–14. https://doi.org/10.1007/978-3-319-27613-7_2/COVER.

Deeks JJ, Higgins JPT AD (editors). Chapter 10: Analysing data and undertaking meta-analyses. Cochrane Handb Syst Rev Interv Version 63 (Updated Febr 2022) Cochrane, 2022 Available from WwwTrainingCochraneOrg/Handbook 2022.

Dreizin D, Letzing M, Sliker CW, Chokshi FH, Bodanapally U, Mirvis SE, et al. Multidetector CT of Blunt Cervical Spine Trauma in Adults. Https://DoiOrg/101148/Rg347130094 2014;34:1842–65. https://doi.org/10.1148/RG.347130094.

Duong MT, Rauschecker AM, Mohan S. Diverse Applications of Artificial Intelligence in Neuroradiology. Neuroimaging Clin N Am 2020;30:505–16. https://doi.org/10.1016/j.nic.2020.07.003.

Ebrahim S, Johnston BC, Akl EA, Mustafa RA, Sun X, Walter SD, et al. Addressing continuous data measured with different instruments for participants excluded from trial analysis: A guide for systematic reviewers. J Clin Epidemiol 2014;67:560–70. https://doi.org/10.1016/j.jclinepi.2013.11.014.

von Elm E, Altman D, Egger M, Pocock S, Gøtzsche, PC Vandenbroucke JSI. The Strengthening the Reporting of Observational Studies in Epidemiology (STROBE) Statement: guidelines for reporting observational studies. Int J Surg 2014;12:1495–9. https://doi.org/10.1016/j.ijsu.2014.07.013.

Erly WK, Oh ES, Outwater EK. The Utility of In-Phase/Opposed-Phase Imaging in Differentiating Malignancy from Acute Benign Compression Fractures of the Spine. AJNR Am J Neuroradiol 2006;27:1183.

Fan J, Ma C, Zhong Y. A selective overview of deep learning. Stat Sci 2021;36:264. https://doi.org/10.1214/20-STS783.

Ferrar L, Jiang G, Adams J, Eastell R. Identification of vertebral fractures: An update. Osteoporos Int 2005;16:717–28. https://doi.org/10.1007/S00198-005-1880-X/METRICS.

Ferrari R. Writing narrative style literature reviews. Eur Med Writ Assoc 2015;24:230–5. https://doi.org/10.1179/2047480615Z.000000000329.

Flynn TW, Smith B, Chou R. Appropriate use of diagnostic imaging in low back pain: A reminder that unnecessary imaging may do as much harm as good. J Orthop Sports Phys Ther 2011;41:838–46. https://doi.org/10.2519/JOSPT.2011.3618/ASSET/IMAGES/LARGE/JOSPT-838-FIG005.JPEG.

Fortin J. An algorithm for understanding spine imaging. Pain Physician 2002;5:102–9. https://doi.org/10.36076/PPJ.2002/5/102.

Frei S. Regarding "Emergency Physician Perceptions of Medically Unnecessary Advanced Diagnostic Imaging." Acad Emerg Med 2015;22:1231–1231. https://doi.org/10.1111/ACEM.12757.

Freund P, Seif M, Weiskopf N, Friston K, Fehlings MG, Thompson AJ, et al. MRI in traumatic spinal cord injury: from clinical assessment to neuroimaging biomarkers. Lancet Neurol 2019;18:1123–35. https://doi.org/10.1016/S1474-4422(19)30138-3.

Furlanetto TS, Sedrez JA, Candotti CT, Loss JF. Reference values for Cobb angles when evaluating the spine in the sagittal plane : a systematic review with meta-analysis. Motricidade 2018;14:115–28. https://doi.org/10.6063/MOTRICIDADE.10890.

Gallet J, Titus H. CR/DR systems: what each technology offers today; what is expected for the future. Radiol Manage 2005;27:30–6.

Glissen Brown JR, Berzin TM. Adoption of New Technologies: Artificial Intelligence. Gastrointest Endosc Clin N Am 2021;31:743–58. https://doi.org/10.1016/J.GIEC.2021.05.010.

Grados F, Fechtenbaum J, Flipon E, Kolta S, Roux C, Fardellone P. Radiographic methods for evaluating osteoporotic vertebral fractures. Jt Bone Spine 2009;76:241–7. https://doi.org/10.1016/J.JBSPIN.2008.07.017.

Gyebnar J, Gulacsi G, Supp GM, Balint PV, Mandl P. Imaging anatomy: Conventional radiography. Ultrason Hand Rheumatol 2018:43–63. https://doi.org/10.1007/978-3-319-74207-6_3/COVER.

Harvey CJ, Blomley MJ. Principles and Precautions of Conventional Radiography. Surg 2003;21:175–8. https://doi.org/10.1383/surg.21.7.175.15965.

Heller M, Fink A. Radiology of Trauma. Berlin, Heidelberg: Springer Berlin Heidelberg; 2000. https://doi.org/10.1007/978-3-642-60917-6.

Hernlund E, Svedbom A, Ivergård M, Compston J, Cooper C, Stenmark J, et al. Osteoporosis in the European Union: Medical management, epidemiology and economic burden: A report prepared in collaboration with the International Osteoporosis Foundation (IOF) and the European Federation of Pharmaceutical Industry Associations (EFPIA). Arch Osteoporos 2013;8:1–115. https://doi.org/10.1007/S11657-013-0136-1/TABLES/67.

Herrera A, Martínez AA, Ferrandez L, Gil E, Moreno A. Epidemiology of osteoporotic hip fractures in Spain. Int Orthop 2006;30:11–4. https://doi.org/10.1007/s00264-005-0026-2.

Higgins JPT, Li T DJ (editors). Chapter 6: Choosing effect measures and computing estimates of effect. Cochrane Handb Syst Rev Interv Version 63 (Updated Febr 2022) Cochrane, 2022 2022.

Hosmer DW, Lemeshow S. Applied Logistic Regression. Appl Logist Regres 2005. https://doi.org/10.1002/0471722146.

Le Huec JC, Thompson W, Mohsinaly Y, Barrey C, Faundez A. Sagittal balance of the spine. Eur Spine J 2019;28:1889–905. https://doi.org/10.1007/S00586-019-06083-1.

Husband DJ, Grant KA, Romaniuk CS. MRI in the diagnosis and treatment of suspected malignant spinal cord compression. Http://DxDoiOrg/101259/Bjr74877740015 2014;74:15–23. https://doi.org/10.1259/BJR.74.877.740015.

INE. Instituto Nacional de Estadística (2019).

International Osteoporosis Foundation. The Global Burden of Osteoporosis: A Factsheet. 2016:40.

Iolascon G, Moretti A, Toro G, Gimigliano F, Liguori S, Paoletta M. Pharmacological Therapy of Osteoporosis: What's New? Clin Interv Aging 2020;15:485–91. https://doi.org/10.2147/CIA.S242038.

Izzo R, Guarnieri G, Guglielmi G, Muto M. Biomechanics of the spine. Part I: Spinal stability. Eur J Radiol 2013;82:118–26. https://doi.org/10.1016/j.ejrad.2012.07.024.

Jagannathan D, Indiran V, Hithaya F, Alamelu M, Padmanaban S. Role of Anatomical Landmarks in Identifying Normal and Transitional Vertebra in Lumbar Spine Magnetic Resonance Imaging. Asian Spine J 2017;11:365–79. https://doi.org/10.4184/ASJ.2017.11.3.365.

Jang HD, Kim EH, Lee JC, Choi SW, Kim HS, Cha JS, et al. Management of Osteoporotic Vertebral Fracture: Review Update 2022. Asian Spine J 2022;16:934–46. https://doi.org/10.31616/ASJ.2022.0441.

Jebri B, Phillips M, Knapp K, Appelboam A, Reuben A, Slabaugh G. Detection of degenerative change in lateral projection cervical spine x-ray images. Https://DoiOrg/101117/122082515 2015;9414:18–25. https://doi.org/10.1117/12.2082515.

Johnell O, Kanis JA. An estimate of the worldwide prevalence and disability associated with osteoporotic fractures. Osteoporos Int 2006;17:1726–33. https://doi.org/10.1007/s00198-006-0172-4.

Kafiabadi S, Rangi P. Cervical spine radiology. Anaesth Intensive Care Med 2017;18:288–91. https://doi.org/10.1016/j.mpaic.2017.03.008.

Kallmes DF, Comstock BA, Heagerty PJ, Turner JA, Wilson DJ, Diamond TH, et al. A randomized trial of vertebroplasty for osteoporotic spinal fractures. N Engl J Med 2009;361:569–79. https://doi.org/10.1056/NEJMOA0900563.

Kallmes MH, Murad PH, Luetmer W, Brinjikji FE, Diehn JG, Jarvik CM, et al. MRI Findings of Disc Degeneration are More Prevalent in Adults with Low Back Pain than in Asymptomatic Controls: A Systematic Review and Meta-Analysis. Am J Neuroradiol 2015;36:2394–9. https://doi.org/10.3174/AJNR.A4498.

Kalra MK, Sodickson AD, Mayo-Smith WW. CT radiation: Key concepts for gentle and wise use. Radiographics 2015;35:1706–21. https://doi.org/10.1148/RG.2015150118/ASSET/IMAGES/LARGE/RG.2015150118.FIG8C.JPEG.

Kanis JA, Delmas P, Burckhardt P, Cooper C, Torgerson D. Guidelines for diagnosis and management of osteoporosis. The European Foundation for Osteoporosis and Bone Disease. Osteoporos Int a J Establ as Result Coop between Eur Found Osteoporos Natl Osteoporos Found USA 1997;7:390–406. https://doi.org/10.1007/BF01623782.

Kanis JA, Oden A, Johnell O, De Laet C, Jonsson B. Excess mortality after hospitalisation for vertebral fracture. Osteoporos Int 2004;15:108–12. https://doi.org/10.1007/s00198-003-1516-y.

Kaptoge S, Armbrecht G, Felsenberg D, Lunt M, O'Neill TW, Silman AJ, et al. When should the doctor order a spine X-ray? Identifying vertebral fractures for osteoporosis care: Results from the European Prospective Osteoporosis Study (EPOS). J Bone Miner Res 2004;19:1982–93. https://doi.org/10.1359/JBMR.040901.

Khan MAW, Arif AS. An Overview of Reports on Clinical Case Report. Anwer Khan Mod Med Coll J 2017;7:50–55. https://doi.org/10.3329/akmmcj.v7i1.31614.

Kim Y-H, Kim S-I, Han S-Y. Diagnosis of Osteoporotic Spinal Fractures. J Korean Soc Spine Surg 2015;22:104–8. https://doi.org/10.4184/JKSS.2015.22.3.104.

Kricun ME. Vertebral Body Size and Shape: A Clue to Underlying Systemic Disease. Contemp Diagnostic Radiol 2002;25:1–5. https://doi.org/10.1097/00219246-200201150-00001.

Kuhberger A, Scherndl T, Ludwig B, Simon DM. Comparative Evaluation of Narrative Reviews and Meta-Analyses. Https://DoiOrg/101027/2151-2604/A000250 2016;224:145–56. https://doi.org/10.1027/2151-2604/A000250.

Kuklo TR. Radiographic Evaluation of Spinal Deformity. Neurosurg Clin N Am 2007;18:215–22. https://doi.org/10.1016/J.NEC.2007.01.009.

Kumar Y, Hayashi D. Role of magnetic resonance imaging in acute spinal trauma: a pictorial review. BMC Musculoskelet Disord 2016;17:310. https://doi.org/10.1186/s12891-016-1169-6.

Kwee RM, Kwee TC. Imaging of facet joint diseases. Clin Imaging 2021;80:167–79. https://doi.org/10.1016/j.clinimag.2021.07.005.

Láinez Ramos-Bossini A, A S-R, Martínez Barbero J, Martín Molina J, Martín Rodríguez J, López Milena G, et al. Cross Sectional Correlate for Integrative Imaging (Anatomical Radiology). In: Gholamrezanezhad A, Assadi M, Jadvar H, editors. Radiol. Med. Diagnostic Imaging A Correl. Approach, Wiley-Blackwell; 2023, p. 52–132.

Láinez Ramos-Bossini A, Redruello Guerrero P, Mesas Hernández C, Prados Salazar J. Docencia basada en impresión 3D a partir de imagen médica para el aprendizaje de la Anatomía Humana. Resultados de una experiencia piloto. In: Buzón García O, editor. Innovación en Educ. Investig. reflexiones y propuestas actuación, Egregius; 2022, p. 223–4.

Láinez Ramos-Bossini A, Rivera Izquierdo M, Redruello Guerrero P, Prados Salazar J. Modelado e impresión 3D basada en imagen médica como herramienta docente en el grado en medicina. In: Gómez García G, Ramos Navas-Parejo M, Rodríguez Jiménez C, de la Cruz Campos J, editors. Teoría y práctica en Investig. Educ. una Perspect. Int., Dykinson; 2021, p. 1903–17.

Láinez Ramos AJ, Láinez Millán B, Redruello Guerrero P, Prados Salazar JC. Implementation of novel technologies for teaching and learning normal and pathological anatomy of the spine: From medical imaging to 3D printing. Entornos Virtuales Para La Educ En Tiempos Pandemia Perspect Metod 2021:944–66.

Lastra Leidinger M, Aragón Royón F, Etxeberria O, Balderas L, Láinez Ramos-Bossini A, López Milena G, et al. A real-world intelligent system for the diagnosis and triage of COVID-19 in the emergency department. Signa Vitae 2022;19:91–102. https://doi.org/10.22514/SV.2022.070/HTM.

Laur O, Nandu H, Titelbaum DS, Nunez DB, Khurana B. Nontraumatic spinal cord compression: Mri primer for emergency department radiologists. Radiographics 2019;39:1862–80. https://doi.org/10.1148/RG.2019190024/ASSET/IMAGES/MEDIUM/RG.2019190024.FIG20C.GIF.

Lee E, Lee JW, Lee J, Lee GY, Kang WY, Yoo BR, et al. Acute benign vertebral compression fractures: “see-through sign” on contrast-enhanced MR images. Eur Spine J 2016;25:3470–7. https://doi.org/10.1007/S00586-015-4312-4.

Lee LIT, Kanthasamy S, Ayyalaraju RS, Ganatra R. The Current State of Artificial Intelligence in Medical Imaging and Nuclear Medicine. Https://DoiOrg/101259/Bjro20190037 2019;1:20190037. https://doi.org/10.1259/BJRO.20190037.

Lenchik L, Rogers LF, Delmas PD, Genant HK. Diagnosis of osteoporotic vertebral fractures: importance of recognition and description by radiologists. AJR Am J Roentgenol 2004;183:949–58. https://doi.org/10.2214/AJR.183.4.1830949.

Lentle B, Koromani F, Brown JP, Oei L, Ward L, Goltzman D, et al. The Radiology of Osteoporotic Vertebral Fractures Revisited. J Bone Miner Res 2019;34:409–18. https://doi.org/10.1002/JBMR.3669.

Lentle B, Trollip J, Lian K. The Radiology of Osteoporotic Vertebral Fractures Redux. J Clin Densitom 2016;19:40–7. https://doi.org/10.1016/J.JOCD.2015.08.009.

Li H, An J, Zhang J, Kong W, Yun Z, Yu T, et al. Comparative efficacy of radiofrequency denervation in chronic low back pain: A systematic review and network meta-analysis. Front Surg 2022;9. https://doi.org/10.3389/FSURG.2022.899538.

Li Y, Yan L, Cai S, Wang P, Zhuang H, Yu H. The prevalence and under-diagnosis of vertebral fractures on chest radiograph. BMC Musculoskelet Disord 2018;19:235. https://doi.org/10.1186/s12891-018-2171-y.

Link TM, Guglielmi G, Kuijk C, Adams JE. Radiologic assessment of osteoporotic vertebral fractures: Diagnostic and prognostic implications. Eur Radiol 2005;15:1521–32. https://doi.org/10.1007/S00330-005-2773-2/METRICS.

Machi LA, McEvoy BT. The Literature Review: Six Steps to Success. SAGE Publications; 2016.

Mahadevan V. Anatomy of the vertebral column. Surg (United Kingdom) 2018;36:327–32. https://doi.org/10.1016/j.mpsur.2018.05.006.

Mahesh M. The Essential Physics of Medical Imaging, Third Edition. Med Phys 2013;40:077301. https://doi.org/10.1118/1.4811156.

Marro A, Bandukwala T, Mak W. Three-Dimensional Printing and Medical Imaging: A Review of the Methods and Applications. Curr Probl Diagn Radiol 2016;45:2–9. https://doi.org/10.1067/J.CPRADIOL.2015.07.009.

Martín-Noguerol T, Oñate Miranda M, Amrhein TJ, Paulano-Godino F, Xiberta P, Vilanova JC, et al. The role of Artificial intelligence in the assessment of the spine and spinal cord. Eur J Radiol 2023;161:110726. https://doi.org/10.1016/j.ejrad.2023.110726.

Moore KL, Dalley AF, Agur AMR. Clinically Oriented Anatomy. Wolters Kluwer/Lippincott Williams \& Wilkins Health; 2013.

Murphey MD. Computed radiography in musculoskeletal imaging. Semin Roentgenol 1997;32:64–76. https://doi.org/10.1016/S0037-198X(97)80038-7.

Naves M, Díaz-López JB, Gómez C, Rodríguez-Rebollar A, Cannata-Andía JB. Determinants of incidence of osteoporotic fractures in the female Spanish population older than 50. Osteoporos Int 2005;16:2013–7. https://doi.org/10.1007/s00198-005-1983-4.

Neeson D, Roberts D. Imaging the spine. Surg (United Kingdom) 2021;39:371–82. https://doi.org/10.1016/j.mpsur.2021.04.007.

Ng S-Y, Bettany-Saltikov J. Imaging in the Diagnosis and Monitoring of Children with Idiopathic Scoliosis. Open Orthop J 2018;11:1500–20. https://doi.org/10.2174/1874325001711011500.

Nissen T, Wynn R. The clinical case report: A review of its merits and limitations. BMC Res Notes 2014;7:1–7. https://doi.org/10.1186/1756-0500-7-264/METRICS.

Noguchi T, Yamashita K, Kamei R, Maehara J. Current status and challenges of percutaneous vertebroplasty (PVP). Jpn J Radiol 2023;41:1. https://doi.org/10.1007/S11604-022-01322-W.

Nogués Solán X, Guerri R, Sol E, Díez-Pérez A. Impacto socioeconómico de la osteoporosis. Rev Osteoporos Metab Min 2010;2:2005–8.

Odén A, McCloskey E V., Johansson H, Kanis JA. Assessing the impact of osteoporosis on the burden of hip fractures. Calcif Tissue Int 2013;92:42–9. https://doi.org/10.1007/s00223-012-9666-6.

Ombregt L. Applied anatomy of the thorax and abdomen. A Syst Orthop Med 2013:e157–68. https://doi.org/10.1016/B978-0-7020-3145-8.00075-2.

Page MJ, McKenzie JE, Bossuyt PM, Boutron I, Hoffmann TC, Mulrow CD, et al. The PRISMA 2020 statement: an updated guideline for reporting systematic reviews. BMJ 2021;372. https://doi.org/10.1136/BMJ.N71.

Pearson K. On the criterion that a given system of deviations from the probable in the case of a correlated system of variables is such that it can be reasonably supposed to have arisen from random sampling . London, Edinburgh, Dublin Philos Mag J Sci 1900;50:157–75. https://doi.org/10.1080/14786440009463897.

Pfirrmann CWA, Metzdorf A, Zanetti M, Hodler J, Boos N. Magnetic resonance classification of lumbar intervertebral disc degeneration. Spine (Phila Pa 1976) 2001;26:1873–8. https://doi.org/10.1097/00007632-200109010-00011.

Piazzolla A, Solarino G, Lamartina C, De Giorgi S, Bizzoca D, Berjano P, et al. Vertebral Bone Marrow Edema (VBME) in Conservatively Treated Acute Vertebral Compression Fractures (VCFs): Evolution and Clinical Correlations. Spine (Phila Pa 1976) 2015;40:E842–8. https://doi.org/10.1097/BRS.0000000000000973.

Del Pino Montes J. Epidemiología de las fracturas osteoporóticas: las fracturas vertebrales y no vertebrales. Rev Osteoporos Metab Miner2 2010;2:8–12.

Pressney I, Hargunani R, Khoo M, Tyler PA. Radiological imaging in the spine. Orthop Trauma 2014;28:106–15. https://doi.org/10.1016/j.mporth.2014.01.007.

Prost S, Pesenti S, Fuentes S, Tropiano P, Blondel B. Treatment of osteoporotic vertebral fractures. Orthop Traumatol Surg Res 2021;107:102779. https://doi.org/10.1016/J.OTSR.2020.102779.

Provaggi E, Leong JJH, Kalaskar DM. Applications of 3D printing in the management of severe spinal conditions. Http://DxDoiOrg/101177/0954411916667761 2016;231:471–86. https://doi.org/10.1177/0954411916667761.

Pugliese L, Marconi S, Negrello E, Mauri V, Peri A, Gallo V, et al. The clinical use of 3D printing in surgery. Updates Surg 2018;70:381–8. https://doi.org/10.1007/S13304-018-0586-5/METRICS.

Quiroga O, Matozzi F, Beranger M, Nazarian S, Gambarelli J, Salamon G. Normal CT anatomy of the spine. Anatomo-radiological correlations. Neuroradiology 1982;24:1–6. https://doi.org/10.1007/BF00344577.

Redruello-Guerrero P, Jiménez-Gutiérrez C, Láinez Ramos-Bossini AJ, Jiménez-Gutiérrez PM, Rivera-Izquierdo M, Benítez Sánchez JM. Artificial intelligence for the triage of COVID-19 patients at the emergency department: a systematic review. Signa Vitae 2022:2–11.

Renner JB. Conventional radiography in musculoskeletal imaging. Radiol Clin North Am 2009;47:357–72. https://doi.org/10.1016/J.RCL.2009.01.005.

Riancho JA, Peris P, González-Macías J, Pérez-Castrillón JL, Cannata Andía J, Cano A, et al. Resumen ejecutivo de las Guías de práctica clínica en la osteoporosis postmenopáusica, glucocorticoidea y del varón (actualización 2022). Rev Osteoporos y Metab Miner 2022;14:5–12. https://doi.org/10.4321/S1889-836X2022000100002.

Ridley LJ, Han J, Ridley WE, Xiang H. Wasp waist sign: Congenital vertebral fusion. J Med Imaging Radiat Oncol 2018;62:166–7. https://doi.org/10.1111/1754-9485.36_12786.

Rihn JA, Anderson DT, Sasso RC, Zdeblick TA, Lenke LG, Harris MB, et al. Emergency evaluation, imaging, and classification of thoracolumbar injuries. Instr Course Lect 2009;58:619–28.

Riley RD, Higgins JPT, Deeks JJ. Interpretation of random effects meta-analyses. BMJ 2011;342:964–7. https://doi.org/10.1136/BMJ.D549.

Ringer AJ, Bhamidipaty S V. Percutaneous Access to the Vertebral Bodies: A Video and Fluoroscopic Overview of Access Techniques for Trans-, Extra-, and Infrapedicular Approaches. World Neurosurg 2013;80:428–35. https://doi.org/10.1016/J.WNEU.2012.09.005.

Ross PD. Clinical consequences of vertebral fractures. Am J Med 1997;103:S30–43. https://doi.org/10.1016/S0002-9343(97)90025-5.

Ruiz Santiago F, Guzmán Álvarez L, Tello Moreno M, Navarrete González P. Plain-film radiography in the study of spinal pain. Radiologia 2010;52:126–37.

Rumrill PDJ, Fitzgerald SM. Using narrative literature reviews to build a scientific knowledge base. Work 2001;16:165–70.

Sanal HT, Akay S. Computerized tomography in the evaluation of musculoskeletal system. Musculoskelet Res Basic Sci 2015:165–82. https://doi.org/10.1007/978-3-319-20777-3_10/COVER.

Schmalstieg WF, Weinshenker BG. Spinal cord compression and myelopathies. Emerg Neurol 2012:235–58. https://doi.org/10.1007/978-0-387-88585-8_13/COVER.

Shapiro SS, Wilk MB. An Analysis of Variance Test for Normality (Complete Samples). Biometrika 1965;52:591. https://doi.org/10.2307/2333709.

Shepard N, Samim M, Kim Y, Razi A. A practical approach to spine magnetic resonance imaging. JBJS Rev 2020;8. https://doi.org/10.2106/JBJS.RVW.19.00099.

Shih CL, Shen PC, Lu CC, Liu ZM, Tien YC, Huang PJ, et al. A comparison of efficacy among different radiofrequency ablation techniques for the treatment of lumbar facet joint and sacroiliac joint pain: A systematic review and meta-analysis. Clin Neurol Neurosurg 2020;195. https://doi.org/10.1016/J.CLINEURO.2020.105854.

Singh A. Foundations of Machine Learning. SSRN Electron J 2019. https://doi.org/10.2139/SSRN.3399990.

Smith GR, Abel MS. Visualization of the Posterolateral Elements of the Upper Cervical Vertebrae in the Anteroposterior Projection1. Https://DoiOrg/101148/1151219 1975;115:219–20. https://doi.org/10.1148/115.1.219.

Sornay-Rendu E, Munoz F, Duboeuf F, Delmas PD. Disc Space Narrowing Is Associated With an Increased Vertebral Fracture Risk in Postmenopausal Women: The OFELY Study. J Bone Miner Res 2004;19:1994–9. https://doi.org/10.1359/JBMR.040904.

Spivak JM, Johnson MG. Percutaneous treatment of vertebral body pathology. J Am Acad Orthop Surg 2005;13:6–17. https://doi.org/10.5435/00124635-200501000-00003.

Standring S. Gray's Anatomy: The Anatomical Basis of Clinical Practice. Elsevier Limited; 2016.

Sterne JAC, Sutton AJ, Ioannidis JPA, Terrin N, Jones DR, Lau J, et al. Recommendations for examining and interpreting funnel plot asymmetry in meta-analyses of randomised controlled trials. BMJ 2011;343. https://doi.org/10.1136/BMJ.D4002.

Student. The Probable Error of a Mean. Biometrika 1908;6:1. https://doi.org/10.2307/2331554.

Suh SW, Sarwark JF, Vora A, Huang BK. Evaluating congenital spine deformities for intraspinal anomalies with magnetic resonance imaging. J Pediatr Orthop 2001;21:525–31.

Swets JA. Measuring the accuracy of diagnostic systems. Science 1988;240:1285–93. https://doi.org/10.1126/SCIENCE.3287615.

Takenaka S, Mukai Y, Hosono N, Fuji T. Major Surgical Treatment of Osteoporotic Vertebral Fractures in the Elderly: A Comparison of Anterior Spinal Fusion, Anterior-Posterior Combined Surgery and Posterior Closing Wedge Osteotomy. Asian Spine J 2014;8:322–30. https://doi.org/10.4184/ASJ.2014.8.3.322.

Târcoveanu E, Roca M, Mihăescu T. [Writing and publication of a clinical case report]. Chirurgia (Bucur) 2011;106:581–4.

Telera S, Raus L, Pipola V, De Iure F, Gasbarrini A. Traumatic Vertebral Fractures. Vertebr Body Augment Vertebroplasty Kyphoplasty Spine Surg 2021:149–58. https://doi.org/10.1007/978-3-030-76555-2_10.

The Global Burden of Osteoporosis: a Factsheet. 2019.

Tins B. Technical aspects of CT imaging of the spine. Insights into Imaging 2010 15 2010;1:349–59. https://doi.org/10.1007/S13244-010-0047-2.

Torres-Velazquez M, Chen WJ, Li X, McMillan AB. Application and Construction of Deep Learning Networks in Medical Imaging. IEEE Trans Radiat Plasma Med Sci 2021;5:137–59. https://doi.org/10.1109/TRPMS.2020.3030611.

Torres C, Hammond I. Computed Tomography and Magnetic Resonance Imaging in the Differentiation of Osteoporotic Fractures From Neoplastic Metastatic Fractures. J Clin Densitom 2016;19:63–9. https://doi.org/10.1016/J.JOCD.2015.08.008.

Truumees E. Medical consequences of osteoporotic vertebral compression fractures. Instr Course Lect 2003;52:551–8.

Urban JPG, Winlove CP. Pathophysiology of the intervertebral disc and the challenges for MRI. J Magn Reson Imaging 2007;25:419–32. https://doi.org/10.1002/JMRI.20874.

Urrutia J, Zamora T, Yurac R, Campos M, Palma J, Mobarec S, et al. An Independent Inter- and Intraobserver Agreement Evaluation of the New AO Spine Thoracolumbar Spine Injury Classification System. Https://DoiOrg/101055/s-0035-1554440 2017;5:s-0035-1554440-s-0035-1554440. https://doi.org/10.1055/S-0035-1554440.

Valladares-Otero A, Christenson B, Petersen BD. Radiologic imaging of the spine. Spine Surg Basics 2014:37–73. https://doi.org/10.1007/978-3-642-34126-7_4/COVER.

Vosper M. Principles of CT. CT Colonography Radiogr 2016:25–39. https://doi.org/10.1007/978-3-319-29379-0_4.

Wake N. 3D Printing for the Radiologist. Elsevier.; 2021.

Waldt S, Gersing A, Brügel M. Measurements and classifications in spine imaging. Semin Musculoskelet Radiol 2014;18:219–27. https://doi.org/10.1055/S-0034-1375565/ID/JR00781-28/BIB.

Walter SD, Yao X. Effect sizes can be calculated for studies reporting ranges for outcome variables in systematic reviews. J Clin Epidemiol 2007;60:849–52. https://doi.org/10.1016/j.jclinepi.2006.11.003.

Wáng YXJ, Santiago FR, Deng M, Nogueira-Barbosa MH. Identifying osteoporotic vertebral endplate and cortex fractures. Quant Imaging Med Surg 2017;7:555–91. https://doi.org/10.21037/QIMS.2017.10.05.

Wardhana A, Ikawaty R, Sudono H. Comparison of Radiofrequency and Corticosteroid Injection for Treatment of Lumbar Facet Joint Pain: A Meta-Analysis. Asian J Anesthesiol 2022;60:53–60. https://doi.org/10.6859/aja.202206_60(2).0003.

Waxenbaum J, Reddy V, Black A, Futterman B. Anatomy, Back, Cervical Vertebrae. StatPearls 2023.

Wcg P, Journal I, Kh N. Writing a pictorial essay. Singapore Med J 2010;51:186–9.

Weiss K, Khoshgoftaar TM, Wang DD. Transfer learning techniques. Big Data Technol Appl 2016:53–99. https://doi.org/10.1007/978-3-319-44550-2_3/TABLES/6.

Williams AL, Al-Busaidi A, Sparrow PJ, Adams JE, Whitehouse RW. Under-reporting of osteoporotic vertebral fractures on computed tomography. Eur J Radiol 2009;69:179–83. https://doi.org/10.1016/j.ejrad.2007.08.028.

Yang E, Suzuki M, Nazarian S, Halperin HR. Magnetic resonance imaging safety in patients with cardiac implantable electronic devices. Trends Cardiovasc Med 2022;32:440–7. https://doi.org/10.1016/J.TCM.2021.08.001.

Yoon SP, Lee SH, Ki CH, Lee YT, Hong SH, Lee HM, et al. Quality of Life in Patients with Osteoporotic Vertebral Fractures. Asian Spine J 2014;8:653–8. https://doi.org/10.4184/ASJ.2014.8.5.653.

Zhang B, Yu K, Ning Z, Wang K, Dong Y, Liu X, et al. Deep learning of lumbar spine X-ray for osteopenia and osteoporosis screening: A multicenter retrospective cohort study. Bone 2020;140:115561. https://doi.org/10.1016/J.BONE.2020.115561.

Zhang L, Pan Y, Wu X, Skibniewski MJ. Introduction to Artificial Intelligence. Lect Notes Civ Eng 2021;163:1–15. https://doi.org/10.1007/978-981-16-2842-9_1/COVER.

Zheng B, Wang X, Zheng Y, Feng J. 3D-printed model improves clinical assessment of surgeons on anatomy. J Robot Surg 2019;13:61–7. https://doi.org/10.1007/S11701-018-0809-2/METRICS.

APÉNDICES

X. APÉNDICES

Apéndice 1. Capítulo de libro en el que se revisan los fundamentos y anatomía radiológica seccional de las principales regiones del cuerpo humano, incluyendo la columna vertebral. Reproducido con permiso de la editorial Wiley-Blackwell. Referencia completa: Láinez Ramos-Bossini AJ, Salmerón Ruiz A, Martínez Barbero JP, Martín Molina JP, Martín Rodríguez JL, López Milena G, Ruiz Santiago F. Cross-sectional correlate for integrative imaging (anatomical radiology). En: Gholamrezanezhad A, Assadi M, Jadvar H. Multidisciplinary Diagnostic Imaging: Radiology-Nuclear Medicine Correlative Imaging. Wiley-Blackwell. ISBN-10: 1119603617. 2021; 52-132.

3

Cross-sectional Correlate for Integrative Imaging (Anatomical Radiology)

Antonio Jesús Láinez Ramos-Bossini[1], Ángela Salmerón-Ruiz[1], José Pablo Martínez Barbero[1], José Pablo Martín Molina[2], José Luis Martín Rodríguez[2], Genaro López Milena[1], and Fernando Ruiz Santiago[1,3]

[1]*Department of Radiology, Virgen de las Nieves University Hospital, University of Granada, Granada, Spain*
[2]*Department of Radiology, San Cecilio University Hospital, University of Granada, Granada, Spain*
[3]*Neuro-traumatology Hospital, Virgen de las Nieves University Hospital, School of Medicine, University of Granada, Granada, Spain*

Relevant Imaging Anatomy and Variants

This chapter aims to describe the essential aspects of normal anatomy and its variants on cross-sectional imaging from a radiological perspective. The imaging techniques that will be reviewed are computed tomography (CT) and magnetic resonance imaging (MRI). To define the anatomical structures precisely, it is important to remember that information from these two imaging modalities is obtained from different types of sources, namely ionizing radiation in the case of CT and radiofrequency pulses in a magnetic field in MRI. Consequently, the ability of each of these examinations to depict anatomical structures differs in terms of both quality and precision. In general, it can be stated that CT is superior in defining bony structures, while MRI is more advantageous for studying soft tissues, including bone marrow, due to its higher contrast resolution.

CT is a cross-sectional imaging method that provides high spatial resolution for anatomical imaging of the human body. The introduction of the helical CT technique in 1989, in which images are acquired during continuous rotation of the X-ray tube with simultaneous movement of the table (and the patient), allowed significant shortening of the scanning time compared to the first sequential acquisition CT devices. The posterior development of multislice CT scanners with an increasing number of detector rows (e.g. from four or 16 rows initially to the latest models with up to 320 rows) made it possible to acquire a large number of slices simultaneously with a tube rotation time of less than 1 second [1, 2].

Although imaging acquisition is performed in the axial plane, submillimeter slices allow the creation of isotropic images with no significant spatial resolution distortion in multiplanar and 3D reconstructions [3]. CT can distinguish different tissues based on their specific X-ray attenuation, providing structural information. Quantitative information can be obtained based on Hounsfield Unit (HU) values, which measure the density of any structure relative to water (0 HU). For instance, the normal density of fat tissue ranges between −190 and −30 HU, and normal soft tissues show attenuation values in the range of 31–100 HU (although increased fat content may reduce this density to as low as 0 or even negative HU values) [4, 5]. Tendons appear hyperdense relative to muscles, with reported values ranging from 75 to 115 HU. The air contained within the paranasal sinuses, lungs or bowel presents density values up to −1000 HU.

Accordingly, so-called "windows" allow optimization of the analysis of certain anatomic regions by setting the value of two parameters: level and width. For example, to study lung parenchyma, a default "lung window" is set at a level of −700 HU with a width of −1000 HU, whereas analysis of brain tissue is conventionally performed with a level of 40 HU and a width of 80 HU. In addition, intravenous administration of iodine contrast can provide relevant information on vascular structures and tissue vascularization. If the acquisition is performed soon after contrast administration (e.g. 15–40 seconds depending on the anatomical region), information on arterial vascularization will be obtained. More delayed acquisitions will provide further information on the venous system and tissue microvascularization.

Radiology-Nuclear Medicine Diagnostic Imaging: A Correlative Approach, First Edition. Edited by Ali Gholamrezanezhad, Majid Assadi, and Hossein Jadvar.

In current multislice CT scanners, the radiation dose can be reduced by selecting appropriate acquisition protocols (e.g. adjusting voltage, slice thickness, and pitch) as well as by automatic modulation of the tube current. Radiation dose and image noise can also be reduced using iterative reconstruction techniques.

Compared to CT, MRI offers better characterization of soft-tissue structures, including the spinal cord. Standard protocols in most anatomical regions should include the basic sequences, namely T1- and T2-weighted images. In addition, fat-suppressed images based on techniques of chemical shift and/or inversion-recovery suppression are usually performed [6]. As with CT, contrast-enhanced protocols after intravenous gadolinium administration are commonly used to analyze the vascular behavior of different structures. More advanced MRI sequences, such as diffusion or perfusion-weighted images, can help further characterization of lesions. Of note, the reader should know that there is substantial protocol variability according to the anatomical region and type of lesion under study. Because this chapter is particularly focused on anatomy, most figures are based on T1- and T2-weighted images.

The chapter is divided into different sections to cover all relevant anatomy "from head to toe." We believe that this structure will facilitate the understanding of the whole chapter. At the end of the chapter, the reader will have a comprehensive overview of the cross-sectional imaging findings on radiological anatomy that nuclear medicine physicians should be aware of in their daily practice.

Anatomy of the Brain

For an adequate knowledge of the radiological anatomy, it is first convenient to conduct a brief review of the radiological semiology of the brain, i.e. how the different structures that make up the brain are depicted in different techniques or sequences.

Semiology of the Brain in Neuroimaging

In general, the density of the gray matter (GM) (cerebral cortex and basal ganglia) is slightly high (about 50 HU) relative to that of the white matter (WM) (about 30 HU) on CT images, probably because of the higher cell density in the former. Comparatively, the cerebrospinal fluid (CSF) is hypodense, with density values close to water (0–5 HU), while parenchymal or dural calcifications and bone structures are hyperdense. To increase the ability for detecting and characterizing lesions, CT examinations can be complemented with the administration of intravenous contrast. Accordingly, vascular CT angiography of supra-aortic vessels (SAV) and circle of Willis (COW), or cerebral venography studies can be performed. In addition, intravenous contrast enables the assessment of the enhancement pattern of vascularized lesions, such as vascular malformations or tumors with a high rate of neovascularization (e.g. meningiomas and glioblastomas) [7]. Moreover, it allows the evaluation of the integrity of the blood–brain barrier (BBB), whose disruption determines high-contrast uptake in high-grade glial tumors, metastases or inflammatory lesions [8].

In MRI, each tissue has a specific signal intensity in different sequences. Accordingly, the combination of the different signal intensities allows the differentiation and characterization of normal tissues, which, in turn, enables the detection of abnormalities and the use of diagnostic algorithms [9]. In general, in T1-weighted sequences, the GM is hypointense relative to the WM, and vice versa in T2-weighted sequences. The CSF is markedly hyperintense in T2-weighted sequences and hypointense in T1-weighted sequences. The use of T2-Flair (Fluid Liquid Attenuation Inversion Recovery) sequences allows the suppression of the free-water signal, and specifically the CSF signal, improving the detection of lesions in the brain parenchyma and the subarachnoid space (SAS). Fat, which is present in the subcutaneous tissue of the skull, facial bones, neck, and back, as well as inside the orbits and deep spaces of the neck (particularly the masticator and parapharyngeal spaces), is hyperintense in both T1- and T2-weighted sequences. Fat-suppression techniques based on different physical approaches (e.g. Dixon, STIR, SPAIR, SPIR or FatSat) are frequently used to improve the detection of lesions.

The most commonly used contrast in MRI is based on gadolinium chelates, which shorten T1 relaxation times, increasing signal intensity. Enhancement is mainly secondary to disruption of the BBB and increased vascularization [10]. Of special interest are the T2 gradient echo and magnetic susceptibility weighted imaging (SWI) sequences, which have higher sensitivity to detect ferromagnetic substances. Accordingly, SWI sequences allow the identification of the substantia nigra and the red nuclei in the midbrain. Of note, blood deposits can be recognized in SWI as hypointense lesions, including intraparenchymal hematomas, subarachnoid hemorrhage (SAH), cortical siderosis or microhemorrhage foci from hypertensive angiopathy [9].

Diffusion sequences are based on MRI properties to detect the movement of protons and, consequently, of water molecules. In an ideal free environment, molecules move in all directions in space. However, the human body contains numerous barriers that hinder the free diffusion of water molecules, causing "diffusion restriction," mainly

in the CNS, the BBB, and cellular barriers (such as myelin). Accordingly, the CNS shows significant restricted diffusion under physiological conditions

Compartments and Structures of the CNS

The CNS comprises a series of intracranial structures. At the supra-tentorial level, the brain is located in the anterior and middle cranial fossae and contains two hemispheres separated by the falx cerebri. In the posterior fossa, the tentorium cerebelli separates the brain stem (composed of midbrain, pons, and medulla oblongata) from the cerebellum (Figure 3.1).

Anatomy of the Coverings of the CNS

The CNS is encased and protected by different bone structures, including the skull, of great anatomical complexity and comprising multiple bones joined to each other and to the facial bones. In addition, the structures of the CNS present an inner lining composed of several membranes known as the meninges [11]. The most external and thickest layer is the dura mater or pachymeninx, which in turn comprises two layers, one that forms the periosteum of the skull and is attached to the inner table; and another one, more internal or meningeal, which makes up the falx cerebri, tentorium, and diaphragma sellae. The dura mater can be distinguished on imaging and is usually less than 2 mm thick. The innermost meningeal layer is the leptomeninx, composed of the arachnoid mater (attached to the inner layer of the inner dura, which is the outer boundary of the SAS) and the pia mater, in direct contact with the brain. The two components of the leptomeninges are not visible on imaging, except in the presence of pathologic processes, in which both layers are usually affected. The fact that these layers are the boundaries of the SAS makes them especially relevant [8, 10].

Anatomy of the Brain Parenchyma

One of the cornerstones of the morphological and functional anatomy of the brain is the concept of somatotopy, according to which there is a specific location in the CNS controlling the functions of the rest of the body, especially the motor and sensory functions [12]. In addition, despite having a similar histological architecture, each structure of the CNS performs different tasks based on its location. The distribution of specific operations in

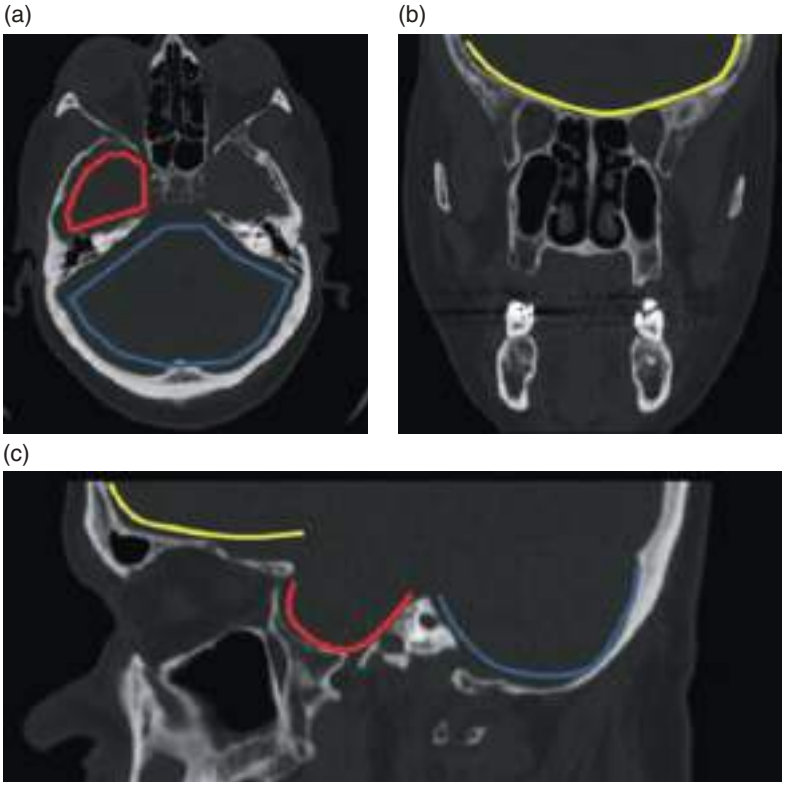

Figure 3.1 Bone anatomy of the cranial fossae. (a) Axial CT image. (b) Coronal CT multiplanar reconstruction (MPR) image. (c) Sagittal MPR CT image. Yellow, anterior cranial fossa; red, middle cranial fossa; blue, posterior cranial fossa.

different cortical regions highlights the importance of the functional anatomy of the brain [13].

The CNS is mainly made up of two types of tissue: the GM, mostly composed of neuronal bodies, and the WM, arranged around the neuronal axons. The GM is mainly present in two locations, namely the cerebral cortex and the deep GM, with the basal ganglia being its most representative example.

Functional Anatomy of the Cerebral Cortex

The cortical GM is formed by the cerebral cortex and cerebellum, being responsible for the main functional tasks according to the anatomical location. During evolutionary development, numerous folds have been formed on the encephalic surface to increase the volume of GM as much as possible. The main consequence of this phylogenetic process is the formation of the so-called sulci and fissures (depressions of the surface), and their corresponding gyri [14].

The brain parenchyma is divided into lobes, which can be defined based on the primary sulci and fissures (Figures 3.2 and 3.3) [11, 14]. Accordingly, the frontal lobes are situated in the anterior pole of the brain, particularly in the anterior fossa and on both sides of the interhemispheric fissure, being separated from the parietal lobes by the central sulcus. The temporal lobes are located in the middle cranial fossa, and the Sylvian fissure separates them from

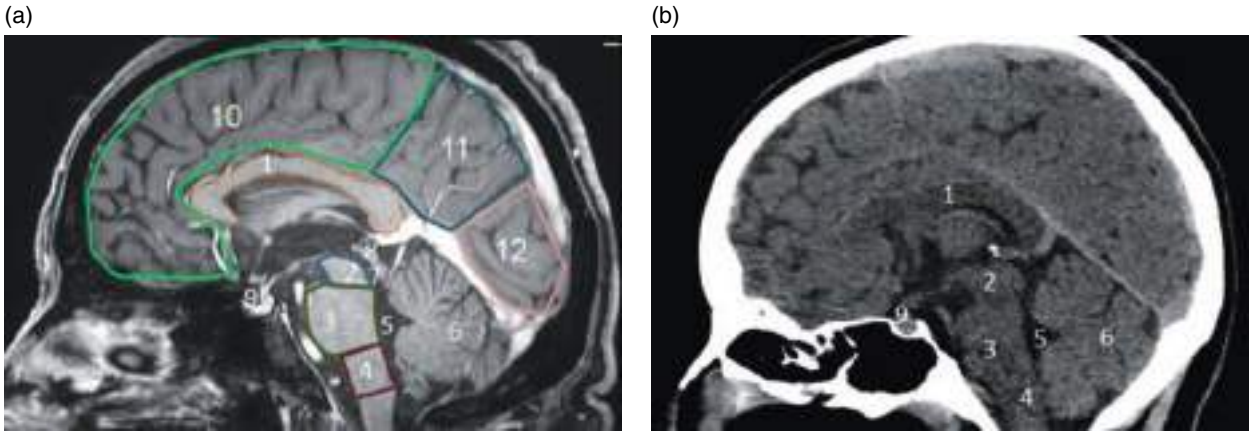

Figure 3.2 Sagittal anatomy of the brain in the midline. (a) Sagittal contrast-enhanced T1-3D weighted magnetic resonance image (MRI). (b) Sagittal noncontrast MPR CT image of the skull. 1, corpus callosum; 2, midbrain; 3, pons; 4, medulla oblongata; 5, fourth ventricle; 6, cerebellar vermis; 7, cerebral aqueduct; 8, quadrigeminal plate; 9, sella turcica; 10, frontal lobe; 11, parietal lobe; 12, occipital lobe.

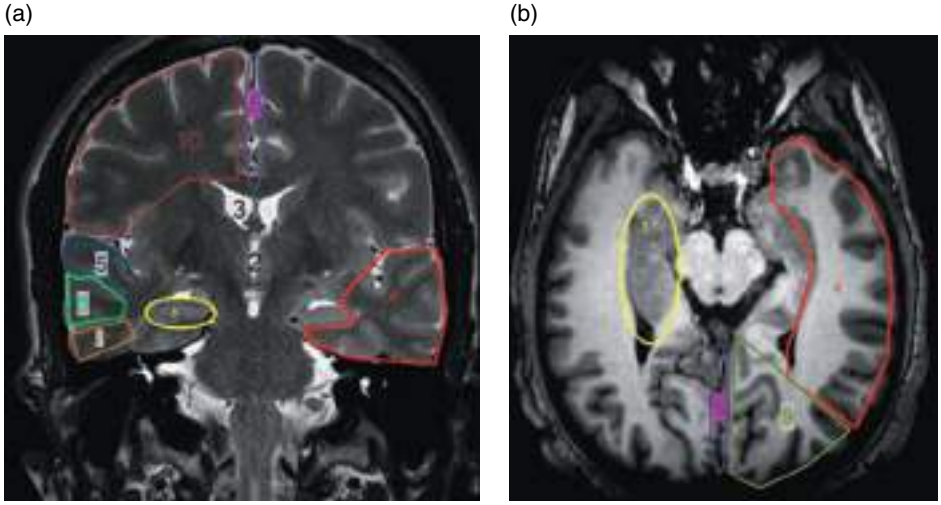

Figure 3.3 Lobar and cortical anatomy. (a) Coronal T2-weighted MRI. (b) Axial T1-3D- weighted MRI (plane at the level of the hippocampus). 1, hippocampus; 2, third ventricle; 3, body of the lateral ventricle; 4, temporal lobe; 5, superior temporal gyrus; 6, middle temporal gyrus; 7, inferior temporal gyrus; 8, interhemispheric fissure; 9, occipital lobe; 10, frontal lobe.

the frontal and parietal lobes. The parietal lobes extend along the postero-superior margin of the convexity of the brain, and their posterior boundaries with the occipital lobe are difficult to define since the parieto-occipital fissure is not always present. The occipital lobes are located in the posterior part of the encephalus, in relation to the occipital bones. Moreover, modern functional neuroanatomy usually considers two other lobes, namely the insular cortex, which is located in the depth of the Sylvian fissure and inferior to the frontal operculum, and the limbic lobe, composed of GM structures and located on both sides of the midline, surrounding the corpus callosum.

It is important to briefly review the most relevant sulci and fissures of the frontal lobes. In the basal face of the frontal lobe, the supraorbital gyri (medial, lateral, anterior, and posterior) are related to the floor of the anterior cranial fossa, and the gyrus rectus, of parasagittal location on both sides of the midline, is related to the cribiform plate of the ethmoid bone and the crista galli. On the lateral face of the frontal lobe, the superior, middle, and inferior frontal gyri can be found. In the latter, immediately above Sylvian fissure, there is an area of paramount importance due to its linguistic function, known as the opercular region (Figure 3.4). It is made up of three adjacent gyri which, from anterior to posterior, are called pars orbitalis, pars triangularis, and pars opercularis.

The primary motor cortex, located in the precentral gyrus, is of special importance. Following a somatotopic arrangement as defined by the Penfield's homunculus, the motor areas of the leg and foot (parasagittal), hand and arm (convexity), and mouth and face (lateral aspect) can be found in this gyrus. A number of anatomical landmarks can be used to locate the central sulcus (Figure 3.4). Accordingly, the motor area of the hand usually adopts a characteristic omega (Ω) or epsilon (ε) shape. In addition, it is helpful to know that the central sulcus does not usually reach the

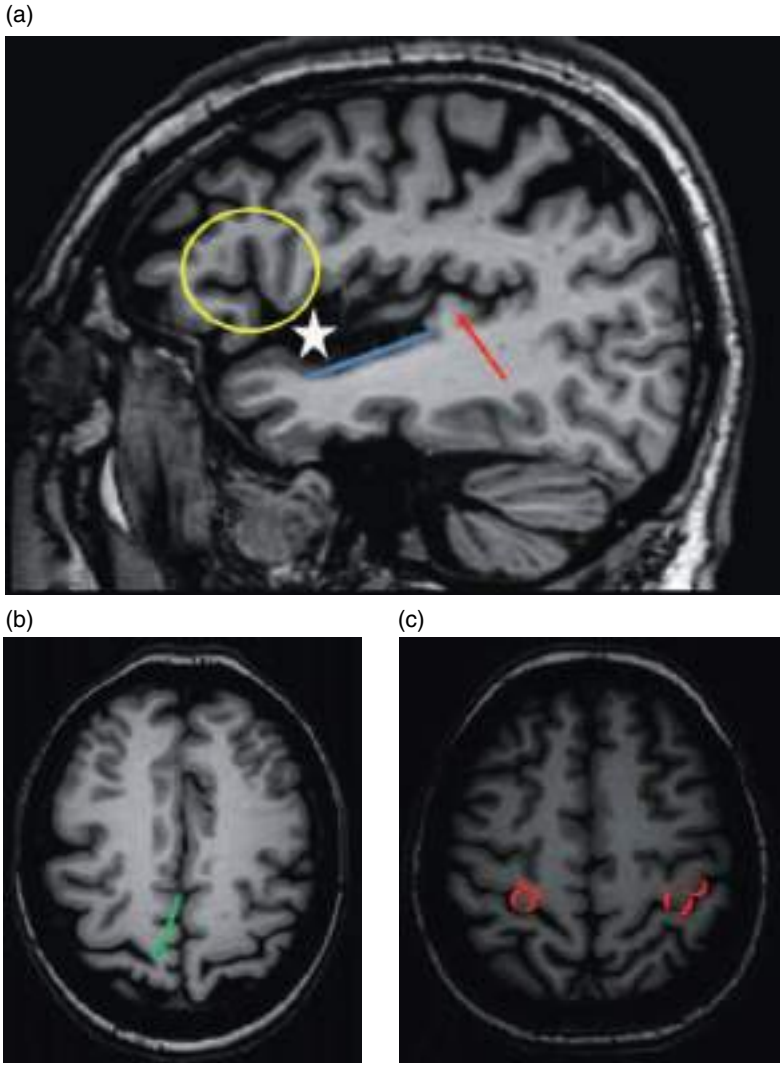

Figure 3.4 Landmarks of cortical anatomy. (a) Sagittal T1-weighted MRI. (b, c) Axial T1-weighted MRI with different angulation. (a) The Sylvian fissure (white asterisk), the superior face of the temporal lobe with the planum temporale (blue line), and the Heschl's gyrus (red arrow). The opercular region (yellow circle) lies above the Sylvian fissure. (b) How the central sulcus does not normally reach the interhemispheric fissure (green arrow). (c) Typical appearances of the motor area of the hand at the central gyrus, i.e. inverted omega shape on the right side and epsilon shape on the left side.

interhemispheric fissure, while the superior frontal sulcus normally ends in the pre-central (rather than the central) sulcus. Furthermore, in MRI, the motor cortex is more hyperintense in T2-weighted images and less well-defined in T1-weighted images, which also helps locate this area.

The lateral face of the temporal lobe includes the inferior, middle, and superior temporal gyri. Its superior face contains the so-called "planum temporale," interrupted in its posterior and deep margin by the Heschl's gyrus, of great relevance for being responsible for auditory processing based on tonotopic coding (Figure 3.4). On the lateral side (usually in the superior temporal gyrus) lies the Wernicke area, also of major importance. In the medial margin of the temporal lobes lie the hippocampi, of special relevance due to their implication in long-term memory. The hippocampal convolution is formed by a folding of the cortex, contains a high density of GM, and is bounded by the choroidal fissure medially (Figure 3.3).

In the parietal lobes, the most relevant part of the cortex is the post-central cortex, responsible for the sensitivity of the body, and with a somatotopic organization similar to the motor cortex. The occipital cortex is located in the posterior and basal pole of the calcarine fissure, being responsible for the visual function.

Anatomy of the Basal Ganglia

The other typical location of GM is the basal ganglia (BG or gray nuclei), which are located in the deep part of the cerebral hemispheres and in the cerebellum. The BG are connected with each other and with the cortex, being part of numerous functional circuits [15].

In the supratentorial compartment, the claustrum is located between the extreme and external capsules. It has a linear morphology and is hypointense in T1-weighted images, but it is usually only visible in volumetric sequences in 3T MRI equipment. Medially, the lenticular nucleus (composed of the putamen and the globus pallidus in its posterolateral and anteromedial portions, respectively) is located between the external and internal capsules. The putamen is hypointense in T1 and slightly hyperintense in T2, while the globus pallidus is isointense relative to the WM in T1 and hypointense in T2. The caudate nuclei lie lateral to the frontal horns and bodies of the lateral ventricles, being isointense relative to the lenticular nuclei. The thalami, of more posterior and inferior location, are difficult to recognize in T1-weighted images because their signal intensity is similar to that of the WM and slightly hyperintense in T2-weighted images (Figure 3.5). The substantia nigra and red nuclei of the midbrain, as well as the subthalamic nuclei, can be identified as hypointense structures in magnetic susceptibility sequences due to their high content in iron (Figure 3.6) [16]. In the cerebellum, the dentate nuclei lie on both sides of the fourth ventricle, with a hypointense central area and hyperintense periphery (Figure 3.7). Under normal conditions, the dentate nuclei are isointense to the WM in T1-weighted images. Nevertheless, it has been recently described that, in patients undergoing repeated examinations with intravenous gadolinium, their signal intensity increases due to interstitial

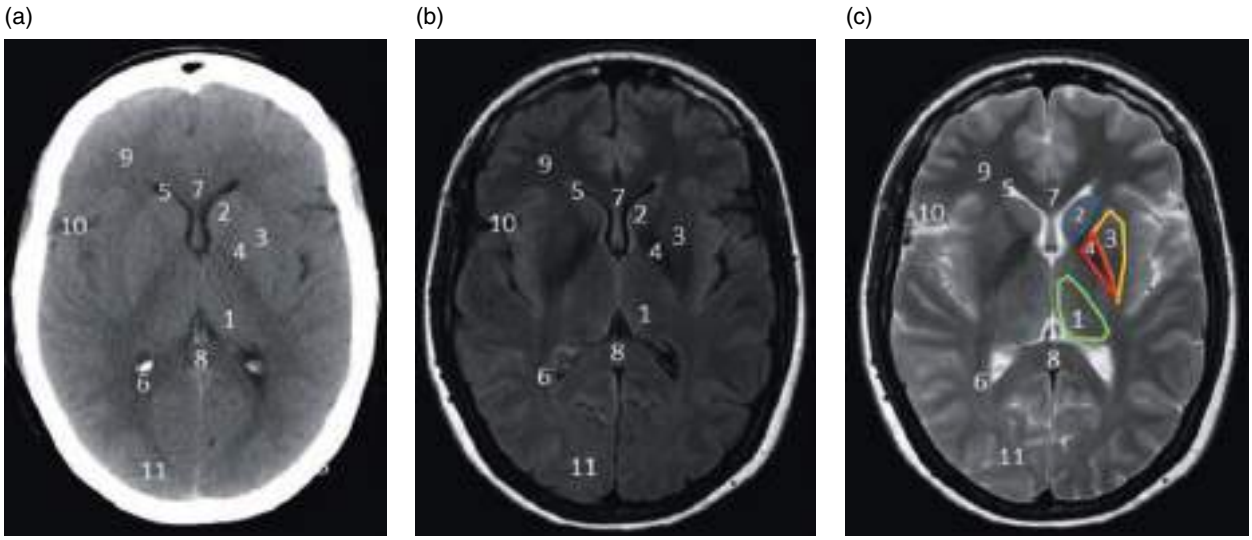

Figure 3.5 Supratentorial axial anatomy, section at the level of the base ganglia. (a) Axial noncontrast CT image. (b) Axial FLAIR T2-weighted MRI. (c) Axial TSE T2-weighted MRI. 1, thalamus; 2, caudate; 3, putamen; 4, globus pallidus; 5, frontal horn of the lateral ventricle; 6, occipital horn of the lateral ventricle; 7, genu of the corpus callosum; 8, splenium of the corpus callosum; 9, frontal lobe; 10, Sylvian fissure; 11, occipital lobe.

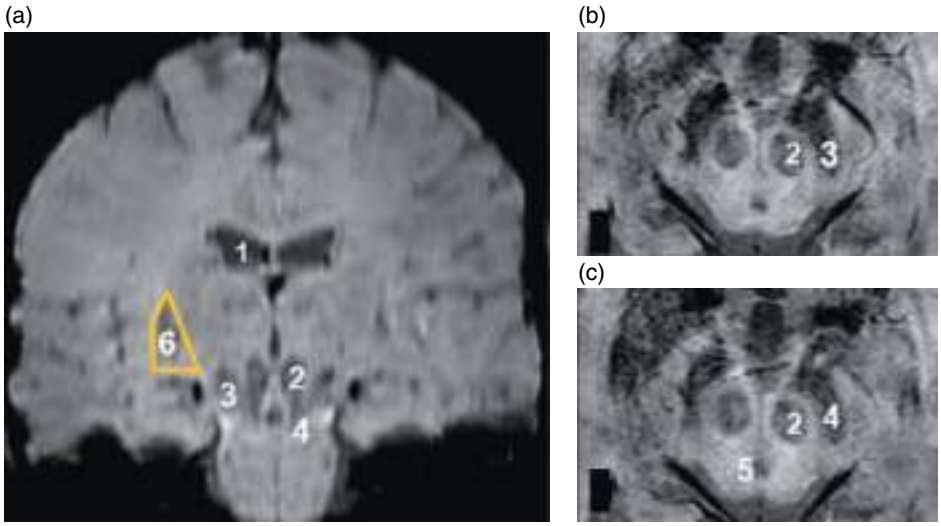

Figure 3.6 Anatomy of the basal ganglia in magnetic susceptibility weighted imaging. (a) Coronal image. (b) Axial image at the level of (3) in (a). (c) Axial image at the level of (4) in (a). 1, body of the lateral ventricle; 2, red nucleus; 3, subthalamic nucleus; 4, substantia nigra; 5, cerebral aqueduct; 6, putamen.

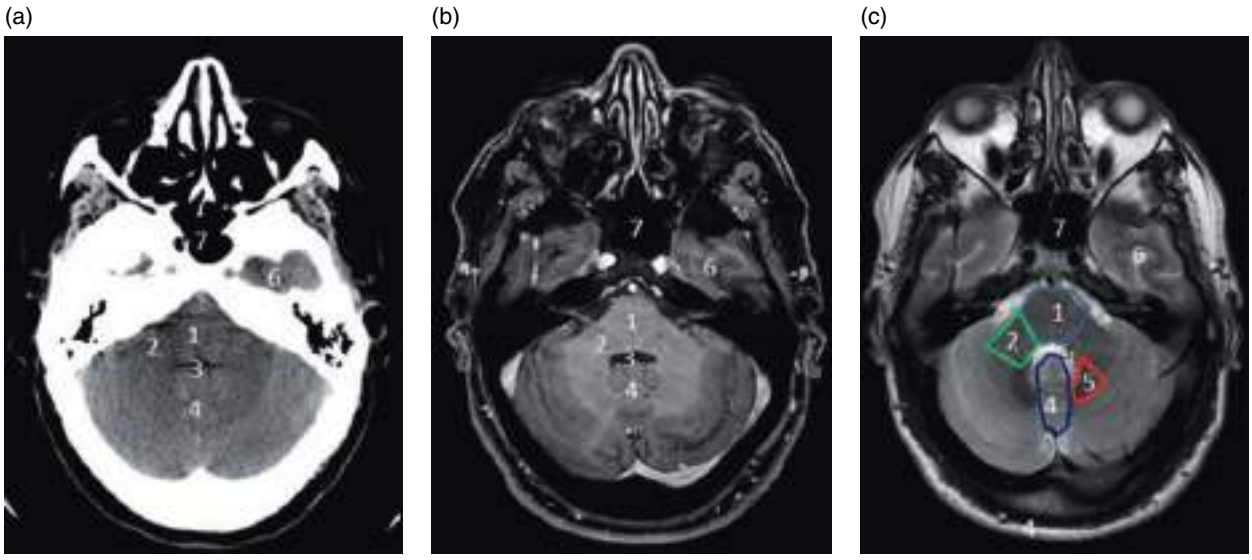

Figure 3.7 Infratentorial axial anatomy, sections at the level of the fourth ventricle. (a) Axial noncontrast CT image. (b) Axial contrast-enhanced T1-3D-weighted MRI. (c) Axial TSE-T2-weighted MRI. 1, pons; 2, middle cerebellar peduncle; 3, fourth ventricle; 4, cerebellar vermis; 5, dentate nucleus; 6, temporal lobe; 7, sphenoid sinus.

gadolinium deposits. There are also GM regions around the cerebral aqueduct of Sylvius and in the lateral walls of the third ventricle, although they do not represent actual nuclei [17].

Anatomy of the White Matter

Historically, the study of the WM by imaging has been difficult. The similar appearance of WM tracts in the different imaging techniques made their individualization almost impossible [13]. However, diffusion tensor imaging (DTI) has allowed anatomical maps of WM fibers to be obtained *in vivo* and noninvasively, leading to a quantum leap in the study of WM.

From the classic anatomical perspective, three main groups of WM fibers can be distinguished, namely association, projection, and commisural. The association fibers communicate cortical neurons from one hemisphere with other neurons more or less nearby, usually from the same functional circuit. The projection fibers connect different

cortical regions with the deep GM from the BG or run toward the spinal cord. Finally, the commissural fibers are responsible for interconnecting the cerebral hemispheres.

The commissural fibers can be easily identified in structural MRI or CT examinations, and should exhibit the same imaging features as the rest of the WM under normal conditions (Figure 3.8). The most relevant anatomical structure within this group is the corpus callosum, formed from anterior to posterior by rostrum, genu (minor forceps), body, and splenium (forceps major). It is located above the lateral ventricles and interconnects the cerebral hemispheres in a massive way. Agenesis of the corpus callosum is usually associated with developmental disorders, although it may be an incidental and asymptomatic finding occasionally. In addition, partial hypoplasia of the corpus callosum can be associated with midline lipomas, of low density in CT and high signal intensity in T1- and T2-weighted images in MRI.

The anterior commissure connects the deep WM of both temporal lobes and is located anterior to the columns of the fornix. The posterior commissure connects both cerebral hemispheres above the cerebral aqueduct, particularly occipital fibers related to light perception. These commissures are especially relevant since the imaginary plane that joins them in the sagittal projection (intercommisural line) is used as a landmark for the axial plane in most MRI studies. They are easily located in sagittal T1-weighted images but may be absent as a variant of normality in some cases. The interthalamic adhesion can sometimes be seen in the midline, at the level of the third ventricle, as an anatomical variant.

The projection fibers originate in the cortex and direct toward the BG, posterior fossa or spinal cord. The most relevant structure within this group of fibers is the corticospinal tract, which arises from the primary motor cortex of the central gyrus and runs inferiorly through the corona radiata, posterior limb of the internal capsule, and cerebral peduncles, reaching the pons, from which they extend to both sides of the midline.

The association fibers are responsible for connecting adjacent cortex areas, which usually belong in the same functional circuit. The "U" or juxtacortical fibers stand out within this group, as well as bundles such as the arcuate fasciculus, which connect the areas related to the language circuit.

Brief Overview of the Cranial Nerves

The cranial nerves are a set of 12 nerves that arise from the encephalus and are involved in sensory functions, motor control of facial muscles, and regulation of glands of the neck. We will briefly review the most relevant cranial nerves from the radiological point of view. Both T2 (e.g. T2-DRIVE 3D or FIESTA) and T13D volumetric sequences with isotropic voxel and high resolution (less than 1 mm) are required for the study of the cranial nerves (Figure 3.9).

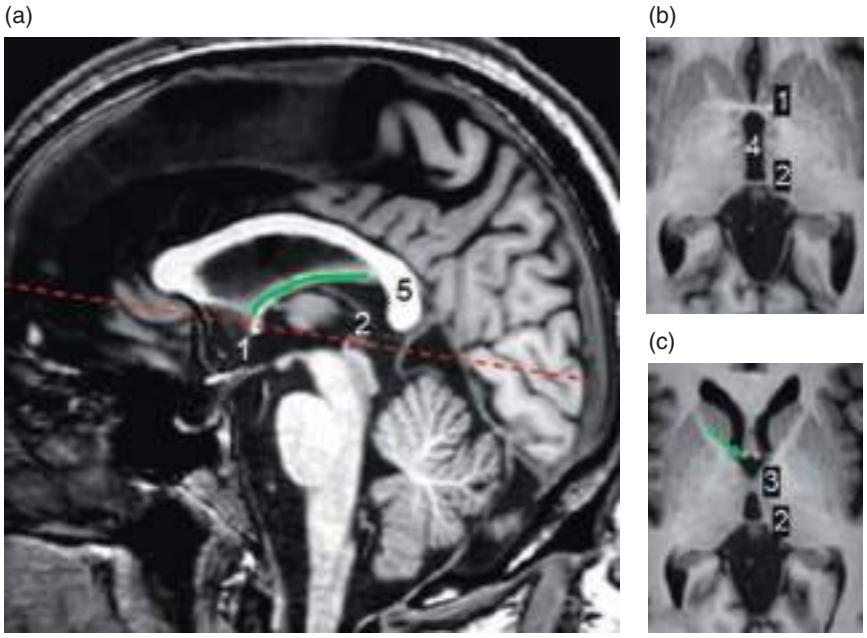

Figure 3.8 Cerebral commissures. (a) Sagittal T1-weighted MRI. (b, c) Axial T1-weighted MRI in two different patients. The intercommissural line, which is used as a landmark to acquire sequences in the axial plane, can be seen in (a) (dashed red line). (b) The anterior and posterior commissures. (c) The interthalamic adhesion, a variant of normality. 1, anterior commissure; 2, posterior commissure; 3, interthalamic adhesion; 4, third ventricle; 5, corpus callosum. Green line (a) and arrow (c) show the fornix.

The first cranial nerve, or olfactory nerve, is located in the anterior cranial fossa, specifically in the olfactory fossa, on both sides of the midline and the crista galli, and closely related to the gyrus rectus of the basal face of the frontal lobes. Its fibers, hypointense relative to the CSF in T2-weighted images, cross the cisternal space toward the cribiform plate.

The second cranial nerve, or optic nerve, arises from the fovea centralis of the ocular globes, and is isointense to the WM in all MRI sequences. In fact, strictly speaking, it is a WM tract and not a peripheral nerve. The optic nerve has an intraconal course within the orbit, a fissural segment by which it exits the orbit, and a cisternal segment prior to crossing over in the optic chiasm, of suprasellar location, and from where the optic tracts and radiations arise.

The fifth cranial nerve, or trigeminal nerve, has its nuclei in the brain stem, and emerges on both sides of the pons. It presents an anterior course toward the Meckle's cave, where the trigeminal ganglion is located. At this point, the nerve trifurcates, although its branches are not radiologically evident. It is easily identifiable in its cisternal course in T2-weighted images. Contact areas between the trigeminal nerve and vascular structures are of special relevance for being a potential cause of trigeminal neuralgia.

The bundle containing the facial and statoacoustic nerves (VII and VIII cranial nerves, respectively) arises from both sides of the pons, crosses the cistern of the pontocerebellar angle, and enters the internal auditory meatus. In the intra-canalicular segment, we can distinguish the VII cranial nerve (supero-anterior) and the cochlear nerve (infero-anterior). The vestibular branches are of posterior location.

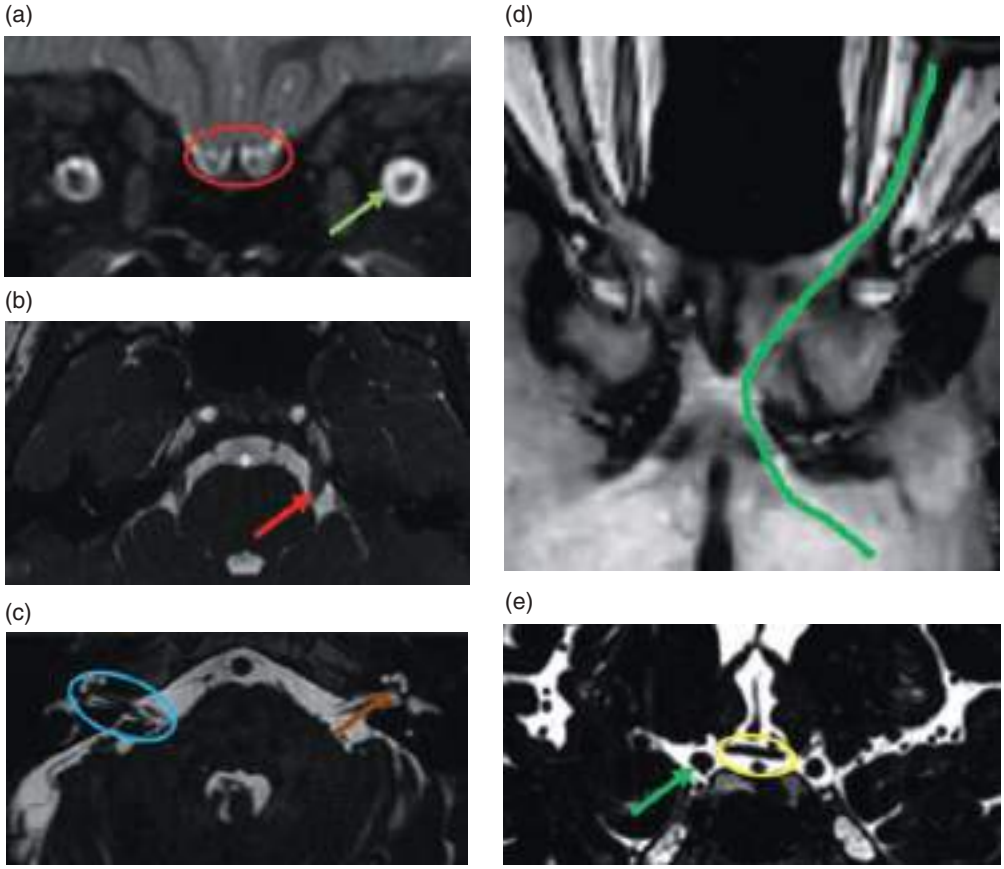

Figure 3.9 Basic anatomy of the cranial nerves. (a, b, c, e) High-resolution 3D DRIVE T2-weighted MRI. (d, e) Oblique axial T1-3D-weighted MRI. (a) Coronal image showing the olfactory nerve in the olfactory groove (red circle) and the optic nerve in its intraorbital segment (green arrow). (b) Axial image showing the trigeminal nerves (red arrow) reaching the Meckel's cave. (c) Axial image showing the cisternal segments (cerebellopontine angle) and intracanalicular segments of statoacoustic and facial nerve bundles (blue circle). The arrival of the cochlear nerves (branch of the VIII cranial nerve) at the cochlea can be appreciated (brown arrow). (d) Axial imaging showing the orbital, cisural, and chiasmatic segments, and optic tracts of the II cranial nerve (green line). (e) Coronal image showing the optic chiasm (yellow circle), medial to the internal carotid arteries (green arrow) and above the sella turcica.

Posterior Fossa

In the anterior part of the posterior fossa the brain stem, consisting of the midbrain, pons, and medulla, can be identified (Figure 3.2). This fundamental structure contains WM projection fibers as well as the nuclei of the cranial nerves. The midbrain is connected to the brain through the two cerebral peduncles. The cerebral aqueduct, which connects the third and fourth ventricles, lies in the dorsal aspect of the midbrain, while the quadrigeminal plate is located posteriorly. The cerebellum consists of a central structure, the vermis, and two hemispheres located on both sides of the posterior cranial fossa, divided into numerous gyri known as cerebellar folia (Figure 3.7). In its most inferior portion, close to the foramen magnum, the cerebellar tonsils are located, and they should not surpass this boundary under normal conditions.

Ventricular System

The approximate volume of CSF in the CNS under normal conditions ranges from 125 to 150 mL [18]. Approximately 80% of this volume is distributed in the SAS (cortical sulci, basal cisterns, and spinal canal) and the rest occupies the ventricular system. It is constantly produced in the choroidal plexuses by an active metabolic process and drainage of interstitial fluid, reaching 450 mL/24 hours, thus its renewal is constant. Its circulation and flow pattern seem to be influenced by blood pressure peaks, as well as by intracranial pressure, presenting oscillations parallel to those of blood pressure. Its reabsorption mainly occurs via parenchymal capillaries into the glymphatic system, although there is also some reabsorption into the arachnoid granulations, which act as valves, by the choroid plexuses and by the nasal lymphatic system.

The spaces containing CSF are the ventricular system and the SAS. The ventricular system consists of four interconnected cavities inside the brain which are covered by a layer of ciliated cells (ependymal cells). At the supratentorial level, both lateral ventricles (consisting of anterior or frontal horns, body, atria, occipital and temporal horns) are connected to the third ventricle through the interventricular foramen (of Monro). The atria are of special relevance, since the choroid plexuses, the key producers of CSF, are normally present at this level. The third ventricle communicates with the fourth ventricle through the cerebral aqueduct (located in the dorsal aspect of the midbrain, closely related to the quadrigeminal plate), which lies in the posterior fossa (Figures 3.2 and 3.7). Its main relations are the posterior aspect of the pons anteriorly, the cerebellar vermis posteriorly, and both cerebellar hemispheres laterally. Through the two foramina of Luschka (lateral) and the foramen of Magendie (central), the fourth ventricle communicates with the SAS.

Neck, Paranasal Sinuses, and Orbit

The most accepted approach to study the neck distinguishes two anatomical spaces: the supra-hyoid and the infra-hyoid neck. The anatomical landmark for this division is the deep cervical fascia (DCF), which is inserted into the base of the skull and converges into the hyoid bone.

There are two main fasciae in the neck: (i) the superficial cervical fascia, which is loose, with fat content and not relevant from the anatomical perspective, and (ii) the DCF, which is composed of several layers (Figure 3.10) and divides the neck into different compartments or functional spaces [19]:

- Superficial or investing layer/fascia (Figure 3.10): envelopes the sternocleiodomastoid (SCD) and trapezium muscles, the parotid gland, the mandible, and the masticatory muscles (masticator space).
- Deep or prevertebral layer/fascia (Figure 3.10): invests the prevertebral and paravertebral muscles.

Between both the superficial and deep layers there are three important fasciae.

The most relevant one is the oropharyngeal fascia or middle layer (Figure 3.10), which defines the pharyngeal mucosal space (containing the nasopharynx and the oropharynx) and includes the pharyngeal mucosa, the constrictor muscles providing muscular support of the pharynx, and lymphatic tissue.

There is another fascia that runs anteromedially from the styloid process to the tensor veli palatini muscle and divides the parapharyngeal space into pre-styloid and retro-styloid.

Finally, the alar fascia (Figure 3.11), a fold of the prevertebral fascia, is located medial to both carotid arteries and posterior to the buccopharyngeal fascia (between the buccopharyngeal and prevertebral fasciae).

The retropharyngeal space, as described below, lies between the buccopharyngeal fascia and the prevertebral fascia (or deep layer). Therefore, the alar fascia separates the retropharyngeal space, more medial, from the carotid space, more lateral (because it has a sagitally-oriented fold). In addition, this fascia divides the retropharyngeal space into two compartments, one located more anteriorly, which is the true retropharyngeal space (extending from the clivus to the first thoracic vertebrae), and another one, more posterior, which is known as the "danger space." The

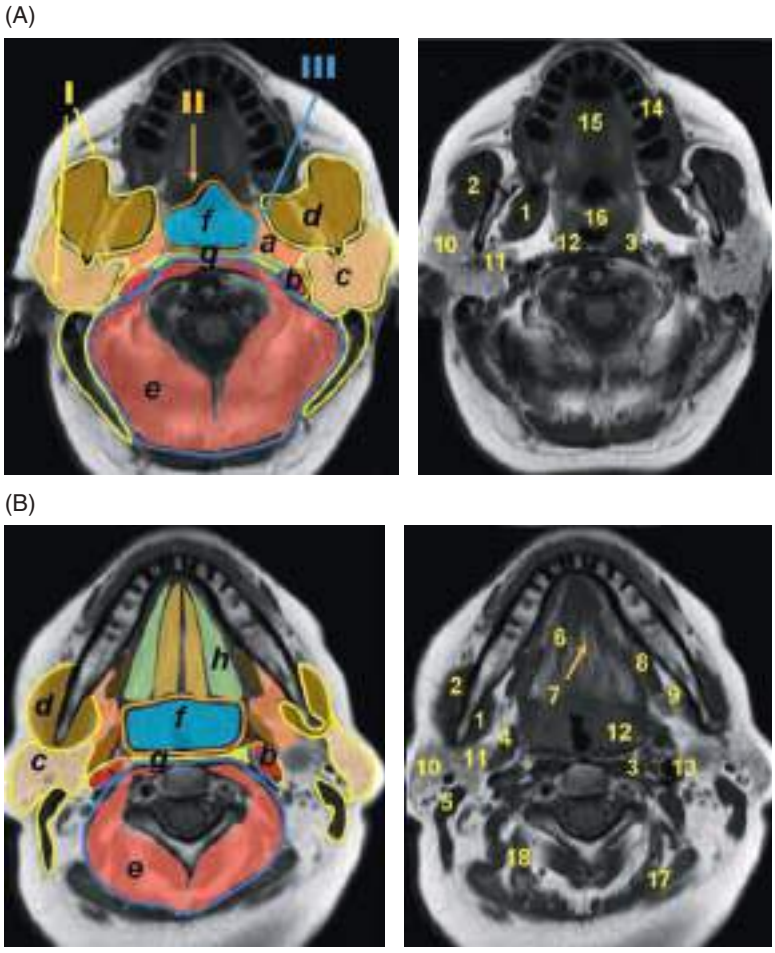

Figure 3.10 Supra-hyoid neck. (A) Axial T1-weighted MRI at the level of the palate. (B) Axial view at the level of the floor of mouth. Cervical fasciae: I, superficial layer of the deep cervical fascia; II, middle layer of the deep cervical fascia; III, deep layer of the deep cervical fascia. Cervical spaces: a, parapharyngeal space; b, carotid space (retro-styloid parapharyngeal space); c, parotid space; d, masticator space; e, perivertebral space; f, pharyngeal mucosal space; g, retropharyngeal space; h, sublingual space. Anatomical structures: 1, pterygoid muscles; 2, masseter muscle; 3, longus colli muscle; 4, posterior belly of the digastric muscle; 5, sternocleidomastoid muscle; 6, geniohyoid muscle; 7, lingual septum; 8, mylohyoid muscle; 9, submandibular gland; 10, parotid gland (superficial lobe); 11, parotid gland (deep lobe); 12, palatine tonsil; 13, internal carotid artery; 14, buccinator muscle; 15, hard palate; 16, soft palate; 17, semispinalis cervicis muscle; 18, splenius capitis muscle.

latter compartment runs more inferiorly to reach the mediastinum, representing a potential communication pathway between the neck and the mediastinum through the retropharyngeal space.

This fascial division allows the extension pathways of pathological processes through the cervical spaces to be analyzed in a structured way.

Compartments of the Supra-hyoid Neck

The DCF defines the pharyngeal, parapharyngeal, carotid, parotid, masticator, retropharyngeal and prevertebral mucosal spaces [20].

Pharyngeal Mucosal Space

The pharyngeal mucosal space is divided into the nasopharynx and the oropharynx and is bounded by the middle layer of the DCF, specifically the buccopharyngeal fascia (Figure 3.10). The superior margin of this fascia surrounds the pharyngeal-basilar fascia (Figure 3.12), which is the aponeurosis of the superior pharyngeal constrictor muscle and is inserted into the base of the skull. The inferior margin of the buccopharyngeal fascia invests the superior and middle pharyngeal constrictor muscles, which provide muscular support to the nasopharynx and oropharynx, respectively.

Nasopharynx The anatomical boundaries of the nasopharynx are (Figure 3.12):

- Anterior: anterior nares.
- Posterior: sphenoid bone.
- Inferior: soft palate.

The lateral boundaries are more anatomically complex. From anterior to posterior, these include the salpingo-pharyngeus muscle, the cartilaginous part of the Eustachian tube, and the prevertebral muscles (longus colli muscle). These structures form folds on both sides of the nasopharynx, specifically (from anterior to posterior) the recess of the Eustachian tube, the torus tubarius, formed by the cartilaginous end of the tube, and the fossa of Rosenmüller, located between the torus

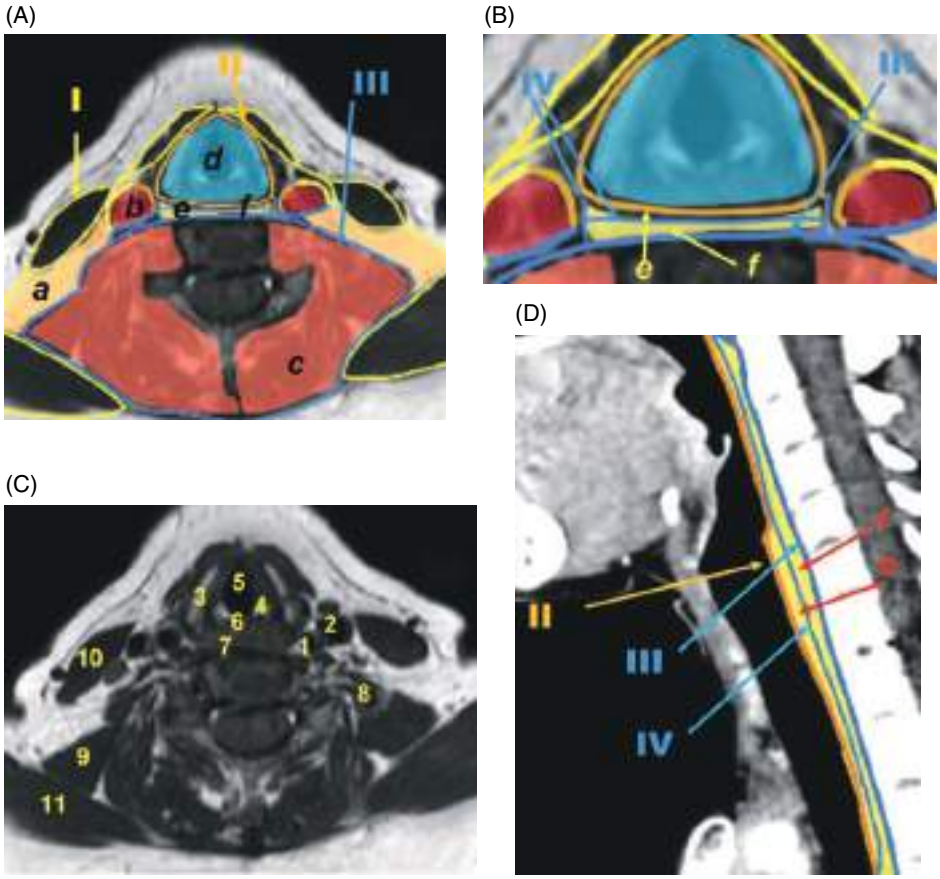

Figure 3.11 Infra-hyoid neck. (A, B) Axial T1-weighted MRI illustrating the fasciae and spaces of the neck. (C) Axial T1-weighted MRI with numbered anatomical structures. (D). Sagittal noncontrast MPR CT image, detail of the retropharyngeal space. Cervical fasciae: I, superficial layer of the deep cervical fascia; II, middle layer of the deep cervical fascia; III, deep layer of the deep cervical fascia; IV, alar fascia. Cervical spaces: a, posterior cervical space; b, carotid space; c, perivertebral space; d, visceral space; e, retropharyngeal space; f, danger space. Anatomical landmarks: 1, internal carotid artery; 2, jugular vein; 3, thyroid cartilage; 4, cricoid cartilage; 5, laryngeal vestibule; 6, post-cricoid region; 7, retropharyngeal space; 8, scalene muscles; 9, levator scapulae muscle; 10, sternocleidomastoid muscle; 11, trapezius muscle.

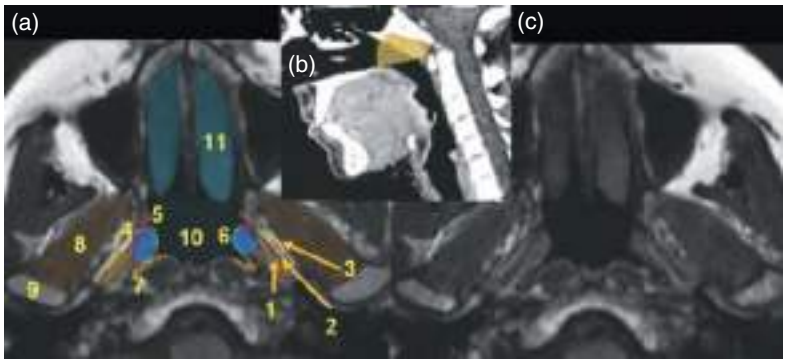

Figure 3.12 Nasopharynx. Axial T1-weighted MRI at the level highlighted in yellow. 1, levator veli palatini muscle; 2, pharyngobasilar fascia; 3, tensor veli palatine muscle; 4, parapharyngeal space; 5, recess of the Eustachian tube; 6, torus tubarius; 7, fossa of Rossenmüller; 8, pterygoid muscles; 9, mandibular condyle; 10, lumen of the nasopharynx; 11, middle turbinate of the nasal fossa.

tubarius and the longus colli muscle, representing one of the most common early sites of origin of nasopharyngeal tumors.

Next to the wall of the nasopharynx, the pharyngobasilar fascia separates the levator veli palatini from the tensor veli palatini muscles (from medial to lateral), the latter of which exhibits a more linear morphology in cross-sectional images. The pharyngobasilar is an aponeurosis of hard consistency related to the superior pharyngeal constrictor muscle and is inserted into the base of the skull. In addition, the pharyngobasilar fascia presents an area of muscular deficiency called the sinus of Morgagni, through which the levator veli palatini muscle and the Eustachian tube run toward the base of the skull. Its importance lies in the fact that it provides a potential communication pathway for tumor extension from the nasopharynx to the base of the skull.

Oropharynx

The anatomical boundaries of the oropharynx are (Figure 3.13):

- Superior: soft palate.
- Inferior: superior aspect of the epiglottis.
- Anterior: the plane formed by the anterior margin of the soft palate, the anterior tonsillar pillar, and the circumvallate papillae, which separates the base and the free edge of the tongue and is bounded by the oral cavity anteriorly.
- Posterior: first cervical vertebrae.
- Lateral (from anterior to posterior): anterior tonsillar pillar, formed by the palatoglossus muscle, the palatine tonsil, and the posterior tonsillar pillar, made up of the palatopharyngeus muscle.

Parapharyngeal Space

The parapharyngeal space was classically divided into pre- and post-styloid with respect to the styloid process. Nevertheless, the pre-styloid parapharyngeal space is currently referred to as the parapharyngeal space (Figure 3.10), while the former post-styloid space is equivalent to the currently known as carotid space (Figure 3.10).

The parapharyngeal (pre-styloid) space is located in the central space of the DCF and predominantly contains fat, in addition to the parapharyngeal venous plexus, other vascular structures such as the ascending pharyngeal artery and, occasionally, minor salivary glands. Its boundaries are established by different layers of the DCF:

- medial: middle layer of the DCF, which surrounds the pharyngeal mucosal space.
- lateral: superficial layer of the DCF, which surrounds the masticator and parotid spaces.
- posterior: carotid sheath, which surrounds the carotid space and is formed by the three layers of the DCF.

This space extends from the base of the skull to the hyoid bone and communicates with the submandibular space directly. It allows potential dissemination of abnormal processes that extend from nearby spaces. In fact, extension by adjacent lesions is the most frequent cause of pathologic involvement of the parapharyngeal space. The parapharyngeal fat is characteristically displaced in one direction or another based on the space from where the pathologic process arises (Figure 3.14).

Carotid Space

As mentioned above, the carotid space corresponds to the classic retro-styloid parapharyngeal space (Figure 3.10). It is located posterior to the styloid process, which extends from the base of the skull to the aortic arch. The three layers of the DCF contribute to form the sheath that surrounds this space. Its supra-hyoid portion contains the internal carotid artery, the jugular vein, lymph nodes, the cranial nerves IX, X and XI (glossopharyngeal, vagus and accessory, respectively), and the cervical sympathetic plexus.

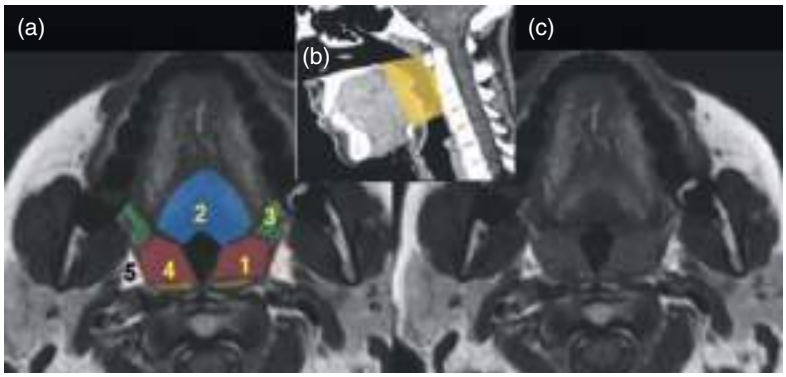

Figure 3.13 Oropharynx. Axial T1-weighted MRI at the level highlighted in yellow. 1, palatine tonsil; 2, base of the tongue; 3, anterior tonsillar pillar (palatoglossus muscle); 4, posterior tonsillar pillar (palatopharyngeal muscle); 5, parapharyngeal space.

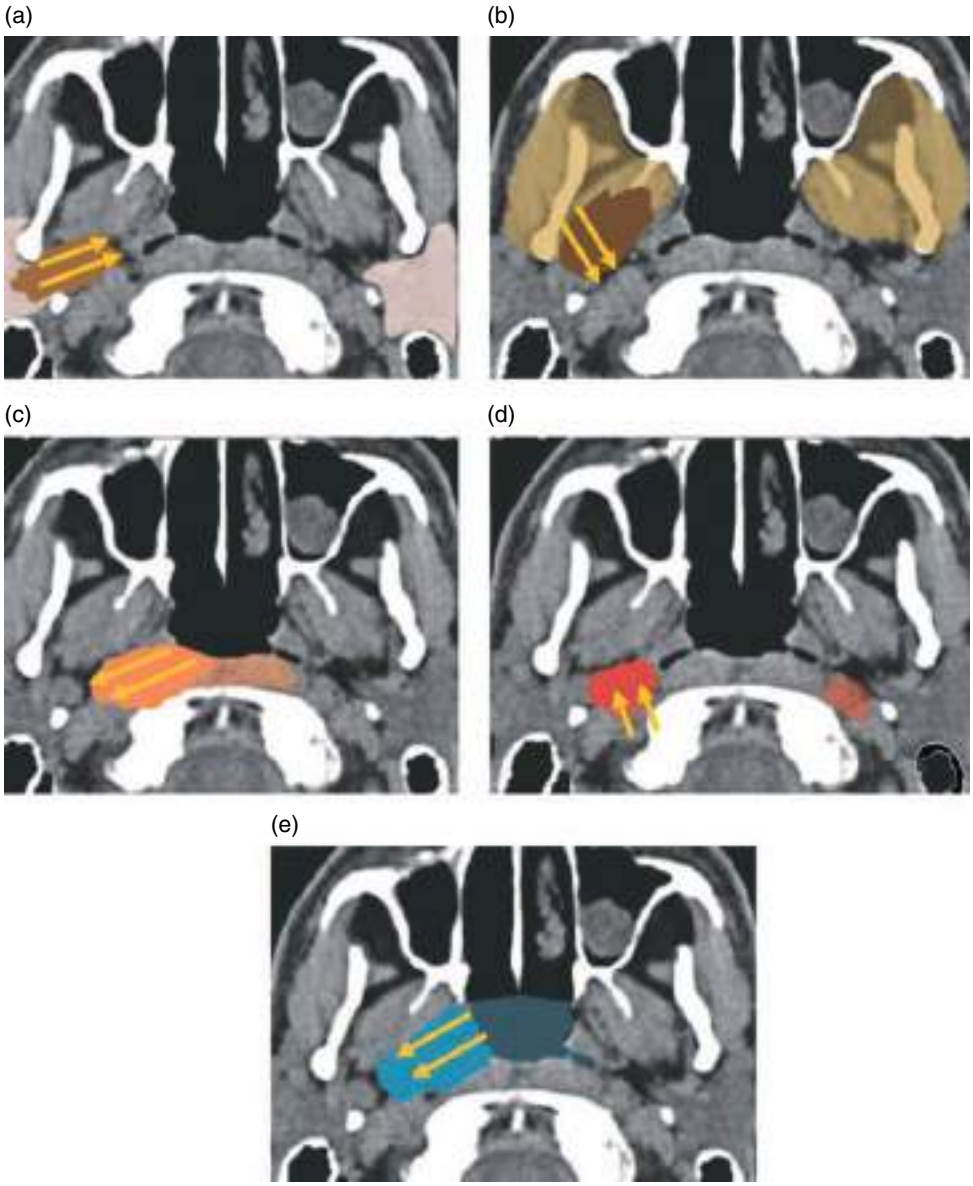

Figure 3.14 Displacement of the fat in the parapharyngeal space based on the location of lesions in adjacent cervical spaces. (a–e) Axial noncontrast CT images. (a) Lesion in the parotid space: antero-medial displacement. (b) Lesion in the masticator space: posteromedial displacement. (c) Lesion in the perivertebral space: lateral displacement. (d) Lesion in the carotid space: anterior displacement. (e) Lesion in the pharyngeal mucosa: postero-lateral displacement.

Masticator Space

The masticator space is a large space bounded by the superficial layer of the DCF. Its anatomical boundaries are (Figure 3.10):

- Inferior: mandibular angle.
- Superior: the masticator space extends medially to reach the insertion of the pterygoid muscles in the base of the skull, inside the foramen ovale. Laterally, it extends to the upper insertion of the temporal muscle in the cranial vault. The zygomatic arch divides this space into the temporal fossa or supra-zygomatic masticator space and the infra-temporal fossa under the zygomatic arch.
- content:
- masticatory muscles: masseter, medial and lateral pterygoid and temporal muscles, which are innervated by the masticatory nerve, the motor portion of the third branch of the V cranial nerve (or trigeminal) which enters the masticator space via the foramen ovale being a potential pathway of perineural invasion from the masticator space to the base of the skull.

- inferior alveolar nerve.
- Mandible.
- Parotid duct.

Buccal Space

The buccal space (Figure 3.15), without true fascial boundaries, is located immediately anterior to the masticator space and contains [21]:

- Buccal fat pad
- Facial artery and vein
- Distal part of the parotid duct
- Buccinator muscle.

Parotid Space

The parotid space (Figure 3.10) contains the following anatomical structures:

- Parotid gland, with intraparotid lymph nodes, surrounded by the superficial layer of the DCF.
- Facial nerve, which forms a plane that divides the parotid gland into its superficial and deep lobes.
- Retromandibular vein (Figure 3.15), which lies medial to the course of the facial nerve at the mandibular angle, being the main anatomical landmark to distinguish the superficial from the deep lobe of the parotid gland on cross-sectional CT images, since the facial nerve is usually not visible at this level.
- External carotid artery.

Retropharyngeal Space

The retropharyngeal space (Figure 3.11) is a virtual space between the pharyngeal constrictor muscles, surrounded

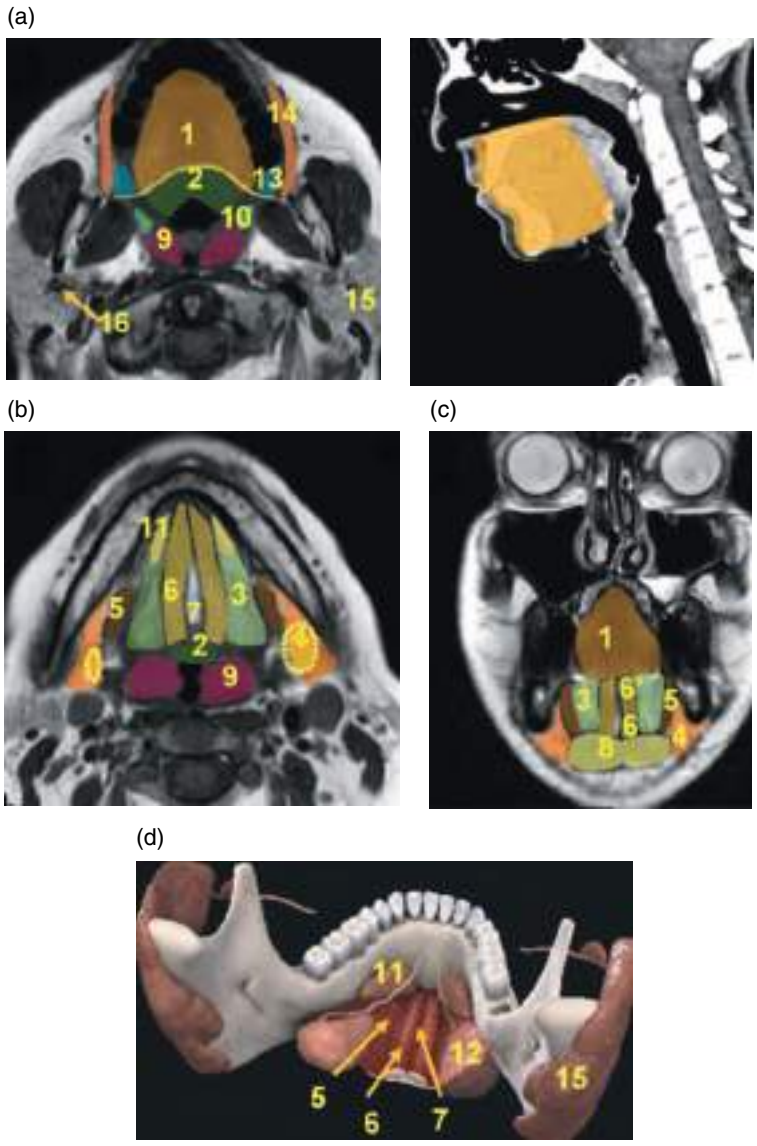

Figure 3.15 Oral cavity (yellow area in the sagittal noncontrast CT image, on the right). (a) Axial T1-weighted MRI at the level of the palate (yellow area in the sagittal noncontrast CT image, on the right). (b) Axial view at the level of the floor of mouth. (c) Coronal T1-weighted MRI. (d) Volume rendering of the floor of mouth with the salivary glands. 1, free edge of the tongue; 2, base of the tongue; 3, sublingual space; 4, submaxillary space; 5, mylohyoid muscle; 6 and 6′, genioglossus-geniohyoid complex, root of the tongue; 7, lingual septum; 8, anterior belly of the digastric muscle; 9, palatine tonsil; 10, anterior tonsillar pillar (palatoglossus muscle); 11, sublingual gland; 12, submandibular glands (encircled by yellow dots); 13, retromolar trigone; 14, buccinator muscle; 15, parotid gland; 16, retromandibular vein.

by the middle layer of the DCF and the prevertebral muscles, which are in turn surrounded by the deep layer of the DCF. A thin line of fat within this space allows its identification on imaging.

The alar fascia separates the retropharyngeal space from the carotid space laterally, and from the danger space posteriorly, representing a pathway for the extension of pathological processes from the retropharyngeal space to the mediastinum (Figure 3.11).

Contents:

- Fat.
- Lymph nodes, only from the level of the nasopharynx to the level of the hyoid bone.

Perivertebral Space

Also called pre-vertebral space, the perivertebral space (Figure 3.10) is bounded by the deep layer of the DCF, which invests the posterior pre- and paravertebral muscles, and is inserted into the transverse processes of the adjacent vertebrae.

The perivertebral space contains elements of the brachial plexus, the phrenic nerve, pre- and paravertebral muscles, vertebrae, vertebral arteries and veins, and the spinal cord.

Oral Cavity

The oral cavity (Figure 3.15) is located anterior to the oropharynx, from which it is separated by a ring of structures formed by the soft palate, the anterior tonsillar pillars, and the circumvallate papillae. Its boundaries are:

- Superior: hard palate, upper alveolar ridge and upper dental arch.
- Lateral: buccae (cheeks).
- Posterior: circumvallate papillae and anterior tonsillar pillars.
- Inferior: mylohyoid muscle or floor of mouth, inferior alveolar ridge and inferior dental arch.

The oral cavity contains the submaxillary and sublingual spaces, which are separated by the mylohyoid muscle and communicated by their free edge posteriorly.

Infectious processes involving both the submaxillary and sublingual spaces (e.g. Ludwig angina) can extend to the parapharyngeal and retropharyngeal spaces and eventually reach the mediastinum. The sublingual space, located above the mylohyoid muscle and lateral to the root of tongue, is formed by the genioglossus and geniohyoid muscles. It contains the following structures:

- lingual nerve
- IX and XII cranial nerves (glossopharyngeal and hypoglossal, respectively)
- lingual artery and vein
- sublingual glands
- deep lobe of the submandibular gland.

The submandibular space, situated inferior and lateral to the mylohyoid muscle, contains the following structures:

- superficial lobe of the submandibular gland
- anterior belly of the digastric muscle
- lymph nodes
- facial artery and vein
- inferior loop of the hypoglossal nerve.

Compartments of the Infra-hyoid Neck

The infra-hyoid neck is formed by the carotid, perivertebral, retropharyngeal, posterior cervical, and visceral spaces. The visceral space is the only specific compartment of the infra-hyoid neck [22, 23].

The first three compartments have already been explained. Accordingly, this section focuses on describing the posterior cervical and the visceral spaces.

Posterior Cervical Space

The posterior cervical space (Figure 3.12) is located between the superficial and deep layers of the DCF, posterior to the sheath of the carotid space and anterolateral to the perivertebral space. It contains fat, the posterior cervical lymph chain, the accessory spinal nerve, and the brachial plexus.

Visceral Space

The visceral space (Figure 3.12) corresponds to the pharyngeal mucosal space in the supra-hyoid neck and is bounded by the middle layer of the DCF. It contains the larynx, hypopharynx, thyroid and parathyroid glands, trachea, esophagus, lymph nodes, and laryngeal nerves.

Next, the larynx and hypopharynx will be described in more detail. Both structures have close anatomical and functional relations.

Larynx The larynx (Figure 3.16) consists of a bony skeleton made up of the hyoid bone and a cartilaginous skeleton formed by the thyroid, cricoid, arytenoid, and corniculated cartilages, and the epiglottis; all of them lined with respiratory mucosa. The larynx is divided into three anatomical spaces, namely the supraglottis, glottis, and subglottis.

The supraglottis or supraglottic larynx extends from the free edge of the epiglottis to the laryngeal ventricles and its main components include the following:

- Epiglottis, attached to the base of the tongue by the medial and lateral glossoepiglottic folds, which define the valleculae.

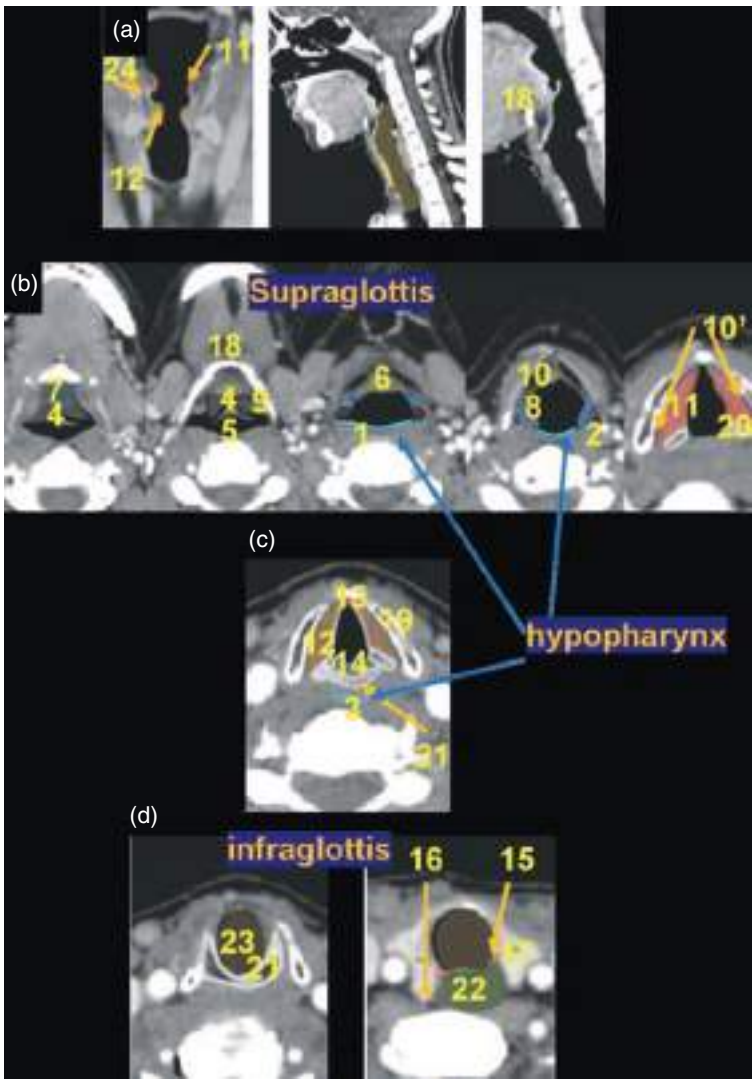

Figure 3.16 Larynx. (a) Coronal (left) and sagittal views (middle and right) of the larynx in the midline, with detail of the laryngeal ventricle and the pre-epiglottic space in the coronal and sagittal planes, respectively. (b) Axial contrast-enhanced CT images of the supraglottic space. (c) Axial noncontrast CT image at the level of the glottis. (d) Axial contrast-enhanced CT images at the infraglottic level. Hypopharynx: formed by 1, posterior pharyngeal wall; 2, pyriform sinus; 3, post-cricoid region. Supraglottis: 4, epiglottis with glossoepiglotic fold and valleculae located on both sides; 5, free edge of the epiglottis; 6, base of the epiglottis; 7, base of the tongue; 8, aryepiglottic folds; 9, pharyngoepiglottic fold; 10, pre-epiglottic space; 10′, paraglottic space, which also extends to the glottis; 11, false vocal cords or bands. Glottis: 12, vocal cords, the vocal ligament lies more medial; 13, anterior commissure; 14, posterior commissure; 10′, paraglottic space. Other structures: 22, esophagus; 17, thyroid gland; 16, parathyroid; 15, recurrent nerve. Bony and cartilaginous anatomy of the larynx: 18, hyoid bone; 19, thyroid; 20, arytenoid; 21, cricoid; 22, esophagus; 23, trachea; 24, laryngeal ventricle; 25, hypopharynx.

- Pre-epiglottic space, located anterior to the epiglottis and posterior to the hyoid bone, thyroid membrane, and thyroid cartilage. Inferiorly, it is continuous with the paraglottic or paralaryngeal space, which lie external to the false vocal cords and, to a lesser extent, the glottis. Both spaces contain fat tissue.
- Laryngeal vestibule, an air space within the supraglottis.
- Aryepiglottic folds, which run inferiorly from the epiglottis to the aytenoid cartilages and separate the laryngeal vestibule from the pyriform sinuses (belonging to the hypopharynx). The aryepiglottic folds end in the false vocal cords distally.
- Laryngeal ventricle, a mucosal fold between the true and false vocal cords. It is usually collapsed.

In the glottis or glottic larynx the following structures can be distinguished:

- Vocal cords, formed by the thyroarytenoid muscle and the vocal ligament.
- Anterior commissure or point of junction of the true vocal cords in the anterior midline.
- Posterior commissure, a mucosal layer between the arytenoid cartilages. Both commissures must not exceed 1 mm thick in cross-sectional images.

The subglottis or subglottic larynx corresponds to the space between the plane located 1 cm below the vocal cords and the inferior margin of the cricoid cartilage.

Hypopharynx The hypopharynz is the part of the visceral space of the infra-hyoid neck that extends from the superior edge of the hyoid bone to the cricoid cartilage (Figure 3.16). It lies posterior to the supraglottis, with the exception of the pyriform sinuses, which are situated more laterally. The hypopharynx consists of three parts:

- Pyriform sinuses, lateral to the aryepiglottic folds and the laryngeal vestibule.
- Posterior wall of the hypopharynx, which is continuous with the posterior wall of the oropharynx.
- Post-cricoid region, which corresponds to the pharyngo-esophageal junction and is usually collapsed.

Lymph Nodes of the Neck

The lymph nodes of the neck are classified into different levels based on cross-sectional anatomy (Figure 3.17). The key anatomical landmarks are the following:

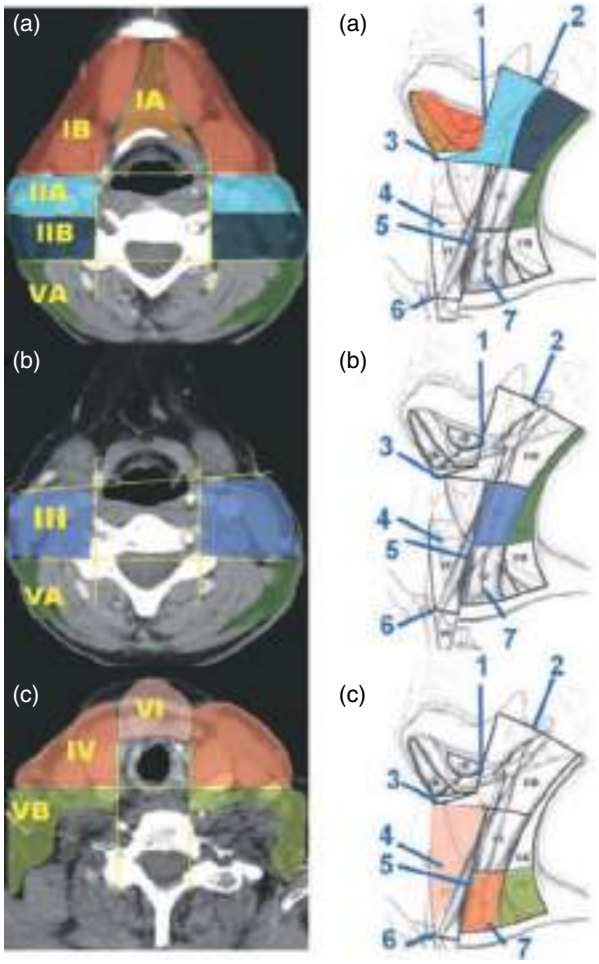

Figure 3.17 Lymph node levels. (a–c) Axial noncontrast CT images, with anatomic illustrations on the right. (a) Submental (IA), submaxillary (IB), upper jugular (IIA and IIB), and upper posterior triangle (VA) lymph nodes. (b) Middle jugular (III) and upper posterior triangle (VA) lymph nodes. (c) Low jugular (IV), lower posterior triangle (VB), and central compartment (VI) lymph nodes. 1, posterior border of the submandibular gland; 2, jugular fossa; 3, posterior border of hyoid bone; 4, inferior margin of cricoid; 5, internal carotid artery; 6, manubrium roof; 7, internal jugular vein.

- Posterior margin of the submandibular gland (which separates level I from level II).
- Hyoid bone, which separates level II from level III.
- Cricoid cartilage, which separates level III from level IV (and sublevels VA from VB).
- Posterior margin of the sternocleidomastoid muscle, which separates levels II, III and IV from level V.
- Medial margin of the internal carotid artery, which separates levels III and IV from level VI.

Levels:

- Level I
  - Level IA (submental). Its boundaries are:
    - Superior: plane of the body of the mandible.
    - Inferior: plane of the hyoid bone.
    - Lateral: medial margins of the digastric muscle.
  - Level IB (submandibular). Its boundaries are:
    - Medial: digastric muscle.
    - Lateral: body of the mandible.
    - Posterior: posterior margin of the submandibular gland.
- Level II (upper internal jugular group). Its boundaries are:
  - Superior: base of the skull.
  - Inferior: hyoid bone.
  - Lateral: sternocleidomastoid muscle.
  - Medial: medial edge of the internal carotid artery.
  - Level IIA: anterior, medial, lateral or posterior to and inseparable from the jugular vein.
  - Level IIB: posterior to and separable from the jugular vein.
- Level III (middle jugular vein group). Its boundaries are:
  - Superior: hyoid bone.
  - Inferior: cricoid cartilage.
  - Posterior: posterior edge of the sternocleidomastoid muscle.
  - Medial: medial margin of the internal carotid artery.
- Level IV (lower internal jugular group). Its boundaries are:
  - Superior: cricoid cartilage.
  - Inferior: clavicle.
  - Posterior: posterior margin of the sternocleidomastoid muscle.
  - Medial: medial margin of the common carotid artery.
- Level V (posterior triangle). Its boundaries are:
  - Anterior: posterior margin of the sternocleidomastoid muscle.
  - Superior: base of the skull.
  - Inferior: clavicle.
  - Posterior: anterior edge of the trapezius muscle.

  - Level VA, from the base of the skull to the cricoid cartilage.
  - Level VB, from the cricoid cartilage to the clavicle.
- Level VI (central compartment). From the hyoid bone to the sternal manubrium, medial to both carotid arteries.
- Level VII (superior mediastinum group). Between the sternal manubrium and the brachiocephalic vein, medial to both carotid arteries.

Sinonasal Region

The sinonasal region has a complex anatomy with many variants of normality [24, 25], some of which can predispose to disease by interfering with the sinus drainage pathways in the nasal cavity (Figure 3.18) [26].

The nasal cavity is located in the central region of the face, above the oral cavity, inferior to the anterior cranial fossa and medial to the orbits. Its boundaries are the following:

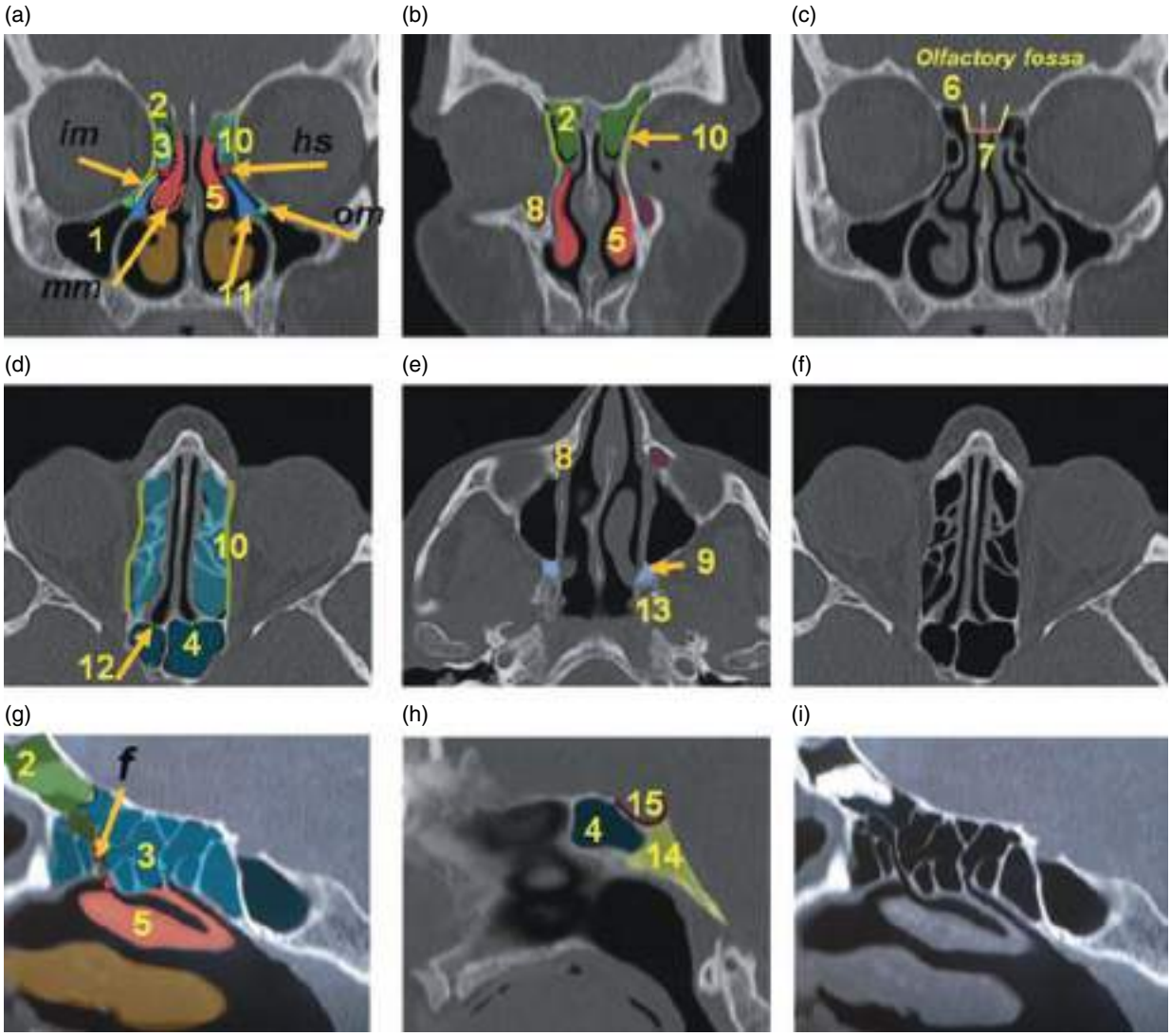

Figure 3.18 Paranasal sinuses. (a–c) Coronal noncontrast MPR CT images (bone window). (d–f) Axial noncontrast CT images (bone window). (g–i) Sagittal noncontrast MPR CT images (bone window). 1, maxillary sinus; 2, frontal sinus; 3, ethmoidal air cells; 4, sphenoid sinus; 5, middle concha; 11, uncinate process; MO, maxillary ostium; MM, middle meatus; HS, hiatus semilunaris. Sphenoethmoidal recess: 12, olfactory fossa; 6, lateral lamella; 7, cribiform plate. Frontal recess: FR (red dots), drainage pathway of the frontal sinus into the middle meatus; 8, nasolacrimal duct; 9, pterygopalatine fossa; 10, lamina papyracea; 13, pterygoid process; 14, clivus; 15, sella turcica.

- Superior wall: olfactory fossa, which is mainly formed by the cribiform plate.
- Inferior wall: hard and soft palate.
- Medial wall: nasal septum.
- Lateral wall: formed by the three conchae or turbinates (superior, middle, and inferior), which form air passages called meatuses between them:
  - the nasolacrimal duct drains into the inferior meatus
  - the frontal sinuses, the anterior ethmoidal air cells and the maxillary sinuses drain into the middle meatus (MM)
  - the posterior ethmoid cells and the sphenoid sinus drain into the superior meatus.

The paranasal sinuses consist of pneumatized spaces within the facial bones that surround the nasal cavity. In childhood, they are present in a rudimentary form, reaching their final configuration during adolescence:

- Frontal sinus [3]: This is not visible on X-rays until the age of 6 years. Its posterior wall is very thin and contacts with the meninges and brain. Its base has a lateral part in close relation to the orbital roof, and its medial wall is continuous with the ethmoid bone.
- Maxillary sinus [1]: This is present at birth. Its superior wall corresponds to the floor of the orbit and is related to the infraorbital nerve. Its inferior wall forms the superior dental arch (root of premolars and first molar). Its posterior wall is the thickest and is related to the pterygopalatine fossa (Figure 3.18).
- Sphenoid sinus: The pneumatization of the sphenoid sinus is evident after the age of 3 years. It is separated by a thin central septum. Its anterior wall is related to the ethmoid cells (Figure 3.18), its posterior wall is bounded by the clivus (Figure 3.18), its superior wall by the sella turcica, and its inferior wall by the nasopharynx. The cavernous sinuses are located on both sides of the lateral walls.
- Ethmoid sinuses: These are divided into anterior and posterior air cells, separated by the lateral insertion of the middle concha into the lamina papyracea (called basal lamina). Their lateral wall is defined by the lamina papyracea of the ethmoid bone, which separates them from the orbit. Their superior wall bounds with the frontal sinuses. The anterior nares are situated inferomedially, and the olfactory fossa and the sphenoid sinus lie posteriorly.

Key anatomical landmarks in CT of the paranasal sinuses [27]:

- Ostiomeatal complex: This consists of a group of anatomical structures that allow the drainage of the frontal and maxillary sinuses and the anterior ethmoid air cells into the MM. It is formed by the maxillary infundibulum (MI), which is the pathway that communicates the maxillary sinus with the MM. Its lateral boundaries are the ethmoid concha [3], which is the most anterior ethmoidal air cells, while it is medially bounded by the uncinate process, related to the lateral wall of the nasal fossa. The MM and the MI converge at the apex of the uncinate process, specifically in the hiatus semilunaris, where the frontal and maxillary sinuses end up draining.
- Sphenoethmoidal recess: This is the drainage pathway of the sphenoidal sinus and posterior ethmoidal air cells into the superior meatus.
- Olfactory fossa: This forms the roof of the nasal cavity. Inferiorly, it contains the cribiform plate, through which the crista galli process arises in its middle zone and divides the olfactory fossa into two cavities. On both sides, the lateral lamellae separate the olfactory fossa from the ethmoidal air cells. The lateral lamella is a very thin bony structure, susceptible to laceration by trauma or surgery.

Orbit

The bone structure of the orbit has the shape of a pyramid with the base situated anterolaterally and the vertex situated posteromedially, converging at the middle cranial fossa (Figures 3.19 and 3.20).

It is formed by the frontal, sphenoid, zygomatic, maxillary, ethmoid, lacrimal, and palatal bones. They form a foramen and two fissures through which vascular and nervous structures communicate the orbit with the middle cranial fossa [28].

Its boundaries are (Figure 3.19):

- Roof: formed by the frontal bone and the lesser wing of sphenoid.
- Floor: weaker and formed by the zygoma and the maxilla.
- Medial wall: lamina papyracea of the ethmoid, palatal, maxillary, lacrimal, and lesser wing of sphenoid.
- Lateral wall: formed by the zygoma and the greater wing of sphenoid.
- Posteriorly, the orbit communicates with the endocranial cavity via the superior orbital fissure, inferior orbital fissure, and optic canal (Figure 3.20).
- Superior orbital fissure, between the greater and lesser sphenoid wings, and through which the III, IV, VI, and VI cranial nerves, superior ophthalmic vein, and sympathetic nerve branches pass. It communicates directly with the cavernous sinus.
- Inferior orbital fissure, between the lateral wall and the floor of the orbit. It communicates with the pterygopalatine fossa, which is an important pathway of

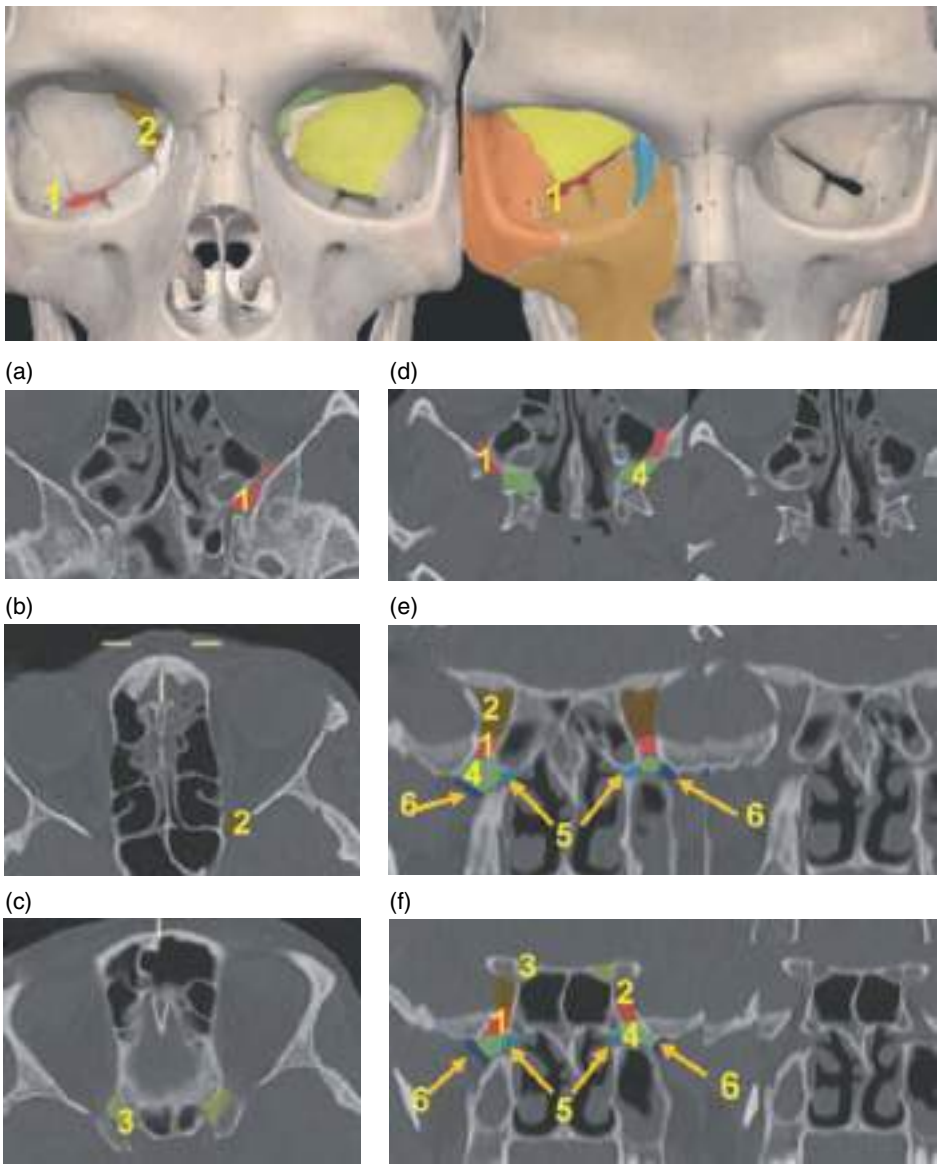

Figure 3.19 Orbital fissures. (l) Volume rendering of the orbits. (a–d) Axial noncontrast CT images of the orbit (bone window). (e, f) Coronal noncontrast MPR CT images (bone window). 1, inferior orbital fissure; 2, superior orbital fissure; 3, optic canal; 4, pterygopalatine fossa; 5, sphenopalatine foramen; 6, pterygomaxillary fissure. The inferior orbital fissure is in direct communication with the pterygopalatine fossa, located on the posterior part of the facial bones (between the posterior wall of the maxillary sinus and the pterygoid process). The pterygopalatine fossa (4) is an important pathway for the extension of lesions. It communicates with the infratemporal fossa of the masticator space laterally via the pterygomaxillary fissure (6), and with the nasal fossa medially via the sphenopalatine foramen (5). The superior orbital fissure communicates with the cavernous sinus.

extension of adjacent lesions. The second trigeminal branch (V2) and the infraorbital nerve pass through this fissure. The pterygopalatine fossa is located between the posterior wall of the maxillary sinus and the pterygoid processes, communicating with the nasal fossa medially via the sphenopalatine foramen, and with the infratemporal fossa of the masticator space laterally via the pterygomaxillary fissure.

- Optic canal, located within the lesser sphenoid wing. The optic nerve passes through this canal.

The orbit can be divided into the preseptal space, the ocular globe, and the retro-ocular spaces (Figure 3.20):

- Preseptal space, anterior to the orbital septum (a): This forms the front edge of the orbit. The orbital septum is inserted into the periosteum of the orbital mar-

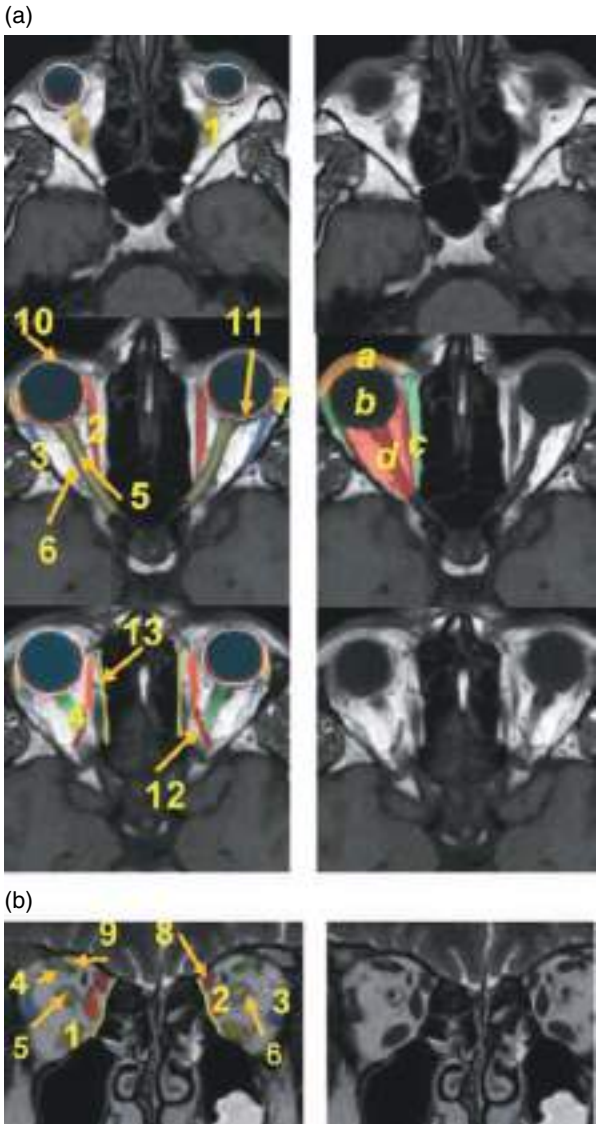

Figure 3.20 Orbit. (a) Axial T1-weighted MRI. (b) Coronal T2-weighted MRI. 1, inferior rectus muscle; 2, medial rectus muscle; 3, lateral rectus muscle; 4, superior rectus muscle; 5, optic nerve; 6, perioptic subarachnoid space; 7, lacrimal gland; 8, superior oblique muscle; 9, levator palpebrae superioris muscle; 10, sclera; 11, choroid; 12, superior ophthalmic vein; 13, lamina papyracea. Spaces of the orbit: a, preseptal space; b, ocular globe; c, extraconal space; d, intraconal space.

gin peripherally, and into the levator palpebrae superioris and the tarsal plate centrally. It separates the preseptal soft tissues (eyelids, orbicularis oculi muscle, eyelid fat) from the ocular globe and the retroocular space.

- Ocular globe (b) [29, 30]: This has a wall formed by three layers:
- sclera and cornea
- vascular uveal tract, formed by the choroid, ciliary bodies and the iris. The choroid becomes visible on MRI after intravenous contrast administration.
- retina.

The inner part of the ocular globe is divided into two cavities by the posterior surface of the lens:

- the anterior segment contains the aqueous humor and is subdivided into an anterior chamber, which extends from the cornea to the iris, and a posterior chamber, from the iris to the lens
- the posterior segment, corresponding to the vitreous body, contains the vitreous humor and is located posterior to the lens.
- Retro-ocular spaces: The space behind the ocular globe is divided into the intraconal and extraconal compartments, based on whether it is inside or outside the musculofascial cone, respectively. The musculofascial cone is formed by the superior, lateral, medial, and inferior rectus muscles. These muscles are inserted posteriorly into the tendinous (or Zinn) ring at the orbital apex. The superior and inferior oblique muscles are not part of the musculofascial cone, although the former is also inserted into the tendinous ring. The levator palpeabrae superioris muscle lies next to the superior rectus muscle, from and they are often difficult to differentiate from each other on imaging.
- Intraconal compartment: This is inside the musculofascial cone and contains fat, the ophthalmic artery, the superior ophthalmic vein, the optic nerve, the perioptic space, and the III, VI, and VI cranial nerves.
- Extraconal compartment: This is outside the muscles of the musculofascial cone. It contains the lacrimal gland and ducts, the IV cranial nerve, and fat.

Thoracic Anatomy: Introduction

The thorax is a complex anatomical region containing vital organs with different densities surrounded by a bone structure which exerts a protective effect. Chest CT is the most sensitive and precise diagnostic imaging method both for depiction of anatomical structures and detection of thoracic pathology.

The significant reduction in acquisition time allows the study of the thorax during a single breath-hold of few seconds, avoiding respiratory motion artifacts and obtaining submillimeter slices with no spacing between them. This results in high spatial resolution in the axial plane and in multiplanar and 3D reconstructions. In addition, the administration of intravascular iodine contrast considerably increases the contrast resolution of this imaging technique.

CT images should always be visualized in mediastinal window (level 40 HU, window width 350 HU) and lung window (level −600 to −700 HU, width 1000–1600 HU), with a standard reconstruction algorithm for the mediastinum and a high-spatial resolution reconstruction for the lung parenchyma (Figure 3.21) [1].

Chest MRI provides high-contrast resolution for soft tissues, high sensitivity to blood flow, multiplanar capability, and absence of ionizing radiations. In addition, it can be used in patients with allergy to iodine contrast. Traditionally, it has been considered a limited technique for the study of the thorax and lungs due to the low proton density of the normal lung and the magnetic susceptibility artifacts caused by air-tissue interfaces. Technical advances with more powerful gradients and the development of faster sequences have expanded its indications. The examinations are performed with a body coil and include fast sequences (gradient echo, turbo spin echo) weighted on T1 and T2. These fast sequences, along with parallel acquisition techniques and matrix sizing, are strategies to allow accelerated acquisition during a single breath-hold to minimize motion artifacts [31].

Anatomy of the Pulmonary Hilum

The pulmonary hilum is a complex anatomical structure containing the lobar and segmental bronchi, pulmonary arteries and veins, bronchial arteries and veins, soft tissue, and lymph nodes. The arrangement of the bronchi, vessels, and lymph nodes and their constant relationships to certain hilar structures allow their precise recognition. Identification of the specific bronchi is essential in the analysis of the pulmonary hilum. The branching pattern of the bronchial tree is usually constant (Figure 3.22) [32].

Anatomy of the Bronchi and Hilar Vessels

Current CT scanners (with 1 mm slice thickness) allow full visibility of the segmental bronchi, although their morphology may vary based on their spatial orientation. The bronchi provide anatomical support to the hilum. The hilar vessels have a constant relationship with the bronchi, thus identification of the hilar bronchi should be the first step to approach the analysis of the hilum.

Most of the segmental hilar arteries can be correctly identified based on their close association with the specific segmental bronchi, which can be traced in consecutive images to identify their origin.

The assessment of the vascular structures of the hilum is facilitated based on specific anatomic levels with respect to the bronchi [33].

Anatomy of the Right Bronchus

The right main bronchus is shorter than the left one and bifurcates into the right upper lobe (RUL) bronchus and the intermediate bronchus. The carina, right main bronchus, and left upper lobe (LUL) bronchus are often visualized in the same slice (Figure 3.23) [34].

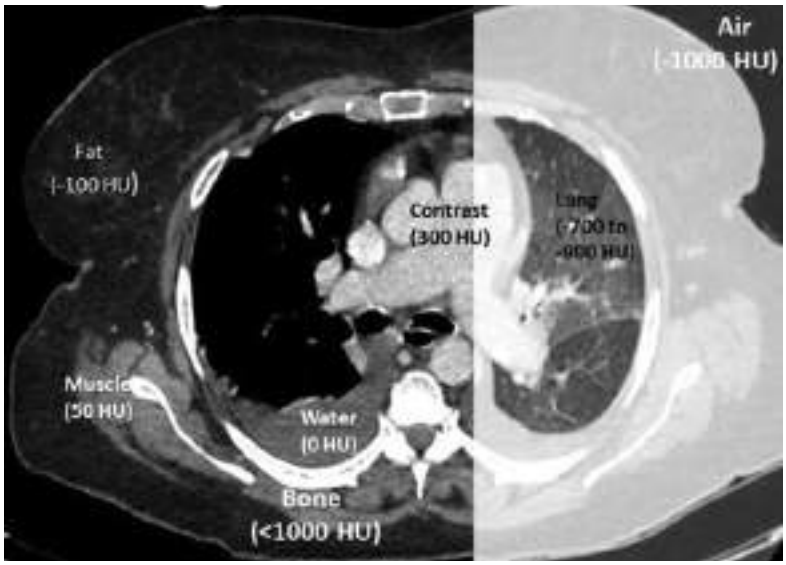

Figure 3.21 Typical Hounsfield unit values of anatomical structures in normal chest CT (left, mediastinal window; right, lung window). Note the right pleural effusion demonstrating water HU values.

Figure 3.22 Normal bronchial tree. LL, lower lobes.

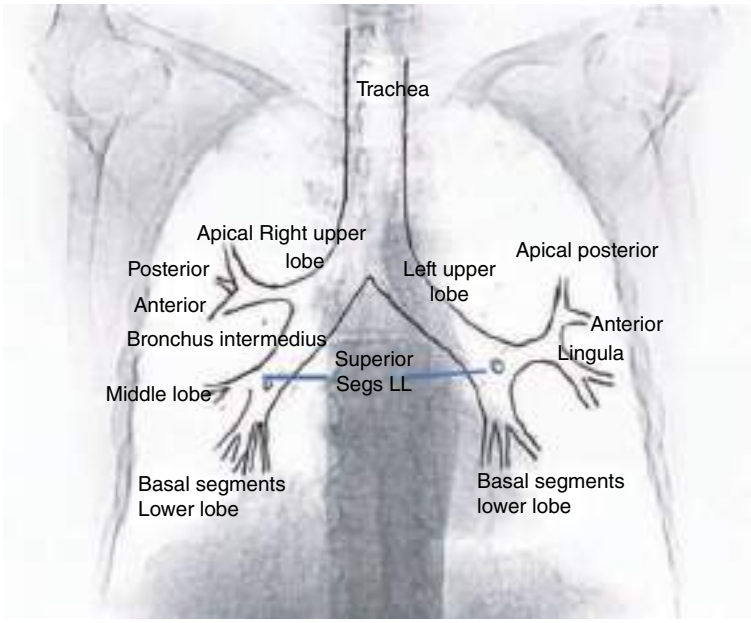

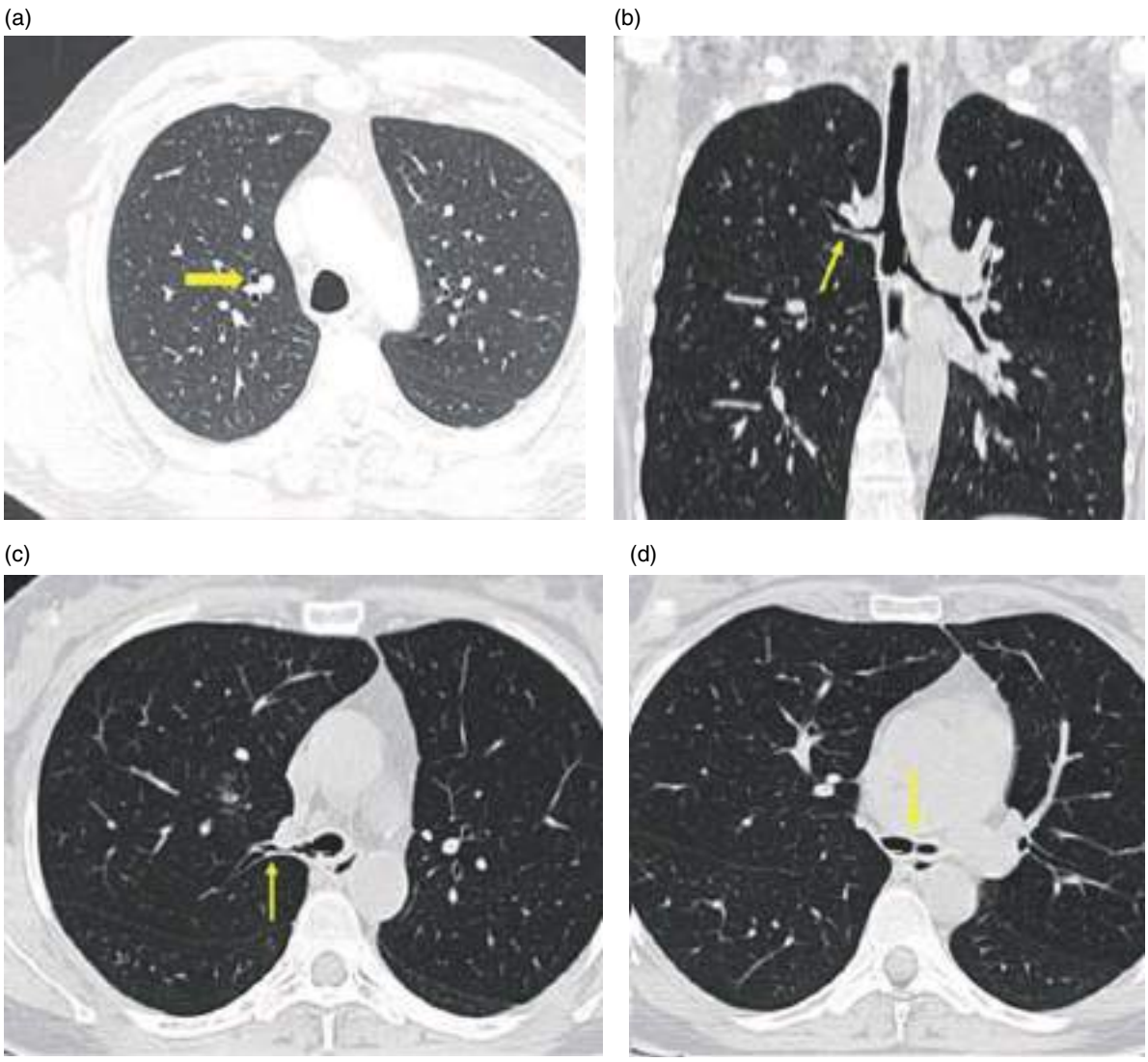

Figure 3.23 Axial CT image (lung window). (a) Apical segment bronchus of the right upper lobe (arrow). Coronal (b) and axial (c) CT images (lung window). (d) Tracheal bronchus (arrows in b and c) approximately 2 cm above the carina (arrow).

Right Upper Lobe Bronchus The RUL bronchus is located at the level or just below the carina. It runs laterally for 1–2 cm before dividing into three segmental branches: apical, anterior, and posterior (Figures 3.23 and 3.24). The posterior wall of the RUL bronchus can be seen as a thin line since it is well delimited from the surrounding lung parenchyma. Its branching pattern is variable, mainly due to differences in the origin of the apical segment bronchus.

- Apical segment bronchus: This becomes visible above the RUL bronchus usually at the level of the distal trachea (Figure 3.23). It is visualized as a rounded structure of air density in the axial plane.
- Anterior and posterior segment bronchi: These emerge as a Y-shaped bifurcation (Figure 3.24). Anatomical variations are rare, the most common being the so-called tracheal bronchus.

The term tracheal bronchus consists of a bronchus arising from the trachea or main bronchus which runs toward the upper lobe territory. This abnormal bronchus usually originates in the right side of the tracheal wall, less than 2 cm superior to the carina, and may provide entire support to the upper lobe or its apical segment. If a branch of the upper lobe bronchus is missing, the tracheal bronchus is defined as "displaced"; if the right upper lobe bronchus has a normal trifurcation into apical, anterior, and posterior segment bronchi, the tracheal bronchus is called "supernumerary."

Intermediate Bronchus The intermediate bronchus measures between 3 and 4 cm in length from the level of the RUL bronchus and gives rise to the middle lobe (ML) and right lower lobe (RLL) bronchi (Figures 3.25–3.27). Its morphology is round or oval in the axial view. Its posterior wall is very well defined, with a maximum thickness of 3 mm, and delimits the apical segment of the RIL bronchus.

Middle Lobe Bronchus The ML bronchus originates from the anterolateral wall of the intermediate bronchus and marks the origin of the RLL bronchus. It extends 1–2 cm before bifurcating into the medial and lateral segment bronchi. Owing to its orientation, its main segment as well as the bronchi of the medial and lateral segments are often seen 1–2 cm below the origin of the ML bronchus (Figure 3.29).

Right Lower Lobe Bronchi The pre-bifurcation segment of the RLL bronchus is very short. Near its origin, it gives rise to the bronchus of the apical segment (Figure 3.28), and the basal bronchial trunk continues for a short distance (Figure 3.29) until it splits off into the four basal segment branches of the RLL (medial, anterior, lateral, and posterior) (Figure 3.30) [34].

- Apical segment: This emerges at the same level or slightly inferior with respect to the origin of the ML bronchus (Figure 3.28).
- Basal trunk and segments of the basal pyramid: Below the origin of the apical segment bronchus, the basal bronchial trunk (or basal trunk) extends inferiorly approximately 5 mm (Figure 3.29).

The basal segments have a typical orientation starting medially and anteriorly in a counter-clockwise direction (M-A-L-P) (Figure 3.30).

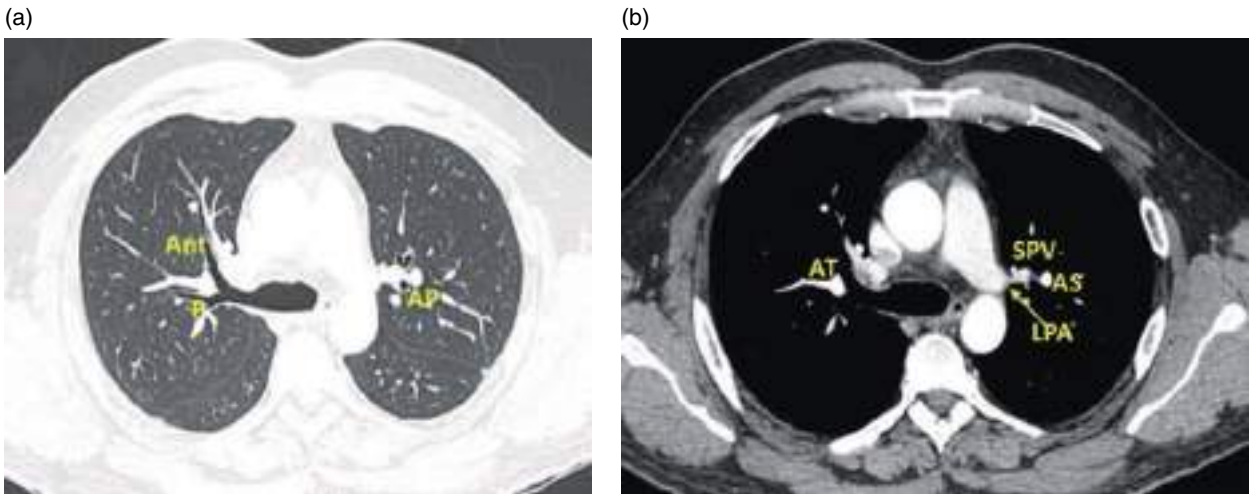

Figure 3.24 (a) Axial CT image (lung window). Right upper lobe bronchus and apicoposterior segment bronchus of the left upper lobe. Ant, anterior; P, posterior; AP, antero-posterior. (b) Axial CT image (mediastinal window). AT, anterior trunk; SPV, superior pulmonary vein; AS, anterior segment artery; LPA, left pulmonary artery.

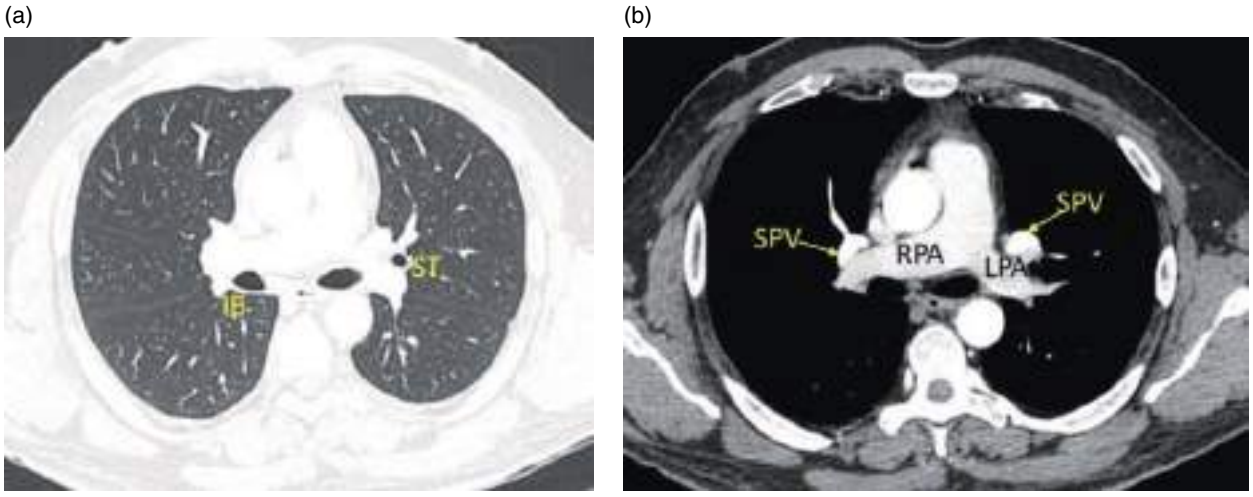

Figure 3.25 (a) Axial CT image (lung window). IB, intermediate bronchus; ST, superior trunk. (b) Axial CT image (mediastinal window). RPA, right pulmonary artery; LPA, left pulmonary artery; SPV, superior pulmonary vein.

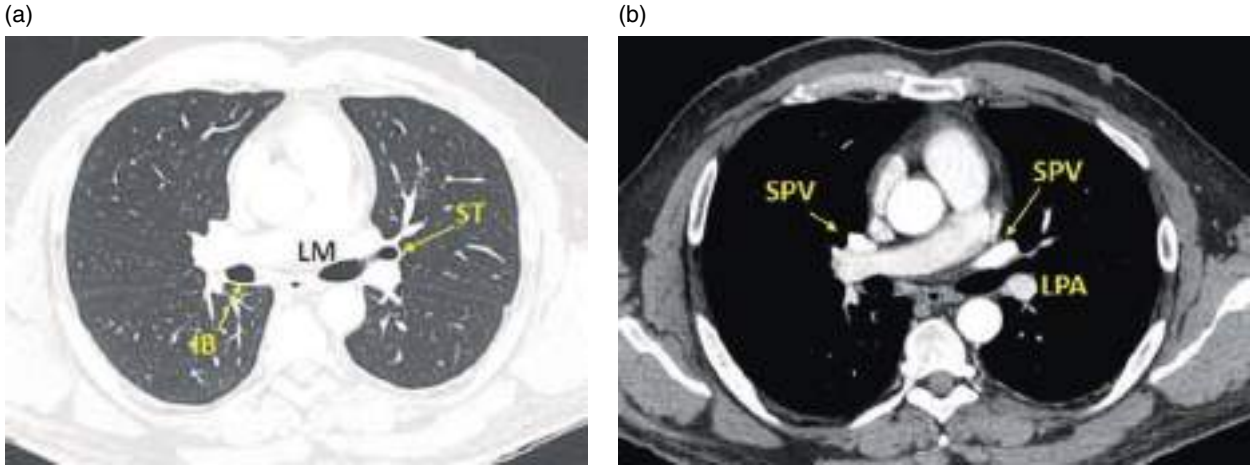

Figure 3.26 (a) Axial CT image (lung window). IB, intermediate bronchus; LM, left main bronchus; ST, superior trunk. (b) Axial CT image (mediastinal window). SPV, superior pulmonary vein; LPA, left pulmonary artery.

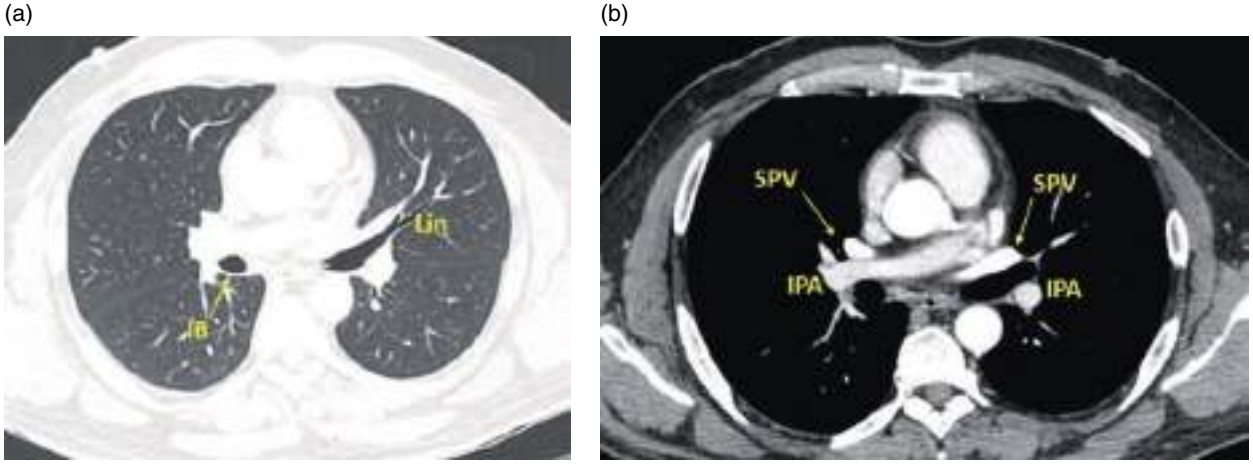

Figure 3.27 (a) Axial CT image (lung window). IB, intermediate bronchus; Lin, lingular bronchus. (b) Axial CT image (mediastinal window). IPA, interlobar pulmonary artery; SPV, superior pulmonary vein.

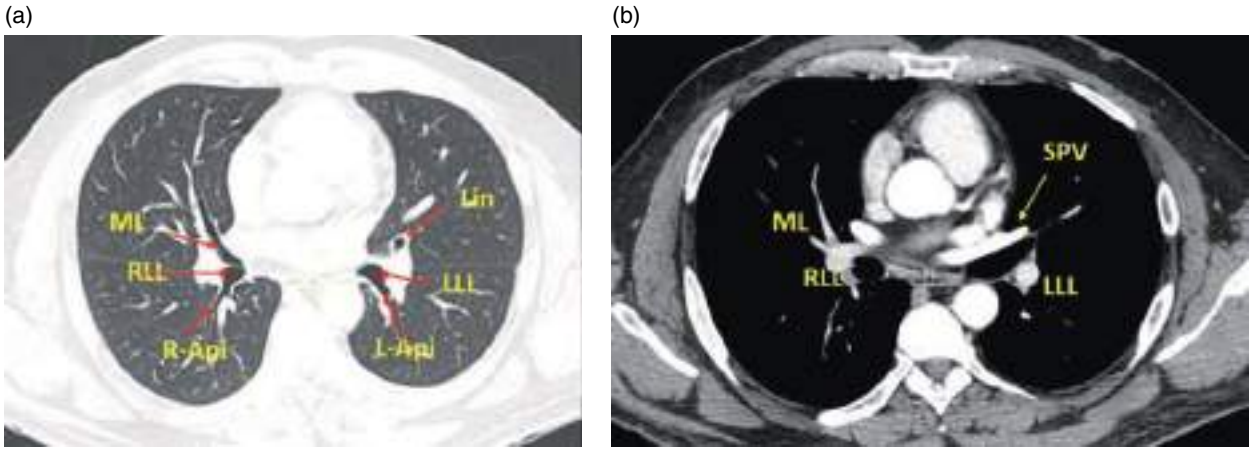

Figure 3.28 (a) Axial CT image (lung window). Middle lobe and apical segment of the right lower lobe bronchi, lingular bronchus, and apical segment of the left lower lobe. ML, middle lobe bronchus; RLL, right lower lobe bronchus; R-Api, apical segment of the right lower lobe bronchus; Lin, lingular bronchus; L-Api, apical segment of the left lower lobe bronchus. (b) Axial CT image (mediastinal window). ML, middle lobe; RLL, LLL, right and left lower lobe arteries, respectively; SPV, superior pulmonary vein.

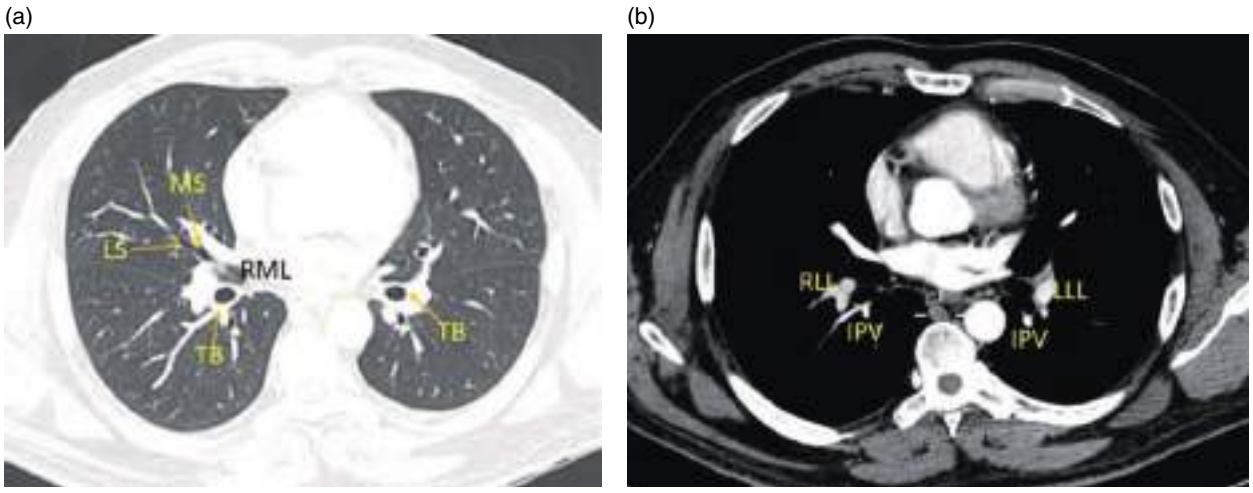

Figure 3.29 Middle lobe and its segments. Trunks of the lower basal lobe. (a) Axial CT image (lung window). ML, middle lobe bronchus; MS, medial segment; LS, lateral segment; BT, basal trunks. (b) Axial CT image (mediastinal window). RLL, LLL, right and left lower lobe pulmonary arteries, respectively; IPV, inferior pulmonary vein.

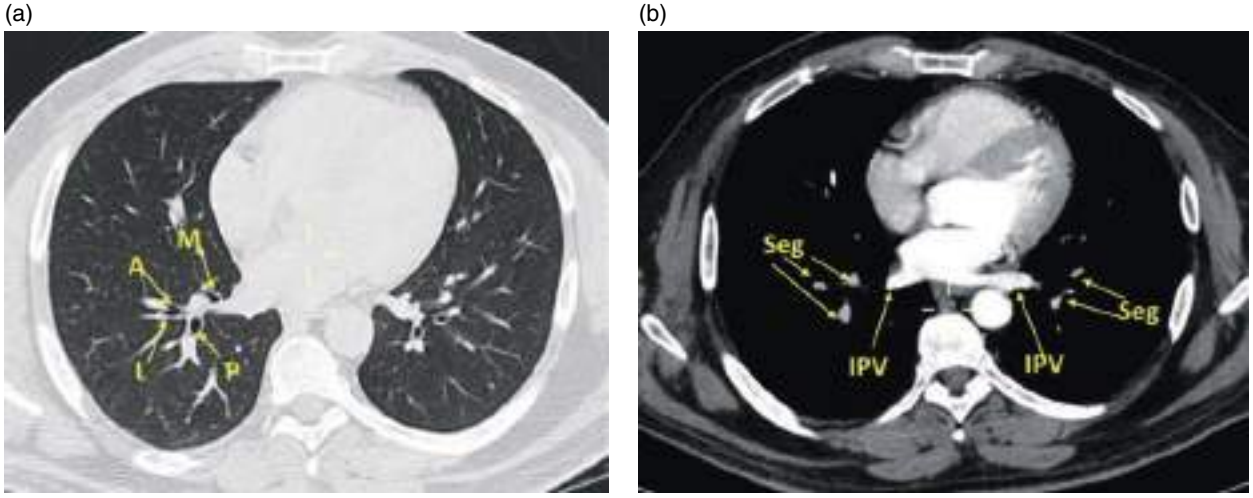

Figure 3.30 Basal segments of the right lower lobe. (a) Axial CT image (lung window). The four basal segments are shown, which in a counter-clockwise direction are the medial basal (M), anterior basal (A), lateral basal (L), and posterior basal (P). (b) Axial CT image (mediastinal window). Seg, segmental arteries; LV, lower pulmonary veins.

Vascular Anatomy of the Right Hilum

The vascular anatomy is best recognized at specific levels in relation to the bronchi [35].

Level of the Carina and Apical Segment Bronchus Next to the level of the carina, one or several branches of the anterior trunk irrigate the apical segment of the RUL and one or several branches of the right superior pulmonary vein drain it. These structures can be seen in cross-sectional images next to the apical segment bronchus (Figure 3.23).

Level of the Right Upper Lobe Bronchus At this level, the anterior trunk has not yet divided and can be easily identified (Figure 3.24). This large vessel is the first main branch of the right main pulmonary artery. A branch of the right superior pulmonary vein, the posterior vein, is located within the angle formed by the bifurcation of the RUL bronchus into its anterior and posterior branches (Figure 3.24).

Level of the Intermediate Bronchus The interlobar pulmonary artery is located anterior and lateral to the corresponding bronchus (Figures 3.25–3.27). The superior right pulmonary vein is located anterior to the right interlobar pulmonary artery and sometimes two veins can be seen.

Level of the Middle Lobe Bronchus At the level of the origin of the ML bronchus, the pulmonary artery of the RLL is located lateral to the external walls of the ML and RLL bronchi. The pulmonary artery of the ML runs parallel to the ML bronchus (Figures 3.28 and 3.29). The superior right pulmonary vein runs anterior and medial to the ML and RLL bronchi until it enters the upper part of the left atrium.

Level of the Basal Segment Bronchus of the Right Lower Lobe Inferior to the origin of the ML bronchus, the pulmonary artery of the RLL usually divides into two shorter trunks, which in turn divide into the four pulmonary arteries of the basal segments (Figures 3.30 and 3.31). The inferior pulmonary veins join to form the inferior pulmonary vein, passing behind the RLL bronchus and its arteries before entering the lower part of left atrium.

Anatomy of the Left Bronchus

The distinctive feature of the left main bronchus is its longer length compared to the right one, thus it can be seen during several contiguous slices below the carina [34].

Left Upper Lobe Bronchus The LUL bronchus is 2–3 cm long (Figure 3.26). In 75% of cases it branches out into an upper trunk and the bronchus of the lingula. The upper trunk gives rise to the bronchi of the anterior and apicoposterior segments (Figures 3.25 and 3.27).

In 25% of cases, the LUL bronchus branches into the posterior apical bronchus, the anterior segmental bronchus, and the lingular bronchus.

- Anterior segment bronchus: Visible above the level of the LUL bronchus (Figure 3.24). Oriented anteriorly.
- Bronchus of the apicoposterior segment: Visible as a rounded air space superior to the origin of the anterior segment bronchus (Figure 3.24).

Lingular Bronchus The lingular bronchus originates from the lower surface of the most distal part of the LUL bronchus and runs inferiorly with an oblique course (Figure 3.27). It subsequently divides into the upper and lower segment bronchi. The upper branch runs more laterally and is closer to the plane of the image in a similar way to the branching pattern of the medial and lateral bronchi of the ML.

Left Lower Lobe Bronchus The LLL bronchus displays a branching pattern similar to that of the RLL bronchus, but there are three basal segments (anteromedial, lateral, and posterior) instead of four.

- Apical segment bronchus: This originates less than 10 mm distal to the origin of the LLL bronchus, being similar in size and arrangement pattern to the apical segment bronchus on the right side (Figure 3.28).
- Basal trunk and segments: The basal trunk is the LLL bronchus itself, which gives rise to the basal segments and is visible below the origin of the apical segment (Figure 3.29). As mentioned above, the configuration of the basal segmental bronchi is similar to that of the contralateral basal pyramid bronchi, except for the fact that the medial and anterior basal bronchi typically originate as a common trunk (Figure 3.31). Accordingly, their clockwise arrangement is M-A (anteromedial)-L-P.

Vascular Anatomy of the Left Hilum

On the left side there are more anatomical variants than on the right side, although the constant relationships between vessels and airways remain [35, 36].

Level of the anterior and posterior apical segments of the LUL The apicoposterior segment bronchus and its arteries and veins are arranged similarly to those on the right side. The artery of the anterior segment of the LUL runs medially to the bronchus of the anterior segment (Figure 3.24).

Level of the LUL Bronchus The left interlobar pulmonary artery causes a large convexity of the posterior part of the hilum and the upper pulmonary vein causes an anterior

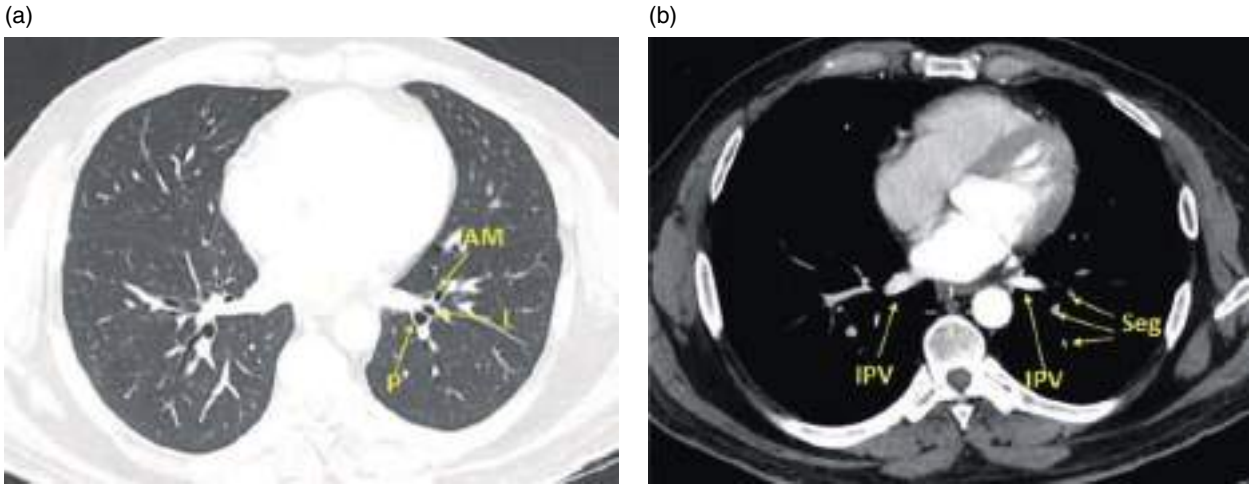

Figure 3.31 Basal segments of the left lower lobe. (a) Axial CT image (lung window). Basal segments in a clockwise direction are the anteromedial basal (AM), lateral basal (L), and posterior basal (P). (b) Axial CT image (mediastinal window). Seg, segmental arteries; IPV, inferior pulmonary veins.

convexity medial to the ascending bronchial trunk (Figure 3.26).

Level of the Lingular Bronchus The left interlobar pulmonary artery can be seen in cross-sectional images lateral to the LLL bronchus, posterolateral to the lingular bronchus, and anterolateral to the apical segment bronchus (Figure 3.27). The superior pulmonary vein passes anteriorly and medially to the corresponding bronchus to enter the left atrium.

Level of the Basal Pyramid Bronchi of the LLL In this region, the anatomy of the lower part of the left hilum is virtually a mirror image of the right side (Figures 3.30 and 3.31). The branches of the pulmonary artery of the LLL are located laterally and posteriorly to the basal bronchus of the LLL. The inferior left pulmonary vein runs anterolateral to the descending aorta and posterior to the bronchi and arteries to enter the left atrium.

Mediastinum

The mediastinum is the compartment located between the two lungs, anterior to the spine, posterior to the sternum, and extending from the thoracic inlet to the diaphragm [37].

The aorta and its branches, the large veins, the pulmonary arteries, the trachea, and the main bronchi serve as precise landmarks to anatomically locate other important mediastinal structures [38, 39].

For a better anatomical understanding, the division proposed by Webb [3] will be followed, considering four compartments in the cranio-caudal direction:

1) Superior or supra-aortic mediastinum.
2) Aortic arch and aorto-pulmonary window.
3) Pulmonary arteries, subcarinal space and azygo-esophageal recess.
4) Heart and paracardiac mediastinum.

Supra-aortic Mediastinum

The trachea is located in a central position inferior to the thoracic inlet (Figure 3.32). The esophagus is positioned posterior to the trachea and slightly displaced to the left (most often) or to the right. It is usually collapsed and looks like a flattened structure with soft tissue density. There may be small amounts of air or fluid in its lumen.

At this level, the supra-aortic vessels, and the subclavian and brachiocephalic veins are also depicted. The latter are the most anterior and lateral visible vessels. They are located immediately behind the clavicular heads. Although they may vary in size, their positions are relatively constant (Figure 3.32).

The right brachiocephalic vein has a vertical course along its entire length. The left brachiocephalic vein is longer and runs horizontally across the mediastinum from left to right (Figure 3.32). This vein has a rather variable location in the cranio-caudal axis.

The trunks of the brachiocephalic, subclavian, and carotid arteries are located posterior to the veins and adjacent to the anterior and lateral walls of the trachea. Their arrangement is relatively constant.

The trunk of the brachiocephalic artery is located in close proximity to the anterior tracheal wall, near the midline or slightly to the right. It is the most variable of all the supra-aortic great vessels.

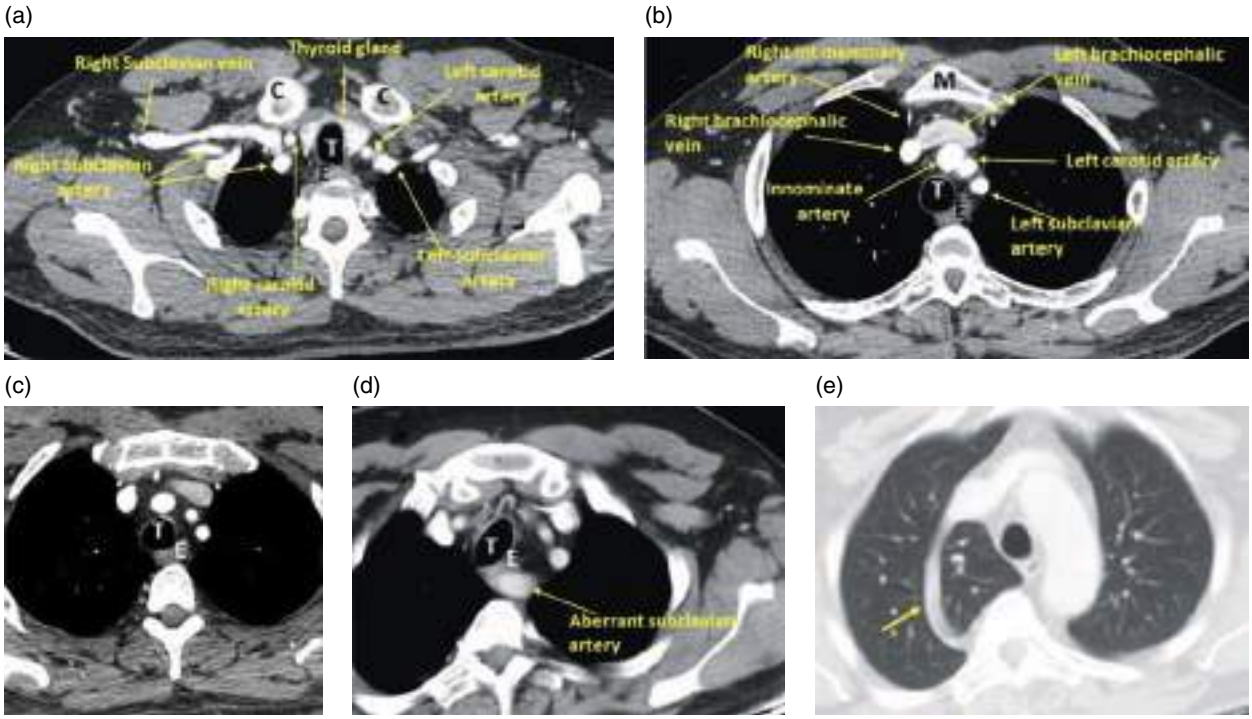

Figure 3.32 Supra-aortic mediastinum. (a–d) Axial contrast-enhanced CT image (mediastinal window). C, clavicle; T, trachea; M, sternal manubrium; E, esophagus. (e) Axial contrast-enhanced CT image (lung window). Arch of the azygos with posterior azygos vein lying more lateral to its normal course (arrow).

The left common carotid artery is located to the left and slightly posterior to the brachiocephalic trunk. It usually has the smallest diameter of the three supra-aortic vessels.

The left subclavian artery is located further posteriorly in most individuals, running along the left side of the trachea or slightly posterior to the midline.

Small vascular branches, the internal thoracic arteries and veins, and the vertebral arteries are also visible at this level.

There is an anatomical variant known as "aberrant right subclavian artery," which consists of a right subclavian artery that courses through the mediastinum from left to right between the esophagus and the vertebral body (Figure 3.32d).

The thyroid gland is also visible in the superior mediastinum, with its right and left lobes located on both sides of the trachea. The density of the thyroid gland is higher than that of the surrounding soft tissues.

There is another congenital anomaly called the azygos lobe, which consists of the arch of the azygos being located in a more superior position than usual, near the point of junction of the brachiocephalic veins. The azygos fissure can be seen defining the pulmonary lobe of the azygos (Figure 3.32e).

Aortic Arch and Aorto-pulmonary Window

At this level several structures can be depicted, including the large mediastinal vessels, the aorta, and the superior vena cava, as well as the mediastinal spaces and different groups of lymph nodes (Figure 3.33).

The aortic arch usually shows a characteristic morphology, although it can be variable. The anterior part of the aortic arch is located anteriorly and slightly to the right of the trachea. It then courses posteriorly, passing to the left side of the trachea. The posterior aortic arch is located anterior and lateral to the spine.

The position of the anterior and posterior parts of the aortic arch may vary depending on the tortuosity and the existence of arteriosclerosis.

The superior vena cava is visible anteriorly and slightly lateralized to the right side of the trachea, with an elliptical morphology on cross-sectional imaging (Figure 3.33).

The appearance of the esophagus is similar to that in upper levels and is located posterior to the trachea, although its course may be variable. It is more frequently located to the left side of the midline (Figure 3.33a–d).

The pre-tracheal space is limited by the aortic arch on the left, the superior vena cava and the mediastinal pleura on the right, and the trachea posteriorly. It has a triangular shape and contains mediastinal fat (Figure 3.33a).

The pre-vascular space also has a triangular shape and is located anterior to the great vessels (superior vena cava and aorta). The apex of this space is posterior to the sternum,

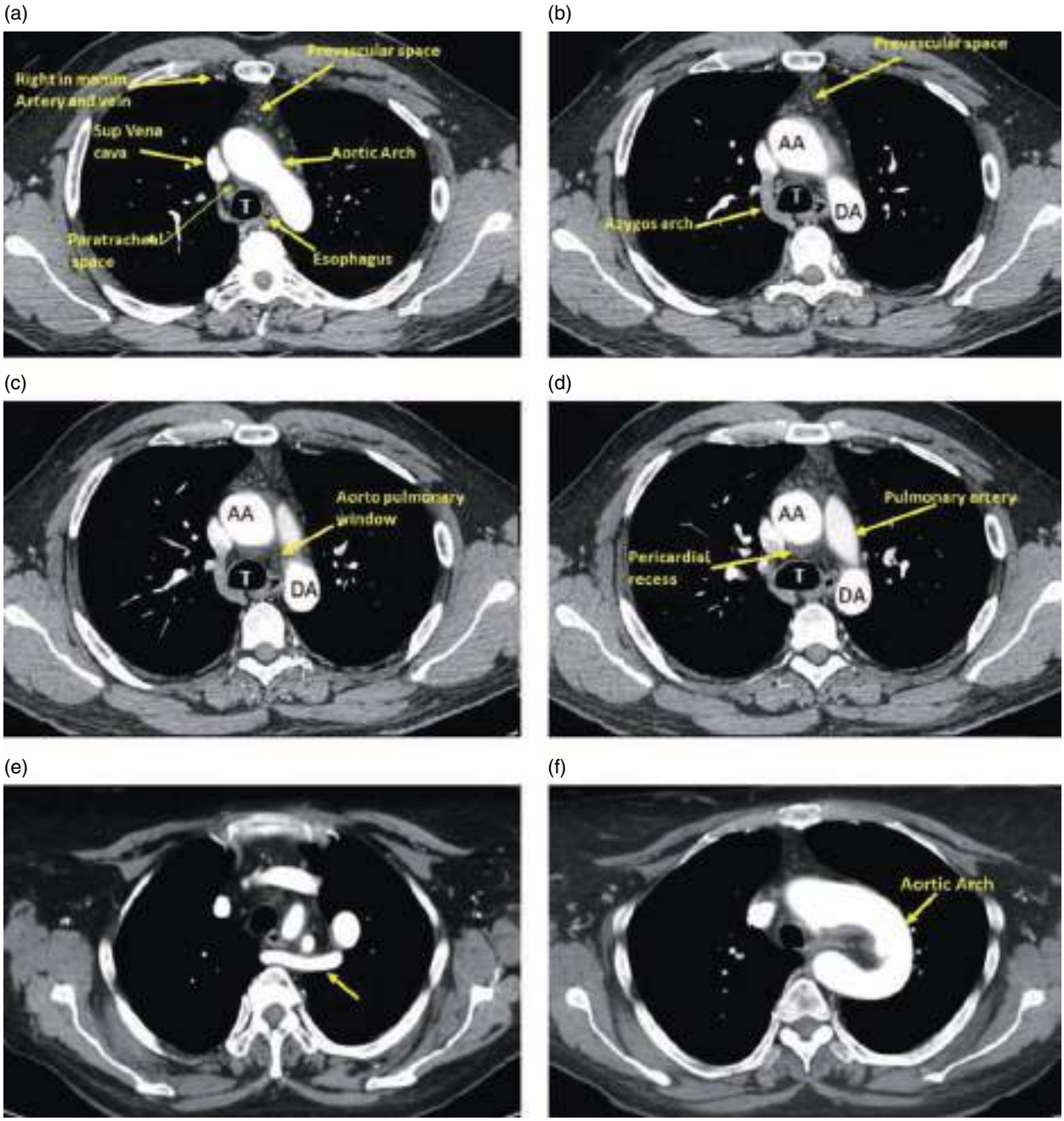

Figure 3.33 Sub-aortic mediastinum. Azygos arch and aorto-pulmonary window. (a–f). Axial contrast-enhanced CT images (mediastinal window). T, trachea; AA, ascending aorta; DA, descending aorta. Note the anatomical variant consisting of elongated left aortic arch with aberrant right subclavian artery (arrows in e and f).

forming the anterior junction line. This mediastinal compartment contains fat, lymph nodes, and the thymus, which involutes with age. The mediastinal pleural reflections lateral to the pre-vascular space can be concave or convex.

At a level below the aortic arch, the ascending and the descending parts of the aorta are visualized as separate structures (Figure 3.33c,d).

In a slightly lower position, the trachea bifurcates into the main bronchi and adopts a triangular morphology prior to the carina.

On the right, the arch of the azygos originates from the posterior wall of the superior vena cava, passes over the right main bronchus, and continues along the mediastinum on the right side and anterior to the spine

(Figure 3.33b). It delimits the right border of the pre-tracheal space. Below the level of the arch of the azygos, the azygos vein can be seen [40].

The aorto-pulmonary window is located on the left side of the mediastinum, inferior to the aorta and above the pulmonary trunk (Figure 3.33c). This space contains fat, lymph nodes, the recurrent laryngeal nerve, and the ligamentum arteriosum (although the latter is usually not visible) [41].

The superior pericardial recess contains a small amount of fluid and can be visualized in the pre-tracheal space immediately posterior to the ascending aorta (Figure 3.13d). It should not be mistaken for a lymph node, and can be distinguished by its typical location, contact with the aortic wall, crescent shape, and fluid-like attenuation.

The anterior recess of the pericardial space can be visualized anterior to the aortic arch, the ascending aorta, and the pulmonary trunk (Figure 3.33d).

Many developmental abnormalities of the aortic arch have been described, such as a double aortic arch, right aortic arch with or without aberrant subclavian artery, and elongated left aortic arch with aberrant right subclavian artery (Figure 3.33e,f).

Pulmonary Arteries, Subcarinal Space, and Azygo-esophageal Recess

At the level of the carina and the main bronchi, the pulmonary trunk divides into the right and left pulmonary arteries (Figure 3.34). The left pulmonary artery is slightly above the right one (around 1 cm).

The emergence of the right pulmonary artery is almost right-angled relative to the pulmonary trunk. It then crosses the mediastinum from left to right anterior to the carina or the main bronchi (Figure 3.34a). This artery serves as the most inferior bound to the pre-tracheal space and the anterior limit of the subcarinal space.

The azygos vein runs parallel to the esophagus on the right side of the mediastinum, contacts laterally with the medial pleural reflection of the RUL, and defines the posterior limit of the azygo-esophageal recess (Figure 3.34).

On the left side, the hemiazygos vein (not always visible) runs parallel to the descending aorta (Figure 3.34b). This

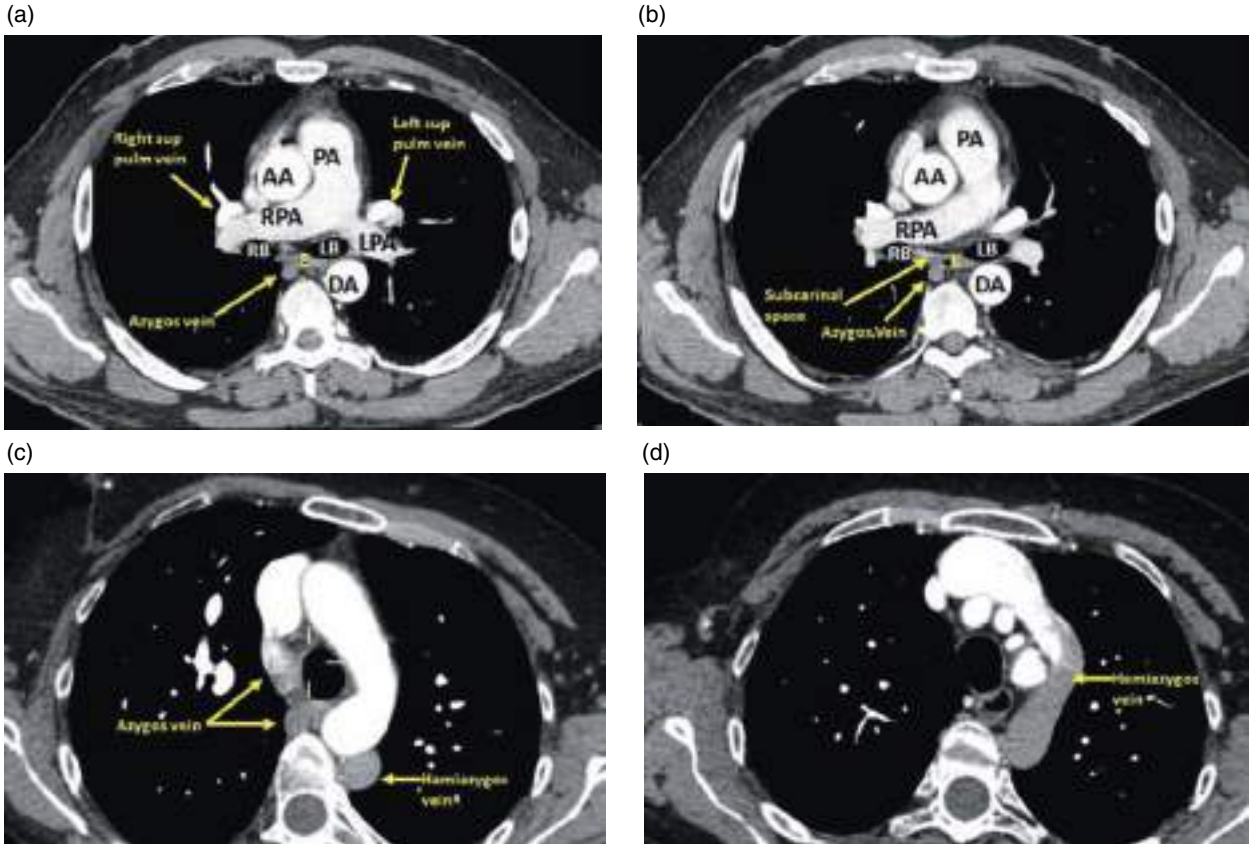

Figure 3.34 (a–d) Axial contrast-enhanced CT images (mediastinal window) at the level of the pulmonary trunk, subcarinal space, and azygo-esophageal recess. AA, ascending aorta; DA, descending aorta; PA, pulmonary artery; RP, right pulmonary artery; LP, left pulmonary artery; RB, right bronchus; LB, left bronchus; E, esophagus. Note the anatomical variant consisting of the hemiazygos vein draining directly into the left brachiocephalic vein.

vein generally drains into the azygos vein through a branch that crosses the midline behind the aorta at the height of the T8 vertebral body.

There are several congenital anomalies of the superior vena cava that can be incidentally found as anatomical variants, including the continuation of the superior vena cava with the azygos-hemiazygos system and, more rarely, the dilated hemiazygos vein draining directly into the left brachiocephalic trunk instead of joining the azygos vein (Figure 3.34c,d).

The region of the mediastinum located just below the carina is known as the sub-carinal space and is limited laterally by the main bronchi. It is closely related to the esophagus and contains lymph nodes (Figure 3.34a).

The azygo-esophageal recess (Figure 3.34) is located inferior to the tracheal carina and the arch of the azygos. The medial part of the right lung contacts the mediastinum where the azygos vein, the esophagus, and the sub-carinal space are located. The contour of the azygo-esophageal recess is usually concave.

Heart and Paracardiac Mediastinum

The pre-vascular mediastinum at the level of the heart becomes thin and practically obliterated because the ventricles come into contact with the anterior chest wall (Figures 3.35 and 3.36).

The azygo-esophageal recess can still be visualized posterior to the heart down to the level of the diaphragm. The left paravertebral space is located posterior to the descending

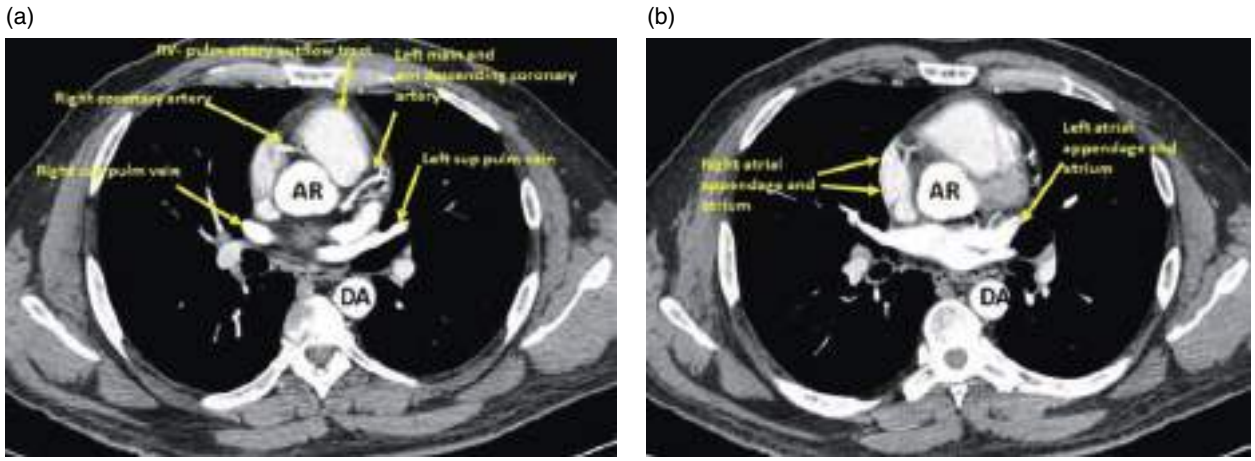

Figure 3.35 Paracardiac mediastinum. (a, b) Axial contrast-enhanced CT images (mediastinal window). AR, aortic root; DA, descending aorta.

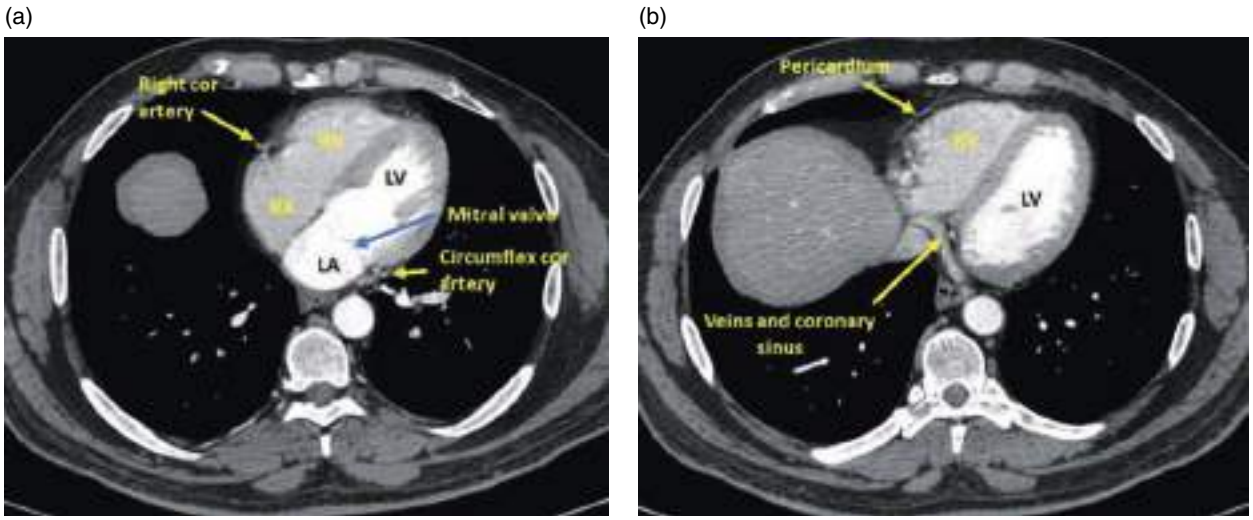

Figure 3.36 Normal cardiac anatomy. (a, b) Axial contrast-enhanced CT images (mediastinal window). RV, right ventricle; LV, left ventricle; RA, right atrium; LA, left atrium; LVO, left ventricular outflow tract; DA, descending aorta.

aorta and contains the hemiazygos vein, fat, and small lymph nodes.

The heart usually has an oblique position relative to the anatomical axes, in such a way that it is oriented from right to left and from top to bottom. In the upper planes, the outflow tract of the left ventricle and the aortic valve are in a central position within the heart (Figure 3.35a). Next to the aortic root it is possible to visualize the exit of the coronary arteries [42].

The outflow tract of the right ventricle is directed toward the left and is visible anterior or slightly to the left of the outflow tract of the left ventricle.

At this level, the entrance of the vena cava into the right atrium, both atrial appendages, and the left atrium are visible (Figure 3.35b).

More inferiorly, the four cardiac chambers can be seen, with the atria separated from the ventricles by the atrioventricular sulcus.

The interventricular septum is oriented inferiorly and toward the left, being slightly convex anteriorly due to the greater pressure in the left ventricle. The lateral aspect or free wall of the left ventricle is usually three times larger than that of the right ventricle. The left ventricle has an elliptical shape.

The right ventricle has a triangular shape and is oriented anteriorly and to the right (Figure 3.36a). In its lower part, the coronary sinus can be seen heading toward the most inferior part of the right atrium (Figure 3.36b). The diameter of the coronary sinus may be increased in the presence of anatomical variants in which a left superior vena cava drains into it. This occurs in two anatomical variants, namely double superior vena cava and persistent superior left vena cava (Figure 3.37).

Thoracic Wall and Pleural Surfaces

Several structures arranged in layers surround the lung and wrap around the inner surface of the chest cavity. The layers of the visceral and parietal pleura surrounding the lung and pleural space are less than 0.5 mm thick.

External to the parietal pleura, the extra-pleural fat separates the parietal pleura from the endothoracic fascia. This fat layer is very thin but may be thicker on the lateral and posterolateral aspects of the ribs.

The thoracic cavity is surrounded by the endothoracic fascia, a fibroelastic layer which covers the surface of the intercostal muscles and the corresponding ribs. Anteriorly, this fascia blends with the perichondrium and periosteum of the costal cartilages and the sternum. In its posterior part, the fascia continues with the prevertebral fascia, which covers the vertebral bodies and the intervertebral discs.

External to the endothoracic fascia there are three layers of intercostal muscles. The innermost intercostal muscle passes between the inner surfaces of the ribs. It is thin and separated from the intercostal muscles by a layer of fat and the intercostal vessels and nerves.

The innermost intercostal muscles are incomplete in the anterior and posterior parts of the thoracic wall. The transverse and subcostal thoracic muscles may occupy the same relative plane.

Anteriorly, the transversus thoracis muscle is made up of four or five muscular strips that arise from the xiphoid process or the lower part of the sternum and pass superolaterally from the second to sixth costal cartilages. The internal thoracic vessels lie external to the transversus thoracis muscle.

Posteriorly, the subcostal muscles, which are thin and rather variable, extend from the inner surface of the angle of the lower ribs, cross one or two ribs and the intercostal spaces, and reach the inner side of the rib above.

On CT, a 1–2 mm thick soft tissue band (the intercostal band) is visible in the anterolateral and posterolateral intercostal spaces at the site in which the lung comes into contact with the thoracic wall (Figure 3.38). This line represents the innermost intercostal muscles, the combination of the visceral and parietal pleural layers, the pleural space containing fluid, the endothoracic fascia and fat layers.

Figure 3.37 Left superior vena cava variants. (a–c) Axial contrast-enhanced CT image (mediastinal window). (a) Double superior vena cava. (b) Persistent left superior vein cava. (c) Dilated coronary sinus.

Figure 3.38 Axial contrast-enhanced CT image (mediastinal window). Intercostal band represented by a thin line corresponding to the innermost intercostal muscle (arrows).

In the paravertebral regions, the innermost intercostal muscle is absent.

Diaphragm

The central portion of the diaphragm is not visualized as a single structure, but its location can be inferred based on the position of the lung bases (in an upper plane) and the abdominal organs (in a lower plane) [43]. As the more peripheral portions of the diaphragm extend inferiorly toward their costal and sternal insertions, the anterior, posterior, and lateral portions of the diaphragm become visible, adjacent to the retroperitoneal fat.

The right and left diaphragmatic crura are tendinous structures that originate inferiorly on the anterior surfaces of the lumbar vertebral bodies and the corresponding intervertebral discs and continue with the anterior longitudinal ligament of the spine. The crura ascend anterior to the spine on both sides of the aorta and then cross anteriorly and medially to join the muscular portion of the diaphragm located in front of the aorta to form the aortic hiatus. The right crus is larger than the left one and originates from the first three lumbar vertebrae. The left crus originates from the first two lumbar vertebrae.

The diaphragmatic crura have a rounded appearance and it is possible to visualize their progressive fusion with the diaphragm in the upper slices.

Diaphragmatic Apertures

The diaphragm is noncontinuous due to various apertures that permit the passage of different anatomical structures from the thorax to the abdomen. The aortic hiatus lies posteriorly and is bounded by the diaphragmatic crura anteriorly and by the vertebral bodies posteriorly. The anatomical structures that pass through this hiatus include the aorta, the azygos and hemiazygous veins, the thoracic duct, the intercostal arteries, and the splanchnic nerves.

The esophageal hiatus is located in a more anterior position, in the muscular portion of the diaphragm. The esophagus, the two portions of the vagus nerve, and small vessels pass through this diaphragmatic aperture.

The inferior caval foramen crosses the fibrous portion of the central diaphragmatic tendon, anteriorly and to the right of the esophageal hiatus.

Of the three diaphragmatic apertures, the aortic hiatus is the one most easily visualized. The esophageal hiatus is visualized as an opening at the junction between the esophagus and the stomach.

The inferior vena caval foramen can be located based on the position of the inferior vena cava (IVC).

Anatomy of the Abdomen

Anatomy of the Hepato-biliary System and Pancreas

Anatomy of the Liver

The liver is located in the right hypochondrium. It is partially peritonealized and covered by a fibrous capsule (Glisson's capsule).

The liver is fixed to the anterior abdominal wall and to the diaphragm by the falciform ligament which contains the ligamentum teres, the coronary ligament, and the two triangular ligaments. In its inferior and medial aspect it is fixed to the stomach and duodenum by the hepatogastric and hepatoduodenal ligaments. The connective tissue of the so-called "bare area" and the IVC, to which the bare area is solidly attached by the hepatic veins (HV), fixes the posterior surface of the liver [44] (Figure 3.39).

The liver has external impressions, which can be seen on its surface. The peritoneum covering the surface of the liver folds back toward the underlying parenchyma, with or without an associated ligament and to a variable depth, creating the fissures of the liver fissures. There are four constant fissures, including the ligamentum teres, ligamentum venosum, gallbladder (or major), and transverse fissures. Fissures are clefts visible on the external surface of the liver which communicate with each other and with the intraperitoneal space. The transverse fissure is a peritoneal fold that forms the hepatic hilum. It contains the bifurcation of the portal vein (PV), the first branch of the hepatic artery (HA), and the common hepatic duct [44] (Figure 3.40).

Classical anatomy of the liver

This is based on external marks which divide the liver into four lobes, namely right, left, caudate (or Spiegel's), and quadrate lobes. This classification is no longer in use in radiology.

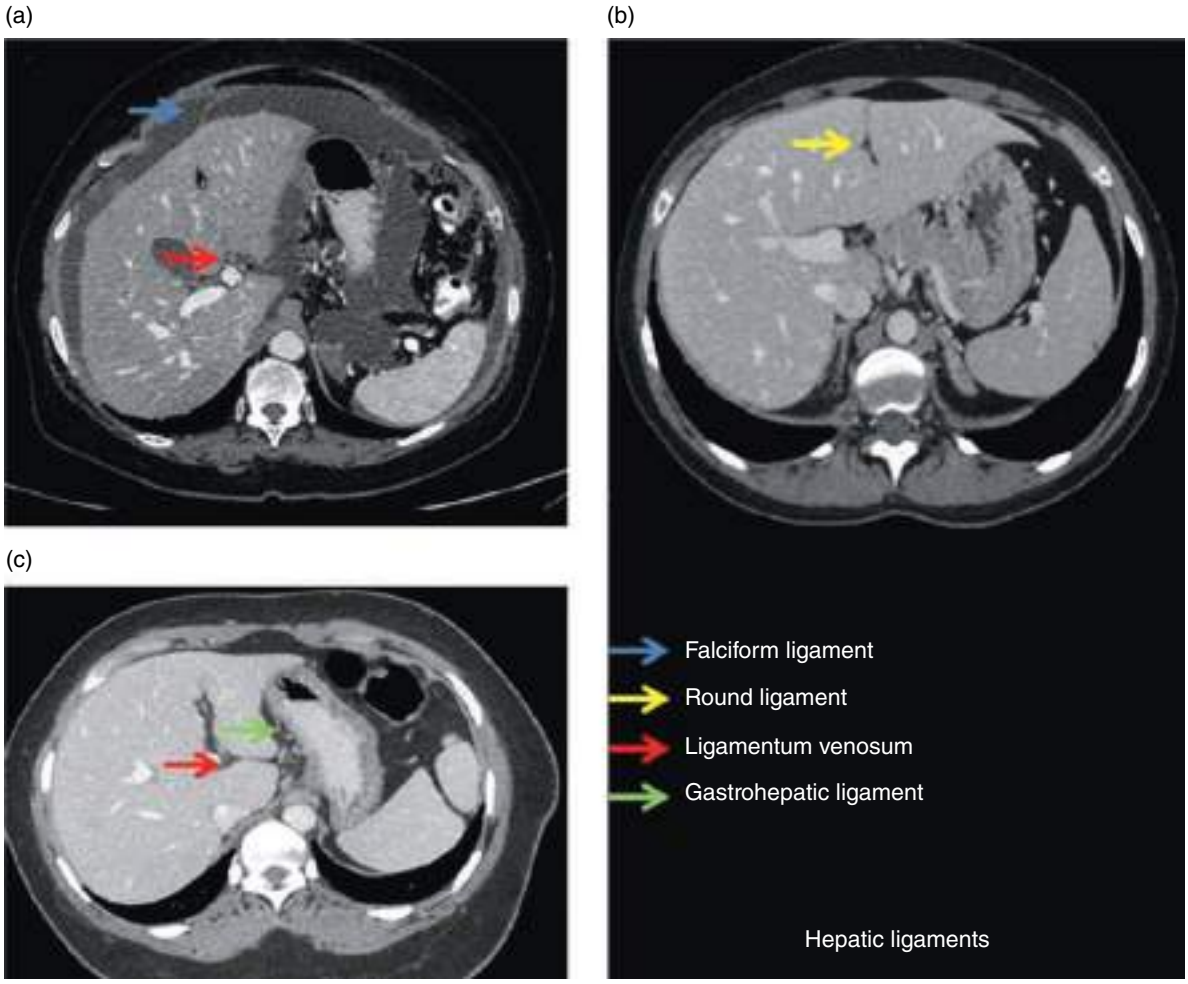

Figure 3.39 Ligaments of the liver. (a–c) Axial contrast-enhanced CT images (portal venous phase).

Functional anatomy

This is based on the intraparenchymal distribution of the afferent blood supply of the liver, with the PV being the main and most easily identifiable landmark. The liver is divided into functional units, each with an independent portal supply, and venous and biliary drainage. Accordingly, removal of one or more units does not compromise the liver function.

Following the initial division of the afferent branches of the hepatic hilum, the liver is divided into right and left hemi-livers. After the second division of the hilum branches, each hemi-liver is further divided into two sections: the right hemi-liver into anterior and posterior, and the left hemi-liver into medial and lateral. The third and final division splits each section into superior and inferior segments [44] (Figure 3.41).

The most representative system to understand the functional anatomy of the liver is the Couinaud classification (Figure 3.42):

- On the transverse plane, the main anatomical landmark is the portal bifurcation through the transverse fissure, which divides the liver into superior and inferior sections. Several vertical planes are then defined for each segment of the liver based on intersections with the transverse plane.
- The middle vertical plane defines the right and left hemi-livers. The anatomical landmark superior to the transverse plane corresponds to the middle hepatic vein (MHV), which separates segment VIII from the superior portion of segment IV. Inferiorly, along the gallbladder and its fissure, this plane separates segment V from the inferior portion of segment IV.
- The right vertical plane separates the right anterior from the right posterior section. Superior to the portal bifurcation, the anatomical landmark is the right hepatic vein (RHV), which separates segment VII from segment VIII. Inferiorly, the limit is rather arbitrary, with the intersection of the RHV coinciding with the bifurcation of the

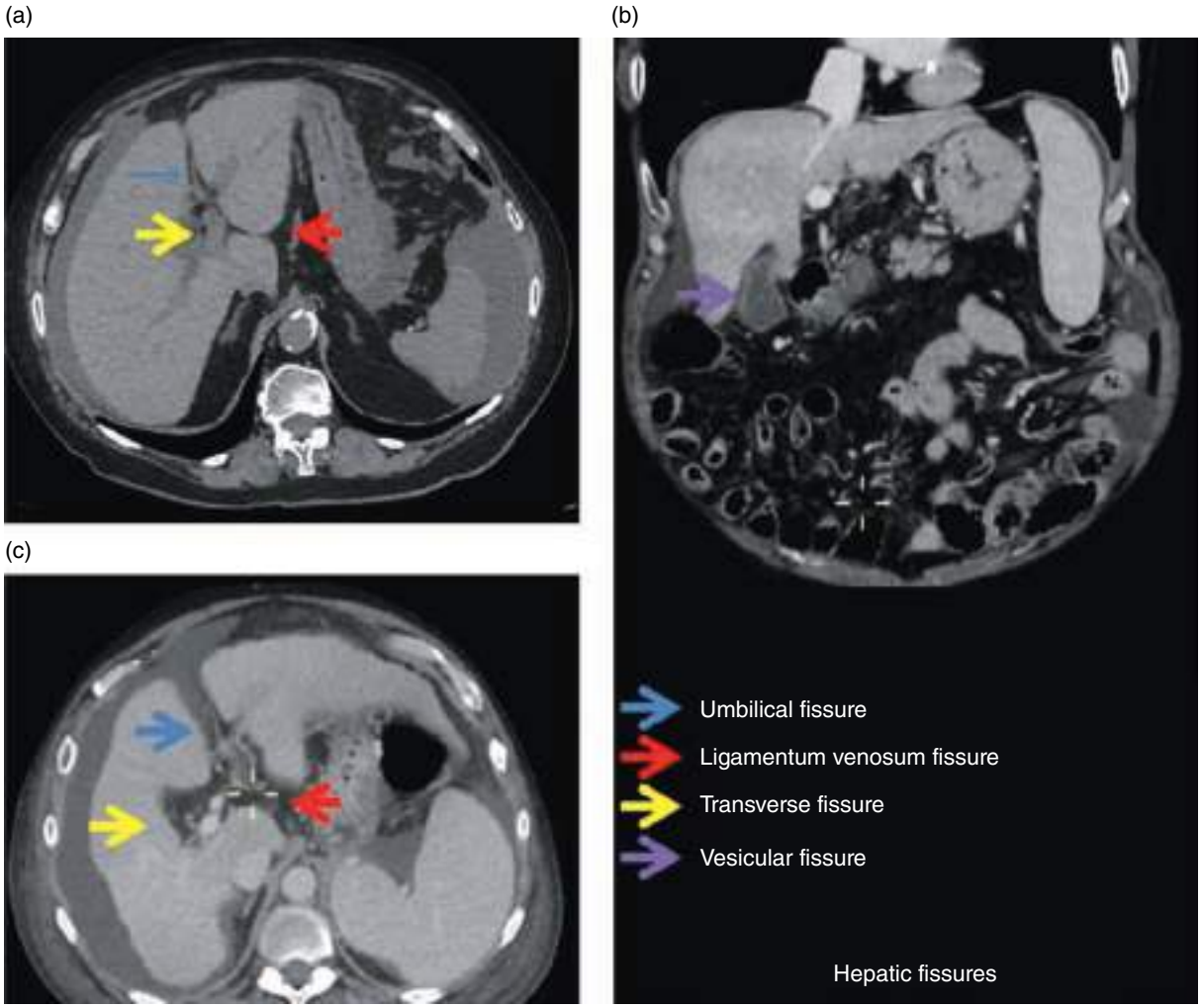

Figure 3.40 Fissures of the liver in a patient with cirrhosis and moderate free ascites. (a) Axial noncontrast CT image. (b) Coronal contrast-enhanced MPR CT image (portal venous phase). (c) Axial contrast-enhanced CT image (portal venous phase).

right portal vein (RPV), separating segment VI from segment V.

- The left vertical plane separates the medial section (segment IV) from the left lateral section (segments II and III). In its upper third, this plane is represented by the left hepatic vein (LHV), in its middle third by the umbilical portion of the left portal vein (LPV), and in its lower third by the fissure of the ligamentum teres.

The posterior sector is formed by segments I and IX. On the left side, the fissure of the ligamentum venosum separates this section from segment II, while the IVC separates it from segment VIII on the right side. Superiorly, it is bounded by the common trunk formed by the MHV and IVC and, posteriorly, by the horizontal portion of the LPV in the transverse fissure [44].

The classification of the International Hepatic Pancreatic Biliary Association (IHPBA) (Brisbone, 2000) is increasingly being used [45, 46]. It unifies both anatomical and surgical terminology, using Arabic numerals and segment 4 is not divided. In addition, it accepts both "section" and "sector" terms, but they are only equivalent to the Couinaud classification in the right liver (Figures 3.41 and 3.42).

The right posterior section (or sector) is made up segments 7 and 6, while the anterior section is formed by segment 5. The left medial section includes segments 4 and 3, and the left lateral sector includes segment 2.

The posterior sector described by Couinaud is independent of the rest of the liver parenchyma and receives vascular supply from right and left branches, draining directly into the VCI via the HVs [45, 46].

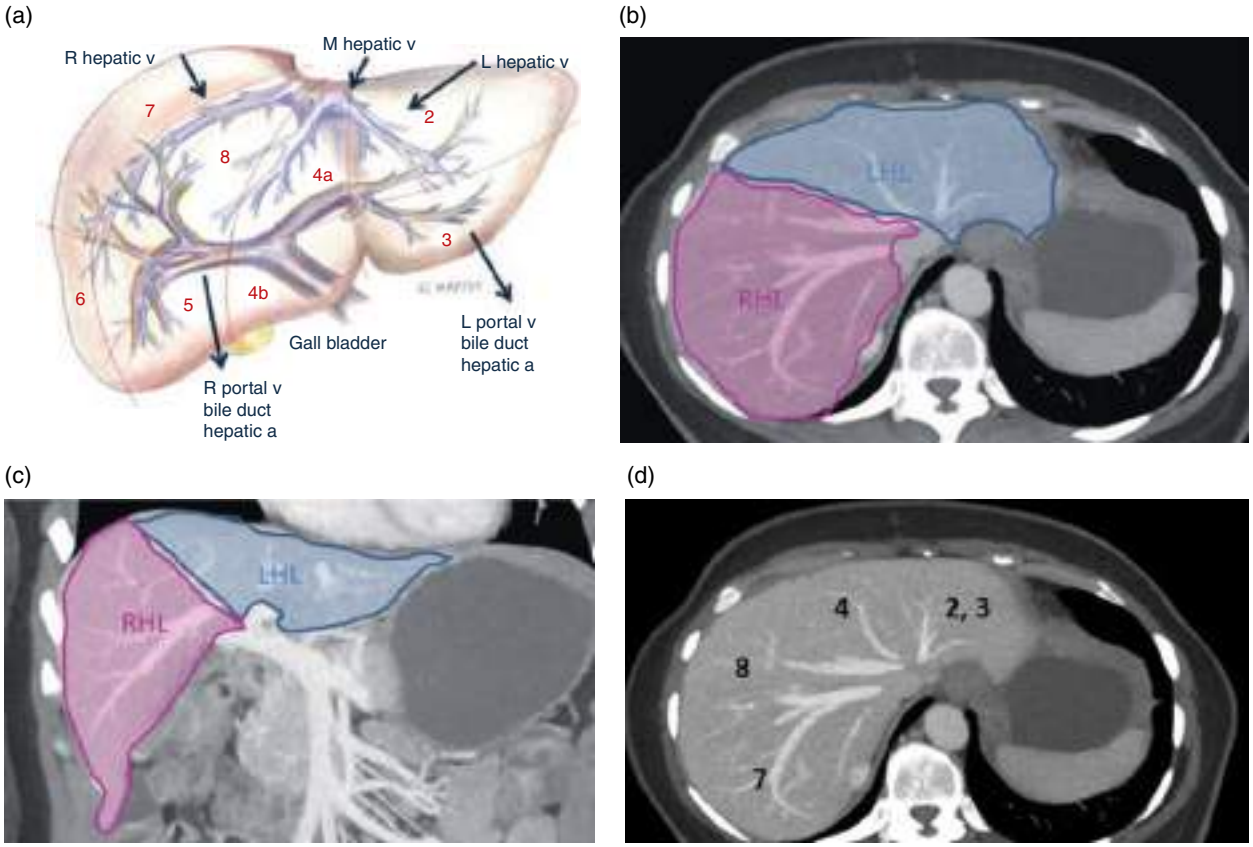

Figure 3.41 First-order division of the afferent vascular supply of the liver, resulting in two lobes. Segments 2, 3, and 4 belong to the left liver, and the other segments belong to the right liver. (a) Schematic diagram, adapted from Abdel-Misih and Bloomston [44]. (b, d) Axial contrast-enhanced CT image at the level of the hepatic veins (portal venous phase). (c) Coronal contrast-enhanced MPR CT image (portal venous phase). RHL, right hepatic lobe; LHL, left hepatic lobe.

Vascularization of the Liver [4] The PV provides 80% of the vascular supply of the liver. The splenic vein and the superior mesenteric vein join to form the PV behind the head of the pancreas. The PV runs toward the hepatic hilum posterior to the bile duct and to the HA at the free edge of the lesser omentum.

In the hepatic hilum, the PV bifurcates into left and RPVs. The LPV presents an abrupt angulation in the site of insertion of the venous ligament and becomes vertical (umbilical portion) medial to the ligamentum teres to vascularize segments 2, 3 and 4. The RPV is further divided into right anterior branch for segments 5 and 8, and right posterior branch for segments 6 and 7. The vascularization of the caudate lobe comes from an independent branch of the LPV [47] (Figure 3.43).

There are several anatomical variants of the PV [48] (Table 3.1 and Figure 3.1).

The HA provides up to 35% of the vascular supply of the liver. The HA arises from the bifurcation of the celiac trunk and is referred to as common hepatic artery (CHA) at this level. Before reaching the liver, the CHA bifurcates into the gastroduodenal artery and the proper HA. The latter further divides into left and right hepatic arteries at the level of the hepatoduodenal ligament [47] (Figure 3.44).

The HA presents numerous anatomical variants (Table 3.2) [48].

The anatomy of HVs is highly variable [48]. In most cases (<35%) there are three main HVs that drain into the IVC. In 60% of the cases, the LHV and MHV form a common trunk prior to enter the IVC. There are numerous accessory veins (most authors consider a vein as accessory when its diameter is equal to or greater than 0.5 cm). The caudate lobe has an independent drainage into the IVC (Figure 3.45).

The right HV is the trunk with the largest diameter and classically drains segments 5, 6, and 7 (Table 3.3).

The middle HV drains the central segments (5, 8, and 4) (Table 3.4).

The left HV drains segments 2 and 3 (Table 3.5).

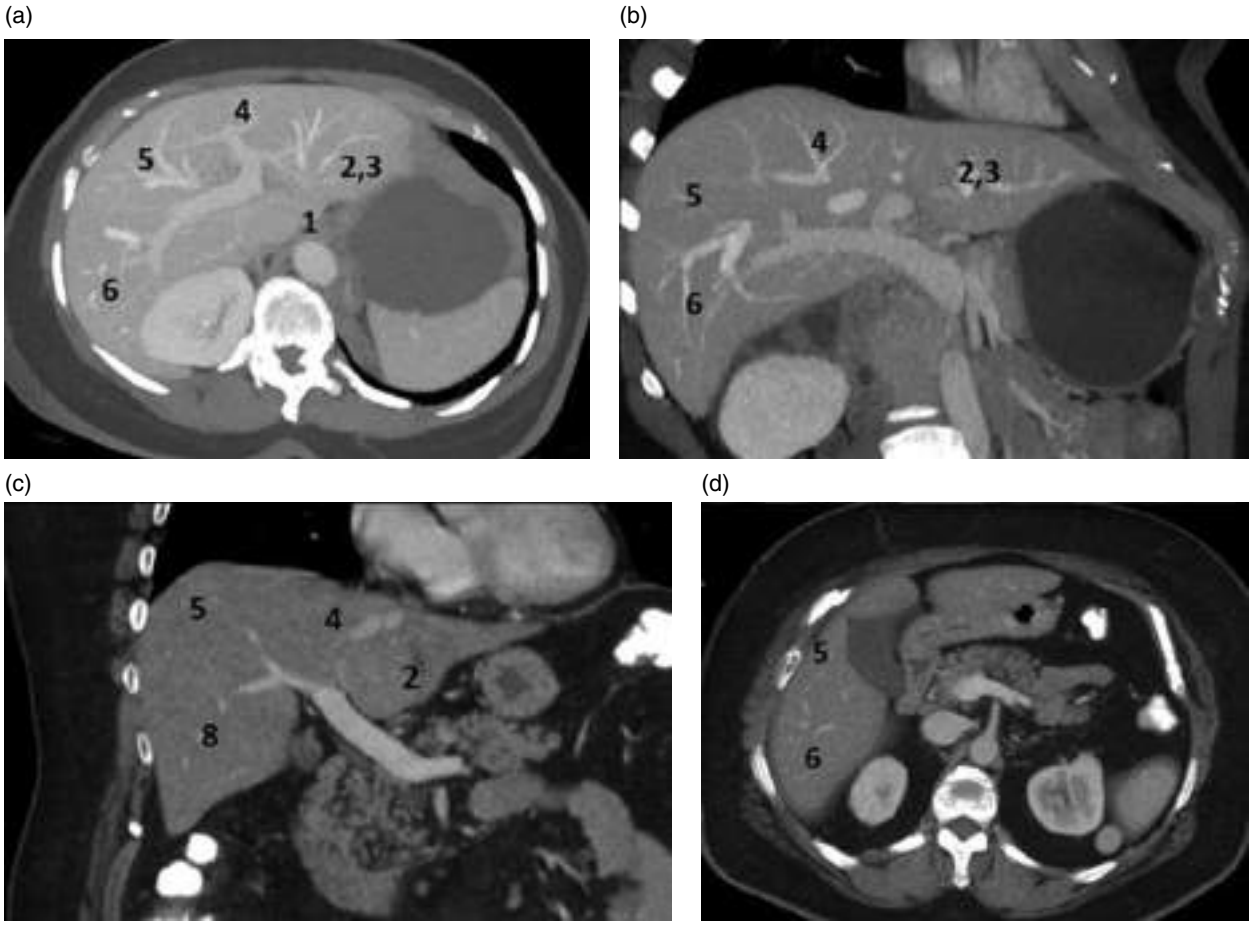

Figure 3.42 Segments of the liver and relations with the portal vein. (a, d) Axial contrast-enhanced CT image (portal venous phase). (b, c) Coronal contrast-enhanced MPR CT image (portal venous phase).

Anatomy of the Biliary System

The anatomy of the biliary system is highly variable. Under normal conditions, the extrahepatic bile duct develops in the 10th week of gestation along with the first-order bile ducts. The intrahepatic bile duct develops in the 12th week from the ductal plate along with the portal system [49] (Figure 3.46).

Intrahepatic Biliary Tree The left intrahepathic bile duct drains segments 2, 3, and 4 via the left hepatic duct. The left intrahepatic bile duct presents four main anatomical variants (Table 3.6).

The right hepatic duct drains segments 5, 6, 7, and 8. The radicals for segments 5 and 8 unite to form the right anterior duct. Analogously, the bile ducts of segments 6 and 7 form the right posterior duct. There is also significant anatomical variability (Table 3.7).

There may be ducts that drain directly into the gallbladder. Currently, it is preferable to use the term "subhepatic duct" over the classic "duct of Luschka." This duct represents an independent drainage pathway next to the hilar plate, thus it may be injured during cholecystectomy if the procedure is performed next to it. In fact, this mechanism could explain many of the post-cholecystectomy biliary leaks.

The caudate lobe is drained by one to three independent ducts (with a maximum of five). The caudate lobe drains into the right posterior or right main duct and the quadrate lobe into the left main duct.

Extrahepatic Biliary Tree The biliary confluence between the right and left hepatic ducts is usually formed in the hepatic hilum, near the transverse fissure, when both ducts join to form the common hepatic duct. More distally, the latter unites to the cystic duct, forming the common bile duct. The latter runs inferiorly through the hepatoduodenal ligament, anterior to the PV and lateral to the HA, and continues its course behind the first duodenal portion. In the ampulla of Vater, the pancreatic duct joins the common bile duct and enters the second part of the duodenum [49, 51].

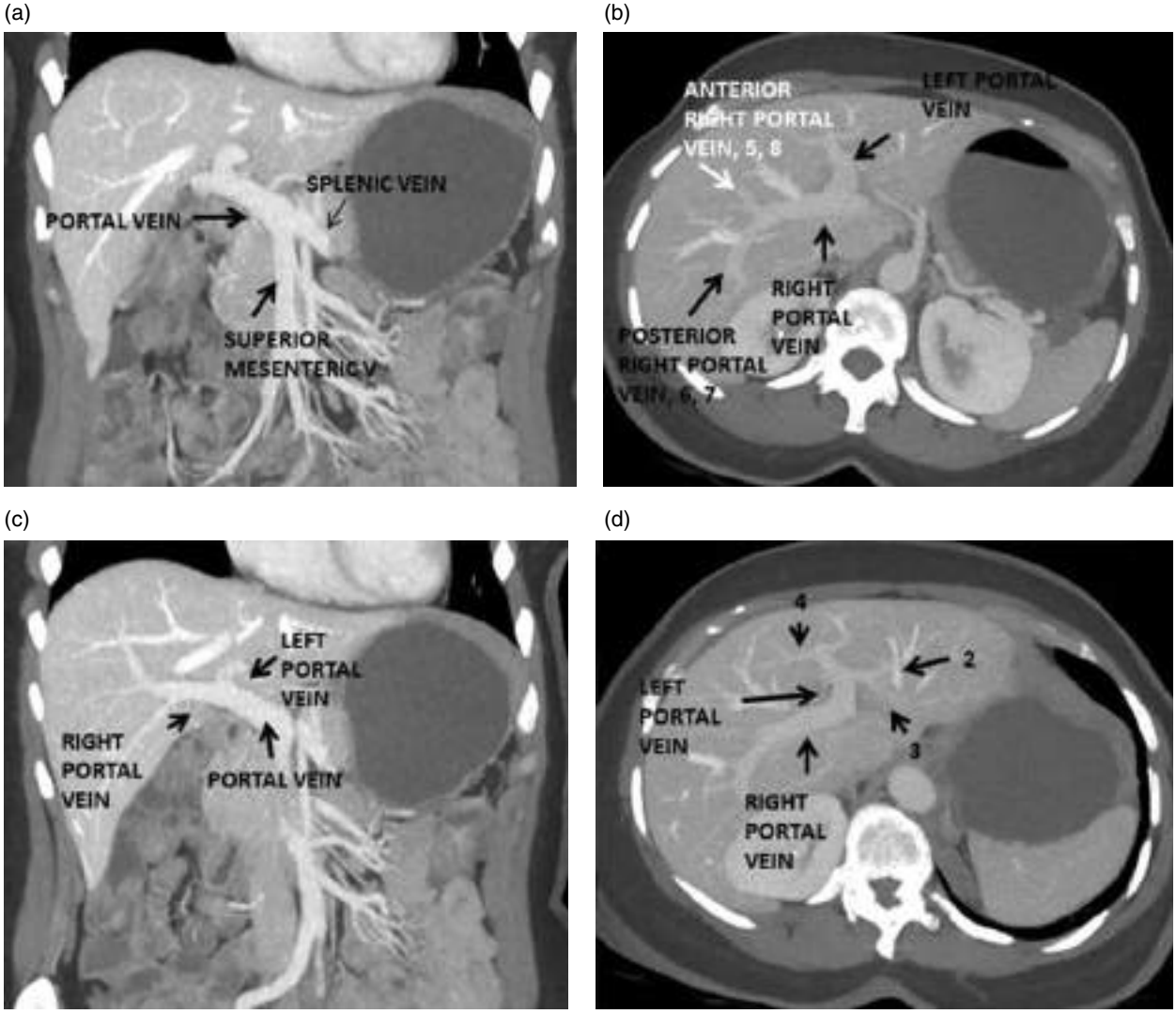

Figure 3.43 Main portal vein and intrahepatic branches. (a, c) Coronal contrast-enhanced MPR CT image (portal venous phase). (b, d) Axial contrast-enhanced CT image (portal venous phase).

Table 3.1 Anatomical variants of the portal vein (see also [Figure 3.1]).

Type	Frequency (%)	Description
I	65–80	MPV divides into RPV and LPV The RPV divides into RAPV and RPPV
II	7–11	Trifurcation of the MPV into LPV, RAPV, and RPPV
III	5–13	Z-type: MPV gives off the RPPV and a common trunk for LPV and RAPV
IV	6	Independent branch for segment 7 from RPV
V	0.1–6	Independent branch for segment 7 from RPV

MPV, main portal vein; RPV, right portal vein; LPV, left portal vein; RAPV, right anterior portal vein; RPPV, right posterior portal vein.
Source: Modified from Catalano et al. [48].

The common bile duct measures between 7 and 11 cm long and has an internal diameter of up to 8 mm under normal physiological pressure [51].

The cystic duct is about 2–4 cm long and has a tortuous course. It usually joins the extrahepatic bile duct halfway, between the PV and the ampulla of Vater, although the site of junction is variable. It marks the division between the common hepatic duct and the common bile duct.

The junction of the common hepatic duct and cystic duct occurs in the upper and distal segment in 75% and 10% of cases, respectively. They may share a common sheath. There are many variants regarding the insertion site, the most common being on the right side of the common hepatic duct (50% of cases), with medial and anterior or posterior insertions occurring in 18% in 31% of cases, respectively. Less frequently, it can be inserted into the

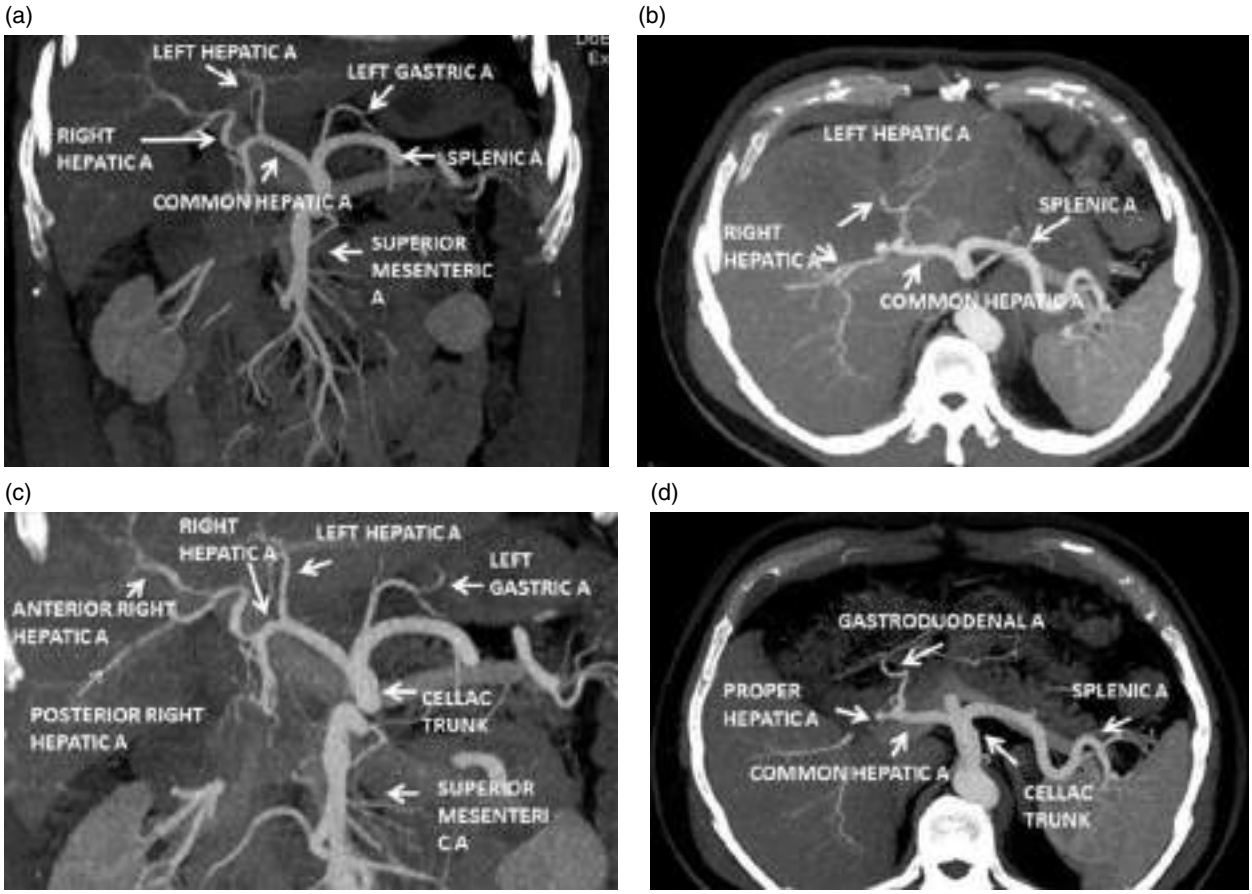

Figure 3.44 Celiac trunk and hepatic artery. (a, c) Coronal contrast-enhanced maximum intensity projection (MIP) CT image (arterial phase). (b, d) Axial contrast-enhanced maximum intensity projection (MIP) CT image (arterial phase).

Table 3.2 Anatomical variants of the hepatic artery Mitchell classification (Figure 3.2).

Type	Frequency (%)	Description
I	55	RHA, MHA, and LHA arise from CHA
II	10	RHA, MHA, and LHA are branches of the CHA LHA is an aberrant branch of the LGA
III	11	RHA and MHA arise from the CHA RHA is an aberrant branch of the SMA
IV	1	Aberrant RHA and LHA
V	8	RHA, MHA, and LHA are branches of the CHA Accessory LHA branch from LGA
VI	7	RHA, MHA, and LHA are branches of the CHA Accessory RHA
VII	1	Accessory RHA and LHA
VIII	4	Aberrant RHA and accessory LHA, or vice versa
IX	4.5	Complete hepatic trunk arising from SMA
X	0.5	Complete hepatic trunk arising from LGA

CHA, common hepatic artery; LGA, left gastric artery; MHA, middle hepatic artery; RHA, right hepatic artery; LHA, left hepatic artery; SMA, superior mesenteric artery.
Source: Catalano et al. [48].

intrapancreatic segment or in the ampulla of Vater, and more rarely into the duodenum [52] (Figure 3.46).

Gallbladder

The gallbladder is a muscular pouch located under the liver. The sphincter of Oddi prevents the flow of bile into

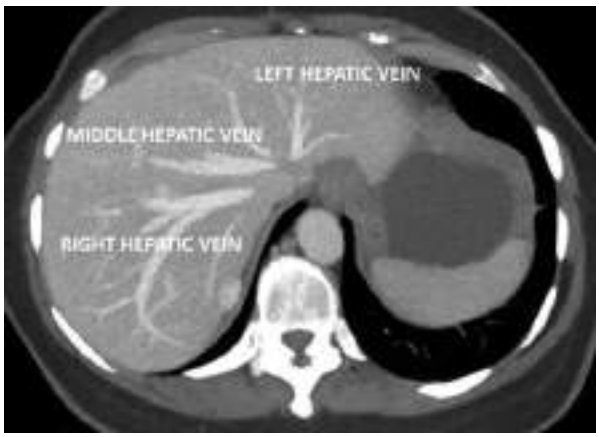

Figure 3.45 Hepatic veins. Axial contrast-enhanced CT image (portal venous phase).

Table 3.3 Anatomical variants of the right hepatic vein.

Type	Description
I	Tributary vein for segment 7
II	Three tributary veins, two form a common trunk and the other is a tributary for segment 7
III	Complete drainage of the right hepatic lobe
IV	An accessory branch is present It is important to measure the distance between the entrance into the IVC of both veins; if >2 cm, consider independent superior and inferior drainage

Table 3.4 Anatomical variants of the middle hepatic vein.

Type	Description
I	Tributary veins for segments 5 and 4 (forming a proximal confluence) and another tributary vein for segment 8
II	Two large segments for segments 8 and 4 (forming a distal trunk), and the other segments are drained by small veins
III	Similar to type I, but with a bifurcation of unequal size for segments 5 and 8, and a small branch for segment 4

the duodenum and allows bile to fill the duct with subsequent retrograde flow into the cystic duct and gallbladder. The volume capacity of the gallbladder is approximately 30 mL, although it can dilate up to 300 mL. It is covered by visceral peritoneum. Anatomically, it is divided into fundus, body, infundibulum (Hartmann's pouch), and neck. Its blood supply is provided by the cystic artery, which is usually a branch of the right HA despite high anatomical variability exists, including its origin in the left HA, proper HA, or even superior

Table 3.5 Anatomical variants of the left hepatic vein.

Type	Description
I	Three veins, two for segment 4 and one for segment 2 Distal confluence The most common variant
II	Common trunk for segments 2 and 3, and receives a tributary for segment 4
III	Similar to type II but there are no tributary veins for segment 4

mesenteric artery. Its venous drainage is via the portal system [51] (Figure 3.46).

Pancreas

The pancreas is a lobulated gland that measures between 15 and 20 cm in length and lies in the anterior pararenal space of the retroperitoneum. It is anatomically divided into four parts: head, neck, body, and tail. The pancreatic head is located on the duodenal flexure, to the right of the superior mesenteric vein. The uncinate process is an inferior prolongation of the hea, and is oriented to the left; it has a triangular shape and its antero-medial edge can be straight or concave. The pancreatic neck is the left portion of the head and lies anterior to the superior mesenteric vein. The body and tail of the pancreas are posterior to the lesser sac and stomach (Figures 3.47 and 3.48).

The main pancreatic duct (of Wirsung) normally measures 3.5 mm at the level of the pancreatic head, 2.5 mm at the body, and 1.5 mm at the pancreatic tail. Its length ranges from 9.5 to 25 cm. There are approximately 27 different ductal configurations. Usually, the main duct has between 25 and 30 lateral branches which drain into it at right angles.

The main pancreatic duct joins the bile duct and drains into the major papilla via the sphincter of Oddi to enter the duodenum. In most cases (80–90%) both ducts join within the sphincter through a muscular wrapping of approximately 10–15 mm in length. The biliopancreatic junction can be long (Y-shape) or short (V-shape). High biliopancreatic sites of junction can favor pancreatic reflux and lead to formation of bile duct cysts [50].

Vascularization of the Pancreas The arterial supply to the pancreatic head is mainly provided by the superior pancreatoduodenal artery, a branch of the gastroduodenal artery (which in turn is a tributary of the CHA), and by the inferior pancreatoduodenal artery, a branch of the superior mesenteric artery. Both of them are located between the pancreas and the duodenum, irrigating the head of the pancreas.

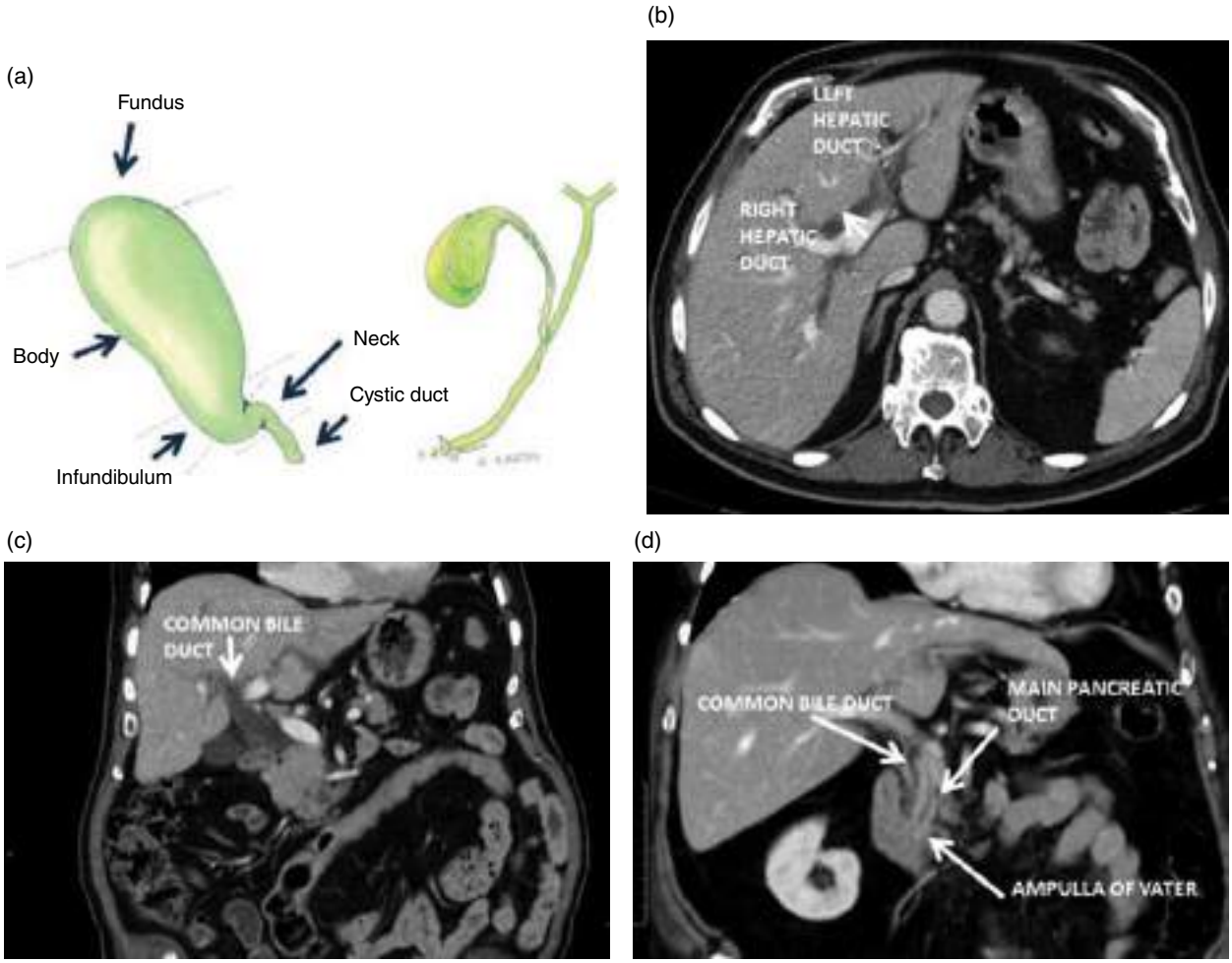

Figure 3.46 Gallbladder and bile duct. (a) Diagram, adapted from Mortele et al. [50]. (b) Axial contrast-enhanced CT image (portal venous phase). (c, d) Coronal contrast-enhanced MPR CT image (portal venous phase).

Table 3.6 Anatomical variants of the left intrahepatic bile duct.

Type	Frequency (%)	Description
I	55	Drainage of lateral segments (2 and 3) into a single duct next to the umbilical fissure, joining the duct for segment 4
II	30	Drainage of lateral segments, plus segment 4 drained by two ducts, one next to the umbilical fissure and the other one close to the biliary confluence
III	10	Independent drainage of segments 2 and 3, and two bile ducts for segment 4 The bile duct for segment 2 is joined next to the hilum
IV	30	Trifurcation, drainage of segments 2 and 3 together by a short bile duct, and drainage of segment 4 which is joined next to the hilum

Table 3.7 Anatomical variants of the right intrahepatic bile duct.

Type	Frequency (%)	Description
I	56	RAD and RPD) merge to form the RHD, which joins the LHD to form the CHD (most common variant)
II	14	Trifurcation: union of the RAD, RPD, and LHD without RHD
IIIa	5	RAD joins the LHD
IIIb	15	RPD joins the LHD
IVa		RAD joins the CHD posterior to the confluence
IVb		RPD joins the CHD posterior to the confluence

AHD, CHD, common hepatic duct; LHD, left hepatic duct; RAD, right anterior duct; RHD, right hepatic duct; RPD, right posterior duct.

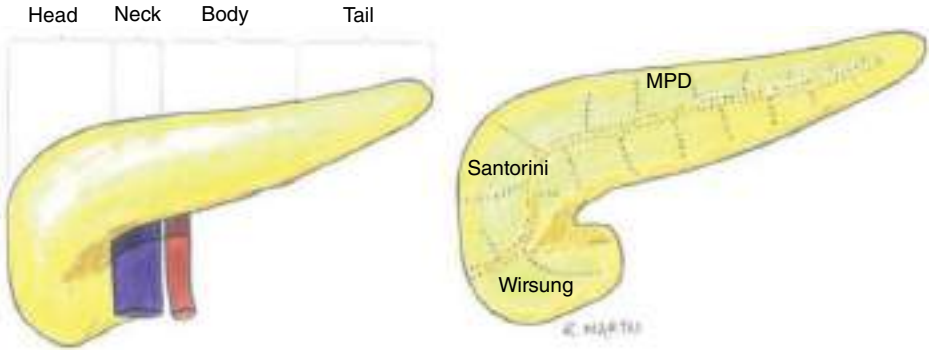

Figure 3.47 Anatomy of the pancreas. Illustration adapted from O'Brien et al. [42].

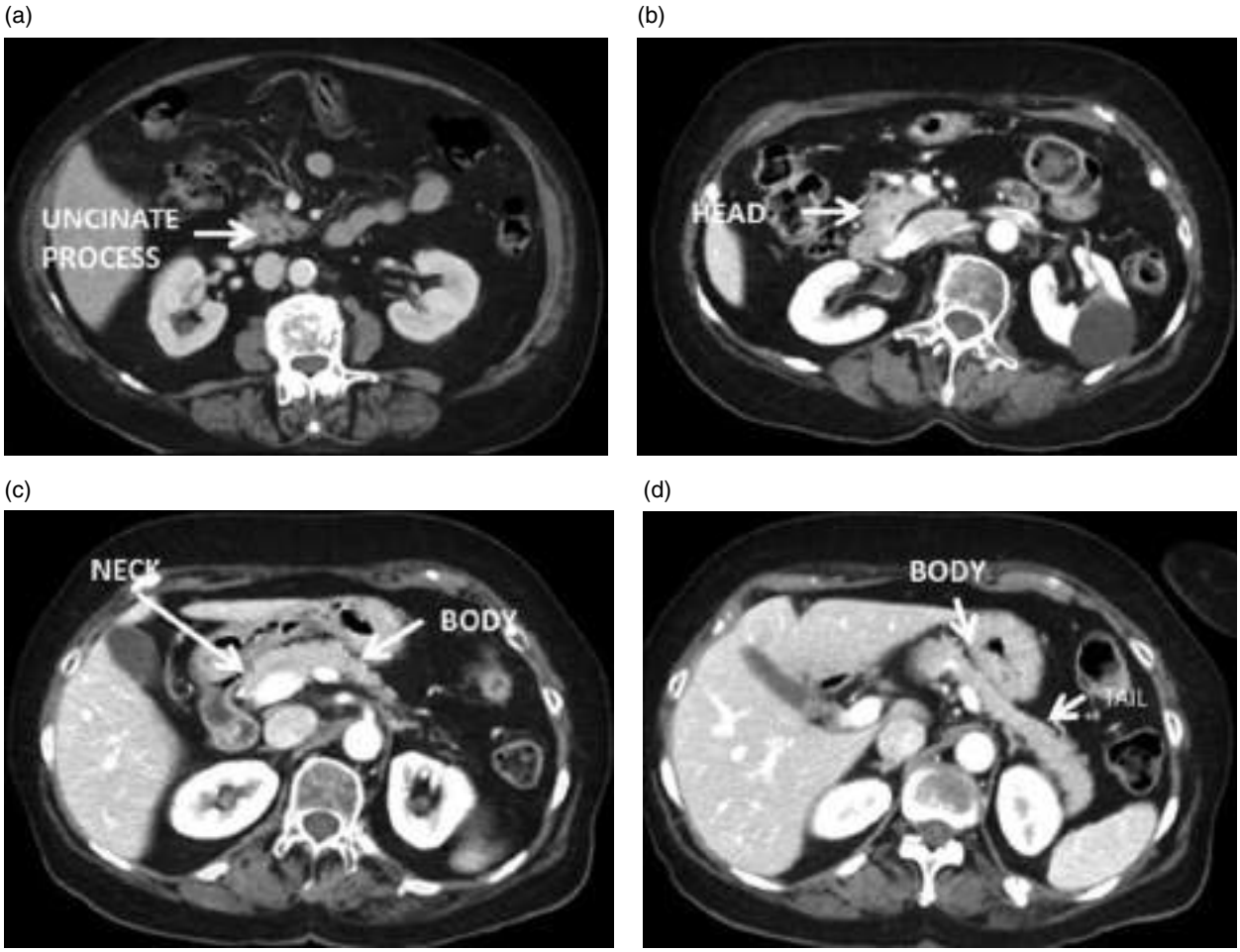

Figure 3.48 Pancreas. (a-d) Axial contrast-enhanced CT image (pancreatic phase).

The arterial vascularization of the neck, body, and tail of the pancreas is primarily provided by pancreatic branches of the splenic artery. The longest and most important branch is the great pancreatic artery.

The venous drainage of the pancreatic neck and body is via the splenic vein, while drainage of the pancreatic head is via the superior mesenteric vein and PV.

Anatomy of the Gastrointestinal System

Stomach

The stomach is composed of five regions, namely the cardia and gastroesophageal junction, fundus, body, antrum, and pylorus. The fundus and body contain acid-secreting glands, while the antrum is lined with an alkaline-secreting epithelium and gastrin-producing endocrine G-cells.

The gastroesophageal junction is closely related to the diaphragm. The fundus and body are oriented vertically, with the spleen lying more lateral, the lateral segment of the left hepatic lobe situated medial and anterior, and the abdominal aorta in a posterior location. The antrum and pylorus are oriented horizontally and related to the transverse colon inferiorly and to the left splenic flexure laterally. The fundus of the gallbladder is suspended above the pylorus [53] (Figure 3.49).

Vascularization of the Stomach The stomach is a richly vascularized organ. The arterial supply is provided by five main arterial branches. The left gastric artery, branch of the trifurcation of the celiac trunk, provides vascular support to the superior portion of the lesser curvature. The right gastric artery, branch of the CHA, irrigates the inferior portion of the lesser curvature. The right gastroepiploic artery, branch of the gastroduodenal artery, provides arterial supply to the antrum and inferior part of the body. The left gastroepiploic artery, branch of the splenic artery, irrigates the superior part of the gastric body. Finally, the splenic artery gives off short gastric arteries that supply the superior portion of the gastric body and fundus [53].

Small Intestine

The mucosa of the small intestine (or bowel) is characterized by presenting the valvulae conniventes (between 1.5 and 2 mm thick) which arise from the second portion of the duodenum and decrease in number as the intestine approaches the ileocecal valve. The small intestine is divided into three functional units: duodenum, jejunum, and ileum.

Duodenum The duodenum is a unique segment of the small intestine with both an intra- and an extraperitoneal portion. It is approximately 25 cm long with a transverse diameter of approximately 2.5 cm. Its mucosal folds are 2 mm thick. It has been classically divided into four differentiated parts. The first portion, also known as duodenal bulb, is intraperitoneal and extends from the gastric pylorus to the neck of the gallbladder. The second portion or descending duodenum includes two flexures (superior and inferior) and extends retroperitoneally from the neck of the gallbladder to the lower lumbar spine. The third portion, also retroperitoneal, crosses the midline

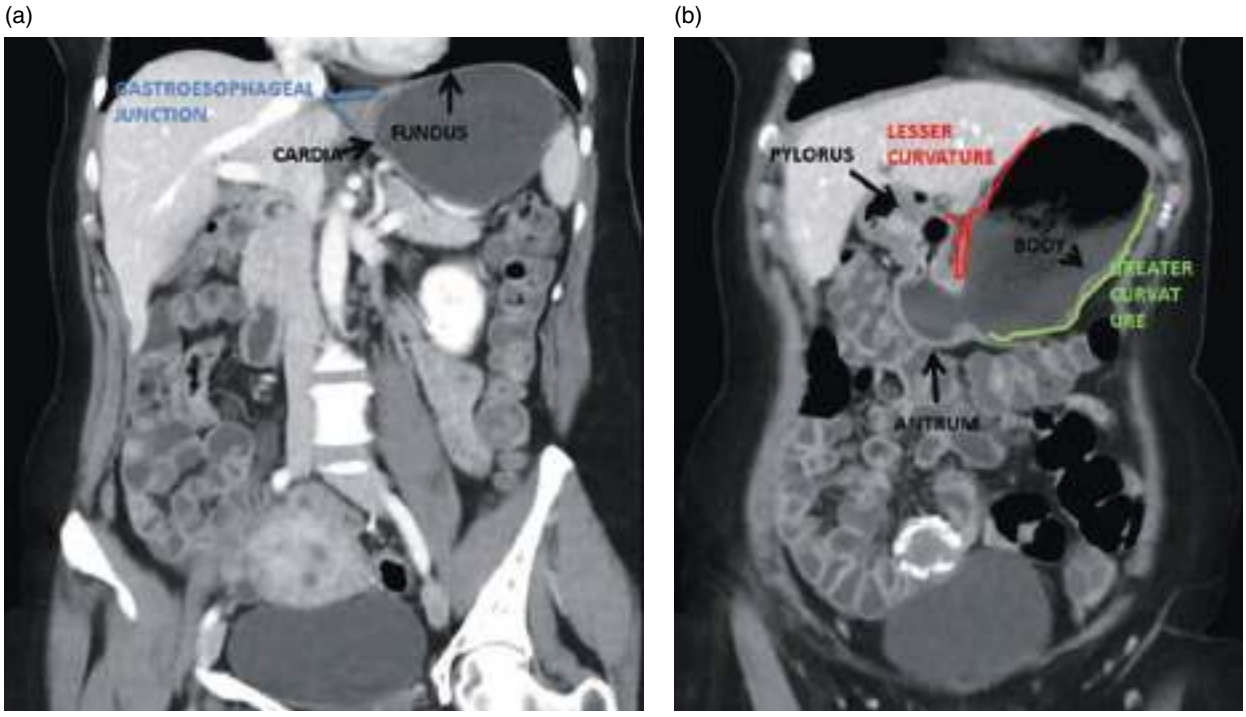

Figure 3.49 Stomach. (a, b) Coronal contrast-enhanced MPR CT image (portal venous phase). Note the presence of a subserosal uterine fibroid with coarse calcifications.

from right to left. Finally, the fourth portion ascends slightly to reach the ligament of Treitz. The serous surface of the duodenum is closely related to the head of the pancreas and forms the pancreaticoduodenal groove, an anatomical space containing the pancreaticoduodenal arterial arcades, mesenteric veins, and lymphatic structures (Figure 3.50).

The main pancreatic duct and the common bile duct usually end in the duodenal papilla to form the ampulla of Vater, which is surrounded by the sphincter of Oddi. The major duodenal papilla is located in the second portion of the duodenum in 75% of cases and in the third portion in the remaining cases [54].

The ligament of Treitz separates the fourth duodenal portion from the first jejunal loops. It lies posterior to the pancreas and anterior to the left renal vein, and is inserted into the duodenum, the esophageal hiatus of the diaphragm, and the celiac trunk. It is not defined by retroperitoneal fat and cannot be identified in CT images [55].

Jejunum and Ileum There are no strictly defined boundaries between the jejunum and ileum, but more than half of the small intestine corresponds to the ileum. An imaginary diagonal line drawn from the right hypochondrium to the left iliac fossa is a conventional landmark used to locate the jejunum in the upper left half and the ileum in the lower right half (Figure 3.51).

Large Intestine

The colon can be normally distinguished from the small intestine based on its different appearance, diameter, and location. The taeniae coli are three longitudinal bands of approximately 8 mm wide that run along the entire length of the colon and are located on its postero-medial, postero-lateral, and anterior walls. The taeniae coli merge at the junction of the vermiform appendix with the cecum and at the recto-sigmoid junction.

The haustra are prominent saccules formed in the spaces between the taeniae coli. The size of the haustras is varia-

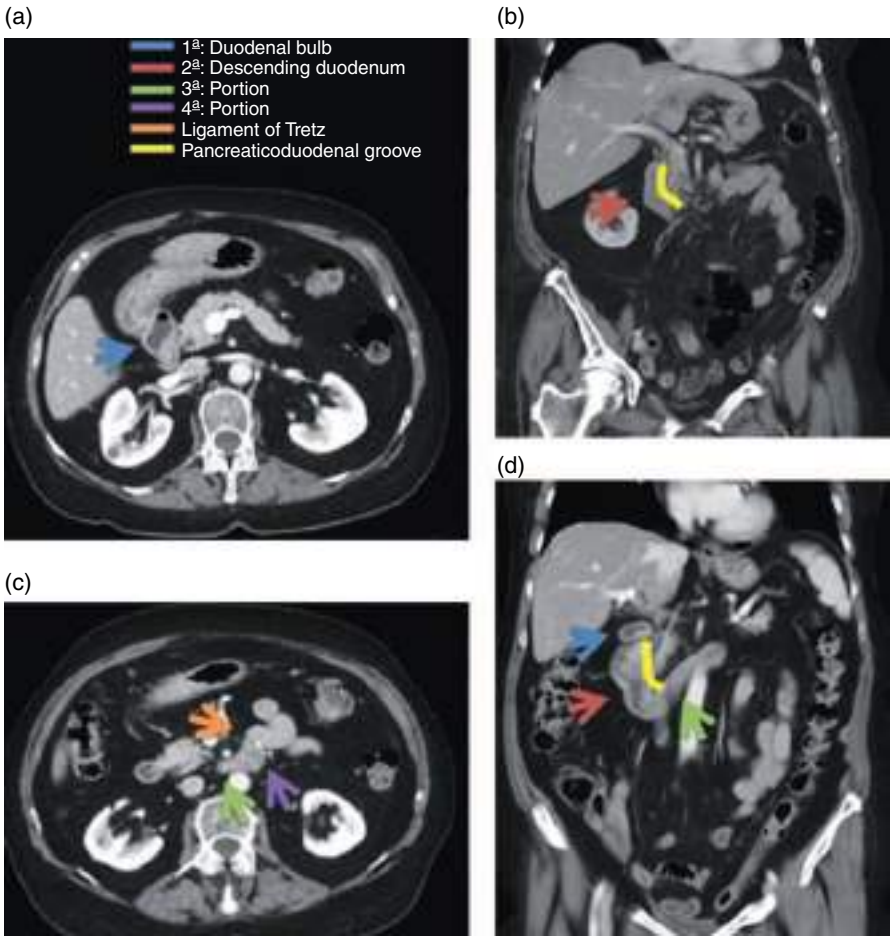

Figure 3.50 Duodenum. (a, c) Axial contrast-enhanced CT image (portal venous phase). (b, d) Coronal contrast-enhanced MPR CT image (portal venous phase).

Figure 3.51 Small intestine. Coronal contrast-enhanced MPR CT image (portal venous phase). Note the presence of a subserosal uterine fibroid with coarse calcifications.

ble, depending on the contraction of the taeniae coli. The epiploic appendages (appendices epiploicae) are small bundles of fatty tissue that run along the taeniae coli and vary in size in relation to the nutritional status. They usually go unnoticed on CT images, except when affected by inflammatory pathology (epiploic appendagitis) (Figure 3.52).

The transverse diameter of the colon is significantly variable. Generally, the largest diameter of the cecum is approximately 9 cm in normal subjects. The transverse colon is about 6 cm in diameter and the descending colon and sigmoid colon are usually about 3 cm in diameter. The wall of the colon is very thin and should measure less than 3 mm thick. The colon usually contains gas, feces in varying degrees of dehydration, and minimal amounts of fluid in its lumen.

The colon usually frames the abdomen and is surrounded by homogeneous fat. However, its position is highly variable, although this often lacks clinical significance. Accordingly, the position of the cecum is related to the length of the mesentery and the degree of retroperitonealization. In addition, the colon can be redundant, resulting in the transverse colon descended into the lower abdomen. Moreover, the colon can be located between the liver and the diaphragm (Chilaiditi sign) [56].

Vascularization of the Bowel

The superior mesenteric artery arises from the abdominal aorta at the level of L1, approximately 1.5 cm inferior to the origin of the celiac trunk and superior to the origin of the renal arteries. It supplies blood to the duodenum via the pancreticoduodenal arcade and irrigates the jejunum, ileum, ascending colon, and usually the transverse colon. The superior mesenteric artery is located to the left of the superior mesenteric vein in its origin. After crossing the third duodenal portion, it enters the mesentery and lies posterior to the mesenteric vein (Figure 3.53).

The tributaries that most frequently arise from the superior mesenteric artery are the inferior pancreaticoduodenal artery, the right colic artery, the middle colic artery, the jejunal arteries, the ileocolic artery, and the ileal arteries (Figures 3.54 and 3.55).

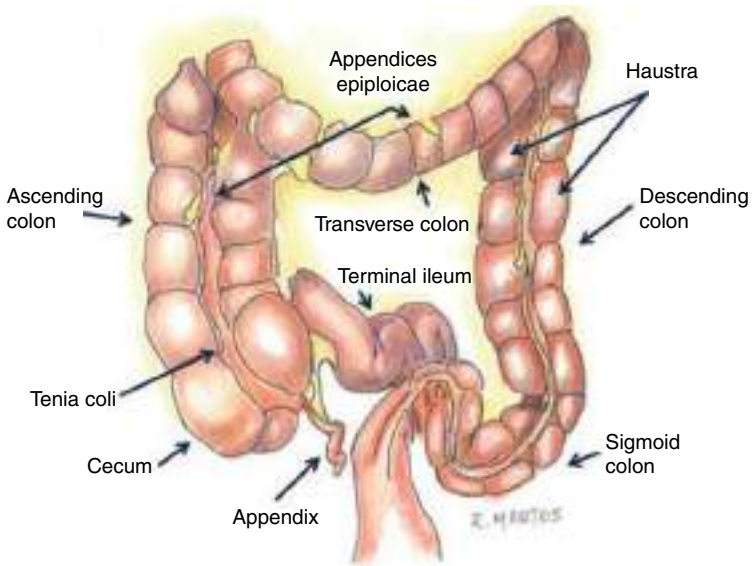

Figure 3.52 Colon. Schematic illustration adapted from Horton et al. [56].

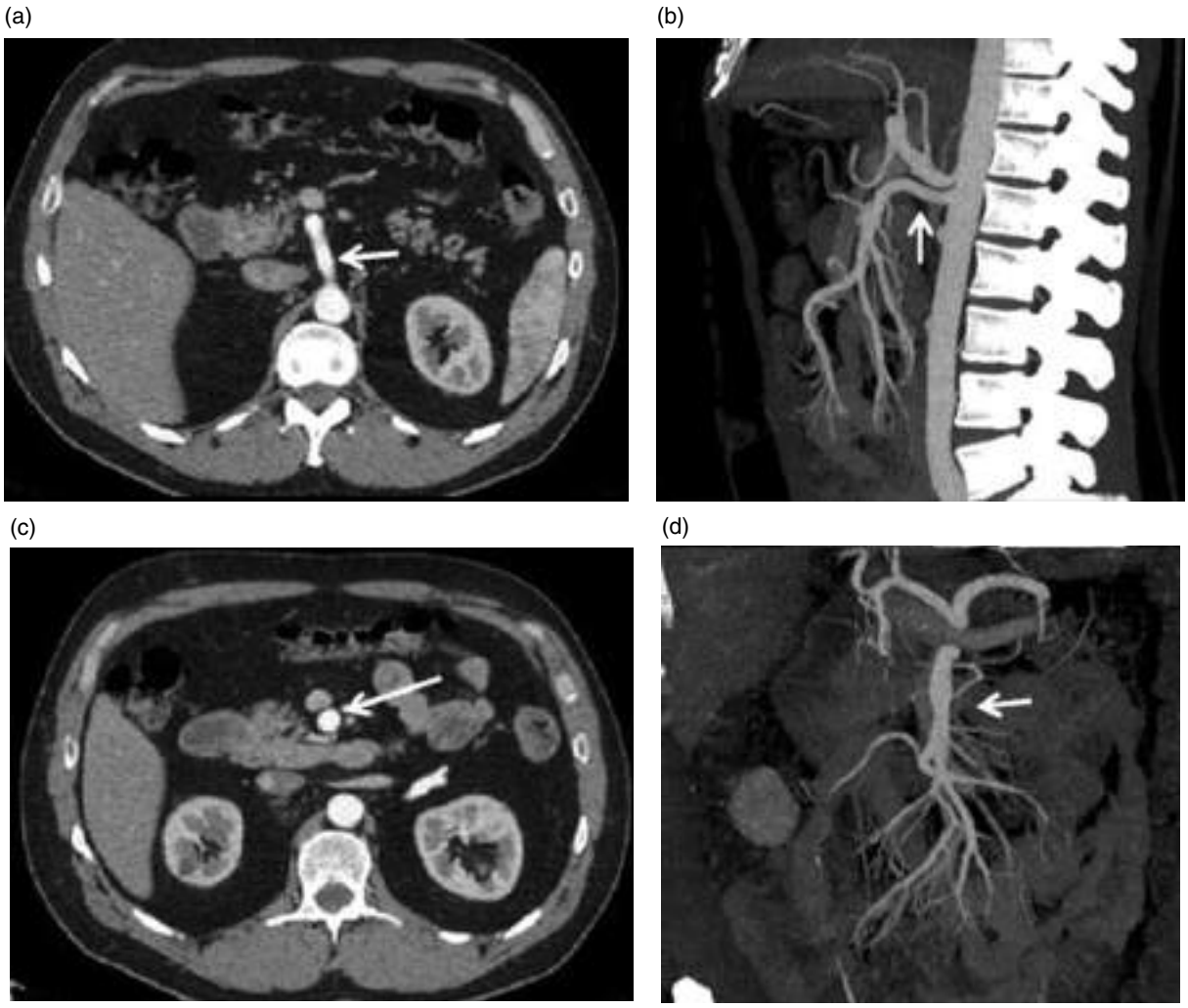

Figure 3.53 Superior mesenteric artery. (a, c) Axial contrast-enhanced CT image (arterial phase). (b) Sagittal contrast-enhanced MIP CT image (arterial phase). (d) Coronal contrast-enhanced MIP CT image (arterial phase).

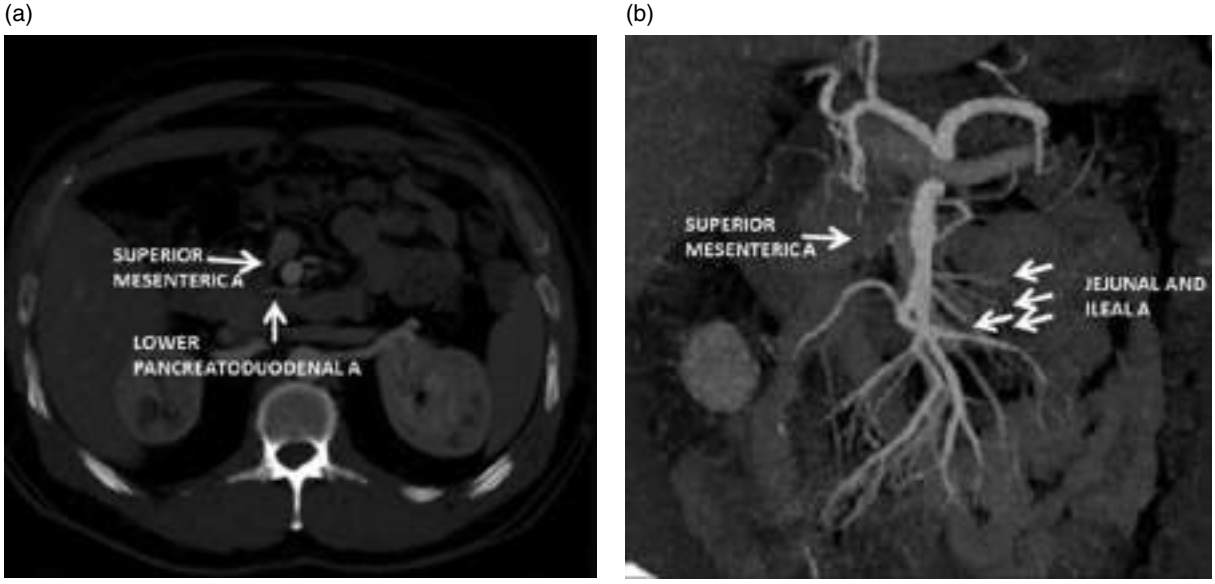

Figure 3.54 Main branches of the superior mesenteric artery. (a) Axial contrast-enhanced CT image (arterial phase). (b) Coronal contrast-enhanced MIP CT image (arterial phase).

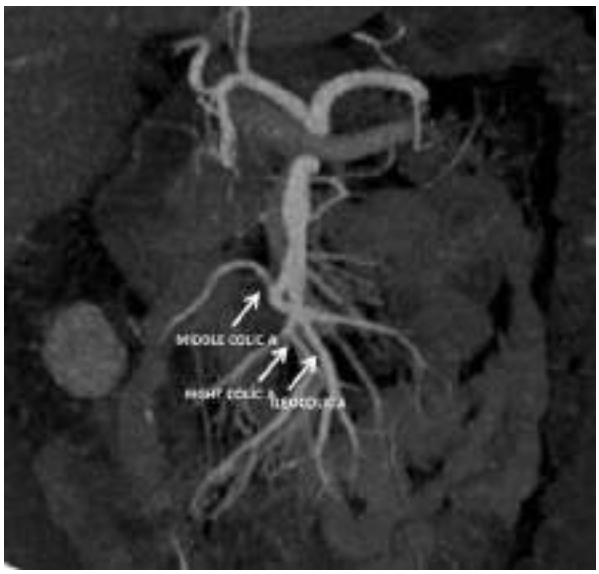

Figure 3.55 Main branches of the superior mesenteric artery. Coronal contrast-enhanced MIP CT image (arterial phase).

The inferior pancreaticoduodenal artery joins the superior pancreaticoduodenal artery (branch of the celiac trunk) to form the pancreatic arcade.

The right colic artery, which is absent in up to 80% of patients, supplies blood to the ascending colon, along with the middle colic and ileocolic arteries.

The middle colic artery usually arises from the right side of the superior mesenteric artery and courses to the right and inferiorly to reach the right lower quadrant, where it anastomoses with the ileocolic artery.

The jejunal arteries (usually four to six branches) arise from the left side of the superior mesenteric artery and supply the jejunum.

The ileocolic artery, which arises from the right side of the superior mesenteric artery, marks the transition between the jejunal and the ileal artery (usually eight to 12 vessels). It supplies the terminal ileum, cecum, and inferior portion of the ascending colon.

The inferior mesenteric artery arises from the aorta, approximately 7 cm below the origin of the superior mesenteric artery, generally above the level of L3. It gives off several arteries from its left side, including the left colic, colosigmoid, recto-sigmoid, and superior rectal arteries (Figure 3.56).

The left colic artery forms an anastomosis with the transverse colon artery, but is absent in up to 12% of individuals.

The colosigmoid artery supplies blood to the descending and sigmoid colon.

Distal to the origin of the recto-sigmoid artery, the inferior mesenteric artery gives off the superior rectal arteries.

The superior mesenteric vein typically consists of a trunk formed by two branches (right and left). It receives blood from numerous veins (ileocolic, gastrocolic, right colic, and middle colic). The superior mesenteric vein joins the splenic vein to form the portal vein.

The inferior mesenteric vein has three main tributaries, the left colic, and the sigmoid and superior rectal veins. The inferior mesenteric vein can drain into the splenic vein or into the superior mesenteric vein [57].

Spleen

The spleen is an intraperitoneal organ located in the left hypochondrium. It has an inverted comma shape and can measure up to 12 cm long and 7 cm thick under normal conditions. Between 10% and 30% of the population

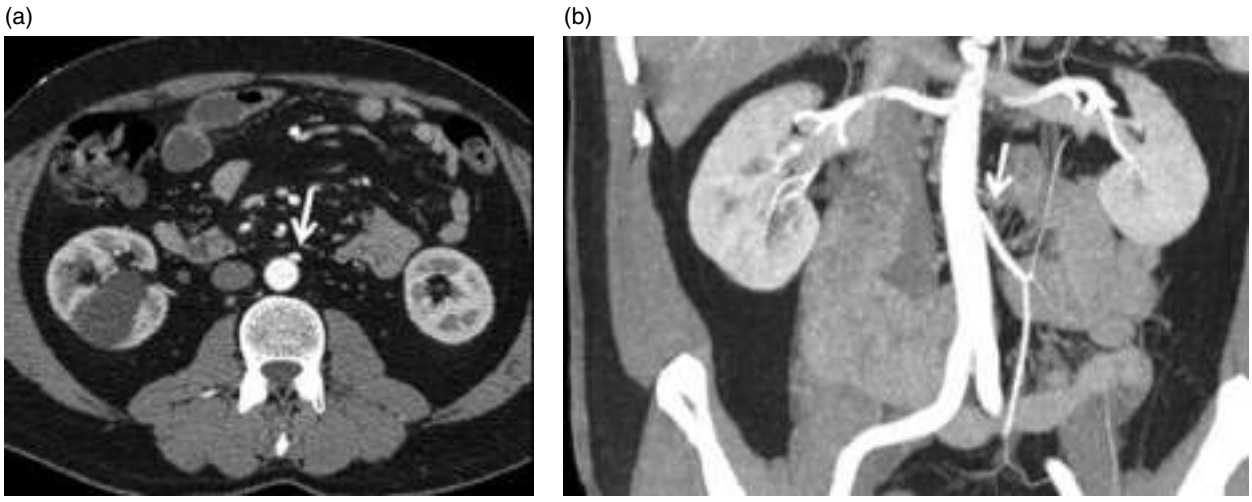

Figure 3.56 Inferior mesenteric artery. (a) Axial contrast-enhanced CT image (arterial phase). (b) Coronal contrast-enhanced MIP CT image (arterial phase).

presents adjacent nodules corresponding to accessory spleens (splenunculi).

The spleen's anatomical boundaries include the phrenicocolic ligament inferiorly, the diaphragm superiorly and postero-laterally, the stomach medially and antero-laterally, and the left kidney postero-medially. The visceral peritoneum covers the fibrous capsule of the spleen except for the splenic hilum, which is retroperitoneal. The splenic hilum contains the splenic artery and vein, lymphatic vessels, and nerves; it is also the site of insertion of the gastrosplenic and splenorenal ligaments. It is often in direct contact with the pancreatic tail [58].

Peritoneum and Mesentery

The peritoneum is an extensive, thin serous membrane made up of a layer of simple epithelium (mesothelium) and loose connective tissue. It is the largest and most complex serous membrane in the body and covers both the abdominal cavity and the abdominopelvic organs.

The parietal peritoneum covers the anterior, lateral, and posterior abdominal and pelvic walls as well as the anterior surface of the retroperitoneal organs, the inferior surface of the diaphragm, and the superior surface of the pelvis.

The visceral peritoneum covers many of the abdominopelvic organs to a variable degree. A number of peritoneal reflections result in the formation of different ligaments, mesentery, and omenta. These reflections contain retroperitoneal areolar tissue, blood, vessels, lymphatic tissue, and nerves. The subperitoneal space represents a communication pathway between the peritoneum and the retroperitoneum. There are intraperitoneal, peritonealized, secondary peritonealized, and partially peritonealized organs [59].

The peritoneal cavity forms a closed pouch in men. In women, it remains open at the orifices of the Fallopian tubes, allowing communication between the intraperitoneal and extraperitoneal pelvis.

Its function is twofold. On the one hand, it provides a lubricated surface (by secreting a small amount of sterile fluid that also has defensive properties against local bacteria) that enables the movement of organs without friction. On the other hand, it serves as a transportation system of fluids. Clearance of the peritoneal fluid is performed through continuous circulation in cephalad direction, which is thought to be caused by changes in the abdominal pressure during breathing and by bowel peristalsis [60].

Several peritoneal structures can be distinguished. To recognize them on imaging, it is essential to remember their typical location and their anatomical relations with other organs and vascular structures.

Mesenteries

The mesenteries are peritoneal reflections which cover different abdominal structures, containing fat, vessels, lymphatic structures, and nerves (Figure 3.57).

- Mesentery: A double fan-shaped peritoneal layer that attaches jejunal and ileal loops to the posterior wall of the abdomen. It extends from the ligament of Treitz to the ileocecal valve. It is currently considered an organ itself.
- Transverse mesocolon: This surrounds the transverse colon and fixes it to the posterior abdominal wall, creating a communication pathway with the retroperitoneum. It divides the peritoneal cavity into two compartments, namely supra and infra-mesocolic.
- Mesosigma: This fixes the sigmoid colon to the posterior wall of the pelvis.

Ligaments

The ligaments are made up of two peritoneal layers and contribute to the fixation and structural support of the abdominal organs. Under normal conditions, the peritoneal ligaments are named after the anatomical structures which they connect.

- Splenorenal ligament: This attaches the spleen to the anterior pararenal space. The splenic vessels run through this ligament (as mentioned above, the splenic hilum is a retroperitoneal space) (Figure 3.58).
- Gastrosplenic ligament.
- Phrenicocolic ligament: This fixes the descending colon to the posterior part of the diaphragm.
- Suspensory ligaments of the liver: Coronary ligaments, triangular ligaments.
- Falciform ligament: This fixes the liver to the anterior wall of the abdomen and contains the obliterated umbilical vein,

Omentum or Epiploon

- Lesser omentum: This results from the combination of the hepatogastric and hepatoduodenal ligaments and connects the lesser curvature of the stomach and proximal duodenum with the liver. Additionally, it covers the lesser sac anteriorly.
- Greater omentum: This is mainly composed of fat and extends anteriorly into the stomach, transverse colon, and small bowel. It is located immediately posterior to the anterior abdominal wall (Figure 3.59).

Peritoneal Compartments

The peritoneal compartments result from the arrangement of the peritoneal structures detailed above, dividing the abdominal cavity into two separate compartments.

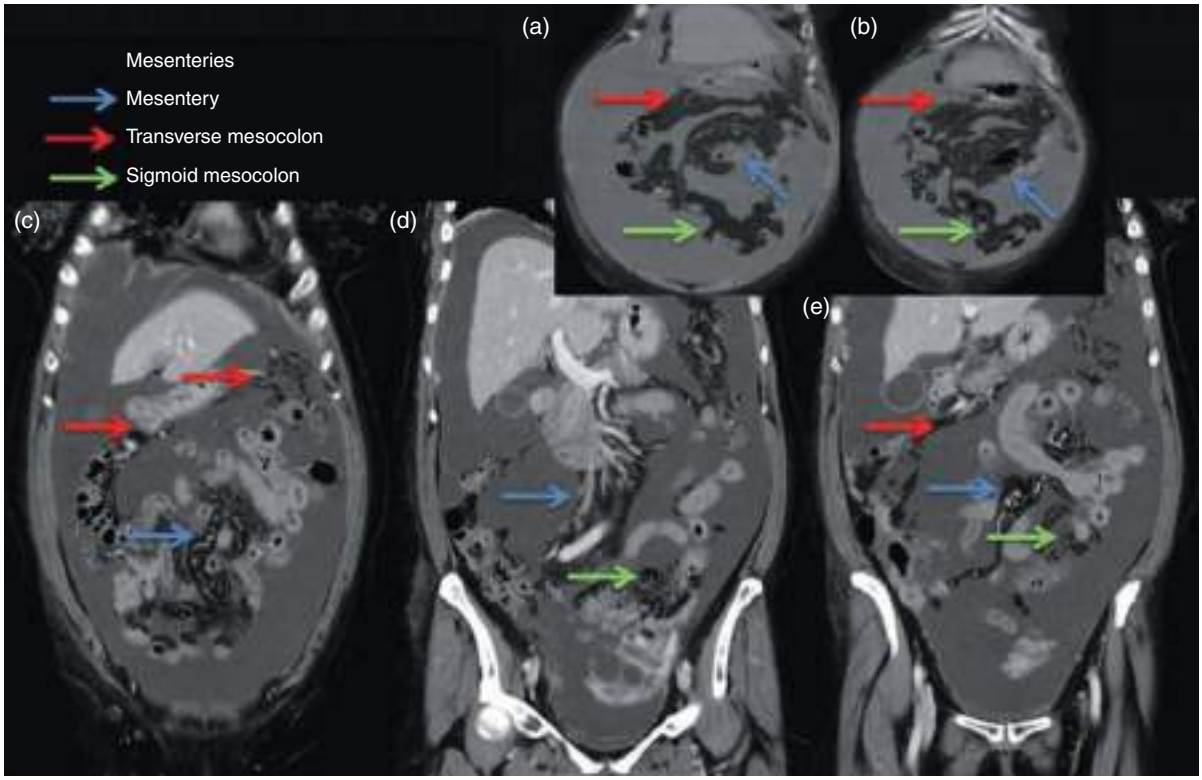

Figure 3.57 Mesenteries in patient with ascites due to peritoneal carcinomatosis secondary to ovarian tumor. (a–e) Coronal contrast-enhanced MPR CT image (portal venous phase).

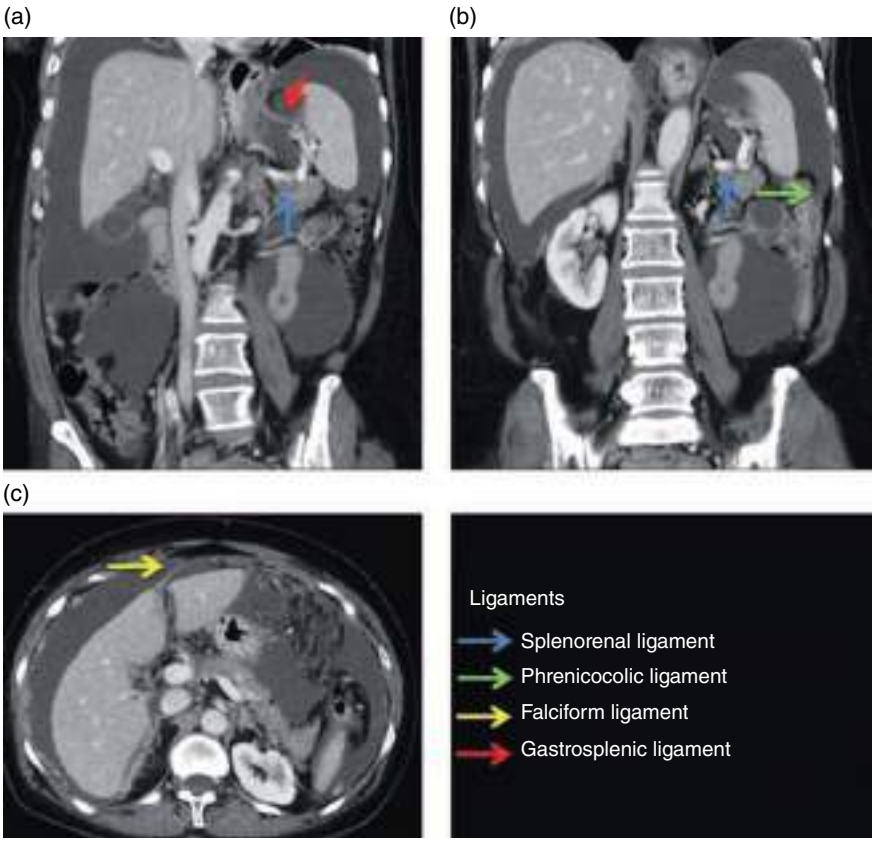

Figure 3.58 Peritoneal ligaments in patient with ascites due to peritoneal carcinomatosis secondary to ovarian tumor. (a, b) Coronal contrast-enhanced MPR CT image (portal venous phase). (c) Axial contrast-enhanced CT image (portal venous phase).

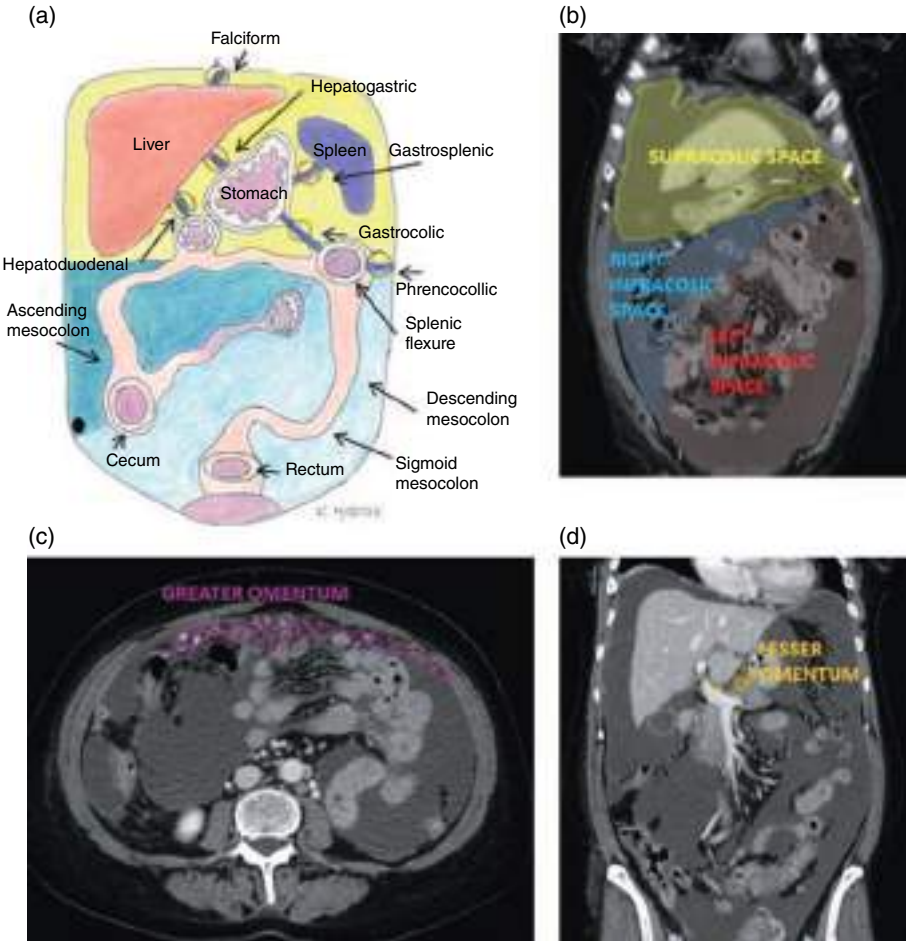

Figure 3.59 Peritoneal compartments and omenta in patient with carcinomatous ascites due to ovarian tumor. (a) Diagram, adapted from Wasnik et al. [60]. (b, d) Coronal contrast-enhanced MPR CT image (portal venous phase). (c) Axial contrast-enhanced CT image (portal venous phase).

Supramesocolic Compartment The supramesocolic compartment is the cavity lying superior to the transverse mesocolon. The falcifom ligament divides this space into the left and right compartments (Figure 3.60).

Right Supramesocolic Space

The right supramesocolic space is divided into three compartments, namely right subphrenic, right perihepatic, and right subhepatic:

- Right subphrenic space: This lies between the right lobe of the liver and the diaphragm.
- Right perihepatic space: This surrounds the anterior and lateral portions of the diaphragm
- Right subhepatic space: This is sub-divided into anterior and posterior spaces: The right anterior subhepatic space is in close contact with the PV and communicates with the omental bursa by the omental foramen (of Winslow). Right posterior subhepatic space is also known as Morison's pouch or hepatorenal space.
- The omental bursa (lesser sac) is an enclosed cavity bounded by the hepatogastric ligament, the posterior wall of the stomach, the duodenum, and the caudate lobe anteriorly, by the pancreas and the posterior parietal peritoneum posteriorly, by the diaphragm superiorly, and by the transverse mesocolon inferiorly. The foramen of Winslow communicates the lesser sac with the rest of the abdominal cavity or greater sac.

Left Supramesocolic Space

The left supramesocolic space is divided into anterior and posterior perihepatic spaces, and anterior and posterior subphrenic spaces.

- Left anterior perihepatic space: This lies anterior to the liver and medial to the falcifom ligament.

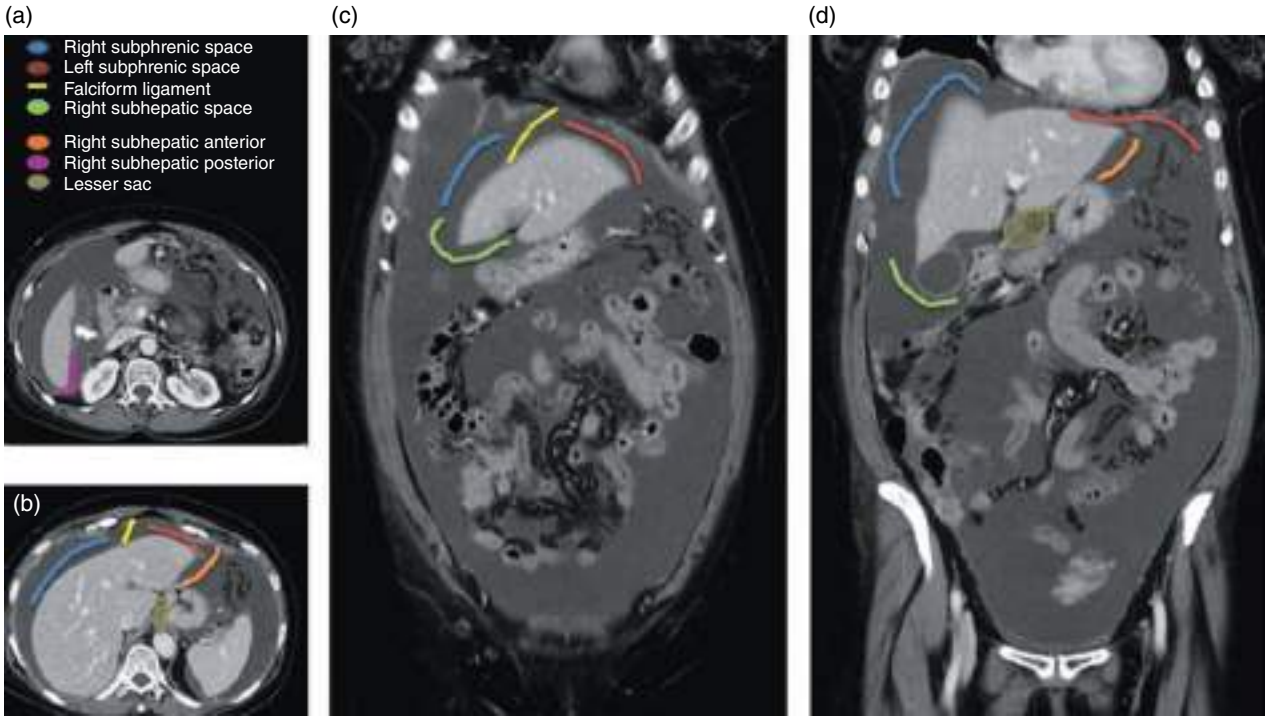

Figure 3.60 Supramesocolic compartments in patient with carcinomatous ascites due to ovarian tumor. (a, b) Axial contrast-enhanced CT image (portal venous phase). (c, d) Coronal contrast-enhanced MPR CT image (portal venous phase).

- Left posterior perihepatic space (gastrohepatic recess): This surrounds the lateral segment of the liver and contacts the stomach.
- Anterior subphrenic space: This is continuous with the left anterior perihepatic space, separating the gastric fundus from the diaphragm.
- Left posterior subhepatic space: This surrounds the spleen and is bounded by the phrenicocolic ligament, which separates this space from the left paracolic gutter.

Inframesocolic Compartment The inframesocolic compartment is divided into right and left spaces. The left inframesocolic space is larger and contains the mesentery. The paracolic gutters are the most lateral parts of these spaces. The right gutter communicates with the right perihepatic and subhepatic spaces superiorly, and the left gutter is bounded by the phrenicocolic ligament superiorly [59–61] (Figure 3.59).

Urinary System

Kidneys

The kidneys are retroperitoneal organs with a disposition parallel to the psoas muscles. They measure approximately 10–14 cm long and 3–5 cm wide. The right kidney is around 2 cm lower than the left one and is slightly smaller (approximately 0.5 cm). It is convex laterally and concave medially. In the craniocaudal orientation, its upper pole lies medially and its lower pole posteriorly.

The kidneys are surrounded by a fibrous capsule to which they are firmly attached. This capsule is surrounded by anterior perirenal fat which, in turn, is defined by the Gerota fascia anteriorly and by the Zuckerkandl's fascia posteriorly.

The renal hilum is located medially. It is composed of adipose tissue and a fibrous fascia. It contains the renal vessels, the collecting system, and lymphatic structures. On imaging, the hilum can be identified entering the kidney within the renal sinus (rich in fat).

The renal parenchyma is formed by the renal cortex and the medullary pyramids. The renal cortex receives 90% of the renal blood flow and is formed by proximal and distal glomeruli and tubules.

The renal medulla contains between eight and 18 pyramids that can be identified on imaging by their typical inverted-cone shape, with the vertex representing the papilla which drains into a minor calyx. The minor calyces are cup-shaped structures that converge into major calyces which drain into infundibula. These, in turn, drain into the renal pelvis. The renal cortex arches between the pyramids forming the columns of Bertin [62].

Anatomical Variants There are frequent anatomical variants of renal development that may lead to a

pseudotumor appearance of the kidneys. The most common variants include the following:

- Column of Bertin hypertrophy: This can simulate a solid focal lesion and is usually located between the upper and middle thirds of the kidney.
- Dromedary hump: This is a focal interpolar protuberance on the lateral edge of the left kidney, formed by the adaptation of the renal contour to the spleen, with which it is in close contact.
- Persistent fetal lobulation: During the neonatal period, the fetal kidneys are divided into lobes by grooves, which normally disappear by the end of gestation. However, they can persist into adulthood.
- Junctional parenchymal defects: These are related to the persistence of a prominent fetal lobulation which includes perirenal fat and leads to fold of the anterior surface of the upper third of the kidneys toward the hilum [63].

Renal Arteries The renal arteries arise from the aorta above the L2 level, immediately cranial to the superior mesenteric artery. They reach the renal hilum anterior to the renal pelvis, where they divide into segmental arteries. The first branch is usually posterior and supplies the posterior and inferior renal segments. The anterior branch divides into four arteries: apical, superior, middle, and inferior. The segmental arteries are divided into lobar, interlobar, arcuate, and interlobular arteries.

Renal Veins The renal cortex drains into the arcuate and interlobar veins. The lobar veins unite to form the main renal vein. The renal veins usually lie anterior to the renal artery. The left renal vein is three times longer than the right renal vein because it drains into the IVC. Unlike the right renal vein, the left renal vein is joined by the left adrenal vein in its superior portion, the left gonadal vein inferiorly, and a lumbar vein posteriorly before draining into the IVC [64].

Ureter

The ureter is an extraperitoneal structure surrounded by fat, with an approximate length of 22–30 cm. It is a dynamic organ and not a simple duct through which urine flows. It conveys urine from the renal papillae to the ureteric orifice in the bladder, regardless of gravity. It is divided into three portions: the proximal (superior) ureter, which extends from the pelviureteric junction to the site where the ureter crosses the sacroiliac joint, the middle ureter, which runs through the bony pelvis and the iliac vessels, and the distal (pelvic or inferior) ureter, which extends from the iliac vessels to the bladder. The distal segment is subdivided into juxta-vesical, intramural, and submucosal portions. Its blood supply comes from the ureteral artery, which runs along the ureter. The superior third of the ureteral artery is irrigated by the aorta and the renal artery, while the middle and inferior ureter receive their arterial supply from the iliac, lumbar, and vesical arteries [65].

Urinary Bladder

When the urinary bladder is distended, it lies almost entirely in the antero-inferior pelvis and enters the major pelvis when it is full. It consists of a muscular bag with the function of collecting, storing, and eliminating urine. It is made up three layers, the internal one corresponding to the urothelium (site of origin of most bladder cancers), muscularis propria (formed by the detrusor muscle of the bladder), and serosa [66].

The urinary bladder has a round or oval shape, with its superior segment being wider, and is divided into fundus, body, apex, and neck. Anteriorly, it contacts the pubic symphysis. In men, it is bounded by the retrovesical space and rectum posteriorly, the prostate, seminal vesicles, obturators, and levator ani muscles inferiorly, and the peritoneum anteriorly. In women, its posterior aspect contacts the vesicouterine space, the uterus, the cervix, and the vagina.

The ureteral orifices and the internal orifice of the urethra define an area known as the trigone.

The dome of the bladder is covered with peritoneum to a varying degree based on the length of the peritoneal reflections. The rest of the surfaces of the bladder are extraperitoneal. During the neonatal period, the apex of the bladder is connected to the umbilicus through the urachus. This duct can persist in adults as a normal anatomical variant. The neck of the bladder is located inferiorly and contains the internal ureteral orifice, in the lower angle of the trigone. The ureters have a short and oblique intramuscular course before opening at the postero-lateral angles of the trigone [67].

The vascular supply of the bladder is via the external iliac arteries, which give off the superior and inferior vesical arteries. It also receives vascular supply from branches of the obturator, uterine, and vaginal arteries.

The bladder's venous drainage is via a complex plexus which ends in the internal iliac vein [68].

Adrenal Glands

The adrenal glands are Y-shaped organs located anterosuperiorly and slightly medial to the superior pole of each kidney in the so-called adrenal space, located in the Gerota fascia and surrounded by fat. The adrenal gland is a bipartite structure comprising the cortex and medulla, each with different embryogenesis, structure, and function. Its

approximate size is 10–12 mm for the body and 6 mm for the limbs [69].

Because they are responsible for hormone production and play a key role in systemic functions, the adrenal glands are richly vascularized. Their arterial supply is via three adrenal arteries (superior, middle, and inferior), which are branches of the superior phrenic, aorta, and renal artery, respectively. Their venous drainage is via a single adrenal vein, the left one draining into the left renal or the inferior phrenic vein and the right one directly into the IVC [70].

Retroperitoneum

The retroperitoneal space is an anatomical compartment bounded by the posterior parietal peritoneum and the transversalis fascia. It is divided into five compartments, two lateral, two posterior, and one central (Figures 3.60 and 3.61).

Lateral Compartments

The lateral compartments are subdivided into three spaces bounded by fasciae: anterior pararenal, perirenal, and posterior pararenal (Figure 3.62).

Anterior Pararenal Space The anterior pararenal space is bounded by the posterior parietal peritoneum anteriorly, by the anterior renal fascia posteriorly, and by the lateroconal fascia laterally. It contains the posterior face of portions of the ascending and descending colon, the duodenum, and the pancreas (Figure 3.63).

Perirenal Spaces The perirenal spaces contain the kidneys and ureters, the adrenal glands, and their corresponding vascular, lymphatic, and nervous structures (Figure 3.64).

The perirenal space has an inverted-cone shape, with the tip directed toward the pelvis and the base placed onto the diaphragm. The anterior edge of this space is formed by the anterior (Gerota) and posterior (Zuckerkandl) renal fasciae. The posterior renal fascia merges with the fascia of the quadratus lumborum muscle. Along with the connective tissue that surrounds the great vessels, there is a theoretical duct that connects both perirenal spaces at the level of L3–L5, known as the Kneeland channel, allowing free diffusion between both anatomical locations.

The superior part of the anterior renal fascia contacts the bare area (nonperitoneal region of the liver) so that the posterior peritoneum and the anterior renal fascia merge, establishing direct contact between the liver and the kidney. This relation explains the involvement of the perirenal space by different processes affecting the liver.

At the inferior end of the perirenal space, the anterior and posterior renal fasciae merge around the ureter.

Posterior Pararenal Space The posterior pararenal space only contains fat and is bounded by the diaphragm superiorly, by the posterior renal fascia anteriorly, and by the transversalis fascia posteriorly (Figure 3.65).

The lower part of the anterior and posterior pararenal spaces unite to form the infrarenal retroperitoneal space, which communicates with the prevesical space and the extraperitoneal spaces of the pelvis.

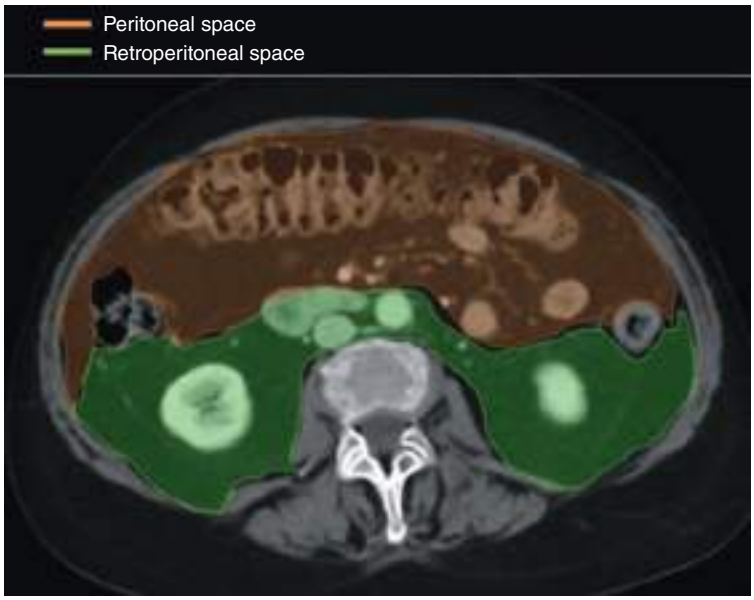

Figure 3.61 Peritoneal and retroperitoneal spaces. Axial contrast-enhanced CT image (portal venous phase).

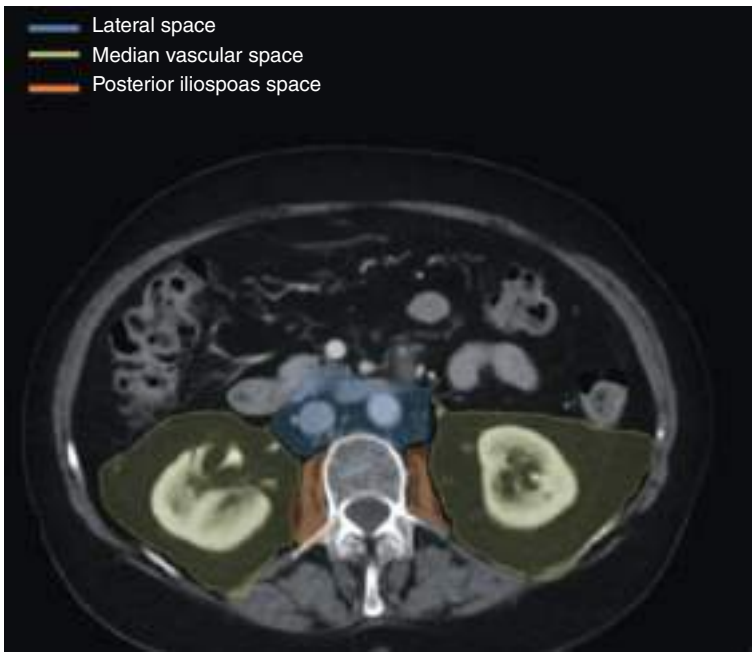

Figure 3.62 Retroperitoneal compartments. Axial contrast-enhanced CT image (portal venous phase).

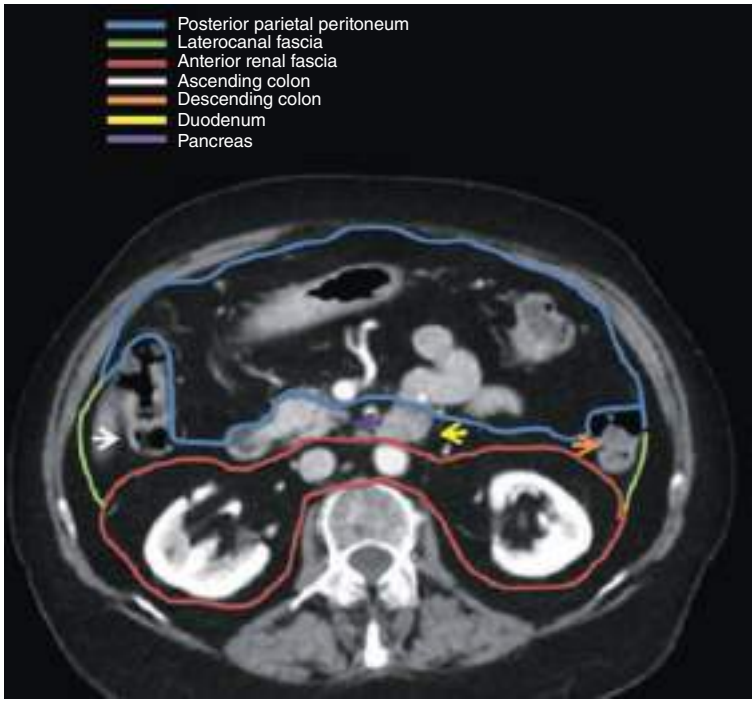

Figure 3.63 Anterior pararenal space. Axial contrast-enhanced CT image (portal venous phase).

Central compartment

The central compartment is a vascular compartment that extends from T12 to L4–L5, located between the two perirenal spaces and posterior to the anterior pararenal space. It contains the abdominal aorta and its branches, the IVC and its afferent vessels, lymphatic chains, and the abdominal sympathetic trunk (Figure 3.62).

Posterior Compartments

The posterior compartments contain the psoas and iliac muscles and are considered to be retroperitoneal despite being located posterior to the transversal fascia because of their frequent involvement in the context of retroperitoneal processes (Figure 3.62).

Figure 3.64 Perirenal space. Axial contrast-enhanced CT image (portal venous phase).

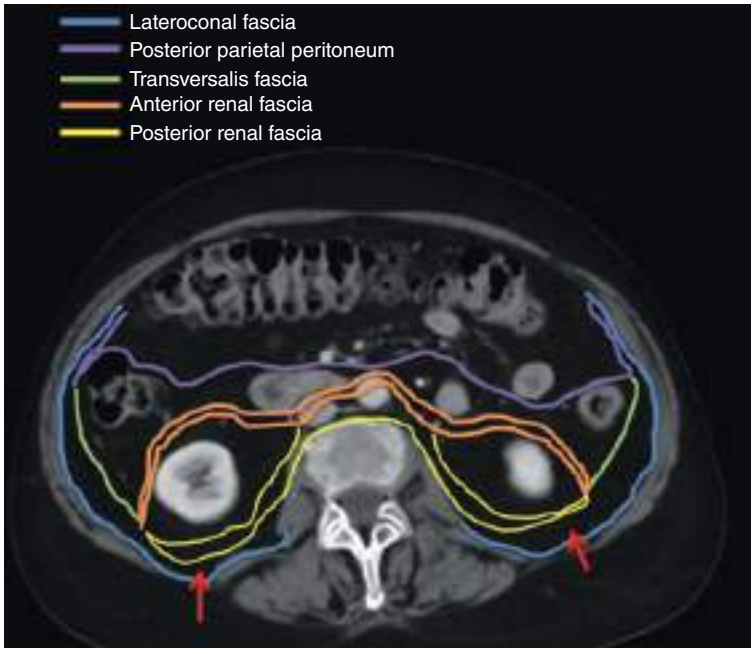

Figure 3.65 Posterior pararenal space. Axial contrast-enhanced CT image (portal venous phase).

Interfascial Plane

The interfascial plane is one of the potential retroperitoneal spaces created between the layers of the renal fasciae.

- Anterior or retromesenteric plane: Thist lies between the anterior pararenal and perirenal spaces and crosses the midline.
- Retrorenal space: This lies between the perirenal and posterior pararenal spaces. It does not cross the midline because it is interrupted by the central compartment.
- Combined intersfascial space: This results from the fusion of the retromesenteric and retrorenal spaces and extends anterior to the psoas muscle and the retroperitoneum of the pelvis.
- Lateroconal plane: This lies between the lateroconal fascia and is communicated with the retromesenteric and retrorenal spaces [59, 71, 72].

Anatomy of the Pelvis

The pelvis is bowl-shaped and presents two openings: one superior, into the abdominal cavity, and one inferior, bounded by the pelvic floor and perineum.

Anatomically, the pelvis is usually divided into true and false pelvis by an oblique line extending from the sacral promontory along the anterior face of S1 to the pubic symphysis.

The greater or false pelvis is located above this plane, containing the ascending, descending, and sigmoid colon as well as ileal loops and the bifurcation of iliac vessels.

The lesser or true pelvis, located below the pelvic brim, contains the reproductive organs, urinary bladder, pelvic ureters, small bowel loops, and rectum [73].

Anatomy of the Female Pelvis

The pelvic cavity is separated into an anterior and posterior space by the broad ligament, which is transversely oriented and contains the uterus in its center. This ligament is the main anatomical landmark to understand the female pelvic anatomy. The round ligaments, attached to the uterus, run antero-laterally through the broad ligament to reach the pelvic wall, where they change their course medially, around the inferior epigastric vessels, to exit the pelvis via the internal inguinal ring and inguinal canal [73].

Uterus and Cervix

The uterus is a smooth, hollow organ which exhibits a pyriform shape with its lower vertex posterior to the urinary bladder and anterior to the rectum. Its position is variable and changes when the bladder is full. It is divided into three segments: fundus, body, and neck (Figure 3.66).

The fundus is located in the superior segment of the uterus, with the uterine tubes arising at this level. It is made up of three layers: the endometrium in contact with the cavity, the junctional zone, and the myometrium. The endometrium is the most central part of the uterus, with a variable thickness along the menstrual cycle, being thicker during the secretory phase than in the follicular phase or menstruation. Its thickness also varies depending on the reproductive age; in postmenopausal women, it should be less than 5 mm. The junctional zone is the innermost layer of the myometrium and should be less than 12 mm thick, whereas the myometrium lies external [74] (Figure 3.66).

There are two peritoneal folds in contact with the uterus: the peritoneal lining of the uterus reflects anteriorly to cover the posterior wall of the bladder at the level of the cervix, forming the vesicouterine recess, which presents two lateral recesses called paravesical fossae.

Posteriorly, the peritoneum is reflected to cover the superior rectum, forming the rectouterine pouch (also known as the cul-de-sac or pouch of Douglas), which is continuous with the para-rectal fossae. This is the most caudal portion of the peritoneal cavity and often presents a mild amount of fluid during ovulation or loops of small intestine [73] (Figure 3.67).

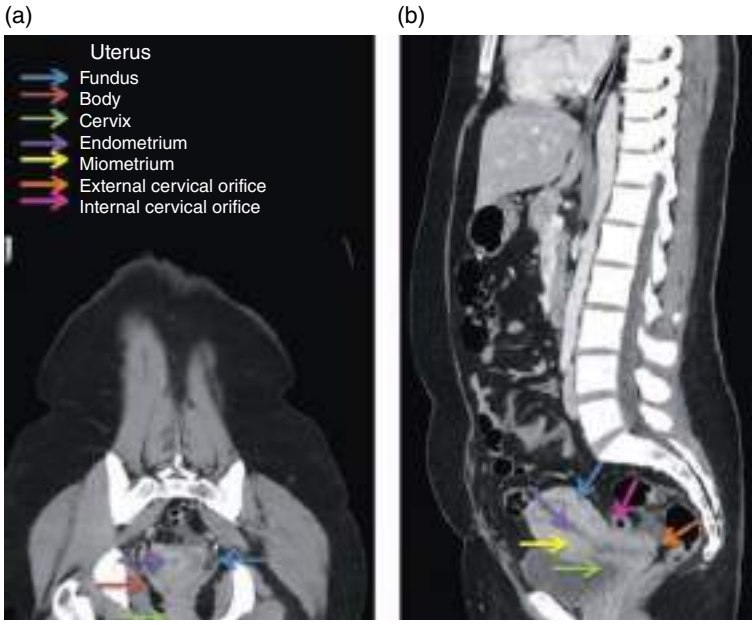

Figure 3.66 Uterus. (a) Axial oblique contrast-enhanced MPR CT image (portal venous phase). (b) Sagittal contrast-enhanced MPR CT image (portal venous phase).

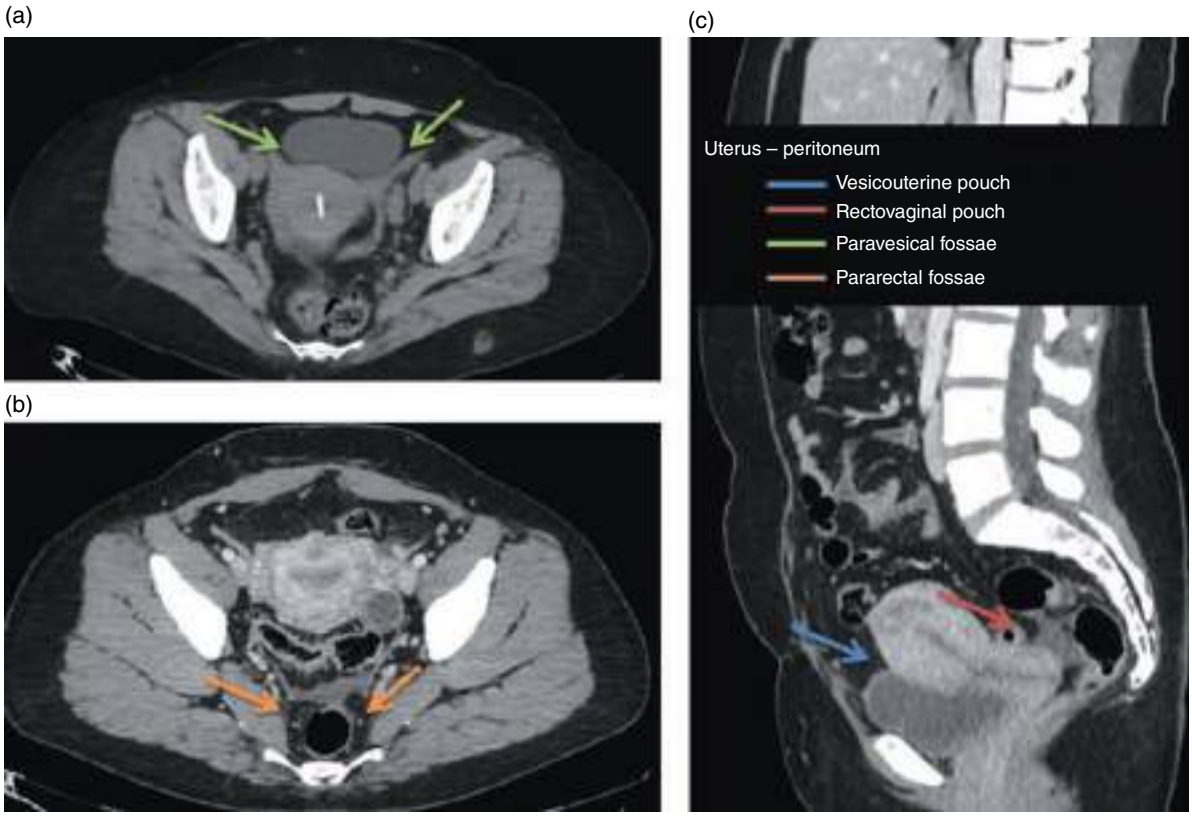

Figure 3.67 Uterus and peritoneum. (a) Axial noncontrast CT image. (b) Axial contrast-enhanced CT image (portal venous phase). (c) Sagittal contrast-enhanced MPR CT image (portal venous phase).

The cervix is separated from the uterine body by the internal cervical orifice [68]. It is cylindrical in shape and protrudes into the vagina, with which it communicates via the external cervical orifice.

The anatomical relation between the body and the cervix changes with reproductive age. The body:cervix ratio is 1:1 in premenopausal women, and 2:1 in reproductive age women. In postmenopausal women, the uterus atrophies and decreases in size to 4–6 cm in length [73].

Ovary: Fallopian Tube

The ovaries are ellipsoid in shape and measure between 2.5 and 5 cm in length. They change in location after pregnancy and with the size of the uterus and degree of bladder distension. In nulliparous women, the ovaries lie within the ovarian fossa (of Waldeyer) on the lateral wall of the pelvis, bounded by the obliterated umbilical artery anteriorly, the external iliac vein superiorly, and the ureter and internal iliac artery posteriorly [73, 75].

The ovary is suspended in the pelvis by the mesovarium, which fixes the ovary to the posterior surface of the broad ligament, by the ovarian ligament, which attaches the ovary to the uterus, and by the suspensory ligament or pelvic infundibulum, which fixes the ovary to the lateral wall of the pelvis. The broad ligament and the mesovarium cannot be identified in CT images unless surrounding ascites is present [74] (Figures 3.68 and 3.69).

In the premenopausal woman, the normal ovary presents follicles, which usually lie peripherally and measure

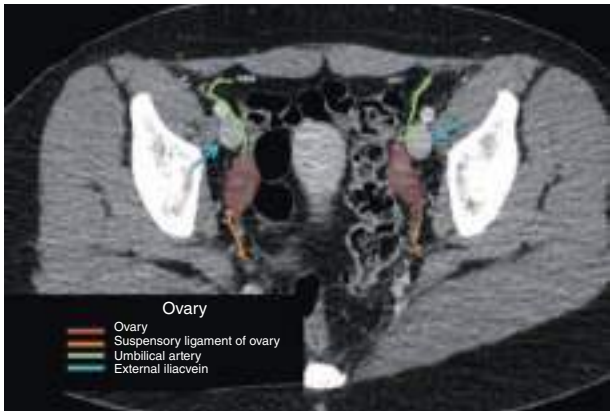

Figure 3.68 Ovary. Axial contrast-enhanced CT image (portal venous phase).

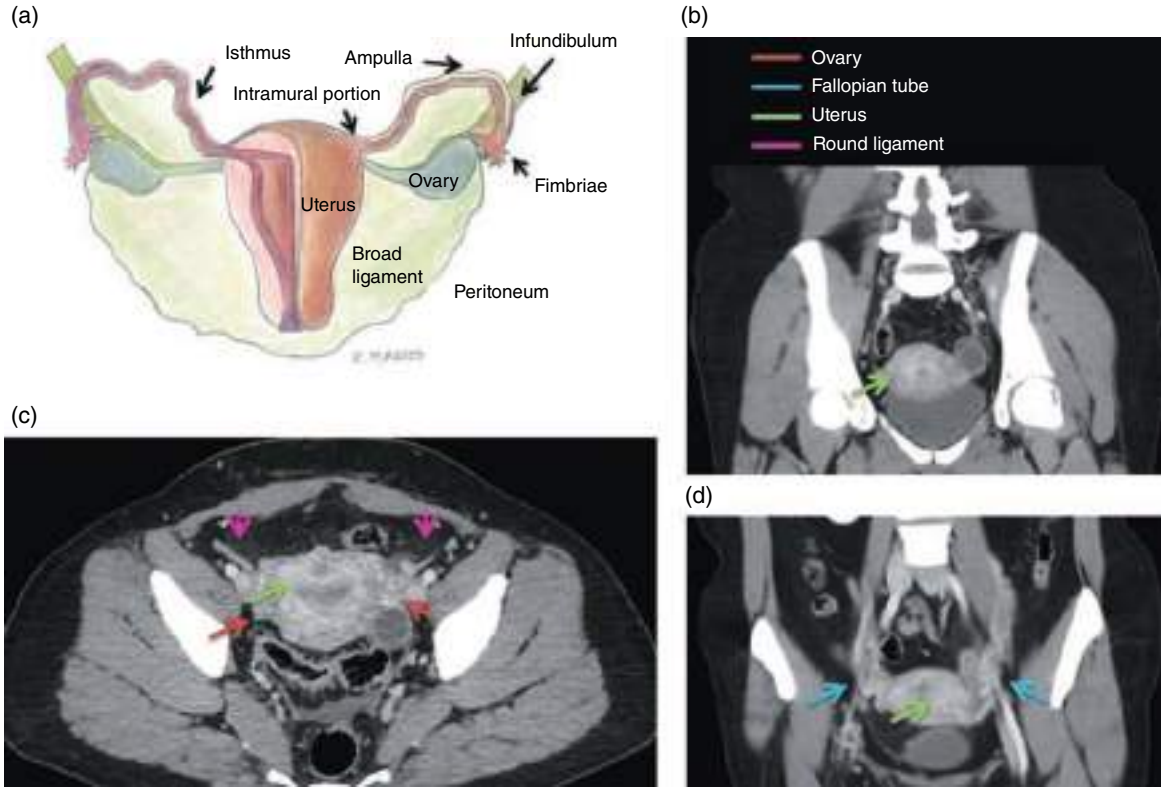

Figure 3.69 Ovary and fallopian tubes. (a) Schematic illustration, adapted from Revzin et al. [76]. (b) Axial contrast-enhanced CT image (portal venous phase). (c) Coronal contrast-enhanced MPR CT image (portal venous phase). (d) Coronal contrast-enhanced MPR CT image (portal venous phase).

less than 3 cm. The corpus luteum cyst is an involutional dominant functional cyst that can be recognized because its wall tends to be more irregular [68].

The fallopian tubes arise from the posterior part of the uterus, at the site of junction between the fundus and body. They are approximately 10 cm long and lie in the superior aspect of the broad ligament. Four portions can be distinguished: intramural (within the myometrium), isthmic (medial third), ampullar (middle distal), and infundibular (distal zone). The distal part of the infundibulum is fimbriate and opens into the peritoneal cavity [73, 76] (Figures 3.68 and 3.69).

Vagina

The vagina is a cylindrical fibromuscular structure measuring approximately 7–9 cm in length (its anterior wall is approximately 6 cm and its posterior wall 9 cm). The vagina extends from the vulva to the cervix superiorly, lying between the urinary bladder and rectum. It forms an angle greater than 90° relative to the uterus. The urogenital diaphragm connects the vagina to the levator ani muscle. It is lined with a stratified squamous epithelium sensitive to strogens. Morphologically, it is divided into thirds: the lower third is located inferior to the base of the bladder, so that the urethra lies anteriorly, the middle third corresponds to the base of the bladder, and the upper third comprises the lateral vaginal fundi (Figure 3.70).

Figure 3.70 Vagina. Sagittal contrast-enhanced MPR CT image (portal venous phase).

Urethra

The female urethra is a thin-walled tubular muscular canal, measuring approximately 40 mm in length. It runs antero-inferiorly from the internal urethral meatus located in the trigone of the bladder and terminates in an external urethral meatus anterior to the vagina. It has three layers: an internal mucosa, vascular submucosa, and an external muscular layer. The urethropelvic ligaments provide structural support to the urethra [68].

Ligaments of the Pelvis

The broad ligament consists of two layers of peritoneum, which surround the uterus and extend laterally to the external wall of the pelvis. It includes the fallopian tube, ovarian ligament, uterine and ovarian vessels, nerves, lymphatic vessels, and a portion of the ureter, along with loose connective tissue and fat, known as the parametrium (Figure 3.69).

On its superior free edge, the broad ligament surrounds the fallopian tube, while the ureter lies in its inferior aspect.

The cardinal or transverse cervical ligament arises from the cervix and superior portion of the vagina, and merges with the fascia of the internal obturator muscle.

The ureterosacral ligament extends posteriorly from the lateral face of the vagina to the anterior body of the sacrum at the second or third sacral vertebrae. Finally, it merges with the cardinal ligaments medially.

The round ligament is a fibromuscular band that arises from the antero-lateral side of the fundus, runs laterally through the broad ligament along the lateral wall of the pelvis to the internal inguinal ring, and ends in the labia majora [77] (Figure 3.71).

The ovary has two supporting ligaments, namely the ovarian ligament and the suspensory ligament or pelvic infundibulum [73].

The suspensory ligament of the ovary is a peritoneal fold containing the ovarian artery and vein. It arises from the ovary and extends antero-laterally over the external iliac vessels to the lateral wall of the pelvis, where it merges with the connective tissue covering the psoas muscle.

Vascularization of the Pelvis

The common iliac arteries give off the internal and external iliac arteries approximately at the level of the lower sacroiliac joint.

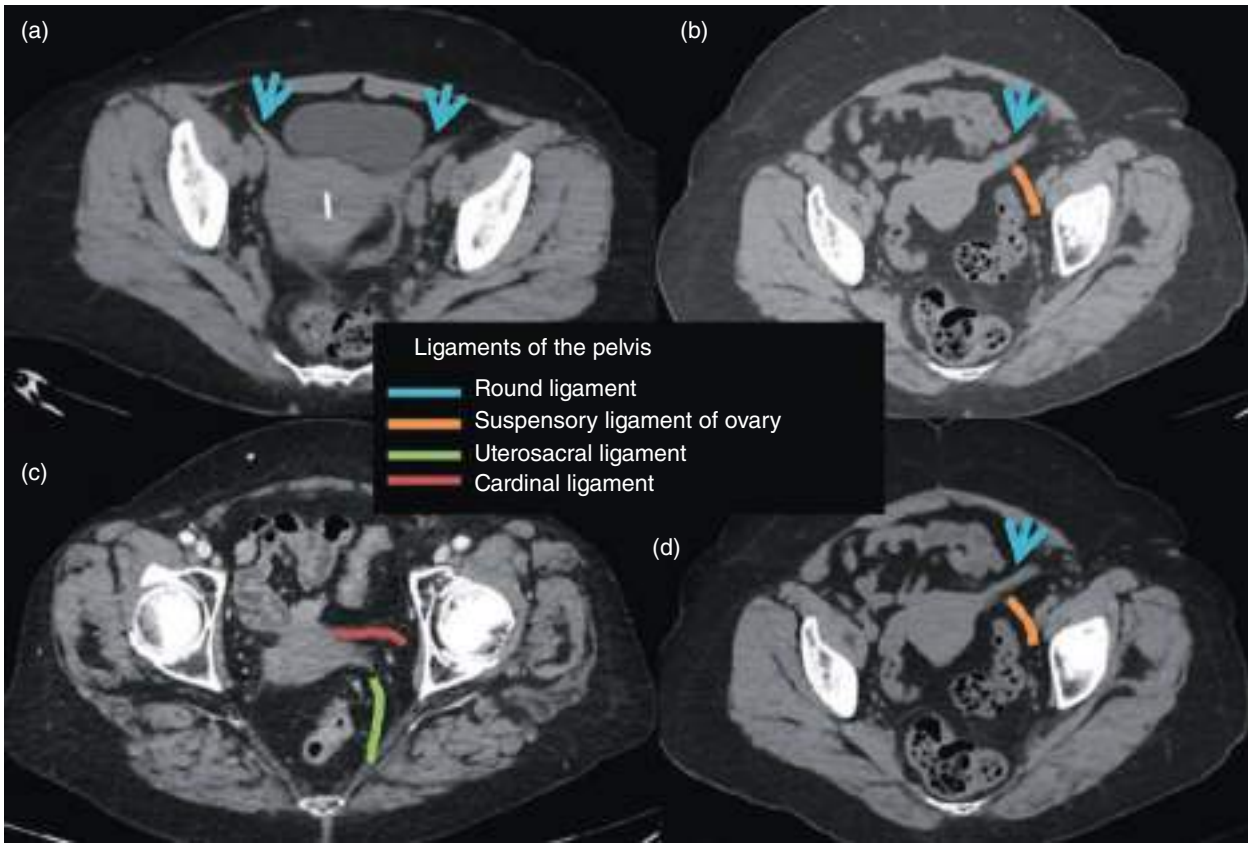

Figure 3.71 Ligaments of the pelvis. (a, b, d) Axial noncontrast CT images. (c) Axial contrast-enhanced CT image.

The paired uterine arteries are branches of the anterior trunk of the internal iliac artery. The uterine artery runs medially above the cardinal ligament through the base of the broad ligament to provide the primary blood supply to the uterus. The artery crosses anterior to the pelvic ureter to reach the cervix and divides into a large uterine branch and a smaller cervico-vaginal branch. Both branches are tortuous and form extensive vascular networks lateral to the uterus and vagina. In the superior segment of the uterus, the uterine artery trifurcates, giving off branches for the fallopian tubes, uterine fundus, and ovary. In addition, the ovaries receive direct blood flow from the ovarian arteries, which arise from the aorta immediately inferior to the renal arteries.

The blood supply of the vagina comes from a network of vessels formed by the anastomosis between the vaginal and uterine branches of the internal iliac artery. The lower two thirds of the vagina are supplied by the middle rectal artery and the internal pudendal arteries [68].

Venous Drainage The venous drainage of the uterus, cervix, upper vagina, and ovaries is via an extensive venous plexus within the parametrium. This plexus eventually drains into veins that run parallel to the arterial blood supply. Venous drainage is via the gonadal vein, with the right one draining into the IVC and the left one into the left renal vein [68, 73].

Rectum

The rectum is an extraperitoneal organ that extends from the rectosigmoid junction to the anorectal ring. Its proximal limit is approximately 15 cm from the anal verge and can be divided into the lower (5 cm from the anal verge), middle (5–10 cm), and upper (10–15 cm) rectum. It is surrounded by fat and by the mesorectal fascia (MRF), which represents the visceral fascia of the extraperitoneal portion of the rectum. The MRF has a funnel shape opened in its anterior portion, in such a way that the posterior insertion of the peritoneum lies higher than its anterior insertion, which forms the anterior peritoneal reflection (Figure 3.72).

The presacral fascia lies posteriorly, in close contact with the sacrum. The MRF and presacral fascia merge at the level of S4 to form the sacrorectal ligament. Anteriorly, the MRF merges with the urogenital septum,

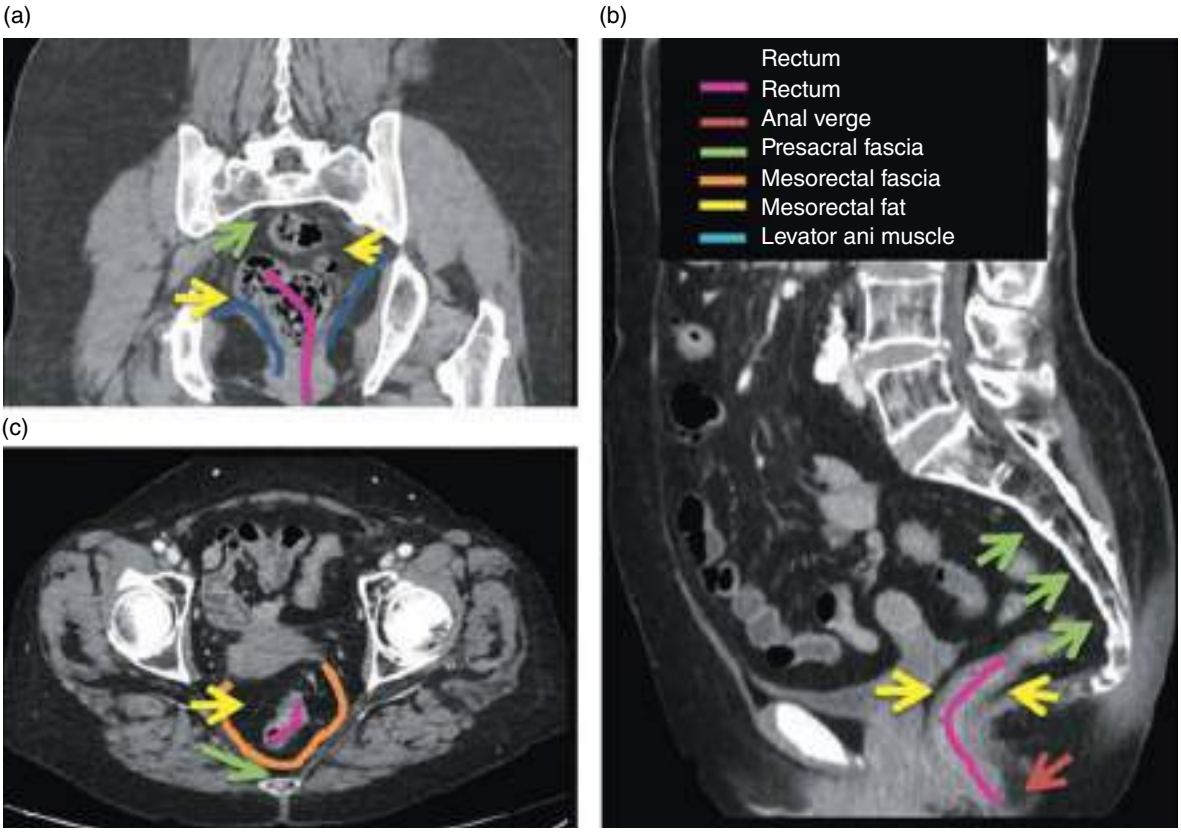

Figure 3.72 Rectum. (a) Coronal noncontrast MPR CT image (portal venous phase). (b) Axial contrast-enhanced CT image (portal venous phase). (c) Sagittal contrast-enhanced MPR CT image (portal venous phase).

forming the rectovaginal septum in women, while it merges with the Denonvilliers' fascia in men [78] (Figure 3.74).

The anal canal is the terminal portion of the large intestine. It is bounded by the rectum at the anorectal junction, which can be recognized because the puborectalis muscle forms a U-shaped sling posteriorly. The inferior boundary is the anal verge. The approximate histological length of the anal canal is 4 cm (Figure 3.72).

The wall of the anal canal has a cylindrical shape. The internal muscular layer is made up of smooth muscle and represents the internal anal sphincter. It is the distal prolongation of the circular muscular layer of the rectum. The external layer is a complex external anal sphincter of striated, skeletal muscles, which keeps the anal lumen closed. Between both layers there is fatty tissue called intersphinteric fat [79].

The external anal sphincter has three separate fiber bundles: deep, superficial, and subcutaneous. The deep fibers merge proximally with the puborectalis muscle, similar to a sling (Figure 3.73).

Both the external and internal sphincters are subsequently attached to the anococcygeal ligament and to the fibrous perineal body anteriorly.

The external sphincter has a series of reinforcements and support structures, which fix the anal canal to pelvic structures, especially the puborectalis muscle (into its superior margin) and the levator ani muscle (Figure 3.73).

The levator ani muscle is the main muscle of the pelvic diaphragm and has three components: ileococcygeal, pubococcygeal, and puborectalis.

The vascularization of the rectum is via three rectal arteries. The superior rectal artery is the terminal branch of the inferior mesenteric artery. It supplies the rectosigmoid junction and the upper rectum. It anastomoses with the middle rectal artery (branch of the internal iliac artery) and with the inferior rectal artery (branch of the internal pudendal artery). The middle rectal artery supplies the lower rectum, seminal vesicles, and prostate. In women it can be replaced by the uterine artery. The inferior rectal artery is responsible for the arterial supply of the anal canal.

Anatomy of the Male Pelvis

Prostate and Seminal Vesicles

The prostate is an exocrine gland found only in men. It has an inverted-cone shape with the base placed superiorly. It lies in the subperitoneal space, posterior to the pubic symphysis and anterior to the rectum. The base is attached to the bladder neck by the prostatic urethra, an anatomical landmark in the prostate, and the apex rests on the urogenital diaphragm contacting the medial surface of the levator ani muscles.

The prostate is made up of a glandular component (70%) and fibromuscular stroma (30%). Its primary function is to secrete an alkaline fluid that makes the semen more fluid.

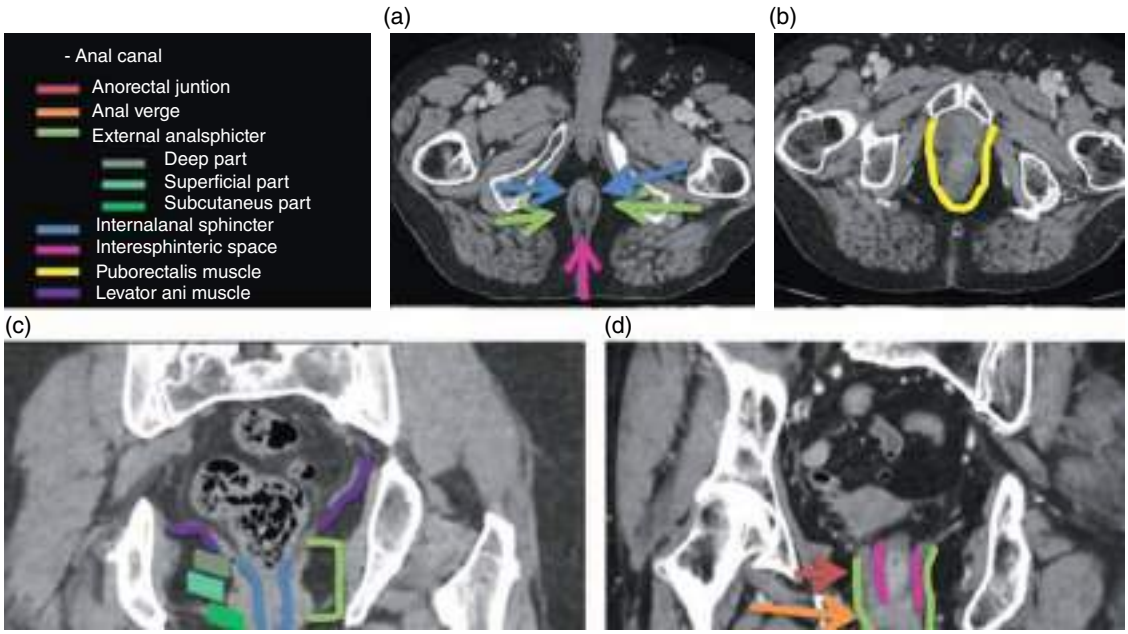

Figure 3.73 Anal canal. (a, b) Axial noncontrast CT images. (c) Coronal noncontrast MPR CT image. (d) Coronal contrast-enhanced MPR CT image (portal venous phase).

The ejaculatory ducts that come from the seminal vesicles open into the prostatic urethra in the so-called prostatic utricle, an area of glandular tissue which can be recognized because it protrudes from the posterior urethral wall [80] (Figure 3.74).

The seminal vesicles receive sperm from the testicles via the vas deferens and their size changes with ejaculation.

There are several classifications of the prostatic anatomy, including traditional divisions into lobes and the more up-to-date zonal classification, which distinguishes four zones, namely transitional, central, peripheral, and anterior fibromuscular stroma (Figure 3.75).

The volumetric contribution of the transitional, central, and peripheral zones changes with age. Prostatic hyperplasia is characterized by a considerable increase in the transitional zone [68, 80].

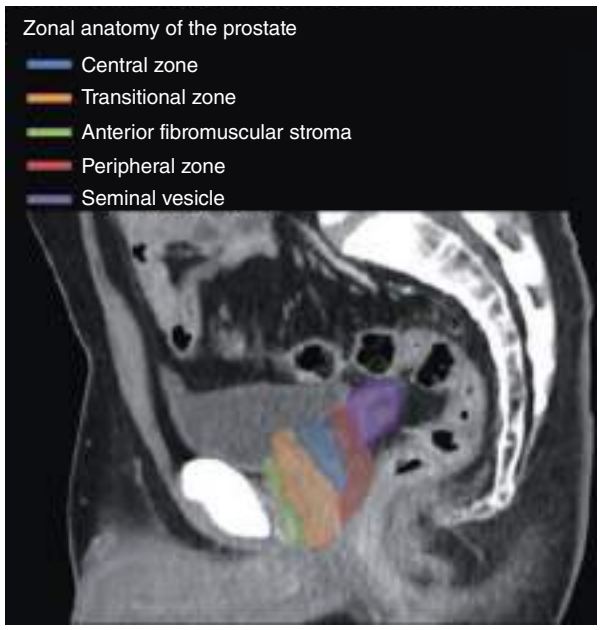

Figure 3.75 Sagittal contrast-enhanced MPR CT image (portal venous phase).

Peritoneal and Extraperitoneal Pelvic Spaces

The inferior terminal portion of both paracolic gutters lies at the inlet of the major pelvis, resulting from the anterior peritonealization of the ascending and left colon and its reflection in the abdominal wall. Both gutters communicate with the peritoneal pelvic spaces.

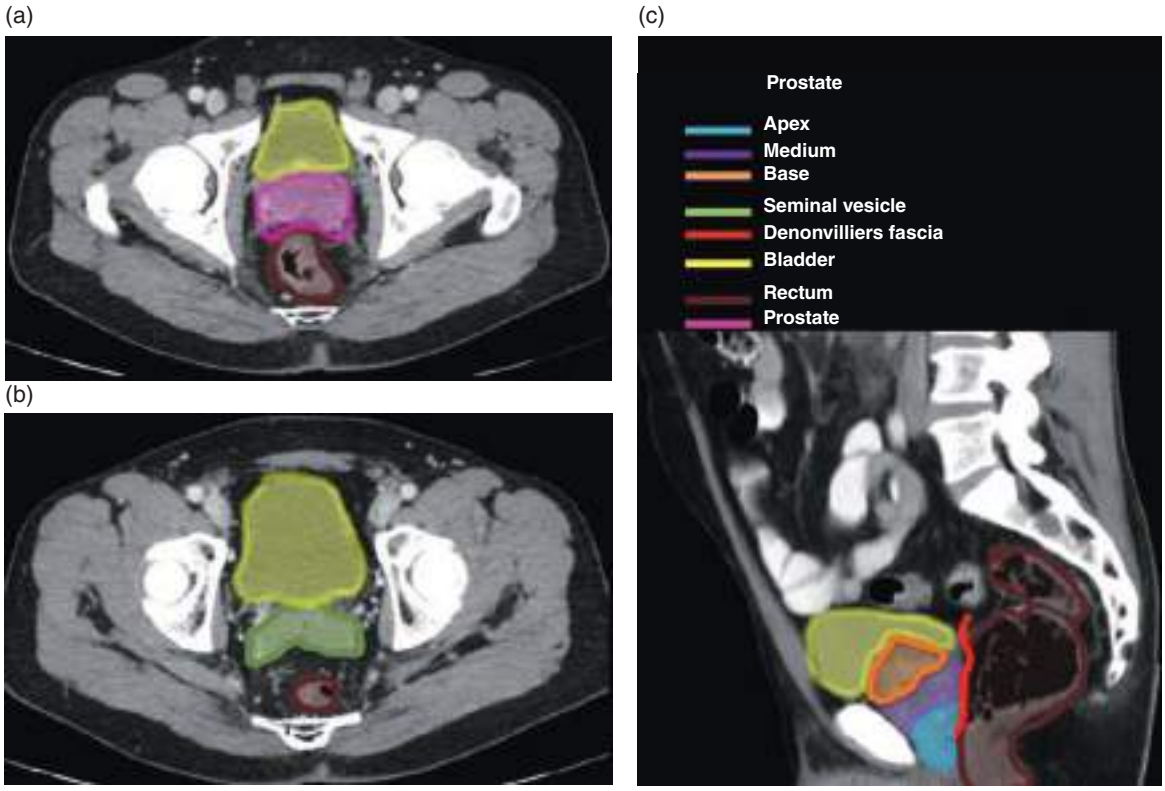

Figure 3.74 (a, b) Axial contrast-enhanced CT image (portal venous phase). (c) Sagittal contrast-enhanced MPR CT image (portal venous phase).

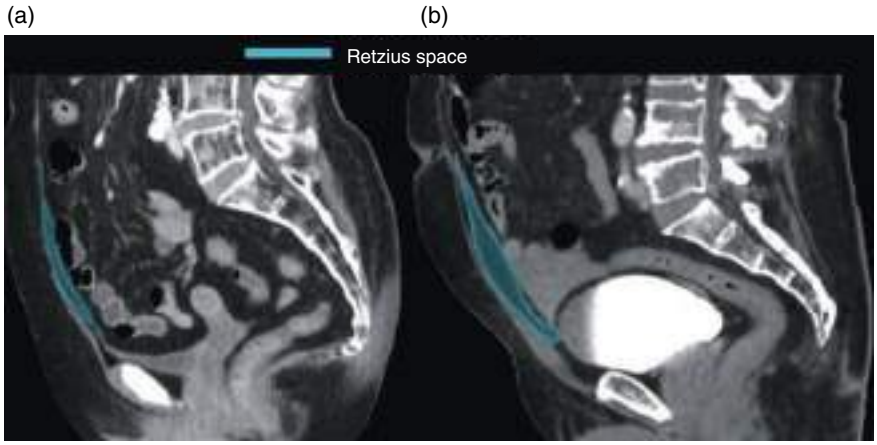

Figure 3.76 (a) Sagittal contrast-enhanced MPR CT image (portal venous phase). (b) Sagittal contrast-enhanced MPR CT image (late venous phase).

The peritoneum covers the superior surface of the extraperitoneal pelvic organs, forming the peritoneal reflections. Three main reflections can be found in women, namely the rectouterine pouch (of Douglas), the vesicouterine pouch, and the anterior vesical space lying between the anterior parietal peritoneum and the anterior vesical wall. In men, the main peritoneal reflection is the rectovesical pouch.

Anterior to the pouch of Douglas, the umbilical folds, which contain the obliterated umbilical artery, divide the pelvic spaces into lateral and medial compartments. On each side, the inferior epigastric artery divides the lateral compartments of the pelvis into lateral and medial inguinal fossae [59].

The prevesical (or Retzius) space is a large extraperitoneal compartment which mainly contains fat. Its anatomical boundaries are the transversalis fascia anteriorly, the umbilicovesical fascia posteriorly, the umbilicus superiorly, and the pubovesical ligament inferiorly. The transversalis fascia is a dense layer of areolar tissue which runs below the diaphragm and covers the posterior aspect of the muscles of the anterior abdominal wall. The umbilicovesical fascia extends in a triangular shape from the umbilicus to the urinary bladder, surrounding the urachus, the medial umbilical ligament (containing the obliterated umbilical arteries) and the urinary bladder, thus separating the prevesical from the perivesical space. Accordingly, the perivesical space contains the urachus, the medial umbilical ligament, and the urinary bladder [81–83] (Figure 3.76).

Spine Anatomy

General Anatomy of the Spine

The normal spine accounts for 24 pre-sacral vertebrae (seven cervical, 12 thoracic, five lumbar). However, transitional abnormalities are frequent, namely sacralization (L5 is fused to sacrum, described in <25% of cases) or lumbarization (S1 is detached from sacrum, described in around 2% of the cases) [84, 85]. The sacrum and coccyx are composed of five and four fused vertebrae, respectively.

The spine can be divided into the following components:

Anterior elements: vertebral bodies and intervertebral discs.

The vertebral bodies have an outer layer of dense cortical bone and an internal cavity composed of cancellous bone and soft tissue (bone marrow). In childhood, the bone marrow contains active hematopoietic tissue (red marrow), which is progressively replaced by fat (yellow marrow) with age. CT is the ideal technique to depict the structural integrity of the cortical and cancellous bone, but it is less sensitive in depicting the marrow component, which may be assessed visually or quantified in Hounsfield units (HU). The value in HU at the medullary cavity of the vertebral body ranges from 256.7 ± 41.8 (mean $\pm$ standard deviation) in the second decade of life to 90.0 ± 25.5 in the ninth decade of life in men, and from 253.5 ± 29.6 to 67.3 ± 41.2 in women, respectively. This decrease is secondary to progressive loss of bone density. Typical density values of cortical bone range from 600 to 3000 HU [86].

MRI depicts cortical bone as a black structure in all sequences, thus minor structural changes may be difficult to appreciate. Nevertheless, due to its greatest contrast resolution, it is the ideal technique to depict the normal and pathological appearance of the bone marrow. The appearance of the bone marrow varies according to the sequence used. Basic sequences to study the bone marrow include T1-weighted and fat suppression techniques, fat-suppressed T2-weighted or STIR. The normal yellow marrow is hyperintense on T1 and hypointense in fat suppressed or STIR sequences. Hematopoietic red marrow shows intermediate signal that is similar or slightly higher than normal intervertebral discs or muscle on T1-weighted images. On fat-suppressed or STIR images, the red marrow has

intermediate-to-high signal intensity (with intermediate being like that of muscle), depending on the degree of cellularity [87].

- Posterior elements: pedicles, laminae, transverse processes, spinous processes, articular apophysis, and joints. The pedicles and laminae enclose the central canal. The transverse processes arise laterally from the junction between the pedicle and laminae, while superior and inferior articular processes arise above and below, respectively. The spinous process arises posteriorly and inferiorly from the junction of the laminae. The orientation of facet joints is measured as the angle of the facet joint articular space relative to the sagittal plane. At the thoracic level, they have a roughly frontal orientation, which becomes more sagittal oblique at the lumbar level.
- Ligaments and soft tissues (muscles, venous plexuses, epidural fat).

The paravertebral or paraspinal muscles are intrinsic muscles that regulate the tone and motion of the spine. They include the transversospinalis muscles medially and the erector spinae muscles laterally. The transversospinalis muscles comprise the semispinalis thoracis, semispinalis cervicis, semispinalis capitis, multifidus, rotatores, interspinalis, and intertransversarii muscles. They assist with rotation and extension. The erector spinae muscles comprise the spinalis, longissimus, and iliocostalis muscles. The iliocostalis forms the most lateral column of paravertebral muscles. The longissimus is the intermediate column of the erector spinae. The spinalis forms the most medial part of the erector spinae group at cervical and dorsal spine. They are responsible for extension of the spine to maintain an erect position.

Nervous tissue: Composed of the spinal cord, nerve roots, and the cauda equina.

The thecal sac and its contents, including the nerve roots, are better visualized on MRI than CT. The surrounding epidural fat and CSF provide an excellent natural contrast tissue on MRI. The dura mater is a dense, fibrous tube enclosing the leptomeninges, CSF, spinal cord, and proximal nerve roots. The spinal dura is continuous with the cranial dura and attaches at the edge of the foramen magnum, C2–C3 bodies, and the posterior longitudinal ligament (PLL). The dura courses inferiorly, surrounding and blending with the filum terminale to distally insert into the coccyx. The arachnoid mater is loosely attached to the dura mater and it is difficult to depict both layers separately on imaging. The pia mater is not distinguishable from the cord on MRI. The cord demonstrates variable shape throughout its course. Accordingly, the cervical spine has an elliptical shape on cross-sectional imaging, becoming rounded in the dorsal spine. It terminates in the conus medullaris, which may be positioned between T11 and L3 in normal conditions. The filum terminale, a fibrous band connecting the conus medullaris with the coccyx, is continuous with the pia mater and surrounded by the cauda equina nerve roots.

The exiting nerve roots can be seen in the lower half of the foramen in the cervical spine and in the superior half in the thoracic and lumbar regions [88].

Regional Anatomy of the Spine

The cross-sectional anatomy of the spine is variable depending on the region and specific location in each region.

Cervical Spine

The cervical spine is made up of seven vertebrae. It has been classically divided into two separate entities: upper (from C1 to C2) and lower (from C3 to C7) [89].

The upper cervical spine consists of atypical joints: the atlanto-occipital and atlanto-axial joints. The dens of C2 articulates with the anterior arch of the atlas, forming the atlanto-axial joint.

The atlas is formed by the anterior and posterior arches joined by the lateral masses, and two lateral transverse processes. The anterior arch has a ventral tubercle on its frontal aspect and the odontoid fovea in its posterior aspect, to articulate with the odontoid process of C2. The dorsal tubercle is in the midline of the posterior arch. A groove for the vertebral artery can be found on the superior border of the posterior arch, posterior to the lateral masses. A bony bridge between the posterior part of the superior articular process and the posterolateral part of the posterior arch of C1 serves as roof for the vertebral artery. It has been described in 5–68% of series and is mostly considered an anatomical variant. It has been referred to with a variety of terms, including ponticulus posticus, arcuate foramen or Kimmerle anomaly [90]. The articular facets for the occipital condyles lie on the superior surface of the lateral masses, and the facet joints for the lateral masses of C2 can be found on their inferior surface. The transverse processes, more prominent than in the rest of the cervical vertebrae, have a foramen for the vertebral artery.

Many variants, mostly without clinical manifestations or craniovertebral junction pathological abnormalities, may affect the atlas. Most anomalies consist of various arch clefts, aplasia, and hypoplasia, which can be best understood by acknowledging the ossification centers of the atlas. The presence of cortical bone at the edges of the defect allows their differentiation from fractures. Posterior rachischisis is the most common anomaly, mainly at the

midline, while anterior arch rachischisis is rarer. The simultaneous presence of both variants is known as "split atlas." Rarer congenital abnormalities, such as atlanto-occipital assimilation or condylar hypoplasia, may lead to craniovertebral junction abnormalities [91] (Figure 3.77).

The axis is characterized by a prominence in the superior aspect of its body known as the odontoid process, which represents the fusion between the body of C2 and an embryonic segment of C1. The lateral masses of the axis contain the articular facets for C1 in their superior aspect. The costo-transverse processes of C2 are smaller than C1 and have a foramen for the passage of the vertebral artery.

Congenital variants of the axis are infrequent. The odontoid process may be absent or hypoplastic, separated from the C2 body (os odontoideum) or present an ossiculum terminale (unfused and detached apical dental fragment) [92].

The lower cervical spine consists of large, flattened vertebrae separated by intervertebral discs. Vertebrae are characterized by the presence of bony prominences, the uncinate processes (UPs), located on the posterolateral edge of the upper endplates. UPs have a shovel-like form and change their orientation from lateral to posterior in the cranio-caudal direction. In addition, their height decreases

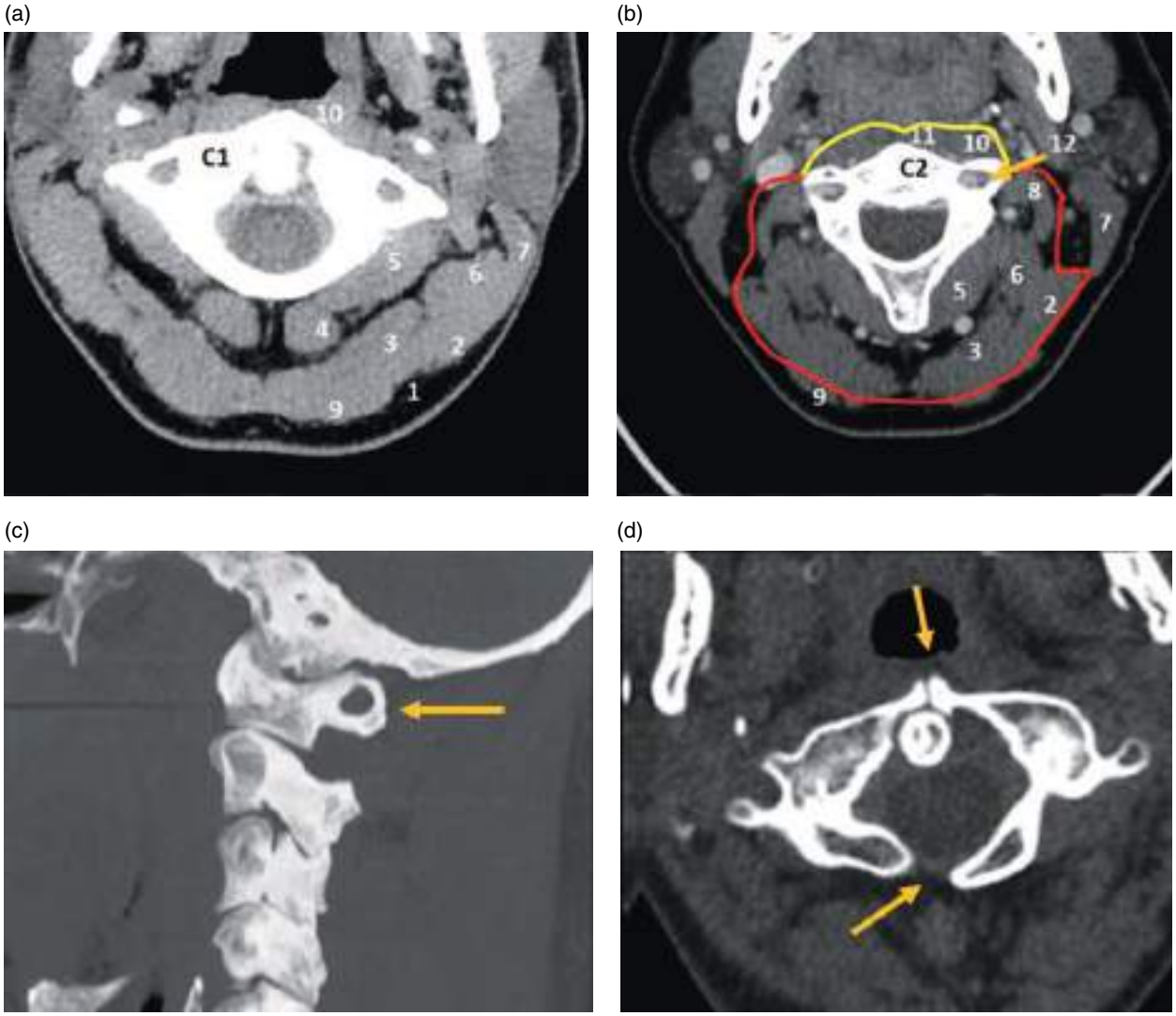

Figure 3.77 Axial CT image at the level of the atlas (a) and axis (b). (c) Arcuate foramen of the atlas (Kimmerle anomaly) (arrow). (d) Split atlas (arrows). 1, cervical fascia, superficial layer; 2, splenius capitis muscle; 3, semispinalis capitis muscle; 4, rectus capitis posterior major muscle; 5, obliquus capitis inferior muscle; 6, longuissimus capitis muscle; 7, sternocleidomastoid muscle; 8, levator scapulae muscle; 9, trapezius muscle; 10, longus capitis muscle; 11, longus colli muscle; 12, vertebral artery. The perivertebral space is subdivided into prevertebral (yellow) and posterior paraspinal (red) spaces.

at the lowest-level cervical spine, but their length increases from C3 to C6 [89, 93].

The vertebra prominens (C7) is atypical in that its long spinous process is not bifid but ends in a rounded tubercle. The foramen in the transverse process is small or absent and does not contain the vertebral artery. The anterior tubercle of the transverse process is also small. Moreover, C7 may have a cervical rib as a transitional abnormality.

The cervical perivertebral space (PVS) surrounds the spine and extends from the skull base to the mediastinum. The deep layer of the deep cervical fascia (DLDCF) divides the PVS into an anterior pre-vertebral space and a posterior para-spinal space, anterior and posterior to the costotransverse process, respectively [94].

The prevertebral space contains the longus colli, longus capitis, and scalenus muscles. The posterior paraspinal space contains the major extensor muscles of the head and neck. The levator scapulae and transversospinalis (multifidus and interspinalis) muscles are located more centrally and anteriorly. The splenius capitis, transversospinalis (semispinalis capitis), and erector (spinalis cervicis, longissimus capitis, and iliocostalis) adopt a more peripheral and posterior position.

The superficial layer of the deep cervical fascia (SLDCF) invests the descending part of the trapezius muscles, which are part of the posterior cervical musculature and are separated from the paraspinal muscles by fat.

Sequential interpretation of the cervical spine anatomy on cross-sectional images requires reference points to depict the normal anatomy. On cross-sectional CT anatomy, the following levels can be defined.

At the level of C1 the arches of the atlas can be seen, as well as the lateral masses and the transverse processes containing the transverse foramen for the vertebral artery. On the medial surface of the lateral masses of the atlas a small tubercle where the transverse ligament get insertion can be found. The odontoid process of the axis is in the middle, posterior to the anterior arch of the atlas, and held by the transverse ligament, among others (Figure 3.77).

At the level of C2, the continuum with the pedicles, laminae, and spinous process can be seen. The costotransverse processes with the foramen for the vertebral artery are located anterolaterally.

In the typical cervical spine, C3–C6, at disc level, the small intervertebral disc which is isodense to muscle may be partially depicted with the vertebral endplates (partial volume artifact). The disc is contoured laterally by the UPs, which represent the medial margin of the foramina, with the lateral limit being the superior articular process of the inferior vertebra. This superior process articulates with the inferior articular process of the upper vertebra.

At the level of the pedicle, the vertebral body in continuum with the pedicles and laminae can be seen. The costotransverse processes with the vertebral artery foramen (VAF) lie anterolaterally. The posterior part of the arch of the VAF ends in the posterior tubercle. The anterior part of the arch of the VAF ends in the anterior tubercle. The tubercles of the transverse processes at C5–C7 have different configurations, which allow their precise identification. The tubercles of C5 are similar in size, resembling a two-humped camel. The anterior tubercle of C6 is the largest and has been referred to as "the carotid tubercle of Chassignac." In C7, the anterior tubercle is rudimentary or absent. The anterior and posterior tubercles are joined by the intertubercular lamellae, which lie lateral to the VAF. The anterior part of the arch of the VAF and the anterior tubercle are remnants of the costal element. Conversely, the posterior part of the arch of VAF, as well as the posterior tubercle and lamella are true transverse processes [95]. The vertebral artery lies in this foramen, with the posterior root ganglion of the nerve lying posteriorly on the lamella (Figure 3.78).

MRI offers a similar picture of the anatomy with higher contrast resolution of the soft tissues. The spinal cord is isointense on T1-weighted images and is surrounded by CSF, which has low signal intensity. In T2-weighted images, the spinal cord is also isointense but surrounded by hyperintense CSF.

Thoracic Spine

The thoracic vertebrae are made up of a body and a posterior arch. On their posterior aspect, at both sides of the body there are two articular costal fossae to articulate with the heads of the ribs. They are demi-facets from T2 to T10. The superior one articulates with the rib of the same vertebral level and the inferior one with the ribs corresponding to the vertebra below. T1 has a complete facet superiorly and a demi-facet inferiorly, whereas a single complete facet is seen at midlevel on T11 and T12. Pedicles are prolonged with the laminae, which join posteriorly to form the spinous process. In the junction between the pedicle and lamina the superior and inferior articular processes can be found, with superior facets to articulate with the inferior zygapophyseal facets of the vertebra above, and inferior facets to articulate with the superior zygapophyseal facets of the vertebra below. Laterally, the transverse articular apophysis from T1 to T10 have a facet to articulate with the posterior arch of the ribs.

Paraspinal muscles are mainly composed by the erector spinalis muscles: iliocostalis, longissimus thoracis, and spinalis thoracis.

On cross-sectional CT anatomy, the following levels can be defined.

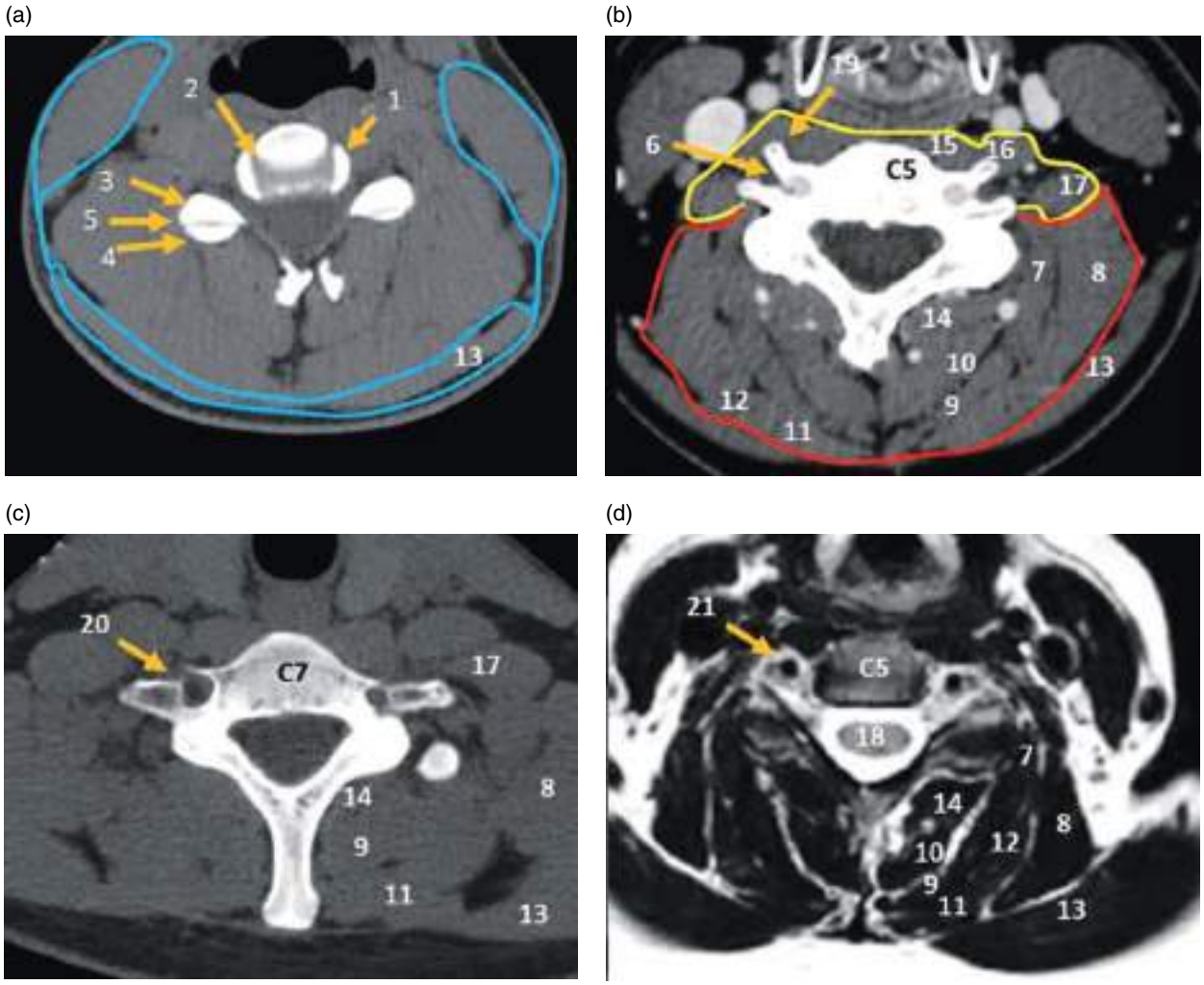

Figure 3.78 Axial CT image at the level of the C4–C5 disc (a), C5 vertebral body (b), and C7 vertebral body (c). (d) Axial T2-weighted MRI at the level of the C5 foramina. 1, uncinate process of C5; 2, uncovertebral joint of C4–C5; 3, superior articular facet of C5; 4, inferior articular facet of C4; 5, facet joint; 6, vertebral artery foramen; 7, longissimus cervicis muscle; 8, levator scapulae muscle; 9, semispinalis capitis muscle; 10, semispinalis cervicis muscle; 11, splenius capitis muscle; 12, splenius cervicis; 13, trapezius muscle; 14, multifidus muscle; 15, longus colli muscle; 16, longus capiti muscle; 17, scalenus medius muscle; 18, spinal cord; 19, costotransverse process of C5; 20, costotransverse process of C7; 21, vertebral artery. The blue line represents the superficial layer of the deep cervical fascia encasing the trapezius and sternocleidomastoid muscles. The perivertebral space is subdivided into prevertebral (yellow) and posterior paraspinal (red) spaces.

At the disc level, the soft tissue density and the small height of the thoracic discs may lead to partial volume artifacts due to overlap with the adjacent vertebral endplates. The superior articular process of the vertebra below is anterior to the inferior articular process of the vertebra above. The lamina and spinous process of the vertebra above may also be partially depicted.

At the level of the upper pedicle, the upper part of the vertebral body connected to the pedicles and laminae can be seen. The head of both ribs articulating with the costal fossae of the vertebral body (costo-vertebral joints) and the tubercles of the ribs articulating with the transverse process (costo-transverse joints) can also be seen.

At the level of the mid pedicle, the continuum with the mid portion of the vertebral body with the pedicles, laminae, and both transverse processes is depicted. A small notch in the posterior aspect of the vertebral body represents the exit of the basivertebral vein.

At the level of the foramina, several structures can be seen, including the inferior part of the vertebral body, the superior articular processes of the vertebra below, and the inferior articular processes of the in-plane vertebra connected to the inferior aspect of the laminae that converge to

the spinous process of the in-plane vertebra. The neural foramen, where the dorsal root ganglion may be identified, is depicted as a gap between the body and the posterior arch. At this level, the ribs articulate with the vertebra below and with the small costal facet of the inferior part of the in-plane vertebra (Figure 3.79).

Lumbar Spine

The five lumbar vertebrae are characterized by a more robust body than other spinal segments. In the normal healthy spine, vertebral bodies increase in width in a cranio-caudal direction, and the distance between the articular processes and pedicles increases accordingly. The arch is formed by the pedicles and laminae, which delimit the central canal. The laminae join posteriorly to form the spinous process. The interlaminar gap is occupied by the ligamenta flava. From the union between the pedicles and laminae, the upper and lower joint processes emerge to articulate with the adjacent vertebrae. The articular facets are markedly vertical, with the superior facets directed posteromedially and medially. The mammillary processes arise on the posterior surface of the superior articular processes, while the accessory process projects back at the root of the transverse process. Both processes represent the stunted transverse process of the thoracic vertebrae. The lumbar transverse processes are located laterally at the junction between the body and the pedicle. They represent the fused costal elements.

At the lumbar level, the rotatores, interspinalis, and intertransversarii muscles form the deep layer of the paraspinal muscles, while the multifidus constitutes the middle layer

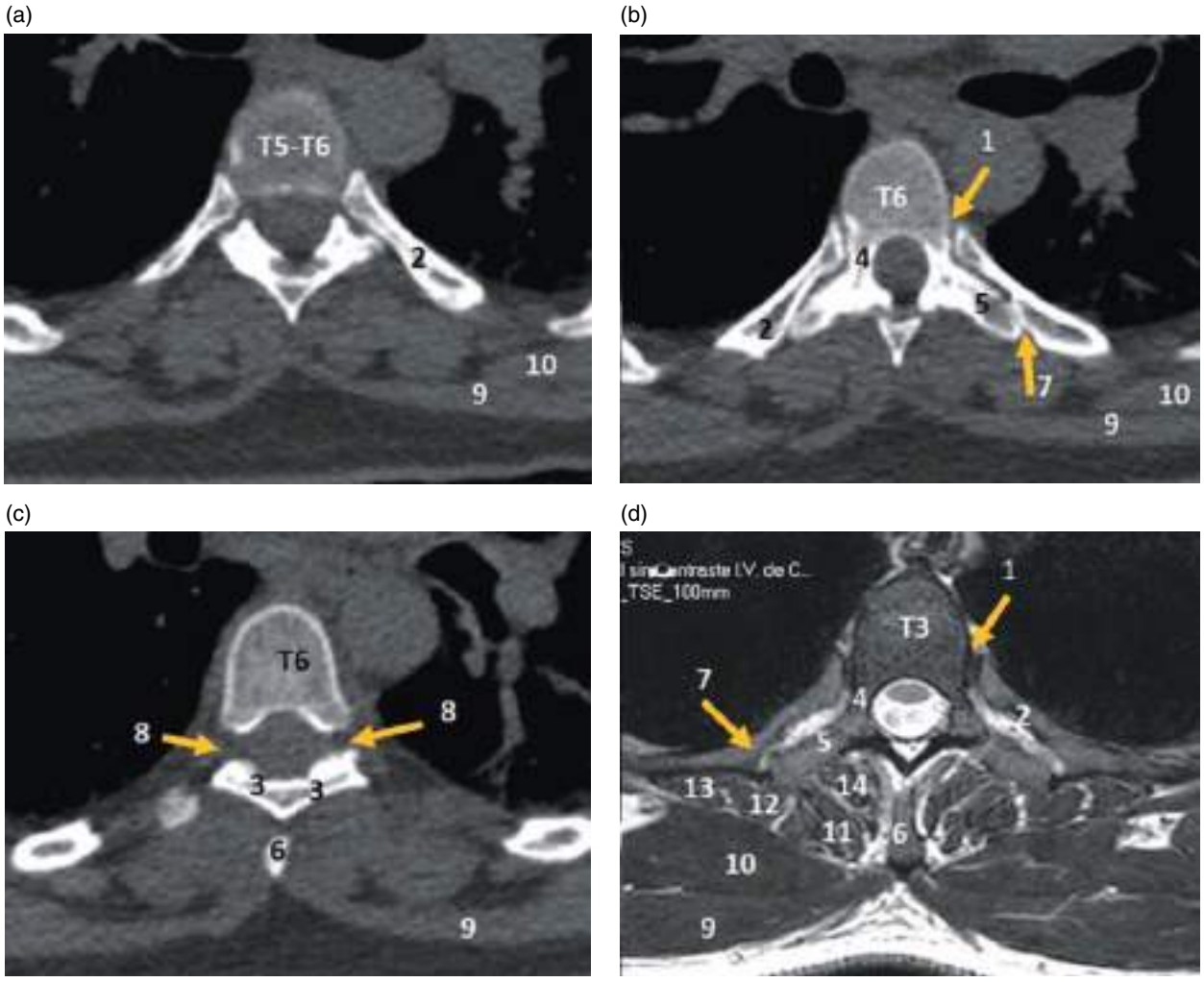

Figure 3.79 Axial CT image at the level of the T5–T6 disc (a), T6 pedicles (b), and T6 foramen (c). (d) Axial T2-weighted MRI at the level of T3. 1, costovertebral joint; 2, rib; 3, lamina; 4, pedicle; 5, transverse process; 6, spinous process; 7, costotransverse joint; 8, vertebral foramen; 9, trapezius muscle; 10, rhomboid major muscle; 11, spinalis thoracis muscle; 12, longissimus muscle; 13, iliocostalis muscle; 14, transversospinalis muscles.

and the erector spinae muscles compose the superficial layer (sacrospinalis muscles formed by the longissimus and iliocostalis muscles). Intrinsic muscles are covered by the posterior thoraco-lumbar fascia (PTLF) and separated from the psoas muscle (P) and the quadratus lumborum muscle (QL) by the middle thoracolumbar fascia [96].

On cross-sectional CT anatomy, the following reference levels can be defined. At the disc level, the typical soft tissue density of the disc can be seen. The superior articular process of the vertebra below is anterior to the inferior articular process of the vertebra above. The facet joints are oriented from posterior to anterior in medial direction. This medial orientation increases from cranial to caudal, reaching the most medialized orientation at L5-S1.

At the level of the lateral recess, the upper endplate of the vertebra can be seen, with or without partial volume average with the intervertebral disc. The lateral recess, also known as Lee's entrance zone, is the most cephalad part of the lateral canal [97]. It is the space between the posterior border of the disc upper vertebral endplate and the upper articular process of the in-plane vertebra and facet joint. The medial and lateral aspects are open, extending from the lateral border of the dura to the superomedial border of the pedicle. The canal is closed by the ligamenta flava posteriorly.

At the pedicle level, the continuum of the vertebral body with the pedicles, laminae, and spinous process can be seen.

At the level of the foramina, the inferior part of the vertebral body which constitutes the anterior limit of the foramen can be found. The dorsal root ganglion and ventral motor root occupy 30% of this space [98]. The posterior border corresponds to the pars interarticularis, while the medial aspect is open to the central canal and the lateral aspect is open to the extraforaminal space (Figure 3.80).

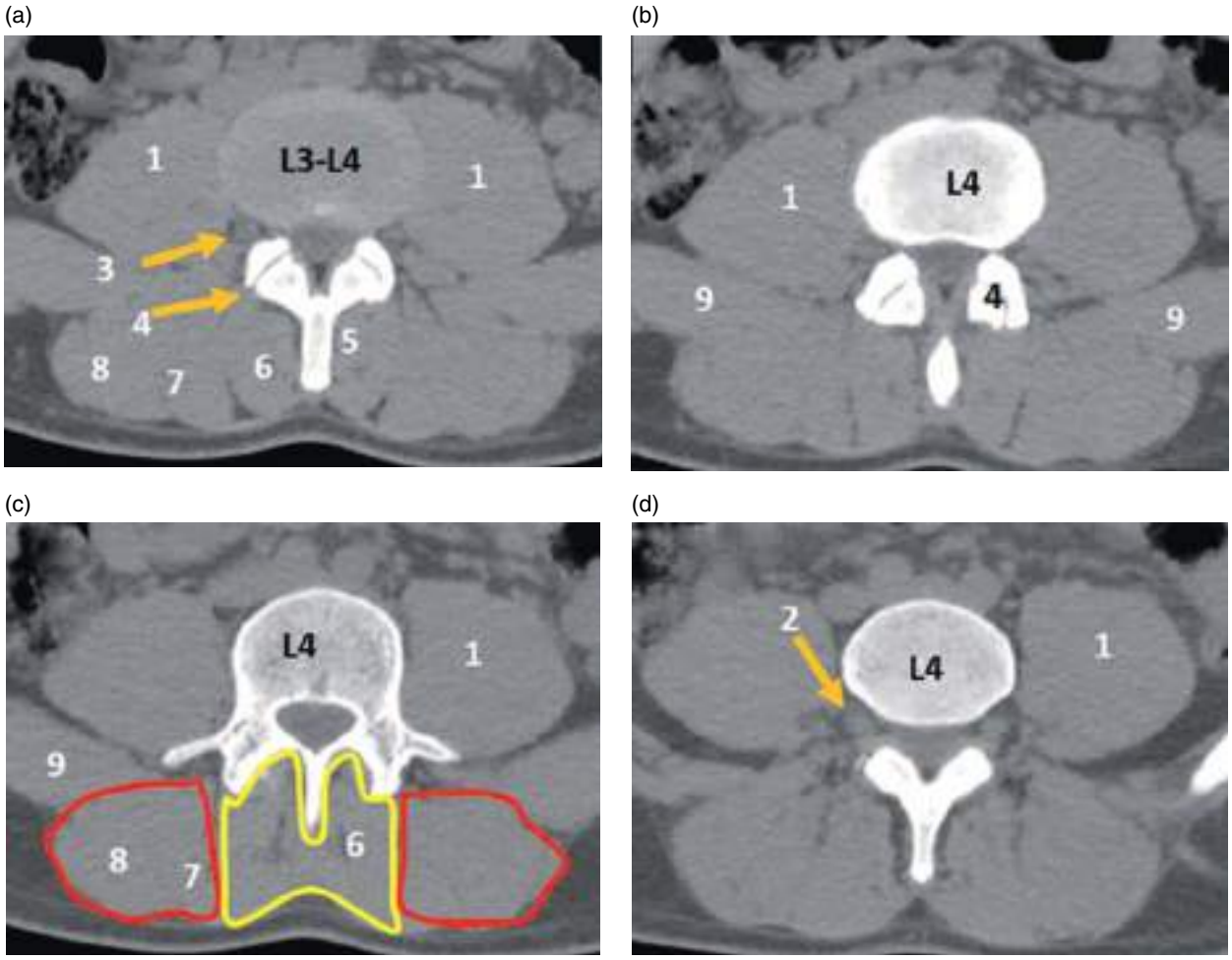

Figure 3.80 Axial CT image at the level of the L3–L4 disc (a), L4 lateral recesses (b), L4 pedicles (c), and L4 foramina (d). 1, psoas muscle; 2, L4 nerve root; 3, L3 nerve root; 4, facet joint; 5, rotator muscles; 6, multifidus muscle; 7, longissimus muscle; 8, iliocostalis muscle; 9, quadratus lumborum muscle; yellow line, transversospinalis muscles; red line, erector spinae muscles.

Sacrum and Coccyx

The sacrum is composed of five fused vertebrae and has a triangular morphology. It is curved on its anterior aspect, both transversely and vertically. The base of the sacrum is formed by the surface of the first sacral vertebra, which is much larger in its transverse diameter than in the anteroposterior axis and has an anterior promontory. Cranially, the superior articular processes articulate with the lower articular facets of L5. The sacred alae are fused rudiments of the pedicles and transverse processes with the bodies and contain the foramina, which communicate with the sacral canal. The apex of the sacrum is formed by the distal end of S5 which has an ovoid articular facet for the coccyx.

The posterior surface of the sacrum is rough and irregular. The medial sacral crest can be seen in the midline, formed by the fusion of four spinous processes and the sacral hiatus at the distal end. The sacral intermediate crest is located medial to each foramen. At S5, two processes project inferiorly from the intermediate crest to limit the sacral hiatus laterally. These cornua or horns articulate with the cornua of the coccyx. Finally, the lateral sacral crest is located lateral to each dorsal foramen.

Anatomy of the Limbs and Joints

The cross-sectional anatomy of the limbs and joint is highly influenced by patient positioning, especially in the case of CT of the upper limbs, where the arms are usually raised and placed behind the patient's head.

Knowledge of cross-sectional anatomy is helpful in delimiting which anatomic spaces or compartments are involved. This is of paramount importance in local staging of the tumors. Because of its high soft tissue contrast resolution, this determination is best accomplished with MRI [99]. According to the Enneking classification in tumors of the musculoskeletal system, any tumor confined to one compartment is considered intra-compartmental (stage T1) and is extra-compartmental (stage T2) when it spreads beyond these natural boundaries [100].

The skin and subcutaneous fat are considered a single compartment. They are separated from deeper tissues by a thick, intervening fascia; however, there are no barriers to stop the longitudinal spread of tumors in this compartment. A lesion inside a single muscle is considered as stage T1. Extension of the tumor beyond the muscle is still considered T1 if it remains confined to a larger compartment by natural barriers such as fascia or tendons. Each bone is considered an individual compartment, bounded by the overlying cortex, periosteum, and articular cartilage. A purely intraosseous lesion is therefore considered T1, whereas a tumor extending from the bone into adjacent soft tissues or vice versa would be considered as stage T2. The space between the bone and overlying tissues is considered a compartment because a lesion could arise in that location without invading the bone or adjacent soft tissues. Each joint is considered a different compartment, bounded by synovial and capsular tissues [99].

Neurovascular structures are not classically considered compartments but must be evaluated during the staging of tumors. Fat, areolar tissue and muscles are relatively poor barriers to tumor spread, and certain regions composed of these tissues are considered completely T2, including the head and neck, paraspinal tissues, periclavicular area, axilla, antecubital fossa, wrist, dorsum of the hand, groin, popliteal fossa, ankle, and dorsum of the foot.

Pelvic Girdle and Lower Limbs

The pelvic is a ring-like structure made up of three components: the sacrum and two coxal or innominate bones. The innominate bones are formed by three components, namely the ilium, ischium, and pubis. The ilium articulates with the auricular facets of S1–S3 posteriorly to form the sacroiliac joints, and both pubic rami articulate anteriorly to form the pubis symphysis. Therefore, the posterior ring is formed by the sacrum and sacroiliac joints, and the anterior ring is formed by the symphysis and pubic rami.

The pelvic brim or linea terminalis (innominate line) is the boundary between the greater pelvis and the lesser pelvis as well as the plane of the pelvic inlet. It is formed by the pectineal line, the arcuate line, and the sacral promontory.

The acetabulum is formed by the conjunction of the three components of the innominate bones. It shows a normal anteversion around 15° with the anterior wall being smaller than the posterior wall. The flat medial surface of the acetabulum that faces the pelvic organs is known as the quadrilateral plate or surface and constitutes the true floor of the acetabulum [101]. It is limited by the greater sciatic foramen posteriorly, the obturator foramen anteriorly, and the pelvic brim superiorly, with a horizontal line joining the ischial spine and the obturator foramen inferiorly [102]. The obturator foramen is bounded superiorly by the inferior aspect of the quadrilateral plate, posteriorly by the anterior portion of the ischium, anteriorly by the interior pubic ramus, and internally by the junction of the ischium and pubis. The obturator foramen is covered by the internal and external obturator muscles. Other important muscles of the pelvis include the psoas iliacus and the gluteus muscles posteriorly.

The acetabulum represents the "socket" of the so-called ball-and-socket joint, with the femoral head, which under normal conditions is a perfect sphere, resembling a ball,

interrupted by the fovea capitis where the ligamentum teres gets inserted.

The greater trochanter of the femur consists of four facets (anterior, lateral, posterior, and superoposterior) which serve as attachments for the gluteus muscles. The lesser trochanter projects medially from the femoral neck-shaft junction and serves as the insertion site for the iliopsoas muscle, which is the primary hip flexor [103] (Figures 3.81 and 3.82).

Above the hip, the pelvic soft tissues can be divided into three essential spaces comprising the iliopsoas, the gluteus medius/minimus, and the gluteus maximus compartments [104]. A lesion confined to a single bone or muscle within the pelvis would be considered as stage T1 [99]. The intra-pelvic region and neurovascular bundles of the lower limb are classified as T2 spaces.

The thigh is made up of three compartments, anterior, posterior, and medial, covered by the fascia lata. The anterior compartment contains the iliotibial tract and the tensor fasciae latae muscle, along with the quadriceps musculature (rectus femoris, vastus medialis, vastus lateralis, and vastus intermedius). The vastus intermedius muscle is sometimes considered a separate fourth compartment. Although the sartorius muscle is an anterior structure proximally and a medial structure in the distal thigh from an anatomic perspective, it is classically considered an anterior compartment structure (Figure 3.83).

The posterior compartment contains the hamstring muscles (semimembranosus, semitendinosus, and biceps femoris) as well as the sciatic nerve. The gracilis and adductor muscles lie within the medial compartment.

The anterior compartment is separated from the medial and posterior compartments by two fascial thickenings projecting from the fascia lata to get inserted in the femur: the medial and lateral intermuscular septa. The medial compartment is separated from the posterior compartment by a thin fascial plane [105].

The lower leg is divided into four compartments covered by the deep crural fascia that blends medially along the entire length of the tibia: anterior, deep posterior,

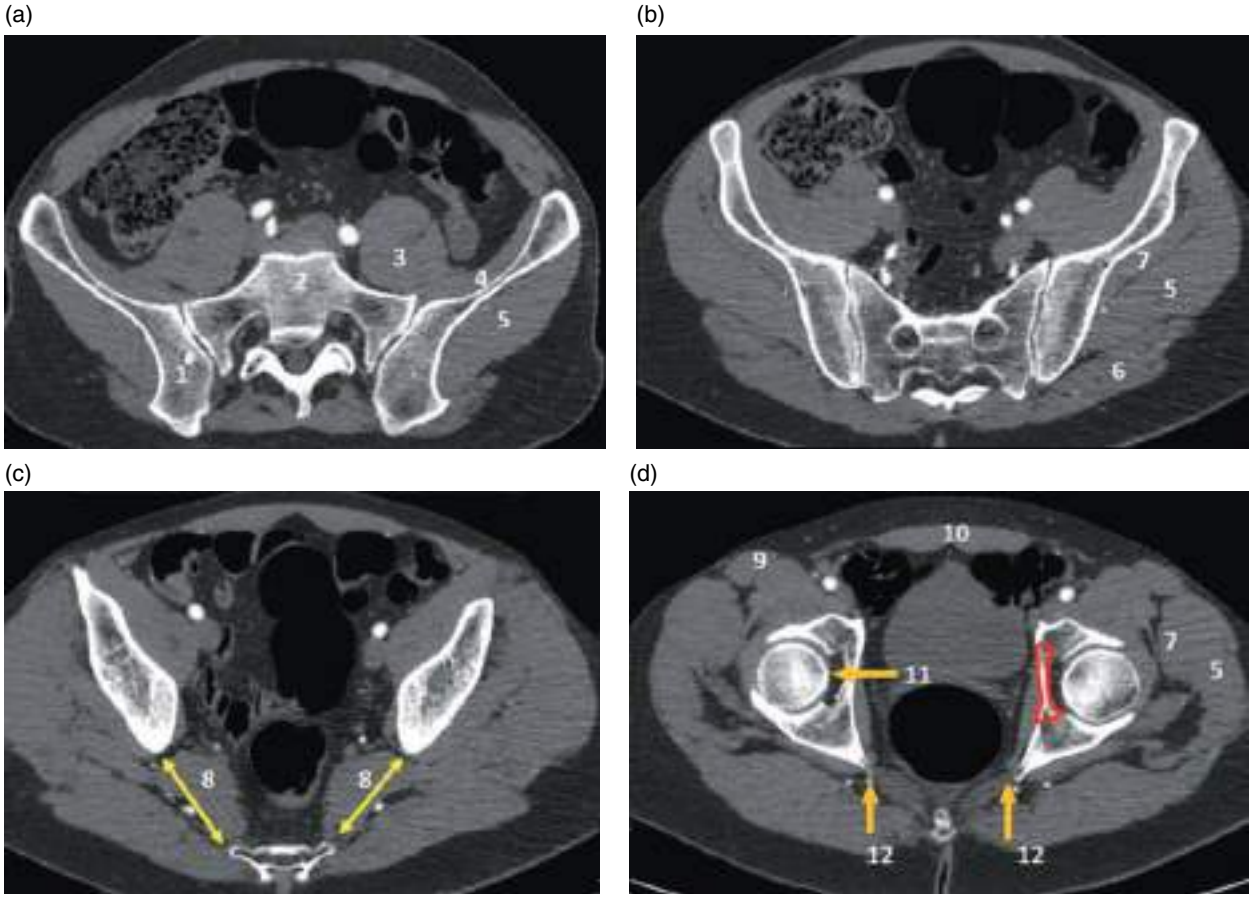

Figure 3.81 Axial CT images of the upper pelvis showing successive slices from cranial (a) to caudal (d). 1, ilium; 2, sacrum; 3, psoas muscle; 4, iliacus muscle; 5, gluteus medius muscle; 6, gluteus maximus muscle; 7, gluteus minimus muscle; 8, piriformis muscle; 9, sartorius muscle; 10, rectus abdominis muscle; 11, acetabulum; 12, ischial spine; red area, quadrilateral plate; double yellow line, greater sciatic foramen.

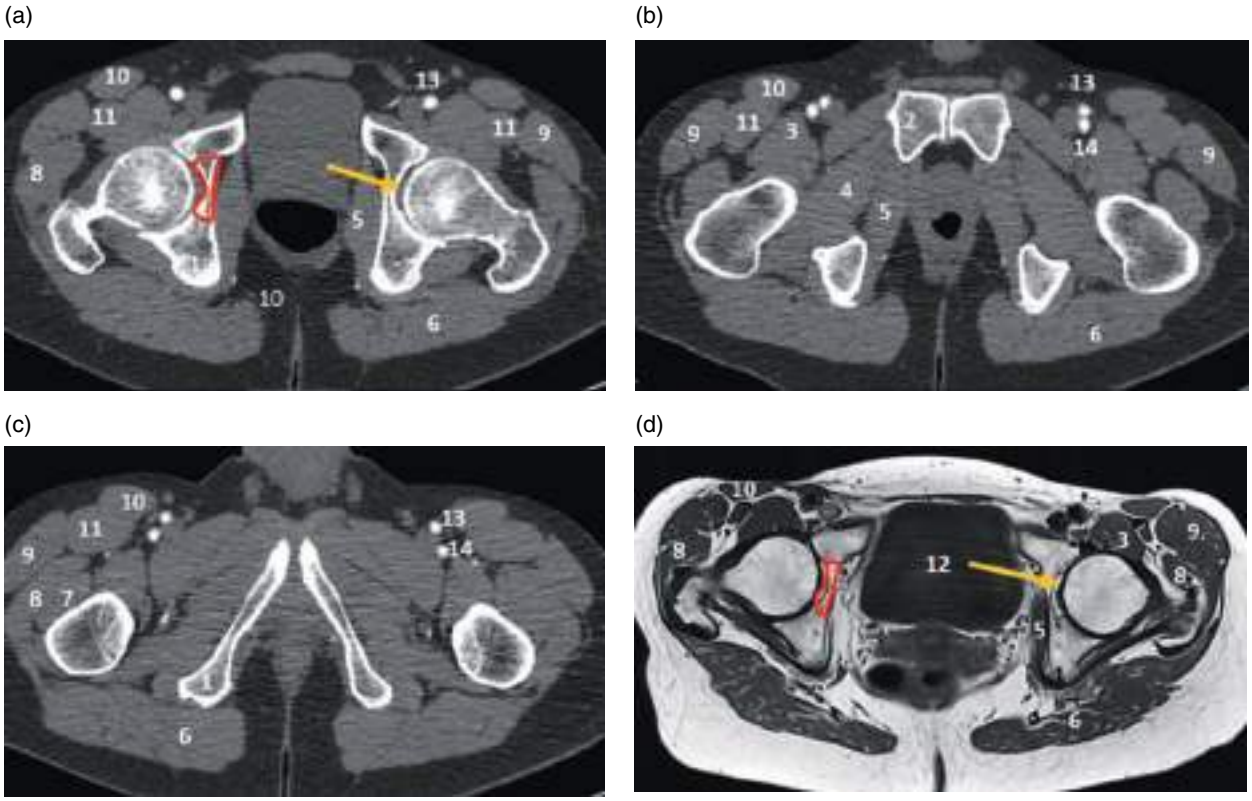

Figure 3.82 Axial CT images of the lower pelvis showing successive slices from cranial (a) to caudal (d). 1, ischial tuberosity; 2, pubis; 3, psoas iliacus muscle; 4, external obturator muscle; 5, internal obturator muscle; 6, gluteus maximus muscle; 7, gluteus minimus muscle; 8, gluteus medius muscle; 9, tensor fasciae latae muscle; 10, sartorius muscle; 11, rectus femoris muscle; 12, acetabulum; 13, femoral artery; 14, deep artery of the thigh; red area, quadrilateral plate.

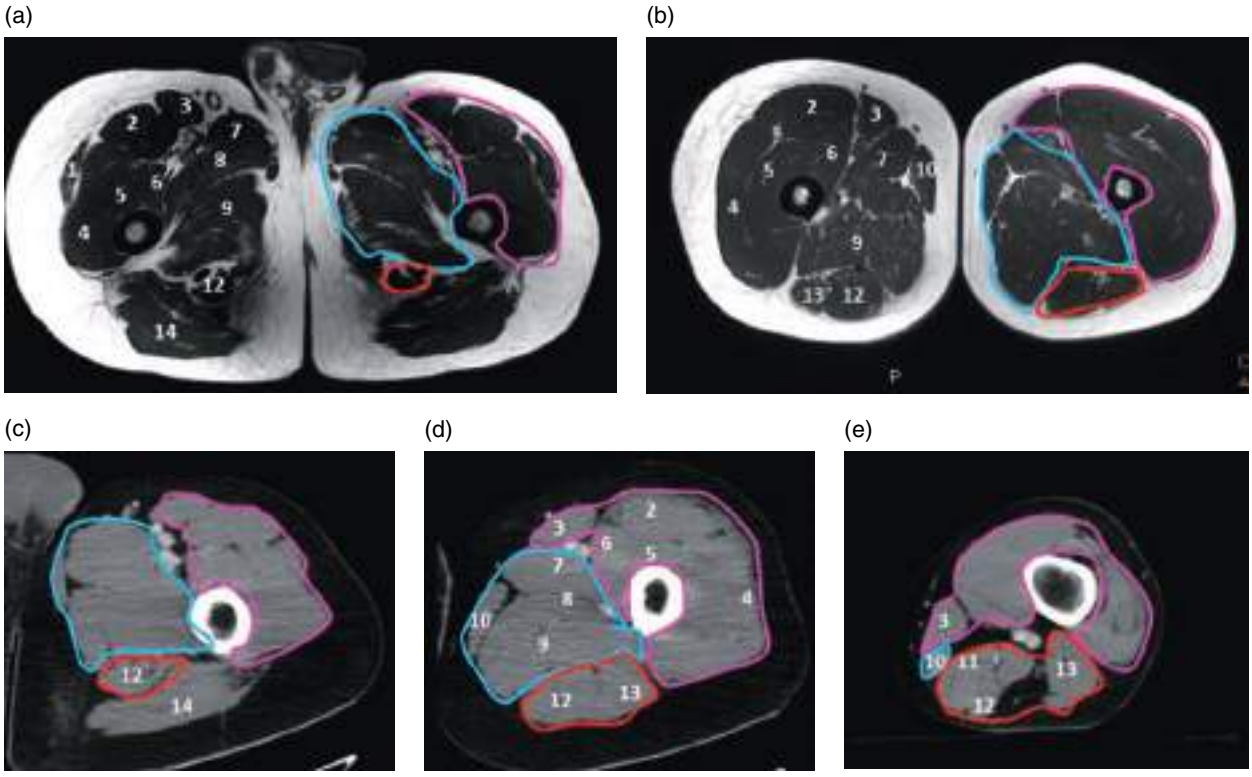

Figure 3.83 Compartments of the thigh in MRI (a, b) and CT images (c–e). The anterior compartment (pink) contains the tensor fasciae latae (1), rectus femoris (2), sartorius (3), vastus lateralis (4), medialis (5), and intermedius (6) muscles. The medial compartment (blue) contains the adductor longus (7), brevis (8), magnum (9), and gracilis (10) muscles. The posterior compartment (red) contains the semimembranosus (11), semitendinosus (12), and biceps (13) muscles. 14, gluteus maximus muscle.

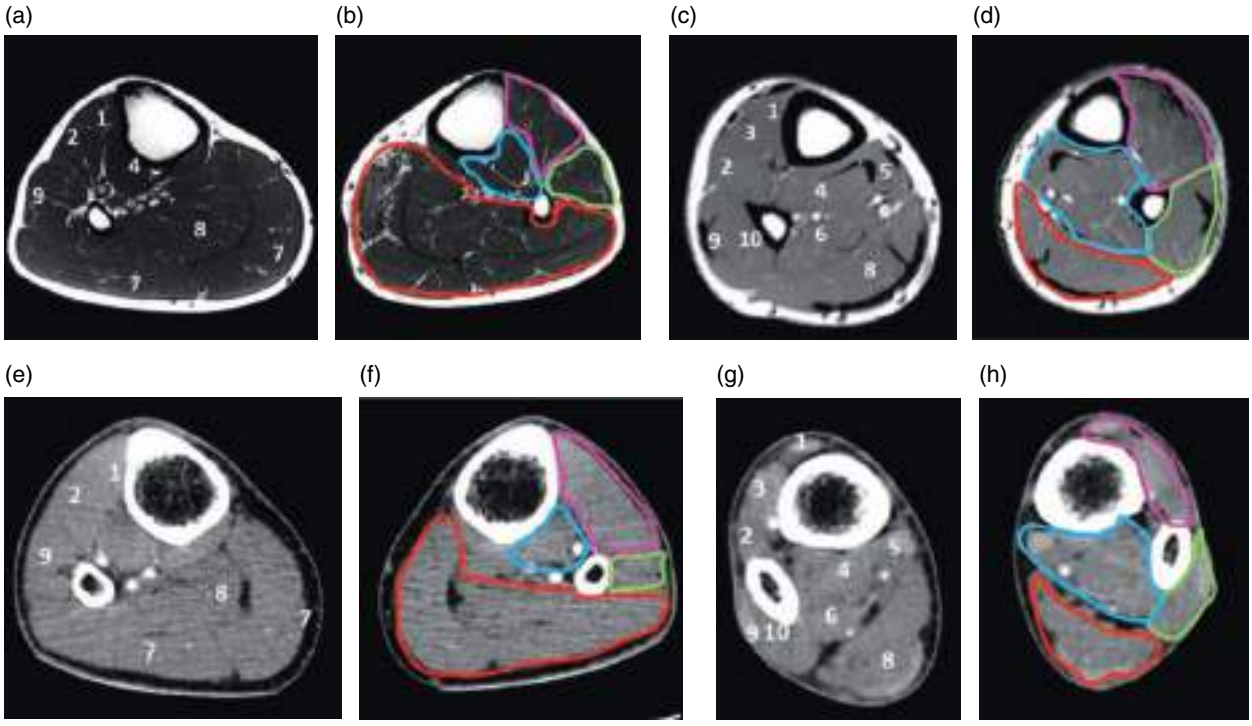

Figure 3.84 Compartments of the leg in MRI [(a and b) proximal and (c and d) distal] and in CT [(e and f) proximal and (g and h) distal]. The anterior compartment (pink) includes the tibialis anterior (1), extensor digitorum longus (2), and extensor hallucis longus (3) muscles. The tibialis posterior (4), flexor digitorum (5), and flexor hallucis longus (6) muscles lie in the deep posterior compartment (blue). The superficial posterior compartment (red) contains the gastrocnemius (7) and soleus (8) muscles (red). The peroneus longus (9) and brevis (10) make up the lateral compartment (green).

superficial posterior, and lateral (Figure 3.84). The anterior compartment contains the extensor muscles, including the tibialis anterior, extensor digitorum longus, and extensor hallucis longus muscles as well as the anterior tibial artery and vein, and the deep peroneal nerve. The anterior compartment is separated from the deep posterior compartment by the interosseous membrane. The tibialis posterior, flexor digitorum, and flexor hallucis longus muscles lie in the deep posterior compartment along with the posterior tibial and peroneal arteries and the posterior tibial nerve. The superficial posterior compartment contains the ankle dorsiflexors, including the gastrocnemius and soleus muscles, and the sural nerve. The peroneal muscles lie in the lateral compartment along with the common and superficial peroneal nerves. The anterior intermuscular septum separates the lateral anterior from the lateral compartment, and the posterior intermuscular septum separates the lateral and posterior compartments. The transverse intermuscular septum separates the musculature of the superficial and deep posterior compartments [105] (Figure 3.84).

The foot is divided into three compartments. The medial compartment contains the abductor hallucis and flexor hallucis brevis muscles. The flexor digitorum brevis, quadratus plantae, lumbrical, and adductor hallucis muscles lie in the central compartment. The lateral compartment contains the abductor digiti minimi and short flexor muscles.

Shoulder Girdle and Upper Limbs

The muscles and fasciae covering the dorsal scapula are considered a compartment. They include the infraspinatus, teres minor, and rhomboid muscles. The supraspinatus muscle is in a separate compartment. The axillary space is considered extra-compartmental [106].

The arm is composed of three compartments. The humerus is considered the bone compartment, while the soft tissues make up the other two compartments (anterior and posterior). The anterior compartment contains the biceps, brachialis, coracobrachialis, and brachioradialis muscles. The triceps muscule comprises the posterior compartment. The medial and lateral intermuscular septa, which attach to the humerus and to the brachial fascia, separate both compartments [106]

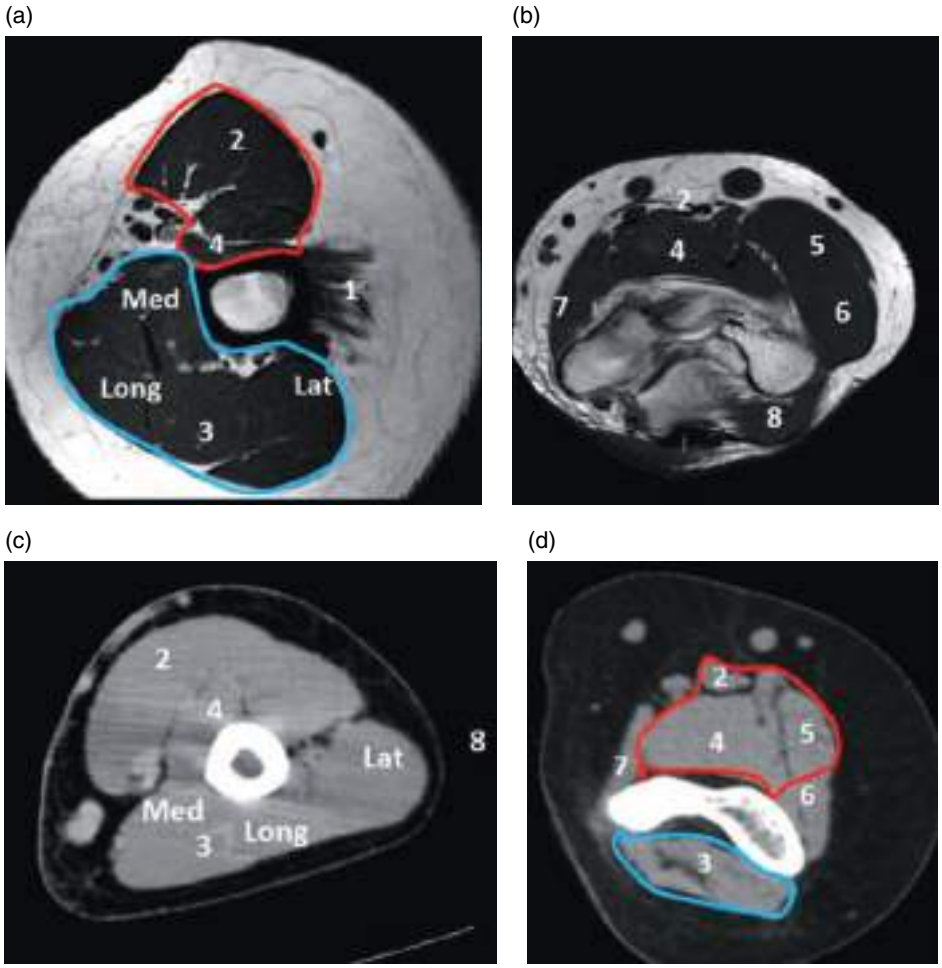

Figure 3.85 Arm compartments. Axial T1 MR sequence of the proximal (a) and distal (b) arms. CT scan of the proximal (c) and distal (d) arms. 1, deltoid; 2, biceps; 3, triceps (long, medial, and lateral heads); 4, brachialis; 5, brachioradialis; 6, extensor carpi radialis longus; 7, pronator teres; 8, anconeus; red, anterior compartment; blue, posterior compartment.

(Figure 3.85). The deltoid is not considered part of either the anterior or posterior arm compartments and occupies the abductor compartment of the shoulder girdle.

In the forearm, the radius and ulna comprise the osseous compartment, while the soft tissues make up two compartments (dorsal and volar). The dorsal compartment contains the extensor muscles; it is separated from the volar compartment by the interosseous membrane. Included superficial muscles are the extensor carpi radialis brevis and longus, extensor digitorum, extensor digiti minimi, and extensor carpi ulnaris. Included deep muscles are the abductor pollicis longus, extensor pollicis brevis, extensor pollicis longus, and extensor indicis. Supinator muscle and brachioradialis also belong to the dorsal compartment.

The flexor muscles are found in the volar compartment. It includes the pronator teres, flexor carpi radialis, palmaris longus, flexor digitorum superficialis, and flexor carpi ulnaris. Deeper volar muscles are separated from the superficial muscles by a transverse septum, including the flexor digitorum profundus, flexor pollicis longus, and the pronator quadratus, distally (Figure 3.86). Other staging systems consider a third compartment, the "mobile wad" or radial compartment of the forearm, composed of the brachioradialis muscle, extensor carpi radialis longus muscle, and extensor carpi radialis brevis muscle.

The palmar soft tissues of the hand are separated into multiple compartments but because they are so compact and have so many neurovascular communications, most lesions involving this region are considered extra-compartmental. The dorsal hand is considered extra-compartmental [106].

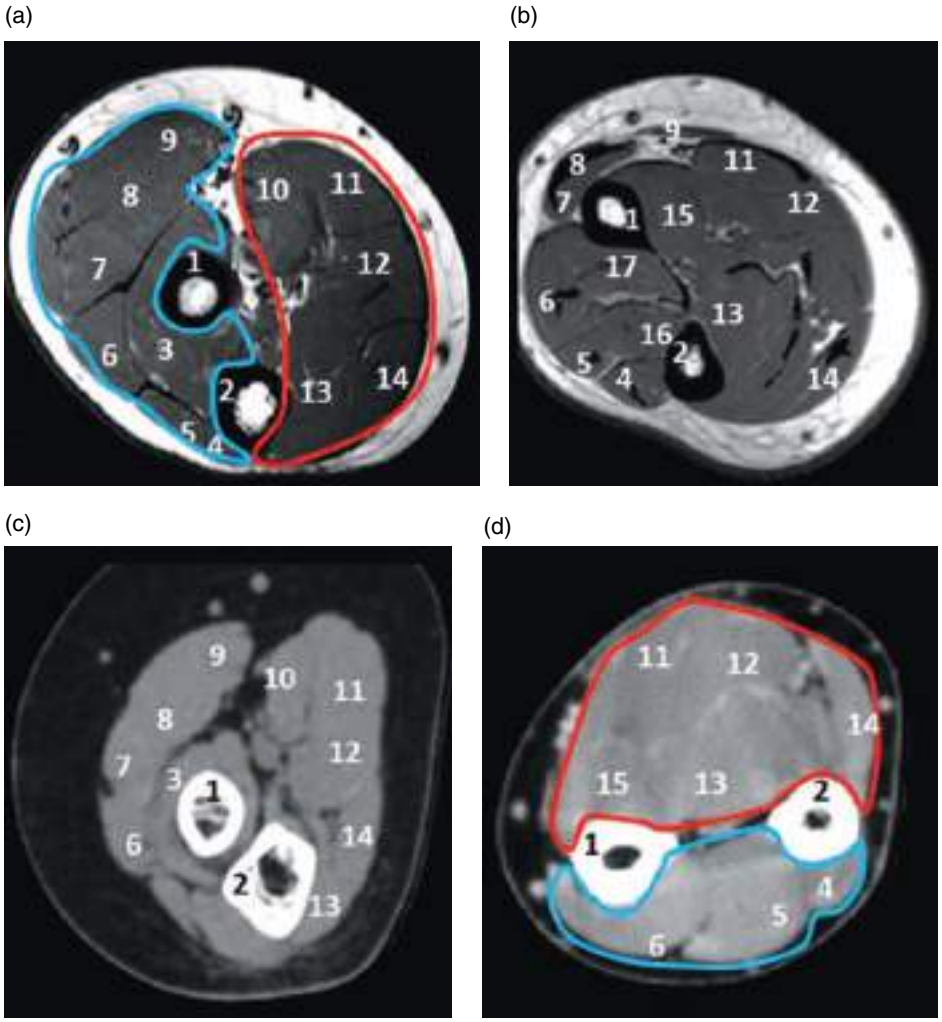

Figure 3.86 Forearm compartments. Axial T1 MR sequence of the proximal (a) and middle (b) forearms. CT scan of the proximal (c) and middle (d) forearms. 1, radius; 2, ulna; 3, supinator; 4, extensor carpi ulnaris; 5, extensor digiti minimi; 6, extensor digitorum; 7, extensor carpi radialis brevis; 8, extensor carpi radialis longus; 9, brachioradialis; 10, pronator teres; 11, flexor carpi radialis; 12, flexor digitorum superficialis; 13, flexor digitorum profundus; 14, flexor carpi radialis; 15, flexor pollicis longus; 16, extensor pollicis longus; 17, abductor pollicis longus and extensor pollicis brevis; red, anterior compartment; blue, posterior compartment.

References

1 Little, B.P. (2015). Approach to chest computed tomography. *Clin. Chest Med.* 36: 127–145.

2 Reguero Llorente, E. and Arauzo Álvarez, E. (2018). Conceptos básicos en la tomografía computarizada de tórax. *Medicina Respiratoria* 11 (1): 23–35.

3 West, A.T.H., Marshall, T.J., and Bearcroft, P.W. (2009). CT of the musculoskeletal system: what is left in the days of MRI? *Eur. Radiol.* 19: 152–164.

4 Goodpaster, B.H., Thaete, F.L., and Kelley, D.E. (2000). Composition of skeletal muscle evaluated with computed tomography. *Ann. N. Y. Acad. Sci.* 904: 18–24.

5 Ross, R. (2003). Advances in the application of imaging methods in applied and clinical physiology. *Acta Diabetol.* 40: S45–S50.

6 Santiago, F.R., García, M.C., Álvarez, L.G., and Moreno, M.T. (2011). Computed tomography and magnetic resonance imaging for painful spinal column: contributions and controversies. *Radiología* 53: 116–133.

7 Yeager, S. (2016). Neuroradiology of the brain. *Crit. Care Nurs. Clin. North Am.* 28 (1): 37–66. https://doi.org/10.1016/j.cnc.2015.10.003.

8 Tumani, H., Huss, A., and Bachhuber, F. (2017). The cerebrospinal fluid and barriers – anatomic and physiologic considerations. In: *Handbook of Clinical Neurology*, 1e (eds F. Deisenhammer, C. E. Teunissen, H. Tumani) vol. 146, 3–20. Elsevier. https://doi.org/10.1016/B978-0-12-804279-3.00002-2.

9 Pukenas, B. (2011). Normal brain anatomy on magnetic resonance imaging. *Magn. Reson. Imaging Clin. N. Am.* 19 (3): 429–437.

10 Smirniotopoulos, J.G., Murphy, F.M., Rushing, E.J. et al. (2007). Patterns of contrast enhancement in the brain and meninges. *Radiographics* 27 (2): 525–551.

11 Lerch, J.P., Van Der Kouwe, A.J.W., Raznahan, A. et al. (2017). Studying neuroanatomy using MRI. *Nat. Neurosci.* 20 (3): 314–326.

12 Casillo, S.M., Luy, D.D., and Goldschmidt, E. (2020). A history of the lobes of the brain. *World Neurosurg.* 134: 353–360. https://doi.org/10.1016/j.wneu.2019.10.155.

13 Talos, I.F., Mian, A.Z., Zou, K.H. et al. (2006). Magnetic resonance and the human brain: anatomy, function and metabolism. *Cell. Mol. Life Sci.* 63 (10): 1106–1124.

14 Campero, A., Ajler, P., Emmerich, J. et al. (2014). Brain sulci and gyri: a practical anatomical review. *J. Clin. Neurosci.* 21 (12): 2219–2225. https://doi.org/10.1016/j.jocn.2014.02.024.

15 Anderson, J.C., Costantino, M.M., and Stratford, T. (2004). Basal ganglia: anatomy, pathology, and imaging characteristics. *Curr. Probl. Diagn. Radiol.* 33 (1): 28–41.

16 Telford, R. and Vattoth, S. (2014). MR anatomy of deep brain nuclei with special reference to specific diseases and deep brain stimulation localization. *Neuroradiol. J.* 27 (1): 29–43.

17 Sciacca, S., Lynch, J., Davagnanam, I., and Barker, R. (2019). Midbrain, pons, and medulla: anatomy and syndromes. *Radiographics* 39 (4): 1110–1125.

18 Stratchko, L., Filatova, I., Agarwal, A., and Kanekar, S. (2016). The ventricular system of the brain: anatomy and normal variations. *Semin. Ultrasound CT MRI* 37 (2): 72–83. https://doi.org/10.1053/j.sult.2016.01.004.

19 Ric Harnsberger, H. (1995). *Handbook of Head and Neck Imaging*, 2e. Sant Luis, Missouri: Mosby.

20 Ric Harnsberger, H., Glastonbury, C.M., Michel, M.A. et al. (2011). *Diagnostico por la Imagen de Cabeza y Cuello*. Marban: Segunda Edición Madrid.

21 Som, P.M., Su Ann, N.G., Stuchen, C. et al. (2012). The MR imaging identification of the facial muscles and subcutaneous Musculoaponeurotic system. *Neurographics* 2 (1): 35–43.

22 Moreno, E.G. and Delago, M.J. (2012). Anatomia Simplificada del Cuello. In: *Radiología de Cabeza y Cuello. Actualizaciones SERAM* (ed. Sociedad Española de Radiologia Medica), 1–11. Madrid: Elsevier.

23 Mukherji, S.K. and Chong, V. (2004). *Atlas of Head and Neck Imaging*. Kew York: Thieme.

24 Dib, O., Chahinez, H., Asma, B. et al. (2017). *CT Anatomy of Paranasal Sinuses*. Viena: Eurpean Congress of Radiology. Educational Exhibit.

25 Padilla, I.G., DeFarias, L.D.P.G., Padilha, B.G. et al. (2012). Anatomical variations of paranasal sinuses at multislice computed tomography: what to look for?. European Congress of Radiology. Viena Educational Exhibit.

26 Vela, J.J.C., Martin, A.B.V., Muñiz, C.M. et al. *Hallazgos en imagen de la patología nasosinusal. Lo que el radiólogo general debe saber*. Granada: XXXI Congreso SERAM. Presentación electrónica educativa.

27 Nouraei, S.A.R., Elisay, A.R., DiMarco, A. et al. (2009). Variations in paranasal anatomy: implications for the pathophysiology or chronic Rhinosinusitis and safety of endoscopic sinus surgery. *J. Otolaryngol. Head Neck Surg.* 38 (1): 32–37.

28 Rodriguez, M., Vega Vigo, C.M., Ruiz, G.G. et al. *La patologia orbitaria en urgencias: Hallazgos radiológicos mediante TCMC*. Granada: XXXI Congreso SERAM. Presentación electrónica Educativa.

29 Georgouli, T., James, T., Tanner, S. et al. (2008). High-resolution microscopy coli MR-eye. *Eye (Lond.)* 22: 994–996.

30 Dobbs, N.W., Budak, M.J., White, R.D., and Zealley, I.A. (2020). MR-eye: high-resolution microscopy coil MRI for the assessment of the orbit and periorbital structures, Part 1. Technique and anatomy. *Am. J. Neuroradiol.* 41: 947–950.

31 Vikram, V., Verdini, D., and Ghoshhajra, B. (2011). Normal magnetic resonance imaging of the thorax. *Magn. Reson. Imaging Clin. N. Am.* 19: 489–506.

32 Webb, W.R. and Higgins, C.B. (2005). *Thoracic Imaging: Pulmonary and Cardiovascular Radiology*. Philadelphia: Lippincott Williams & Wilkins.

33 Naidich, D.P., Khouri, N.F., Scott, W.J. et al. (1981). Computed tomography of the pulmonary hila, 1: normal anatomy. *J. Comput. Assist. Tomogr.* 5: 459–467.

34 Naidich, D.P., Terry, P.B., Stitik, F.P., and Siegelman, S.S. (1980). Computed tomography of the bronchi. 1. Normal anatomy. *J. Comput. Assist. Tomogr.* 4: 746–753.

35 Park, C.K., Webb, W.R., and Klein, J.S. (1978). Inferior hilar window. *Radiology* 1991: 163–168.

36 Proto, A.V. and Rost, R.C. (1985). CT of the thorax: pitfalls in interpretation. *Radiographics* 5 (5): 736–738.

37 Zylak, C.J., Pallie, W., and Jackson, R. (1982). Correlative anatomy and computed tomography: a module on the mediastinum. *Radiographics* 2 (4) https://doi.org/10.1148/radiographics.2.4.555.

38 Proto, A.V. (1987). Mediastinal anatomy: emphasis on conventional images with anatomic and computed tomographic correlations. *J. Thorac. Imaging* 2: 1–48.

39 Whiting, P., Singatullina, N., and Rosser, J.H. (2015). Computed tomography of the chest: I. basic principles. *BJA Educ.* 15 (6): 299–304.

40 Smathers, R.L., Buschi, A.J., Pope, T.L. et al. (1982). The azygos arch: normal and pathologic CT appearance. *AJR Am. J. Roentgenol.* 139: 477–483.

41 Aquino, S.L., Duncan, G.R., and Hayman, L.A. (2001). Nerves of the thorax: atlas of normal and pathologic findings. *Radiographics* 21: 1275–1281.

42 O'Brien, J.P., Srichai, M.B. et al. (2007). Anatomy of the heart at multidetector CT: what the radiologist needs to know. *Radiographics* 27: 1569–1582.

43 Panicek, D.M., Benson, C.B. et al. (1988). The diaphragm: anatomic, pathologic, and radiologic considerations. *Radiographics* 8 (3): 385–425.

44 Abdel-Misih, S.R. and Bloomston, M. (2010). Liver anatomy. *Surg. Clin. North Am.* 90 (4): 643–653.

45 Pang, Y.Y. (2002). The Brisbane 2000 terminology of liver anatomy and resections. HPB 2000; 2:333-39. *HPB (Oxford)* 4 (2): 99; author reply -100. PubMed PMID: 18332933. Pubmed Central PMCID: 2020531.

46 Strasberg, S.M. and Phillips, C. (2013). Use and dissemination of the Brisbane 2000 nomenclature of liver anatomy and resections. *Ann. Surg.* 257 (3): 377–382. PubMed PMID: 22895397.

47 Mathew, R.P. and Venkatesh, S.K. (2018). Liver vascular anatomy: a refresher. *Abdom. Radiol. (NY)* 43 (8): 1886–1895. PubMed PMID: 29696320.

48 Catalano, O.A., Singh, A.H., Uppot, R.N. et al. (2008). Vascular and biliary variants in the liver: implications for liver surgery. *Radiographics* 28 (2): 359–378. PubMed PMID: 18349445.

49 Abou-Khalil, J.E. and Bertens, K.A. (2019). Embryology, anatomy, and imaging of the biliary tree. *Surg. Clin. North Am.* 99 (2): 163–174. PubMed PMID: 30846027.

50 Mortele, K.J., Rocha, T.C., Streeter, J.L., and Taylor, A.J. (2006). Multimodality imaging of pancreatic and biliary congenital anomalies. *Radiographics* 26 (3): 715–731. PubMed PMID: 16702450.

51 Keplinger, K.M. and Bloomston, M. (2014). Anatomy and embryology of the biliary tract. *Surg. Clin. North Am.* 94 (2): 203–217. PubMed PMID: 24679417.

52 Turner, M.A. and Fulcher, A.S. (2001). The cystic duct: normal anatomy and disease processes. *Radiographics* 21 (1): 3–22; questionnaire 288–94. PubMed PMID: 11158640.

53 Soybel, D.I. (2005). Anatomy and physiology of the stomach. *Surg. Clin. North Am.* 85 (5): 875–894, v. PubMed PMID: 16139026.

54 McNeeley, M.F., Lalwani, N., Dhakshina Moorthy, G. et al. (2014). Multimodality imaging of diseases of the duodenum. *Abdom. Imaging* 39 (6): 1330–1349. PubMed PMID: 24811767.

55 Kim, S.K., Cho, C.D., and Wojtowycz, A.R. (2008). The ligament of Treitz (the suspensory ligament of the duodenum): anatomic and radiographic correlation. *Abdom. Imaging* 33 (4): 395–397. PubMed PMID: 17653583.

56 Horton, K.M., Corl, F.M., and Fishman, E.K. (2000). CT evaluation of the colon: inflammatory disease. *Radiographics* 20 (2): 399–418. PubMed PMID: 10715339.

57 Iannaccone, R., Laghi, A., and Passariello, R. (2004). Multislice CT angiography of mesenteric vessels. *Abdom. Imaging* 29 (2): 146–152. PubMed PMID: 15290936.

58 Etchison, A., Menias, C.O., Ganeshan, D.M. et al. (2020). A review of anatomy, pathology, and disease spread in the perisplenic region. *Abdom. Radiol. (NY)* 46 https://doi.org/10.1007/s00261-020-02736-8. PubMed PMID: 32949273.

59 Tirkes, T., Sandrasegaran, K., Patel, A.A. et al. (2012). Peritoneal and retroperitoneal anatomy and its relevance for cross-sectional imaging. *Radiographics* 32 (2): 437–451. PubMed PMID: 22411941.

60 Wasnik, A.P., Maturen, K.E., Kaza, R.K. et al. (2015). Primary and secondary disease of the peritoneum and mesentery: review of anatomy and imaging features. *Abdom. Imaging* 40 (3): 626–642. PubMed PMID: 25189130.

61 Yoo, E., Kim, J.H., Kim, M.J. et al. (2007). Greater and lesser omenta: normal anatomy and pathologic processes. *Radiographics* 27 (3): 707–720. PubMed PMID: 17495288.

62 Wasnik, A.P., Mazza, M.B., Lalchandani, U.R., and Liu, P.S. (2011). Normal and variant abdominal anatomy on magnetic resonance imaging. *Magn. Reson. Imaging Clin. N. Am.* 19 (3): 521–545; viii. PubMed PMID: 21816329.

63 Akbar, S.A., Shirkhoda, A., and Jafri, S.Z. (2003). Normal variants and pitfalls in CT of the gastrointestinal and genitourinary tracts. *Abdom. Imaging* 28 (1): 115–128. PubMed PMID: 12483399.

64 Tuna, I.S. and Tatli, S. (2014). Contrast-enhanced CT and MR imaging of renal vessels. *Abdom. Imaging* 39 (4): 875–891. PubMed PMID: 24615510.

65 Bhargava, P., Dighe, M.K., Lee, J.H., and Wang, C. (2012). Multimodality imaging of ureteric disease. *Radiol. Clin. N. Am.* 50 (2): 271–299, vi. PubMed PMID: 22498443.

66 Wentland, A.L., Desser, T.S., Troxell, M.L., and Kamaya, A. (2019). Bladder cancer and its mimics: a sonographic pictorial review with CT/MR and histologic correlation. *Abdom. Radiol.* 44 (12): 3827–3842. PubMed PMID: 31676920.

67 Shinagare, A.B., Sadow, C.A., Sahni, V.A., and Silverman, S.G. (2011). Urinary bladder: normal appearance and mimics of malignancy at CT urography. *Cancer Imaging* 11: 100–118. PubMed PMID: 21771710. Pubmed Central PMCID: 3205759.

68 Wasnik, A.P., Mazza, M.B., and Liu, P.S. (2011). Normal and variant pelvic anatomy on MRI. *Magn. Reson. Imaging Clin. N. Am.* 19 (3): 547–566; viii. PubMed PMID: 21816330.

69 Allen, B.C. and Francis, I.R. (2015). Adrenal imaging and intervention. *Radiol. Clin. N. Am.* 53 (5): 1021–1035. PubMed PMID: 26321451.

70 Lattin, G.E. Jr., Sturgill, E.D., Tujo, C.A. et al. (2014). From the radiologic pathology archives: adrenal tumors and tumor-like conditions in the adult: radiologic-pathologic correlation. *Radiographics* 34 (3): 805–829. PubMed PMID: 24819798.

71 Coffin, A., Boulay-Coletta, I., Sebbag-Sfez, D., and Zins, M. (2015). Radioanatomy of the retroperitoneal space. *Diagn. Interv. Imaging* 96 (2): 171–186. PubMed PMID: 25547251.

72 Osman, S., Moshiri, M., Robinson, T.J. et al. (2015). Subperitoneal extension of disease processes between the chest, abdomen, and the pelvis. *Abdom. Imaging* 40 (6): 1858–1870. PubMed PMID: 25403702.

73 Paramasivam, S., Proietto, A., and Puvaneswary, M. (2006). Pelvic anatomy and MRI. *Best Pract. Res. Clin. Obstet. Gynaecol.* 20 (1): 3–22. PubMed PMID: 16275093.

74 Yitta, S., Hecht, E.M., Slywotzky, C.M., and Bennett, G.L. (2009). Added value of multiplanar reformation in the multidetector CT evaluation of the female pelvis: a pictorial review. *Radiographics* 29 (7): 1987–2003. PubMed PMID: 19926758.

75 Saksouk, F.A. and Johnson, S.C. (2004). Recognition of the ovaries and ovarian origin of pelvic masses with CT. *Radiographics* 24 (Suppl. 1): S133–S146. PubMed PMID: 15486237.

76 Revzin, M.V., Moshiri, M., Katz, D.S. et al. (2020). Imaging evaluation of fallopian tubes and related disease: a primer for radiologists. *Radiographics* 40 (5): 1473–1501. PubMed PMID: 32822282.

77 Gui, B., Valentini, A.L., Ninivaggi, V. et al. (2014). Deep pelvic endometriosis: don't forget round ligaments. Review of anatomy, clinical characteristics, and MR imaging features. *Abdom. Imaging* 39 (3): 622–632. PubMed PMID: 24557639.

78 Ayuso Colella, J.R., Pages Llinas, M., and Ayuso, C.C. (2010). Staging rectal cancer. *Radiologia* 52 (1): 18–29. PubMed PMID: 20022073. Estadificacion del cancer de recto.

79 Erden, A. (2018). MRI of anal canal: normal anatomy, imaging protocol, and perianal fistulas: Part 1. *Abdom. Radiol.* 43 (6): 1334–1352. PubMed PMID: 28840368.

80 Yacoub, J.H. and Oto, A. (2018). MR imaging of prostate zonal anatomy. *Radiol. Clin. N. Am.* 56 (2): 197–209. PubMed PMID: 29420976.

81 Kim, S.W., Kim, H.C., Yang, D.M., and Min, G.E. (2013). The prevesical space: anatomical review and pathological conditions. *Clin. Radiol.* 68 (7): 733–740. PubMed PMID: 23465701.

82 Asakage, N. (2018). Paradigm shift regarding the transversalis fascia, preperitoneal space, and Retzius' space. *Hernia* 22 (3): 499–506. PubMed PMID: 29488129.

83 Luk, L. and Taffel, M.T. (2020). Cross-sectional anatomy of the male pelvis. *Abdom. Radiol.* 45 (7): 1951–1960. PubMed PMID: 31919648.

84 Wigh, R.E. (1980). The thoracolumbar and lumbosacral transitional junctions. *Spine (Phila Pa 1976)* 5 (3): 215–222.

85 Ruiz Santiago, F., Láinez Ramos-Bossini, A.J., Wáng, Y.X., and López, Z.D. (2020). The role of radiography in the study of spinal disorders. *Quant. Imaging Med. Surg.* 10 (12): 2322–2355.

86 Schreiber, J.J., Anderson, P.A., Rosas, H.G. et al. (2011). Hounsfield units for assessing bone mineral density and strength: a tool for osteoporosis management. *J. Bone Joint Surg. Am.* 93: 1057–1063.

87 Alyas, F., Saifuddin, A., and Connel, D. (2007). MR imaging evaluation of the bone marrow and marrow infiltrative disorders of the lumbar spine. *Magn. Reson. Imaging Clin. N. Am.* 15: 199–219.

88 Grenier, J.-M. and Wessely, M.A. (2007). Magnetic resonance imaging of the spinal cord. *Clin. Chiropr.* 10: 205–217.

89 Nguyen, C., Sanchez, K., Roren, A. et al. (2016). Anatomical specificities of the degenerated cervical spine: a narrative review of clinical implications, with special focus on targeted spinal injections. *Ann. Phys. Rehabil. Med.* 59: 276–281.

90 Songa, M.S., Leea, H.J., Kima, J.T. et al. (2017). Ponticulus posticus: morphometric analysis and its anatomical implications for occipito-cervical fusion. *Clin. Neurol. Neurosurg.* 157: 76–81.

91 Smoker, W.R. (1994). Craniovertebral junction: normal anatomy, craniometry, and congenital anomalies. *Radiographics* 14 (2): 255–277.

92 Akobo, S., Rizk, E., Loukas, M. et al. (2015). The odontoid process: a comprehensive review of its anatomy, embryology, and variations. *Childs Nerv. Syst.* 31: 2025–2034.

93 Lee, T.H., Kim, S.J., and Chung, I.H. (2012). Morphometrical study of uncinate processes and vertebral body of cervical spine. *J. Korean Neurosurg. Soc.* 51: 247–252.

94 Mills, M.K. and Shah, L.M. (2015). Imaging of the perivertebral space. *Radiol Clin. NA.* 53 (1): 163–180.

95 Fenart, R. (2008). Considerations on the phylogeny of the axial skeleton. *J. Dentofacial Anom. Orthod.* 11: 138–153.

96 Bierry, G., Kremer, S., Kellner, F. et al. (2008). Disorders of paravertebral lumbar muscles: from pathology to cross-sectional imaging. *Skelet. Radiol.* 37: 967–977.

97 Lee, C.K., Rauschning, W., and Glenn, W. (1988). Lateral lumbar spinal canal stenosis: classification, pathologic anatomy, and surgical decompression. *Spine (Phila Pa 1976)* 13: 313–320.

98 Lee, S.Y., Kim, T.H., Oh, J.K. et al. (2015). Lumbar stenosis: a recent update by review of literature. *Asian Spine J.* 9 (5): 818–828.

99 Anderson, M.W., Temple, H.T., Dussault, R. et al. (1999). Compartmental anatomy: relevance to staging and biopsy of musculoskeletal tumors. *AJR* 173: 1663–1671.

100 Enneking, W.F., Spanier, S.S., and Goodman, M.A. (2003). A system for the surgical staging of musculoskeletal sarcoma, 1980. *Clin. Orthop. Relat. Res.* 415: 4–18.

101 Scheinfeld, M.H., Dym, A.A., Spektor, M. et al. (2015). Acetabular fractures: what radiologists should know and how 3D CT can aid classification. *Radiographics* 35: 555–577.

102 ElNahal, W.A., Abdel Karim, M., Khaled, S.A. et al. (2018). Quadrilateral plate fractures of the acetabulum: proposition for a novel classification system. *Injury* 49: 296–301.

103 Jesse, M.K., Petersen, B., Strickland, C. et al. (2013). Normal anatomy and imaging of the hip: emphasis on impingement assessment. *Semin. Musculoskelet. Radiol.* 17: 229–247.

104 Bosch, U. and Tscherne, H. (1992). The pelvic compartment syndrome. *Arch. Orthop. Trauma Surg.* 111: 314–317.

105 Toomayan, G., Robertson, F., and Major, N. (2005). Lower extremity compartmental anatomy: clinical relevance to radiologists. *Skelet. Radiol.* 34: 307–313.

106 Toomayan, G.A., Robertson, F., Major, N.M., and Brigman, B.E. (2006). Upper extremity compartmental anatomy: clinical relevance to radiologists. *Skelet. Radiol.* 35: 195–201.

Apéndice 2. **Capítulo de libro sobre la implementación de tecnologías de impresión 3D para el estudio de la anatomía normal y patológica de la columna vertebral.** Reproducido con permiso de la editorial Dykinson. Referencia completa: Láinez Ramos-Bossini AJ, Láinez Millán B, Redruello Guerrero P, Prados Salazar JC. Implementation of novel technologies for teaching and learning normal and pathological anatomy of the spine. From medical imaging to 3D printing. En: Innovación en educación: investigaciones, reflexiones y propuestas de actuación. Editorial Dykinson. ISBN 978-84-1377-640-8. 2021; 944-966.

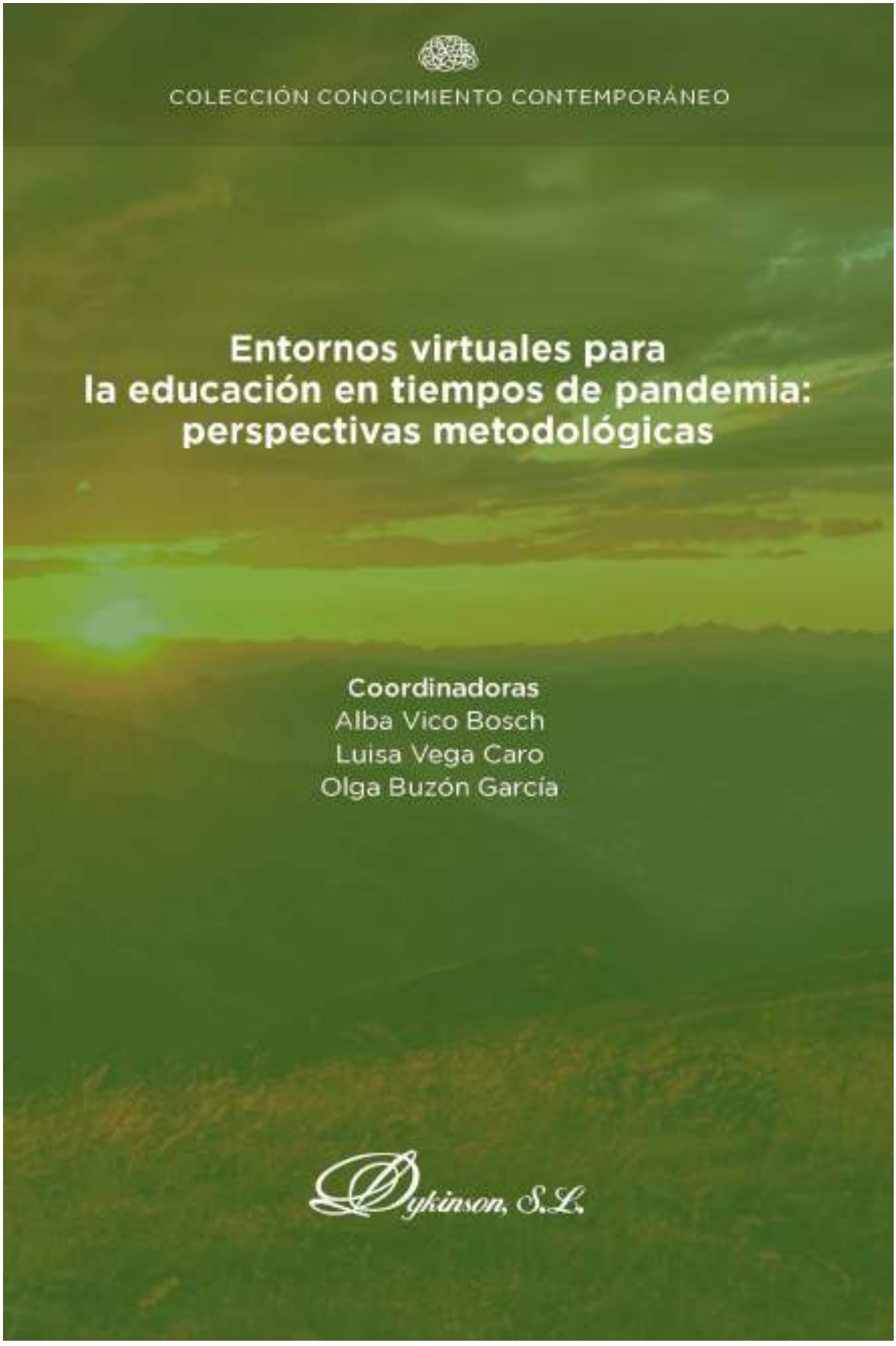
COLECCIÓN CONOCIMIENTO CONTEMPORÁNEO
Entornos virtuales para la educación en tiempos de pandemia: perspectivas metodológicas
Coordinadoras
Alba Vico Bosch
Luisa Vega Caro
Olga Buzón García
Dykinson, S.L.

ENTORNOS VIRTUALES PARA LA EDUCACIÓN EN TIEMPOS DE PANDEMIA: PERSPECTIVAS METODOLÓGICAS

ENTORNOS VIRTUALES PARA LA EDUCACIÓN EN TIEMPOS DE PANDEMIA: PERSPECTIVAS METODOLÓGICAS

Coordinadoras

ALBA VICO BOSCH
LUISA VEGA CARO
OLGA BUZÓN GARCÍA

Dykinson, S.L.

2021

CAPÍTULO 42

IMPLEMENTATION OF NOVEL TECHNOLOGIES FOR TEACHING AND LEARNING NORMAL AND PATHOLOGICAL ANATOMY OF THE SPINE. FROM MEDICAL IMAGING TO 3D PRINTING

ANTONIO JESÚS LÁINEZ RAMOS-BOSSINI
Hospital Universitario Virgen de las Nieves
Granada, Spain

BÁRBARA LÁINEZ MILLÁN
School of Medicine.
University of Glasgow, Scotland

PABLO REDRUELLO GUERRERO
Departamento de Anatomía y Embriología Humana.
Facultad de Medicina. Universidad de Granada, España

JOSÉ CARLOS PRADOS SALAZAR
Departamento de Anatomía y Embriología Humana.
Facultad de Medicina. Universidad de Granada, España

1. INTRODUCTION

Spatial understanding of 3D anatomy from 2D images is usually difficult for undergraduate medical students, probably due to limitations in the ability to rotate static 2D illustrations, which are the cornerstone of traditional ways of learning anatomy in university curricula (Triepels et al., 2020). These limitations may translate into problems in recognizing anatomy in the clinical setting (Saltarelli et al., 2014). In addition, knowledge of skeletal anatomy is a fundamental aspect in the educational curriculum of undergraduate medical students (Wu et al., 2018). However, this topic often receives insufficient allocation of time throughout the medical program and there are variable opinions on which aspects are of the essence for medical students, motivating different authors to determine which knowledge is core in this field (Webb et al., 2019). Efforts are still needed to reach international consensus on

the relevance of musculoskeletal contents at undergraduate levels. Moreover, theoretical knowledge needs to be complemented by practical skills, particularly in medicine, thus medical schools should find ways to successfully transfer neuromusculoskeletal knowledge to clinical practice(González Blum et al., 2020). In our experience, the vertebral column is one of the most complex anatomical regions to understand, both in normal and pathologic conditions, due to the intrinsic particularities in terms of bone morphology, joints, ligaments, biomechanics, and pathologies.

In fact, although students usually learn the key characteristics of pathologies of the vertebral column, for instance, osteoarthritis, they rarely obtain the opportunity to visualize this process using clinical data from real-life patients to form 3D models of pathological anatomy. Advanced medical imaging and 3D printing technology allow students to consolidate basic anatomical knowledge relating to the spine and relate this to the susceptibility of different areas of the vertebral column to conditions such as osteoarthritis or a prolapsed intervertebral disc. Moreover, 3D models could help students differentiate between similar conditions; given that enthesophytes, osteophytes and ankylosing spondylitis can appear similar on radiographs, a 3D model can highlight key features used for their identification.

The COVID-19 pandemic has also emphasized the need for a combination of different learning approaches to take full advantage of the benefits of each methodology whilst simultaneously compensating for individual limitations. Furthermore, blended learning techniques make anatomy teaching more accessible to students everywhere, allowing them to obtain specific knowledge regarding normal and pathological conditions of the spine outside of a stereotypical setting, i.e. a classroom or dissecting room, without compromising learning. Students should be able to access this information by themselves to consolidate their knowledge and help them develop the spatial navigation skills which will be crucial in clinical practice, specifically appreciating the importance of the position of certain structures relative to others, a necessary skill for the procedural training which will take place during the clinical years of their education.

1.1. Emerging technologies for anatomy teaching: Medical imaging

Over the past decades, innovations in computer technology have radically transformed the practices of anatomical education and research (Trelease, 2016). Currently, a wide spectrum of radiologic technologies are available, allowing the construction, presentation, clinical application, and educational potential of medical imaging including multiplanar reformats, minimum intensity projections, segmentation, volume-rendering, surface-rendering, fly-throughs, virtual endoscopy, angiography, and cine-loops (Tam, 2010). Of particular interest for advanced anatomy learning is the possibility of generating Statistical 3D Shape Models based on collections of volume rendering models, allowing ‘a new kind of anatomy’ that facilitates both quantitative analysis of anatomical variation and educational visualization (Ambellan et al., 2019). With these significant advances in imaging technology, some argue that dissection anatomy is outdated and labor-intensive, whereas three-dimensional images are more accessible and time-effective for today's students (Day & Ahn, 2010).

The emergence of dynamic visualizations of 3D models in anatomy curricula may be an adequate solution for visuo-spatial difficulties encountered with traditional static learning, as they provide direct visualization of change throughout the viewpoints (Berney et al., 2015). Moreover, the importance of medical imaging is not limited to anatomy learning in theoretical terms, but it is a core skill for medical practice. In fact, a study by Orsbon et al. in which 93 physicians were surveyed on their opinion on what anatomical knowledge is most relevant in their practice, it was found that medical imaging was considered highly important compared to other anatomic contents such as embryology or lymphatic anatomy (Orsbon et al., 2014). The increasing sophistication with which radiology can depict the human body, combined with electronic availability of the resulting images, has been advocated to have a significant role in anatomy teaching (Miles, 2005), and modern pregraduate curricula should count on radiology for improving normal anatomy, pathology and clinical diagnosis (Kainberger & Kletter, 2007). Not only may advanced medical imaging impact the spatial

anatomy knowledge, but it has also been found to be preferred by students over traditional learning methods (Tan et al., 2012).

1.2. Emerging technologies for anatomy teaching: 3D printing

The teaching of human anatomy is undergoing significant changes in recent years due to the impact of medical imaging technologies and the development of 3D printing techniques, among other factors (15). In the last decade, remarkable improvements in 3D printing technologies have made it possible to distribute them to an increasingly wide audience due to factors such as lower costs, simplification of the assembly process and increasingly intuitive software development. 3D printing techniques were introduced into the medical and biomedical fields in 2000 and have potential value in clinical practice (3,16). Different technologies are currently available for 3D printing applied to medical education, including stereolithography, selective laser sintering and fused deposition modeling (17). Among the different applications of these technologies, surgical planning stands out, where 3D models have shown enormous utility in addressing infrequent pathologies such as Eagle's syndrome (18), congenital cardiac pathologies (19), various kidney pathologies (20) or in highly complex surgeries such as the separation of Siamese twins (21). Likewise, models have been used for other procedures such as intra-cavitary brachytherapy (22) and it is being evaluated in different populations, paying special attention to pediatric age (23). In addition, various ad hoc models have been developed to train resident physicians in specific procedures. For example, Odom et al. developed a homemade spinal model for simulation to teach ultrasound guidance for lumbar puncture (24). Similarly, specific models have been printed for fine needle thyroid puncture practices (25) and for early learning in interventional cardiology (26). All of the above is extremely useful for clinical practice, especially in advanced stages of specialized training.

1.3. Introducing advanced medical imaging and 3D printing technologies in our institution

Despite the undoubted usefulness of advanced medical imaging technologies and 3D printing in the teaching of human anatomy, the reality is that most universities in Spain are still established in traditional teaching models focused on the use of illustrations and cadaveric dissection. Among the causes that limit the introduction of new advanced technologies, it is worth highlighting the decreasing number of radiology specialists involved in the teaching of Human Anatomy, which is due to different reasons (high clinical care pressure, little recognition of the role of the radiologist in the university , expansion of access to teaching human anatomy to professionals without medical training such as biologists or pharmacologists, etc.); the need for a cohesive multidisciplinary team for the proper use of 3D printing technologies (engineering and medical imaging); or the reluctance of teachers to modify their teaching guidelines.

In addition, the COVID-19 pandemic has generated an unprecedented situation in modern education in our country and its impact on the face-to-face teaching paradigm has required a joint effort to implement effective online learning measures. This is especially important in subjects whose idiosyncrasies require the use of materials or other physical elements that are difficult to access, such as in anatomy practices where access to dissection rooms has been impossible.

Within the framework of the teaching innovation project “Design and 3D printing of anatomical models using radiological imaging techniques and artificial intelligence for medical education” led by our research team at the University of Granada, we have specifically addressed this problem in the Medical Degree. To do so, we have implemented an innovative teaching system using medical imaging examinations and 3D printed models.

2. OBJECTIVES

Under the assumption that advanced medical imaging and 3D printing technologies offer a significant improvement in undergraduate teaching in terms of academic performance and student satisfaction, the aim of this work is to present the proposed teaching methodology and the results of this initial experience in a selected cohort of undergraduate medical students,

3. METHODS

We have developed a field study to introduce advanced medical imaging and 3D printing technologies as accessory tools for learning human anatomy. To do this, we designed three paradigms of learning both for the normal and pathologic spine: ideal anatomical models of the spine, using traditional 2D illustrations and interactive 3D models available in our practice room; medical imaging examinations (computed tomography and magnetic resonance imaging); and 3D printed models. Regarding the latter learning method, normal and pathologic spine models were 3D printed from digital models available in open online resources such as Thingiverse and medical image segmentation, respectively. For image segmentation, 3D Slicer was used, and posterior 3D modeling was performed with MeshMixer (Autodesk®). The models were 3D printed in Bibo 2 Dual Laser (Bibo®), Ender 3 Pro and Creality LD-002h (Creality®) 3D printers. Figure 1 shows the steps followed throughout the process of 3D printing, and figures 2 to 5 show examples of each of these learning paradigms.

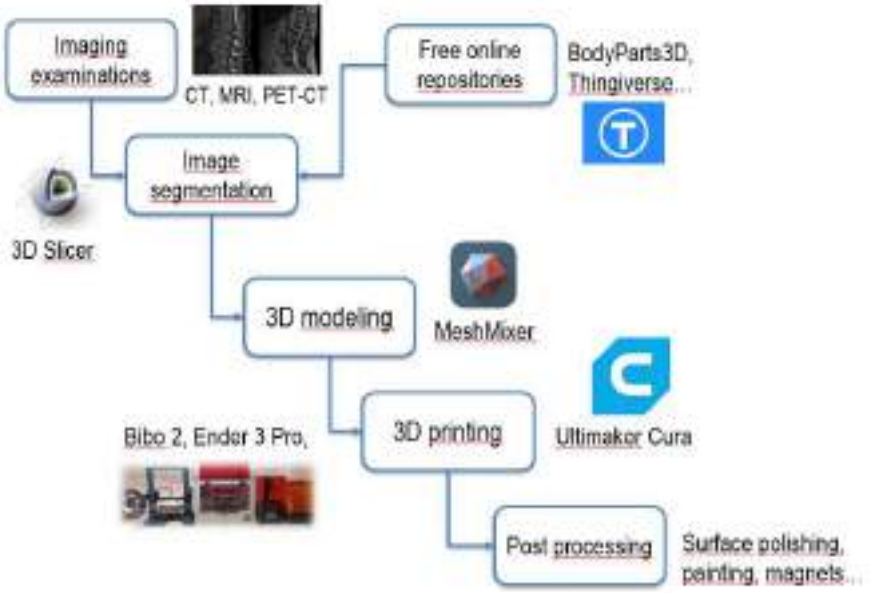

FIGURE 1. Flow diagram of the steps followed to 3D printing anatomical models in the study.

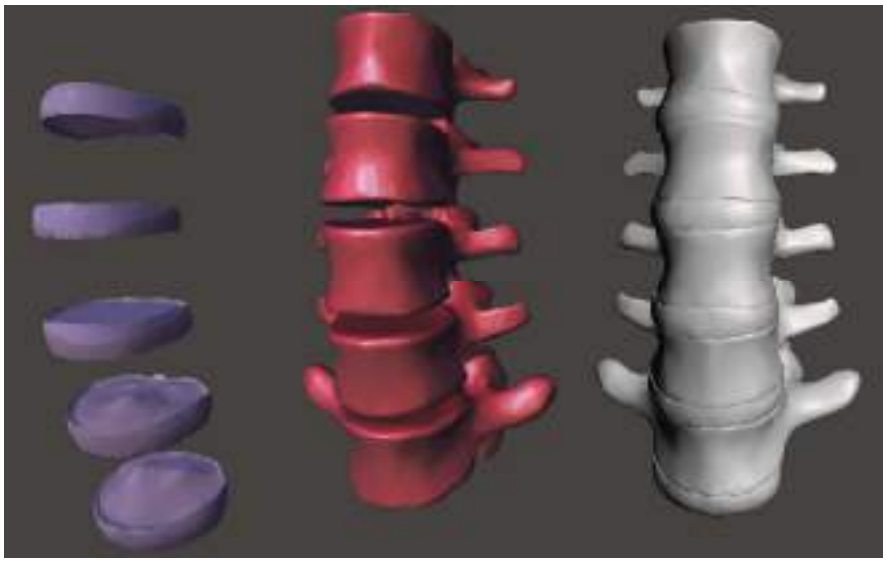

FIGURE 2. Example of interactive 3D models used as learning paradigm for spinal anatomy teaching using MeshMixer (AutoDesk®).

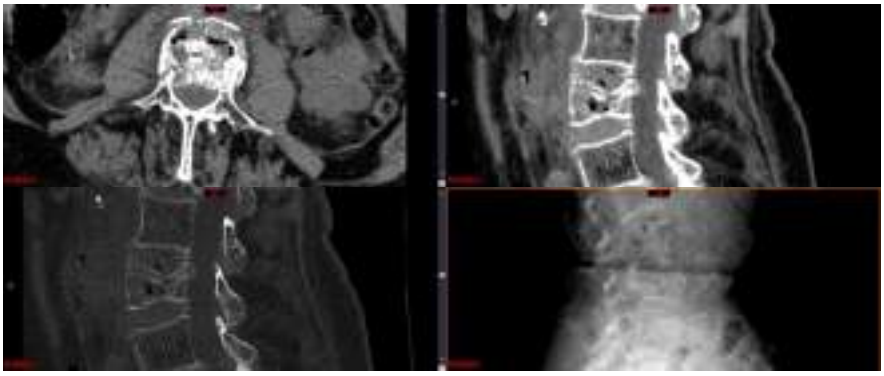

FIGURE 3. Example of computed tomography images and plain radiography used as learning paradigm for spinal anatomy teaching using the advanced Carestream viewer (Philips®).

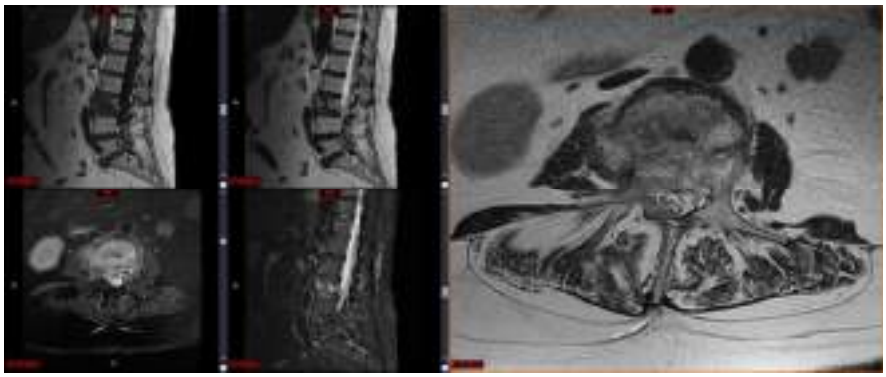

FIGURE 4. Example of computed tomography images and plain radiography used as learning paradigm for spinal anatomy teaching using the advanced Carestream viewer (Philips®).

FIGURE 5. Example of 3D printed models of the spine used as learning paradigm for spinal anatomy teaching. The models were printed using the Bibo 2 Dual Extrusion 3D printer.

Twenty undergraduate medical students were offered each of these different models to learn basic concepts relating to the normal and pathologic spine. After the learning period, students were examined by a short multiple-choice test on spinal anatomy containing 20 questions with 4 possible answers and only 1 correct answer. Some examples of questions from the test are the following:

1. With regard to the joints of the spine and their ligaments, it is true that:

A. The posterior longitudinal ligament lies dorsal to the vertebrae

B. The spinal canal is located between the anterior and posterior longitudinal ligaments

C. The anterior longitudinal ligament holds the odontoid process in place

D. The joints between transverse processes are pivot joints

E. Zygapophyseal joints become more congruent as the vertebral column descends

2. With regard to the degeneration of the spine, it is true that:

A. The formation of anterior osteophytes is rare

B. Herniated intervertebral discs are more common in the thoracic segment than in the lumbar segment

C. The anteroposterior diameter of the spinal canal is usually decreased in degenerative spine conditions

D. Scoliosis is a typical degenerative pathology of the spine

E. Osteoporotic vertebral fractures are more common in men than in women

The number of correct answers was compared with that of another group of 20 medical students matched by academic year and sex, who had been subject to conventional learning on spine anatomy. For each question, the rate of correct answers was compared between both groups. In addition, overall differences between students who passed the test were compared (cut-off point: at least 12 correct answers). Chi-squared test was applied (or Fisher's exact test if the conditional criteria for the former were not met). P-values <.05 were considered significant. Statistical analyses were performed using the SPSS version 23.0 software. Figure 6 shows the flow diagram of the study.

FIGURE 6. Flow diagram of the study.

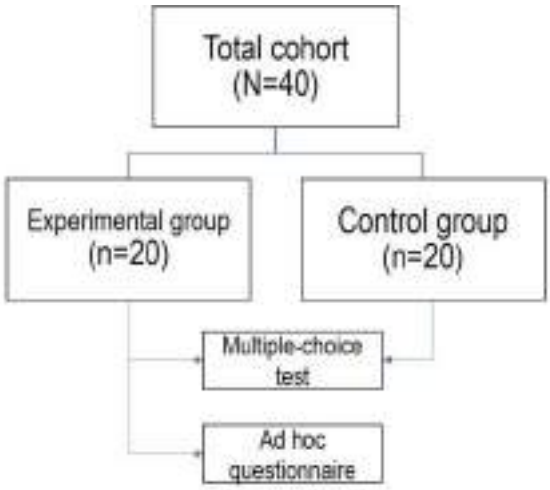

Finally, a short ad hoc questionnaire designed by the professors based on their experience and feedback of students from the experimental group was used to assess the overall satisfaction with each method. In particular, the questionnaire included the following questions.

- Please rate from 0 (none) to 10 (maximum) your satisfaction with the illustration-based teaching you have received and the plastic 3D models you have used.
- Please rate from 0 (none) to 10 (maximum) your satisfaction with the advanced medical imaging-based teaching you have used.
- Please rate from 0 (none) to 10 (maximum) your satisfaction with teaching using models obtained through 3D printing.
- In addition, 10 open questions on the advantages and limitations of the learning methodology were recorded. Open questions included the following:
- What advantages do you consider that illustrations and 3D plastic models have in the teaching of Human Anatomy?

– What limitations do you consider that illustrations and 3D plastic models have in the teaching of Human Anatomy?

– Do you think that the anatomical knowledge that you have obtained through the use of illustrations and 3D plastic models will be useful in your professional future? Please state the reasons for your answer

– What advantages do you consider that medical imaging has in the teaching of Human Anatomy?

– What limitations do you consider that medical imaging has in the teaching of Human Anatomy?

– Do you think that the anatomical knowledge that you have obtained through the use of medical imaging will be useful in your professional future? Please state the reasons for your answer.

– What advantages do you consider that 3D printing has in the teaching of Human Anatomy?

– What limitations do you consider that 3D printing has in the teaching of Human Anatomy?

– Do you think that the anatomical knowledge that you have obtained through the use of medical imaging will be useful in your professional future? Please state the reasons for your answer.

– Which suggestions would you give us to improve the quality of practical teaching in Human Anatomy?

4. RESULTS

Both groups were comparable in terms of age, sex and average Anatomy grades. The characteristics of students in both groups are shown in **Table 1**.

TABLE 1. Characteristics of experimental and control groups. Results are expressed as mean (standard deviation).

Variable	Group 1 (experimental)	Group 2 (control)	P-value
Age	20 (2.15)	20.25 (3.57)	.58
Sex distribution (% women)	70	60	.44
Average Anatomy grades (0-10)	7.71 (1.26)	8.05 (1.18)	.81

The group of students exposed to our methodology showed a greater number of correct answers in the multiple-choice test, reaching statistical significance in 8 questions. However, the rate of students who passed the test did not significantly differ between both. **Table 2** shows the results of multiple choice test in both groups.

*Table 2. Rate of correct answers in each group. *Significant p-value.*

Question	Group 1	Group 2	P-value
1	15	13	.49
2	16	16	1
3	18	15	.21
4	20	16	.04*
5	18	14	.11
6	5	1	.08
7	10	3	.02*
8	14	8	0.6
9	19	14	.04
10	10	8	.53
11	18	15	.21
12	15	13	.49
13	18	18	1
14	18	10	.01*
15	16	8	.01*
16	19	12	.01*
17	17	13	.14
18	19	10	.001*
19	17	10	.02*
20	17	8	.003*
Rate of students who passed	16	11	.09

Regarding the ad hoc questionnaire, the overall satisfaction with each method was higher with the use of medical imaging, followed by 3D printing technologies (table 3).

TABLE 3. Overall satisfaction with each learning paradigm in the experimental group. Data are presented as mean (standard deviation).

Method	**Satisfaction**
Illustrations and plastic 3D models	6.1 (2)
Advanced medical imaging	9.3 (0.8)
3D printing technologies	8.8 (0.8)

Open answers on the followed methodology also showed that students were very satisfied with the use of advanced medical imaging and 3D-printed models in learning, as they helped depict examples of specific pathologies, including osteoarthritis or vertebral fractures.

The main limitations regarding the use of illustrations were the difficulties in visualizing the 3D rotation of the spine, whereas 3D plastic models were considered to be stereotypical and not able to show spinal pathologies. Regarding medical imaging technologies, several students highlighted that they lacked knowledge on the fundamentals of magnetic resonance imaging so that they felt that they could not adequately interpret some findings on the images. Finally, the main limitations of 3D printing technologies were the relatively low representativeness of 3D printed models for non-bony conditions, and the need to understand basic concepts of medical imaging examinations.

5. DISCUSSION

The increasing development of advanced medical imaging modalities along with emergent technologies such as 3D printing is transforming the ways in which medical education is implemented throughout different environments and contexts, including undergraduate university curricula, Masters' and PhD programs, and medical residency programs.

Although cadaveric dissection is considered the gold standard for teaching anatomy, an increasing number of 3D visualization methods for teaching anatomy are being developed, among other factors due to the limited availability of cadavers, the high costs associated with their maintenance, and the ethical debate surrounding the use of cadavers (Ghosh, 2017; Triepels et al., 2020). Conversely, 3D printing techniques applied to medical education are less expensive and customizable in nature (Casciato et al., 2018). In fact, a meta-analysis by Yammine and Violato concluded that the use of a 3D tool resulted in greater knowledge of spatial anatomy in comparison with traditional methods (Yammine & Violato, 2015) as students can physically observe and manipulate the 3D topographic features.

It has been hypothesized that 3D printed materials allow students to visualize structures in unique ways, enabling them to consolidate their understanding of complex human anatomy, such as that of vertebrae, emphasizing the importance of nearby structures through superimposition. 3D printing is therefore useful when building training simulators, which have a unique quality in that they are able to imitate tissues in the human body so students can become acclimated to the anatomical landmarks which are crucial for successful execution of clinical procedures; this is a practical experience which they cannot obtain from textbooks.

Chen et al. conducted a RCT in which 79 junior medical students were randomised into three groups, using 3D-printed skulls, cadaveric skulls and atlas, respectively, to study basicranial structures via an introductory lecture and a self-directed learning session (Chen et al., 2017). Several damaged structures were found in the cadaveric skulls as well as the 3D models, but the latter were repaired using digital software. The

3D models provided a detailed anatomical information of the skull and each section of the skull bone was coloured differently to aid in anatomical education and minimize the differences between interventions. There were no statistical differences in the pre-test scores, however, the 3D group's performance was superior in the post-test (combination of theory and laboratory tests). The author attributed the fact that the 3D group performed better to the structural variation and damaged structures in the cadavers. The use of colour in the specimens may have also been a contributing factor to the success of the 3D models. Furthermore, this study argues in favour of the sustainability of 3D printing in the context of anatomy teaching, as the printer cost $500 and the raw materials cost $14, reducing expenses significantly in the long-term.

3D printed models enable direct interaction with the content, which aids in the promotion of "deep learning" and helps students apply these concepts to clinical practice, once again highlighting how 3D printing is essential when training students in specialties which rely heavily on extensive anatomical knowledge, including surgery, histopathology and radiology. Indeed, surveys given to a sample of medical students and surgeons reveal that they all shared the opinion that 3D models would be beneficial in medical education and should be integrated into medical school curricula (Yuen, 2020).

An important factor in learning is student engagement and attention, which can vary throughout lectures, but visual aids and active learning methods have shown promise in helping teachers maintain students' attention on the content, ultimately facilitating the recollection of information. These arguments support the positive influences of 3D models om educational outcomes compared to traditional learning methodologies.

In addition, 3D prints allow students to study increasingly complex pathologies of the spine, observing their progression over time. Hence, clinical knowledge can be obtained via a scaffolding approach in a "spiral curriculum". Such techniques can be utilized in teaching modalities such as small-group problem-based learning, especially since small-group learning provides higher efficiency than anatomy lectures. Teachers must make use of a wide range of resources to ensure that the

desired learning outcomes are met; to accomplish this task, it is necessary to create a learning environment containing appropriate educational activities to achieve certain outcomes. In terms of teaching anatomy, students must obtain an integrated view and understanding of 3D structures, which are also essential in comprehending the function of organs, also indirectly contributing to the teaching of physiology. 3D-printed models hold the potential to ensure that this process is productive and tailored to student needs, as they can easily use them to take part in interactive group work and independent learning (Yuen, 2020).

The advantages of 3D printing in medical education have been found in specific scenarios. However, it is precisely due to the rapid evolution of novel educational methodologies that the available literature on their effectiveness is still scarce. Nonetheless, significant efforts are being made to implement state-of-the-art technologies in undergraduate medical teaching and training in these scenarios. Students, specifically surgical residents, can learn the importance of 3D-printed models based on the patient's own measurements, with data obtained from medical imaging, in surgical planning and training with personalized implants, especially in traditionally complicated neurosurgical procedures such as screw placement, students can practice using 3D-printed models of the cervical spine or using personalized guidance templates adapted to the patient, thus minimizing the risk of intraoperative complications and improving outcomes. 3D printing therefore has the potential to improve medical education ranging from theoretical learning to practical clinical skills.

Medical imaging-based 3D printing has also proven to be very useful in specific anatomy-related topics such as embryology. Embryology is notorious amongst medical students for the difficulty of visualization of developing structures; embryonic folding is an example of a topic which medical students struggle to picture, but 3D printing is a technology which can help in resolving this issue. Young et al. developed a series of 3D prints from digital data collected by CT imaging of archived preserved human embryonic and fetal specimens to improve embryological understanding in medical students. The authors concluded that this approach has enormous potential to allow embryology students

access to both local and international collections of human gestational material (Young et al., 2019).

Das and Mitchell conducted a comparative study between traditional (textbooks, physical models, cadaveric dissection) and recent (electronic) techniques as training aids to teach the surgical anatomy of the lumbar spine (Das & Mitchell, 2013). Similarly to our approach, these authors compared three different methodologies (paper-based images, a 3D plastic model and a semitransparent computer model). They found that the computer model gave the best results to determine the location of structures, followed by the paper-based images. Interestingly, the authors found that, although 3D plastic models were less useful for learning, they proved to be helpful for understanding bone anatomy and fractures of the pelvis and spine, but not of the upper and lower limbs. Intrinsic differences in bone complexity between these anatomical structures was hypothesized to be the cause of these findings. This study is relevant as it showed the insufficiency of traditional learning methods for practical medical learning. However, this study did not include 3D printed models or advanced medical imaging, thus their outcomes are not directly comparable to our study.

Li et al. conducted a randomized controlled study on 120 medical students to investigate the impact of 3D printed models on the identification of spinal fracture in medical students as well as for assessing sex-related differences in benefits compared with 2D and 3D presentations (Li et al., 2015). They found that 3D printed models markedly improved the identification of complex spinal fracture anatomy by medical students and was equally appreciated and comprehended by both sexes. This is especially relevant in pre-clinical years, given that students have not yet had surgical experience and have not observed these fractures intraoperatively, a more suitable way to picture them and acquire a more accurate representation of the impacts of complex fractures is through 3D printed models. Accordingly, the authors recommended the use of 3D printing technologies to improve undergraduate medical education.

Apart from the potential advantages of 3D printed models in anatomy learning, 3D printing technologies provide other important advantages,

such as adaptability to students' needs, correlation with medical imaging (Rengier et al., 2010), model accuracy (Xu et al., 2017), potential applications to anatomy-related fields (e.g., simulation of surgical implants), or reduced costs. Regarding this last point, Li et al. reported that the cost of spine, upper limb and lower limb models was approximately $6–$10.50, which is significantly less expensive that available commercial models (Láinez Ramos-Bossini et al., 2021).

Interestingly, we observed that the overall satisfaction of students was higher regarding the use of advanced medical imaging compared to 3D printing. This could be due to several reasons, such as the benefits of online learning since there are a significant number of resources to improve radiological understanding (e.g., radiopaedia, IMAIOS). However, it should be noted that the satisfaction rates with both medical imaging and 3D printing were similar, and significantly higher compared to traditional learning methods (i.e., illustrations). In our study, students' opinions on the use of 3D printing technologies revealed that they perceive that the knowledge acquired will be useful in their professional futures, and they considered that these technologies improve practical knowledge in relation to anatomy learning. Other aspects stressed in the answers to the ad hoc questionnaire included the importance of teamwork, communication and shared knowledge derived from the interaction between students and a multidisciplinary team of educators.

This study presents several limitations. First, the sample size was low and the control and experimental groups had not been randomized. Second, the multiple-choice questionnaire was developed by consensus between professors, not following specific topics, which could entail assessment biases. In the future, international syllabus consensus such as that of the Delphi panel (Webb et al., 2019) would be recommended. These limitations are understandable considering the pilot nature of the study.

6. CONCLUSIONS

3D printing represents an emerging technology with enormous potential, both for understanding normal and pathological anatomy and for training in interventional techniques. It is necessary to know about the different aspects related to software and hardware to obtain the maximum benefit of this technology.

This innovative methodology, which has not been used previously in our country to our knowledge, showed promising initial results and offers a new way of understanding human anatomy. Overall, our teaching project sheds light on the suitability of advanced medical imaging and 3D printing to outline the pathophysiology of degenerative spine conditions. Finally, it is important to stress the innovative nature of our project, since there are, to our knowledge, no previous experiences of this kind in Spain.

7. ACKNOWLEDGMENTS

The authors wish to express their gratitude to all the teachers of the course "Segmentation and 3D printing of anatomical models from medical imaging tests: theoretical-practical course for biosanitary students", especially to David López Cornejo for his work as co-director. We also show our gratitude for the help provided by the members of the ArquiM3D-X project and the Mediterranean Center of the University of Granada for facilitating the development of the course.

8. REFERENCES

Ambellan, F., Lamecker, H., von Tycowicz, C., & Zachow, S. (2019). Statistical Shape Models: Understanding and Mastering Variation in Anatomy. Advances in Experimental Medicine and Biology, 1156, 67–84. https://doi.org/10.1007/978-3-030-19385-0_5

Berney, S., Bétrancourt, M., Molinari, G., & Hoyek, N. (2015). How spatial abilities and dynamic visualizations interplay when learning functional anatomy with 3D anatomical models. Anatomical Sciences Education, 8(5), 452–462. https://doi.org/10.1002/ASE.1524

Casciato, D., Builes, N., & Singh, B. (2018). Using Three-Dimensional Printing to Enhance Cross-Sectional Anatomy Instruction. Journal of the American Podiatric Medical Association, 108(4), 304–310. https://doi.org/10.7547/16-137

Chen, S., Pan, Z., Wu, Y., Gu, Z., Li, M., Liang, Z., Zhu, H., Yao, Y., Shui, W., Shen, Z., Zhao, J., & Pan, H. (2017). The role of three-dimensional printed models of skull in anatomy education: a randomized controlled trail. Scientific Reports, 7(1). https://doi.org/10.1038/S41598-017-00647-1

Das, S., & Mitchell, P. (2013). Comparison of three aids for teaching lumbar surgical anatomy. British Journal of Neurosurgery, 27(4), 475–478. https://doi.org/10.3109/02688697.2013.771723

Day, C., & Ahn, C. (2010). Commentary: the importance of musculoskeletal medicine and anatomy in medical education. Academic Medicine : Journal of the Association of American Medical Colleges, 85(3), 401–402. https://doi.org/10.1097/ACM.0B013E3181CD4A89

Ghosh, S. (2017). Cadaveric dissection as an educational tool for anatomical sciences in the 21st century. Anatomical Sciences Education, 10(3), 286–299. https://doi.org/10.1002/ASE.1649

González Blum, C., Richter, R., Fuchs, R., Sandeck, F., & Heermann, S. (2020). An interprofessional teaching approach for medical and physical therapy students to learn functional anatomy and clinical examination of the lower spine and hip. Annals of Anatomy = Anatomischer Anzeiger : Official Organ of the Anatomische Gesellschaft, 231. https://doi.org/10.1016/J.AANAT.2020.151534

Kainberger, F., & Kletter, K. (2007). Diagnostic imaging in pregraduate integrated curricula. RoFo : Fortschritte Auf Dem Gebiete Der Rontgenstrahlen Und Der Nuklearmedizin, 179(11), 1137–1144. https://doi.org/10.1055/S-2007-963509

Láinez Ramos-Bossini, A., Rivera-Izquierdo, M., Redruello Guerrero, P., & Prados Salazar, J. (2021). Modelado e impresión 3D basada en imagen médica como herramienta docente en el grado en medicina. In G. Gómez García, M. Ramos Navas-Parejo, C. Rodríguez Jiménez, & J. de la Cruz Campos (Eds.), Teorìa y práctica en investigación educativa: una perspectiva internacional. Dykinson.

Li, Z., Li, Z., Xu, R., Li, M., Li, J., Liu, Y., Sui, D., Zhang, W., & Chen, Z. (2015). Three-dimensional printing models improve understanding of spinal fracture--A randomized controlled study in China. Scientific Reports, 5. https://doi.org/10.1038/SREP11570

Miles, K. (2005). Diagnostic imaging in undergraduate medical education: an expanding role. Clinical Radiology, 60(7), 742–745. https://doi.org/10.1016/J.CRAD.2005.02.011

Orsbon, C., Kaiser, R., & Ross, C. (2014). Physician opinions about an anatomy core curriculum: a case for medical imaging and vertical integration. Anatomical Sciences Education, 7(4), 251–261. https://doi.org/10.1002/ASE.1401

Rengier, F., Mehndiratta, A., von Tengg-Kobligk, H., Zechmann, C., Unterhinninghofen, R., Kauczor, H., & Giesel, F. (2010). 3D printing based on imaging data: review of medical applications. International Journal of Computer Assisted Radiology and Surgery, 5(4), 335–341. https://doi.org/10.1007/S11548-010-0476-X

Saltarelli, A., Roseth, C., & Saltarelli, W. (2014). Human cadavers Vs. multimedia simulation: A study of student learning in anatomy. Anatomical Sciences Education, 7(5), 331–339. https://doi.org/10.1002/ASE.1429

Tam, M. (2010). Building virtual models by postprocessing radiology images: A guide for anatomy faculty. Anatomical Sciences Education, 3(5), 261–266. https://doi.org/10.1002/ASE.175

Tan, S., Hu, A., Wilson, T., Ladak, H., Haase, P., & Fung, K. (2012). Role of a computer-generated three-dimensional laryngeal model in anatomy teaching for advanced learners. The Journal of Laryngology and Otology, 126(4), 395–401. https://doi.org/10.1017/S0022215111002830

Trelease, R. (2016). From chalkboard, slides, and paper to e-learning: How computing technologies have transformed anatomical sciences education. Anatomical Sciences Education, 9(6), 583–602. https://doi.org/10.1002/ASE.1620

Triepels, C., Smeets, C., Notten, K., Kruitwagen, R., Futterer, J., Vergeldt, T., & Van Kuijk, S. (2020). Does three-dimensional anatomy improve student understanding? Clinical Anatomy (New York, N.Y.), 33(1), 25–33. https://doi.org/10.1002/CA.23405

Webb, A., Green, R., & Woodley, S. (2019). The development of a core syllabus for teaching musculoskeletal anatomy of the vertebral column and limbs to medical students. Clinical Anatomy (New York, N.Y.), 32(8), 974–1007. https://doi.org/10.1002/CA.23319

Wu, A.-M., Wang, K., Wang, J.-S., Chen, C.-H., Yang, X.-D., Ni, W.-F., & Hu, Y.-Z. (2018). The addition of 3D printed models to enhance the teaching and learning of bone spatial anatomy and fractures for undergraduate students: a randomized controlled study. Annals of Translational Medicine, 6(20), 403–403. https://doi.org/10.21037/ATM.2018.09.59

Xu, W., Zhang, X., Ke, T., Cai, H., & Gao, X. (2017). 3D printing-assisted preoperative plan of pedicle screw placement for middle-upper thoracic trauma: a cohort study. BMC Musculoskeletal Disorders, 18(1), 348. https://doi.org/10.1186/s12891-017-1703-1

Yammine, K., & Violato, C. (2015). A meta-analysis of the educational effectiveness of three-dimensional visualization technologies in teaching anatomy. Anatomical Sciences Education, 8(6), 525–538. https://doi.org/10.1002/ASE.1510

Young, J., Quayle, M., Adams, J., Bertram, J., & McMenamin, P. (2019). Three-Dimensional Printing of Archived Human Fetal Material for Teaching Purposes. Anatomical Sciences Education, 12(1), 90–96. https://doi.org/10.1002/ASE.1805

Yuen, J. (2020). What Is the Role of 3D Printing in Undergraduate Anatomy Education? A Scoping Review of Current Literature and Recommendations. Medical Science Educator, 30(3), 1321. https://doi.org/10.1007/S40670-020-00990-5

Apéndice 3. Estudio de campo sobre la utilidad de la impresión 3D basada en imagen médica como método de enseñanza para la comprensión de la anatomía normal y patológica de la columna vertebral. Reproducido con permiso de Dykinson SL. Referencia completa: Láinez Ramos-Bossini AJ, Redruello Guerrero P, Quiñonero Muñoz FJ, Prados Salazar JC. Desarrollo de un programa formativo reducido para la adquisición de habilidades teórico-prácticas en impresión 3D basada en imagen médica. En: Innovación en educación: investigaciones, reflexiones y propuestas de actuación. Editorial Egregius. ISBN 978-84-18167-64-5. 2021; 302-322.

3.1. Estrategia de búsqueda en PubMed

16,#10 OR #14,,,"(1950/01/01:2020/07/31[Date - Completion] AND (""vertebroplasty""[MeSH Terms] OR ""cementoplasty""[MeSH Terms] OR ""vertebral augmentation""[Text Word]) AND ""osteoporo*""[MeSH Terms]) OR (1950/01/01:2020/07/31[Date - Completion] AND (""vertebroplasty""[MeSH Terms] OR ""cementoplasty""[MeSH Terms] OR ""vertebral augmentation""[Text Word]) AND ""spinal fractures""[MeSH Terms] AND (""conservative treatment""[Text Word] OR ""conservative management""[Text Word] OR ""usual care""[Text Word] OR ""non surgical treatment""[Text Word] OR ""non surgical management""[Text Word] OR ""usual care""[Text Word] OR ""standard medical therapy""[Text Word] OR ""placebo""[Text Word] OR ""sham""[Text Word]))","1,271",09:27:55

15,#1 AND #2 AND #3 AND #4 AND #5,,,"1950/01/01:2020/07/31[Date - Completion] AND (""vertebroplasty""[MeSH Terms] OR ""cementoplasty""[MeSH Terms] OR ""vertebral augmentation""[Text Word]) AND ""osteoporo*""[MeSH Terms] AND ""spinal fractures""[MeSH Terms] AND (""conservative treatment""[Text Word] OR ""conservative management""[Text Word] OR ""usual care""[Text Word] OR ""non surgical treatment""[Text Word] OR ""non surgical management""[Text Word] OR ""usual care""[Text Word] OR ""standard medical therapy""[Text Word] OR ""placebo""[Text Word] OR ""sham""[Text Word])",154,09:26:12

14,#1 AND #2 AND #4 AND #5,,,"1950/01/01:2020/07/31[Date - Completion] AND (""vertebroplasty""[MeSH Terms] OR ""cementoplasty""[MeSH Terms] OR ""vertebral augmentation""[Text Word]) AND ""spinal fractures""[MeSH Terms] AND (""conservative treatment""[Text Word] OR ""conservative management""[Text Word] OR ""usual care""[Text Word] OR ""non surgical treatment""[Text Word] OR ""non surgical management""[Text Word] OR ""usual care""[Text Word] OR ""standard medical therapy""[Text Word] OR ""placebo""[Text Word] OR ""sham""[Text Word])",227,09:25:48

13,#1 AND #2 AND #3 AND #4,,,"1950/01/01:2020/07/31[Date - Completion] AND (""vertebroplasty""[MeSH Terms] OR ""cementoplasty""[MeSH Terms] OR ""vertebral augmentation""[Text Word]) AND ""osteoporo*""[MeSH Terms] AND ""spinal fractures""[MeSH Terms]","1,026",09:25:31

12,#1 AND #2 AND #5,,,"1950/01/01:2020/07/31[Date - Completion] AND (""vertebroplasty""[MeSH Terms] OR ""cementoplasty""[MeSH Terms] OR ""vertebral augmentation""[Text Word]) AND (""conservative treatment""[Text Word] OR ""conservative management""[Text Word] OR ""usual care""[Text Word] OR ""non surgical treatment""[Text Word] OR ""non surgical management""[Text Word] OR ""usual care""[Text Word] OR ""standard medical therapy""[Text Word] OR ""placebo""[Text Word] OR ""sham""[Text Word])",287,09:25:00

11,#1 AND #2 AND #4,,,"1950/01/01:2020/07/31[Date - Completion] AND (""vertebroplasty""[MeSH Terms] OR ""cementoplasty""[MeSH Terms] OR ""vertebral augmentation""[Text Word]) AND ""spinal fractures""[MeSH Terms]","1,836",09:24:39

10,#1 AND #2 AND #3,,,"1950/01/01:2020/07/31[Date - Completion] AND (""vertebroplasty""[MeSH Terms] OR ""cementoplasty""[MeSH Terms] OR ""vertebral augmentation""[Text Word]) AND ""osteoporo*""[MeSH Terms]","1,198",09:24:20

9,#1 AND #5,,,"1950/01/01:2020/07/31[Date - Completion] AND (""conservative treatment""[Text Word] OR ""conservative management""[Text Word] OR ""usual care""[Text Word] OR ""non surgical treatment""[Text Word] OR ""non surgical management""[Text Word]

OR ""usual care""[Text Word] OR ""standard medical therapy""[Text Word] OR ""placebo""[Text Word] OR ""sham""[Text Word])","336,802",09:23:40
8,#1 AND #4,,,"1950/01/01:2020/07/31[Date - Completion] AND ""spinal fractures""[MeSH Terms]","14,928",09:23:33

7,#1 AND #3,,,"1950/01/01:2020/07/31[Date - Completion] AND ""osteoporo*""[MeSH Terms]","58,694",09:23:24

6,#1 AND #2,,,"1950/01/01:2020/07/31[Date - Completion] AND (""vertebroplasty""[MeSH Terms] OR ""cementoplasty""[MeSH Terms] OR ""vertebral augmentation""[Text Word])","2,952",09:23:10

5,(((((((conservative treatment[Text Word]) OR (conservative management[Text Word])) OR (usual care[Text Word])) OR (non-surgical treatment[Text Word])) OR (non-surgical management[Text Word])) OR (usual care[Text Word])) OR (standard medical therapy[Text Word])) OR (placebo[Text Word])) OR (sham[Text Word]),,,""""conservative treatment""[Text Word] OR ""conservative management""[Text Word] OR ""usual care""[Text Word] OR ""non surgical treatment""[Text Word] OR ""non surgical management""[Text Word] OR ""usual care""[Text Word] OR ""standard medical therapy""[Text Word] OR ""placebo""[Text Word] OR ""sham""[Text Word]","366,776",09:22:13

4,spinal fracture[MeSH Terms],,,""""spinal fractures""[MeSH Terms]","15,014",09:21:13

3,osteoporo*[MeSH Terms],,,""""osteoporo*""[MeSH Terms]","58,990",09:20:48

2,((vertebroplasty[MeSH Terms]) OR (cementoplasty[MeSH Terms])) OR (vertebral augmentation[Text Word]),,,""""vertebroplasty""[MeSH Terms] OR ""cementoplasty""[MeSH Terms] OR ""vertebral augmentation""[Text Word]","3,062",09:20:33

1,(""1950/01/01""[Date - Completion] : ""2020/07/31""[Date - Completion])",,,1950/01/01:2020/07/31[Date - Completion],"29,051,514",09:20:05

3.2. Estrategia de búsqueda en EMBASE

#21,"#4 AND #5 AND #19",703,17 Sep 2020
#20,"#4 AND #19",1390,17 Sep 2020
#19,"#10 OR #14",931956,17 Sep 2020
#18,"#4 AND #5 AND #7 AND #10 AND #14",25,17 Sep 2020
#17,"#4 AND #5 AND #7 AND #14",61,17 Sep 2020
#16,"#4 AND #5 AND #14",69,17 Sep 2020
#15,"#4 AND #14",123,17 Sep 2020
#14,"'placebo'/exp AND [1-1-1950]/sd NOT [1-8-2020]/sd",358492,17 Sep 2020
#13,"#4 AND #5 AND #7 AND #10",581,17 Sep 2020
#12,"#6 AND #10",661,17 Sep 2020
#11,"#4 AND #10",1305,17 Sep 2020
#10,"'conservative treatment'/exp AND [1-1-1950]/sd NOT [1-8-2020]/sd",595884,17 Sep 2020
#9,"#6 AND #7",3074,17 Sep 2020
#8,"#4 AND #7",4515,17 Sep 2020
#7,"'spine fracture'/exp AND [1-1-1950]/sd NOT [1-8-2020]/sd",36359,17 Sep 2020

#6,"#4 AND #5",3754,17 Sep 2020
#5,"osteoporo* AND [1-1-1950]/sd NOT [1-8-2020]/sd",170070,17 Sep 2020
#4,"#1 OR #2 OR #3",7514,17 Sep 2020
#3,"'vertebral augmentation'/exp AND [1-1-1950]/sd NOT [1-8-2020]/sd",56,17 Sep 2020
#2,"'cementoplasty'/exp AND [1-1-1950]/sd NOT [1-8-2020]/sd",7314,17 Sep 2020
#1,"('percutaneous vertebroplasty'/exp OR 'percutaneous vertebroplasty') AND [1-1-1950]/sd NOT [1-8-2020]/sd",7211,17 Sep 2020

3.3. Estrategia de búsqueda en Cochrane

Search Name: VERTEBROPLASTY

Date Run: 17/09/2020 22:11:32

Comment:

ID	Search	Hits
#1	vertebroplasty	364
#2	(vertebroplasty) AND (osteoporo*) (Word variations have been searched)	268
#3	(Bone cement injection as vertebral augmentation therapy for osteoporotic vertebral compression fractures) (Word variations have been searched)	4
#4	(vertebroplasty) with Cochrane Library publication date Between Jan 1950 and Jul 2020 (Word variations have been searched)	359

Apéndice 4. Estrategias de búsqueda y análisis incluidos como material suplementario en el trabajo 7. También se encuentran disponibles en el material suplementario del artículo referido: Láinez Ramos-Bossini AJ, López Zúñiga D, Ruiz Santiago F. Percutaneous vertebroplasty versus conservative treatment and placebo in osteoporotic vertebral fractures: meta-analysis and critical review of the literature. Eur Radiol. 2021;31(11):8542-8553. doi:10.1007/s00330-021-08018-1.

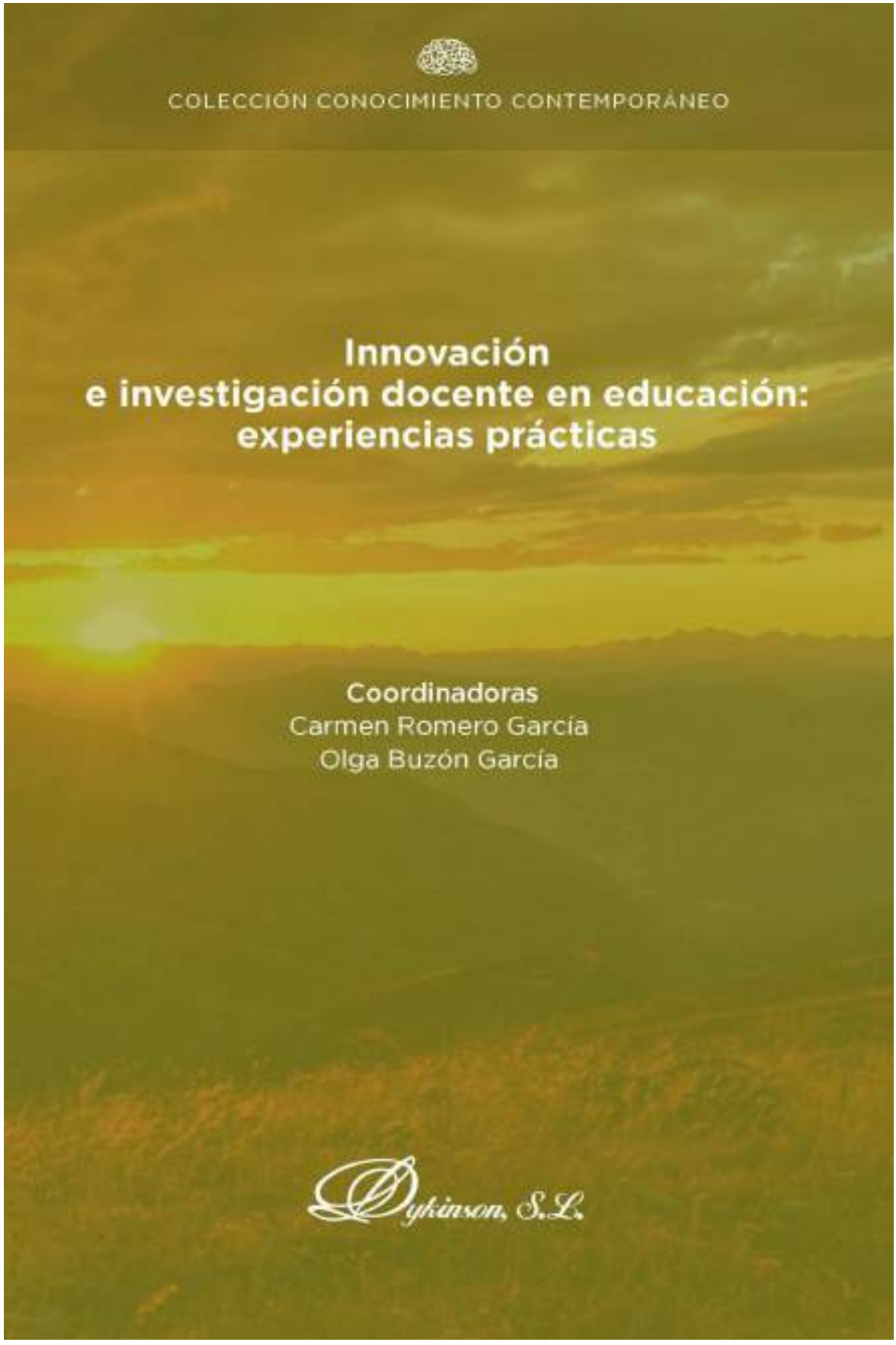
COLECCIÓN CONOCIMIENTO CONTEMPORÁNEO
Innovación
e investigación docente en educación:
experiencias prácticas
Coordinadoras
Carmen Romero García
Olga Buzón García
Dykinson, S.L.

INNOVACIÓN E INVESTIGACIÓN DOCENTE EN EDUCACIÓN: EXPERIENCIAS PRÁCTICAS

INNOVACIÓN E INVESTIGACIÓN DOCENTE EN EDUCACIÓN: EXPERIENCIAS PRÁCTICAS

Coordinadoras

CARMEN ROMERO GARCÍA
OLGA BUZÓN GARCÍA

Dykinson, S.L.

2021

CAPÍTULO 14

DOCENCIA BASADA EN IMPRESIÓN 3D A PARTIR DE IMAGEN MÉDICA PARA EL APRENDIZAJE DE LA ANATOMÍA HUMANA. RESULTADOS DE UNA EXPERIENCIA PILOTO

ANTONIO JESÚS LÁINEZ RAMOS-BOSSINI
Hospital Universitario Virgen de las Nieves
Granada, España

PABLO REDRUELLO GUERRERO
Departamento de Anatomía y Embriología Humana
Facultad de Medicina. Universidad de Granada, España

CRISTINA MESAS HERNÁNDEZ
Departamento de Anatomía y Embriología Humana
Facultad de Medicina. Universidad de Granada, España

JOSÉ CARLOS PRADOS SALAZAR
Departamento de Anatomía y Embriología Humana
Facultad de Medicina. Universidad de Granada, España

1. INTRODUCCIÓN

En los últimos años se han producido cambios sin precedentes en la forma de entender la anatomía humana gracias al desarrollo de las nuevas técnicas de imagen médica e impresión 3D (Láinez Ramos-Bossini et al., 2021). El salto de calidad a la hora de abordar el estudio del cuerpo humano gracias a estas tecnologías está teniendo una clara repercusión en la docencia de esta disciplina, de manera especialmente notable en los estudios de Grado y Posgrado. Así, en comparación con las formas clásicas de enseñanza sustentadas en un abordaje pedagógico monolítico basado en ilustraciones, modelos tridimensionales estereotipados y disección de cadáver, las herramientas actuales (visores online, estudios de imagen médica avanzada, impresión 3D, etc.) permiten al estudiantado aproximarse a la anatomía humana de forma práctica, adaptativa y real. En efecto, existen numerosos proyectos y recursos

centrados en la didáctica de la anatomía humana y especialidades clínicas afines como la radiología o medicina nuclear. En la **tabla 1** se recogen algunos de estos proyectos de interés.

TABLA 1. *Recursos online para el aprendizaje de anatomía humana y áreas afines.*

Recurso	Área principal	URL	Idioma(s)
Visible Human Project	Anatomía Humana, Radiología	https://www.nlm.nih.gov/research/visible/applications.html *	Inglés
Digital Anatomist Project	Anatomía Humana, Radiología	http://da.si.washington.edu/da.html	Inglés
IMAIOS	Anatomía humana, radiología, medicina nuclear	https://www.imaios.com/es	Inglés, Español, otros
AnatomyTV	Anatomía humana, radiología	https://www.anatomy.tv/welcomer	Inglés
BodyParts3D	Anatomía Humana, impresión 3D	https://lifesciencedb.jp/bp3d/	Inglés, Japonés
Radiopaedia	Radiología, Medicina Nuclear	https://radiopaedia.org/	Inglés

* En la URL se recogen las distintas aplicaciones que forman parte del recurso.
Fuente: elaboración propia

1.1. Impresión 3D basada en imagen médica

Una de las herramientas más recientemente desarrolladas con clara aplicabilidad a la enseñanza de la anatomía es la impresión 3D. Aunque esta tecnología existe desde la década de 1980 (Wake, 2021), hasta hace pocos años no se han desarrollado modelos de uso doméstico, lo que permite su expansión a distintos sectores más allá de la industria. Como consecuencia, la impresión 3D se ha desplegado en distintas vertientes relacionadas con la medicina (Tack et al., 2016; Wang et al., 2016), entre las cuales cabe destacar el ámbito de la planificación prequirúrgica (Ganguli et al., 2018; Pugliese et al., 2018) el empoderamiento de los pacientes en la toma de decisiones (Biglino et al., 2015) y la docencia de la anatomía humana (Chytas et al., 2020). En efecto, encontramos

diversos estudios que ilustran la variada casuística anatómica que puede recrearse de manera fidedigna y personalizada gracias a la impresión 3D abarcando, entre otros, patologías infrecuentes como el síndrome de Eagle (Czako et al., 2020), patologías cardíacas congénitas (Moore et al., 2018), diversas patologías renales (Sun & Liu, 2018) o cirugías de elevada complejidad como la separación de siameses (Villarreal et al., 2020). Ello da cuenta del gran potencial de esta tecnología en el ámbito de la enseñanza médica. Más allá de ilustrar de manera teórica las posibilidades de la impresión 3D en el ámbito médico, diversos estudios han demostrado su utilidad siguiendo metodologías regladas como ensayos de campo. En el ámbito particular de la docencia, se han publicado revisiones sistemáticas y metaanálisis que concluyen que la impresión 3D ofrece ventajas significativas en la docencia médica (Chytas et al., 2020; Fleming et al., 2020). No obstante, los resultados publicados hasta la fecha deben ser interpretados con precaución dado que el número de estudios publicados es aún escaso y heterogéneo, especialmente aquellos que generan un mayor nivel de evidencia científica. Dado que el principal factor limitante es la reciente expansión de las tecnologías de impresión 3D (ligado a una dificultad moderada en lo que al desarrollo de habilidades que permitan su utilización se refiere), cabe esperar que en los próximos años se genere suficiente evidencia científica para generalizar el uso de estas tecnologías en la educación médica.

1.2. Conocimientos y destrezas necesarias para el dominio de la impresión 3D. ¿Es posible adquirirlas en tiempos de pandemia?

No podemos desvincular el desarrollo de cualquier actividad académica reciente del contexto sociosanitario en que nos hemos visto inmersos desde la declaración de la pandemia COVID-19, el cual ha generado una situación sin precedentes que ha obligado a tomar estrictas medidas de prevención en las aulas universitarias en nuestro país. Esto resulta de especial relevancia en asignaturas ligadas a la anatomía ya que el desarrollo adecuado de sus contenidos teórico-prácticos exige casi indefectiblemente la utilización de modelos 3D, disección de cadáver, etc. En este sentido, la impresión 3D puede suponer una gran ventaja

en el ámbito académico, pues posibilita el acceso a modelos coste-eficientes y personalizados que los estudiantes pueden utilizar fuera de las aulas.

Sin embargo, aprovechar al máximo las posibilidades de la impresión 3D requiere disponer de espacios y equipos suficientemente adaptados para tiempos de pandemia, lo que no siempre es posible. Enseñar al alumnado cómo obtener sus propios modelos a partir de impresión 3D podría suponer una solución de compromiso, ya que permitiría habilitar y coordinar tiempos de máquina para que los propios estudiantes impriman sus modelos, rentabilizando los tiempos disponibles para el uso de salas. No obstante, aprender cómo funciona una impresora 3D requiere un conocimiento, al menos parcial, del *hardware* de impresión, aspecto difícilmente enseñable a través de docencia *online*. No obstante, la amplitud y variada naturaleza de los aspectos que es necesario dominar para hacer un uso adecuado de esta técnica, fundamentalmente aquellos relativos al *software*, pueden resultar suficientes si se dispone de personal que gestione los espacios y equipos de impresión 3D disponibles en espacios institucionales habilitados a tal efecto. Ello justifica holgadamente la realización de un curso centrado en contenidos específicos, como es la anatomía radiológica normal y patológica, los fundamentos de las técnicas de imagen médica avanzada, el uso de visualizadores DICOM, las herramientas de segmentación manual y semiautomática disponibles, el modelado 3D o el software de rebanado (*slicing*). Mediante la adquisición de competencias de nivel básico-intermedio por parte del alumnado, se les capacita para preparar modelos de impresión 3D. Así, es posible sobrevenir las dificultades impuestas por la pandemia a través de un curso centrado en el aprendizaje y dominio de estas habilidades y recursos, aunque ello no implique un dominio completo de la impresión 3D basada en imagen médica.

1.2. Innovación docente en tiempos de pandemia

En el marco del proyecto de innovación docente "Diseño e impresión 3D de modelos anatómicos mediante técnicas de imagen radiológica e inteligencia artificial para la enseñanza de la medicina" liderado por nuestro equipo de investigación en la Universidad de Granada, hemos

abordado específicamente este problema. Para ello, hemos implementado un innovador sistema de enseñanza utilizando imagen médica y modelos impresos en 3D. La hipótesis de partida principal del proyecto radica en que la imagen médica avanzada y, especialmente, las tecnologías de impresión 3D, ofrecen una mejora significativa en la docencia de grado en términos de rendimiento académico y satisfacción estudiantil.

En resumen, la docencia en anatomía humana está reinventándose gracias a disciplinas y tecnologías emergentes como la imagen médica avanzada, los modelos interactivos digitales y la impresión 3D. En el difícil contexto de la enseñanza universitaria derivado de la pandemia por COVID-19, estas herramientas han desplegado su enorme potencial. Sin embargo, algunas limitaciones, como el manejo avanzado de *software* y *hardware* específico o el conocimiento de áreas específicas (p.ej., anatomía radiológica), deben ser consideradas para el éxito de su aplicación. Precisamente estas limitaciones justifican los aún escasos (aunque crecientes) proyectos de innovación docente que incorporan la impresión 3D en la docencia de anatomía humana en España.

2. OBJETIVOS

El objetivo principal del presente trabajo es presentar los resultados de un curso piloto de impresión 3D basada en imagen médica para la enseñanza de la anatomía humana. Este objetivo principal se desglosa en varios objetivos secundarios que se describen a continuación.

2.1. OBJETIVOS SECUNDARIOS

- Describir las características (formato, extensión, cronograma, número de estudiantes, etc.) del curso piloto.
- Analizar el perfil académico (Grado, Posgrado) de los estudiantes inscritos en el curso.
- Evaluar el grado de interés de los alumnos por la impresión 3D biomédica.

– Evaluar el nivel de competencias adquiridas en las habilidades básicas de impresión 3D por parte del alumnado del curso.

– Evaluar el grado de satisfacción del alumnado con el curso.

– Evaluar las ventajas y limitaciones del curso, con especial atención a los aspectos condicionados por el formato *online*.

3. METODOLOGÍA

3.1. CARACTERÍSTICAS DEL CURSO PILOTO

Se planificó un curso piloto interdisciplinar de 32 horas de duración (3 créditos ECTS), cuyo título fue "Segmentación e impresión 3D de modelos anatómicos a partir de pruebas de imagen médica: curso teórico-práctico para estudiantes biosanitarios". Debido a las restricciones de presencialidad impuestas por el escenario COVID-19, el formato de celebración fue virtual y en tiempo real, con la excepción de la última clase, que se planteó desde el inicio como presencial siempre que la situación sociosanitaria lo permitiera. El curso se desarrolló a través del Centro Mediterráneo de la Universidad de Granada[1] durante los meses de abril y mayo, mediante dos clases teórico-prácticas semanales de 4 horas de duración, hasta un total de 8 sesiones. En la tabla 1 se describen los contenidos principales de las sesiones del curso.

Debido al carácter piloto del curso, se estableció un número máximo de alumnos permitidos de 30. Además de incluirse en el catálogo de cursos ofrecidos por el Centro Mediterráneo, la difusión del curso se realizó mediante invitación genérica a través del correo institucional de la universidad así como de las redes sociales del proyecto ArquiM3D-X[2], en las cuales se utilizaron carteles publicitarios describiendo el título, modalidad, duración y convalidación de créditos ECTS del curso (inicialmente solo se aprobaron los créditos de enseñanza universitaria, que

[1] https://cemed.ugr.es/

[2] Twitter (@arquim3dx) e Instagram (arquim3d)

posteriormente serían convalidables en las facultades de Odontología, Ciencias del Deporte y Medicina).

TABLA 2. *Sesiones teórico-prácticas llevadas a cabo durante el curso piloto.*

Sesión	Contenidos	Duración
1	Bienvenida y presentación del curso. Definición de los objetivos y destrezas que el alumnado alcanzará al finalizar el programa teórico-práctico a través de un cronograma definido.	1 hora
	Revisión de la historia de la impresión 3D. Tecnologías, hardware y materiales más utilizados en impresión 3D.	I hora
	Terminología empleada en el *software* y *hardware* de la impresión 3D.	I hora
	Aplicaciones de la impresión 3D en la práctica clínica: desde el entrenamiento para el abordaje del dolor al empoderamiento del paciente.	I hora
2	Utilidad y potencialidad de la impresión 3D para el alumnado de medicina y ciencias de la salud. Una visión en primera persona.	I hora
	Diseño y personalización de un modelo simple para impresión 3D con Tinkercad. Introducción al *software* de impresión 3D *Ultimaker Cura*. Parámetros básicos de impresión. Taller práctico: diseño de salvaorejas para impresión 3D.	3 horas
3	Resultados de la impresión de los modelos elaborados por el alumnado (*timelapse* de la impresión 3D). Aspectos a tener en cuenta para evitar problemas frecuentes en la impresión 3D. Resolución de dudas y problemas.	I hora
	Neuroanatomía básica y aplicaciones de la impresión 3D en Neurología y especialidades afines.	I hora
	Introducción a la anatomía radiológica: pruebas de imagen (radiografía simple, ecografía, TC, PET-TC y RM). Introducción al software 3D Slicer. Semiología radiológica básica de la anatomía del abdomen y pelvis en tomografía computarizada y resonancia magnética.	I hora
	Anatomía radiológica torácica en tomografía computarizada. Aspectos esenciales y algunas claves para la segmentación 3D	0,5 horas
	Neuroanatomía radiológica en tomografía computarizada y resonancia magnética. Aspectos esenciales y algunas claves para la segmentación 3D	0,5 horas
4	Segmentación de un modelo anatómico vertebral a partir de un estudio de tomografía computarizada utilizando *3D Slicer*. Adaptación del modelo para su impresión con funciones básicas de *Meshmixer*. Preparación del fichero definitivo optimizado para impresión con *Ultimaker Cura*.	4 horas
5	Aplicaciones biomédicas de la impresión 3D: de la teoría a la práctica.	1 hora
	Repositorios de modelos 3D generales y específicos de anatomía (*Thingiverse, 3Dcult, 3D Body parts*). Aplicaciones clínicas de la impresión 3D. Ampliación de la anatomía radiológica con revisión de variantes anatómicas y patologías estructurales. Visores de archivos DICOM gratuitos y repositorios de acceso abierto.	3 horas
6	Funciones más avanzadas de *Meshmixer*: utilización de soportes de árbol, corte y unión de piezas mediante booleanos, orientación y solidificación. Herramientas para la numeración y personalización de modelos anatómicos. Preparación de modelo anatómico segmentado para impresión 3D por partes y unión mediante sistema de imanes.	4 horas
7	Introducción a las funciones avanzadas de impresión 3D: uso de doble extrusión, soportes solubles, retracción y posprocesado. Aclaraciones, repaso y *feedback* de lo aprendido.	4 horas
8	Sesión de clausura del curso*. Entrega de modelos anatómicos impresos. Consejos para el posprocesado. Encuestas de satisfacción. Proyecto ARQUIM3D-X y formación continuada.	4 horas

En la figura 1 se muestra uno de los carteles publicitarios del curso. El precio del curso para los estudiantes se estableció para cubrir los gastos derivados de la gestión de convalidación de créditos, pues los docentes renunciaron a sus honorarios. Todos los estudiantes participaron de manera voluntaria.

FIGURA 1. *Cartel publicitario del curso (fuente: Centro Mediterráneo, Universidad de Granada, España).*

Fuente: https://cemed.ugr.es/

El perfil de los docentes incluyó cinco especialistas clínicos hospitalarios (tres especialistas en Radiodiagnóstico, un especialista en Neurología y un especialista en Medicina Preventiva y Salud Pública), una especialista en Medicina Familiar y Comunitaria, un graduado en Ingeniería Electrónica, una terminóloga y un docente universitario del departamento de Anatomía Humana y Embriología.

Los criterios de evaluación del curso fueron claramente establecidos desde el inicio del curso, computándose las calificaciones de cada estudiante mediante la asistencia y participación (70% de la nota final) y tres pruebas de evaluación consistentes en la preparación de un modelo sencillo de impresión 3D (10% de la nota final), la segmentación y posprocesado simple de un modelo anatómico vertebral a partir de tomografía computarizada (10% de la nota final), y el posprocesado avanzado de un modelo 3D de hígado (10% de la nota final). Las calificaciones correspondientes a la asistencia y participación fueron otorgadas tras el análisis de la asistencia a los participantes (registro de asistencia al inicio y final de cada clase); se permitió un máximo de 1 ausencia no justificada y se restó un 10% sobre la calificación correspondiente por cada sesión a la que no se acudió, hasta un máximo de 3 (no se permitió faltar a más de 3 sesiones en el curso), y el número de intervenciones (mínimo de 4 intervenciones por estudiante para obtener la máxima puntuación). Así, si un estudiante faltó a 3 sesiones de forma no justificada y participó activamente, su calificación fue de 5 puntos sobre 7, mientras que quienes faltaron a 1 o ninguna sesión y participaron activamente obtuvieron los 7 puntos. Para la evaluación de las tareas, los docentes encargados de explicar los requisitos de esta analizaron mediante una lista de comprobación predefinida si la tarea del estudiante cumplía con las especificaciones, deduciéndose 1 punto por cada fallo menor y 3 puntos por cada error mayor. El retraso injustificado en la entrega del modelo respecto a la fecha límite establecida se penalizó con 2 puntos.

Tras la finalización del curso, los estudiantes fueron invitados a rellenar una encuesta voluntaria en formato semiestructurado que los docentes del curso prepararon conjuntamente con el Centro Mediterráneo a partir de la retroalimentación recibida durante el curso y experiencias previas

recientes en otros cursos realizados con un perfil similar de alumnado (grados y posgrados biosanitarios)[3]. Los cuestionarios incluyeron preguntas dirigidas sobre la evaluación de los contenidos del curso y calidad docente, puntuadas de 1 (menor) a 10 (mayor), así como preguntas abiertas con respuesta de extensión breve.

4. RESULTADOS

4.1. Características del alumnado del curso piloto

Al inicio del curso todas las plazas fueron ocupadas, por lo que el total de estudiantes matriculados fue de 30 (edad media: 22,15; ratio de mujeres: 69,23%). De estos, 4 abandonaron el curso antes de la segunda semana, por lo que la ratio de participación fue del 86,6%. Los motivos de abandono fueron: laboral (1 alumno), carga académica (2 alumnos) y no precisado (1 alumno). Los 26 alumnos que finalizaron el curso obtuvieron una calificación media de 9,4/10. Todos rellenaron la encuesta voluntaria. El 88,46% era alumnado de pregrado (Grados en Odontología, Medicina y Bioquímica) y el 11,54% de Posgrado.

4.2. Interés y satisfacción del alumnado con el curso piloto

Los motivos principales para participar en el curso fueron: interés intelectual y cultural (24,18%), mejora de curriculum (23,08%) y reconocimiento de créditos (16,67%). Las principales vías informativas por las que los alumnos asistieron al curso fueron: información a través de un amigo (73,08%), redes sociales (19,23%), listas de distribución (15,38%), web institucional (11,54%), información a través del profesorado (7,69%) y correo electrónico (3,85%). La temporalidad del conocimiento de los cursos docentes a través del Centro Mediterráneo mostró que la mayoría de los estudiantes no conocía la institución en cursos previos (76,92%) o la conocía del año anterior (11,54%); el resto

[3] Por ejemplo, el director del curso y varios docentes participaron un mes antes en el curso “Producción y traducción de artículos científicos (III ed.)”, también realizado a través del Centro Mediterráneo de la UGR (https://cemed.ugr.es/curso/21on03/)

conocía de estos cursos dos años antes (3,85%) o con mayor antelación (7,69%).

Respecto a la evaluación de la calidad del curso, los alumnos otorgaron puntuaciones muy elevadas (media: 9,56; desviación estándar: 0,31). En la **tabla 3** se muestran los aspectos evaluados y la puntuación obtenida.

TABLA 3. *Aspectos relacionados con la calidad del curso que fueron evaluados por el alumnado y puntuación correspondiente (0-10)*.

Aspecto evaluado	Puntuación
El título del curso expresa claramente el contenido del mismo	9,81
El número total de horas dedicadas al curso es adecuado	9,23
El número total de horas dedicadas a cada tema es adecuado	9,12
Accesibilidad de los/as directores/as	9,69
Debate y comunicación entre los asistentes	9,62
En conjunto, el grado de satisfacción con el curso es	9,88

Respecto a la evaluación del profesorado, los alumnos otorgaron puntuaciones muy elevadas (media: 9,92; desviación estándar: 0,07). En la tabla 4 se muestran los aspectos evaluados y la puntuación obtenida.

TABLA 4. *Aspectos relacionados con el profesorado que fueron evaluados por el alumnado y puntuación correspondiente (0-10)*.

Aspecto evaluado	Puntuación
Claridad en la exposición	9,92
Metodología utilizada	10,00
Dominio del tema	9,96
Material de apoyo	9,81
Cumplimiento de horarios establecidos	9,96
Disponibilidad del profesorado	9,85
En conjunto, la puntuación del profesorado	9,92

La encuesta también incluyó dos ítems sobre aspectos genéricos, en los que también se observaron puntuaciones muy altas: Material técnico y audiovisual (9,92); administración Centro Mediterráneo (9,73).

Las preguntas abiertas mostraron un alto grado de satisfacción y algunas limitaciones o áreas de mejora. A continuación, se recogen diversas respuestas del estudiantado, seleccionadas al azar.

4.3. Respuestas del alumnado al cuestionario abierto

4.3.1. Respuestas libres del alumnado sobre el curso seguido

Se recogen a continuación diversas respuestas seleccionadas al azar con relación al curso piloto.

> Me gustaría que fuera incluso más largo el curso
>
> Sería ideal en otras circunstancias poder hacer el curso de manera presencial
>
> Se podría mejorar haciendo un par más de talleres prácticos, pues todas las técnicas y herramientas son muy interesantes, y estaría bien hacer más trabajos.
>
> Más horas de curso, para poder hacer alguna práctica más, y la posibilidad de hacer prácticas al mismo tiempo que el profesor para así poder adquirir las destrezas en la sesión
>
> Más horas de clase, es súper interesante. Incluso incluir más contenido.
>
> Muy bien impartido, sin embargo la distribución del horario podría disponerse de otra manera para facilitar una correcta atención por parte de los alumnos y no resulte muy pesado
>
> Me ha parecido muy interesante tanto el contenido como la disposición y variación de perfiles que nos habéis mostrado y que de esta forma como la impresión 3D se aplica múltiples campos. Desde mi punto de vista añadiría quizá un campo en el que se nos forme sobre el diseño 3D y no únicamente sobre la segmentación e impresión 3D
>
> Estoy muy satisfecho con el curso impartido y los docentes. Me ha parecido muy interesante y he aprendido mucho. Estoy convencido de que seguirá siendo de interés en los próximos años y evolucionará a mejor, si cabe.

Enhorabuena por el curso. Ha sido muy interesante y muy bien organizado. Para futuras ediciones, si no se pueden ampliar el número de horas, creo que sería maravilloso quizá resumir un poco los aspectos relacionados con las aplicaciones, para poder incorporar más talleres prácticos para aprender a segmentar situaciones patológicas, como por ejemplo tumor. Imagino que con las técnicas vistas, ya se proporcionan las herramientas para poder meternos de lleno en cualquier situación por nuestra cuenta, pero creo que el programa del curso se podría ver muy enriquecido incorporando un taller de este estilo. En cualquier caso, ha sido un curso estupendo y unas horas muy bien aprovechadas. Gracias por vuestro tiempo, y gracias también por vuestra iniciativa y paciencia :)

Posibilidad de realizar los modelos que se adaptan más a nuestra carrera

Es casi necesario realizar el curso de forma presencial para afianzar el conocimiento relativo al hardware

Como ya comenté e insisto, que en el campo de la odontología podría ser bastante interesante introducirlo como materia extra o con alguna optativa para obtener un aprendizaje más amplio y, noción del presente de cara al mundo laboral y de investigación.

Me hubiera gustado realizar cosas o centrarnos más en mi área, Odontologia pero por lo demás ha sido genial

4.3.2. Respuestas libres del alumnado sobre la organización del curso

Se recogen a continuación diversas respuestas seleccionadas al azar en relación a la organización del curso.

Más publicidad para darse a conocer; Ha sido buena; Bien organizado; Todo bien; Muy buena organización con respecto a la atención al alumnado y su propaganda de los cursos; Adecuado, curso perfectamente organizado; La verdad que Centro de Mediterráneo lo ha hecho muy bien :); Es muy oportuno que el Centro Mediterráneo ofrezca a la sociedad cursos de tan alto interés para complementar la formación de los alumnos; Muy acorde; Todo ha sido correcto; En general, bastante bien organizado, como petición se podría ampliar el curso en un mes y medio o dos, con por ej. 3h por sesión; Magnífica.

4.3.3. Respuestas libres del alumnado sobre otros temas de interés

Se recogen a continuación diversas respuestas seleccionadas al azar en relación con otros temas de interés.

Como he dicho hubiera estado también bien más largo el curso

Enfoque hacia la odontología

Ofrecer horas de presencialidad.

La verdad que me ha gustado el curso mucho y veo poco margen de mejora.

Docentes muy competentes y han explicado todo genial. Han estado muy involucrados. Muy satisfecha

Mejora en cuanto horario

Evaluar si el rendimiento de los ordenadores o portátiles es adecuado, previamente

al inicio de las actividades. Si bien, se han dado todas las facilidades para facilitar estos problemas.

Sin duda cuando el formato sea presencial el feed back del curso será mucho mayor.

Me ha parecido muy bien tal y como es. No obstante, seguro que evoluciona durante los años y, sin duda, creo que muchos alumnos repetirán en otras ediciones.

Mayor contenido específico sobre Odontología

Nada que mejorar

5. DISCUSIÓN

El curso piloto que hemos desarrollado en el contexto de un Proyecto de innovación docente de la Universidad de Granada (Diseño e impresión 3D de modelos anatómicos mediante imagen médica e inteligencia artificial para la educación médica) ha generado resultados prometedores en colaboración con el proyecto ArquiM3D-X (*Proyecto ArquiM3D-X*, n.d.). El alumnado demostró adquirir habilidades adecuadas para comprender y segmentar estructuras a partir de estudios de imagen médica, posprocesarlos e imprimirlos en 3D. Debe tenerse en cuenta que la adquisición de estas competencias no es sencilla, pues es necesario familiarizarse con distintos programas informáticos (Tinkercad, 3D Slicer, MeshMixer, Ultimaker Cura y visualizadores DICOM

como Radiant), cada uno de los cuales presenta numerosas herramientas. Como es lógico, los contenidos desarrollados y las prácticas evaluadas se adaptaron al nivel de los estudiantes, asumiendo que no partían de conocimientos previos. Además de estos conocimientos de software, se dedicaron varias clases específicas a explicar los fundamentos de imagen médica por tomografía computarizada (TC) y resonancia magnética (RM), ya que estas técnicas seccionales fueron empleadas en los ejercicios de demostración y en las tareas de los estudiantes pues son la base de la mayor parte de aplicaciones de la impresión 3D basada en imagen médica (Bartikian et al., 2019). Las elevadas calificaciones del estudiantado en las prácticas entregadas demuestran que adquirieron los conocimientos necesarios para segmentar las imágenes de TC aplicando diferentes filtros como el umbral, similar al concepto de ventana frecuentemente utilizada en TC (Wolpert, 1979), y reconocieron estructuras cuya anatomía puede considerarse moderadamente compleja (especialmente para estudiantes de Grado), como son las vértebras de la columna cervical alta (Louie et al., n.d.). En resumen, la adecuada consecución de los objetivos previstos por parte del alumnado del curso demuestra el éxito del curso en términos de adquisición de competencias.

Por otra parte, el grado de satisfacción observado en el cuestionario semiestructurado administrado de forma voluntaria al estudiantado fue muy elevado. Todos los ítems incluidos en dicho cuestionario obtuvieron calificaciones superiores a 9 puntos, siendo 10 el máximo. No obstante, debe tenerse en cuenta que dicho cuestionario no está validado formalmente, aunque concuerda con los criterios que el profesorado del curso consideró relevantes y viene utilizándose de manera rutinaria en distintos cursos realizados en el Centro Mediterráneo desde hace años, utilizándose como criterio de referencia para comparar los distintos cursos que se organizan en dicha institución vinculada a la Universidad de Granada en aras de permitir una comparación relativamente homogénea entre los diferentes cursos. Los resultados son públicos y están a disposición a cualquier usuario en la web de dicha institución[4]. En relación a

[4] URL (fecha de consulta: 07/08/2021):

las preguntas abiertas, la retroalimentación del alumnado sobre los aspectos mejorables y limitaciones del curso destacan la conveniencia de prolongar la duración del curso, la distribución de las horas lectivas (clases muy concentradas, considerando que se realizaron durante el curso académico), el interés por la aplicación de la impresión 3D al ámbito de la Odontología y la necesidad de realizar algunos seminarios de forma presencial para adquirir un conocimiento más práctico del *hardware* de impresión 3D. Es necesario hacer algunas consideraciones sobre estas áreas de potencial mejora.

En primer lugar, el interés por prolongar la duración del curso probablemente obedece a varios motivos como la complejidad del contenido y variedad de *software* empleado, pues como se ha comentado previamente, se trataron diversos aspectos que pueden resultar difíciles de aprender, especialmente para alumnos sin formación reglada en radiología e imagen médica. Debe tenerse en cuenta que los docentes ofrecieron tutorías *online* para practicar aquellas tareas en las que los alumnos encontraran problemas. También se convocó una tutoría presencial en aulas equipadas con ordenadores por si existían limitaciones de software (nótese que, para algunas tareas, los requisitos de rendimiento gráfico son relativamente altas). En este sentido, consideramos que, además de estructurar los contenidos de forma más espaciada y prolongada en el tiempo, y promover la realización de un mayor número de talleres para practicar, sería conveniente establecer un sistema de cribado para evaluar y, posiblemente, clasificar al alumnado en función de los conocimientos previos sobre los aspectos fundamentales del curso (anatomía humana, imagen médica e impresión 3D). Otra opción sería establecer itinerarios específicos en función del Grado de procedencia y/o curso académico. Esto permitiría, indudablemente, una mayor adaptación de los contenidos teórico-prácticos relevantes al perfil del alumnado, y podría ser especialmente importante para grados como Odontología, que en este caso constituyó el mayor porcentaje relativo de participantes del curso (superior al 50%).

https://cemed.ugr.es/wp-content/uploads/2021/05/21ON18-MEMORIA.pdf (téngase en cuenta que los resultados son preliminares y podrían estar sujetos a modificaciones).

En segundo lugar, la distribución de las horas lectivas fue otro aspecto reseñado por el alumnado. No parece descabellado si se considera que las clases fueron de 4 horas seguidas durante dos días a la semana en horario de tarde (de 16:00 a 20:00 horas). Téngase en cuenta que la mayor parte del alumnado llegaba al curso tras una intensa jornada de clases por la mañana, por lo que no debe extrañar que se prefiera tener clases de menor duración. No obstante, también debe considerarse que las clases fueron grabadas (con el consentimiento explícito de los estudiantes) ya que, debido al carácter no presencial del curso, el equipo docente optó por poner el material impartido a disposición del alumnado que por cualquier razón no pudiera atender síncronamente al curso de forma puntual; y, por otra parte, se decidió concentrar el curso para finalizarlo durante un mes para evitar el solapamiento del mismo con los exámenes finales del curso académico. En cualquier caso, la retroalimentación obtenida en este sentido fue bastante homogénea por parte de los alumnos, y por parte de los docentes también fue evidente el desgaste producido por jornadas tan intensas. Por lo tanto, de cara a futuras ediciones del curso, se hará un esfuerzo importante por evitar concentrar los horarios del curso en clases de 4 horas de duración. Como vías alternativas podría considerarse el formato semipresencial con clases síncronas y asíncronas o un mayor número de clases de menor duración (2 horas) entre semana.

En relación a la conveniencia de introducir prácticas y contenidos específicos para Odontología y otras áreas específicas dentro de las Ciencias Biosanitarias, deben tenerse en cuenta varias cuestiones. En primer lugar, esta limitación es lógica, no solo por el carácter piloto del curso, sino porque la mayor parte de docentes son médicos de formación. El curso se ofertó a las áreas biosanitarias afines considerando las nociones comunes en cuanto a Anatomía Humana, ya que se trata de una asignatura compartida, aunque evidentemente los contenidos específicos difieren sustancialmente en función del grado (por ejemplo, en Medicina se imparten tres asignaturas de Anatomía Humana que abarcan la totalidad del cuerpo, mientras que en Odontología se da un mayor protagonismo a las áreas anatómicas relevantes para el ejercicio práctico). Paradójicamente, el número de créditos ECTS convalidables fue

sustancialmente mayor en Odontología (3 ECTS) que en Medicina (1 ECTS), lo que puede explicarse teniendo en cuenta la escasa proporción de créditos de optatividad que se ofertan en esta última en relación a la primera (menos de un 5% del total de créditos de la carrera), lo que se traduce en una menor facilidad por parte de las comisiones académicas para otorgar créditos a cursos no incluidos en la oferta curricular del Grado. Sea como fuere, parece claro que existe un gran interés por parte del alumnado y la comisión académica del Grado en Odontología por introducir las tecnologías de impresión 3D como componente formativo del alumnado, por lo que en futuras ediciones del curso prevemos la introducción de contenidos específicos de interés particular para esta área, en particular la introducción de impresión 3D basada en resina (tecnologías SLA y similares) y anatomía radiológica del macizo facial. Nuevamente, el establecimiento de criterios de cribado o clasificación del perfil de alumnos durante la preinscripción del curso podría resultar de gran utilidad para determinar las necesidades de los estudiantes.

Por último, a juicio de los docentes del curso, la mayor limitación del curso concierne a la falta de formación en hardware de impresión 3D. Este aspecto fue determinado antes de iniciar el curso debido a las restricciones en la presencialidad impuestas por la pandemia COVID, no pudiéndose optar por formatos semipresenciales dado que las medidas de distanciamiento social eran muy restrictivas en las fechas en que se desarrolló la mayor parte del curso. No obstante, dado el elevado interés docente de mostrar al alumnado las características físicas de los equipos de impresión 3D, ya desde el inicio del curso se planteó que la última sesión del curso sería presencial siempre que la situación sociosanitaria lo permitiese (como en efecto ocurrió). Aunque evidentemente no se pudieron impartir talleres específicos sobre el *hardware* de impresión 3D, en la sesión de clausura del curso se contó con una de las impresoras del equipo docente en el aula para que los alumnos pudieran verla de primera mano en funcionamiento. Cabe reseñar que el certificado de participación en el curso permite a los estudiantes acceder y utilizar las impresoras 3D disponibles en nuestro laboratorio, por lo que en futuras ediciones resultará de especial importancia asegurar que los alumnos disponen de conocimientos suficientes del hardware, si bien siempre

existe una monitorización de los equipos de impresión 3D por parte de nuestro personal docente e investigador.

Al margen de las potenciales áreas de mejora, propias de un curso piloto, la experiencia global del curso ha sido muy gratificante para estudiantes y alumnos. El esfuerzo por parte de ambos colectivos para optimizar el aprendizaje de un campo tan emergente e innovador también queda fuera de toda duda. Los resultados de la experiencia nos animan a continuar en la tarea de introducir la impresión 3D basada en imagen médica como un componente formativo de elevado interés para la formación de nuestros estudiantes. Considerando la efervescencia de estas tecnologías en el ámbito biosanitario, ya implantadas en numerosos hospitales en el contexto de Unidades de Impresión 3D clínica (Wake, 2021) así como en la práctica de numerosas clínicas de Odontología (Kessler et al., 2020), estamos convencidos de que el alumnado contará con conocimientos de gran importancia en su futuro laboral. Confiamos en que la retroalimentación recibida y el escenario de vuelta a la presencialidad nos permita optimizar las características y contenidos de este curso en futuras ediciones.

6. CONCLUSIONES

La experiencia piloto desarrollada muestra unos resultados prometedores y pone de manifiesto la importancia de las nuevas tecnologías de impresión 3D basada en imagen médica como herramientas emergentes para la docencia de la anatomía humana. No obstante, existen algunas limitaciones que deben ser consideradas en el futuro.

7. AGRADECIMIENTOS/APOYOS

Los autores desean mostrar su agradecimiento a todos los docentes del curso “Segmentación e impresión 3D de modelos anatómicos a partir de pruebas de imagen médica: curso teórico-práctico para estudiantes biosanitarios”, especialmente a David López Cornejo por su labor de codirección. Igualmente mostramos nuestra gratitud por la ayuda prestada por los miembros del proyecto ArquiM3D-X y al Centro

Mediterráneo de la Universidad de Granada por facilitar el desarrollo del curso.

8. REFERENCIAS

Bartikian, M., Ferreira, A., Gonçalves-Ferreira, A., & Neto, L. (2019). 3D printing anatomical models of head bones. *Surgical and Radiologic Anatomy : SRA*, *41*(10), 1205–1209. https://doi.org/10.1007/S00276-018-2148-4

Biglino, G., Capelli, C., Leaver, L., Schievano, S., Taylor, A., & Wray, J. (2015). Involving patients, families and medical staff in the evaluation of 3D printing models of congenital heart disease. *Communication & Medicine*, *12*(2–3), 157–169. https://doi.org/10.1558/CAM.28455

Chytas, D., Johnson, E. O., Piagkou, M., Tsakotos, G., Babis, G. C., Nikolaou, V. S., Markatos, K., & Natsis, K. (2020). Three-dimensional printing in anatomy teaching: current evidence. In *Surgical and Radiologic Anatomy* (Vol. 42, Issue 7, pp. 835–841). Springer. https://doi.org/10.1007/s00276-020-02470-2

Czako, L., Simko, K., Thurzo, A., Galis, B., & Varga, I. (2020). The Syndrome of Elongated Styloid Process, the Eagle's Syndrome—From Anatomical, Evolutionary and Embryological Backgrounds to 3D Printing and Personalized Surgery Planning. Report of Five Cases. *Medicina*, *56*(9), 458. https://doi.org/10.3390/medicina56090458

Fleming, C., Sadaghiani, M. S., Stellon, M. A., & Javan, R. (2020). Effectiveness of Three-Dimensionally Printed Models in Anatomy Education for Medical Students and Resident Physicians: Systematic Review and Meta-Analysis. *Journal of the American College of Radiology*. https://doi.org/10.1016/j.jacr.2020.05.030

Ganguli, A., Pagan-Diaz, G., Grant, L., Cvetkovic, C., Bramlet, M., Vozenilek, J., Kesavadas, T., & Bashir, R. (2018). 3D printing for preoperative planning and surgical training: a review. *Biomedical Microdevices*, *20*(3). https://doi.org/10.1007/S10544-018-0301-9

Kessler, A., Hickel, R., & Reymus, M. (2020). 3D Printing in Dentistry-State of the Art. *Operative Dentistry*, *45*(1), 30–40. https://doi.org/10.2341/18-229-L

Láinez Ramos-Bossini, A., Rivera-Izquierdo, M., Redruello Guerrero, P., & Prados Salazar, J. (2021). Modelado e impresión 3D basada en imagen médica como herramienta docente en el grado en medicina. In G. Gómez García, M. Ramos Navas-Parejo, C. Rodríguez Jiménez, & J. de la Cruz Campos (Eds.), *Teorìa y práctica en investigación educativa: una perspectiva internacional*. Dykinson.

Louie, P. K., An, H. S., & Samartzis, D. (n.d.). *Atlas of spinal imaging : phenotypes, measurements and classification systems*.

Moore, R., Riggs, K., Kourtidou, S., Schneider, K., Szugye, N., Troja, W., D'Souza, G., Rattan, M., Bryant, R., Taylor, M., & Morales, D. (2018). Three-dimensional printing and virtual surgery for congenital heart procedural planning. *Birth Defects Research*, *110*(13), 1082–1090. https://doi.org/10.1002/BDR2.1370

Proyecto ArquiM3D-X. Último acceso: Septiembre 5, 2021, disponible en https://arquim3dx.com/

Pugliese, L., Marconi, S., Negrello, E., Mauri, V., Peri, A., Gallo, V., Auricchio, F., & Pietrabissa, A. (2018). The clinical use of 3D printing in surgery. *Updates in Surgery*, *70*(3), 381–388. https://doi.org/10.1007/S13304-018-0586-5

Sun, Z., & Liu, D. (2018). A systematic review of clinical value of three-dimensional printing in renal disease. *Quantitative Imaging in Medicine and Surgery*, *8*(3), 311–325. https://doi.org/10.21037/QIMS.2018.03.09

Tack, P., Victor, J., Gemmel, P., & Annemans, L. (2016). 3D-printing techniques in a medical setting: a systematic literature review. *Biomedical Engineering Online*, *15*(1), 115. https://doi.org/10.1186/s12938-016-0236-4

Villarreal, J. A., Yoeli, D., Masand, P. M., Galvan, N. T. N., Olutoye, O. O., & Goss, J. A. (2020). Hepatic separation of conjoined twins: Operative technique and review of three-dimensional model utilization. *Journal of Pediatric Surgery*. https://doi.org/10.1016/j.jpedsurg.2020.06.047

Wake, N. (2021). *3D Printing for the Radiologist*. Elsevier.

Wang, Y.-T., Yang, X.-J., Yan, B., Zeng, T.-H., Qiu, Y.-Y., & Chen, S.-J. (2016). Clinical application of three-dimensional printing in the personalized treatment of complex spinal disorders. *Chinese Journal of Traumatology = Zhonghua Chuang Shang Za Zhi*, *19*(1), 31–34. https://doi.org/10.1016/j.cjtee.2015.09.009

Wolpert, S. (1979). Appropriate window settings for CT anatomic measurements. *Radiology*, *132*(3), 775. https://doi.org/10.1148/132.3.775A

Apéndice 5. Meta-análisis sobre la eficacia de la radiofrecuencia en el tratamiento del síndrome facetario lumbar (trabajo aún no publicado, actualmente enviado para publicación a revista de impacto).

Efficacy of Radiofrequency in Lumbar Facet Syndrome: A Systematic Review and Meta-Analysis of Placebo-Controlled Randomized Clinical Trials

Abstract

Background: Lumbar facet syndrome (LFS) is one of the main causes of chronic low back pain (LBP) and can be treated using radiofrequency (RF) sensory denervation. The aim of this work is to analyze the efficacy of RF in LFS through a systematic review and meta-analysis of randomized clinical trials (RCTs) with placebo control.

Materials and methods: A systematic search was conducted in the Medline (PubMed), Scopus, Web of Science databases, and the Cochrane Central Register of Controlled Trials (CENTRAL). The variables of interest were pain, functional status, quality of life (QoL), and global perceived effect (GPE) measured at different time intervals: short (<3 months), medium (>3 and <12 months), and long term (>12 months).

Results: Eight RCTs with placebo control (sham procedure) were included. RF showed significant benefits over placebo in pain relief in the short, medium and long term, as well as improvement in functional disability in the short and long term. No statistically significant differences were observed in QoL or quantitative GPE, but benefits for RF were observed in dichotomous GPE. Subgroup analyses showed more benefits for RF in LBP <1 year in the short term and in RCTs that did not require performing an MRI for patient selection.

Conclusions: RF demonstrated significant improvements in LFS in terms of pain and functionality, but the benefits in terms of QoL and GPE are inconclusive. Duration of LBP and performing an MRI as inclusion criteria might influence treatment response and should be explored in further investigations.

Keywords: Lumbar facet syndrome; radiofrequency; placebo; meta-analysis; randomized controlled trial.

Key points:

1. We conducted a systematic review and meta-analysis of placebo-controlled randomized clinical trials to evaluate the efficacy of radiofrequency (RF) in lumbar facet syndrome (LFS).
2. RF provided significant pain relief and improved functionality in LFS compared to placebo. However, the evidence for benefits in quality of life and global perceived effect was inconclusive.
3. Duration of low back pain and performing an MRI prior to RF may influence therapeutic response, and should be explored in future research.

Clinical relevance statement:

This study provides evidence that radiofrequency treatment for lumbar facet syndrome can significantly reduce pain and improve functionality. The duration of low back pain and performing an MRI prior to treatment may influence therapeutic outcomes and should be further explored.

Introduction

Low back pain (LBP) is a very common health problem in the adult population, with an estimated incidence of 5% and a lifetime prevalence of 60 to 80% [1,2]. Chronic pain syndromes develop in 10 to 20% of these patients and represent a significant source of disability [2]. Among the multiple causes of chronic LBP, lumbar facet syndrome (LFS) accounts for up to 40% of cases [3]. LFS is characterized by the degeneration of the zygapophyseal or facet joints of two adjacent lumbar vertebrae, resulting from repetitive mechanical stress, inflammatory processes, or infections [4]. The facet joint is the only synovial joint in the spinal column, and its sensory innervation is provided by the medial branch of the dorsal root [5]. The pain associated with LFS can radiate to the gluteal region and the posterior aspect of the leg, is exacerbated by lumbar extension and improves with slight lumbar flexion [6]. To confirm LFS, it is often necessary to perform a diagnostic blockage test [7].

The therapeutic approach to LFS should be multimodal, including hygienic-dietary measures, physical therapies, and pharmacological interventions [8-10]. In non-responders, second-line treatments include local anesthetic and corticosteroid infiltration, and radiofrequency (RF) of the medial branch of the dorsal root [11,12], all of which are frequently performed by musculoskeletal and interventional radiologists. The latter procedure involves sensory denervation of the facet joint by applying an electrical field around a nerve, which alters the transmission of painful stimuli, either through direct nerve injury (continuous RF, CRF) or modulation of nerve impulses (pulsed RF, PRF) [13,14].

To date, various randomized clinical trials (RCTs) have been conducted comparing the efficacy of RF with placebo [15-17], intra-articular infiltration of anesthetics and corticosteroids, and different RF modalities [18-20]. However, systematic reviews and meta-analyses of these trials have shown contradictory results [21,22], which have been attributed to factors, including small sample sizes [15,23], significant differences in baseline variables, heterogeneous inclusion and exclusion criteria [21], presence or absence of prior diagnostic blocks [15,24], short follow-up periods [16,17,25], or differences in outcome measures and RF technique used [18,19,26]. Additionally, various biases in different stages of the clinical trials have been noted [9,27].

Therefore, high-quality scientific evidence is needed to update and compare the results obtained from RCTs comparing RF versus placebo. Such evidence should consider potential biases and confounding factors that may impact the analysis, shedding light on the efficacy and clinical indications of RF treatment for LFS.

The aim of this study is to conduct a systematic review and an updated meta-analysis of placebo-controlled RCTs examining the efficacy of RF in the treatment of chronic LBP caused by LFS.

Materials and methods

Eligibility criteria

The PRISMA (Preferred Reporting Items for Systematic Reviews and Meta-Analyses) guidelines [28] were followed to collect and report the results obtained. The design and selection criteria were based on the PICOS strategy: adult patients with chronic LBP due to LFS (P), treated with RF-based procedures (I) compared to placebo (C), and clinical outcomes (pain, functional status, quality of life [QoL], and perceived global effect) (O). Only RCTs were included (S).

Therefore, the inclusion criteria were: RCTs on RF versus placebo for LFS that included quantitative results for at least one of the primary outcomes, original data, and adult populations. The exclusion criteria were: locations or conditions other than LFS (e.g., cervical, thoracic, disc pathology, or sacroiliac pain), RF modalities other than PRF or CRF, quasi-experimental or observational designs without a control group, letters, editorials, or conference proceedings.

Information sources and search strategy

A systematic search was conducted in PubMed, Scopus, Web of Science, and Cochrane Central Register of Controlled Trials (CENTRAL) databases. The search included literature published up to 31st May 2023. A search equation using the MeSH terms "facet joint," "zygapophyseal joint," "low back pain," "radiofrequency," "efficacy" was used, combining them with the boolean operators AND and OR. Only human studies with abstracts written in English or Spanish were considered, without any other restrictions. Additionally, to optimize the number of relevant results, studies of potential interest from the reference lists of the selected articles were reviewed.

The literature search was conducted by the authors PMJG and AJLRB. All titles and abstracts of interest were reviewed. An article that could not be unequivocally excluded based on its title and abstract was considered potentially relevant. Then, the full text of the non-excluded articles was evaluated to determine if they met all the eligibility criteria. Discrepancies were solved by consultation to the third author (FRS).

Variables analyzed and data extraction

The treatment-related outcomes included:

-Pain relief, measured by the Visual Analog Scale (VAS) or other quantitative scales (e.g., Numeric Rating Scale, NRS).

-Improvement in functional disability measured by the Roland-Morris Disability Questionnaire (RMDQ) and the Oswestry Disability Index (ODI).

-Improvement in QoL measured by the Euro-Qol in 5 dimensions and other scales (e.g., SF-36 QoL Questionnaire, 6-item QoL scale).

-Global perceived effect (GPE) measured by the GPE scale or surrogate scores on overall subjective assessment measured as quantitative data or as data that could be grouped as dichotomous variables (e.g., pain relief <50% or >50% compared to baseline, or bad/moderate vs good/excellent overall patient satisfaction).

These variables were grouped according to the time at which they were measured as follows: short-term (<3 months), medium-term (3-12 months), and long-term (>12 months). If any RCT reported several measurements within one of those intervals, the data from the last one were selected.

The primary outcome measure was pain relief. The secondary outcome measures were improvement in functional status, QoL, and perceived global effect.

The data from the selected articles were extracted by the author. The data were stored in anonymized spreadsheets and the software Review Manager Web (RevMan Web) version 5.4.0 [29].

Risk of bias and publication bias

The Cochrane Risk of Bias Tool v. 2 was used to systematically address the presence of potential biases. For each RCT, the risk of bias was classified as low, intermediate, or high. Publication bias was analyzed through funnel plots.

Statistical analysis

For variables measured on different scales (e.g., functional status), standardized mean differences (SMDs) with a 95% confidence interval (CI) were calculated. In the case of different scales with the same range (e.g., pain), mean differences (MDs) were applied, as in Shih et al. (2020) [11]. When standard deviations (SDs) were not available for a given variable, they were calculated using the standard error (SE) through the formula $SD = SE \cdot \sqrt{N}$. For studies with sample sizes greater than 70 patients, SD was estimated from 95% confidence intervals using the formula $SD =$

$\sqrt{N} \cdot \frac{(U_L - L_L)}{3.92}$, and for studies with smaller sample sizes, SD was estimated using the formula $SD = \sqrt{N} \cdot \frac{(U_L - L_L)}{4.13}$. If SDs or 95% CIs were not available, SD values were imputed based on the median of SDs from all studies in the same group [32].

The inverse variance-weighted method with a random-effects model was applied to quantitative outcomes, and the Mantel-Haenszel method was applied for dichotomous GPE variables. The I^2 statistic was used to analyze heterogeneity among studies (non-relevant, moderate, or substantial, with cutoff values of $I^2 < 40\%$, $40\% < I^2 < 75\%$, and $I^2 > 75\%$, respectively) [33]. Sensitivity analyses were performed in cases of significant heterogeneity ($I^2 > 40\%$) by sequentially removing each study to estimate its contribution to the overall analysis. Two-tailed tests were conducted, with significance set at $p < 0.05$. Statistical analyses were performed using RevMan web [29].

Results

Baseline characteristics of patients

The RCTs included in the meta-analysis encompassed data from 472 patients, with 249 in the RF group and 223 in the placebo group. The smallest RCT included 30 patients (Gallagher et al., 1994), while the largest included 150 patients (Moussa et al., 2020). Of the eight included studies, seven compared CRF with placebo, and one (Tekin et al., 2007) compared CRF, PRF, and placebo. Therefore, data from the latter were analyzed based on the corresponding subgroups, following the example of Maas et al. (2015) [27]. **Table 1** summarizes the baseline characteristics of the participants in each study.

Pain relief

Pain relief was measured using the VAS in all studies except Van Tilburg et al. (2016), who used the 11-NRS. Statistically significant differences were found favoring RF over placebo in the short (MD -1.01; 95% CI -1.98 to -0.04; p = 0.04), medium (MD -1.42; 95% CI -2.41 to -0.43; p = 0.005), and long term (MD -1.12; 95% CI -1.57 to -0.68; p < 0.00001). Heterogeneity among the studies was high, particularly in the short and medium-term analyses (I^2 = 90% and 91%, respectively). The results of the analysis are shown in **Figure 2**.

Improvement in functional status

Statistically significant benefits of RF over placebo were observed in the short (SMD -0.94; 95% CI -1.73 to -0.14; p = 0.02) and long term (SMD -0.74; 95% CI -1.09 to -0.39; p < 0.0001). For medium term outcomes, a trend toward significance favoring RF was observed (SMD -1.43; 95% CI -3.24 to -0.37; p = 0.12). Overall, significant differences favoring RF were found (SMD -1.04; 95% CI -1.65 to -0.44; p < 0.0007). Heterogeneity was high, particularly in the short and medium term (I^2 = 87% and 90%, respectively). The results are shown in **Figure 3**.

Improvement in QoL

Only two RCTs (Nath et al., 2008; Van Kleef et al., 1999) included results on QoL, using different questionnaires. QoL was analyzed for short and medium term outcomes combined, and no statistically significant differences were observed (SMD -0.28; 95% CI -0.75 to 0.18; p = 0.23). Heterogeneity among the studies was low (I^2 = 0%). The results of the analysis are shown in **Figure 4**.

Global Perceived Effect

GPE was analyzed in six RCTs (15,16,18,19,23,25). No statistically significant differences were found in GPE measured as a continuous variable (SMD 0.04; 95% CI -0.55 to 0.63; p = 0.90). The heterogeneity among studies was moderate (I^2=64%)

Moussa et al. (2020), Van Wijk et al. (2005), and Tekin et al. (2007) measured GPE as variables that could be grouped as dichotomous. In the short term, the results showed a trend toward significance favoring RF (OR 0.55; 95% CI 0.31 to 1; p = 0.05). In the medium and long term, statistically significant differences favoring RF were observed (OR 0.22; 95% CI 0.06 to 0.78; p = 0.02). Overall, significant benefits in favor of RF over placebo were found (OR 0.38; 95% CI 0.24 to 0.6; p < 0.0001). Heterogeneity was low (I^2 = 0-3%). The results of the analysis are shown in **Figure 5**.

Risk of bias and publication bias

A high risk of bias was detected in several RCTs, specifically for performance (n = 1), detection (n = 1), attrition (n = 3), information (n = 1), and other biases (n = 6). **Figure 6** summarizes the analysis of risk of bias in the RCTs included in the meta-analysis.

Regarding publication bias, funnel plots were obtained only for pain and functional status due to the low number of studies in the other analyzed variables [35]. The funnel plots did not suggest publication bias (**Supplementary File 1**).

Subgroup analysis

Low back pain duration prior to patient inclusion

Regarding pain relief in the short term, the RCTs that established LBP duration >1 year in the inclusion criteria [15,19,23] showed no significant differences, while significant differences favoring RF were found in the group of LBP <1 year [16-18,25,34] (MD -1.16; 95% CI -2.11 to -0.20). In the medium and long term there were similar results between both groups.

For functional status, significant differences favoring RF were found in both groups in the medium and long term. Although no significant differences were observed in the short term in either group, a trend toward significance (p = 0.11) was observed in the group of LBP <1 year. **Supplementary File 2** presents the forest plots for the subgroup analyses.

MRI prior to patient inclusion

Regarding pain relief, the RCTs that included the performance of MRI as an inclusion criterion [15,19,25] showed significant differences favoring RF in the long term (MD: -1.21; 95% CI -1.40 to -1.02), but not in the short or medium term. In the RCTs where the previous performance of MRI was not established as inclusion criterion [16-18,23,34], significant differences favoring RF were found in the short term (MD -1.42; 95% CI -2.35 to -0.50), with a trend toward significance in the medium (p = 0.11) and long (p = 0.08) term.

For functional status, no significant differences were found in the group with prior MRI in the short term, but significant differences favoring RF were found in the medium (SMD: -3.12; 95% CI: -3.72 to -2.53) and long (SMD: -0.69; 95% CI: -1.14 to -0.24) term. In the other group, significant differences were observed in the short, medium and long term. **Supplementary File 3** presents the forest plots for the subgroup analysis.

Sensitivity analysis

The sensitivity analysis showed differences in pain and functional status when excluding certain studies in different time intervals. Specifically, for pain, the exclusion of the studies by Gallagher et al. (1994) in the medium term and Moussa et al. (2020) in the long term led to significant

modifications (from "favorable to RF" to "no significant differences"). In the short term, no significant variations in the overall effect size were observed.

Regarding functional status, the exclusion of Van Kleef et al. (1997) in the short term led to significant modifications (from "significant in favor of RF" to "not significant"), and a reduction in heterogeneity (I^2 from 87% to 51%). Similarly, the exclusion of Moussa et al. (2020) in the medium term led to significant modifications (from "not significant" to "favorable to RF"), associated with significant changes in heterogeneity (from 95% to 0%). No sensitivity analysis was conducted for the remaining comparisons due to the low number of studies.

Discussion

This meta-analysis included eight placebo-controlled RCTs with a total of 472 patients (249 in the experimental group and 223 in the sham group). The results indicate that RF provides significant benefits in terms of pain relief and improvement in functional disability in the short, medium, and long term compared to placebo, which is consistent with previous studies [15,19,23]. However, the benefits in terms of QoL and perceived global effect are inconclusive, mainly due to the low number of RCTs that evaluated these variables in a comparable manner, although there are cues suggesting favorable benefits in GPE, consistent with previous studies [36]. Overall, the analysis of risk of bias indicates that the quality of the studies is adequate, although there may be information biases, as reported elsewhere [27,36]. Although no clear signs of publication bias were found, its assessment is limited due to the low number of RCTs. A high heterogeneity was found among studies, with the sensitivity analysis showing a mild influence of some studies (e.g., Gallagher et al., Moussa et al).

Several systematic reviews and meta-analyses on this topic have been published. For example, a systematic review of RCTs conducted by Leggett et al. (2014) reported short-term benefits in favor of RF [37], while Manchikanti et al. (2015) found long-term pain relief benefits with level II evidence [38]. These findings contradict a Cochrane review published by Maas et al. (2015), which reported the absence of high-quality studies suggesting benefits of RF in chronic LBP [27]. More recently, Lee et al. (2017) published a meta-analysis with 7 RCTs and a total of 454 patients [39] which found benefits favoring RF compared to the control group in pain relief for up to 12 months, in line with our findings. Similarly, Chen et al. (2019) evaluated the efficacy of RF in the treatment of LFS and sacroiliac joint pain [36], and reported favorable results for RF in pain relief, functionality, and QoL. Very recently, the meta-analysis conducted by Janapala et al. (2021) concluded that there is level II evidence in favor of RF efficacy [40]. These results are consistent with our findings, which includes the largest number of placebo-controlled RCTs published to date, and focuses exclusively on traditional RF modalities (continuous and pulsed).

A noteworthy aspect of our study is the evaluation of QoL, which has only been assessed in the previous meta-analysis by Chen et al. (2019). We found no significant differences between groups, although the number of RCTs included is very low. In addition, we conducted an analysis on GPE and found significant differences in favor of RF. However, the number of studies is limited, warranting a more comprehensive and standardized approach when assessing QoL and GPE in future research.

The subgroup analysis based on the duration of LBP suggests an influence on the response to RF, being more favorable in less chronic cases. These findings could be explained by differences in structural spine changes or central sensitization phenomena [41]. The other subgroup analysis shows that patients who did not undergo an MRI before inclusion in the study reported more pain relief in the short term. This could be explained by a selection bias, as patients with different conditions that could show a more favorable response to RF might have been included, or by the influence of MRI on patients' expectations of treatment [42, 43].

This meta-analysis has several strengths and limitations. Remarkable strengths include the quantitative analysis of QoL and GPE, which have been poorly analyzed in previous studies [36], and the subgroup analyses conducted, which allowed to suggest hypotheses to consider in future research. Regarding the limitations, there is a relatively low number of RCTs which limits the

statistical power of the meta-analysis [44], high heterogeneity in study design, inclusion criteria, and outcome measures.

Conclusion

Radiofrequency treatment for lumbar facet syndrome provides significant benefits compared to placebo in terms of pain relief in the short, medium, and long term, as well as improved functionality in the short and long term. However, the evidence for benefits in quality of life and perceived global effect is inconclusive. The duration of low back pain and performing an MRI before treatment may influence therapeutic response. Future clinical trials should investigate the long-term effects of RF, its impact on quality of life, and define appropriate criteria for patient selection.

References

1. Hoy D, Brooks P, Blyth F, Buchbinder R (2010) The Epidemiology of low back pain. Best Pract Res Clin Rheumatol 24:769–781. https://doi.org/10.1016/J.BERH.2010.10.002

2. Wu A, March L, Zheng X, et al (2020) Global low back pain prevalence and years lived with disability from 1990 to 2017: estimates from the Global Burden of Disease Study 2017. Ann Transl Med 8:299–299. https://doi.org/10.21037/ATM.2020.02.175

3. Ruiz Santiago F, Láinez Ramos-Bossini AJ, Wáng YXJ, López Zúñiga D (2020) The role of radiography in the study of spinal disorders. Quant Imaging Med Surg 10:2322–2355. https://doi.org/10.21037/qims-20-1014

4. Cohen SP, Raja SN (2007) Pathogenesis, diagnosis, and treatment of lumbar zygapophysial (facet) joint pain. Anesthesiology 106:591–614. https://doi.org/10.1097/00000542-200703000-00024

5. Kaplan M, Dreyfuss P, Halbrook B, Bogduk N (1998) The ability of lumbar medial branch blocks to anesthetize the zygapophysial joint. A physiologic challenge. Spine (Phila Pa 1976) 23:1847–1852. https://doi.org/10.1097/00007632-199809010-00008

6. Hooten WM, Cohen SP (2015) Evaluation and Treatment of Low Back Pain: A Clinically Focused Review for Primary Care Specialists. Mayo Clin Proc 90:1699–1718. https://doi.org/10.1016/J.MAYOCP.2015.10.009

7. Perolat R, Kastler A, Nicot B, et al (2018) Facet joint syndrome: from diagnosis to interventional management. Insights Imaging 9:773–789. https://doi.org/10.1007/S13244-018-0638-X/FIGURES/11

8. Van Tulder MW, Koes BW, Bouter LM (1997) Conservative treatment of acute and chronic nonspecific low back pain. A systematic review of randomized controlled trials of the most common interventions. Spine (Phila Pa 1976) 22:2128–2156. https://doi.org/10.1097/00007632-199709150-00012

9. Juch JNS, Maas ET, Ostelo RWJG, et al (2017) Effect of Radiofrequency Denervation on Pain Intensity Among Patients With Chronic Low Back Pain: The Mint Randomized Clinical Trials. JAMA 318:68–81. https://doi.org/10.1001/jama.2017.7918

10. Baroncini A, Maffulli N, Eschweiler J, et al (2021) Management of facet joints osteoarthritis associated with chronic low back pain: A systematic review. Surgeon 19:e512–e518. https://doi.org/10.1016/J.SURGE.2020.12.004

11. Shih CL, Shen PC, Lu CC, et al (2020) A comparison of efficacy among different radiofrequency ablation techniques for the treatment of lumbar facet joint and sacroiliac joint pain: A systematic review and meta-analysis. Clin Neurol Neurosurg 195:. https://doi.org/10.1016/J.CLINEURO.2020.105854

12. Zhou Q, Zhou F, Wang L, Liu K (2016) An investigation on the effect of improved X-rays-guided radiofrequency thermocoagulation denervation on lumbar facet joint syndrome. Clin Neurol Neurosurg 148:115–120. https://doi.org/10.1016/J.CLINEURO.2016.07.018

13. Lee DW, Pritzlaff S, Jung MJ, et al (2021) Latest Evidence-Based Application for Radiofrequency Neurotomy (LEARN): Best Practice Guidelines from the American Society of Pain and Neuroscience (ASPN). J Pain Res 14:2807–2831. https://doi.org/10.2147/JPR.S325665

14. Contreras Lopez WO, Navarro PA, Vargas MD, et al (2019) Pulsed Radiofrequency Versus Continuous Radiofrequency for Facet Joint Low Back Pain: A Systematic Review. World Neurosurg 122:390–396. https://doi.org/10.1016/J.WNEU.2018.10.191

15. Nath S, Nath CA, Pettersson K (2008) Percutaneous lumbar zygapophysial (facet) joint neurotomy using radiofrequency current, in the management of chronic low back pain: A randomized double-blind trial. Spine (Phila Pa 1976) 33:1291–1297. https://doi.org/10.1097/BRS.0B013E31817329F0

16. van Wijk R, Geurts J, Wynne H, et al (2005) Radiofrequency denervation of lumbar facet joints; double-blind; sham lesion-controlled trial. Clin J Pain 21:335–344

17. Leclaire R, Fortin L, Lambert R, et al (2001) Radiofrequency facet joint denervation in the treatment of low back pain: A placebo-controlled clinical trial to assess efficacy. Spine (Phila Pa 1976) 26:1411–1416. https://doi.org/10.1097/00007632-200107010-00003

18. Tekin I, Mirzai H, Ok G, et al (2007) A comparison of conventional and pulsed radiofrequency denervation in the treatment of chronic facet joint pain. Clin J Pain 23:524–529. https://doi.org/10.1097/AJP.0b013e318074c99c

19. Moussa WM, Khedr W, Elsawy M (2020) Percutaneous pulsed radiofrequency treatment of dorsal root ganglion for treatment of lumbar facet syndrome. Clin Neurol Neurosurg 199:. https://doi.org/10.1016/J.CLINEURO.2020.106253

20. Ambrosio L, Vadalà G, Russo F, et al (2023) Interventional Minimally Invasive Treatments for Chronic Low Back Pain Caused by Lumbar Facet Joint Syndrome: A Systematic Review. Glob spine J 13:1163–1179. https://doi.org/10.1177/21925682221142264

21. Wardhana A, Ikawaty R, Sudono H (2022) Comparison of Radiofrequency and Corticosteroid Injection for Treatment of Lumbar Facet Joint Pain: A Meta-Analysis. Asian J Anesthesiol 60:53–60. https://doi.org/10.6859/aja.202206_60(2).0003

22. Li H, An J, Zhang J, et al (2022) Comparative efficacy of radiofrequency denervation in chronic low back pain: A systematic review and network meta-analysis. Front Surg 9:. https://doi.org/10.3389/FSURG.2022.899538

23. van Kleef M, Barendse GAM, Kessels A, Voets HM, Weber WEJ, de Lange S (1999) Randomized trial of radiofrequency lumbar facet denervation for chronic low back pain. 6

24. Civelek E, Cansever T, Kabatas S, et al (2012) Comparison of effectiveness of facet joint injection and radiofrequency denervation in chronic low back pain. Turk Neurosurg 22:200–206. https://doi.org/10.5137/1019-5149.JTN.5207-11.1

25. Van Tilburg CWJ, Schuurmans FA, Stronks DL, et al (2016) Randomized sham-controlled double-blind multicenter clinical trial to ascertain the effect of percutaneous radiofrequency treatment for sacroiliac joint pain: Three-month results

26. Nebreda C, Vallejo R, Salvador E, et al (2016) Estudio comparativo entre la radiofrecuencia térmica o convencional y la radiofrecuencia pulsada en el tratamiento del dolor de origen en la artropatía facetaria lumbar. Rev la Soc Esp del Dolor 23:170–174. https://doi.org/10.20986/RESED.2016.3417/2016

27. Maas ET, Ostelo RWJG, Niemisto L, et al (2015) Radiofrequency denervation for chronic low back pain

28. Moher D, Liberati A, Tetzlaff J, et al (2009) Preferred reporting items for systematic reviews and meta-analyses: the PRISMA statement. PLoS Med 6:. https://doi.org/10.1371/JOURNAL.PMED.1000097

29. Review Manager Web (RevMan Web). Version 5.4.0 (15 Jun 2023)

30. Higgins JPT, Li T DJ (editors) Chapter 6: Choosing effect measures and computing estimates of effect. In: Cochrane Handb. Syst. Rev. Interv. version 6.3 (updated Febr. 2022). Cochrane, 2022.

31. Walter SD, Yao X (2007) Effect sizes can be calculated for studies reporting ranges for outcome variables in systematic reviews. J Clin Epidemiol 60:849–852. https://doi.org/10.1016/j.jclinepi.2006.11.003

32. Ebrahim S, Johnston BC, Akl EA, et al (2014) Addressing continuous data measured with different instruments for participants excluded from trial analysis: A guide for systematic reviewers. J Clin Epidemiol 67:560–570. https://doi.org/10.1016/j.jclinepi.2013.11.014

33. Deeks JJ, Higgins JPT AD (editors) Chapter 10: Analysing data and undertaking meta-analyses. In: Cochrane Handb. Syst. Rev. Interv. version 6.3 (updated Febr. 2022). Cochrane, 2022. Available from www.training.cochrane.org/handbook.

34. Gallagher J, Petriccione di Vadi PL W (1994) Radiofrequency facet joint denervation in the treatment of low back pain: a prospective controlled double-blind study to assess its efficacy. Pain Clin 7:193-8:

35. Sterne JAC, Sutton AJ, Ioannidis JPA, et al (2011) Recommendations for examining and interpreting funnel plot asymmetry in meta-analyses of randomised controlled trials. BMJ 343:. https://doi.org/10.1136/BMJ.D4002

36. Chen CH, Weng PW, Wu LC, et al (2019) Radiofrequency neurotomy in chronic lumbar and sacroiliac joint pain: A meta-analysis. Medicine (Baltimore) 98:e16230. https://doi.org/10.1097/MD.0000000000016230

37. Leggett LE, Soril LJJ, Lorenzetti DL, et al (2014) Radiofrequency ablation for chronic low back pain: a systematic review of randomized controlled trials. Pain Res Manag 19:e146–e153. https://doi.org/10.1155/2014/834369

38. Manchikanti L, Kaye AD, Boswell M V, et al (2015) A systematic review and best evidence synthesis of effectiveness of therapeutic facet joint interventions in managing chronic spinal pain

39. Lee CH, Chung CK, Kim CH (2017) The efficacy of conventional radiofrequency denervation in patients with chronic low back pain originating from the facet joints: a meta-analysis of randomized controlled trials. Spine J 17:1770–1780. https://doi.org/10.1016/J.SPINEE.2017.05.006

40. Janapala RN, Manchikanti L, Sanapati MR, et al (2021) Efficacy of Radiofrequency Neurotomy in Chronic Low Back Pain: A Systematic Review and Meta-Analysis. J Pain Res 14:2859–2891. https://doi.org/10.2147/JPR.S323362

41. Sanzarello I, Merlini L, Rosa MA, et al (2016) Central sensitization in chronic low back pain: A narrative review. J Back Musculoskelet Rehabil 29:625–633. https://doi.org/10.3233/BMR-160685

42. Crown S (1978) Psychological aspects of low back pain. Rheumatol Rehabil 17:114–124. https://doi.org/10.1093/RHEUMATOLOGY/17.2.114

43. van Wijk RMAW, Geurts JWM, Lousberg R, et al (2008) Psychological predictors of substantial pain reduction after minimally invasive radiofrequency and injection treatments for chronic low back pain. Pain Med 9:212–221. https://doi.org/10.1111/J.1526-4637.2007.00367.X

44. Turner RM, Bird SM, Higgins JPT (2013) The Impact of Study Size on Meta-analyses: Examination of Underpowered Studies in Cochrane Reviews. PLoS One 8:e59202. https://doi.org/10.1371/JOURNAL.PONE.0059202

Figure and legends

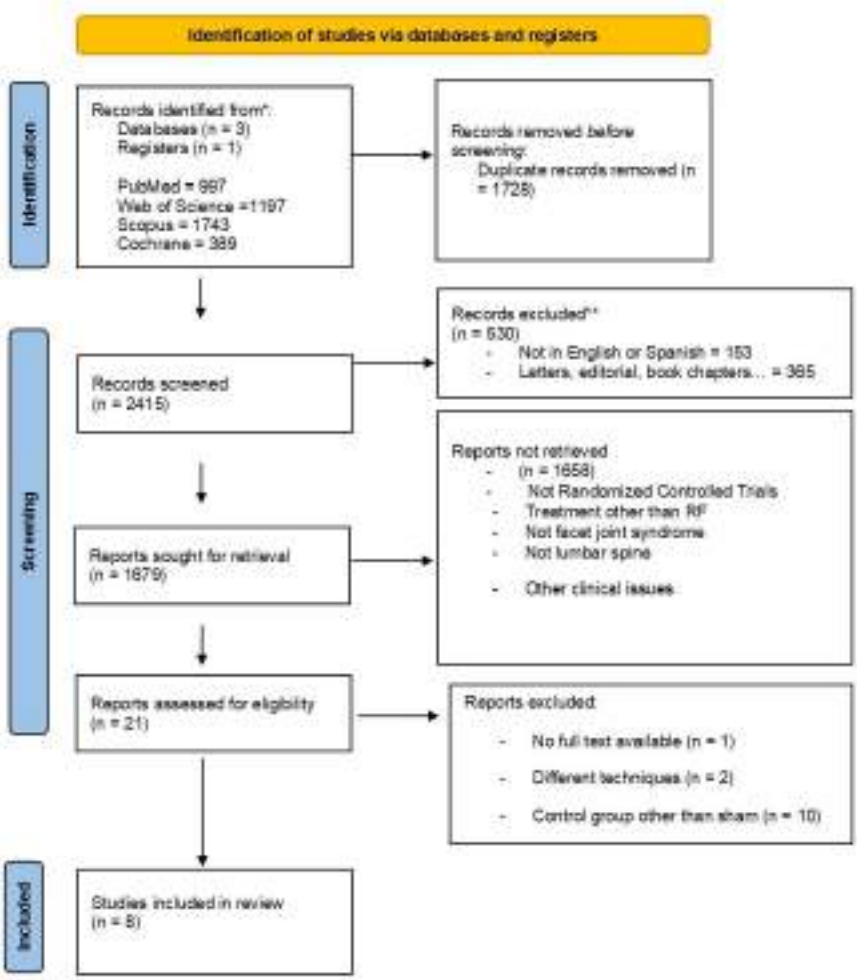

Figure 1. Flow diagram of the study.

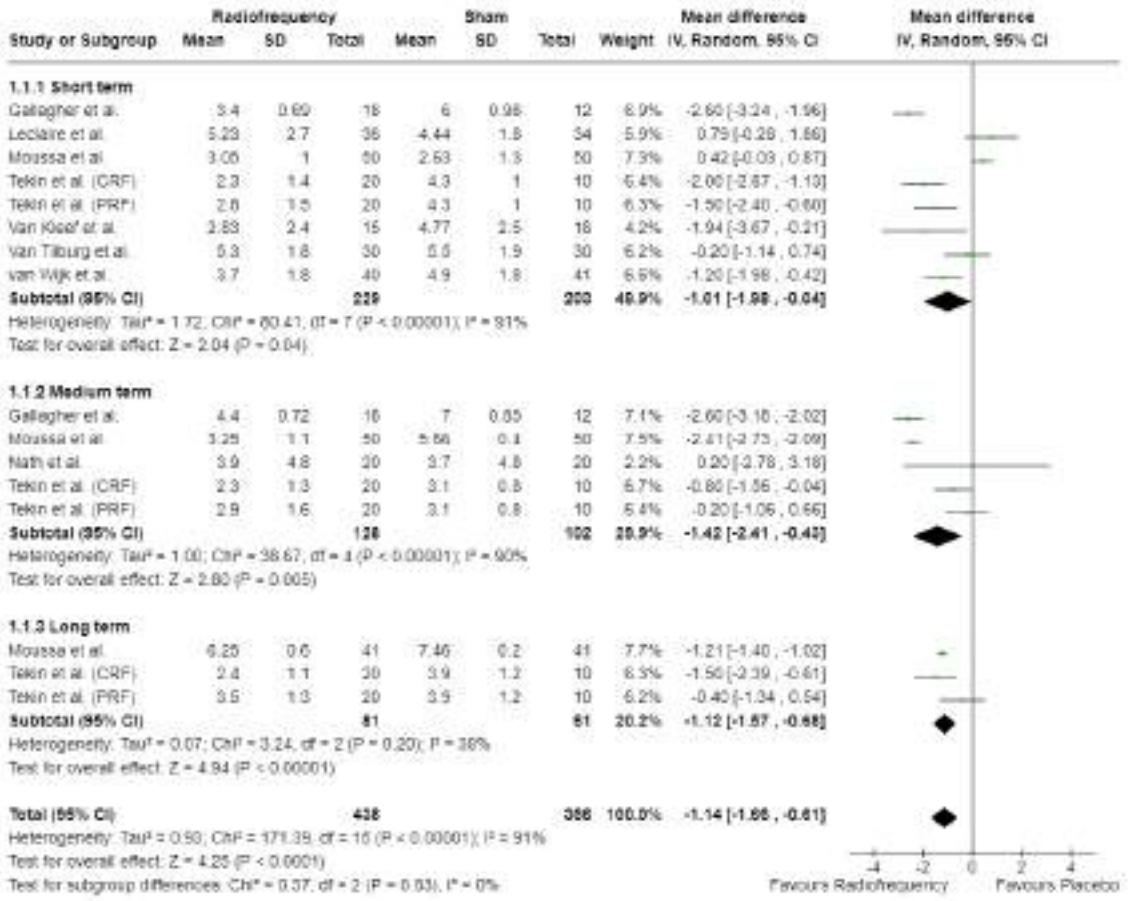

Figure 2. Forest plot comparing radiofrequency versus sham for pain relief at different time intervals after treatment or sham intervention.

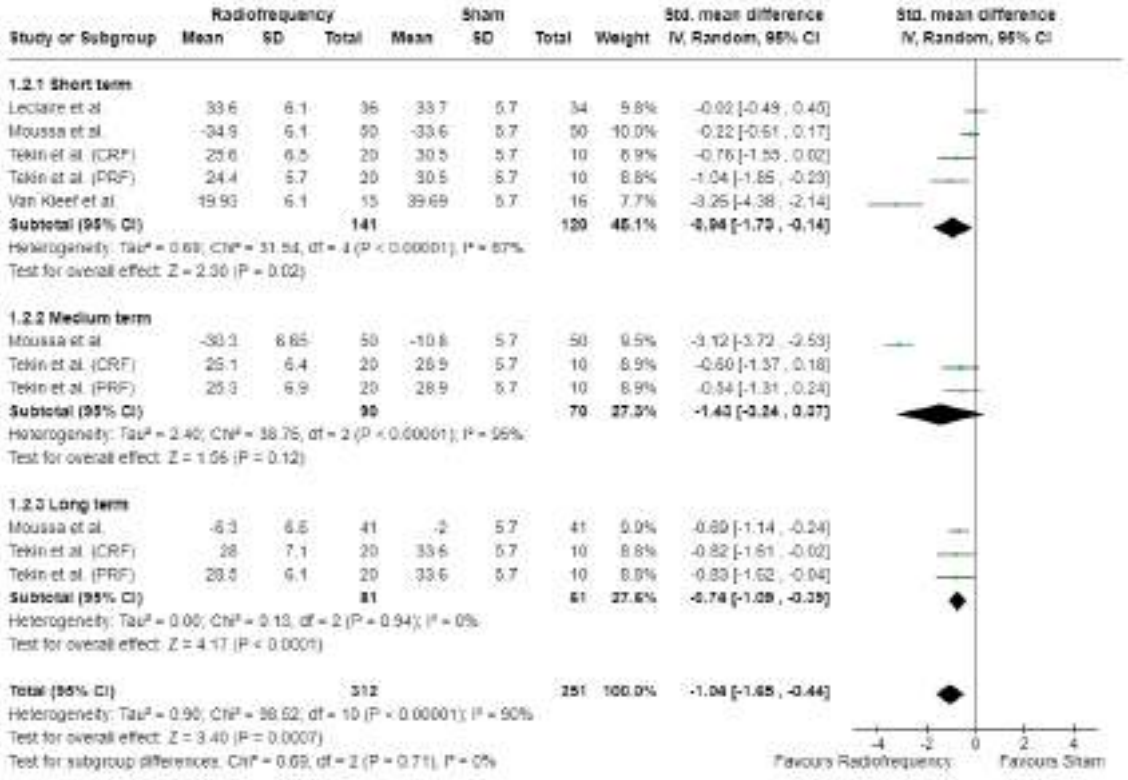

Figure 3. Forest plot comparing radiofrequency versus placebo for improvement in functional disability at different time intervals after treatment or sham intervention.

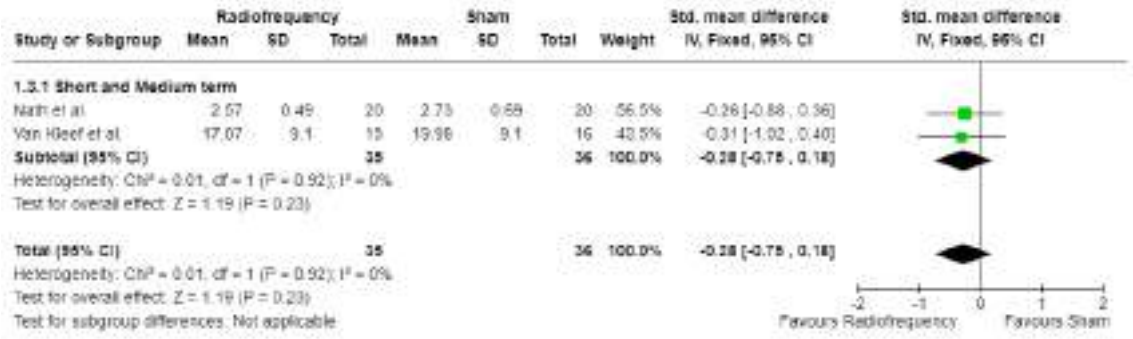

Figure 4. Forest plot comparing RF treatment with placebo for improvement in quality of life at different time intervals after treatment or sham intervention.

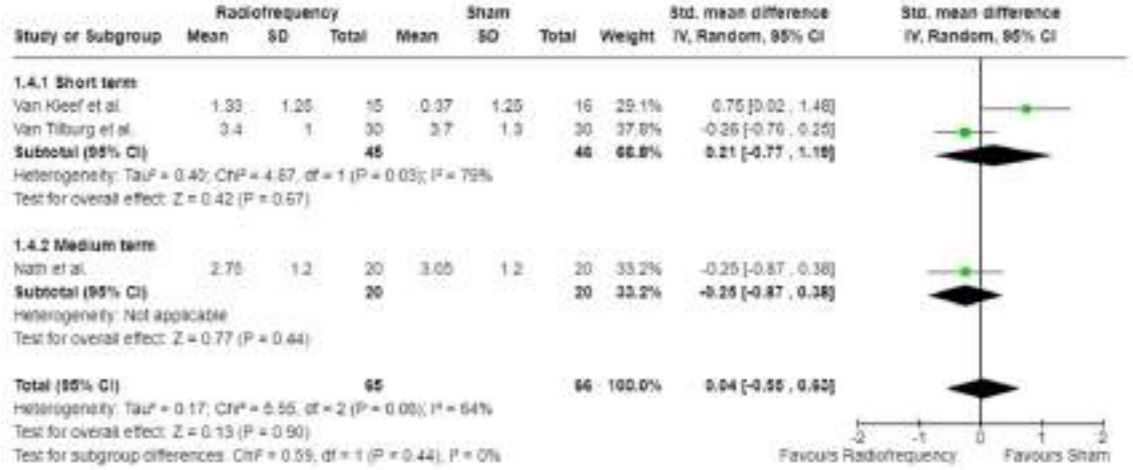

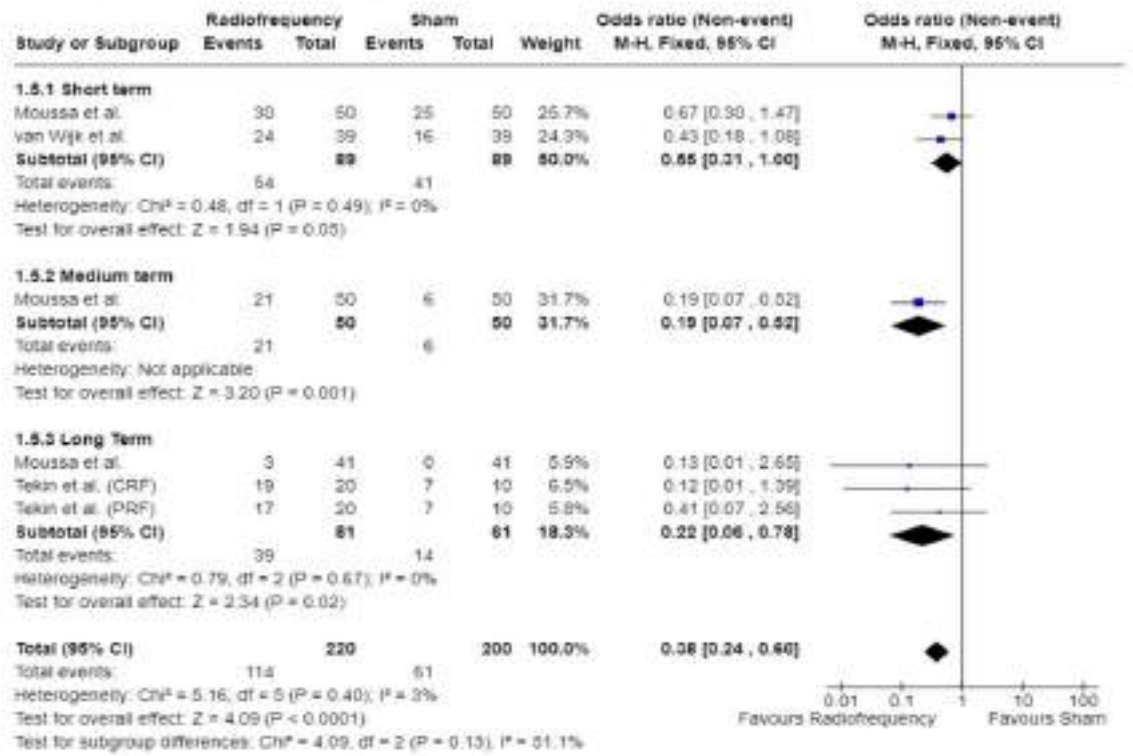

Figure 5. Forest plot comparing radiofrequency versus placebo for global perceive effect (GPE) at different time intervals after treatment or sham intervention. Top, GPE measured as a continuous variable. Bottom, GPE measured as a dichotomous variable.

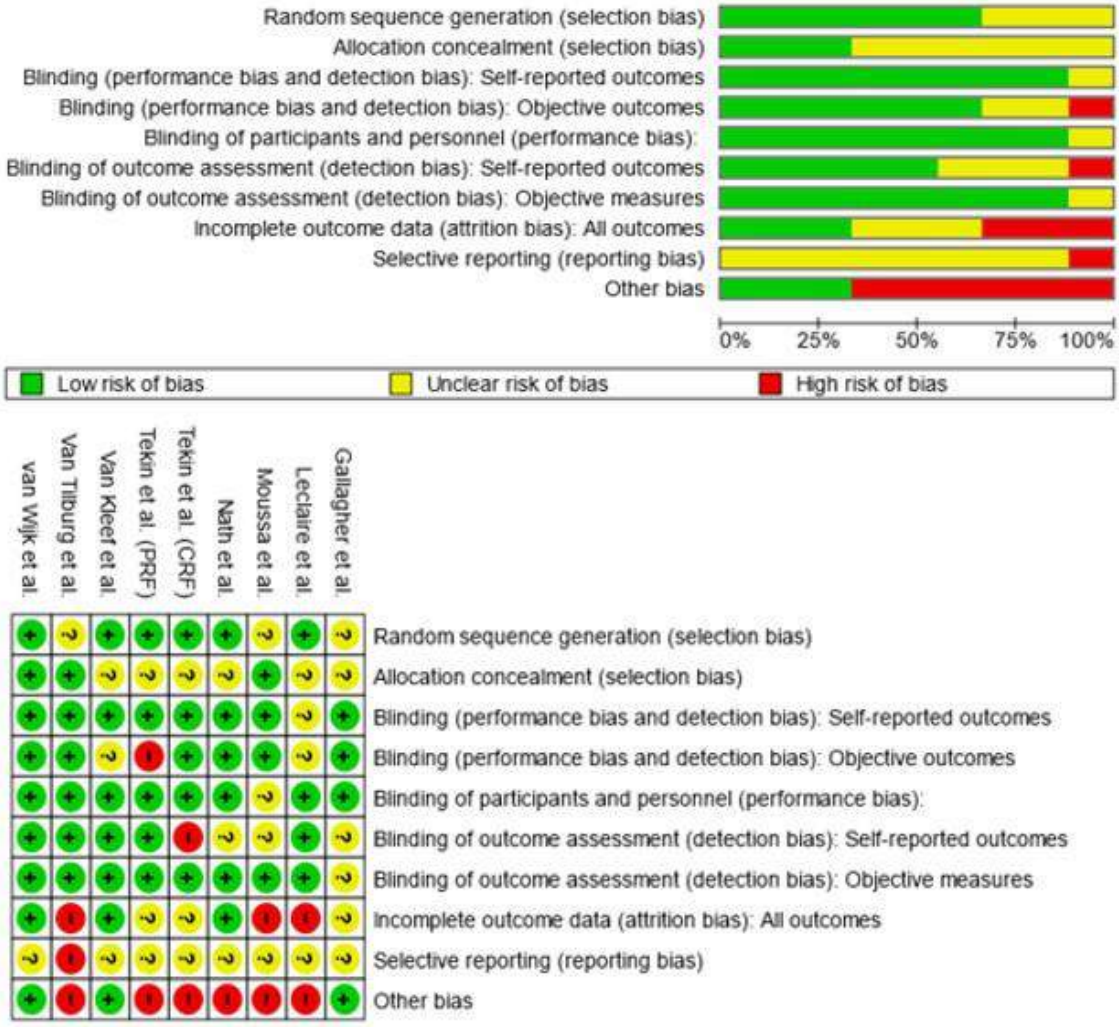

Figure 6. Risk of bias assessment for the trials included in the meta-analysis. Each evaluated item is indicated as "+" for low risk of bias, "?" for unclear risk, and "-" for high risk.

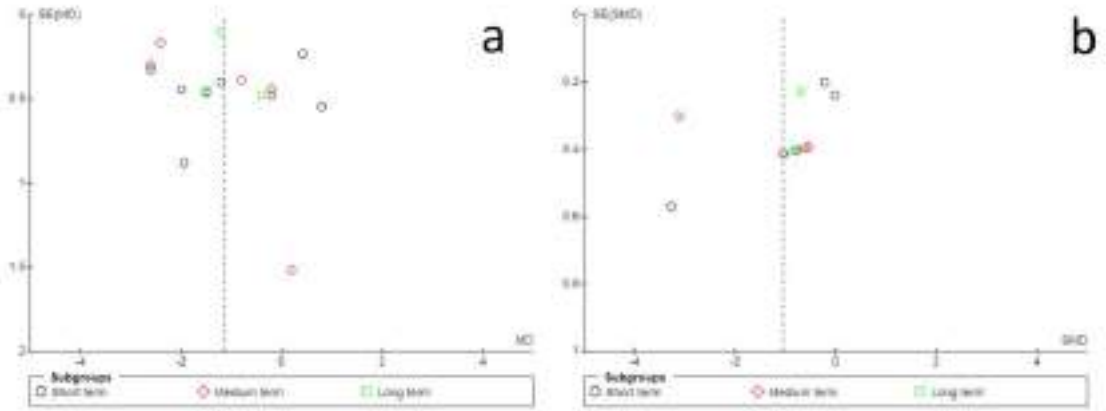

Supplementary File 1. Funnel plots of the included trials in the meta-analysis for the variables of pain (a) and functional status (b).

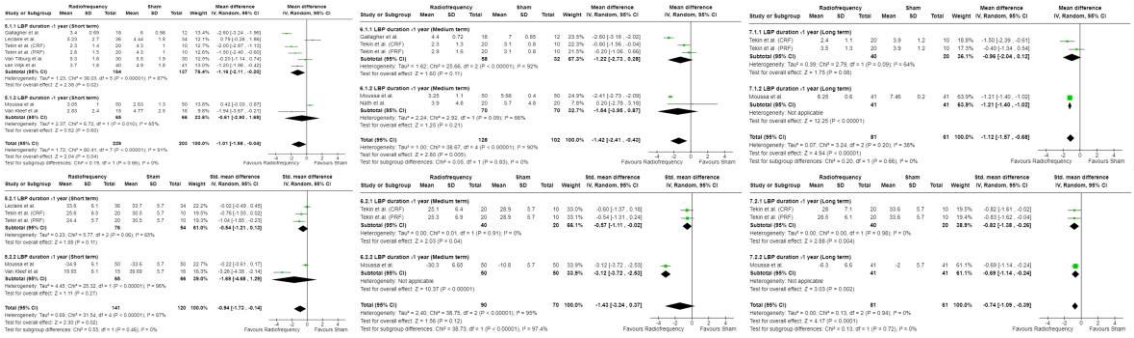

Supplementary File 2. Subgroup analysis based on the duration of low back pain as an inclusion criterion. Top row, Pain in the short (left), medium (center) and long (right) term. Bottom row, Functional status in the short (left), medium (center) and long (right) term.

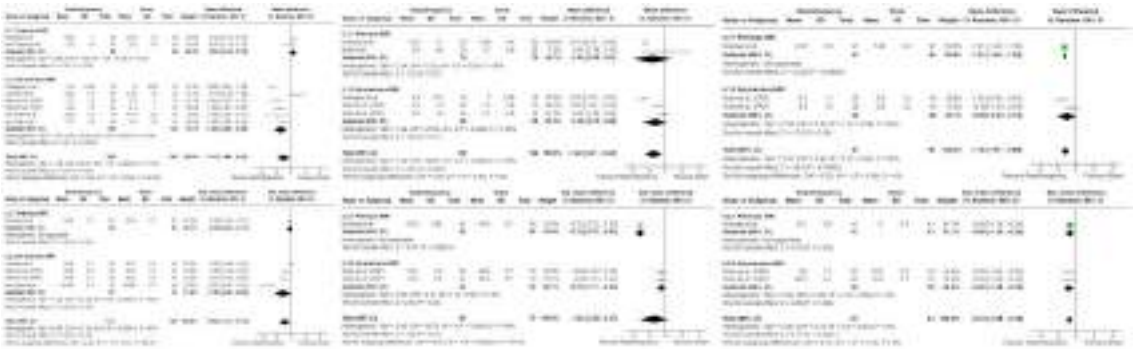

Supplementary File 3. Subgroup analysis based on having performed magnetic resonance imaging as an inclusion criterion. Top row, Pain in the short (left), medium (center) and long (right) term. Bottom row, Functional status in the short (left), medium (center) and long (right) term.

PROGRAMA DE DOCTORADO EN MEDICINA CLÍNICA Y SALUD PÚBLICA

UNIVERSIDAD DE GRANADA

2023